

Berichte

zur Polar-
und Meeresforschung

667
2013

Reports
on Polar and Marine Research



The Sea Ice Thickness in the Atlantic Sector of the
Southern Ocean

Axel Behrendt

 HELMHOLTZ
| GEMEINSCHAFT

Alfred-Wegener-Institut
Helmholtz-Zentrum für Polar-
und Meeresforschung
D-27570 BREMERHAVEN
Bundesrepublik Deutschland

ISSN 1866-3192

Hinweis

Die Berichte zur Polar- und Meeresforschung werden vom Alfred-Wegener-Institut Helmholtz-Zentrum für Polar- und Meeresforschung in Bremerhaven* in unregelmäßiger Abfolge herausgegeben.

Sie enthalten Beschreibungen und Ergebnisse der vom Institut (AWI) oder mit seiner Unterstützung durchgeführten Forschungsarbeiten in den Polargebieten und in den Meeren.

Es werden veröffentlicht:

- Expeditionsberichte
(inkl. Stationslisten und Routenkarten)
- Expeditions- und Forschungsergebnisse
(inkl. Dissertationen)
- wissenschaftliche Berichte der
Forschungsstationen des AWI
- Berichte wissenschaftlicher Tagungen

Die Beiträge geben nicht notwendigerweise die Auffassung des Instituts wieder.

Notice

The Reports on Polar and Marine Research are issued by the Alfred-Wegener-Institut Helmholtz-Zentrum für Polar- und Meeresforschung in Bremerhaven*, Federal Republic of Germany. They are published in irregular intervals.

They contain descriptions and results of investigations in polar regions and in the seas either conducted by the Institute (AWI) or with its support.

The following items are published:

- expedition reports
(incl. station lists and route maps)
- expedition and research results
(incl. Ph.D. theses)
- scientific reports of research stations
operated by the AWI
- reports on scientific meetings

The papers contained in the Reports do not necessarily reflect the opinion of the Institute.

The „Berichte zur Polar- und Meeresforschung“
continue the former „Berichte zur Polarforschung“

* Anschrift / Address

Alfred-Wegener-Institut
Helmholtz-Zentrum für Polar-
und Meeresforschung
D-27570 Bremerhaven
Germany
www.awi.de

Editor:
Dr. Horst Bornemann

Assistant editor:
Birgit Chiaventone

Die "Berichte zur Polar- und Meeresforschung" (ISSN 1866-3192) werden ab 2008 als Open-Access-Publikation herausgegeben (URL: <http://epic.awi.de>).

Since 2008 the "Reports on Polar and Marine Research" (ISSN 1866-3192) are available as open-access publications (URL: <http://epic.awi.de>)

The Sea Ice Thickness in the Atlantic Sector of the Southern Ocean

Axel Behrendt

**Please cite or link this publication using the identifier
hdi:10013/epic.41879 or <http://hdl.handle.net/10013/epic.41879>**

ISSN 1866-3192

Axel Behrendt
Alfred-Wegener-Institut
Helmoltz-Zentrum für Polar- und Meeresforschung
Bussestraße 24
D-27570 Bremerhaven

E-Mail: axel_beh@web.de

Die vorliegende Arbeit ist die inhaltlich leicht veränderte Fassung einer Dissertation, die am Alfred-Wegener-Institut in der Sektion Messende Ozeanographie des Fachbereichs Klimawissenschaften angefertigt und 2013 dem Fachbereich 1 für Physik und Elektrotechnik der Universität Bremen vorgelegt wurde.

Contents

1	Introduction and Objectives	5
1.1	The climate system	5
1.2	Sea ice as a climate component	7
1.2.1	Biological aspects	10
1.2.2	Sea ice and climate change	12
1.3	Motivation and scientific goals	14
2	Antarctic Sea Ice	19
2.1	The structure, growth and life cycle of sea ice	19
2.1.1	First-year ice	23
2.1.2	Multiyear ice	25
2.2	Formation, growth and melt of an ice cover	26
2.3	The drift of sea ice	33
2.4	The sea ice thickness distribution	35
2.5	Variability and trends of Antarctic sea ice	39
2.5.1	Variability	39
2.5.2	Trends	51
3	Measuring Sea Ice Thickness	55
3.1	Drilling	55
3.2	Ground penetrating radar	56
3.3	The ASPeCt programme	57
3.4	Airborne laser profilometry	57
3.5	Electromagnetic induction sounding	58
3.6	Satellite altimetry	60
3.7	Other satellite methods	62
3.8	Upward looking sonar	63
4	Data and Methodology	71
4.1	Data	71
4.1.1	ULS data	71
4.1.2	Satellite data	74
4.1.3	Model data	75
4.2	Methods	77
4.2.1	Detrended fluctuation analysis	77
4.2.2	Correlation analysis	78
4.2.3	Singular spectrum analysis	79
4.2.4	Multichannel singular spectrum analysis	82

4.2.5	EOF and SVD analysis	84
5	Data Processing and Data Quality	87
5.1	Data processing	87
5.2	Data quality	96
5.2.1	Accuracy	96
5.2.2	Systematic error	112
5.3	M-SSA gap filling	116
5.4	Summary	122
6	Variability of Sea Ice Draft	125
6.1	Qualitative descriptions	125
6.2	Monthly draft statistics	133
6.3	Ice season duration	144
6.4	Spectral analysis	147
6.5	Autocorrelation	158
6.5.1	Short-range correlation	158
6.5.2	Long-range correlation	161
6.6	Summary	164
7	Correlation Analysis	167
7.1	Covariation with water masses	167
7.2	Linear correlation	172
7.3	Summary	203
8	Summary and Conclusions	205
	List of Acronyms	210
	List of Symbols	212
	References	214
	List of Figures	229
	List of Tables	233
	Appendix	234
	Acknowledgements / Danksagung	244

Zusammenfassung

Antarktisches Meereis ist immernoch eine schwer zu erfassende geophysikalische Größe. Zum einen ist es nur schwer zugänglich, zum anderen lässt sich seine Dicke noch nicht verlässlich von Satelliten aus bestimmen. In dieser Arbeit wurden anhand von Sonarmessungen mittels *upward looking sonar* (ULS) Schwankungen der Meeresdicke im Weddellmeer untersucht. ULS-Geräte messen den Tiefgang des Meereises als Proxy für Meereisdicke. Zwischen beiden Größen besteht ein linearer Zusammenhang. Ein einheitlicher und umfangreicher ULS-Datensatz wurde hergestellt und hinsichtlich seiner Qualität bewertet. Die gewonnenen Zeitreihen wurden untersucht auf: Variabilität, Trends, regelmäßige Schwankungen und Autokorrelation. Eine Korrelationsanalyse brachte Aufschluss über die geophysikalischen Antriebe für Schwankungen der Meereisdicke und deren Zusammenhang mit der Klimavariabilität in der Südhemisphäre. Abhängig von der Jahreszeit, kann der Eistiefgang mit einer Genauigkeit von 5-12 cm gemessen werden. Es konnte zusätzlich gezeigt werden, dass systematische Fehler durch hohe Eiskonzentrationen mit einem einfachen Schallgeschwindigkeitsmodell vermieden werden können. Regelmäßige Schwankungen mit Perioden von unter einem Jahr und bis zu 3-4 Jahren konnten in den Zeitreihen nachgewiesen werden. Weiterhin wurde festgestellt, dass die Meereisdicke signifikante Langzeitkorrelation auf Zeitskalen von bis zu 8 Jahren aufweist. Trends des Eistiefgangs wurden in drei Regionen des Weddellmeeres gefunden: (1) Ein starker Rückgang um ca. 2 m an der Spitze der Antarktischen Halbinsel zwischen den Perioden 1991-1992 und 2005-2007. (2) Ein statistisch signifikanter Trend von -3 cm pro Jahr im nordöstlichen Weddellmeer in der Zeit 2001-2005. (3) Ein statistisch signifikanter Trend von +9 cm pro Jahr im südöstlichen Weddellmeer in den Jahren 2000-2004. Die Abnahme der Eisdicke an der Halbinsel konnte durch veränderte Driftverhältnisse erklärt werden und ist damit nicht temperaturbedingt. Dennoch ist das Eis in den letzten Jahren deutlich empfindlicher gegenüber Schwankungen der Lufttemperatur geworden. Der Trend im nordöstlichen Weddellmeer wurde mit der sinkenden Eisadvektion aus dem zentralen Weddellmeer erklärt. Für den Aufwärtstrend im südöstlichen Weddellmeer kann angenommen werden, dass er durch ansteigende Advektion von dickerem Eis und sinkende Temperaturen durch zunehmende Südwinde hervorgerufen wurde. Es wurde festgestellt, dass der gemessene Eistiefgang auf verschiedene Klimamoden - wie z.B. *El Niño Southern Oscillation* (ENSO) - reagiert, auf Grund von: (1) Advektion von dickerem oder dünnerem Eis aus anderen Regionen über die ULS-Position, (2) schwankenden Lufttemperaturen und (3) schwankender Intensität der Eisdrift und Eisdeformation.

Abstract

The remoteness of the Antarctic sea ice field and the fact that there is still no reliable way to measure its thickness from satellites renders it one of the most difficult geophysical parameters to measure. In this study, variations in sea ice thickness were examined by means of upward looking sonar (ULS) measurements in the Weddell Sea. ULS instruments measure the subsurface portion (draft) of the ice as a proxy for sea ice thickness. Both quantities are linearly related. A consistent and extensive data set of sea ice draft was produced and its quality was investigated in detail. The obtained draft time series were studied in terms of variability, trends, oscillations and autocorrelation. A correlation analysis was performed to examine the geophysical driving mechanisms for changes in sea ice thickness and their relation to climate variability in the Southern Hemisphere. It was shown that sea ice draft can be measured with an accuracy of 5-12 cm, depending on the season. Furthermore, it was demonstrated that biases introduced by high ice concentration can be avoided by applying a simple sound speed model. Different significant oscillations with sub-annual periods and periods of up to 3-4 years were found in the draft time series. It was also shown that autocorrelation of sea ice thickness extends over up to eight years. Trends in the ice draft could be observed in three regions of the Weddell Sea: (1) A strong decline of about 2 m at the tip of the Antarctic Peninsula between the periods 1991-1992 and 2005-2007. (2) A statistically significant trend of -3 cm per year in the northeastern Weddell Sea during 2001-2005. (3) A statistically significant trend of +9 cm per year in the southeastern Weddell Sea during 2000-2004. The decrease in ice thickness in the peninsula region was found to be due to changing patterns of ice advection and is therefore not the result of temperature changes. The ice thickness, however, has become more sensitive to surface air temperature in the recent years. The trend in the northeastern Weddell Sea was explained by reduced ice advection from the central Weddell Sea. The upward trend in the southeastern Weddell Sea can be assumed to be the result of increasing advection of thicker ice from further south in combination with falling air temperatures due to increasing southerly winds. It was found that the measured sea ice draft responds to different large-scale climate modes and processes - such as *El Niño Southern Oscillation* (ENSO) - due to: (1) advection of thinner or thicker ice from other regions over the ULS position, (2) varying surface air temperatures and (3) changing drift speed and ice deformation.

"We must explore our domain, it is a fine heritage and worth exploring..."

Lincoln Ellsworth, 1934

1

Introduction and Objectives

To put the presented work into a broader perspective, this chapter gives an overview of the Earth's climate system. This also allows for a better understanding of the importance of sea ice for the global climate. The first section outlines the sources of climate variability and the problem of global warming. In the following section, the role of sea ice in the climate system is described. The scientific goal of this dissertation is described in the third section.

1.1 The climate system

The Earth's climate system is complex. A wide range of internal processes, interactions, variable boundary conditions and external influences create a variable climate which has changed throughout the history of planet Earth. Climate varies from place to place, depending on latitude and the presence of water, vegetation, geographical factors and even human settlements [Baede *et al.*, 2001]. Climate also varies on different time scales: over seasons, decades and longer periods, such as ice ages.

In common parlance the term "weather" refers to the fluctuating state of the atmosphere characterised by the temperature, wind, precipitation, clouds and other weather elements [Baede *et al.*, 2001]. Weather systems emerge and decay rapidly and have only limited predictability. "Climate" means the average weather in terms of the temporal and spatial mean and its variability [Baede *et al.*, 2001]. The notion "climate system" refers to the interacting network of (1) the atmosphere, (2) the hydrosphere, (3) the lithosphere, (4) the pedosphere, (5) the biosphere and (6) the cryosphere. Forced by various mechanisms, the dynamic interplay of these components is responsible for natural variations of the climate.

The radiation balance:

The main driver of the climate system is short wavelength solar radiation (mainly visible light and ultraviolet) with longer wavelength radiation (mainly infrared) being emitted by the Earth back to space [Bigg, 2003]. To maintain thermal equilibrium, the Earth should radiate at an effective emission temperature of -18°C with typical wavelengths in the infrared part of the electromagnetic spectrum [Lemke and Olbers, 2007]. However, the observed average surface temperature on Earth is about 15°C . The difference of 33°C can be attributed to the natural greenhouse effect. Greenhouse gases, such as carbon dioxide (CO_2), methane (CH_4), nitrous oxide (N_2O) or ozone (O_3), trap heat inside the climate system by absorbing the Earth's infrared radiation and partly re-emitting it back to the surface [Trenberth et al., 2009; Pierrehumbert, 2011]. In this way the natural greenhouse effect influences the radiation balance of the Earth. Additionally to the greenhouse effect, two more processes alter the Earth's radiation balance: Changes in the incoming solar radiation and changes in the fraction of solar radiation that is reflected back to space (albedo).

Climate variability:

The Earth's climate is influenced by (a) changes in external forcings and (b) internal variability.

(a) External forcings include natural phenomena and human-induced variations. Examples are: Changes in the solar radiation (e.g. by changes in the Earth's orbit or in the Sun itself), volcanic activity or the anthropogenic greenhouse effect.

Ice ages, that occur in regular cycles for the last nearly three million years, are linked to periodic variations in the Earth's orbit around the Sun. These *Milanković-Cycles* alter the amount of solar insolation on Earth [Herterich, 2002]. The resulting changes inside the climate system are amplified or weakened by internal feedback mechanisms, which are yet to be fully understood [Lisiecki, 2010]. Volcanoes can inject large amounts of aerosols into the atmosphere, which results in a measurable decline of the global temperatures, e.g. after the *Mount Pinatubo* eruption in 1991 [Graf, 2002]. The anthropogenic greenhouse effect is a result of human-induced changes in the composition of the atmosphere, mainly due to burning of fossil carbon which was removed from the climate system millions of years ago [Dukes, 2003].

(b) The components of the climate system are linked by fluxes of mass, heat and momentum and are therefore open and interrelated [Baede et al., 2001]. The physical, chemical and biological interactions are versatile and occur on a wide range of space and time scales. This means that the components of the climate system are never in equilibrium, and variability is intrinsic to climate itself [Baede et al., 2001]. A prominent example of an internal climate variation is the *El Niño* Southern Oscillation (ENSO) in the tropical Pacific.

Another example is the large-scale ocean circulation, whose variations affect the amount of transported heat and water masses. During ice ages the circulation was subject to large, abrupt fluctuations (*Heinrich- and Dansgaard-Oeschger events*) which had considerable climatic impacts in both hemispheres [Rahmstorf, 2002; Clark et al., 2002].

The response of the climate system to internal and external factors is further complicated by different kinds of feedbacks and non-linear interactions between the components of the climate system [Baede et al., 2001; Hense, 2002].

The contemporary global climate change:

As demonstrated by increasing global average air and ocean temperatures [Hansen et al., 2010], melting of Arctic sea ice and rising global average sea levels, warming of the climate system is

beyond argument. Northern Hemisphere temperatures are already moving outside the patterns of natural climate variability [Rybski *et al.*, 2006].

During the period 1906-2005 global average surface temperatures have increased by 0.74°C [Bernstein *et al.*, 2007] (Fig. 1.1). Over the period 1985-2009 the temperatures have increased by 0.19°C per decade [Allison *et al.*, 2009] and all top ten warmest years ever measured occurred after 1998. The warmest global surface ocean temperatures ever measured occurred in July 2009¹ and the heat content in the upper ocean shows a robust warming trend [Lyman *et al.*,

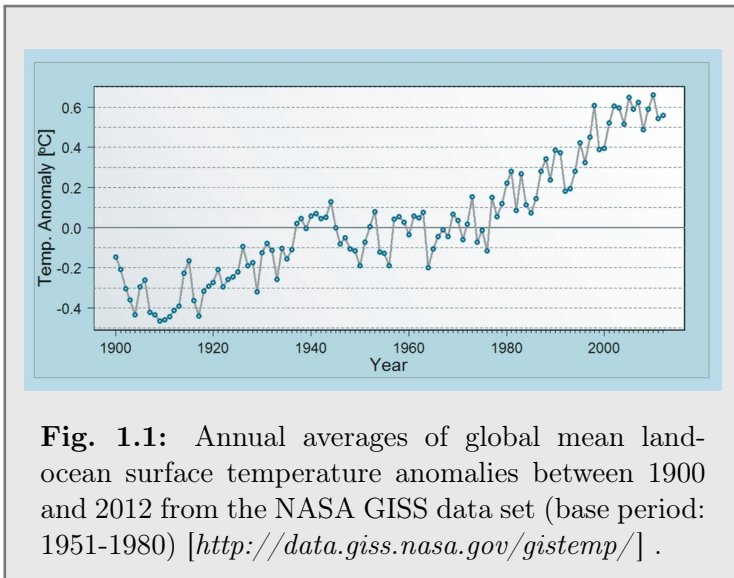


Fig. 1.1: Annual averages of global mean land-ocean surface temperature anomalies between 1900 and 2012 from the NASA GISS data set (base period: 1951-1980) [<http://data.giss.nasa.gov/gistemp/>].

2010]. In the recent years, science has made great strides in determining the potential causes that are responsible for the observed climate change during the twentieth century. Today, a large body of research provides strong evidence that greenhouse gases released to the atmosphere by human activities are the main cause of contemporary global warming. In 2009, the global carbon emissions from fossil fuel combustion and cement production were 8.4 ± 0.5 Gt [Friedlingstein *et al.*, 2010]. This corresponds to 30.8 billion tons of CO_2 . In 2008, the CO_2 emissions from fossil fuel combustion, cement production and gas flaring were

41% above the emissions in 1990 [Le Quéré *et al.*, 2009] and in 2011 54% above [Peters *et al.*, 2012]. But also other greenhouse gases, like CH_4 , N_2O and halocarbons, have anthropogenic sources and increased significantly since the beginning of the industrial era. The effect of increasing emissions combines with the changing patterns of land-use, such as deforestation. This further enhances the greenhouse effect by reducing the natural sinks for carbon dioxide and by increasing the carbon emission from the land, e.g. through increased biomass decay and biomass burning [Karl and Trenberth, 2003; IPCC, 2007; Endlicher and Gerstengarbe, 2007; Lemke and Olbers, 2007].

1.2 Sea ice as a climate component

Presently, ice covers 11% of the land surface and up to 8% of the oceans [Lemke and Olbers, 2007]. The high albedo of ice and snow is relevant to the radiation budget in the atmosphere and thus the global temperatures. Ice and snow reflect most of the solar radiation back to space, while open sea and bare ground absorb most of the solar radiation as heat. Polar regions absorb less solar radiation, due to their high albedo and the spherical shape of the Earth. The resulting temperature differences induce winds and ocean currents, that transport heat from tropical to polar latitudes [Lemke and Olbers, 2007]. In this way the ice and snow covered surfaces in high latitude regions contribute an important cooling function for the whole planet [Prestrud, 2007]. Induced by a warming climate, a shrinking ice cover can lead to a higher absorption of solar radiation, which in turn accelerates the melting (*ice-albedo feedback*). Polar

¹Based on the NOAA data set: <https://www.ncdc.noaa.gov/cmb-faq/anomalies.php>.

regions are therefore particularly sensitive to global warming [Anisimov *et al.*, 2007]. Sea ice can be thought of as a thin layer of frozen ocean surface. It forms and melts with the seasons and affects its physical and biological environment, the global climate and even human activity. While the open ocean reflects 5-6% of the sunlight [Bigg, 2003], sea ice reflects up to 90% and thus hinders the transfer of energy into the upper ocean. Furthermore, sea ice is one of the most expansive geophysical parameters: On an annual average it covers approximately 23×10^6 km², about 6.5% of the ocean surface [Lemke and Olbers, 2007]. Therefore it significantly contributes to the average albedo of the Earth and affects the radiation balance of the whole planet.

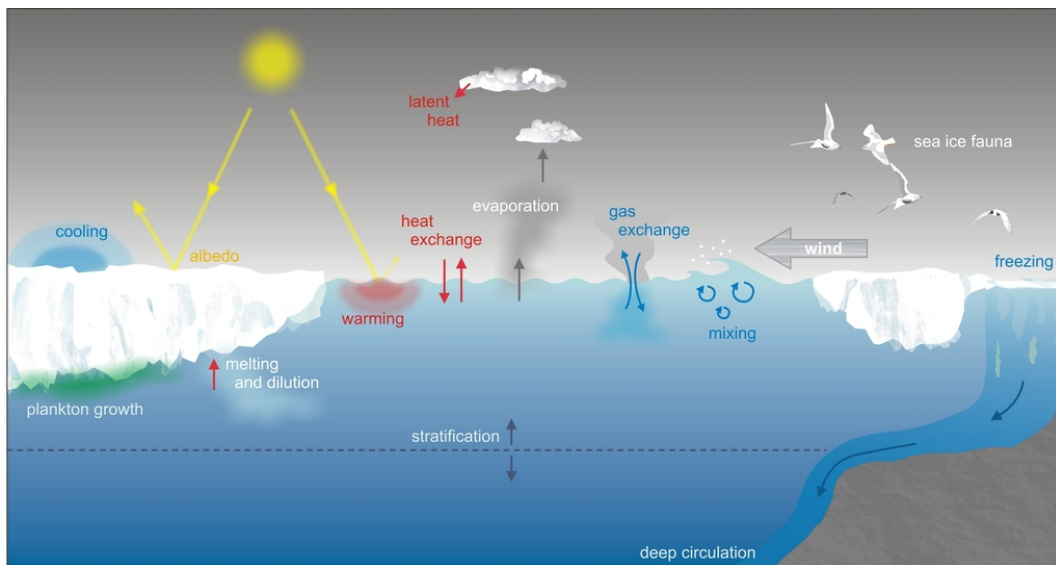


Fig. 1.2: Physical, chemical and biological processes that are influenced or inhibited by the presence of sea ice.

Sea ice acts as a blanket on the ocean surface which insulates the atmosphere from fluxes of oceanic heat and moisture (Fig. 1.2). In this way it affects weather processes like cloud formation and cools the air above the ice. Studies in the Antarctic found that the influence of the sea ice cover on the surface air temperatures is strongest in summer [Yuan and Li, 2008]. The cooling in summer is supported by the high albedo, which prevents the heating of the sea ice and, consequently, the atmosphere. In winter, when solar radiation is absent, the sea ice cover extracts heat from the air blown across the surface and emits long-wave radiation [Diekmann and Hellmer, 2010]. Therefore, sea ice has a profound influence on the regional climate and the polar physical environment [Scott and Simmon, 2009]. But also the mid-latitudes could be affected by the polar sea ice cover. A reduced sea ice extent could alter the meridional temperature gradient and in turn weaken the westerly winds in mid-latitudes. Such effects are hard to detect, but have been confirmed by circulation models [Lemke, 1994; Lemke and Olbers, 2007].

A sea ice cover also prevents dissolved gases and particles from entering the atmosphere. Algae and other microorganisms produce volatile organic compounds which contribute in different ways to the composition of the marine atmosphere. A prominent example is the sulfur compound Dimethylsulfide² (DMS; (CH₃)₂S), which provides about 50% of the global biogenic

²DMS is responsible for the typical odour of the ocean, which can also be smelled near lakes or at the shores of rivers.

sulfur input to the atmosphere. The oxidation of DMS in the atmosphere is a major source for cloud condensation nuclei. Sea ice mitigates the air-sea exchange of DMS, but itself contains high amounts of it, which are released during ice melt [Kiene *et al.*, 2007, and references therein]. Another example: Paleoclimatic investigations suggest that the large-scale retreat of southern sea ice during the last deglaciation (17.000 yrs BP - 10.000 yrs BP) allowed the winds to drive more effectively the exchange between surface and deep waters in the Southern Ocean [Skinner *et al.*, 2010]. In this way the shrinking of the sea ice cover enhanced the release of CO₂ from the deep ocean to the atmosphere.

The sea ice cover also insulates the ocean against the atmosphere. Acting as a lid on the ocean surface, it reduces the uptake of atmospheric heat and gases into the water. In open water, breaking surface waves are an important pathway for atmospheric gases to enter the ocean. In regions where strong winds mix the surface waters, enhanced levels of dissolved oxygen and other gases can be observed. Once a sea ice cover has formed, it creates a barrier for atmospheric gases and shields the ocean from wind stress, which reduces turbulent mixing processes in the surface layer. Since the beginning of the industrial era, the oceans absorbed almost half of the anthropogenic CO₂ [World Ocean Review, 2010]. However, the deep waters produced close to the Antarctic continent (see below) contain only little concentrations of anthropogenic CO₂, which can be partly attributed to the presence of sea ice that hampers the oceanic CO₂-uptake [Sabine *et al.*, 2004; Hauck *et al.*, 2010].

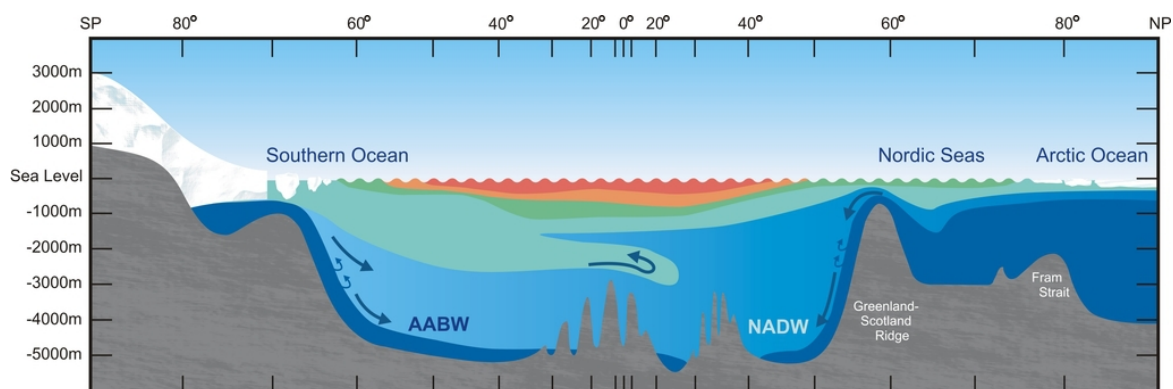


Fig. 1.3: Cross-section through the Atlantic Ocean, with the South Pole (SP) in the far left and the North Pole (NP) in the far right. The cold and dense water formed through freezing of sea ice and ocean cooling in higher latitudes is visualised as dark blue layer along the bottom [modified from: <http://www.bccr.no/biac>].

Today, many polar field experiments are designed to quantitatively determine the transfer of heat, mass and momentum between ocean and atmosphere [Diekmann and Hellmer, 2010]. The obtained values are used to parameterise modern sea ice models, which are coupled to circulation models for climate projections and future greenhouse scenarios.

The most striking feature of sea ice is its contribution to the formation of deep and bottom waters. In most parts of the world's ocean warmer water masses lie above colder ones. But a few regions in the polar oceans are characterised by weak thermal stratification. In winter, they are exposed to intense buoyancy loss through cooling and formation of sea ice, and subsequent deep-reaching convection mixes the surface waters to great depth [Marshall and Schott, 1999]. When ocean water freezes, the ions of the salts cannot enter the crystal structure of the ice and are expelled into the surrounding water. This makes the water more saline and, consequently, denser, causing the water to sink into deeper layers or to the bottom. Antarctic Bottom Water

(AABW) and North Atlantic Deep Water (NADW) are the largest deep water masses produced in the polar oceans (Fig. 1.3) and spread throughout the world's ocean basins. Not only they ventilate the deep ocean with oxygen, but they also transport other natural and anthropogenic substances from the ocean surface to the abyss where they can be stored for centuries [*Diekmann and Hellmer, 2010*].

The thermohaline ocean circulation (THC), or more commonly the *great ocean conveyor*, is driven by fluxes of heat and fresh water across the sea surface and subsequent interior mixing of heat and salt [*Rahmstorf, 2006*]³. As the polar deep waters determine the exchange of heat and salt between the surface layer and the interior ocean, they represent an important driving mechanism of the THC. Freezing and melting of sea ice therefore plays a significant role in global ocean circulation. The THC contributes to the mild European climate through its oceanic poleward heat transport in the Atlantic, peaking at about 1.2 PW (1.2×10^{15} W) at 24°N [*Clark et al., 2002*].

When sea ice melts, it leads to a freshening of the surface water layer, thereby stabilising the stratification. The formation and decay of sea ice from a mixed water mass is thus an efficient distillation process, that contributes to the formation of fresh water lying above more saline and denser water [*Notz, 2005*]. Sea ice - when moved away from its region of origin by winds and currents - can transport fresh water over large distances.

Thickness and extent of sea ice are controlled by thermodynamic and dynamic processes, which can change within hours, over days, from one season to another or even over decades. As the thin surface layer of the ocean must lose heat to form sea ice, thermal factors exert the main influence on the extent of the ice cover [*Doronin and Kheisin, 1977*]. Apart from wind, variations in the atmospheric temperatures and the oceanic heat flux are therefore mainly responsible for north and southward shifts of the sea ice boundary. Sediment-based reconstructions of the sea ice extent in Fram Strait (Arctic Ocean) showed, that the ice boundary has varied in concert with climate variability and circulation changes in the North Atlantic Ocean over the past 30.000 years [*Müller et al., 2009; Nørgaard-Pedersen, 2009*].

Also the thickness of sea ice is crucially determined by thermal factors. For example, in the central Arctic Ocean even the summer temperatures are not high enough to completely melt the ice cover. This multiyear ice can reach thicknesses of several metres.

Although the general positions of the polar sea ice covers are not greatly altered by ocean currents and wind, the ice mass within the cover is in constant motion. Changing directions of wind and currents can cause ice floes to converge and form pressure ridges, which increase the ice thickness. But also large open areas within the ice pack⁴, like the so-called *polynyas*, can be created, when ice within a region is continually removed by winds and currents. In polynyas the ocean loses up to 50 times more heat to the atmosphere than is taken up due to solar radiation through an equally sized area in equatorial latitudes [*Olbers, 2002*].

1.2.1 Biological aspects

Sea ice is important for the polar ecosystems because many warmblooded animals like seals, foxes, polar bears, penguins and other birds depend on sea ice as a platform for feeding, resting or reproduction. Analyses of seabird communities in the South Pacific found the most distinctive of all communities to be the one comprising that associated with the Antarctic sea ice,

³See also *Broecker [1991]* and *Kuhlbrodt et al. [2007]*.

⁴The term *pack ice* refers to free drifting sea ice, in contrast to *landfast ice* (or "fast ice") which remains connected to the coast or ice shelves.

whereas the composition of lower-latitude communities were less defined and included much overlap [Tynan *et al.*, 2010]. During winter, most bird species in open water communities are forced to migrate northwards because of the ice cover and the lack of sunlight, which reduces food availability for them. The sea ice community on the contrary remains robust year-round and its ice-adapted species, like the *snow petrel* (Fig. 1.4a), reach their heaviest body masses in winter [Tynan *et al.*, 2010].

Large baleen whales forage near the ice edge in both the Arctic and Antarctic. The sea ice habitat acts as a particularly important nursery for krill larvae [Cotté and Guinet, 2007] that feed on ice algae during winter and spring. As these zooplankton concentrations become available with the disappearing of sea ice in spring, the whales tend to follow the seasonal retreat of the ice edge. Other whale species, like the *minke* in the Antarctic and the *bowhead*, *beluga* and *narwhal* in the Arctic, occur regularly within the sea ice zone. These species are able of

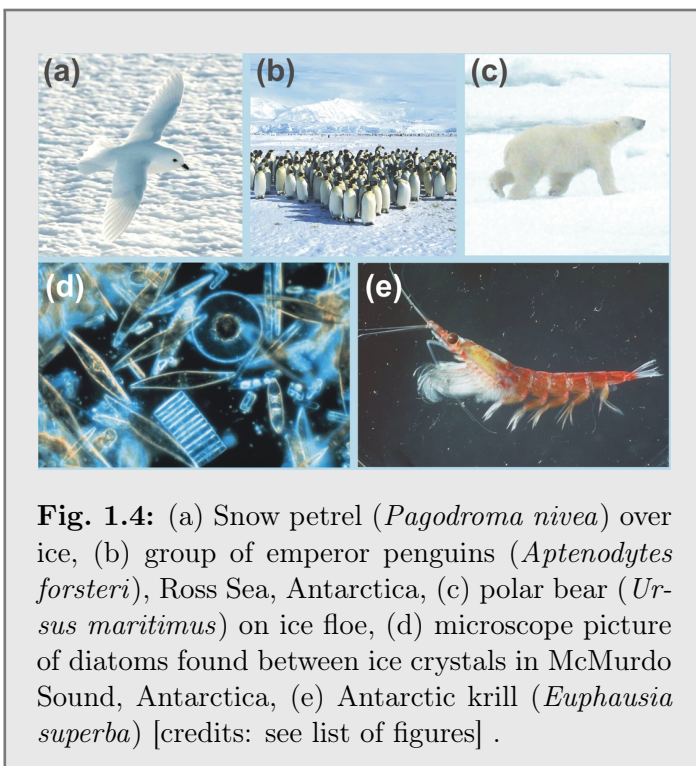


Fig. 1.4: (a) Snow petrel (*Pagodroma nivea*) over ice, (b) group of emperor penguins (*Aptenodytes forsteri*), Ross Sea, Antarctica, (c) polar bear (*Ursus maritimus*) on ice floe, (d) microscope picture of diatoms found between ice crystals in McMurdo Sound, Antarctica, (e) Antarctic krill (*Euphausia superba*) [credits: see list of figures] .

breaking new ice with their backs [Tynan *et al.*, 2010] and are highly dependent on zooplankton and fish associated with sea ice. Changes in the extent and thickness of the ice might affect the migratory patterns, the foraging success and thus the population structures of whales. The *ringed seal* in the Arctic and the *Weddell seal* in the Antarctic prefer coastal landfast ice for overwintering and reproduction [Tynan *et al.*, 2010]. They mainly depend on the ice as a refuge from marine predators and for weaning their pups. Many seal species hunt for fish in the sea ice zone or feed on krill associated with the ice. Some of them rely on drift ice in shallow regions where they hunt for benthic prey. In the Arctic *polar bears* are confined to the seasonally ice-covered areas where they search for seals, walrus or belu-

gas. "*Polar bears represent a highly specialised species in that they evolved into existence only because of the presence of an unexploited niche for a surface predator on sea ice*" [Tynan *et al.*, 2010]. The access to its prey species can be crucially affected by the sea ice conditions.

Antarctica and the subantarctic waters south of 50°S are habitat for more than ten penguin species. Five of them nest on the Antarctic continent. The *emperor penguin* and the *Adélie penguin* assemble in large colonies of up to 10.000 birds and strongly associate with sea ice. For example, the emperor penguin requires stable ice floes for moulting and landfast ice for breeding.

Less conspicuous but highly diverse and abundant are the microbiota living on or within the ice. Melt ponds on the ice surface are typically inhabited by different microorganisms, such as bacteria, ice algae, *flagellates* and *ciliates* [Spindler, 1994]. The abundance of the different species is determined by the salinity, the temperature and the light conditions in the water.

Living organisms are also found in the numerous porous spaces within the ice. The pockets and channels formed during ice growth are filled with concentrated brine and represent an im-

portant habitat for microbiota and small crustaceans like *copepods*. The most diverse group of sea ice microorganisms are *diatoms* (Fig. 1.4d). These unicellular photosynthetic microalgae occupy different ice habitats with some 200 species in the Antarctic and about 300 in the Arctic [Spindler, 1994]. As the ice melts in spring and summer, it can release algae to the water, which leads to major algal blooms near the ice edge. Ice floes that are occupied by large numbers of diatoms sometimes show an intense brown colouration. The dense mats of algae on the underside of ice floes attract other organisms which graze on them [Spindler, 1994]. Zooplankton - like the Antarctic krill *Euphausia superba* (Fig. 1.4e) - can aggregate in huge swarms under the ice and is able to fully exploit the ice environment, particularly by scraping algae from the under-ice surface [Eicken, 1992]. Krill stocks can exceed 1.5 billion tons (the total mass of people approximates 0.5 billion tons) and represent an important food source for different whale species, squids, penguins and seals [Thomas and Dieckmann, 2002].

Biological research in polar waters focused for many years on diatom communities. As diatoms make up more than 90% of the photosynthetic organism diversity in sea ice [Arrigo *et al.*, 2010], they contribute a large part to the primary production in the polar oceans. The primary production in Antarctic sea ice alone amounts to 63 Tg to 70 Tg (1 Tg = 10^9 kg) carbon per year [Thomas and Dieckmann, 2002]. During photosynthesis inorganic nutrients and CO₂ are fixed by the diatoms. Larger zooplankton, such as copepods and krill, consume diatoms and egest fecal pellets, which form aggregates together with other dead organic matter and sink. On their way down to deeper layers the aggregates are consumed by bacteria, which release dissolved CO₂ as a product of respiration. However, a fraction of the sinking organic matter is not consumed and sinks to the ocean floor where it is buried in the sediments. This chain of processes is referred to as "biological pump". It removes carbon in organic form from the surface and turns it into dissolved or sedimented inorganic carbon at great depths [Ducklow *et al.*, 2001]. In this way carbon from atmospheric CO₂ can be stored in the deep ocean for millions of years. Without this sequestration mechanism today's atmospheric CO₂ concentrations would be considerably higher.

1.2.2 Sea ice and climate change

In both scientific and popular literature climatic changes of the polar regions receive much attention. Many characteristics of sea ice - like its extent, thickness, growth and melt rates - react sensitively to changes in heat and momentum of the atmosphere and the ocean and are therefore important indicators of climatic changes.

Regarding the scenario of global warming, especially for the polar regions the temperature changes are expected to be much higher than in other regions of the Earth. There are several reasons for an amplified polar warming: First, as ice and snow melt, darker land and ocean surfaces absorb more solar energy (*ice-albedo feedback*). Second, a greater fraction of extra energy from greenhouse gases goes into warming the atmosphere rather than evaporation, like in the tropics. Third, the polar troposphere is thinner than in warmer latitudes and thus requires less energy input per degree temperature increase. Fourth, as warming reduces the extent of sea ice, more oceanic heat goes into the atmosphere [ACIA, 2004; Notz, 2005]. Another reason is the increasing transport of water vapour from lower latitudes into the dry polar regions due to the enhanced hydrological cycle [Dommenges and Flöter, 2011].

In fact, the two polar regions have experienced contrasting climatic changes in the recent decades. The Arctic has been marked by extensive retreat of sea ice throughout the year, with a decrease of over 10% per decade for the period 1979-2006 [Turner and Overland, 2009]. This

is much faster than the climate models predicted. In September 2012 Arctic sea ice shrank to an average extent of $3.4 \times 10^6 \text{ km}^2$ (Fig. 1.5) [NSIDC, 2012]. Furthermore, the average Arctic sea ice thickness at the end of the melt season decreased by 53% in over 40 years [Kwok and Rothrock, 2009]. Arctic temperatures increased twice as much as the global mean warming, with a resultant loss of permafrost and a reduction in snow cover [Turner and Overland, 2009]. In contrast to the Arctic, the total Southern Hemisphere sea ice extent has slightly increased in the period since 1979⁵. Our knowledge about the long-term development of Southern Hemisphere sea ice thickness is still very limited (see next sections). The Antarctic temperature

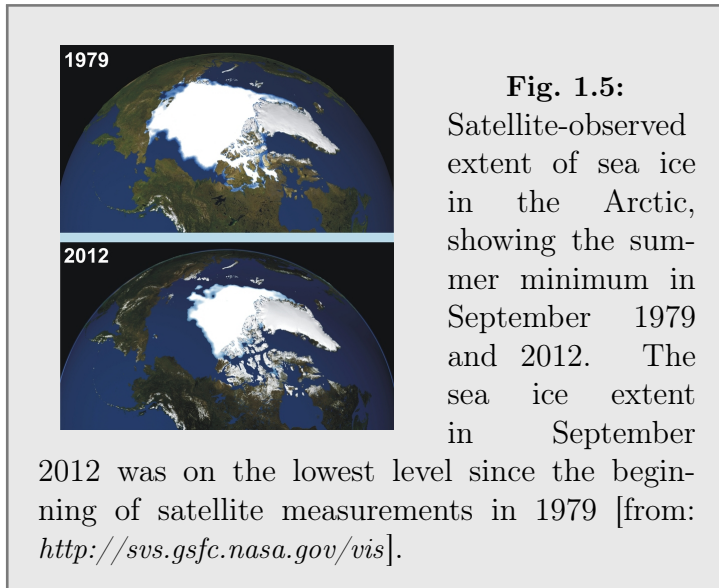


Fig. 1.5: Satellite-observed extent of sea ice in the Arctic, showing the summer minimum in September 1979 and 2012. The sea ice extent in September

2012 was on the lowest level since the beginning of satellite measurements in 1979 [from: <http://svs.gsfc.nasa.gov/vis>].

trends are very variable across the continent. Combining temperature observations from research stations and satellites, a recent study found a significant warming across much of the west Antarctic continent since 1957, with trends exceeding 0.1°C per decade [Steig *et al.*, 2009]. The Antarctic Peninsula warmed by 3°C since the 1950s. This trend is among the largest on Earth for that period. Contrary to West Antarctica, temperature data from research stations show a weak cooling around much of the coast of East Antarctica and the South Pole. These temperature patterns can be partly attributed to the changing atmospheric circulation

in response to the human-induced ozone depletion in the Antarctic stratosphere [Turner and Overland, 2009].

Historic measurements of ocean temperatures in the Southern Hemisphere compared with measurements collected in the 1990s indicate, that the Southern Ocean has warmed substantially since the 1930s, with 80% of the warming concentrated south of 30° [Gille, 2008]. The reasons for this apparent warming trend are still an active area of research [Mayewski *et al.*, 2009].

However, experiments with global climate models confirmed that the observed changes in Arctic and Antarctic temperatures can not be explained with natural climate variability alone. They are directly attributable to human influence [Gillett *et al.*, 2008]. In some model simulations the inclusion of sea ice processes (in both hemispheres) accounts for 37% of the global warming simulated for doubled atmospheric CO_2 . Based on these simulations it was furthermore estimated that the global impact of sea ice changes is, on average, to warm the surface air by 0.107 K for each 10% ice concentration decrease [Parkinson, 2004].

Since the polar sea ice covers significantly alter the freshwater balance of the oceans, a large-scale loss of sea ice could affect the strength of the THC. Melting Arctic sea ice can change the freshwater flux into the convection regions of the Nordic Seas and thus weaken the production of NADW. On the other hand, a thinning of Arctic sea ice would possibly go along with increased rates of new ice formation during winter [Notz, 2005]. The following increase in the salinity of the underlying water would in turn strengthen the bottom water formation. The feedback mechanisms between sea ice and THC have been investigated using computer models but are not yet fully understood [Lohmann and Gerdes, 1998; Stocker *et al.*, 2001]. Studies with coupled ice-ocean models suggest, that the formation of Southern Ocean sea ice and the associated

⁵The current state of Antarctic sea ice is described in detail in chapter two.

production of AABW controls to some extent the formation of NADW. According to *Shin et al.* [2003], the enhanced production of southern sea ice during the last glacial maximum caused a large mass of AABW, which made the deep-ocean heavier and thus increased the oceanic vertical stability. This was followed by a weaker and shallower NADW circulation. Contrary, a Southern Ocean warming and the accompanying sea ice retreat during the end of the last ice age may have preconditioned a stronger NADW formation [*Knorr and Lohmann*, 2003]. On the other hand, there are also indications that the THC itself could serve as a trigger for sea ice switches which result in abrupt climate shifts, such as the Dansgaard-Oeschger events [*Gildor and Tziperman*, 2003].

Retreat of sea ice will also lead to more absorption of solar radiation in the ocean surface, which in turn heats the lower atmosphere. Analyses of long-term weather data suggest, that the diminishing Northern Hemisphere sea ice cover has had a leading role in the recent Arctic temperature amplification [*Screen and Simmonds*, 2010]. Observations and model studies for the Southern Ocean indicate, that regional sea ice changes are strongly associated with the temperature increase on the Antarctic Peninsula [*Turner et al.*, 2005; *Steig et al.*, 2009].

The loss of summer sea ice can also change the moisture supply to coastal regions. It will also be likely to alter the calving rates of glaciers that are still shielded by sea ice for much of the year [*Anisimov et al.*, 2007]. In the Southern Ocean, where large ice shelves exist, sea ice shields the ice shelf from the surrounding ocean. When sea ice decreases, it exposes the ice shelf margin to ocean waves, increasing the instability and possibly contributing to a collapse of the shelf [*Meier et al.*, 2010].

Reduction of sea ice has also impacts on ice-associated food-webs and ecosystems, e.g. due to changes in the biodiversity, distribution and productivity of marine biota. In the Southern Ocean there is a marked reduction in the biomass of Antarctic krill, due to regional reductions in the sea ice extent [*Anisimov et al.*, 2007]. The loss of krill and other crustaceans adapted for life at the sea ice edge will seriously impact their predators, such as albatrosses, seals, whales and penguins. For example, the Arctic fish species *Boreogadus saida* (polar cod) feeds on krill and plankton, and its habitat is therefore closely associated with sea ice. The polar cod itself is a prime food source for many marine mammals, such as ringed seals. The polar bear, a top predator, is in turn highly dependent on ringed seals. This illustrates how food webs in polar regions may be seriously disrupted by changing sea ice conditions. The loss of krill due to sea ice retreat could also have other far-reaching impacts, perhaps even affecting the effectivity of the biological pump in parts of the Southern Ocean [*Anisimov et al.*, 2007, and references therein].

As changes in sea ice accompanied by changes in ocean temperatures are likely to alter the distribution of fish stocks, important food and income sources and thus economic activities are also affected. In the Arctic, previously frozen areas become seasonally or even permanently navigable. Besides increasing the prospects for marine transport, this could provide greater access to Arctic resources such as fish, oil and gas [*Gerland et al.*, 2007].

1.3 Motivation and scientific goals

The descriptions given so far illustrate that sea ice is a pivotal part of the global climate system and a crucial factor for polar food webs. Examining the changes of sea ice has thus become an important field in modern Earth system science. Today, the global sea ice cover is mostly mapped with passive microwave sensors and active synthetic aperture radar (SAR) from

satellites. Microwave radiation is hardly affected by clouds and moisture in the atmosphere. The most important passive microwave sensors used today are the SSM/I (Special Sensor Microwave/Imager) instrument on board DMSP (Defense Meteorological Satellite Programme) satellites and the AMSR-E (Advanced Microwave Scanning Radiometer - Earth Observing System) on board NASA's *Aqua* satellite. Sea ice and water emit substantially different amounts of radiation, the sensors can therefore easily distinguish sea ice from ocean [Meier *et al.*, 2009]. SSM/I and AMSR-E provide global daily images of all sea ice-covered regions, and their data have been used to study trends in sea ice extent in different regions of the polar sea ice covers [e.g. Parkinson and Comiso, 2008]. Radar altimeters are non-imaging active microwave sensors which determine the altitude of the reflecting surface, e.g. the height of the sea ice surface above sea level [Meier *et al.*, 2010] (see chapter 3). Radar altimeters are carried by *ENVISAT*, *ERS-2* and the new *CRYOSAT-2*. The *CRYOSAT-2*⁶ mission is especially designed to measure the ice-covered regions of the Earth. Other altimeters use visible light, like the GLAS (Geoscience Laser Altimeter System) instrument on board NASA's *ICESat*⁷ (see chapter 3). This altimeter uses laser beams to measure the sea ice freeboard (the portion of the ice above sea level).

Except for altimetry, all satellite-borne mapping methods are well established techniques in the remote sensing of Arctic and Antarctic sea ice. But they mostly yield two-dimensional information about the ice cover, such as: (1) concentration (that fraction of the ocean covered by ice), (2) extent (the area enclosed by the ice edge - operationally defined as the 15% concentration contour), (3) the total area of ice within its extent (i.e. extent weighted by concentration), (4) the area of multiyear ice within the total extent, (5) its growth and melt rates and (6) its drift velocity [Lemke *et al.*, 2007]. Ice extent and concentration are the only sea ice variables for which observations are available since 1979. These observations were used in many studies and have greatly advanced our knowledge of the variability and trends of the global sea ice cover. However, a complete assessment of the state of the global sea ice cover and its mass balance requires additional information about the third dimension: the sea ice thickness. But the thickness of sea ice is a parameter for which large-scale observation from space is still elusive. Basin-wide monitoring of sea ice thickness can therefore be regarded as the "holy grail" of modern sea ice observations [IGOS, 2007].

As the thickness distribution of sea ice is not routinely measured from space, its exploration still relies on different airborne and in-situ techniques. Each method has its specific set of advantages, and some of them represent high technological challenges⁸.

Most of our knowledge about the long-term development of Arctic sea ice thickness comes from upward sonar measurements carried out by military submarines during the cold war and the following years [e.g. Rothrock *et al.*, 2008]. Airborne methods - like laser profilometry and in the recent years electromagnetic (EM) induction sounding - were applied in many scientific field campaigns in the Arctic [e.g. Forsberg *et al.*, 2001; Haas *et al.*, 2010]. Also the traditional drilling method has been widely used to approximate the Arctic ice thickness distribution [e.g. Eicken and Lange, 1989]. For the Antarctic the situation is different. Due to the lack of a large-scale programme of submarine observations in the Southern Hemisphere, most of our knowledge about Antarctic sea ice thickness comes from drill-hole measurements [Haas, 2010]. However, as drilling is restricted to the accessible regions of the sea ice cover, the measurements are biased.

⁶The satellite was launched in April 2010 by the European Space Agency (ESA).

⁷The ICESat mission ended in August 2010. ICESat-2 is scheduled for launch in early 2016.

⁸The methods for measuring ice thickness are described in detail in chapter three.

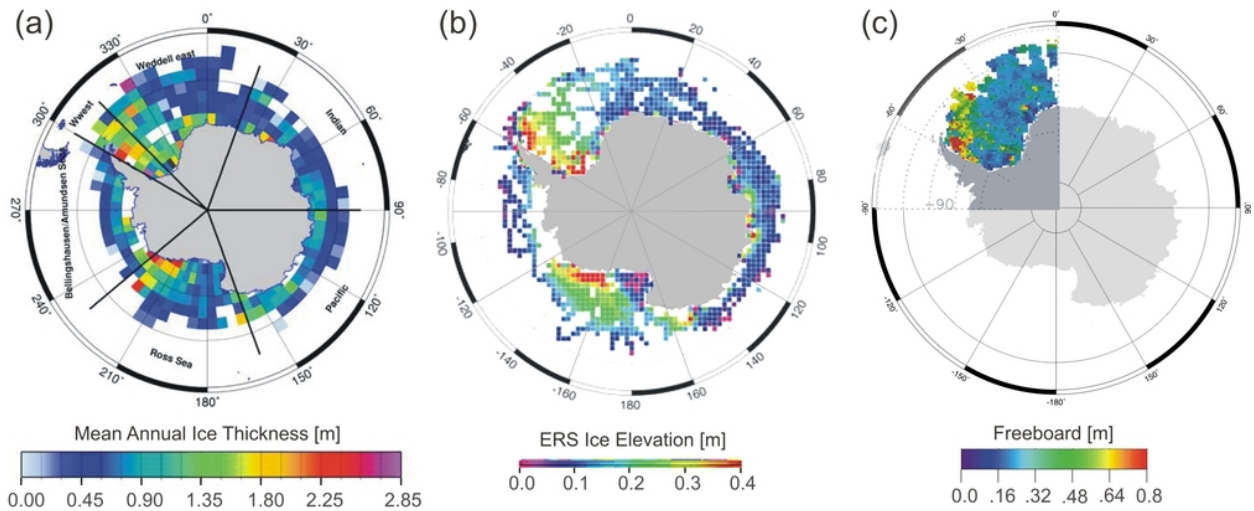


Fig. 1.6: (a) Antarctic sea ice thickness derived from ship-based observations (ASPeCt) between 1981-2005 [Worby *et al.*, 2008], (b) April-September mean sea ice freeboard measured by satellite radar altimetry (*ERS-1/2*) between 1995-2002 [Giles *et al.*, 2008], (c) mean snow freeboard in the Weddell Sea measured by satellite laser altimetry (*ICESat*) in October and November 2005 [after Zwally *et al.*, 2008].

Furthermore, it provides only "snapshots" of sea ice thickness. In the recent years the ASPeCt (Antarctic Sea Ice Processes and Climate) programme compiled visual ship-based observations of sea ice thickness from numerous voyages to the Antarctic. These data provide valuable information about the seasonal evolution of the sea ice thickness around Antarctica, but do not offer insights into its long-term variability (Fig. 1.6a) [Worby *et al.*, 2008]. Groundbased and airborne EM thickness profiling has been performed in the Antarctic e.g. by Haas *et al.* [2008]. But a systematic large-scale programme of EM-surveys by aircraft is still not established. First satellite-borne radar and laser altimetry experiments provided almost basin-wide [e.g. Giles *et al.*, 2008; Zwally *et al.*, 2008] (Fig. 1.6b,c) or first basin-wide [Kurtz and Markus, 2012] estimations of Antarctic sea ice thickness. But these methods still suffer from uncertainties induced by the snow cover on the sea ice, as different snow types and melting snow can alter the rate of signal backscatter significantly. Basin-scale thickness measurements from satellites are just beginning and still very uncertain. Therefore, they need to be further developed [IGOS, 2007].

To date, the only way of performing quasi-continuous long-time observations of ice thickness is the measurement of ice draft (the subsurface portion of sea ice) by moored Upward Looking Sonars (ULS⁹). ULS instruments are attached to oceanographic moorings and determine sea ice draft by measuring the travel times of sound signals reflected by the underside of sea ice (see chapter 3). When moored at different locations, ULS instruments allow synoptic realtime monitoring of the sea ice cover and its topography with high horizontal and vertical spatial resolution.

⁹Sometimes also called *Ice Profiling Sonar* (IPS).

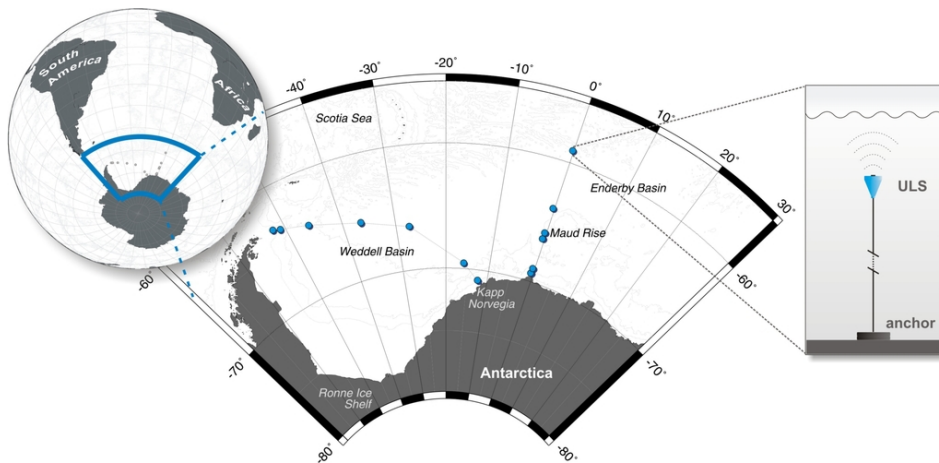


Fig. 1.7: Map of the Atlantic sector of the Southern Ocean, showing the 13 mooring positions (blue circles) in the Weddell Sea. Right: Schematic of a moored ULS.

Since 1990 the Alfred Wegener Institute (AWI) deploys moored ULS instruments on 13 positions along the prime meridian and a transect in the central Weddell Sea (Fig. 1.7). The Weddell Sea represents a key region for the formation of dense and deep water masses which feed the global ocean conveyor belt [Fahrbach *et al.*, 2004]. The AWI ULS-array is the largest array of continuously measuring ice-profiling sonars deployed in the Southern Ocean and provides a unique data set of Antarctic sea ice thickness.

The processing of the raw ULS data is a complicated procedure which has been improved several times since the deployment of the first sonars. The full data set thus comprises data which have been processed applying three methods since 1990. Furthermore, the ULS instrument technology and the signal properties of a new generation of ULS instruments has been improved during the recent years. To assure a stable data quality, one of the first goals of this thesis was therefore to assimilate all available ULS data and to quantify the remaining error as good as possible.

The instruments are deployed by *RV Polarstern* for measurement periods of 2-3 years and operate under harsh conditions. The success rate of moored ULSs is therefore reduced, due to regularly occurring instrument failures or lost instruments which were torn off their moorings by passing icebergs. As a result, most of the obtained ice draft time series are gappy and give rise to problems in the analysis of spatio-temporal variability. Another goal of this thesis was therefore to fill the data gaps in the draft record and to assess the quality of the applied data imputation method. The processed data were combined with filled data to generate time series long enough for further investigation of interannual variability.

An important part of this thesis is the investigation of possible correlations between sea ice thickness changes and changes of other atmospheric and oceanic parameters, such as wind speed, ice drift and surface air temperature. The main scope was to find the dominant features in the variability of the sea ice thickness and to identify its forcing mechanisms in the ocean and in the atmosphere. This also includes the investigation of possible climate-relevant long-term trends.

The ULS data also serve an important function in validating other measurement techniques. As the satellite algorithms for retrieving sea ice thickness are still under development, their preliminary results need to be validated. Therefore, the final outcome of this thesis is a consistent data set of ULS sea ice drafts, which can be used to validate results of new satellite algorithms and coupled ice-ocean models. As sea ice draft and thickness are linearly related,

the term *draft* will sometimes be used as synonym for ice thickness in the following chapters. The first four chapters of this thesis are based on present literature. The results of this study are presented in chapters 5, 6 and 7.

The main goals and questions of this thesis can be summarised as follows:

- Processing of new ULS data and assimilation of the different data.
- Imputation of missing data and assessment of the results.
- Determination of the ULS measurement accuracy.
- Preparation of a complete data set of sea ice drafts for the validation of satellite data and sea ice models.
- Where does the Weddell Sea ice thickness vary?
- Are there trends in the ice draft?
- What are the dominant forcing mechanisms of changes in sea ice thickness?

"I have hydrophobia. But I
know something about ice..."

Peter Høeg, Miss Smilla's
Feeling for Snow

2

Antarctic Sea Ice

In the following chapter I give an overview on the life cycle of sea ice and the physical relations that are important for sea ice thickness. In the first section I qualitatively outline the formation, growth and decay of sea ice. The following sections contain a more detailed physical treatment of the thermodynamics, the dynamics and the thickness distribution of a sea ice cover. In the last section I review the variability and trends of Antarctic sea ice. This chapter is mainly based on the works of *Weeks* [1998], *Petrich and Eicken* [2010], *Wadhams* [2000], *Haas* [2010] and *Lemke* [1994].

2.1 The structure, growth and life cycle of sea ice

Water is a substance with numerous anomalies. The most striking one is its density maximum in the liquid phase. Under normal pressure (1013 mbar) the density of cooling water rises until a temperature of 277 K (4°C) is reached. When the water is cooled further, its density declines, even if the water is supercooled (i.e. cooled below the freezing point at 273 K) [*Ludwig and Paschek*, 2005]. However, the behaviour of seawater is different. The addition of salts lowers the temperature of maximum density and the freezing point of the water, and increases its density. For most of the ocean's water the range of salinity is from 34.60 to 34.80 parts per thousand [*Stewart*, 2006]. When the salinity exceeds 24.70 parts per thousand, the temperature of maximum density disappears (Fig. 2.1b). Cooling of ocean water therefore causes the water to become denser until the freezing point is reached, which itself is depressed to around -1.9°C by the presence of salt ions that hinder the formation of a regular crystal structure.

The ice which forms under the conditions encountered at the Earth's surface is called *ice I(h)*. Hydrogen bonds (H-O bonds) between the water molecules favour a hexagonal arrangement with each oxygen atom located at the centre of a tetrahedron with four other oxygen atoms at the apices (Fig. 2.1a) [*Weeks*, 1998]. According to the *Bernal-Fowler rules* each oxygen atom is connected to two hydrogen atoms via chemical bonds and to another two hydrogen atoms via H-O bonds. The resulting open structure is responsible for the low density of frozen water compared to its liquid phase, in which breaking H-O bonds allow closer packing of the water

molecules. In ice I(h)-crystals the oxygen atoms are arranged in a series of hexagonal planes which are called *basal planes*, or in the notation of Miller indices (*0001*) planes. The basal plane corresponds to the direction of easy ice growth under geometrically unconstrained conditions [Weeks, 1998]. Its interface is smooth at the molecular level. The axis perpendicular to these planes is called *c-axis* and plays an important role in describing the growth and orientation of ice crystals. Prism faces perpendicular to the basal plane are rough at the molecular level [Petrich and Eicken, 2010]. The directions of the three *a-axes* correspond to the rows of oxygen atoms in a basal plane, and coincide with the directions of the dendritic arms of snowflakes and frazil ice crystals (see below) [Weeks, 1998].

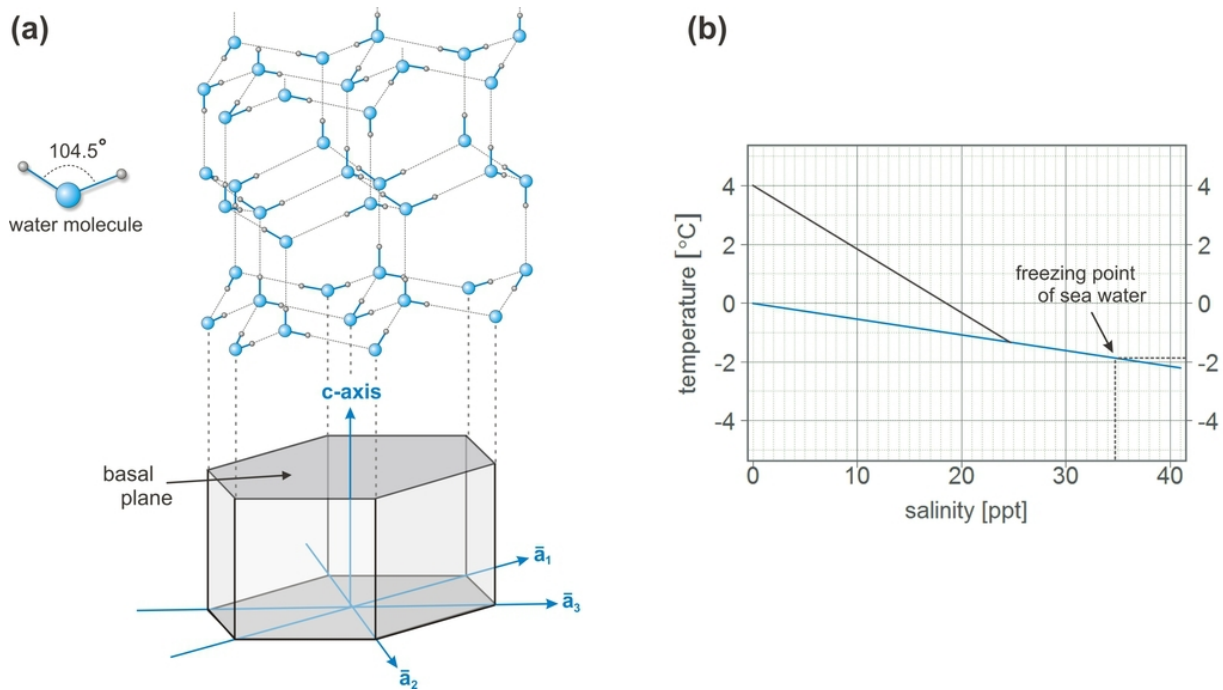


Fig. 2.1: (a) Schematic diagram showing the crystal structure of ice I(h) [after Weeks, 1998], (b) salinity-temperature diagram for water. Black line: temperature of maximum density. Blue line: freezing temperature.

Even at temperatures higher than the freezing point, small structurally ordered regions develop for very short times in the water. Their arrangement corresponds to the hexagonal crystal lattice of ice [Doronin and Kheisin, 1977]. Since water molecules bound to other molecules have less energy than isolated molecules, they are in a "potential well". For a transition from one equilibrium state to another the molecule therefore needs to overcome a certain energy barrier. In the supercooled state the mean energy of the water molecules is less than the height of this barrier [Doronin and Kheisin, 1977]. As the fluctuations of the state parameters of seawater (temperature, pressure, salinity) are wide enough to ensure the crossing of the energy barrier, supercooling under natural conditions is typically very low ($\sim 0.01^\circ\text{C}$ to 0.1°C) [Weeks, 1998]. Significant supercooling is also restricted by the presence of particles and small impurities in the seawater, because the energy required to produce a crystallisation-nucleus on a solid wall of a foreign body is less than that required in a homogeneous medium [Doronin and Kheisin, 1977]. The growth of sea ice crystals is therefore always initiated by natural seeding processes (heterogeneous nucleation). The greatest catalysing effect have those seeds, whose geometrical dimensions of the crystal cells are close to that of the lattice of ice. If the seeds consist of small ice crystals, water molecules that enter the electric field of the seeds do not require additional

energy to join the crystal structure [Doronin and Kheisin, 1977]. In this case the amount of supercooling is very small.

Homogeneous nucleation on the contrary occurs due to fluctuation of the state parameters of the water. This type of nucleation requires pure fresh water devoid of any impurities and occurs at -39°C [Wilson *et al.*, 2003]. In practice, this never happens in seawater and can only be achieved under special laboratory conditions¹.

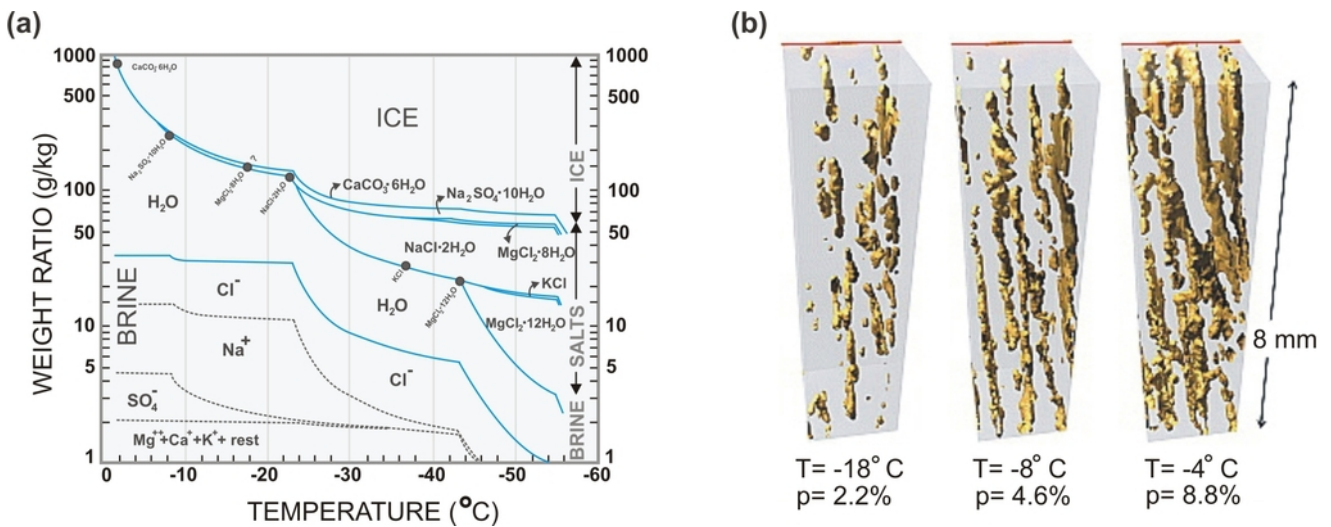


Fig. 2.2: Phase diagram of sea ice. The curves indicate the mass fraction of ice, salts and brine present in seawater at different temperatures [after Assur, 1960], (b) X-ray tomography images of artificially grown sea ice, showing the thermal evolution of the brine pore space (p: porosity) [Pringle *et al.*, 2009].

The salts in seawater, mainly $\text{NaCl} \cdot 2\text{H}_2\text{O}$ (*hydrohalite*) and $\text{Na}_2\text{SO}_4 \cdot 10\text{H}_2\text{O}$ (*mirabilite*), are not incorporated as solid solutions in the ice crystals. However, sea ice samples usually have salinities of around 5‰ [Lemke and Hilmer, 2003], which are caused by liquid inclusions of concentrated brine. These are physically entrapped as layers between the crystals and grain boundaries during growth of the ice crystals. This mechanism allows for a retention of 10% to 40% of the salt ions in the ice [Petrich and Eicken, 2010]. Sea ice can therefore be considered as a porous medium consisting of solid freshwater ice and a system of channels and pockets containing liquid salty brine. As the temperatures fall, freezing reduces the size of the channels and increases the salinity of the brine (Fig. 2.2b). This process continues until the eutectic point is reached at -8.2°C for mirabilite and -22.9°C for hydrohalite [Weeks, 1998], where the salts precipitate in solid form.

The brine content and therefore the porosity of sea ice is a function of temperature and age of the ice. Young ice generally has a higher salt content and thus a higher bulk density than older ice [Lemke, 1994]. Several processes were suggested to contribute to the loss of salt during the life cycle of sea ice: (1) Molecular salt diffusion, caused by a salinity gradient and leading to a slow downward motion of salt within the brine pockets, (2) brine expulsion through pore volume loss during freezing, (3) gravity drainage of brine in the upper parts of the ice floe, induced by cooling from above during winter and (4) flushing, which refers to a washing-out of salty brine with relatively fresh surface meltwater during summer. Recently, Notz and Worster [2009] demonstrated that brine expulsion and salt diffusion do not contribute to any measurable salt loss from sea ice. Their laboratory experiments and measurements on Arctic sea ice

¹Very detailed physical descriptions of ice crystallisation phenomena can be found in Wettlaufer [1998].

showed that all salt loss from sea ice is due to gravity drainage in winter and flushing during summer. In this way the desalination of sea ice contributes to dense water mass formation and hence to the global ocean circulation (see section 1.2). The brine volume of sea ice determines to a large extent its mechanical and electrical properties, the latter being especially important for remote sensing². As a two-phase, two-component, reactive porous medium, sea ice can be described by the "mushy layer" equations [Feltham *et al.*, 2006].

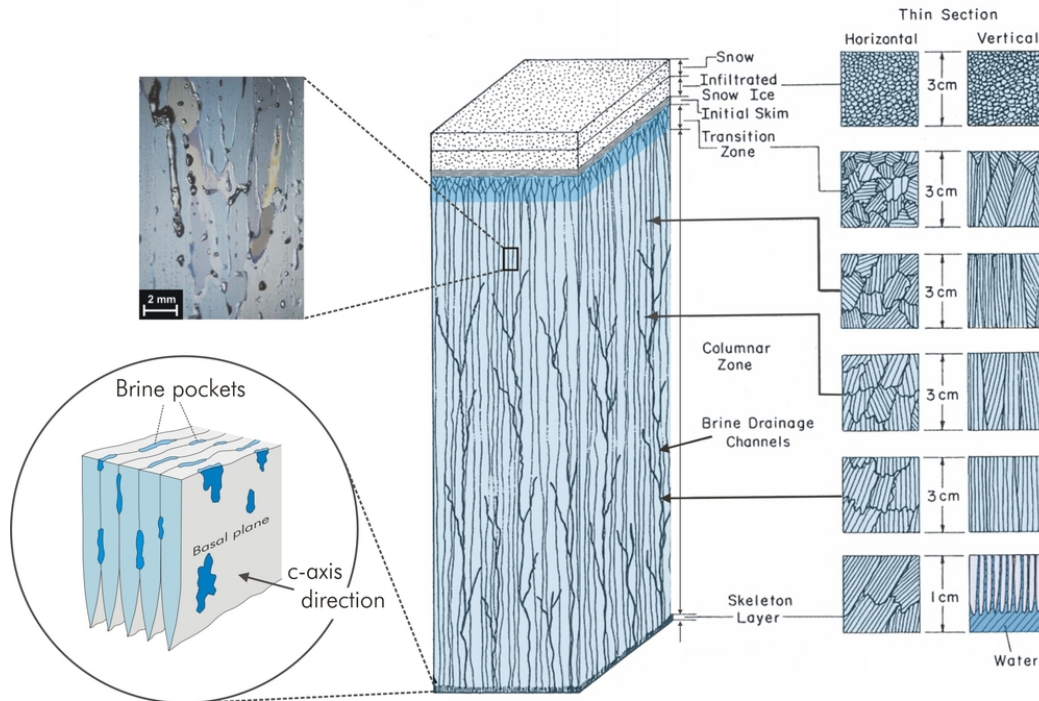


Fig. 2.3: The vertical stratigraphy of sea ice [after Schwarz and Weeks, 1977; Løset *et al.*, 2006]. The photograph in the upper left shows the brine pockets along the grain boundaries in a thin section of first-year ice [Timco and Weeks, 2010].

When the ocean surface cools to the freezing point during winter, ice crystals are formed within the mixed upper water layers. These crystals form a suspension until a closed surface layer is created, which further consolidates during the freezing process. Once a continuous ice cover is established across the sea surface, the ice/water interface advances downwards during ice growth and rejects salt ions. This leads to an increase in the salinity of the thin adjacent water layer. To maintain thermodynamic equilibrium, the interface between water and sea ice is always at the respective melting/freezing point. As the freezing point decreases with increasing salinity, the rising salt concentration in the adjacent water is accompanied by a drop in temperature [Petrich and Eicken, 2010]. Due to the gradient in salinity, the thin saline boundary layer that is in contact with the ice loses salt ions through convection to the less saline ocean water below. But the heat transport through the boundary layer to the colder ice interface is faster than the transport of salt ions away from the interface. The layer is therefore cooled below the freezing point [Petrich and Eicken, 2010]. This phenomenon is called *constitutional supercooling* and does not occur during the growth of lake ice.

²Detailed descriptions of the dielectric properties of sea ice are given by Petrenko [1993], Lemke [1994] and Kaleschke [2003].

As the sea surface is rarely calm, the *c*-axes of crystals in the upper parts of sea ice tend to be randomly oriented, resulting in a granular texture (Fig. 2.3). In a process called *geometric selection*, ice crystals with their *c*-axis oriented in horizontal (or near horizontal) direction grow faster and cut off those crystals from the melt, whose *c*-axes are more oriented perpendicular to the freezing interface. The surviving crystals have therefore preferred growth directions which are oriented perpendicular to the freezing interface, resulting in a typical columnar growth structure [Weeks and Gow, 1978]. Below the transition zone from granular to columnar ice, the ice therefore grows in submillimetre-thick vertical lamellae that are separated by narrow films of brine (Fig. 2.3). It is this *skeletal layer* of ice lamellae that provides the habitat for large concentrations of diatoms and many other microorganisms living on the underside of sea ice. The width of the ice lamellae and the spacing of the brine layers depends on different factors, such as ice-growth rate, salinity of the underlying water and the velocity of ocean currents under the ice [Petrich and Eicken, 2010]. For example, when the ice gets thicker and its growth rate declines, the distance between the brine layers increases.

The vertical stratigraphy and the microcrystalline structure of sea ice reflects to a large extent its history of development, which is described for the different ice types in the following subsections.

2.1.1 First-year ice

The term *first-year ice* refers to sea ice of no more than one year's growth. During the initial ice formation crystals grow into a supercooled melt. The evolution of first ice crystals forming in calm water is somewhat similar to the freezing of fresh water or the development of snowflakes³. These crystals start as small spheres of pure ice with a diameter of 2 mm to 3 mm, then change



Fig. 2.4: (a) Frazil streaks on turbulent water in a lead, (b) rafted sheets of nilas, (c) white first-year ice [credits: see list of figures].

to circular discs that grow outward laterally in the basal planes, and finally change to dendritic stars [Weeks, 1998]. Their *c*-axes are mostly oriented perpendicular to the sea surface, as this is the only stable floating orientation in the water. However, even under calm conditions the *c*-axes of the upper ice crystals in an initial skim are never entirely oriented vertically. The dendritic crystals are very fragile and soon break up into random-shaped crystal fragments, that form a viscous suspension in the surface waters which is called *frazil* (or *grease ice*⁴) [Wadhams, 2000]. The density of this suspension gradually increases as the crystal fragments coagulate. This growth process is sometimes referred to as "collision breeding" and involves collisions with other ice aggregates or particles that are present in the water [Weeks, 1998]. Where the wind

³See Furukawa [1997].

⁴Sometimes the term *grease ice* refers to a later stage of coagulated frazil.

initiates Langmuir circulation in the boundary layer, frazil sometimes forms oily streaks on the sea surface (Fig. 2.4a). Some aspects of frazil growth are yet to be fully understood, such as the transition from loose frazil masses into solid granular ice [Petrich and Eicken, 2010].

Under calm conditions the coagulation process soon leads to a solid surface layer of thin ice, called *nilas* (Fig. 2.4b). In its early stage, when it is only a few centimetres thick, nilas is transparent, has a dark appearance and easily bends on waves [Wadhams, 2000]. As the ice sheet grows thicker, it changes to grey ice (10 cm to 15 cm) and finally to white ice (15 cm to 30 cm) (Fig. 2.4c). After the formation of a continuous layer of nilas a different growth process takes place: *Congelation growth* refers to a process in which the heat loss is one-dimensional upward through the ice to the atmosphere. It is the classic *Stefan-problem* of thermodynamic ice growth (see section 2.2). Congelation ice is added layer by layer to an existing ice sheet and leads to the typical columnar structure shown in figure 2.3, as the direction of easy growth is parallel to the direction of the upward heat flow, i.e. with horizontal c-axes of the crystals. This thermal conductivity advantage of vertically growing crystals is the reason for the geometric selection mentioned earlier. As the downward growth continues, the advancing crystals become larger.

First-year ice evolved under calm conditions usually has a very narrow top layer of granular ice, followed by the transition zone between the upper 25 cm to 50 cm of the ice, where geometric selection occurs. Below this lies the columnar zone that consists of vertically elongated ice crystals, making up the majority of the ice sheet.

Where the wind speeds are higher, especially in the Antarctic, the initial formation process of sea ice is slightly different (Fig. 2.6). Turbulent waters maintain the stage of frazil, instead of

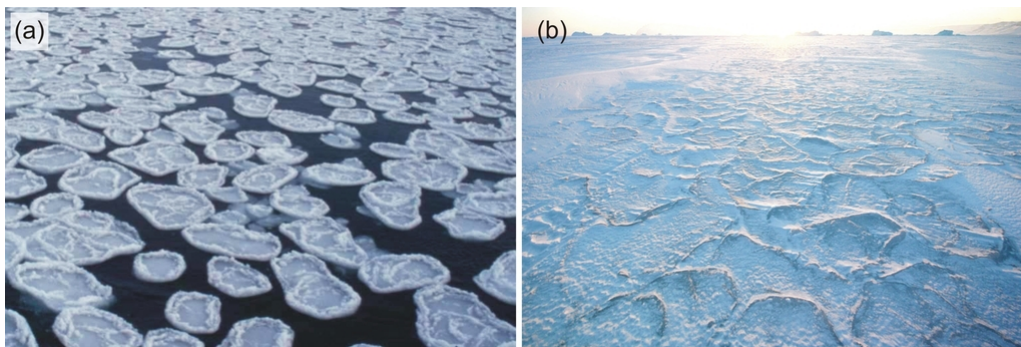


Fig. 2.5: (a) Pancake ice, (b) consolidated pancake ice [credits: see list of figures].

forming nilas. Winds and waves further compress the frazil suspension and form small lumps of slush, which grow larger and solidify by accretion and freezing. This leads to the so-called *pancake ice*, which consists of decimetre-sized pans which bump and rub against each other⁵ (Fig. 2.5a). The individual pans gradually grow until they may reach 3 m to 5 m diameter and 50 cm to 70 cm thickness [Wadhams, 2000]. When the contact regions of the adjoining pans open through the passage of waves, new frazil crystals form in the exposed water and act as glue between the pans [Weeks, 1998]. Herded by the wind, many pancakes further adhere together and form larger composites. This sequence of events was frequently observed in Antarctic waters and became known as the *pancake cycle* [Lange et al., 1989].

Inside the ice cover, where the waves are calmed, the pancake composites accumulate into larger

⁵In very cold winters, pancake ice can form in freezing rivers.

groups that finally freeze together. This kind of first-year ice sheet is known as *consolidated pancake ice* (Fig. 2.5b). Stratigraphic analyses of such ice revealed, that it consists of stacks of tilted pancakes, frozen together with frazil ice in between. First-year ice that evolved under turbulent conditions therefore has broad top layers (typically around 20 cm) of granular ice [Lemke, 1994]. When the consolidated pancake ice is thick enough and cuts off the open water surface, congelation growth adds a layer of columnar ice, which was found to be typically only a few centimetres thick in Antarctic first-year ice [Wadhams, 2000].

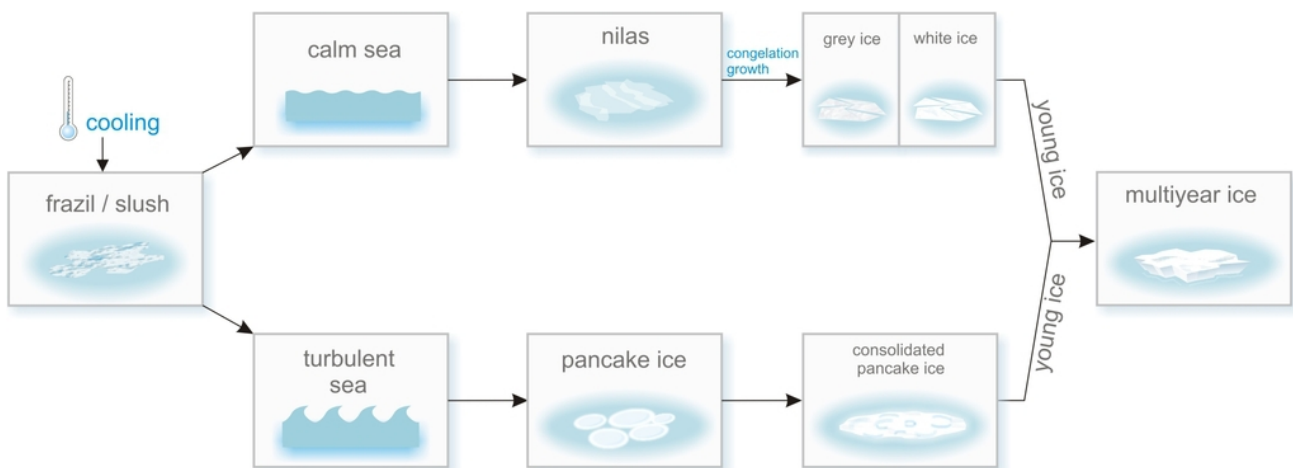


Fig. 2.6: The life cycle of sea ice.

When the sea ice and the overlying snow cover start warming with the onset of summer, the internal melt leads to percolation and occasionally refreezing of meltwater. If the temperatures remain high for a long time, the ice disintegrates and the meltwater works its way down through the pores and channels and flushes out much of the remaining brine. Especially the upper layer of multiyear ice (see below) is subjected to repeated melting and freezing. In the lower layers either the fresh meltwater refreezes or the remaining channels are filled with seawater, which forms young sea ice that penetrates into the structure of the old ice [Doronin and Kheisin, 1977].

2.1.2 Multiyear ice

When sea ice survives one or more summer seasons it is called *multiyear ice*. The sea ice grows thicker every year until it reaches a thickness maximum, at which the summer melt equals the winter growth. From this point on, its thickness oscillates through an annual cycle [Wadhams, 2000]. Calculations of equilibrium thicknesses indicated that - depending on the climatic conditions - it lies in the range of 3 m to 5 m after a first-year growth of 2 m [Weeks, 1998]. In the Arctic, where a large area of multiyear ice exists, the sea ice is either transported by the transpolar drift or circulates in the Beaufort Gyre, which can take up to 10 years. In the Antarctic most multiyear ice is second-year ice and is mainly found in the Weddell Sea.

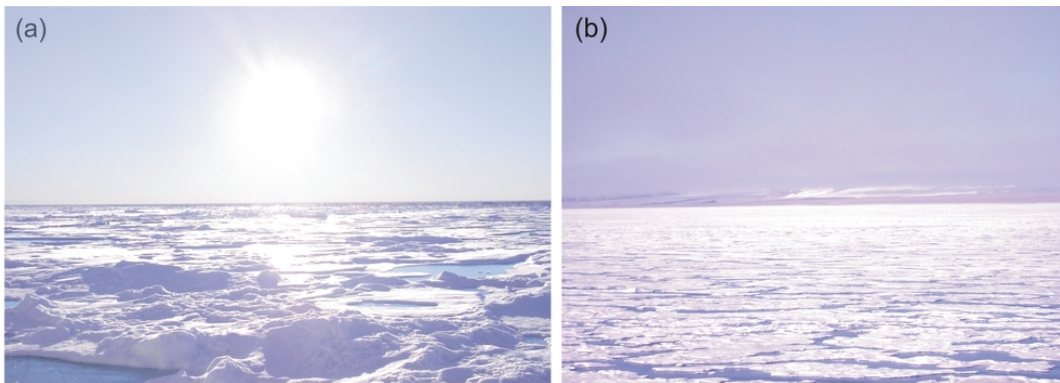


Fig. 2.7: (a) The rough surface of a multiyear ice cover, (b) melt ponds on Arctic multiyear ice.

The vertical stratigraphy of multiyear ice often shows alternating layers of frazil and congelation ice, as ridging and rafting piles up the ice from different years. Sometimes the top layer of frazil is completely removed through melting, and the multiyear ice entirely consists of columnar ice [Lemke, 1994]. However, analyses of ice cores showed that frazil dominates in Antarctic multiyear ice, whereas the percentage of frazil in Arctic multiyear ice is less [Weeks, 1998]. One reason for the higher amount of frazil in the Antarctic is that the northern sea ice edge is frequently disturbed by intense storms, favouring the initiation of the pancake cycle. Additionally, close to the Antarctic continent strong katabatic winds flow off the ice sheet, drive the sea ice away from the coast and create large polynyas, which also favours the production of frazil. The large amount of snow falling on Antarctic sea ice leads to flooding of the ice/snow interface. This results in the formation of snow-ice, or *infiltration ice*, which consists of microgranular ice crystals (Fig. 2.3). In some regions of the Antarctic this type of ice makes up a considerable part of the ice cover.

The stratification of multiyear sea ice is also affected by meltwater that accumulates at the underside of the ice in the summer-fall period. The meltwater entering the saline and cold seawater rapidly freezes and forms summer layers of very fine ice crystals. Further inflow of meltwater from above leads to larger crystals of clear freshwater ice, whose structure is comparable to that of congelation ice [Doronin and Kheisin, 1977]. The density of multiyear sea ice decreases every year, as the brine is gradually replaced by ice. The low salinity of the upper layer of multiyear ice enables the discrimination between first-year ice and multiyear ice by satellite sensors. In the melt season this is not possible, as the water or wet snow on top of the ice disturbs the microwave remote sensing signals [Sandven and Johannessen, 2006].

Due to rafting and ridging, multiyear ice has a rougher surface than young ice, especially in the Arctic where the ice floes tend to converge (Fig. 2.7a). Also the bottom of multiyear ice is rougher and forms a characteristic landscape of bulges and depressions. Furthermore, the low brine content makes it mechanically stronger, turning it into a hard barrier for icebreakers [Wadhams, 2000]. During the spring-summer melting the surface of multiyear ice gets smoothed, as the sails of the pressure ridges melt and depressions are filled with melt water [Lemke, 1994]. This can be frequently observed in the Arctic (Fig. 2.7b).

2.2 Formation, growth and melt of an ice cover

The following section describes the thermal buildup of an ice cover and the thermodynamic processes determining the growth and melt rates of sea ice. Frazil growth under turbulent

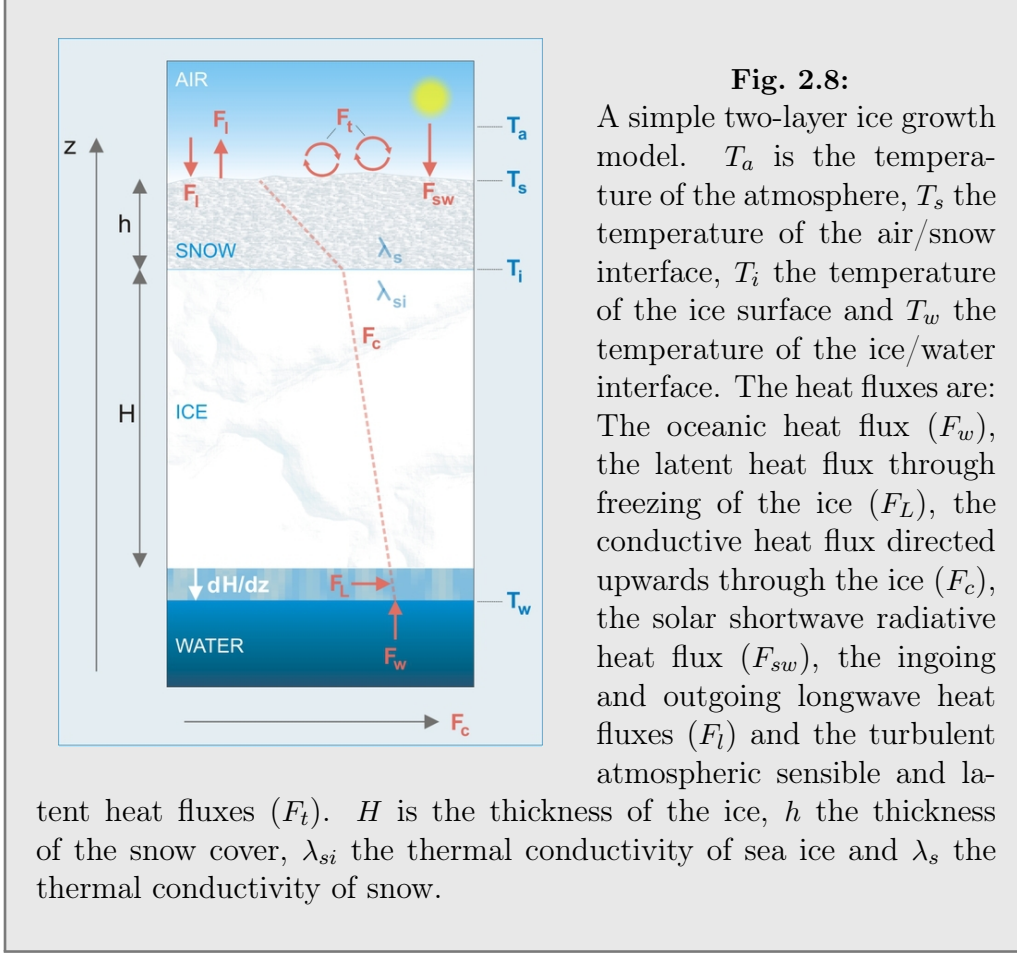
conditions is therefore not discussed here. The descriptions mainly follow the bookchapter of *Petrich and Eicken* [2010].

Once the first individual ice crystals have formed in calm ocean water, crystallisation rapidly spreads over large areas because of the large number of crystallisation nuclei in the surface layer of the ocean. Due to cooling from above and the resulting heat flux through the ice to the atmosphere, the initial sheet of nilas starts thickening. Its growth rate is determined by the energy balance at the ice/water interface, i.e. the underside of the ice. The upward conductive heat flux from the interface into the ice (F_c) and the oceanic heat flux from the water into the ice (F_w) are balanced by the release or uptake of latent heat (L_{si}) [*Petrich and Eicken*, 2010]. This means that the difference between the two heat fluxes is compensated by the latent heat liberated during freezing of the water or taken up to melt the ice:

$$\rho_i L_{si} \frac{dH}{dt} = F_c - F_w. \quad (2.1)$$

Here, dH/dt is the sea ice thickness change with time and ρ_i the density of pure ice. When directed upwards to the atmosphere, the heat flux is positive. Without the oceanic heat flux and the radiative heating of the ice by the sun, the ice cover would grow thicker as long as the surface temperature of the ice was less than the freezing point of the seawater at the ice bottom [*Petrich and Eicken*, 2010]. However, the ocean always contains a reservoir of heat, which maintains an oceanic heat flux of up to several tens of W m^{-2} in the Antarctic. As the winter equilibrium thickness is crucially determined by the balance $F_c = F_w$, Antarctic first-year ice only reaches a thermodynamic growth maximum of 0.5 m to 0.7 m [*Petrich and Eicken*, 2010, and references therein], although the temperatures of the winter atmosphere in some regions may remain at -25°C for several weeks.

Even at times and under climatological conditions where the waters are expected to be ice covered, there are some areas within the ice pack which remain ice free. These polynyas can form by two mechanisms: The first mechanism leads to the so called "latent heat polynyas" and creates open areas in the ice cover by continually removing newly formed ice via winds and ocean currents [*Smith et al.*, 1990]. The new ice which forms in the polynya provides the latent heat to keep the area ice free. The second mechanism includes convective exchange with the deeper ocean. When warm deep water enters the surface layer it can locally melt the existing ice cover or prevent the formation of new ice [*Smith et al.*, 1990]. In such "sensible heat polynyas" the oceanic heat flux can increase to several hundred W m^{-2} [*Petrich and Eicken*, 2010]. This heat flux from the ocean to the atmosphere is one of the reasons why north polar winters are less frigid than those of the south polar region [*Smith et al.*, 1990].



As the vertical temperature gradients in sea ice are usually much larger than the horizontal gradients [Leppäranta, 1993], the oceanic heat and the latent heat of freezing are conducted upwards through the ice and are finally released to the atmosphere. The energy balance at the upper ice surface as well as the thermal properties of the ice and the overlying snow cover determine the rate at which this heat is released [Petrich and Eicken, 2010]. Compared to the balance at the underside of the ice, for the heat balance at the ice surface some more fluxes need to be considered. A sea ice surface at steady temperature ($dT/dt = 0$) requires that the following incoming and outgoing heat fluxes are balanced: (1) the solar radiative shortwave flux penetrating into the ice, (2) the incoming longwave flux, (3) the outgoing longwave flux, (4) the turbulent atmospheric sensible and latent heat fluxes, (5) the heat flux due to melting of the ice surface and (6) the conductive heat flux from the interior of the ice [Petrich and Eicken, 2010] (Fig. 2.8).

Both the heat balance at the ice surface and the heat balance at the bottom are coupled through the conductive heat transfer, which can be expressed by the *heat transfer equation*:

$$\frac{\partial T}{\partial t} = \frac{1}{\rho_i c_{si}} \frac{\partial}{\partial z} \left[\lambda_{si} \frac{\partial T}{\partial z} \right] - \frac{\partial F_{sw}}{\partial z} = \frac{\lambda_{si}}{\rho_i c_{si}} \frac{\partial^2 T}{\partial z^2} - \frac{\partial F_{sw}}{\partial z}. \quad (2.2)$$

Here, λ_{si} is the thermal conductivity of the ice and c_{si} the heat capacity of the ice. The heat transfer equation describes the diffusive propagation of a temperature signal in sea ice by the change of temperature with time [Petrich and Eicken, 2010]. The term $(\lambda_{si}/\rho_i c_{si})$ on the right hand side is referred to as *thermal diffusivity*. It indicates the propagation rate of the

temperature fluctuation. The thermal diffusivity can be calculated from the changes of the vertical temperature profiles in sea ice [Lemke, 1994].

For calculating sea ice thickness changes, equation (2.2) takes the form:

$$\frac{\partial H}{\partial t} = \rho_i c_{si} \frac{\partial T}{\partial t} = \frac{\partial}{\partial z} \left[\lambda_{si} \frac{\partial T}{\partial z} \right] - \frac{\partial F_{sw}}{\partial z}. \quad (2.3)$$

Equation (2.3) becomes nonlinear due to the temperature dependence of λ_{si} and c_{si} . But also the other terms depend on surface and air temperature in a non-linear way. The solution of this problem requires numerical techniques which would be far beyond the scope of this chapter⁶.

However, the problem can be approached by a simple two-layer model. The model was first proposed by *J. Stefan*⁷ and provides reasonable predictions of ice growth. Stefan's law makes use of the assumptions mentioned above, that heat linearly conducted through the ice is exactly balanced by the latent heat of fusion of newly formed ice [Allison, 1979]. Considering Stefan's two-layer model with snow and ice (Fig. 2.8), we assume the temperature at the ice/ocean interface (T_w) to be at the freezing point and the oceanic heat flux (F_w) to be known. The net longwave radiation fluxes (F_l) and the turbulent heat fluxes (F_t) can be linearly approximated as a function of surface and air temperature:

$$F_a = -k(T_a - T_s), \quad (2.4)$$

where F_a is the net atmospheric heat flux and k is an effective heat transfer coefficient between surface and atmosphere [Petrich and Eicken, 2010]. The thermal conductivity λ_{si} is assumed to be homogeneous throughout the ice, which leads to linear vertical temperature profiles. The conductive heat flux is largely determined by the heat flux to the atmosphere. By using the conductive heat flux equation $F_c(z) = \lambda(\partial T/\partial z)$ for the snow layer (h) and the ice layer (H) and with continuity in temperature, the net conductive heat flux is

$$F_a = F_c = -\frac{T_a - T_w}{\frac{1}{k} + \frac{H}{\lambda_{si}} + \frac{h}{\lambda_s}}, \quad (2.5)$$

where λ_s is the thermal conductivity of snow. Note that this equation is only valid in the absence of solar heating and ice surface melting, e.g. for conditions encountered during polar winter. Inserting this net heat flux at the upper surface into the energy balance at the bottom (equation 2.1) leads to the equation

$$\rho_i L_{si} \frac{dH}{dt} = -\frac{T_a - T_w}{\frac{1}{k} + \frac{H}{\lambda_{si}} + \frac{h}{\lambda_s}} - F_w. \quad (2.6)$$

To allow ice thickness calculations solely based on air temperature, some more simplifications have to be made: (1) The oceanic heat flux (F_w) is neglected and (2) we assume that h increases with time proportionally with H ($h = rH$). Integrating the modified equation (2.6) over time then leads to the equation

⁶Several approaches to the solution are discussed by *Doronin and Kheisin* [1977].

⁷*Josef Stefan*, Austrian physicist (1835-1893). See also *Crepeau* [2008].

$$H^2 + \frac{2\lambda_{si}}{k} \left(1 + \frac{\lambda_{si}}{\lambda_s} r\right)^{-1} H = \frac{2\lambda_{si}}{\rho_i L_{si}} \left(1 + \frac{\lambda_{si}}{\lambda_s} r\right)^{-1} \int -(T_a - T_w) dt. \quad (2.7)$$

For absence of snow ($r = 0$) and a constant surface temperature ($dT_s/dt = 0 \Rightarrow k \rightarrow \infty$), we obtain Stefan's law for ice growth:

Stefan's Law

$$H^2 = \frac{2\lambda_{si}}{\rho_i L_{si}} \int_0^T (T_w - T_a) dt \quad (2.8)$$

Josef Stefan called this equation "*Kältesumme*" [Crepeau, 2008], where H is the ice thickness after time $t = T$. It follows from Stefan's law that the thickness of ice increases with the square root of time (Fig. 2.9), which implies that thin ice grows faster than thick ice. Stefan's law initially did not make allowance for changes of the heat content within the ice, i.e. it applied only for ice of zero specific heat. This problem can be solved by using an *effective* latent heat. A more serious drawback of Stefan's law is that it assumes the oceanic heat flux to be zero [Leppäranta, 1993]. As shown by figure 2.9, including an oceanic heat flux in equation (2.8) may be sufficient to obtain a reasonable match to the observed ice growth:

$$H = \sqrt{\frac{2\lambda_i}{\rho_i L_{si}} \sum_0^T (T_w - T_a) t - \frac{1}{\rho_i L_{si}} \sum_0^T F_w t}. \quad (2.9)$$

But there still remain systematic departures from the simple model in equation (2.9), indicative of a variable oceanic heat flux [Allison, 1979]. Usually, the oceanic heat flux during ice growth starts at high values (typically 20 W m^{-2} to 40 W m^{-2}) and decreases as the ice grows thicker. This behaviour can be explained by thermohaline convection caused by the salt rejection from the ice. The following density instabilities initiate convection in the underlying water, which in turn brings relatively warm deep water up to the sea ice bottom. As the ice growth rate decreases, the rate of brine rejection also drops, decreasing the convection and the heat transfer to the ice [Allison, 1979]. Rapid melting and freezing of the ice, changes in ice concentration and modifications to the ice bottom roughness also alter the ice/ocean interaction [Holland *et al.*, 1997]. The oceanic heat flux is therefore strongly dependent on the ice thickness distribution. Another reason for the decrease of the oceanic heat flux during winter is the reduced insolation through ice-free areas and thin ice. The ice drift is also responsible for changes of F_w , as the ice may move into regions of higher or lower heat fluxes, e.g. by passing oceanic frontal zones. The oceanic heat flux can be calculated from turbulent heat transfer in the ocean. Alternatively it can be derived from ocean-models or from the difference between the measured latent and conductive heat fluxes [Purdie *et al.*, 2006].

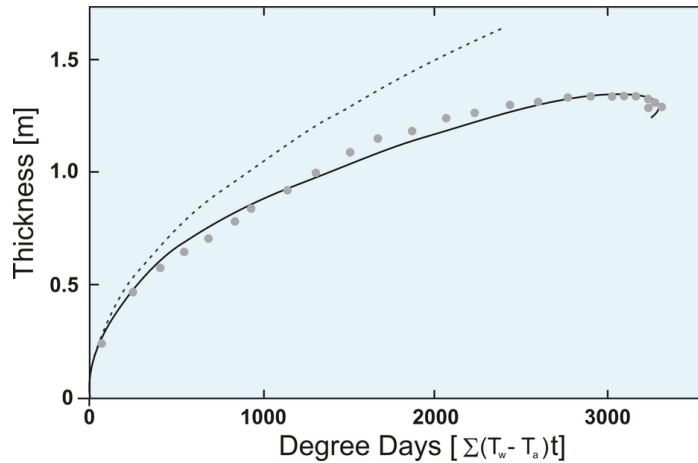


Fig. 2.9: Observed ice thickness at Mawson (Antarctica). The grey circles represent 10 day measured values of ice thickness. The dashed line is from Stefan's law (equation 2.8) and the solid line is from Stefan's law modified to include an oceanic heat flux (equation 2.9) of $F_w = 9 \text{ W m}^{-2}$ [after Allison, 1979].

Several other relationships were found to simplify the predictions for ice growth⁸. One example is the relation

$$H^2 + 5.1 H = 6.7 \Theta, \quad (2.10)$$

where H is in cm and Θ is in degree days ($\Theta = \int (T_w - T_a) dt$).

The snow cover on sea ice, which is also not considered in Stefan's law, alters the heat budget and is therefore important to ice growth. Owing to the large temporal variations, the snow problem poses a great challenge for modelling work. Snow reflects most of the sunlight ($\sim 87\%$ compared to $\sim 50\%$ reflectivity of bare ice) and serves as a thermal insulator on the ice. The conductive heat flux (F_c) can be reduced by up to 50%, just by depositing a snow layer of a few centimetres. Model simulations indicate that the thick snow cover on Antarctic sea ice approximately halves the ice thickness in the Weddell Sea [Petrich and Eicken, 2010]. A possible way of extending Stefan's law by a set of equations to include the effects of a snow cover on sea ice growth is discussed by Leppäranta [1993]⁹. When the snow cover becomes thick enough to depress the ice surface below the sea surface, infiltration ice forms at the top surface of ice floes. This has serious consequences for the remote sensing of sea ice. Usually, snow is fairly transparent to microwave remote sensing wavelengths. This is not the case if the snow is wet or it contains layers of thin ice [Sandven and Johannessen, 2006]. The dielectric properties of snow-ice are different from that of pure snow, which changes the remote sensing signals from the ice. At the snow/ice interface the snow is quickly re-crystallised after melting, which also has an effect on radar return signals.

The analytic methods of thermal growth described above (i.e. Stefan's law and its modifications) are powerful tools for obtaining first-order approximations of sea ice growth. However, a precise quantitative analysis of sea ice growth requires numerical models. The model of Maykut and Untersteiner, proposed in 1971, is still the basis for understanding the thermodynamics of

⁸See Wadhams [2000].

⁹Another detailed discussion about the influence of snow on the buildup of sea ice can be found in Doronin and Kheisin [1977].

sea ice [Wadhams, 2000; Lemke and Hilmer, 2003]. This model includes time-dependent vertical diffusion processes within the ice, time-dependent specific heat and thermal conductivity, effects of internal heating due to solar radiation and the storage of heat in the brine pockets¹⁰.

As we have seen, the limiting factors of sea ice growth are oceanic and solar heating, i.e. the heat fluxes into the ice from above and below. These heat fluxes also determine the ice melt starting with the onset of summer. In the Arctic the increasing insulation and rising air temperatures completely melt the thin snow layer, resulting in the formation of meltwater pools, which can cover a considerable area on the ice surface in the melt season. As the meltwater reduces the albedo of the ice, the melt ponds grow deeper and wider and their water works its way down to the underside of the ice. Through cracks and leads in the disintegrating ice cover the ocean absorbs more and more heat from solar radiation. This increases the oceanic heat flux and thus initiates the accelerated melting of the ice at the underside.

Antarctic sea ice responds quite differently from Arctic sea ice during the summer melt period. As the summer air temperatures rise only sporadically above 0°C around most of Antarctica, atmospherically-induced summer surface melting appears far less extensive than in the Arctic [Drinkwater and Liu, 2000]. On Antarctic sea ice, most of the thick snow cover is retained throughout the summer and insulates the ice from warm air temperatures. Melt ponds are therefore not common in the Antarctic. This is also due to the cold atmosphere that effectively cools the sea ice surface even during summer. Instead of surface melting, absorption of solar short wave radiation by the ocean through small openings and leads, and the resulting oceanic heat flux that exceeds the conductive heat flux are the most effective ice removal processes in austral summer [Drinkwater and Liu, 2000]. As a result, the desalination process is less effective and maintains a relatively higher mean salinity in Antarctic multiyear ice. In the Antarctic a large fraction of sea ice also continues to move seaward into high oceanic heat flux regimes after the ice growth stops. There it breaks up and eventually melts at the retreating edge [Wadhams, 2000].

As discussed above, the presence of brine and the associated phase changes mean that sea ice does not have a fixed melting point. When the upper sea ice surface initially receives a net heat flux into the ice, the sea ice therefore warms and melts on a microscopic scale, rather than reducing its thickness. The ice thickness starts declining, when the continued warming raises the ice temperature to the bulk melting point and surface ablation takes place [Petrich and Eicken, 2010].

Stefan's law shows that the ice growth slows as the ice becomes thicker with time. As there are always oceanic heat fluxes penetrating into the ice, at some point the ice growth stops. At this point the conductive heat flux out of the ice equals the oceanic heat flux into the ice. This maximum thickness can be calculated by setting $dH/dt = 0$ in equation (2.6) and using the proportionality between snow and ice thickness ($h = rH$):

$$H_{eq} = -\lambda_{si} \frac{T_a - T_w}{F_w} \left(1 + \frac{\lambda_{si} r}{\lambda_s} \right)^{-1}. \quad (2.11)$$

This maximum thickness lies at ~ 0.5 m for typical conditions encountered in Antarctic waters: $T_a - T_w = -20$ K, $\lambda_{si} = 2$ W m⁻¹K⁻¹, $F_w = 20$ W m⁻², $\lambda_{si}/\lambda_s = 10$ and $r = 0.3$ (i.e. flooding) [Petrich and Eicken, 2010].

¹⁰A thorough description of the Maykut and Untersteiner-model is given by Wadhams [2000].

As pointed out by *Doronin and Kheisin* [1977], sea ice can be regarded as an index of thermal interaction between the atmosphere and the ocean. In this sense the equilibrium thickness of multiyear ice (subsect. 2.1.2) is considered as a thickness that does not vary from year to year under given climatic conditions and is subject only to internal changes. The equilibrium thickness therefore indicates any trend toward climatic changes in the polar regions. Thus, in regions where a sea ice cover is not in its equilibrium state, additional sinks or sources of heat can be assumed [*Doronin and Kheisin*, 1977]. But variations in sea ice thickness can also be a result of the ice drift. The ice drift transforms level ice (i.e. purely thermodynamically grown ice) into deformed and ridged ice, and therefore significantly alters its thickness and morphology.

2.3 The drift of sea ice

A sea ice cover can be regarded as the moving interface between wind and ocean currents. The response of the ice cover to these forces are leads, pressure ridges and coastal polynyas. To understand the nature of ice drift, it is essential to consider all internal and external forces acting on moving sea ice. The momentum balance for drifting sea ice is expressed by Newton's Third Law of Motion, comprising all forces acting on a unit area of the sea ice cover:

Sea ice momentum balance

$$m \frac{d\mathbf{V}_i}{dt} = \boldsymbol{\tau}_a + \boldsymbol{\tau}_w + \boldsymbol{\tau}_c + \boldsymbol{\tau}_i + \boldsymbol{\tau}_t \quad (2.12)$$

where m is the mass per unit area, \mathbf{V}_i the ice drift velocity, $\boldsymbol{\tau}_a$ the wind stress, $\boldsymbol{\tau}_w$ the water stress, $\boldsymbol{\tau}_c$ the Coriolis force, $\boldsymbol{\tau}_i$ the internal ice stress and $\boldsymbol{\tau}_t$ the force due to sea surface tilt. With the term $\boldsymbol{\tau}_i$ the ice rheology is included into the balance. However, air stress, water stress and the Coriolis force are the dominant forces acting on sea ice [*Wadhams*, 2000]. Wind and ocean forcing of sea ice is therefore a classical boundary layer problem where wind is a purely external force, but the dynamics of ice and water are highly coupled [*Leppäranta*, 1998].

Wind stress and water stress can both be described by quadratic drag laws. As the oceanic boundary layer is much thinner than the atmospheric boundary layer, the difference between the drag of smooth ice and ridged ice is relatively greater for water [*Wadhams*, 2000]. Freezing of ice decreases the density stratification near the surface and thus supports the vertical momentum transfer. Thereby it increases the water drag. Melting on the contrary reduces the water drag [*Wadhams*, 2000]. The Coriolis¹¹ force, or more precisely the *Coriolis effect*, must be included because all governing equations for geophysical motions are written in a reference framework rotating with our planet. As a result, all observed bodies are accelerated in a certain direction due to Earth's rotation. In the Southern Hemisphere, the Coriolis force is turned by 90° to the left of the ice motion vector (in the Northern Hemisphere to the right). The Coriolis force takes its maximum at the poles and is zero at the Equator. As the Coriolis force is proportional to mass, it is much stronger for the motion of icebergs than for the drift of sea ice. Winds and ocean currents are the sources of internal ice stress. Each area within the ice cover is

¹¹*Gaspard Gustave Coriolis*, French Physicist (1792-1843).

affected by stress transmitted by the adjoining parts of the ice sheet. The extent to which a unit area of the ice cover is affected by the surrounding ice is a function of the mechanical properties of the ice [Wadhams, 2000]. But also the thickness distribution (see next section) is an important factor. In some climate models the term of internal ice stress is neglected, i.e. the ice drift is approximated by a "free drift solution". Other models allow for a free drift only as long as the ice is thinner than a preset threshold value (usually 4 m)¹². The last term in the momentum balance is the force acting on sea ice due to the tilt of the sea surface. Due to Earth's rotation, ocean currents, thermohaline effects and tides, the ocean is neither uniform nor at rest. Therefore, its surface does not necessarily correspond to the *geoid*. The geoid is a surface of constant potential energy that coincides with mean sea level over the oceans, i.e. the level of the ocean surface if it were completely at rest¹³. The surface topography, i.e. the tilt of the sea surface, causes a horizontal pressure gradient force which is balanced by the Coriolis force. The resulting equilibrium current is called *geostrophic current* (\mathbf{V}_{wg}) [Wadhams, 2000]. Over periods of a few days τ_t is negligible, but becomes stronger over periods of several months [Wadhams, 2000].

Empirical studies of ice motion confirmed that the vector of ice drift is almost in the direction of the geostrophic wind vector (\mathbf{V}_{ag}) and the ice drift speed is proportional to the geostrophic wind speed [Kottmeier and Sellmann, 1996]. The turning angle (θ_a) between geostrophic wind and surface wind (\mathbf{V}_a) is about 25°. Of the same size is the angle between the current velocity at the bottom of the oceanic boundary layer and the current velocity at the ice underside [Wadhams, 2000].

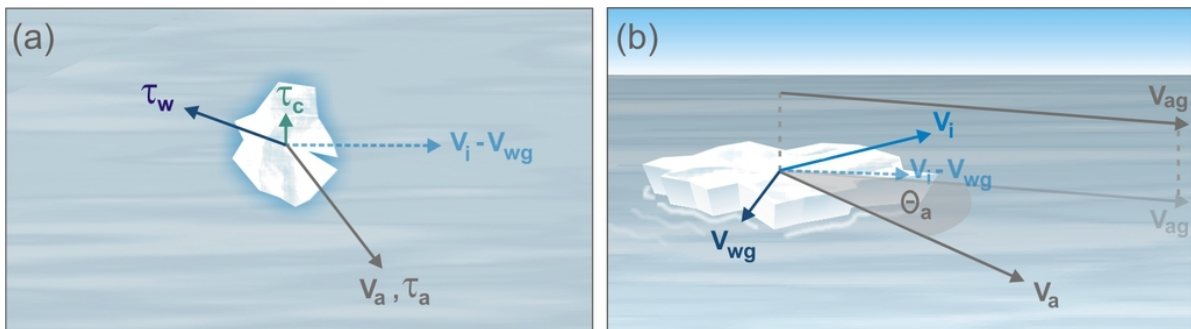


Fig. 2.10: (a) Momentum balance for a freely drifting ice floe in the Southern Hemisphere, as seen from above. The vectors of the forces are shown relative to the geostrophic ocean current [after Martinson and Wamser, 1990] (symbols: see text). The water drag is not directly opposed to the ice drift because the oceanic boundary layer is set in motion by the traction of the ice on it. \mathbf{V}_i : Ice drift with geostrophic ocean current. (b) Velocity diagram for free ice drift [after Kottmeier and Sellmann, 1996].

In a very simple case the sea surface tilt stress is set to zero. Furthermore, e.g. in the case of very thin ice, the Coriolis term is also zero. It follows that in the absence of a geostrophic ocean current, the ice drift is in the direction of the geostrophic wind, as the angles for wind and water are of the same size [Wadhams, 2000] (Fig. 2.10b). This enables the calculation of the ice drift from the geostrophic wind field which is available from model data. Studies on Arctic sea ice revealed that the ice moves at roughly 1% of the mean wind speed, and with an angle of 18° to the right of the surface wind. For the Weddell Sea the numbers were found to be 1.6% and 10° to 15° to the left, respectively [Haas, 2010, and references therein]. Average values of sea ice

¹²See Lemke and Hilmer [2003].

¹³See Stewart [2006] for details.

drift in the Weddell Sea are 0.5% to 1.5% of the geostrophic wind velocity [Schmitt, 2005, and references therein]. "Away from coastal boundaries, geostrophic wind explains more than 70% of the variance of daily ice motion in both winter and summer" [Kwok and Comiso, 2002b].

2.4 The sea ice thickness distribution

As we have seen in the previous section, the ice pack is subject to wind and ocean currents and is therefore in constant motion. As a result, the sea ice breaks up into single ice floes or larger aggregates of floes separated by open areas (so-called *leads*), which form as a result of ice drift divergence. Leads rapidly refreeze in winter and their newly formed ice can be easily crushed under convergent ice drift conditions. In regions of convergent wind or current directions the ice floes are pushed together and collide with each other. The resulting ice stress can become very large and breaks the ice into fragments, which are finally pushed onto and below the edges of the floes (Fig. 2.11a) [Haas, 2010]. The enormous power of converging ice floes is able to destroy whole ships, as dramatically shown by the loss of Ernest Shackleton's¹⁴ sailing ship *Endurance* in 1915 (Fig. 2.11b).

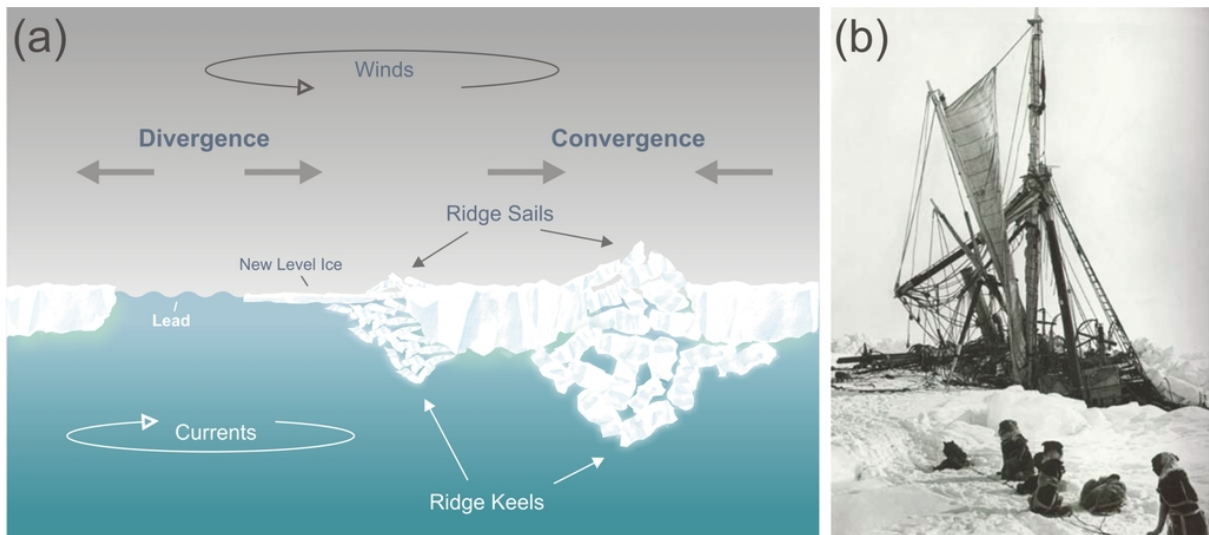


Fig. 2.11: (a) Pressure ridges formed by convergent wind and ocean currents. Ridges consist either of crushed thin ice from refrozen leads (left) or of thick, buckled ice floes (right) [modified from Haas, 2010]. (b) Ernest Shackleton's *Endurance*, crushed by ice in the Weddell Sea (November 1915) [from: www.coolantarctica.com].

Due to the dynamic interaction, the ice pack is composed of many different thicknesses of ice. Variable is also the snow layer on the ice and the network of leads in an ice cover. Pressure ridges are much thicker than thermodynamically grown level ice and obey some statistical laws. The sea ice thickness distribution is a very fundamental attribute of an ice regime, and the shape of its distribution indicates to some extent the degree of ice deformation. Hence, interpreting ice thickness data in terms of climate change is very difficult, as a locally increased production of pressure ridges may offset the thermodynamic thinning of sea ice [Wadhams, 1994]. As the ice thickness combines with the ice drift to the mass transport of sea ice, the thickness distribution regulates the transport of freshwater out of the polar oceans.

¹⁴Sir Ernest Henry Shackleton, Anglo-Irish explorer (1874-1922).

The theory of sea ice thickness distribution was first introduced by *Thorndike et al.* [1975]. Considering a region $\mathbf{R} = \{R, \mathbf{x}\}$ of area R surrounding some point \mathbf{x} , the thickness distribution is the probability density function (PDF) of ice thickness

$$g(H) dH = \frac{dA(H, H + \Delta H)}{R}, \quad (2.13)$$

where H is the ice thickness and $dA(H, H + \Delta H)$ the areal fraction of R covered with ice of thickness between H and $(H + \Delta H)$ [Haas, 2010]. The PDF $g(H)$ can therefore be interpreted as the likelihood that a point will have thickness H . The cumulative distribution $\int_0^H g(H') dH'$ is simply the fractional area of ice thinner than H [Babko et al., 2002] and, by construction, the integral of $g(H)$ over all thicknesses (from 0 to ∞) is one. In practice, $g(H)$ can be obtained by dividing a frequency histogram of measured ice thickness data by the bin-width (dH) [Haas, 2010]. It is important to note that $g(H)$ is the sample distribution function for the region \mathbf{R} and is therefore not necessarily equal to the underlying PDF [Flato, 1998].

The thickness distribution is a function of both time and position and is maintained by a balance of thermal and mechanical processes [Thorndike, 1992]. Its temporal development is given by

Ice volume conservation

$$\frac{\partial g}{\partial t} = \nabla \cdot (\mathbf{V}_i g) - \frac{\partial(fg)}{\partial H} + \Omega \quad (2.14)$$

which can also be interpreted as the conservation of ice volume. Here, $f(H, \mathbf{x}, t) = dH/dt$ is the thermodynamic growth rate of ice of thickness H at time t and at point \mathbf{x} , and Ω is a function that mechanically redistributes ice from one thickness to another [Wadhams, 1994]. The redistribution function itself is a functional of H and $g(H)$ and models the formation of pressure ridges and leads.

The first term on the right hand side of equation (2.14) describes the divergence of ice due to drift (see previous section). The ice divergence creates polynyas and leads in which new ice can form. The divergence removes ice of a certain thickness and creates a delta signal at zero thickness in the thickness distribution [Haas, 2010].

The term of thermodynamic growth has already been discussed in section 2.2. As $f = dH/dt$ is dependent on the sea ice thickness itself, it not only includes the ice growth, but also the melt of very thick ice due to the oceanic heat flux (Fig. 2.12). When averaged over an annual cycle, it therefore causes thin ice to grow thicker and thick ice to become thinner [Wadhams, 1994].

The distribution function Ω describes the process of deformation due to ice convergence, in which thin ice is transformed into thicker ice classes by mechanical processes, such as ridging and rafting. This term is the least understood and poses a serious problem to sea ice models, as it depends to a large extent on small-scale mechanics and friction between the ice floes [Haas, 2010].

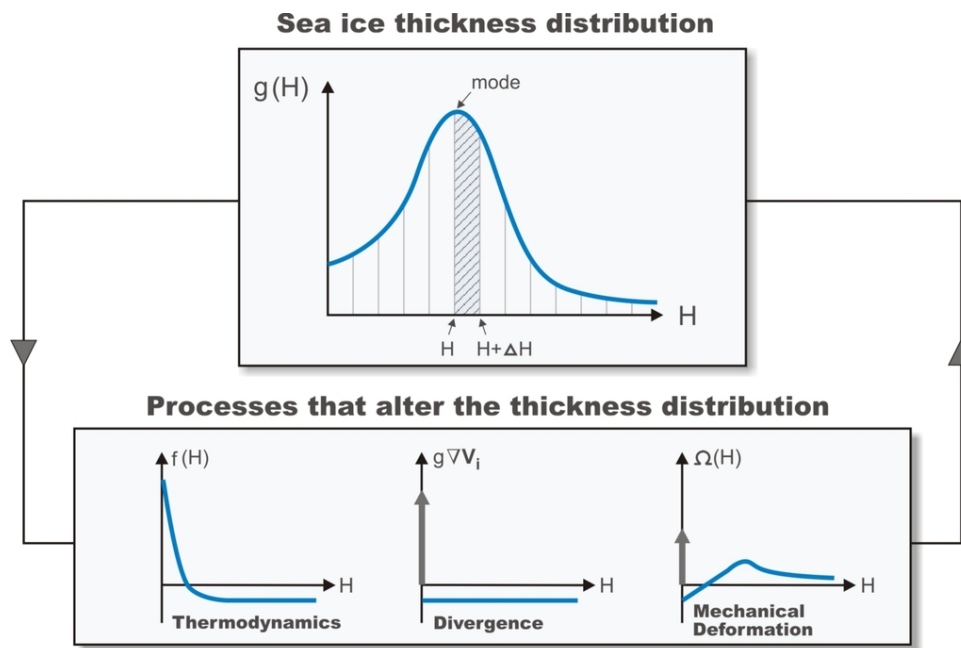


Fig. 2.12: Different physical processes that affect the sea ice thickness distribution [modified from Haas, 2010].

The different melt rates of sea ice depend on the ice thickness distribution. For example, the heat flux through pressure ridges is lower than through new level ice, which makes the pressure ridges melt faster [Haas, 2010]. Their keels may also reach into warmer deep water. On the other hand, the melt rate itself affects the thickness distribution, as demonstrated by melt ponds on the sea ice surface. These significantly reduce the surface albedo and thus absorb more energy than the neighbouring snow or ice surfaces [Haas, 2010]. The processes that influence the sea ice thickness distribution are therefore part of complex feedbacks and are therefore extensively studied.

Depending on the degree of deformation, pressure ridges can contribute 30% to 80% to the total volume of an ice cover [Haas, 2010]. The average ice thickness distribution in regions with large numbers of pressure ridges is determined by the prevailing atmospheric circulation regimes. In such regions the mean ice thickness is more determined by pressure ridges than by level ice [Haas, 2010].

As shown in figure 2.11, pressure ridge sails and keels have nearly triangular shapes. When multiyear keels erode to semi-elliptical profiles, the shape of a pressure ridge cross-section is therefore a triangle with rounded crests. Typical keel draft to sail height ratios are of the order 3-4:1 [Wadhams, 1994]. Very deep ridge keels can reach drafts of more than 40 m, with keel to sail ratios exceeding 10:1 [W. Dierking, personal communication, 2012]. Ridge sails in the Arctic can reach heights of up to 13 m, whereas the sail height of Antarctic ridges rarely exceeds 1 m [Allison, 1997]. The maximum height to which a pressure ridge can build depends on the ice composition.

The tail of $g(H)$ (Fig. 2.12), which typically comprises most of the ridged ice, was found to fit a negative exponential distribution [Wadhams, 1994]. Consequently, the sail heights and keel drafts show a similar distribution.

As mentioned in chapter one, little is known about regional ice thickness distributions in the Antarctic, due to the lack of systematic measurements. However, repeated surveys and ob-

servations - like the *Polarstern* expeditions "Winter Weddell Sea Project" (WWSP) in 1986, "Winter Weddell Gyre Study" (WWGS) in 1989 and "Winter Weddell Outflow Study" (WWOS) in 2006 - provided thickness distributions mainly from ice core drillings and laser profiling, but also from ground penetrating radar (GPR) measurements and EM-surveys. Observations during WWSP showed that the modal ice thickness was about 50 cm to 60 cm and that observed maximum keel drafts of pressure ridges were about 6 m [Wadhams, 1994].

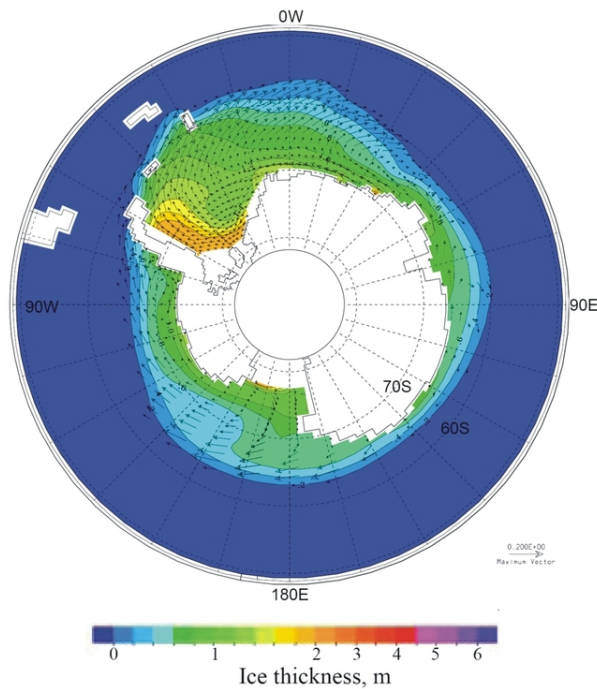


Fig. 2.13: Model results of mean sea ice thicknesses (colours) around Antarctica for the winters 1985-1993. The arrows represent the mean ice drift [after Timmermann *et al.*, 2002].

Antarctic sea ice thickness is 0.87 ± 0.91 m, which is 40% higher than the mean level ice thickness of 0.62 m. The high standard deviation compared to the mean of 0.87 m reflects the highly variable nature of Antarctic sea ice thickness in different regions [Worby *et al.*, 2008]. The highest percentages of ridging are observed in the western Weddell Sea. Mean sea ice thicknesses in this region range from less than 1 m in the south to a range of 1.5 m to 2.5 m along the Antarctic Peninsula [Worby *et al.*, 2008].

The typical pattern of Antarctic sea ice thickness is shown in figure 2.13. The thickest ice is found near the continent, as temperatures are coldest in high latitudes and the ice shears along the coast. In the Atlantic sector the Weddell Gyre carries ice from the eastern Weddell Sea southward towards the Filchner-Ronne Ice Shelf and then northward along the eastern side of the Antarctic Peninsula [Wadhams, 1994]. The Peninsula forms a natural barrier for the drifting ice, where it is sporadically compressed and becomes thicker. The Weddell Sea is the region with the highest amount of perennial ice in Antarctica.

Annual Antarctic fast ice tends to grow to a maximum thermodynamic thickness of 1.5 m to 2.0 m [Worby *et al.*, 2008, and references therein]. But in the Weddell Sea pack ice zone the ice rarely grows thermodynamically to more than 0.5 m. A recent study compiling data from the ASPeCt programme found that the long-term mean and standard deviation of total

2.5 Variability and trends of Antarctic sea ice

2.5.1 Variability

The large-scale variability of the global sea ice cover has been studied since 1978 using satellite passive-microwave data. The two most important parameters to quantify the expansion of the sea ice cover are: (1) The sea ice extent (i.e. the integrated sum of the areas of all data elements with at least 15% ice cover) and (2) the sea ice area (i.e. the sum of all actual ice areas) [Comiso, 2010]. The Antarctic sea ice extent shows a strong seasonal cycle (Fig. 2.14) with a minimum in February (austral summer) and a maximum in September (austral winter). Whereas the growth season takes about seven months, the decay period takes only five months. This can be attributed to the oceanic heat flux, which moderates the ice growth in autumn/winter and accelerates the retreat of the ice in spring/summer [Comiso, 2010].

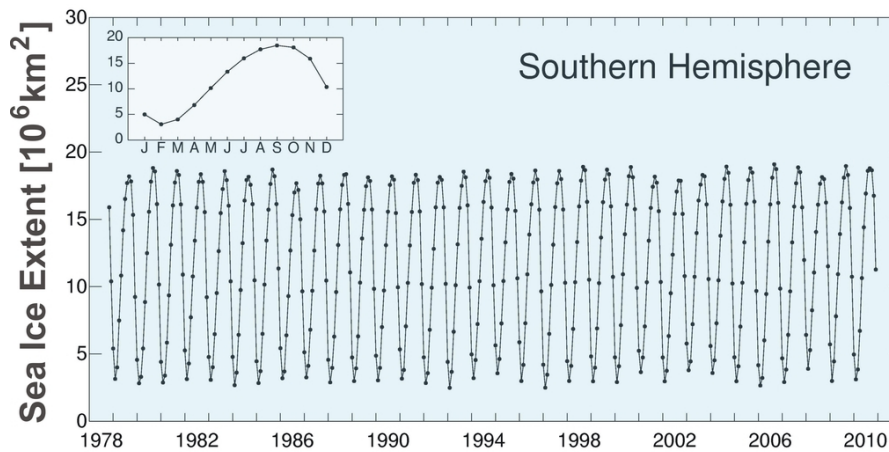
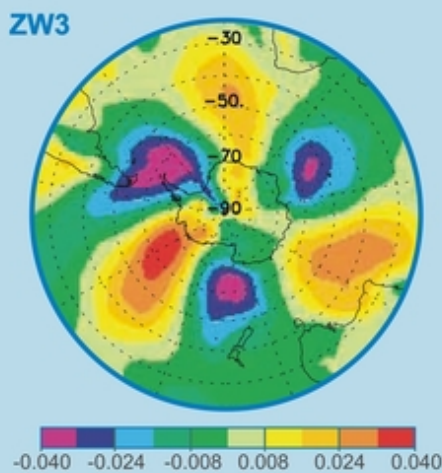
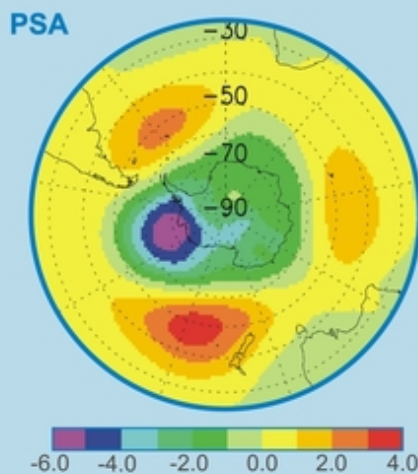
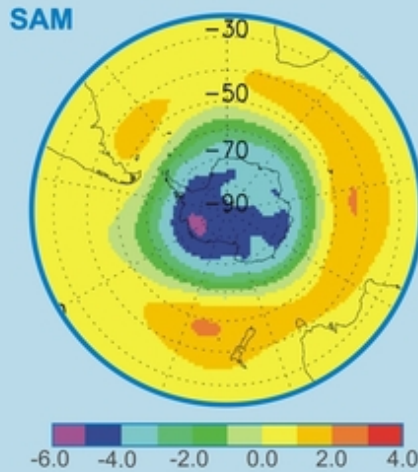


Fig. 2.14: Time series of the extent of Antarctic sea ice (monthly averages). The inset shows the annual cycle, which is computed as a 33 years average (1978-2010) of the monthly mean values [after Parkinson and Cavalieri, 2012].

The September sea ice extents in the Southern Hemisphere in the period 1978-2006 range from a maximum of $18.9 \times 10^6 \text{ km}^2$ in 2006 to a minimum of $17.5 \times 10^6 \text{ km}^2$ in 1986. The February ice extents range from a maximum of $3.75 \times 10^6 \text{ km}^2$ in 2003 to a minimum of $2.46 \times 10^6 \text{ km}^2$ in 1993 [Cavalieri and Parkinson, 2008]. The interannual variability of the sea ice extent anomalies in austral summer (February) is much larger than that in austral winter (September). The time period with the most rapid decay of southern sea ice is January. During February a large fraction of the coastal areas around Antarctica is already ice-free. When the ice freeze-up starts in march, these areas are again covered with thin ice. In September the sea ice extent reaches its maximum, and in October it starts to retreat. The decline of the ice cover becomes very rapid in November and continues throughout December and January until a new cycle of ice growth starts.

The variability of Antarctic sea ice parameters is strongly influenced by ocean-atmosphere modes of climate variability in the Southern Hemisphere. The dominant modes are shown in the box on the next page. These modes are also present in the 850 hPa height anomaly field as EOF1 (SAM), EOF2 (PSA) and EOF3 (ZW3) and explain 27-33%, ~22% and 9% of the total variance, respectively [Schmitt, 2005].

Modes of Climate Variability in the Southern Hemisphere



The *Southern Annular Mode (SAM)* - also known as *Antarctic Oscillation (AAO)* - is the dominant pattern in the tropospheric circulation variability of the Southern Hemisphere. Its signature is a zonally symmetric (wavenumber 0) meridional seesaw in atmospheric mass between 45°S and south of 60°S. The SAM involves zonal winds and alternation of mass between these latitudes. Strongest negative correlations are found in the coastal areas near the Antarctic continent and in the Ross and Amundsen Seas. Strongest positive correlations are concentrated over the Indian and southwest Pacific Oceans.

The *Pacific South America Pattern (PSA)* represents the high latitude response to the *El Niño Southern Oscillation (ENSO)* events in the tropical Pacific. During warm events (*El Niño*) it consists of a low pressure centre east of New Zealand, a high pressure centre in the subpolar southeast Pacific (Bellinghousen and Amundsen Seas), and another low pressure centre over the South Atlantic. The PSA pattern responds to cold events (*La Niña*) with the opposite phase for all three anomalous centres [Yuan and Li, 2008].

The *Zonal Wave Three (ZW3)* is the major asymmetric part in the large-scale atmospheric circulation of the extratropical Southern Hemisphere. It is quasi-stationary and has a maximum near 50°S. Its position is determined by the distribution of the mid-latitude land masses, so that its ridges roughly coincide with the southern continents. ZW3 is a dominant feature in meridional winds on daily, seasonal and interannual time scales [Raphael, 2007]. In some years, however, an eastward propagating zonal wavenumber-2 pattern, known as the *Antarctic Circumpolar Wave (ACW)*, dominates.

SAM, PSA: Linear regression coefficients of standardised climate indices on sea level pressure. The unit is hPa per one unit standard deviation of each index [Yuan and Li, 2008].

ZW3: Eigenvector of the leading EOF mode of standardised anomalous meridional wind at 300 hPa [Yuan and Li, 2008].

SAM & SAO

The SAM has the form of a meridional dipole with the node centred at 45°S. The SAM explains 50% of the monthly mean sea level pressure (SLP) variance over Antarctica [Gong and Wang, 1999]. It has also been identified in various other pressure height levels, surface temperatures and zonally averaged wind fields. In the SAM the latter show strongest anomalies in the upper troposphere [Thompson and Wallace, 2000, and references therein].

The variability of the SAM can be objectively expressed as the difference in the normalised zonally averaged SLP between 45°S and 65°S, which defines the SAM-Index [Gong and Wang, 1999]. Alternative definitions of the SAM-Index are the first EOFs of the Southern Hemisphere extratropical SLP, geopotential height or zonal winds, respectively. In the high index state the subtropical highs develop stronger and the subpolar lows develop deeper, and vice versa in the low index state. A high SAM-Index represents a stronger westerly circumpolar flow and is also associated with a significant cooling over Antarctica, with correspondingly low geopotential heights, and a warming over the Antarctic Peninsula [Kwok and Comiso, 2002a; Gillet *et al.*, 2006]. Since the 1960s the SAM exhibits a significant positive trend toward its positive phase

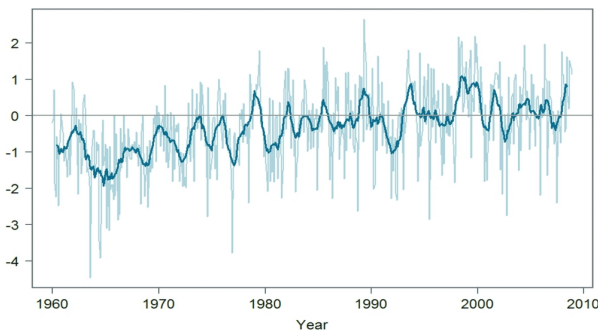


Fig. 2.15: SAM-Index (EOF-1 of SLP) after <http://jisao.washington.edu/data/aao/slp>. Thin line: monthly mean values. Bold line: 12 months running means.

and several model studies have furthermore linked the trend to global warming [Thompson and Solomon, 2002].

The SAM was also found to show a strong seasonality, with the lower troposphere (850 hPa) showing largest variability during May-October. The less active seasons with low variability correspond to times when the polar vortex is strong with westerly winds (austral winter: June-August) or when the polar vortex is weak or easterly (February-March) [Thompson and Wallace, 2000]. When considered as monthly time series over long periods, the spectral distribution of the SAM is dominated by decadal variability [Yuan and Li, 2008].

The main impact of a high SAM-Index on the Antarctic sea ice area is a pronounced dipole pattern between increased sea ice concentrations (SIC) in the eastern Ross/Amundsen Sea and decreased concentrations in the Bellingshausen/northern Weddell Sea (Fig. 2.16). This pattern has the form of a standing wave and is referred to as *Antarctic Dipole* (ADP). It is also found in surface air temperature fields and, moderately, in SLP fields. The ADP is the dominant mode of variability in the Antarctic sea ice field (EOF1 of SIC) and tends to propagate eastward within its basins (see below) [Yuan and Martinson, 2001]. It is therefore affected not only by SAM, but also by the other climate modes in the Southern Hemisphere.

(Fig. 2.15). "Positive" means that pressures over Antarctica are relatively low compared to those in the mid-latitudes [Marshall, 2003]. The index is therefore highest when the normalised high latitude SLP values are lower than those in the mid-latitudes and both time series are strongly anticorrelated. The positive trend is strongest in austral summer (December-February) and not present in austral spring (September-November) [Jones *et al.*, 2009]. It was shown that the trend in the SAM is largely due to photochemical ozone loss in the southern polar stratosphere, and

several model studies have furthermore linked the trend to global warming [Thompson and Solomon, 2002].

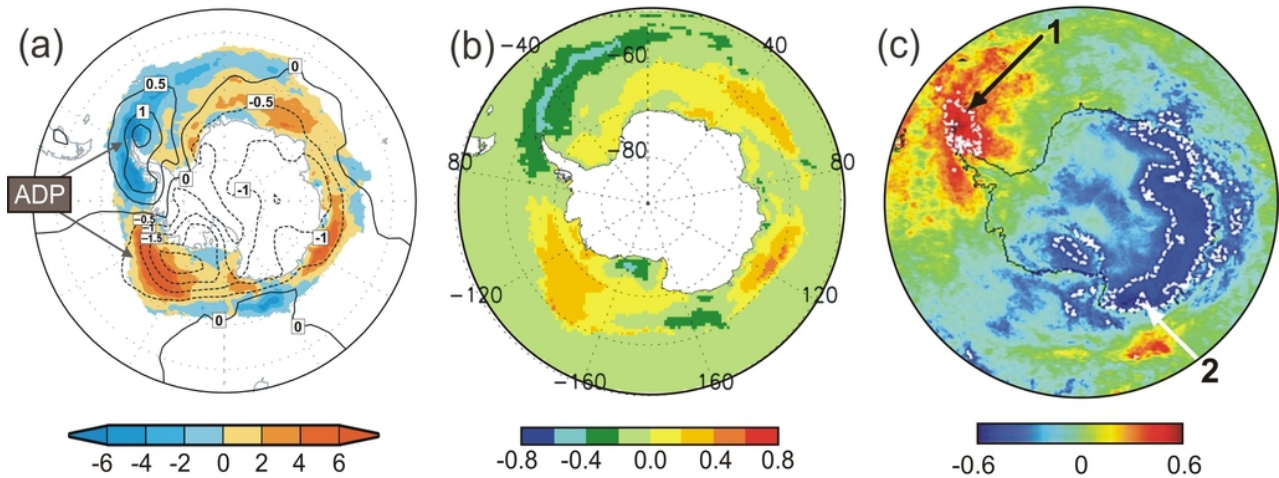


Fig. 2.16: The impacts of the SAM on the southern ocean sea ice area. **(a)** Regression map of the satellite-based Antarctic sea ice concentrations (shaded) and air temperature at 2 m (contour) anomalies on the standardised AAO-Index (1979-2002). The regression coefficients indicate changes in the ice concentration (%) and air temperature ($^{\circ}\text{C}$) corresponding to one unit deviation change in the SAM-Index [Liu *et al.*, 2004]. ADP: Antarctic Dipole. **(b)** Correlation coefficients between sea ice concentration anomalies (lag 2 months) and time series of the SAM (1978-2002) [Yuan and Li, 2008]. **(c)** Correlation maps obtained by regression of surface temperature anomalies (from AVHRR) upon the SAM-Index (1982-1998). The white lines mark the ± 0.4 positive (1) and negative (2) correlation levels [Kwok and Comiso, 2002a].

According to Liu *et al.* [2004], one positive unit of deviation change in the AAO-Index goes along with increases in SIC of $\sim 3\%$ to 7% in the eastern Ross/Amundsen Sea and a decrease of the same magnitude in the Bellingshausen/northern Weddell Sea. Recently, Yuan and Li [2008] found that the response of sea ice on the large-scale atmospheric patterns is largest after a delay of two months (Fig. 2.16b).

The changes in SIC are a consequence of surface heat flux and ice advection. During times of high SAM-Index polarities an anomalously strong cyclonic circulation in the southeast Pacific (Amundsen Sea) leads to southerly winds with an associated equatorward mean heat flux at the surface in the Ross/Amundsen Sea, which enhances sea ice growth [Liu *et al.*, 2004]. The strong surface westerlies associated with positive phases of the SAM induce an enhanced Ekman drift to the north, that transports sea ice and cold water equatorward. This leads to thinner ice, more open water areas and increased ice production near the coast. The new ice is advected northward, leading to an increased ice thickness away from the coast [Liu *et al.*, 2004].

Contrary, in the Bellingshausen/northern Weddell Sea (around the Antarctic Peninsula) a high SAM-Index leads to a strong poleward heat flux through warm northerly winds and reduces sea ice growth in that region (Fig. 2.16a,c) [Stammerjohn *et al.*, 2008]. Furthermore, a high SAM-Index shifts the strengthened westerlies southward, which results in stronger ice advection away from the peninsula, particularly in the western Weddell Sea. As noted by van den Broeke [2000], the pronounced south-north orientation of the peninsula makes it more sensitive to circulation changes with a zonal component than other sectors of the Antarctic coast. The strengthened westerly flow during high SAM-Index transports relatively warm air from the Pacific sector over the Antarctic Peninsula. Additionally, part of the flow veers at the mountain chain and becomes more northerly, leading to a greater advection of warm air from lower

latitudes into the peninsula region [Marshall *et al.*, 2006, and references therein]. Also Kwok and Comiso [2002a] confirmed that the warming at the peninsula over the period 1982-1998 can largely be attributed to the positive trend of the SAM. The rising surface temperatures in the sea ice region (Fig. 2.16c) can be interpreted as an increase of the area of thinner first-year ice in winter and longer periods with open water in summer. There is generally only little relation between the SAM and the position of the ice edge [Kwok and Comiso, 2002a]. The winter ice edge position in the peninsula region is more related to meridional (north-south) winds that modulate the ice drift [Harangozo, 2006, and references therein]. Especially in the ADP region the SAM is detectable in the timings of autumn-winter sea ice advance and spring-summer sea ice retreat, which together determine the ice season duration [Stammerjohn *et al.*, 2008]. The highest covariability is found between sea ice advance (March-May) and SAM, as the equatorward expansion of the ice is physically unconstrained (no continental boundary to the north). The advance of sea ice may therefore more readily capture climate signals, e.g. through storm forcing. The sea ice anomalies are strongest when SAM and ENSO (see below) peaks coincide, indicating that the high latitude response of the sea ice field to ENSO is modulated by SAM [Stammerjohn *et al.*, 2008]. Overall, the SAM affects sea ice less than the other climate patterns [Yuan and Li, 2008].

The semi-annual oscillation (SAO) is another climate oscillation with roughly symmetric pattern. Because of ocean heat storage, the cooling of air masses at the ocean-dominated latitude 50°S is delayed compared the cooling at the more continental-dominated latitude 65°S during the autumn equinox [Meehl, 1991]. Due to the resulting temperature gradient, the low-pressure trough around Antarctica contracts and intensifies during the equinox in March. A similar effect leads to a contraction and intensification during the spring equinox in September: The air masses at 65°S warm more rapidly than those at 50°S , which again causes a larger temperature gradient between the two latitudes. In June and December the low-pressure trough expands and weakens again [Meehl, 1991]. Thus, the SAO involves a twice-yearly intensification and poleward shift of the circumpolar atmospheric low-pressure trough. The SAO in the meridional temperature gradient induces responses in mean winds, cyclone characteristics and surface currents [Simmonds, 2003]. For example, in March and September the westerly surface winds are strongest south of 50°S whereas in June and December they are strongest north of 50°S [Meehl, 1991].

Whereas the SAM-Index is defined in the SLP anomaly fields, the SAO-Index is defined as the difference between the zonal mean SLP at 50°S and the zonal mean SLP at 65°S . However, this index shares much variance with the SAM-Index [Yuan and Li, 2008]. But in contrast to SAM, the variability of SAO is not necessarily controlled by the pressure variability over the Antarctic continent [Yuan and Li, 2008]. The SAO is also to some extent related to the Southern Oscillation and the ZW3 [Meehl, 1991].

The SAO is also partly responsible for the temporally asymmetric behaviour of the ice extent, which advances slowly equatorward in autumn and retreats rapidly in spring [Enomoto and Ohmura, 1990]. Watkins and Simmonds [1999] showed that the open water area in retreating Antarctic sea ice surges in November, when the large winter ocean/continental temperature gradient relaxes. During this time, the circumpolar trough advances northwards, crosses the sea ice edge and thus exposes the central pack to easterly winds. This induces an Ekman transport of sea ice to the south and thus rapidly increases the fraction of open water in the ice. In the study of Yuan and Li [2008] SAO has a stronger impact on the sea ice variability in the ADP than SAM.

ENSO, SOI & PSA

ENSO is the largest climatic cycle on decadal and sub-decadal time scales [Turner, 2004]. Usually, the trade winds in the equatorial Pacific region are pushing warm water masses westwards to the Indonesian coast. As a result, nutrient-rich water wells up close to the South American west coast and the warm rising air over Indonesia creates a low pressure centre. Contrary, the subsiding air masses create a high pressure centre over the South American west coast. During an ENSO event (*El Niño*) the trades in the western equatorial Pacific weaken - or sometimes

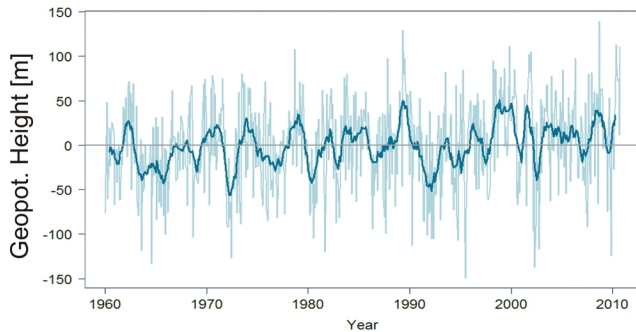


Fig. 2.17: PSA-Index after Yuan and Li [2008]. Thin line: monthly mean values. Bold line: 12 months running means. Negative (positive) peaks of the index mark an *El Niño* (*La Niña*) event.

[Trenberth, 1997; Collins et al., 2010]. The evolution of the ENSO cycle is expressed by the *Southern Oscillation-Index* (SOI), which is the normalised difference in surface pressure between Tahiti and Darwin (Australia). The Southern Oscillation refers to the seesaw in the surface pressure anomalies between these two regions. The tropical ENSO signal is propagated to southern high latitudes via the stationary Rossby Wave¹⁵. This wave train responds to the change in tropical convection due to the anomalous heating (or cooling), and forms the PSA¹⁶ pattern with a high pressure centre in the Amundsen/Bellinghausen Seas during *El Niño* conditions or a low pressure centre during *La Niña* conditions [Yuan, 2004; Baba et al., 2006]. The Amundsen/Bellinghausen pressure anomaly represents the largest action centre in the Southern Ocean pressure field [Yuan and Li, 2008]. During an *El Niño* event, it brings warm air from lower latitudes to the polar region in the Ross/Amundsen Sea sector (reducing the sea ice extent) and cold air from the Antarctic continent to the open ocean in the Bellinghausen/northern Weddell Sea sector (increasing the sea ice extent) [Hobbs and Raphael, 2010]. The opposite mechanism applies for a *La Niña* event. Via the PSA, ENSO is therefore strongly correlated with the ADP (Fig. 2.18b) and has the largest influence on southern sea ice among the climate modes [Yuan and Li, 2008].

The eastern Pacific and western Weddell Sea regions are very sensitive to extrapolar climate. The temperature anomalies in the ADP region were found to represent the largest ENSO signal outside the tropical Pacific [Yuan and Li, 2008, and references therein]. Yuan and Martinson [2001] therefore used the first EOF of the surface air temperatures south of 20°N (Fig. 2.18a) to predict changes in the sea ice extent anomalies associated with the ADP. They found that the ADP responds more consistently to *La Niña* conditions than to *El Niño* conditions.

The ADP pattern in the temperature anomalies is reversed in the sea ice anomalies (pos. temp.

even reverse direction for a few weeks - and produce westerly wind bursts [Stewart, 2006]. This launches an eastward propagating wave that carries warm water towards South America. The surface temperatures offshore of Ecuador and Peru warms by 2°C to 4°C and reduces the temperature contrast between east and west. This further reduces the trades and accelerates the development of *El Niño* [Stewart, 2006]. The opposite situation (i.e. anomalously cold water in the tropical east Pacific and anomalously warm water near Indonesia) is called *La Niña*

¹⁵The process of "atmospheric teleconnection" is described in detail by Liu et al. [2002] and Yuan [2004].

¹⁶The PSA pattern was first discussed by Karoly [1989].

anomalies→less ice, neg. temp. anomalies→more ice). The ENSO signal starts to affect the temperature and pressure fields at southern high latitudes in summer. After being triggered by tropical forcing, the ENSO signal in the ADP grows in the sea ice field as the Southern Hemisphere approaches austral winter. ENSO and ADP closely share interannual variance in periods from 3-5 years [Yuan, 2004].

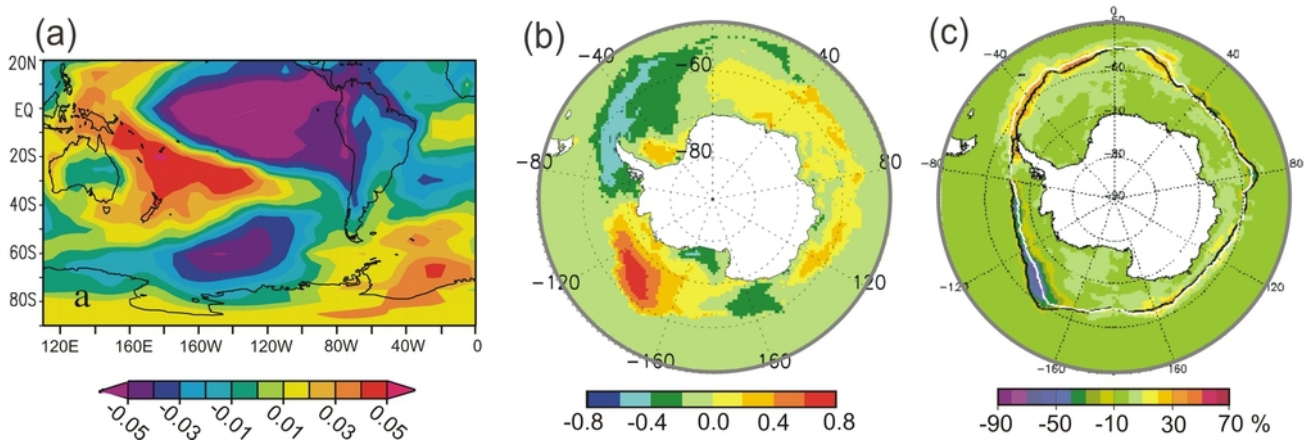


Fig. 2.18: The impacts of ENSO on the Southern Ocean sea ice area. (a) The leading EOF mode of the surface temperature anomaly in the Pacific and Atlantic south of 20°N (1975-1999). The eigenvector contains 18% of the total variance and suggests a link between the typical ENSO pattern in the tropical Pacific and the ADP with one pole in the South Pacific and another one in the Weddell Sea [Yuan and Martinson, 2001]. (b) Correlation coefficients between sea ice concentration anomalies (lag 2 months) and time series of the PSA-Index (1978-2002) after Yuan and Li [2008]. Note that the PSA-Index is low (high) for *El Niño* (*La Niña*). (c) Mean sea ice concentration at each month following *La Niña* events in the years 1985/89/96/99 subtracted from the mean sea ice concentration at each month following *El Niño* events in 1980/83/88/92/97. The figure shows the ENSO impact in the following September. The white (black) line indicates the mean ice edge following *El Niño* (*La Niña*) events [after <http://www.ldeo.columbia.edu/~xyuan/adp>].

The impact of ENSO on the ADP in SIC is strongest in the outer sea ice zone, whereas the influence on the centre of the pack after *El Niño*/*La Niña* events is rather small (Fig. 2.18c). Significantly cold surface air temperatures over the central/western Weddell and Bellinghousen Seas covary with warm temperatures over the Ross/Amundsen Seas during strongly negative peaks of the SOI (*El Niño*) [Kwok and Comiso, 2002b]. A signal with opposite polarity occurs during *La Niña* conditions, i.e. warm air temperatures over the central/western Weddell and Bellinghousen Seas and cold temperatures over the Ross/Amundsen Seas. A similar pattern was found in sea surface temperatures and ice surface temperatures [Kwok and Comiso, 2002b]. A record high sea surface temperature (SST) anomaly within a large midlatitude region of the south-central Pacific (Amundsen Sea sector) occurred during the mature phase of the recent *El Niño* (2009-2010) [Lee et al., 2010].

Hobbs and Raphael [2010] studied the variability of anticyclones (high pressure centres) associated with the PSA and their relation to sea ice. They suggested that the PSA-pressure system close to the Weddell Sea has a role in explaining the teleconnection of tropical Pacific variability to the Southern Hemisphere high latitudes. Furthermore, they concluded that meridional thermal advection, and not the ice motion, is the dominant mechanism by which pressure anomalies influence the sea ice field on seasonal and longer time scales. This is consistent with the findings of Yuan and Li [2008], who emphasise that sea ice fields share much less variance with wind

fields than they do with pressure and summer temperature fields.

Also earlier studies have indicated the importance of the teleconnection between Weddell Sea ice and the tropics. Historical sea ice data compiled from ship-based observations in the marginal ice zone (MIZ) were used to investigate composites of Weddell Sea ice extent at extremes of the ENSO cycle [Carleton, 1988]. There were lower SICs (more open water) in the December-January period of *El Niño* events compared with previous years. This could be attributed to an enhanced cyclonic atmospheric circulation during *El Niño* events, leading to increased southerly flow and divergence of the pack. Carleton [1989] investigated the relationships of the SOI with satellite-derived Antarctic sea ice extents (1973-1982), taking autocorrelations of all time series into account. Again the author found the most significant correlations in the Weddell Sea sector, with the ice extent changes lagging the SOI. Data of sea ice extent show a significant spectral peak in the Weddell Sea, with a quasi-quadrennial period resembling the ENSO signal [Gloersen, 1995], and detrended monthly sea ice edge anomalies, spatially averaged into 12° longitude bands, contain significant spectral peaks at periods of ~5 and 1.5-2 years [Yuan and Martinson, 2000]. Moreover, some sectors (including the Weddell Sea) show significant correlations between sea ice edge anomalies and the *Niño-3-Index*, which is the SST averaged over the eastern equatorial Pacific. It was also found that the cross-correlations between sea ice and the *Niño-3-Index* extend over a large range of lead-lag relationships, i.e. changes in sea ice extent presage extra-polar climate and vice versa [Yuan and Martinson, 2000]. This makes it difficult to identify any lag as representative and hence the direction of causality.

Also the upper ocean-atmosphere-sea ice system in the Weddell Sea responds to extrapolar climate variability. During *El Niño* events, the bulk stability in the Weddell Gyre increases, whereas the oceanic heat flux decreases [Martinson and Iannuzzi, 2003]. The bulk stability indicates the amount of surface buoyancy stabilising the surface water column and allowing sea ice formation. Changes in bulk stability, mixed layer salinity and the temperature of the circumpolar deep water show highest correlations to ENSO at the northern rim of the Weddell Gyre (57-60°S) [Martinson and Iannuzzi, 2003]. This was attributed to the enhanced (reduced) cyclonic forcing of the Weddell Gyre during *El Niño* (*La Niña*) events, and the associated migration of the northern rim of the gyre.

Some studies discussed above also found that the high latitude response to ENSO is modulated by SAM. For example, ENSO and SAM related SLP anomalies in the South Pacific are positive during *El Niño* and/or negative SAM (-SAM), and negative during *La Niña* and/or positive SAM (+SAM) [Stammerjohn et al., 2008]. The recent trend in SAM is consistent with the increased occurrences of *El Niño* events, and the variability of SAO also shows some association with recent trends in ENSO [Carleton, 2003].

ZW3 & ACW

The ZW3 was first discussed by *van Loon and Jenne* [1972]. *Raphael* [2004] introduced a ZW3-Index (Fig. 2.19) as the normalised deviation of the 500 hPa geopotential height values at the ZW3 ridges from its three-monthly mean. A high ZW3-Index is associated with strong meridional components in the flow, whereas a low ZW3-Index indicates a stronger zonal flow

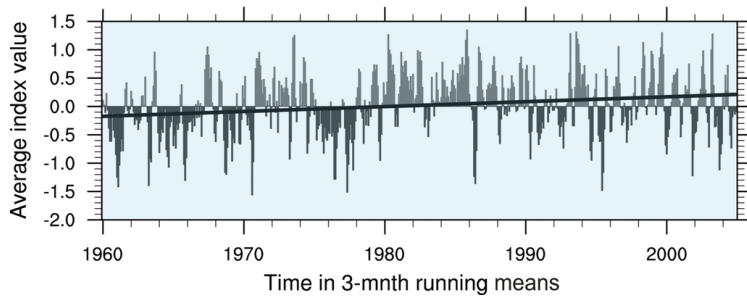


Fig. 2.19: ZW3-Index after *Raphael* [2007]. The index was calculated from the 500 hPa zonal anomalies of geopotential height and shows a positive trend (bold line) with a significant slope of 0.386. The trend represents a shift toward a more meridional flow pattern.

[*Raphael*, 2004]. "Where the anomaly of ZW3 is positive (in the ridges of the wave pattern) the flow is expected to be counterclockwise and diverging, and where it is negative (in the troughs of the wave pattern) the flow is expected to be clockwise and converging" [*Raphael*, 2007]. The largest energy loading in ZW3 occurs in 3- to 4-year periods, likely associated with ENSO variability, as the marked fluctuation in sign and magnitude of the ZW3-Index coincides with several ENSO events [*Raphael*, 2004; *Yuan and Li*, 2008]. During strong

SAM events, the flow is more zonal and leads to a weak ZW3 appearance [*Massom et al.*, 2008]. Although the 500 hPa height fields are dominated by a ZW1 pattern (90% explained spatial variance), the ZW3 (8% explained spatial variance) has a clear effect on the SICs. This is because the ZW3 forces an alternating pattern of equatorward (colder) and poleward (warmer) air flow and the southern edges of the pattern extend far enough to reach the sea ice field [*Raphael*, 2007; *Udagawa et al.*, 2009]. The strongest correlations were found between ZW3 and the third EOF (i.e. the principal component (PC) of EOF3) of the SIC field [*Raphael*, 2007]. This means, that ZW3 has only small influence on the ADP. The correlations were strongest in the period April-June, which shows once again that the response of sea ice to climate variability is strongest during its northward expansion in the growth season. The three regions of significant positive correlations - the Ross and Weddell Seas and off the Amery Ice Shelf (Fig. 2.20a) - are indicative of increased SIC and are influenced by southerly airflow. In the regions of negative correlations the flow becomes more northerly and the SICs are reduced, as the poleward flow of warm air forced by a strong ZW3 can lead to warmer upper layers and a deeper mixed layer in the ocean [*Raphael*, 2007].

Yuan and Li [2008] used a ZW3-Index which is slightly different to the one defined by *Raphael* [2007] and shares 36% of variance with their PSA-Index. The link to ENSO is supported by the fact that the strongest branch of the ZW3 occurs in the South Pacific and coincides with the central pressure system of the PSA. In the study of *Yuan and Li* [2008] the ZW3-Index is rather independent from SAM and SAO. This ZW3-Index has a large impact on the SIC in the ADP (more than *Raphael's* ZW3), which is quite similar to the impact of the PSA and thus much stronger than the impacts of SAM and SAO (Fig. 2.20b).

The ZW3 pattern in combination with a weak *La Niña* event in 2005 caused an extreme ice compaction and mean ice thicknesses of >5 m in the Bellinghousen and eastern Amundsen Seas. This could be attributed to the juxtaposition of an anomalous low pressure centre at 130°W and a high pressure centre at 60°W , which created persistent northerly winds across the

region in between [Massom *et al.*, 2008].

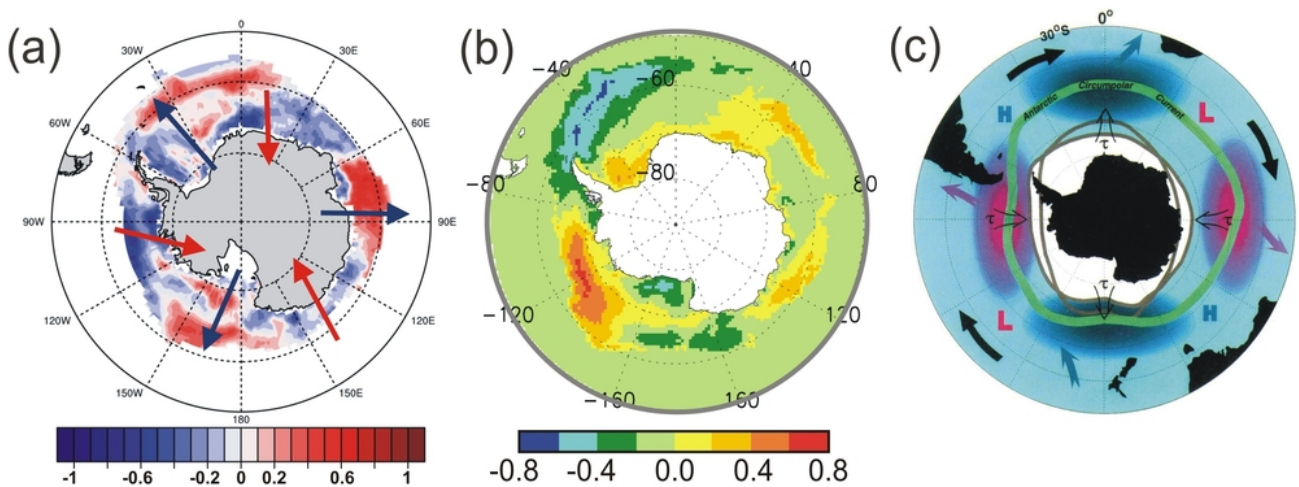


Fig. 2.20: The impacts of ZW3 and ACW on the Southern Ocean sea ice area. **(a)** Correlation of the ZW3-Index after *Raphael* [2007] and sea ice concentration for the period April-June. The blue (red) arrows indicate the anomalous meridional flow of cold (warm) air according to the troughs and ridges of the ZW3 pattern. **(b)** Correlation coefficients between sea ice concentration anomalies (lag 2 months) and time series of the ZW3-Index (1978-2002) after *Yuan and Li* [2008]. **(c)** Summary of interannual variations in SST (red: warm, blue: cold), SLP (bold H and L), meridional wind stress (τ), and sea ice extent (grey lines), together with the mean course of the ACC (green belt). Black arrows depict the eastward motion of anomalies during propagation of the ACW. The other arrows indicate the communications between the ACC and the subtropical gyres [White and Peterson, 1996].

Contrary to the ZW3 the Antarctic Circumpolar Wave (ACW) is a propagating anomaly. It has a zonal wavenumber-2 pattern (ZW2), propagates eastward at speeds of 6-8 cm s⁻¹ and has a dominant period of about 4-5 years. Hence, it takes 8-10 years for individual phases to travel around the Antarctic continent [White and Peterson, 1996]. The existence of the ACW has been detected in SST, sea ice extent, SLP and meridional surface wind, and it is most intense in the Pacific sector of the Southern Ocean. The behaviour of the wave is strongly associated with the air-sea interaction in this region and involves lower (higher) SLP followed by negative (positive) SSTs, more (less) extensive sea ice and oceanic upwelling (downwelling) [Carleton, 2003; Simmonds, 2003].

The initial warm (cold) SST anomaly that launches the ACW in the ice-ocean system first appears east of Australia, stretches eastward and coalesces one year later with warm (cold) anomalies, which originate in the Indian Ocean and spread eastward north and south of Australia. Further in the east, it merges with a warm (cold) anomaly that has moved from the Antarctic Circumpolar Current (ACC) north into the Peru Current and then west in the subtropics [Peterson and White, 1998].

Initially, the local ocean-atmosphere coupling in the ACC was thought to be fully responsible for the ACW [Qiu and Jin, 1997]. But the SST anomalies appearing east of Australia were shown to be directly linked to the ENSO cycle via a regional Hadley cell in the atmosphere [Peterson and White, 1998]. Although the ACW and ENSO were shown to be associated, the extent to which this is true is still unclear. Complex EOF analyses with SST and 500 hPa geopotential height fields revealed that the ACW is forced by the PSA pattern and that SLP anomalies lead SST anomalies by about five months [Cai and Baines, 2001].

A number of recent studies indicate that the ACW can be considered as a superposition of two

interannual signals in combination with the eastward flowing ACC. One signal is the ZW3 and the other one is the ZW2 pattern, which is responsible for most of the propagating character of the ACW and is strongly coupled to ENSO [Venegas, 2003]. As a result, the propagating ACW signal is only present at times when the ZW2 part dominates over the ZW3 signal. This

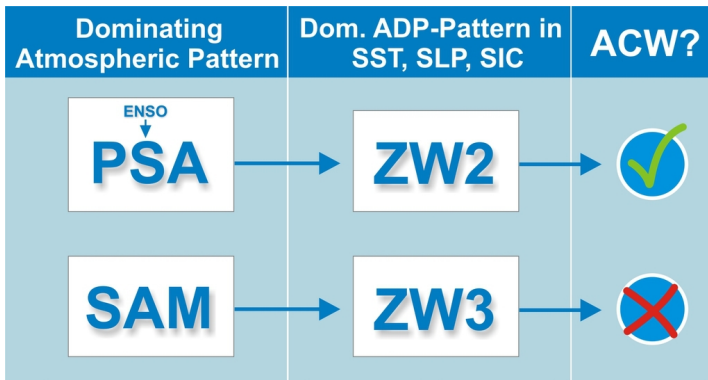


Fig. 2.21: The dominant atmospheric and oceanic patterns during years of ACW occurrence and years of non-propagating anomalies [after Udagawa *et al.*, 2009].

was the case in the period 1985-1994 [Cai and Baines, 2001; Venegas, 2003]. The SIC anomalies in the MIZ induced by the ACW are the result of both dynamic and thermodynamic effects: (1) ice compaction/dilation due to ice drift, (2) ice growth/melt due to cold/warm meridional winds, and (3) ice growth/melt due to SST anomalies in the ACC [Venegas *et al.*, 2001]. The ice pack is less concentrated during the passage of warm SST anomalies and poleward meridional surface wind anomalies. Furthermore, the eastward propagation of the ACW in the winter ice pack exhibits

maximum variability along the sea ice edge and extending 400-600 km into the ice field [Gloersen and White, 2001]. The variations in the SICs are directly linked to variations in the adjacent SST, and the upper ocean temperatures carry the memory of the ACW into the sea ice field from one winter to the next. Thus, the SST influences the SIC in the developing winter ice pack through its thermal inertia and by warming the overlying air carried by poleward winds over the sea ice [Gloersen and White, 2001].

Sea ice extent plays not a driving role in the ACW but is affected by it [Simmonds, 2003, and references therein]. The positive correlation peaks between sea ice extent and the Niño-3-Index propagate eastward at speeds corresponding to the circumpolar wave [Yuan and Martinson, 2000]. The strongest portion of the ACW signal in sea ice is found in the ADP region, suggesting that both are related. A much weaker signal propagates outside the dipole region. Udagawa *et al.* [2009] explain the four-year cycle of the ACW as follows: The negative and positive structure of the ADP is excited during periods of a strong PSA-Index and is retained in the ocean by thermal inertia, persisting until the next year. In the following winter, this signature moves eastward in association with the ACC. Two years later, the same atmospheric forcing as in the first year, but with reversed phase, again excites the dipole of the SIC and moves eastward until the following year. In the fourth year, the cycle starts again. Thus, the periodic atmospheric forcing excites the dipole, and the ocean makes the dipole propagate eastward, i.e. it plays a role as a carrier of the dipole. Udagawa *et al.* [2009] also revealed that a switch in the dominant atmospheric pattern in the period 1985-1994 was responsible for the propagating ACW signal. In the years of rotation, the PSA pattern with a four year cycle is predominant in the troposphere, whereas the SAM variance is subdominant. In the nonpropagating years the variance of the SAM dominates (Fig. 2.21).

These studies corroborate the view that the ADP is excited by extra-polar teleconnections with ENSO, and its anomaly is advected out of the dipole area by the ACC [Yuan and Martinson, 2001]. In other areas of the Southern Ocean (e.g. the central Weddell Sea or East Antarctica) ZW3 is more dominant, and propagating signals of the ACW are less distinct.

However, the ACW signal was also detected in the joint monthly SIC, SLP and ice drift anoma-

lies in the Weddell Sea. It can be identified as an oscillation with four-year period in the strength of the Weddell Gyre, which is associated with ice accumulation in the central Weddell Sea and is termed "Weddell Sea Oscillation" [Venegas and Drinkwater, 2001].

The ACW also seems to be associated with SAO, in that the weakening of the SAO in the late 1970s was followed by a strengthening of the ACW in the early 1980s. Contrary, the recovery of the SAO in the late 1990s was followed by a much weaker ACW [Simmonds, 2003].

All described climate modes are defined in different atmospheric variables and have, more or less, different spectral distributions [Yuan and Li, 2008]. But as we have seen, they are not completely independent from each other. For example, SAM and ENSO were found to be associated: 25% of the year-to-year variability in the SAM is linearly related to fluctuations in ENSO [L'Heureux and Thompson, 2006]. The changes in the sea ice field must therefore be considered as a superposition of effects caused by different climate modes. The atmosphere, the upper ocean and the sea ice alternatively force one another. This leads to feedbacks between these components and results in the observed variability of the system [Venegas and Drinkwater, 2001]. The physical and dynamical causalities for the described climate modes are discussed elsewhere [Yuan and Li, 2008, and references therein].

A recently conducted multivariate analysis of Antarctic sea ice confirmed the above described correlations of sea ice extent with ENSO and SAM (Fig. 2.22). But also correlations with other physical parameters were found, such as global air surface temperature, global sea surface temperature, atmospheric CO₂ concentration, total solar irradiance and ozone concentration [de Magalhães Neto et al., 2012]. Most of the significant correlations were found in the Pacific Sector of the Southern Ocean. The additional cluster analysis showed that in general the minimum sea ice extent shows highest covariability with ozone depletion and total solar irradiance, the mean sea ice extent covaries with global average air temperature, global average sea surface temperatures

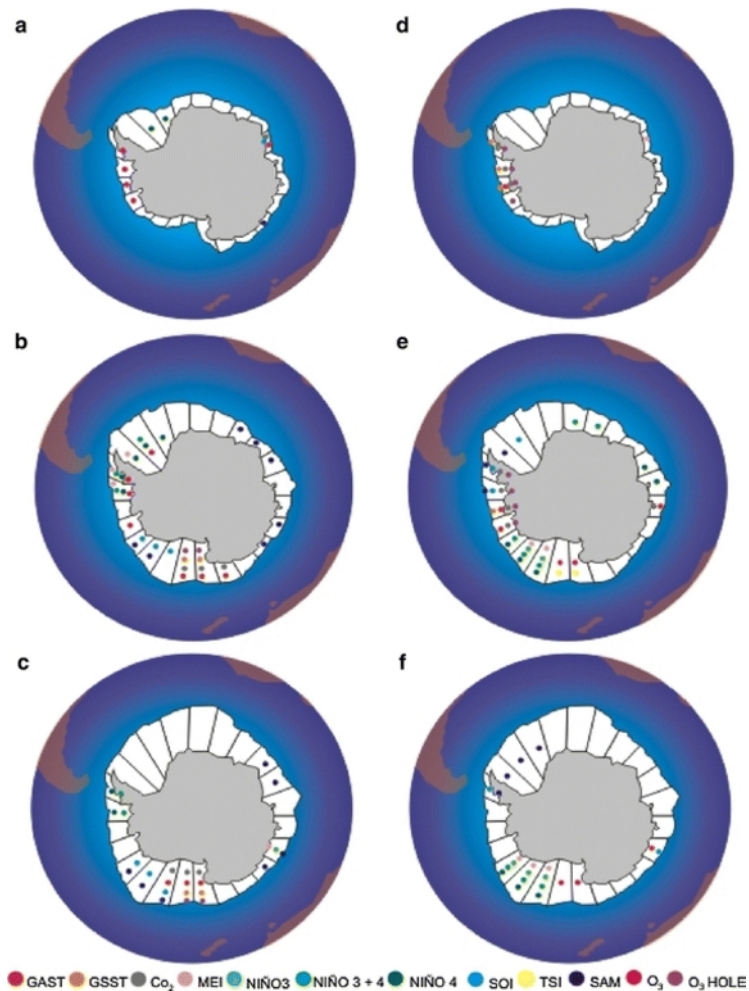


Fig. 2.22: The response of Antarctic sea ice extent to different climate-related parameters. The left column (a,b,c) shows positive significant correlations and the right column (d,e,f) shows negative significant correlations with minimum (a,d), mean (b,e) and maximum (c,f) sea ice extent [de Magalhães Neto et al., 2012]. GASST: Global average surface temperature, global sea surface temperature. GSST: Global sea surface temperature. MEI: Multivariate ENSO index. TSI: Total solar irradiance.

and global CO₂ concentrations, while the maximum sea ice extent shows highest similarity with SAM and ENSO variability [*de Magalhães Neto et al.*, 2012].

2.5.2 Trends

Contrary to Northern Hemisphere sea ice, the trends in the southern sea ice extent are weakly positive (Fig. 2.23 & Table I). For the entire Southern Hemisphere the significant trend in sea ice extent for the 30-year period **1979-2008** is $1.2 \pm 0.2\%$ per decade. For the same period, the trend in Weddell Sea and Indian Ocean ice extent is $1.2 \pm 0.5\%$ and $2.1 \pm 0.6\%$ per decade, respectively. In the Western Pacific the trend is insignificant ($0.8 \pm 0.7\%$ per decade). The strongest trends occur in the ADP region, with $4.9 \pm 0.6\%$ per decade in the Ross Sea and $-7.1 \pm 0.9\%$ per decade in the Bellinghousen/Amundsen Seas [*Comiso*, 2010]. The dipole pattern is therefore also present in trends of sea ice extent, and the same pattern is found in the trends of SICs [*Raphael*, 2007]. These trends are also consistent with the trends in surface temperature around Antarctica.

In austral autumn, the trend in southern sea ice extent is highest (3.1%), whereas in austral winter, spring and summer the trends are about the same (0.8%, 0.7% and 1.0%, respectively) [*Comiso*, 2010]. The trends show a mode-2 pattern around Antarctica, with positive trends at 0° and 180° and negative trends at roughly 270°E and 120°E. This pattern is most pronounced in winter and spring, whereas in summer and autumn the trends are strongest around West Antarctica and in the western Ross Sea [*Comiso*, 2010].

In the whole Weddell Sea sector the yearly trend is positive (Fig. 2.23), whereas the seasonal trends differ in sign: The winter and spring trends for the period **1979-2006** are negative and the summer and autumn trends are positive [*Cavaliere and Parkinson*, 2008]. For the sea ice extent minimum the trend is positive in the central Weddell Sea and for the sea ice extent mean and maximum it is positive in the eastern and negative in the western Weddell Sea [*de Magalhães Neto et al.*, 2012]. Significant trends were also found in the length of the sea ice season. Most of the Ross Sea underwent a lengthening of the sea ice season during the period 1979-1999. In the Amundsen Sea and almost the entire Bellinghousen Sea on the contrary the ice season has become shorter [*Parkinson*, 2002]. The contrasting trends for the 21-year period in large parts of the Bellinghousen Sea and in the northern/northwestern Ross Sea are significant at the 99% confidence level. In the Weddell Sea the results are mixed. The northwestern part has experienced a shortening of the ice season and the south-central part has undergone a lengthening of the ice season [*Parkinson*, 2002]. Considering the total change over the period 1979-2004, sea ice is retreating 31 ± 10 days earlier and advancing 54 ± 9 days later in the region west of the Antarctic Peninsula and in the southern Bellinghousen Sea [*Stammerjohn et al.*, 2008]. In the western Ross Sea on the contrary the sea ice is retreating 29 ± 6 days later and advancing 31 ± 6 days earlier. Whereas the highest variability occurs mainly in the outer pack ice regions, the high-trending regions lie largely within the inner pack ice regions [*Stammerjohn et al.*, 2008]. The sources for the sea ice trends are still not completely identified. It is clear that none of the significant trends present in the climate modes of the Southern Hemisphere (e.g. SAM, ENSO, PSA) can be translated into trends in Southern Hemisphere sea ice [*Liu et al.*, 2004; *Yuan and Li*, 2008]. Only *Raphael* [2007] found a relation between the long-term behaviour of ZW3 and the SICs off the Amery Ice Shelf, near 0° longitude and in the Ross Sea for the months April-June, i.e. for sea ice advance.

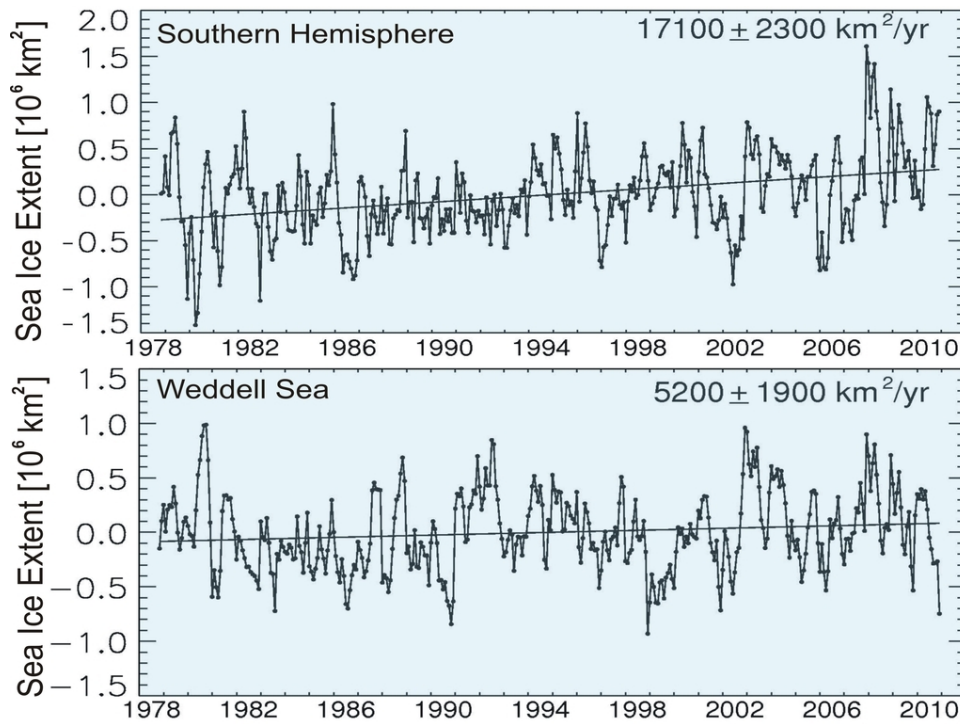


Fig. 2.23: Sea ice extent monthly deviations for the entire Southern Hemisphere and the Weddell Sea [after *Parkinson and Cavalieri, 2012*].

Table I: Trends in monthly Southern Ocean sea ice extent for 1979-2010 [after *Parkinson and Cavalieri, 2012*]

Sector/Region	Linear Trend [$\text{km}^2 \text{ yr}^{-1}$]
Southern Hemisphere	$17,100 \pm 2,300$
Weddell Sea	$5,200 \pm 1,900$
Indian Ocean	$5,900 \pm 1,100$
West Pacific	400 ± 800
Ross Sea	$13,700 \pm 1,500$
Bellinghousen/Amundsen Seas	$-8,200 \pm 1,200$

The sudden increase in Antarctic sea ice area in 2009 and 2010 compared to the years before was shown to be a result of the switch from one satellite sensor to another [*Screen, 2011*].

The contrasting trends between northern and southern sea ice are captured by few general circulation model (GCM) scenarios for increased global CO_2 levels. The hemispheric difference in these model experiments is partly a result of the large thermal inertia of the larger ocean area in the Southern Hemisphere, compared to the Northern Hemisphere [*Cavalieri et al., 1997*]. However, most of the contemporary climate models simulate decreases in Antarctic sea ice extent over the past 30 years [*Maksym et al., 2012*]. Many possible mechanisms responsible for the positive trend are discussed by *Parkinson* [2004], *Zhang* [2007], *Liu and Curry* [2010], *Turner et al.* [2009], *Sigmond and Fyfe* [2010] and *Maksym et al.* [2012]. However, a recent

study found that the observed asymmetric trends in Antarctic sea ice extent are largely due to trends in the local meridional sea ice motion in response to changing atmospheric pressure systems and winds [Holland and Kwok, 2012]. In the Weddell Sea the trend in northward sea ice drift is accompanied by a loss in sea ice concentration, which is mainly caused by ice dynamics [Holland and Kwok, 2012].

There are also approaches to extend the sea ice record further back into the pre-satellite era. This can be achieved by using historical information from whale hunters [de la Mare, 1997; Ackley et al., 2003] or ice cores [Curran et al., 2003; Foster et al., 2006; Wolff et al., 2006]. These studies indicate that after 1950 the ice extent shows a declining trend from about 59.3°S latitude to 60.8°S latitude, which corresponds to a 20% decrease.

To date, satellite-derived long-term trends can only be obtained for areal measures of sea ice, e.g. ice extent or concentration. Also the reconstructions of past sea ice only provide estimations of ice coverage and ice edge position, rather than ice thickness. For the measurement of today's sea ice thickness different techniques are available, which are described in the following chapter.

The forcings of sea ice variability described in the preceding pages are also expected to affect sea ice thickness. For example, at mooring AWI-207 - at the tip of the Antarctic Peninsula - an increasing SAM may reduce the sea ice thickness through rising air temperatures. The increasing PSA-index could result in less advection of thicker ice from the southern Weddell Sea towards AWI-207. Both mechanisms would explain the observed decline of the ice draft in this region (see chapter 4). Also the increasing ZW3 could influence the meridional ice drift and thus the measured ice draft at the tip of the peninsula. The relative influence of these modes on ice draft is tested in the last chapter of this thesis.

On the prime meridian the increasing southerly winds [Holland and Kwok, 2012; Schweggmann, 2012] associated with ZW3 are expected to advect more thicker ice from coastal regions to the north. This would imply rising ice thickness away from the coast, for example at the moorings AWI-231 and AWI-232, and frequent opening of coastal polynyas, where only few ice draft records exist (see chapter 4). The rising westerly winds associated with SAM could also contribute to a northward transport through Ekman drift. However, as seen on figure 2.22, correlations of different climate modes with sea ice concentration in the eastern Weddell Sea are sparse. More correlations with ice draft are therefore expected at AWI-207, which lies in the Antarctic Dipole.

As shown in chapter 4 (Fig. 4.1), the ice draft exhibits contrasting trends between AWI-207 (Antarctic Peninsula) and AWI-232 (prime meridian). ZW3 has an opposite polarity between these two regions. It is therefore expected that ZW3 - and thus meridional ice advection - is to some extent responsible for the contrasting changes in ice thickness in the southeastern and northwestern Weddell Sea.

The mooring position AWI-232 in the southeastern Weddell Sea lies close to the alternating Coats Land anomaly in sea ice concentration [Venegas and Drinkwater, 2001]. Thus, it can be expected that the anomaly leaves an imprint of the Weddell Sea Oscillation in sea ice thickness upstream in the coastal current at AWI-232.

"Ein Abenteuer, aber doch eines, das kalkuliert ist wie ein Geschäft, eine Verwegenheit mit allen Künsten der Vorsicht."

Stefan Zweig, *Der Kampf um den Südpol*, 1927

3

Measuring Sea Ice Thickness

This chapter provides an overview of the different techniques for measuring the thickness of sea ice. Most of the methods used today are indirect measurements. The purpose of this chapter is to compare the methods by their accuracies and advantages, and to highlight the capabilities of ULS measurements.

3.1 Drilling

Drilling a hole into the ice and lowering a ruler into the hole is the simplest and the most traditional direct method of measuring ice thickness (Fig. 3.1). Drilling is the only method which simultaneously allows the determination of the thicknesses of the snow cover, the ice draft and the ice freeboard [Haas, 2010]. Usually gas- or battery-driven motors are used for the ice augers. A very rapid technique is the hot water drill. Hot water is pumped with high pressure through a heavy bronze probe, which melts its way quickly down through the ice [Wadhams, 2000].



Fig. 3.1: Drilling of sea ice [credit: see list of figures].

Rothrock [1986] estimated that a mean ice thickness with a standard error of 30 cm could be obtained by drilling 62 independent random holes, and that this error could be reduced to 10 cm by increasing the number of holes to 560. To approximate the shape of $g(h)$ (thickness distribution) it may in some regions be sufficient to measure thickness along a profile of around 1 km length, with sample spacings of 10 m. In the work of *Eicken and Lange* [1989] the spatial autocorrelation function of the measured ice thicknesses in Fram Strait has its first zero at 185 m, implying that the samples become independent at this distance. But for other sea ice regions this is not necessarily the case. *Lange and Eicken* [1991] report decorrelation lengths smaller than 50 m in the outflow region of the Weddell Gyre. In other regions of the Antarctic large ice floes consist of consolidated pancake ice. These

are very homogeneous and their thickness variability is usually rather small. It is therefore not sufficient to sample only one or two particular floes in a certain area. The ice floes in a neighbouring area can represent a different age or ice class [Wadhams *et al.*, 1987]. Another problem with drilling is that it has to include the degree of ridging. Taking mean values from the results of drilling across unridged floes may underestimate the true mean ice thickness. Worby *et al.* [1996] therefore included ridges in their drillings and found a minimum mean ridge height of 0.5 m for the Bellinghousen and Amundsen Seas.

Another disadvantage of drilling is that it provides only snapshots, rather than time series of ice thickness. As it is mostly restricted to the accessible regions of an ice cover, the results of drilling also tend to be biased towards thin ice. On the other hand, drilling mostly does not account for newly grown level ice, which also contributes to the thickness distribution.

As they are very time-consuming and need a lot of work during expensive field campaigns, drillings usually have poor spatial and temporal resolution. Hence, it is not an appropriate method for determining the shape of $g(H)$. However, sea ice drilling provides a very accurate data set for validating the derived ice thicknesses of other methods [Wadhams, 2000].

3.2 Ground penetrating radar

Another in-situ method of measuring sea ice thickness is the ground penetrating radar (GPR). The best way of using GPRs is pulling a sledge over the ice with the radar mounted on it (Fig. 3.2). This enables to obtain profiles of several kilometres length. A GPR sends radar signals, generally between 50 and 250 MHz, in nadir direction through the ice. Due to the high di-

electric contrast at the ice-ocean interface, the signal is reflected and then detected by the instrument. The time delay between transmission and detection of the signal can be converted into ice thickness. This conversion depends critically on the knowledge of the velocity of the radar wave in the ice. As sea ice is a multilayered medium, where each layer is characterised by its density and the size of air pockets and brine inclusions, the propagation speed will vary with the changing dielectric constant [Holt *et al.*, 2009]. Therefore, the propagation speed is modelled based on theoretical assumptions about sea ice salinity, tem-



Fig. 3.2: Sledge with integrated GPR system [Holt *et al.*, 2009].

perature, crystal structure, brine inclusions and density [Holt *et al.*, 2009]. This also accounts for volume scattering effects and absorption loss inside the ice. The propagation speed can also be calculated from data obtained by drillings carried out parallel to the GPR-measurements. Most studies using GPR on sea ice have been carried out with limited success. However, Sun *et al.* [2003] demonstrated that GPR is suitable for displaying the position and micro-morphology of the sea ice bottom surface. Holt *et al.* [2009] used an ultrawideband radar with two channels: A low-frequency mode that operates at 50 MHz to 250 MHz to measure ice thicknesses in the range of 1 m to 7 m and a high-frequency mode that operates at 300-1300 MHz to capture thinner ice between 0.3 m to 1 m thickness. The reason for this selection is the changing penetration depth, which increases with decreasing frequency. The high bandwidth increases the vertical resolution of the GPR. The mean differences to drillings and EM-measurements are about 15 cm [Holt *et al.*, 2009].

3.3 The ASPeCt programme

The ASPeCt (Antarctic Sea Ice Processes and Climate) programme was established by the Scientific Committee on Antarctic Research (SCAR) in 1997. The initial focus of the programme was to gather information of sea ice observations from Australian, German, US and Russian icebreakers that operate in the Antarctic sea ice zone. Today, it contains the data of 23,391 individual ship-based observations collected from 81 voyages to Antarctica over the period 1981-2005, plus 1,663 aircraft-based observations [SCAR, 2009]. Besides the position, the data include hourly observations of total ice concentration and an estimate of the areal coverage, thickness, floe size, topography, and snow cover of the three dominant ice thickness categories within a radius of approximately 1 km around the ship [SCAR, 2009].

The ASPeCt data set has significant regional and seasonal gaps. Therefore it is not possible to estimate the interannual or even decadal variability of the sea ice thickness around Antarctica. However, ASPeCt represents the most comprehensive data set available on circumpolar Antarctic sea ice thickness [Worby *et al.*, 2008]. Worby *et al.* [2008] used the data set to approximate the sea ice thickness distribution around Antarctica by incorporating the ship observations into a simple ridge model. The ASPeCt data have also been used to validate passive microwave-derived ice edge locations [Worby and Comiso, 2004] and coupled sea ice-ocean models [Timmermann *et al.*, 2004].

3.4 Airborne laser profilometry

Airborne laser altimeters consist of pulsed laser diodes that are mounted on an airplane or a helicopter. The diodes send laser beams with a wavelength of 904 nm to 905 nm (infrared) to the sea ice surface and measure the distance between the airborne platform and the terrain below. The technique is also referred to as "*Airborne Laser Mapping*", "*LIDAR Mapping*" (LIDAR: Light Detection And Ranging) or "*Airborne Laserscanning*".

The distance to the sea ice surface is determined by measuring the time-of-flight of a short laser pulse. The location and altitude of the plane is determined by GPS-Sensors (GPS: Global Positioning System). The sea ice freeboard is calculated from the derived distance and information about the aircraft's altitude and the mean sea level. Altitude and sea level are known from GPS and modern geoid models. Finally, the freeboard height is used to infer the sea ice thickness.

The footprint of the laser beam on the ice surface is typically about 8 cm to 20 cm for altitudes of 30 m to 50 m. The typical precision of a laser measurement is about 2.5-5 cm [Tan *et al.*, 2012; Hvidegaard and Forsberg, 2002]. LIDAR profiles of sea ice freeboard can be many hundred kilometres long, depending on the range of the aircraft. In the early LIDAR measurements the raw data had to be high-pass filtered to remove the height variations of the aircraft. This led to biases in the final surface elevation data¹. Today, modern GPS sensors and inertial measurement units (IMU), that measure the yaw, pitch and roll of the aircraft, allow for a better correction of the data. Also the new geoid models contribute to a better accuracy [e.g. Forsberg and Skourup, 2005].

Modern altimeter systems work with movable mirrors that scan a swath (typically around 250 m wide) over the sea ice (Fig. 3.3). This expands the former quasi-one dimensional measurements to a two dimensional band of sea ice elevation data.

¹See Granberg and Leppäranta [1999].

The basic equation for the ice freeboard from altimetry is

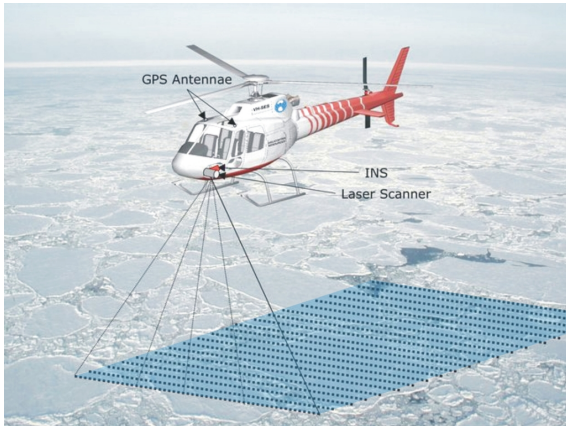


Fig. 3.3: LIDAR measurement of sea ice. INS: Inertial Navigation System [credit: see list of figures].

ice density and the density of salt water [Hvidegaard and Forsberg, 2002]. The primary error sources are measurement errors from the laser, IMU and GPS, errors in the geoid, filtering errors and errors in the conversion from ice freeboard to ice thickness. Taking all these error sources into account Hvidegaard and Forsberg [2002] calculated an accuracy of 1 m for their final ice thickness estimates.

LIDAR sensors can only collect data during good weather conditions and when the cloud cover is above the aircraft. It is not possible to measure during snowstorms, rain or fog, as the laser signal is scattered by water droplets or snow flakes. Like drilling, GPR and EM-sounding, laser profilometry only provides information about the temporal evolution of sea ice thickness when it is conducted regularly and in the same area over long periods of time. Altimetry from aircraft is not very expensive compared to other methods.

Many laser profilings of sea ice have been carried out in the Arctic since the early 1970s [Wadhams, 2000, and references therein]. Only few studies are available for the Antarctic [e.g. Dierking, 1995]. Most of these studies are mainly concerned with producing ridge statistics.

3.5 Electromagnetic induction sounding

The EM technique has become a widespread tool for measuring sea ice thickness [Pfaffling et al., 2005]. EM instruments were initially mounted on a sledge or kanu and pulled over the sea ice surface (like GPR), or they were lowered by a crane from the deck of an icebreaker. Modern EM instruments are either towed under helicopters, like the "EM-bird" (Fig. 3.4), or mounted on a fixed wing aircraft.

While sea ice is almost an electrical insulator, seawater has considerably higher conductivities. The EM instrument generates a primary EM field (typically 10 kHz to 100 kHz) which penetrates through the sea ice and induces eddy currents in the water below. These currents generate a secondary EM field which is sensed by a receiver coil inside the EM instrument [Haas, 2010]. The measured phase and amplitude depend on the distance between the eddy currents at the water surface (i.e. the ice underside) and the coil [Haas, 2010]. For an EM instrument in contact with the sea ice this distance is equivalent to the ice thickness. The

$$F = h_{GPS} - H_{laser} - N, \quad (3.1)$$

where F is the freeboard height, h the height of the aircraft determined by GPS, H the laser range and N the geoid height (see also figure 3.6). The contribution of the sea surface topography is more or less eliminated by high-pass filtering the data at the end [Hvidegaard and Forsberg, 2002].

Assuming isostatic equilibrium, the measured freeboard heights F can be converted into ice thickness T by a linear relationship: $T = K \times F$. The constant of proportionality K is usually calculated based on empirical values of snow depth,

instrument measures the apparent electrical underground conductivity, i.e. the thicker the sea ice, the smaller the apparent conductivity. If the EM instrument is towed by a helicopter or mounted to a plane, the height above the ice surface has to be determined by a laser altimeter or a sonar range finder.

To obtain the sea ice thickness, the measured height is subtracted from the EM-derived distance. Three main approximations are made for transforming the EM data into ice thickness: (1) The seawater conductivity is assumed to be known and constant. This assumption is generally satisfied. (2) The sea ice conductivity is assumed to be zero. This is not always true (see below). (3) The ice bottom is considered to be one-dimensional. This is true as long as level sea ice is considered [Pfaffling *et al.*, 2005]. A small bias is introduced into the ice thickness estimates by these approximations. This systematic error governs the helicopter EM ice thickness accuracy [Pfaffling *et al.*, 2005].

The induced eddy currents have lateral extents (footprints) of between 3.7 and 10 times the distance between the EM instrument and the water surface [Haas, 2010]. EM measurements therefore tend to underestimate the thickness of deformed ice, such as ridge keels, while mean values for full ridge cross-profiles agree reasonably well [Haas, 1998]. The currents are affected by water within ridged and deformed ice structures. The ice thickness is also underestimated when surface flooding occurs or water-filled layers form inside the ice. The ice conditions during the melt season introduce greater scatter into the ice-thickness versus apparent conductivity relation, as the ice conductivity can vary in greater ranges than in winter [Haas *et al.*, 1997]. Over level ice the accuracy of helicopter-borne EM measurements was shown to be better than 10 cm. However, it is still unclear how the EM method performs over ridged ice, compared to other methods [Haas, 2010, and references therein]. There may also be other effects that introduce errors, e.g. by influencing the EM field. For example, EM-bird movements may disturb the induction geometry. Like satellite altimetry, EM surveys yield the total (ice-plus-snow) sea ice thickness. However, the influence of uncertainties in the snow depth on the final thickness estimates is much less compared to altimetry [Haas *et al.*, 2010]. The snow and ice thicknesses are typically calculated from the apparent conductivity by using a one-dimensional multilayer model in which conductivity is assumed to vary only with depth [Reid *et al.*, 2003]. The AWI and the University of Alberta (Canada) use EM-birds (Fig. 3.5) that operate at frequencies of 3.6 and 112 kHz. The instruments have an overall length of 3.4 m with a coil spacing of 2.7 m. Their low weight (100 kg) allows the operation by any kind of helicopter [Haas, 2010].

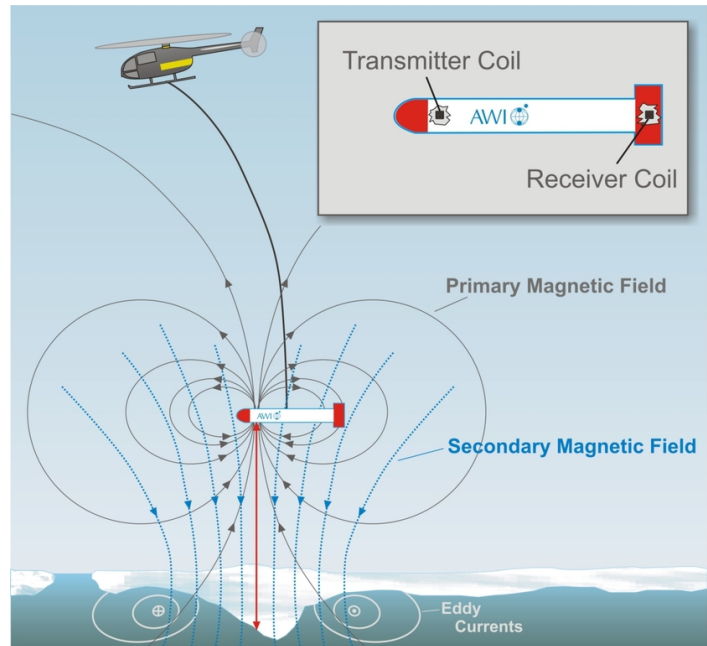


Fig. 3.4: The EM-bird measurement principle. The red line depicts the distance determined by the EM instrument [redrawn from: Holladay *et al.*, 1990]. The bird is operated 15-20 m above the ice surface.



Fig. 3.5: The EM-Bird on the helicopter deck of an icebreaker [credit: A. Pfaffhuber]

There have been several EM studies with fixed wing aircrafts and helicopters in the Arctic [e.g. *Haas et al.*, 2005; *Haas et al.*, 2010]. In the Antarctic, the EM-bird was used by *Haas et al.* [2008] to study the thickness distribution of an ice floe in the Weddell Sea. However, most of the studies applying the EM technique in the Antarctic were ship-based observations with portable or crane-lowered EM instruments [e.g. *Haas*, 1998; *Worby et al.*, 1999; *Reid et al.*, 2003; *Weissling et al.*, 2011].

3.6 Satellite altimetry

The measurement of sea ice freeboard by laser and radar satellite altimetry has developed rapidly during the recent decade. The laser altimeter GLAS on *ICESat* for example uses electromagnetic radiation at a wavelength of 1064 nm (near-infrared) and performs one measurement every 170 m with a footprint diameter of approximately 64 m. Similar to altimetry from aircrafts, the time delay between the transmission of the signal and the detection of the echo is used to infer the distance between the satellite and the terrain below. A radar altimeter, as carried by the *ERS* satellites, typically measures at around 13.8 GHz every 330 m, but with a footprint diameter of several kilometres [*Haas*, 2010]. Due to the pulse-limited signals and the typical orbit repeat period of 30 days, large areas of the sea ice are not covered by the altimeters. Sufficient accuracy for large areas can therefore only be obtained with significant spatial and temporal averaging [*Haas*, 2010]. The new radar altimeter carried by *CRYOSAT-2* has a better spatial resolution, due to a footprint size of approximately 250 m.

The orbit of a satellite, and thus the height above a reference ellipsoid (h_{ell}), can be determined with accuracies of a few centimetres. The ellipsoid is a sphere flattened at the poles and approximates the Earth surface. To obtain the mean surface elevation above the reference ellipsoid for the altimeter footprint, the measured distance, e.g. through laser altimetry, (H_{las}) is subtracted together with the geoid (N) and the dynamic sea surface height (Δh) from the orbit (Fig. 3.6a):

$$F = h_{ell} - H_{las} - N - \Delta h. \quad (3.2)$$

The dynamic sea surface height (dynamic topography) contains contributions from ocean currents, steric sea surface height changes, atmospheric pressure loading, and ocean and Earth

tides [Spreen *et al.*, 2006]. The geoid is not known precisely enough, therefore it is not possible to simply subtract the geoid from the measured total sea surface height above the ellipsoid in order to obtain the dynamic topography. As there are also no measurements of Δh , it has to be determined from the altimeter data themselves [Spreen *et al.*, 2006]. Therefore, satellite altimetry relies on the detection of open water as a reference level. Open water patches generally have a lower reflectivity and can be used as tie-points to interpolate the water level². As there are in most cases not only open water patches but also ice floes within the altimeter footprint, the retrieved sea surface is biased [Kwok *et al.*, 2009].

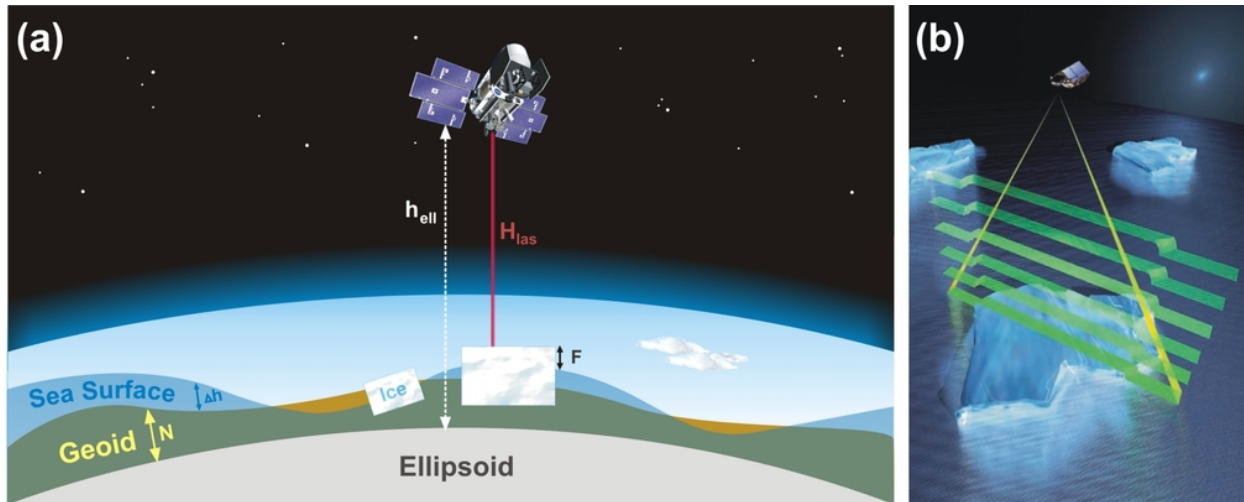


Fig. 3.6: (a) The principle of satellite laser altimetry. F : sea ice freeboard (including the snow cover), h_{ell} : orbit height of the satellite, H_{las} : measured distance, Δh : sea surface topography. (b) Satellite radar altimetry [credit for (b): ESA-AOES Medialab].

Laser and radar altimeters are different in the way the radiation penetrates into snow and ice. The infrared laser radiation is scattered at the upper snow surface, i.e. it does not penetrate through the snow layer on the sea ice. Radar signals on the contrary penetrate through fresh snow, and the backscattered signal is generally believed to originate from the snow/ice interface (Fig. 3.10). However, there are indications that radar signals are disturbed by old and metamorphic snow [Haas, 2010]. Due to the different penetration characteristics between laser and radar, the measured freeboard heights also differ. The equations for the conversion of the ice freeboard to ice thickness are therefore not the same. As a result, uncertainties in the knowledge of the snow thickness induce an error in the calculated ice thickness from laser altimetry which is twice as large as the respective thickness error in radar altimeter data [Haas, 2010]. For the conversion of ice freeboard to ice thickness the snow thickness has to be known and is usually taken from climatology (if available).

The sea ice drafts determined by the laser altimeter GLAS were found to be within 0.5 m of the ice draft measured by ULSs at the same location in the Arctic [Kwok and Cunningham, 2008]. The thickness error due to the combined uncertainty of ICESat freeboard and AMSR-E derived snow depth is 0.58 m [Yi *et al.*, 2011]. If the uncertainties in the ice/water density variables are additionally taken into account, the error in the thickness estimates increases to 0.7 m [Kwok and Cunningham, 2008]. It is also not entirely clear whether the satellite-derived freeboards represent mean values, modal values or maximum values [Haas, 2010].

Both laser and radar altimetry have been used to determine the sea ice thickness in the Arctic

²See Kwok *et al.* [2009] for details.

ocean [e.g. *Laxon et al.*, 2003; *Kwok and Cunningham*, 2008]. In the Antarctic, negative ice freeboards and flooded and refrozen snow are more common than in the Arctic. Moreover, snow depth climatologies, such as the ones for the Arctic, do not exist for the Antarctic. This complicates the satellite measurements of sea ice freeboard in that region. The freeboard elevations of Antarctic sea ice determined through radar altimetry by *Giles et al.* [2008] were found to be overestimated, most probably due to the snow cover on the ice. The snow cover on Antarctic sea ice consists of a mixture of different snow types, soft slabs, icy layers and slush [*Massom et al.*, 2001]. If the snow depth is underestimated, the ice thickness will be overestimated and vice versa. Therefore, snow and ice density and their influence on radar penetration need to be further investigated.

The first studies applying satellite laser altimetry over the Weddell Sea showed that *ICESat* provided a unique capability for measuring Antarctic sea ice freeboards [*Yi et al.*, 2011; *Zwally et al.*, 2008]. The altimeter has been successfully used for sea ice studies in single regions of the Antarctic [e.g. *Xie et al.*, 2011]. The first basin-scale study of Antarctic sea ice thickness using *ICESat* was provided by *Kurtz and Markus* [2012]. However, the studies also demonstrated that many assumptions have to be made for the freeboard retrieval, each of which leading to inaccuracies in the final result. For example, a laser altimeter is subject to cloud contamination, which can sometimes significantly reduce the amount of useful data. Moreover, as described above, laser altimetry suffers much more from uncertainties in the estimation of the snow depth than the radar technique.

3.7 Other satellite methods

Other methods use imaging satellite instruments to estimate sea ice thickness. As long as it is not yet covered by snow, thin ice has a warmer surface than thick ice. It is therefore possible to determine the thickness of snow-free ice up to 0.5 m thick by means of thermal infrared techniques, such as the AVHRR sensor³ [*Haas*, 2010]. For this method the surface air temperature over the ice has to be known. Similarly, passive microwave temperatures, as observed by SSM/I, can be used to derive thin ice thicknesses of up to 0.2 m [*Haas*, 2010].

As second- and multiyear ice has different surface properties compared to young ice, the strength of radar backscatter provides estimates on the relative amount of thick multiyear and thin first-year ice. This technique can also indicate the degree of ridging within an ice cover [*Haas*, 2010, and references therein].

Another method is currently developed for the ESA Soil Moisture and Ocean Salinity (*SMOS*) satellite, launched in November 2009. It uses 21 cm L-band microwave imaging to determine ice thicknesses of up to 50 cm. The thickness is derived from brightness temperatures, which are a function of ice concentration, the emissivities of ice and water, the water temperature and the bulk temperature of the ice. The uncertainties of the method range from 2 cm (for ice thicknesses of up to 10 cm) to 12 cm (for ice thicknesses between 40 and 50 cm). The advantage of this technique is its high temporal resolution. Contrary to other satellite missions *SMOS* is able to provide daily maps of ice thickness. However, the *SMOS* algorithm can not be applied to ice in the melting season [*Kaleschke et al.*, 2010].

Su and Wang [2012] used data from the Moderate Resolution Imaging Spectroradiometer (MODIS) on board the NASA satellite *Terra* to estimate the ice thickness in the semi-enclosed

³For a discussion of the method see *Yu and Lindsay* [2003].

Bohai Sea (China) with high accuracy. The ice thickness was obtained through an exponential relation between ice albedo and ice thickness.

3.8 Upward looking sonar

Sea ice draft measured by ULSs is a good proxy for ice thickness. The basic principle of a ULS draft measurement is transmitting ultrasonic sound pulses towards the surface and measuring the elapsed time for the sound signal to propagate through the water to the ice bottom and back. Knowing the sound velocity (c), the travel time (t) can be converted into a distance (Fig. 3.7a). With the precise knowledge of the instrument depth (z), the detected time intervals can be used to calculate the draft (d) of the sea ice:

$$d = z - c \frac{t}{2} \cos(\alpha). \quad (3.3)$$

When the ULS is positioned under an open water area, the measured sonar distance equals the ULS depth.

The instruments used for this thesis are the ULS types ES-300 V, ES-300 VI and ES-300 VIII, manufactured by Christian Michelsen Research (CMR) in Norway. These instruments operate with sound pulses of 300 ± 15 kHz, which corresponds to a wavelength of roughly 5 mm. The pulses are transmitted with 1 s offset in bursts of four pulses (Fig. 3.7b) by a piezo-ceramic transducer. The bursts are transmitted in intervals of 2 min to 15 min, where the length of the interval depends on the available battery capacity. The travel times of the echoes are recorded with a resolution of $4.3 \mu\text{s}$ or $13 \mu\text{s}$ and stored as 8 or 16-bit digitised voltage values. In this way, the ULS can record more than hundred thousand data cycles during deployment periods of several years. Furthermore, the instruments separately store the variable V_{env} , which is the highest value of the echo PDF. This *envelope voltage* is the logarithmically amplified echo amplitude, with the gain of the amplifier increasing approximately proportional to the square of the sound pulse travel time [Strass, 1998]. It can be regarded as a measure of the target strength of the ice/water interface (see box *Underwater Acoustics*). The sonars also contain a dual axis clinometer (tilt sensor), that measures the inclination angle (α) with an accuracy of 1° , a pressure sensor for determining the instrument depth (accuracy: 0.01 bar), a temperature sensor and a realtime clock. Tilt, temperature and pressure are measured at the same rate as the sound pulse travel times (2 min to 15 min).

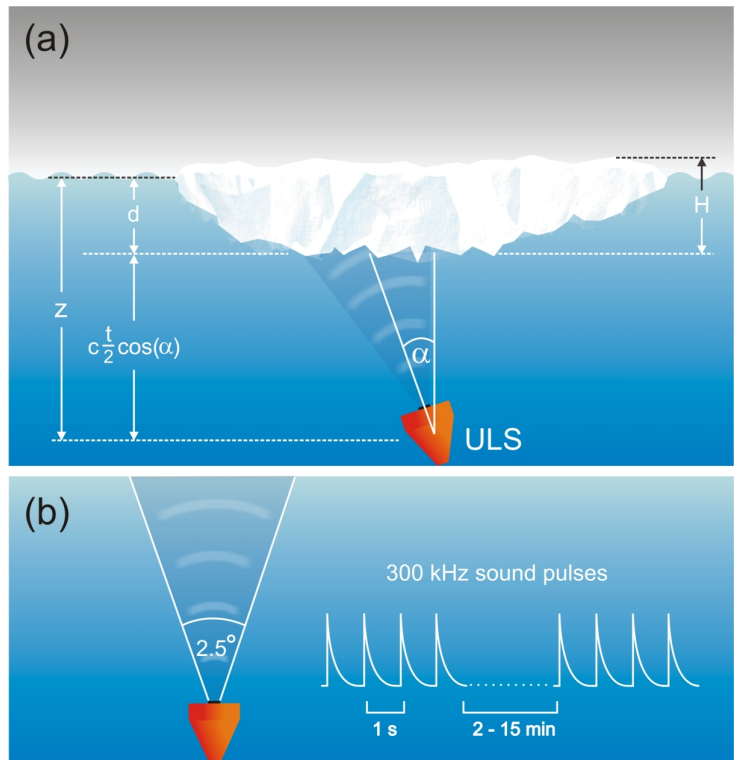


Fig. 3.7: The ULS measurement principle.

The measured pressure (p) is always the sum of the hydrostatic pressure (p_h) and the atmospheric pressure (p_a). The depth is therefore given by the relation

$$z = (p - p_a)/\rho_w g, \quad (3.4)$$

where ρ_w is the density of the seawater and g is the acceleration of gravity. If not taken into account, surface pressure variations may cause a small error in the measured distance. This implies that surface air pressure would have to be observed permanently at the mooring sites. This is not possible on an hourly or shorter basis in remote open ocean areas. The pressure data are therefore taken from atmospheric model reanalysis of the European Centre for Medium-Range Weather Forecasts (ECMWF). The data have a temporal resolution of 6 h and were completed by linear interpolation at the mooring positions. When the ULS-mooring position lies near the coast, the pressure data can alternatively be taken from coastal weather stations, like in the pioneering ULS study of *Melling et al.* [1995].

The opening angle of the acoustic beam of 2.5° at -3 dB⁴ (Fig. 3.8) (2° for ES-300 V) results in an ensonified surface window (footprint) of 7.5 m for an instrument at 170 m depth. This in turn results in a bias, as the window contains ice of different thicknesses.

The draft can be converted into total ice thickness (H_{tot}) by assuming isostatic equilibrium⁵:

$$H_{tot} = (\rho_w d - \rho_s z_s)/\rho_i. \quad (3.5)$$

Here, ρ_w , ρ_s and ρ_i are the densities of water, snow and ice, respectively, and z_s is the snow thickness. An alternative method is the use of empirical relations obtained from drillings in the Weddell Sea:

$$H_{tot} = 0.028 + 1.012d \quad (3.6)$$

[*Harms et al.*, 2001, and references therein]. ULS measurements are not free from uncertainties. The choice of the sampling rate is always a trade-off between approximation of the real sea ice thickness distribution and battery or data storage capacity. This choice is sensitive to the probability distribution of the ice drift velocity. For example, when the movement of the ice exceeds the length of the ULS footprint between two sonar bursts, the sea ice profile will be undersampled [*Melling et al.*, 1995]. When the sample rate is too high, large amounts of redundant data will occur [*Melling et al.*, 1995].

Another uncertainty arises due to the variation of the sound speed in the water column between ULS and the sea ice bottom. These are mainly due to seasonal changes of oceanographic conditions. The two-way travel time of the signal is therefore

$$T(t) = 2 \int_0^{R(t)} \frac{dr}{c(z-r, t)}, \quad (3.7)$$

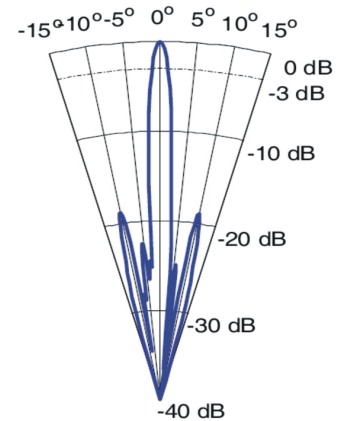


Fig. 3.8: The directivity pattern of the sonar transducer *Reson TC2078* [*Reson*, 2010].

⁴See appendix for more information on the ULS sound transducer.

⁵Note that isostatic equilibrium is usually determined by the whole ice floe.

where $R(t)$ is the range to the target, z the instrument depth and $c(x, t)$ the sound speed profile. In the Arctic, sound speed variations caused an apparent change in distance to the surface of 0.15 m to 0.2 m for moored ULSs at 72 m depth [Melling *et al.*, 1995]. Evaluating the integral (equation 3.7) for each sonar pulse is not possible. Density profiles, from which the sound speed

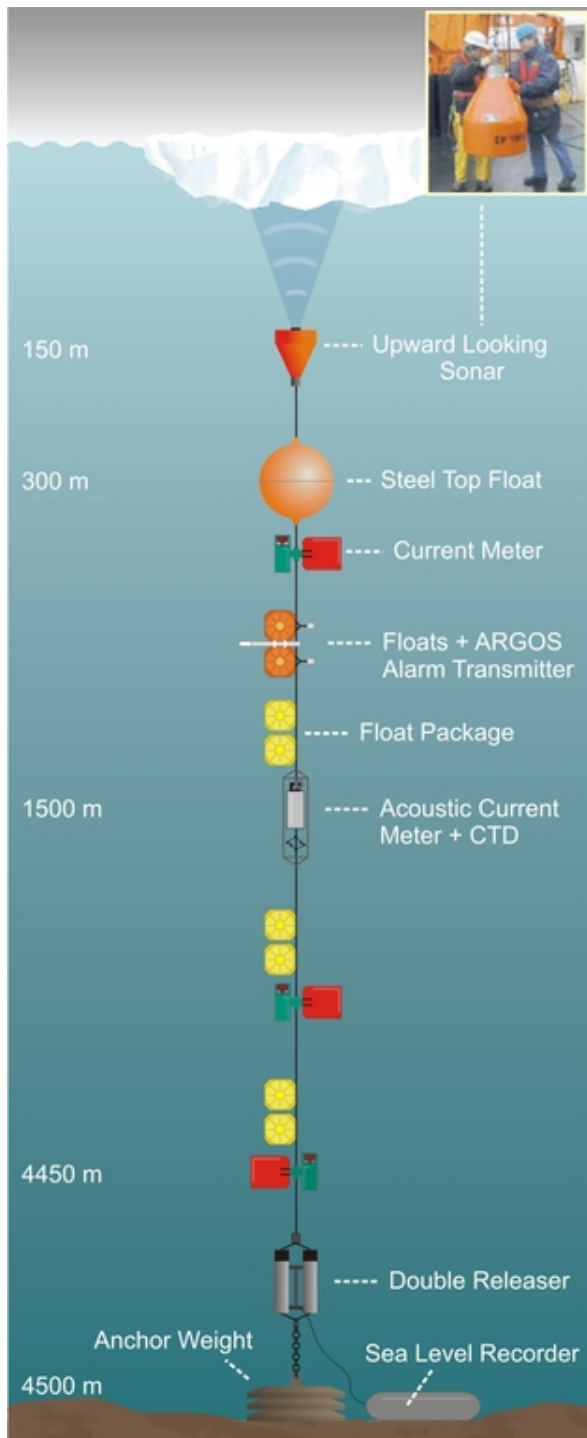


Fig. 3.9: Mooring arrangement with ULS.

instruments for sea ice monitoring has been published until today, and most of them were conducted in the Arctic Ocean. Vinje *et al.* [1998] used the ES-300 ULS for monitoring the ice thickness in Fram Strait. Other studies using ULSs in combination with ADCPs were mainly

can be calculated, are usually measured with CTD (Conductivity/Temperature/Depth) probes from ships and are therefore very sparse. Strass [1998] applied a mixed layer model combined with CTD measurements to generate vertical profiles of sound speed and calculated time series of vertical harmonic mean sound speeds. The time series (not shown) has a clear annual cycle and indicates changes in vertical mean sound speed of up to 2.5 m s^{-1} , which corresponds to a range error of 0.24 m. The most convenient way of coping with the effect of sound speed variations is to derive the range corrections from the apparent draft of open water areas that pass through the sonar footprint [Melling *et al.*, 1995]. The ULS instruments are attached to the top of an oceanographic mooring and placed around 150 metres below the sea surface to avoid the disturbing influence by surface gravity waves and the damage due to passing icebergs (Fig. 3.9). Moorings are the only available tool to perform oceanographic long-term observations at a fixed place in the ocean. A mooring consists of a *Kevlar* rope that can be up to several thousand metres long. An anchor (about 1 t weight) holds the mooring on the sea floor. To keep the rope nearly vertically in the water column, plastic covered evacuated glass spheres are attached to the rope. These buoyant floats also force the mooring back to the sea surface after the rope is released from the bottom weight. The rope can be released by a sound signal which is sent from a ship. A mechanical actuator, mounted directly above the bottom weight, receives the signal and separates the rope from the weight. Moorings may be equipped with various oceanographic measuring and sampling instruments, such as current meters, temperature and salinity sensors or sediment traps.

Only a limited number of studies applying ULS

carried out in the Canadian Beaufort Sea and investigated the seasonal evolution of the ice cover as well as the statistics of different ice classes, leads and pressure ridges [Melling and Riedel, 1995; Melling and Riedel, 1996; Melling and Riedel, 2005]. Apart from some very early studies - cited by Melling and Riedel [1996] - ULS instruments were also deployed in the Barents Sea [Abrahamsen *et al.*, 2006] and the Sea of Okhotsk [Fukumachi *et al.*, 2003]. In the Southern Hemisphere a single ULS was deployed off the coast of East Antarctica, but with limited success [Worby *et al.*, 2001].

Mounted on military nuclear submarines sonar systems allow for long-range, basin-scale transects and contributed to our knowledge of the evolution of Arctic sea ice thickness over nearly five decades [e.g. Kwok and Rothrock, 2009]. However, they were not performed in a systematic manner [Haas, 2010]. The accuracy of 0.25 m is largely determined by power and gain settings changed by the crew during the cruise, and due to the changing bias introduced by the varying footprint size along the submarine track [Rothrock and Wensnahan, 2007].

Sea ice draft can also be measured using ADCPs. But these measurements are less accurate than ULS measurements, mainly due to the applied hardware signal-preprocessing and the modelling of the sound speed profile [Shcherbina *et al.*, 2005; Hyatt *et al.*, 2008].

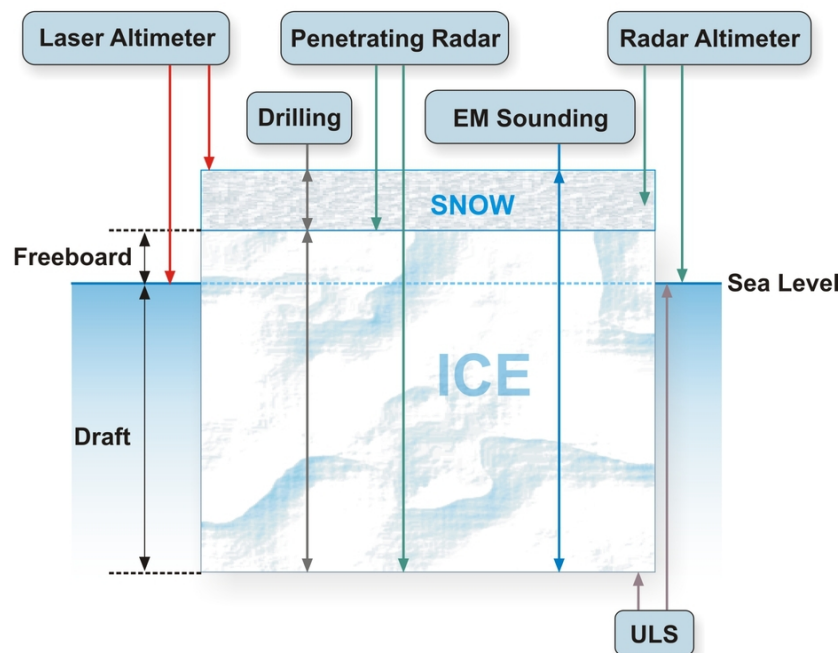


Fig. 3.10: Sea ice thickness measurement techniques and their capabilities [modified from: Holt *et al.*, 2009].

Underwater Acoustics

Sound in the ocean propagates as a longitudinal wave, i.e. as regular back-and-forth movements of water molecules. Because the water is compressible, this motion is accompanied by changes in pressure. These pressure changes can be detected by hydrophones. The instantaneous intensity of a plane sound wave of pressure p is

$$p = \rho_w c u, \quad (3.8)$$

where u is the velocity with which the fluid parcels oscillate back and forth (german: *Schallschnelle*) and c is the propagation velocity of the sound wave: $c = \sqrt{1/\beta\rho_w}$, where β and ρ_w are the adiabatic compressibility and the density of seawater, respectively. The proportionality factor $\rho_w c$ in equation (3.8) is called *specific acoustic resistance* (or specific acoustic impedance) of the fluid. With a mean underwater sound velocity of 1500 m/s the acoustic impedance of seawater is approximately 1.5×10^6 Rayle (1 Rayle = 1 kg m⁻²s⁻¹) [Urick, 1983]. The variation of the speed of sound in the ocean depends on temperature, salinity and pressure, as all three parameters influence the density of the water. The changes of the sound speed with depth pose a problem to the accuracy of the ULS data. The energy carried by a sound wave consists of kinetic energy of the particles in motion and potential energy of the stresses in the medium [Urick, 1983]. The energy crossing a unit area per second is measured by the intensity (I) of the wave, which, integrated over the duration of the wave, gives the energy flux density E :

$$I = p u = \frac{p^2}{\rho_w c} \Rightarrow E = \frac{1}{\rho_w c} \int_0^{\infty} p^2(t) dt. \quad (3.9)$$

The sound wave, which is transmitted by the ULS, reflected by the sea ice bottom and then detected by the ULS receiver, loses energy through different processes. For example, the wave is weakened by transmission loss on its way to the ice and back. Transmission loss occurs mainly due to the regular weakening of the signal as it spreads outward from the source, and due to attenuation. The term attenuation comprises different processes, such as scattering or absorption [Urick, 1983]. Sources for absorption are e.g. the viscosity of the water, or magnesium sulphate and boron molecules which are deformed by the pressure wave [Bradley and Stern, 2008]. A typical value of a sound absorption coefficient under winter hydrographic conditions is 0.067 dB/m for 300 kHz [Francois and Garrison, 1982].

Another source for the loss of energy is the reflection at the ice/water boundary, as the ice bottom consists of the skeletal layer (Fig. 2.3) which is not totally flat. Nevertheless, the laws of specular sound reflection can be applied for the ice/water interface.

For a sound wave in medium 1 (seawater) incident on medium 2 (skeletal layer) the reflection coefficient R for angles of incidence less than the critical angle is

$$R = \frac{(\rho_2/\rho_1) \cos(\alpha) - \sqrt{(c_1/c_2)^2 - \sin^2(\alpha)}}{(\rho_2/\rho_1) \cos(\alpha) + \sqrt{(c_1/c_2)^2 - \sin^2(\alpha)}}, \quad (3.10)$$

where ρ_1 and ρ_2 stand for the densities of the two media, α is the angle of incidence and c_1 and c_2 are the sound velocities in the two media [Langleben, 1970]. The reflection coefficient represents the ratio of reflected to incident wave amplitudes. It follows that the stronger the contrast in the acoustic impedances of the two media, the more wave energy is reflected. The reflection coefficient also increases with increasing angle of incidence [Langleben, 1970], until the critical angle is reached, where total internal reflection occurs. Given the much larger contrast in the acoustic impedances, the reflectivity of the water/air interface is higher than that of the water/ice interface. The amplitude reflection coefficients of a skeletal layer of smooth first-year ice at normal incidence ($\alpha = 0^\circ$), measured with wide-beam (7°) sonars at 300 kHz was between 0.017 and 0.04 [Garrison *et al.*, 1991].

The median coefficients measured with a narrowbeam (2.1°) sonar at 400 kHz on young sea ice in the Beaufort Sea were even lower ($R = 0.0044$) [Melling, 1998]. This means, that only a very small fraction of the initial energy of the sound wave is reflected by sea ice, and very strong sound transducers are needed. The reflection is not only reduced by the skeletal layer, but also when the sonar signal is diffusely scattered between the troughs and ridges at the underside of deformed ice. An echo therefore always consists of a coherently reflected component and an incoherently scattered component (noise or reverberation) from the skeletal layer and the deformed surface. The *signal-to-noise ratio* (S/N) is the ratio of the two components:

$$\gamma = \frac{I_{refl}}{I_{scatt}}, \quad (3.11)$$

where I_{refl} is the intensity of the coherently reflected signal and I_{scatt} is the intensity of the incoherently scattered signal. Theoretically, the S/N decreases with increasing frequency, surface roughness and sonar beamwidth [Stanton *et al.*, 1986].

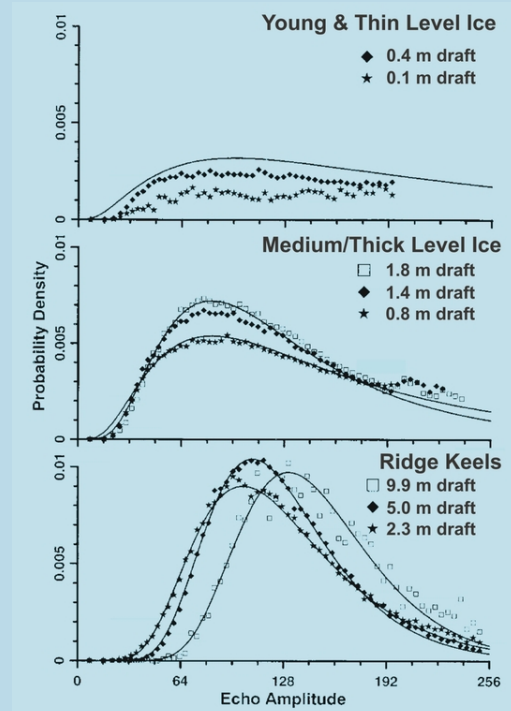


Fig. 3.11: Probability density of echo amplitude for three ice regimes segregated by range. Lognormal functions are plotted as curves [Melling, 1998].

But it was shown that also narrowbeam ULSs mainly detect the incoherent signal of sea ice, and coherent reflection is rarely received [Melling, 1998]. The PDFs of the ULS echo amplitudes fit a lognormal distribution [Melling, 1998]. As indicated by the lognormal fits, the echoes from level ice are on average stronger than those from deformed ice and also fluctuate more widely (Fig. 3.11). Furthermore, it was found that open water in leads has a reflection coefficient which is at least 10 times larger than that of a few centimetres of congelation ice [Jezek *et al.*, 1990].

The *target strength* (TS) refers to the echo intensity returned by an underwater target in relation to the incident intensity from a distant source [Urlick, 1983]. For a circular plate of flat, rigid skeletal ice in the far field it is

$$TS = 20 \log \left[R \left(\frac{\pi a^2}{\lambda} \right) \frac{2J_1(\beta)}{\beta} \cos(\alpha) \right] \text{ [dB]}, \quad (3.12)$$

where a is the radius of the plate, λ the acoustic wavelength, $\beta = [(4\pi a)/\lambda] \sin(\alpha)$ and J_1 the Bessel function [Garrison *et al.*, 1991]. The Bessel function describes the zeros in the diffraction pattern of a circular disc. For measurements with 80 kHz on skeletal layers at the underside of small cylindrical sea ice blocks and $\alpha = 0^\circ$, the TS was found to be about 10 dB [Garrison *et al.*, 1991].

The reflected signal is detected, if its intensity exceeds the detection threshold (DT) of the receiver:

$$SL - 2TL + TS - RL > DT. \quad (3.13)$$

Here, RL stands for reverberation level, TL for transmission loss and the source level (SL) refers to the initial intensity of the wave at the time of transmission.

"The first principle is that you must not fool yourself - and you are the easiest person to fool..."

Richard Feynman, 1974

4

Data and Methodology

4.1 Data

4.1.1 ULS data

The first six ULSs were deployed in November 1990, on the transect spanning the Weddell Sea from Kapp Norvegia to Joinville Island at the tip of the Antarctic Peninsula. They were recovered and redeployed in 1992 and measured until the next recovery in 1995, yielding more than four years of ice draft data. However, half of the data were lost, due to flooded instruments or lost moorings. Furthermore, the data output of the remaining instruments was partly reduced for unknown reasons, so that their success rate was about 86%.

From 1996 on, the measurements were concentrated on the prime meridian, with six ULSs (Fig. 4.1). At the peninsula AWI-207 continued measuring in the years 1996 and 1997 and from 2005 until 2011, and AWI-206 in 1996, 1997 and from 2008 to 2011. The loss rate due to flooded instruments or lost moorings since 1996 is about one third, and the success rate of the remaining instruments is 78%. All moorings are deployed at fixed positions in water depths of more than 900 m, some of them in depths exceeding 4500 m.

The pressure sensors of AWI 206-4 and AWI 227-3 failed completely. The drafts of these two instruments were therefore taken from the study of *Harms et al.* [2001]. They were processed with a different procedure which also allowed for a simple interactive correction of the data. However, this method was technically not as sophisticated as the one used in this thesis. The correction of the two data occurred by means of the pressure record of the instrument below the ULS. Since the recording intervals of the two instruments differed significantly, interpolated pressure time series had to be used, which can lead to disturbing aliasing effects. The data of AWI 206-4 and AWI 227-3 therefore have to be considered with care and were excluded from the analyses in the presented work.

Strass and Fahrbach [1998] published first results of draft measurements from the western transect between 1990 and 1994. They demonstrated, that the ice growth undergoes a distinct

annual cycle in the central Weddell Sea, whereas in the boundary regions temporal changes of ice thickness occur more irregularly. It was shown, that sea ice with a draft of less than one meter is transformed into thicker ice by ridging and rafting during its circulation through the Weddell Sea.

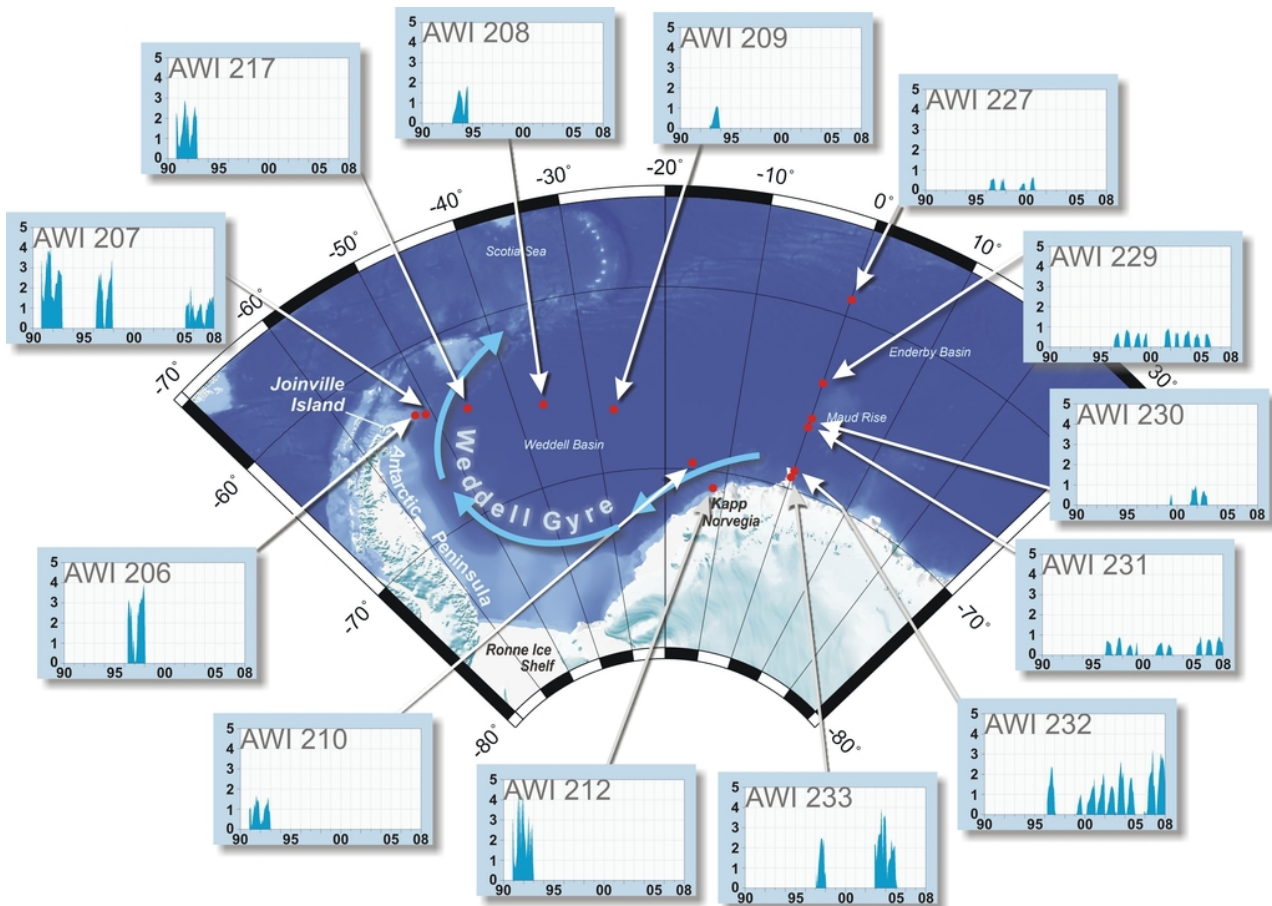


Fig. 4.1: Monthly mean values of sea ice draft (in metres) of the available ULS data from 1990 to 2007.

In 2001 the AWI ULS data have been used for two volume transport studies. *Harms et al.* [2001] used ULS data from both transects for estimations of the annual mean ice export from the Weddell Sea. They established empirical relations between annual mean ice draft and the length of the sea ice season to fill the time gaps in the ULS data record with proxy ice thickness information. By combining ice thickness with ice drift speed derived from the geostrophic wind field, the annual mean ice export out of the Weddell Sea was estimated for the period 1979-1998. *Drinkwater et al.* [2001] applied an improved strategy and used SSM/I-derived ice drift velocities combined with ULS ice thickness information to estimate monthly mean ice volume transports out of the Weddell Sea for the period 1992-1998. To fill data gaps with proxy data, they combined ULS information with ERS satellite observations of radar backscatter to establish an empirical relation between ice thickness and the rate of change of backscatter with incidence angle. It was shown that *Harms et al.* [2001] significantly overestimated the net ice

Table II: Available ULS-data

ULS Number	Instrument Type	Soft- ware	Depth [m]	Lograte [min]	Deployment Period	Position		Ana- lysts
						Lat	Lon	
AWI 206-4 [•]	ES-300 V	3.0	157	15	05/96 - 04/98	63°29.6'S; 52°06.1'W		H [×]
AWI 207-2 [°]	ES-300 V	1.0	165	8	11/90 - 11/92	63°45.1'S; 50°54.3'W		W/B
AWI 207-4 [°]	ES-300 V	3.0	174	15	05/96 - 04/98	63°43.3'S; 50°49.2'W		W/B
AWI 207-6 [°]	ES-300 VIII [◊]	4.5	148	3	03/05 - 03/08	63°42.2'S; 50°52.2'W		W/B
AWI 208-3 [•]	ES-300 V	1.0	125	4	01/93 - 01/95	65°37.7'S; 36°29.4'W		W/B
AWI 209-3 [°]	ES-300 V	1.0	100	4	12/92 - 01/95	66°37.4'S; 27°07.2'W		W/B
AWI 210-2 [°]	ES-300 V	1.0	151	8	12/90 - 12/92	69°39.6'S; 15°42.9'W		W/B
AWI 212-2 [•]	ES-300 V	1.0	135	8	12/90 - 12/92	70°54.7'S; 11°57.8'W		W/B
AWI 217-1 [°]	ES-300 V	1.0	141	8	11/90 - 11/92	64°25.1'S; 45°51.0'W		W/B
AWI 227-3 [•]	ES-300 V	1.0	156	8	04/96 - 01/97	59°01.8'S; 00°00.0'W		H [×]
AWI 227-4 [•]	ES-300 VI	4.0	145	3	01/97 - 05/98	59°04.3'S; 00°01.3'E		W/B
AWI 227-6 [°]	ES-300 VIII	4.0	143	8	03/99 - 12/00	59°04.2'S; 00°04.4'E		W/D
AWI 229-1 [°]	ES-300 V	3.0	165	15	04/96 - 05/98	63°59.6'S; 00°00.3'W		W/B
AWI 229-2 [°]	ES-300 VIII	4.1	150	4	05/98 - 03/99	63°58.5'S; 00°04.6'W		W/D
AWI 229-3 [°]	ES-300 V	3.0	125	4	03/99 - 12/00	63°57.8'S; 00°02.3'E		W/D
AWI 229-4 [°]	ES-300 V	3.0	148	4	12/00 - 12/02	63°57.9'S; 00°02.4'E		W/D
AWI 229-5 [°]	ES-300 VIII [◊]	4.3	147	4	12/02 - 02/05	63°57.2'S; 00°00.2'W		W/D
AWI 229-6 [°]	ES-300 VIII [◊]	4.5	147	1	02/05 - 12/05	63°57.2'S; 00°00.4'W		W/D
AWI 230-2 [•]	ES-300 V	3.0	153	4	01/99 - 12/00	66°00.3'S; 00°10.6'W		W/D
AWI 230-3 [•]	ES-300 VI	4.0	170	4	12/00 - 12/02	66°00.3'S; 00°10.4'E		W/D
AWI 231-1 [•]	ES-300 V	3.0	160	15	04/96 - 05/98	66°30.0'S; 00°00.4'W		W/B
AWI 231-2 [°]	ES-300 VIII	4.1	186	4	05/98 - 01/99	66°30.06'S; 00°01.1'W		W/D
AWI 231-3 [°]	ES-300 V	3.0	102	4	01/99 - 12/00	66°29.9'S; 00°00.9'W		W/D
AWI 231-4 [°]	ES-300 VIII	4.0	179	4	12/00 - 12/02	66°30.0'S; 00°01.8'W		W/D
AWI 231-6 [°]	ES-300 VIII [◊]	4.5	151	1	02/05 - 12/05	66°30.7'S; 00°01.9'W		W/D
AWI 231-7 [°]	ES-300 VIII [◊]	4.3	120	2	12/05 - 03/08	66°30.7'S; 00°01.9'W		W/B
AWI 232-1 [•]	ES-300 V	3.0	147	15	04/96 - 02/97	69°00.0'S; 00°00.0'W		W/B
AWI 232-4 [•]	ES-300 VI	4.0	169	4	01/99 - 12/00	68°59.7'S; 00°01.9'E		W/D
AWI 232-5 [°]	ES-300 VIII	4.0	181	4	12/00 - 12/02	68°59.5'S; 00°02.2'W		W/D
AWI 232-6 [°]	ES-300 VIII [◊]	4.3	175	4	12/02 - 02/05	68°59.9'S; 00°00.3'W		W/D
AWI 232-8 [°]	ES-300 VIII [◊]	4.3	125	2	12/05 - 03/08	68°59.8'S; 00°00.1'W		W/B
AWI 233-2 [•]	ES-300 VI	4.0	154	3	02/97 - 04/98	69°24.2'S; 00°00.0'E		W/B
AWI 233-6 [°]	ES-300 VIII [◊]	4.3	165	4	12/02 - 02/05	69°23.7'S; 00°04.0'W		W/D

Analysts: **W**: H. Witte, **B**: A. Behrendt, **D**: W. Dierking, **H**: S. Harms

Pressure Sensors: [•]Druck PDCR 130/W, [◊]Lucas Schaevitz P9066-0101, [•]damaged pressure sensor

[◊]: XDR included, [×]: different processing algorithm

volume transport across the western transect.

In 2002 *Timmermann et al.* validated the BRIOS-2 ice-ocean model with the ULS data and found that sea ice thickness is well reproduced.

Connolley [2005] used the ULS-data set to compare satellite-based (SSM/I) sea ice concentrations with ULS-derived concentrations. He reported the SSM/I values to be in good agreement with the ULS ice concentrations but considered the ULS concentrations to be more reliable.

Sea ice thickness and ice salinity are directly related to salt fluxes which help drive global ocean models. *Renner and Lytle* [2007] compared sea ice thickness and concentration simulated by four global coupled ocean-atmosphere models (used by the IPCC) with the ULS data. The authors found that all models could capture the seasonal cycle of the ice growth but three models underestimated the ice thickness and one model overestimated the ice thickness.

Giles et al. [2008] determined the freeboard of Antarctic sea ice through satellite radar altimetry. Their comparison with the AWI ULS data showed that the ERS ice elevations were larger than the expected ice freeboard.

In 2009, *Timmermann et al.* validated the simulated sea ice thickness from the global Finite Element Sea Ice Ocean Model (FESOM) with ULS data. Their model showed remarkable agreement with the ULS data for the prime meridian section and the central Weddell Sea. But due to the limited model resolution, the ice thickness was significantly underestimated near the Antarctic Peninsula (AWI-207, AWI-217) and near Kapp Norvegia (AWI-212).

Schwegmann [2012] used the newer ULS data to compare them with data of the FESOM model. In some years both data agree fairly well, whereas in other years the model underestimates or overestimates the ice thickness.

ULS-data available at: <http://doi.pangaea.de/10.1594/PANGAEA.785565>

4.1.2 Satellite data

Sea ice concentration:

The ice concentration data used for this study are Bootstrap Sea Ice Concentrations from the *Nimbus-7* satellite Scanning Multichannel Microwave Radiometer (SMMR) and SSM/I sensors of the DMSP satellites *F8*, *F11* and *F13* [*Comiso*, 1999/2008]. The data set has been generated using the Bootstrap Algorithm and consists of sea ice concentrations derived from gridded brightness temperatures. The concentrations range from 0 to 100%, with a retrieval accuracy of approximately 5 to 10% [*Comiso*, 1999/2008]. The data set has a temporal resolution of one day and covers the period from 26 October 1978 to 31 December 2007. Gridded fields are provided by the US National Snow and Ice Data Center (NSIDC) on an azimuthal equal area projection (EASE grid) with a spatial resolution of 25 km. The positions are given in respective grid coordinates.

Data available at: <http://nsidc.org/data>

Sea ice drift:

The ice drift data used for this thesis are the Polar Pathfinder Daily Ice Motion Vectors of *Fowler* [2003/2007], provided by the NSIDC. The data combine information from visible and thermal channels from AVHRR and daily composites of brightness temperature fields from SSM/I (85.5 GHz) and SMMR (37 GHz) [*Fowler*, 2003/2007]. The vectors represent the pixel displacement between the acquisition times of two images with the same spatial coverage and

are calculated by an optimal interpolation method for all areas where ice concentration exceeds 50% [Schwegmann *et al.*, 2011; Schwegmann, 2012]. The daily maps are provided on a 25×25 km EASE grid (see above). In the Weddell Sea the ice motion vectors underestimate the mean drift velocity of drifting buoys by 34.5% [Schwegmann *et al.*, 2011]. The highest differences between the two types of data occur from July to November for the u-component of the drift (zonal drift). However, the general drift patterns of both data were found to be in good agreement.

Data available at: <http://nsidc.org/data>

4.1.3 Model data

ECMWF:

Daily surface wind fields (10 m level), sea level pressure and surface air temperatures (2 m level) were taken from the ERA-Interim reanalysis project, the latest global atmospheric reanalysis produced by the ECMWF [Dee *et al.*, 2011]. Reanalysis data provide a coherent record of all atmospheric parameters over the entire globe - such as cloud cover, surface thermal radiation and moisture flux - from the past to the present. This is achieved by combining a large number of different observations and measurements together within a model. The advantage of reanalysis is that it only uses a single version of the data assimilation system. The output is therefore not affected by changes in method [Dee *et al.*, 2011].

To date, ERA-Interim covers the period from 1 January 1989 onwards, and continues to be extended forward in near-real time [Dee *et al.*, 2011]. The data are provided on 1.5° longitude-latitude grids and include analyses, forecasts or combinations of both, at different time steps. The high quality of the ECMWF pressure fields over Antarctica was confirmed e.g. by Renwick [2004] and King [2003].

Data available at: http://data-portal.ecmwf.int/data/d/interim_daily

NCEP/NCAR:

Another reanalysis project is conducted by the *National Centers for Environmental Prediction* (NCEP), which are part of the NOAA (USA), in cooperation with the NCAR (*National Center for Atmospheric Research*) in the USA. For this project data from many different sources (such as rawinsonde, ship, satellite and aircraft measurements) are assimilated in a system which is kept unchanged over the entire reanalysis period. The gridded data are classified into three quality classes: A-C. Class A, the most reliable one, indicates that the variable is strongly influenced by observations, whereas class B values are also affected by the analysis. Class C indicates that there are no observations affecting the variable [Kalnay *et al.*, 1996]. Most NCEP/NCAR data used for this thesis (e.g. geopotential heights and wind fields on different pressure levels) are among the class A products [Yuan and Li, 2008].

NCEP/NCAR reanalysis provides many atmospheric variables on different pressure levels. The data are provided on 2.5° longitude-latitude grids over the entire globe from 1948 to present. Details of the reanalysis system are explained by Kalnay *et al.* [1996].

Data available at: <http://www.esrl.noaa.gov/psd/data/reanalysis/reanalysis.shtml>

Sea ice models:

For comparison with the ULS data, sea ice thicknesses derived from two different climate models were used. The FESOM model is described in detail by *Schwegmann* [2012] and *Timmermann et al.* [2009]. FESOM is a finite element ocean model combined with a dynamic-thermodynamic sea ice model and has an unstructured surface triangular grid with 26 vertical levels. The resulting 3-D mesh consists of tetrahedra [*Schwegmann*, 2012]. The sea ice component assumes linear temperature gradients in the ice, negligible heat storage within the ice and allows for snow layers. It includes the energy balance introduced in section 2.2 and the momentum balance introduced in section 2.3. Additionally, it models lateral ice growth and lead formation and uses an elastic-viscous-plastic rheology for ice deformation [*Schwegmann*, 2012].

The MIT GCM (Massachusetts Institute of Technology General Circulation Model) is a coupled dynamic-thermodynamic sea ice ocean model on Arakawa C and B grids. It uses dynamic momentum equations and a viscous-plastic law for internal ice stresses. The model assumes a linear temperature profile and a constant ice conductivity, i.e. zero heat capacity for ice [*Losch et al.*, 2010]. It also allows for a modification of the heat fluxes and the albedo by a snow layer. For this work, the sea ice thickness of each grid cell was averaged over nine grid cells (including all eight neighbouring cells) as the model performs better on slightly larger spatial scales [*M. Losch*, personal communication, 2012].

Data available at: AWI: *Ralph Timmermann*, *Martin Losch*

4.2 Methods

4.2.1 Detrended fluctuation analysis

The detrended fluctuation analysis (DFA) was used to detect long-range correlations in ice draft time series. When geophysical data are affected externally by trends, it is usually not a simple task to distinguish those from long-range fluctuations intrinsic in the data. DFA systematically removes trends of different order from the time series, which enables a precise investigation of its scaling behaviour [Kantelhardt *et al.*, 2001].

Short-range correlations are usually detected by the autocorrelation function $C(s)$, which declines exponentially: $C(s) \propto \exp(-s/s_x)$, where s denotes the lag and s_x the characteristic decay time. For long-range correlations $C(s)$ obeys the power law $C(s) \propto s^{-\gamma}$, with the exponent $0 < \gamma < 1$. However, $C(s)$ is often strongly affected by noise or non-stationarities superimposed on the time series and is therefore not an appropriate method for detecting long-range correlations [Kantelhardt *et al.*, 2001]. DFA bypasses these problems. It basically consists of three steps:

First, a cumulated version of the original time series $\mathbf{d}(n)$ is formed by

$$\mathbf{d}(n) = \sum_{t=1}^n \mathbf{d}_t. \quad (4.1)$$

This series of length N is then cut into $N_s \equiv [N/s]$ non-overlapping segments of equal length s . This is repeated in backward direction, starting from the end of the time series, such that $2N_s$ elements are obtained in total. In the second step, for each segment ν a least-squares fit is calculated to subtract the local trend from the element. The detrended segment of duration s is then defined as $\mathbf{d}_s(n) = \mathbf{d}(n) - p_\nu(n)$, where $p_\nu(n)$ is the fitting polynomial in the ν -th segment [Kantelhardt *et al.*, 2001]. The fitting polynomials can be linear (DFA1), quadratic (DFA2) or of higher order. Due to equation (4.1), an n -th order DFA eliminates trends of order $n - 1$ in the original time series. In the third step, the so-called fluctuation function is calculated. To do this, the variance for each segment ν is first calculated by averaging over all data points in segment ν :

$$F_s^2(\nu) = \langle \mathbf{d}_s^2(n) \rangle = \frac{1}{s} \sum_{t=1}^s \mathbf{d}_s^2[(\nu - 1)s + t]. \quad (4.2)$$

Next, the value of the fluctuation function $F(s)$ is calculated by averaging over all segments of length s and taking the square root:

$$F(s) = \sqrt{\frac{1}{2N_s} \sum_{\nu=1}^{2N_s} F_s^2(\nu)}. \quad (4.3)$$

The procedure is repeated many times, thereby increasing the length of the segments in each step until the full fluctuation function is obtained. The variance increases with increasing duration s of the segments [Kantelhardt *et al.*, 2001]. In case of long-range correlation in the initial time series, the fluctuation functions for different fitting-polynomial orders p increase by the power law $F^{(p)}(s) \propto s^\alpha$, where the parameter α is an estimation of the *Hurst exponent*. This exponent is related to the fractal dimension, which describes the degree of complication

of self-similar objects [Mandelbrodt, 1987]. α is related to γ (see above) through $\alpha = 1 - \gamma/2$. Thus, for long-range correlations we have $\alpha > 0.5$, whereas $\alpha = 0.5$ indicates the absence of long-range correlations. The exponent α can be found by linear fits to the fluctuation function in double logarithmic plots. The slope of the fit is directly related to α .

The high performance of the DFA-method was confirmed by Weron [2002]. DFA has been used in different studies, e.g. for detecting the long time memory in global warming simulations [Blender and Fraedrich, 2003], and it also contributed to the detection of anthropogenic warming in global temperature data sets [Rybski et al., 2006].

4.2.2 Correlation analysis

Correlation analysis was applied by using the standard linear correlation coefficient of Pearson. Additionally, Spearman's rank correlation is calculated to account for the non-Gaussian distribution of the observed variables. Both methods are widely used standard techniques and are described e.g. by Schönwiese [1992]. Additionally, the squared correlation coefficient was calculated to estimate the shared variance of the correlated time series [Schönwiese, 1992].

The significance of correlations was tested by applying the method of Ebisuzaki [1997]. This method estimates the statistical significance of a computed correlation coefficient accounting for the autocorrelation present in most geophysical time series. As the serial correlation of a time series decreases the effective sample size, i.e. the number of independent observations, it also affects the correlation coefficient. Due to low-pass filtering, for example to suppress remaining signals of the annual cycle in anomaly time series, the serial correlation is even enhanced. The method of Ebisuzaki [1997] is relatively insensitive to serial correlation.

To test the significance of a correlation ρ_{ab} between two series A and B, "bootstrap" methods usually generate a large number of random series by shuffling the elements of series A. The obtained random series are then correlated against series B to find the significance level of the initial correlation ρ_{ab} by evaluating the statistical distribution of the randomly generated correlations. Shuffling all elements of a serially correlated time series usually destroys its autocorrelation. But random series with zero autocorrelation are not suitable to test the significance of ρ_{ab} calculated from serially correlated time series.

The presented method resamples the time series in the frequency domain, rather than the time domain and thereby retains the power spectrum of the series. The sampled random time series therefore still has the same autocorrelation as the original series. The first step is to compute the discrete Fourier transform of the first series, a_i , by

$$\tilde{a}_k = \frac{2 - \delta_k}{N} \sum_{j=0}^{N-1} a_j e^{2\pi i j k / N}, \quad \delta_k = \begin{cases} 0 & \text{for } k \in \{0, N/2\} \text{ (even } N), \\ 1 & \text{otherwise} \end{cases} \quad (4.4)$$

where N is the length of the original time series A. Then a Fourier series \tilde{r}_k is created in the following way:

$$\begin{aligned} \tilde{r}_0 &= 0 \\ \tilde{r}_k &= |\tilde{a}_k| e^{i\Theta_k}, \quad \text{for } 0 < k < \frac{N}{2} \\ \tilde{r}_{N/2} &= \sqrt{2} |\tilde{a}_{N/2}| \cos(\Theta_{N/2}), \quad \text{for even } N, \end{aligned}$$

where Θ_k is a uniform random variable from $[0, 2\pi)$. This step creates a Fourier series with random phases and the same power spectrum as the original series A. The last step creates the inverse Fourier transform and gives a random time series with the same autocorrelation as the original series A [Ebisuzaki, 1997]:

$$r_j = Re \sum_{k=0}^n \tilde{r}_k e^{-2\pi i j k / N}, \quad n = \begin{cases} \frac{N}{2} & \text{for even } N \\ \frac{N-1}{2} & \text{for odd } N. \end{cases} \quad (4.5)$$

Once a large number of these surrogate series is created, they are correlated against the time series B. To reject the null hypothesis of zero correlation ($\rho_{ab} = 0$) at the α significance level, only $\alpha \times 100\%$ of the correlations have to be larger than ρ_{crit} , assuming $|\rho_{ab}| > \rho_{crit}$. The high performance of this method is demonstrated in detail in the paper of Ebisuzaki [1997].

4.2.3 Singular spectrum analysis

Singular Spectrum Analysis (SSA) is a very powerful tool in modern time series analysis. SSA is an EOF-based method which can be applied for various purposes: Trend analysis, smoothing, extraction of seasonality or cycles with varying periods and amplitudes, filling of data gaps, and for finding structures in short time series [Hassani, 2007]. In climate science SSA is mostly used to detect modulated oscillations in meteorological or geophysical records. In the presented work it was applied to ice draft anomalies.

The basic idea of SSA is sliding a window down a time series and looking for patterns that account for a high proportion of the variance [Allen and Smith, 1996]. One may think of an EOF analysis of a single time series, rather than of a field of time series. SSA analysis typically involves four steps which are known as the *caterpillar method*:

Step 1: Embedding:

The considered time series \mathbf{d} of length N , $\mathbf{d}(t) : t = 1 \dots N$, is first centred to have zero mean. Sliding a window of width M down the time series produces a set of M lagged vectors, which are then arranged in a $(N' \times M)$ matrix \mathbf{D} , which is called the *trajectory matrix*:

$$\mathbf{D} = \begin{pmatrix} D_{11} & D_{12} & \dots & D_{1M} \\ D_{21} & D_{22} & \dots & D_{2M} \\ \vdots & \vdots & \ddots & \vdots \\ D_{N'1} & D_{N'2} & \dots & D_{N'M} \end{pmatrix} \xrightarrow[\text{N=6}]{\text{M=3}} \mathbf{D} = \begin{pmatrix} d_1 & d_2 & d_3 \\ d_2 & d_3 & d_4 \\ d_3 & d_4 & d_5 \\ d_4 & d_5 & d_6 \end{pmatrix}. \quad (4.6)$$

The window width M defines the longest periodicity that can be detected by SSA. Increasing M increases the spectral resolution of the method. \mathbf{D} is a *Hankel* matrix, i.e. all elements along the skew diagonals are equal. It consists of M lag-shifted copies of $\mathbf{d}(t)$, which are $N' = N - M + 1$ long [Kondrashov and Ghil, 2006].

Step 2: EOF Analysis:

In the next step the trajectory matrix is used to form the *lag-covariance matrix* \mathbf{C}_D :

$$\mathbf{C}_D = \frac{1}{N'} \mathbf{D}^T \mathbf{D}. \quad (4.7)$$

The lag-covariance matrix has the dimensions $(M \times M)$. This way of computing \mathbf{C}_D is the method of *Broomhead and King* [1986]. An alternative approach is the method of *Vautard and Ghil* [1989]¹. Once the lag-covariance matrix is computed, it is diagonalised and its eigenvalues are ranked in decreasing order:

$$\mathbf{\Lambda}_D = \mathbf{E}_D^T \mathbf{C}_D \mathbf{E}_D, \quad (4.8)$$

where $\mathbf{\Lambda}_D$ is a diagonal matrix containing the eigenvalues and \mathbf{E}_D contains the eigenvectors (EOFs) of \mathbf{C}_D . The total variance of the time series $\mathbf{d}(t)$ is given by the trace of \mathbf{C}_D , and the eigenvalues λ_k explain the partial variance in the direction of \mathbf{E}_k . The *principal components* \mathbf{a}_k can be obtained by projecting the time series onto each EOF:

$$\mathbf{a}_k(t) = \sum_{j=1}^M \mathbf{d}(t+j-1) e_k(j). \quad (4.9)$$

The trajectory matrix can be reconstructed through

$$\mathbf{D} = \sum_{j=1}^M \mathbf{a}_j \mathbf{e}_j^T = \mathbf{D}'_1 + \mathbf{D}'_2 + \dots + \mathbf{D}'_M, \quad (4.10)$$

where the matrices \mathbf{D}'_j are elementary matrices of rank one. Each elementary matrix is related to one eigenvector and an eigenvalue of \mathbf{C}_D which explains a certain fraction of the variance in $\mathbf{d}(t)$ (Fig. 4.2).

Step 3: Grouping:

In the grouping step the elementary matrices \mathbf{D}'_j can be splitted into groups, corresponding to a certain kind of signal in $\mathbf{d}(t)$, which can then be summed. From the sum a new trajectory matrix \mathbf{D}_2 can be constructed containing only signal components corresponding to the group of selected eigenvalues [*Hassani, 2007*]. The selection of the eigenvalues and thus the amount of variance to retain can be based on a "scree diagram" (eigenvalue spectrum). Summing up all elementary matrices $\mathbf{D}'_{1,\dots,M}$ would give the initial trajectory matrix \mathbf{D} .

Step 4: Diagonal Averaging:

The final step extracts the time series from \mathbf{D}_2 , which is an additive component of the initial time series $\mathbf{d}(t)$ [*Hassani, 2007*]. The first operation in this step is also called *Hankelisation*, as it turns the matrix \mathbf{D}_2 into a Hankel matrix by replacing every element by the average of the respective skew diagonal. The elements of the new time series are then read from the skew diagonals, like in matrix \mathbf{D} on the right hand side of equation 4.6.

With \mathcal{K} as the set of EOFs on which the reconstruction is based, M_t as the normalisation factor, L_t as the lower bound of summation and U_t as the upper bound of summation, the new time series $\mathbf{r}_{\mathcal{K}}(t)$ can thus be obtained by

$$\mathbf{r}_{\mathcal{K}}(t) = \frac{1}{M_t} \sum_{k \in \mathcal{K}} \sum_{j=L_t}^{U_t} a_k(t-j+1) e_k(j), \quad (4.11)$$

[*Kondrashov and Ghil, 2006*] where

¹Both versions of computing \mathbf{C}_D are explained in the paper of *Allen and Smith* [1996].

$$(M_t, L_t, U_t) = \begin{cases} \left(\frac{1}{t}, 1, t\right) & \text{for } 1 \leq t \leq M-1 \\ \left(\frac{1}{M}, 1, M\right) & \text{for } M \leq t \leq N' \\ \left(\frac{1}{N-t+1}, t-N+M, M\right) & \text{for } N'+1 \leq t \leq N. \end{cases}$$

For extracting significant oscillations in a time series it is sufficient to stop at step two of the SSA procedure and to evaluate the spectrum of eigenvalues. According to SSA theory, every harmonic oscillation present in the time series produces two eigenvalues, a sine and a cosine with equal frequencies, amplitudes and phases [Hassani, 2007]. As both eigenvalues of such a pair explain the same amount of variance, oscillations in $\mathbf{d}(t)$ can be detected by finding plateaus in the plotted eigenvalue spectrum. However, as noted by Allen and Smith [1996] the pair selection criterion can be misleading when trends are present in the data.

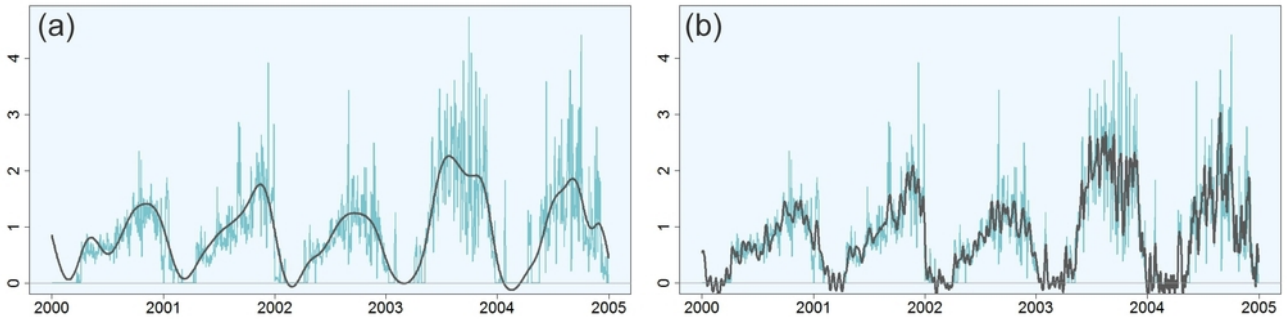


Fig. 4.2: (a) Light thin line: Daily mean ice draft time series (in metres). Dark bold line: The same series reconstructed with the first 10 eigenvalues. (b) Dark bold line: The same series as in (a), reconstructed with the first 50 eigenvalues.

Furthermore, considering only the high ranked eigenvalues of the spectrum as significant may be wrong, as true systems are mostly contaminated with coloured noise. Also the stability of an EOF pair to varying window widths is not a sufficient condition for significant oscillations. SSA should therefore never be used without an appropriate significance test [Allen and Smith, 1996].

The significance test developed by Allen and Smith [1996] is based on a Monte Carlo approach. First, the mean, variance and lag-1 autocorrelation are estimated from $\mathbf{d}(t)$ in order to simulate a large number of random AR(1) processes corresponding to these parameters². From each process a *surrogate lag-covariance matrix* \mathbf{C}_R is computed and projected onto the EOFs of the original data:

$$\mathbf{\Lambda}_R = \mathbf{E}_D^T \mathbf{C}_R \mathbf{E}_D. \quad (4.12)$$

The statistical distribution of the diagonal elements in $\mathbf{\Lambda}_R$ is used to find the 2.5th and 97.5th percentiles. These are plotted as error bars in the eigenvalue spectrum of the initial lag-covariance matrix \mathbf{C}_D . 95% of the surrogate realisations then lie within those limits. The null hypothesis to be rejected is: *The time series has been generated by AR(1) noise*. But for

²For details of the algorithm see Allen and Smith [1996].

a pair of sinusoidal EOFs considered as signal the true confidence level is in fact lower than 95% [Allen and Smith, 1996]. When the signal EOFs are determined, one aims to proof at the 95% (or 97.5%) level that the remainder of the time series has been generated by AR(1) noise. The described test therefore includes a second stage: If some components of the time series are believed to represent significant signals after stage one of the test, the second stage checks whether the remainder of the time series is attributable to AR(1) noise. This test makes use of steps three and four of the caterpillar method.

First, matrix \mathbf{D}_2 is constructed using only the eigenvalues which were identified as signal. The AR(1) process parameters are then estimated, such that when added to the time series $\mathbf{r}_K(t)$, this composite has the same variance and lag-1 autocorrelation as the original series $\mathbf{d}(t)$ [Allen and Smith, 1996]. Like in stage one, the AR(1) surrogates are centred, and new lag-covariance matrices \mathbf{C}_R are calculated. Their eigenvalue spectrum is used to calculate the desired error bars. To overcome the problem of artificial variance-compression described by Allen and Smith [1996], the matrices \mathbf{C}_D and \mathbf{C}_R are projected onto the EOFs of the composite null hypothesis \mathbf{E}_N , rather than the EOFs derived from the data itself:

$$\mathbf{\Lambda}'_D = \mathbf{E}_N^T \mathbf{C}_D \mathbf{E}_N, \quad (4.13)$$

$$\mathbf{\Lambda}'_R = \mathbf{E}_N^T \mathbf{C}_R \mathbf{E}_N. \quad (4.14)$$

The eigenvectors \mathbf{E}_N are calculated by diagonalising the lag-covariance matrix \mathbf{C}_N , which is based on the composite null hypothesis that the data only consist of the selected signal component plus AR(1) noise. In spectral analysis the results of SSA are presented as EOF scree diagrams, ordered by frequency.

4.2.4 Multichannel singular spectrum analysis

Multi-channel singular spectrum analysis (M-SSA) was used to fill data gaps in the ice draft record. The method of Kondrashov and Ghil [2006] takes advantage of both spatial and temporal correlations.

Contrary to single channel SSA (see above) M-SSA is applied to a field of L time series (channels), each of which N data points long. The channels can be arranged in a $(L \times N)$ matrix $\mathbf{d}_{ln: l=1,\dots,L, n=1,\dots,N}$. Both SSA ($L = 1$) and standard principal component analysis ($M = 1$) are special cases of M-SSA [SpectraWorks, 2011]. The basic part of the procedure is very similar to SSA and is therefore only briefly described here.

In the first step the $(N' \times M)$ trajectory matrix $\widetilde{\mathbf{X}}_l$ is created for each channel of \mathbf{d}_{ln} , for a given window M . All trajectory matrices are then arranged in the *full augmented trajectory matrix* with dimensions $(N' \times LM)$:

$$\widetilde{\mathbf{D}} = (\widetilde{\mathbf{X}}_1, \widetilde{\mathbf{X}}_2, \dots, \widetilde{\mathbf{X}}_L). \quad (4.15)$$

From $\widetilde{\mathbf{D}}$ the symmetric *grand covariance matrix* is computed:

$$\widetilde{\mathbf{C}}_D = \frac{1}{N'} \widetilde{\mathbf{D}}^T \widetilde{\mathbf{D}}, \quad (4.16)$$

which has the dimensions $(LM \times LM)$. The blocks of $\widetilde{\mathbf{C}}_D$ are given by

$$\tilde{\mathbf{C}}_{l,l'} = \frac{1}{N'} \tilde{\mathbf{X}}_l^T \tilde{\mathbf{X}}_{l'}. \quad (4.17)$$

The entries of $\tilde{\mathbf{C}}_{l,l'}$ are in turn given by

$$(C_{l,l'})_{j,j'} = \tilde{C}_{IJ} = \frac{1}{N'} \sum_{t=1}^{N'} X_l(t+j-1)X_{l'}(t+j'-1), \quad (4.18)$$

where $I = j + M(l - 1)$ and $J = j' + M(l' - 1)$ [*SpectraWorks*, 2011]. The grand covariance matrix thus has the appearance

$$\tilde{\mathbf{C}}_D = \frac{1}{N'} \begin{pmatrix} \tilde{\mathbf{X}}_1^2 & \tilde{\mathbf{X}}_1^T \tilde{\mathbf{X}}_2 & \dots & \tilde{\mathbf{X}}_1^T \tilde{\mathbf{X}}_L \\ \tilde{\mathbf{X}}_2^T \tilde{\mathbf{X}}_1 & \tilde{\mathbf{X}}_2^2 & \dots & \tilde{\mathbf{X}}_2^T \tilde{\mathbf{X}}_L \\ \vdots & \vdots & \ddots & \vdots \\ \tilde{\mathbf{X}}_L^T \tilde{\mathbf{X}}_1 & \tilde{\mathbf{X}}_L^T \tilde{\mathbf{X}}_2 & \dots & \tilde{\mathbf{X}}_L^T \tilde{\mathbf{X}}_L \end{pmatrix}. \quad (4.19)$$

The principal diagonal of $\tilde{\mathbf{C}}_D$ contains the temporal covariances (like in SSA), while all other diagonals contain cross-channel, i.e. spatial covariances³.

The gap-filling technique is based on the assumption that the dominant oscillations or trends in a geophysical time series are represented by the leading EOFs [*Kondrashov and Ghil*, 2006]. Using the selected EOFs, the data gaps are filled iteratively by reconstructing the original time series step by step. All time series of the field are first centred, and their gaps are filled with zeros. Next, the M-SSA algorithm is performed and the time series are reconstructed with only the first EOF. As a result, the data gaps of the original time series are filled with non-zero values. In the next iteration step the same procedure is started again, but this time with the filled time series. The new covariance matrix is diagonalised and the series are again reconstructed with the first EOF to obtain new values in the filled data gaps. If these steps are repeated loopwise, the filled values growth larger until they converge. The loop can be escaped by programming a simple convergence test. In a second outer-loop iteration the already filled series are reconstructed by adding a second EOF to the algorithm. This step therefore adds more variance to the filled data. The inner loop is again repeated until convergence and the outer loop is restarted by adding one more EOF. This procedure can be repeated until the maximum number of EOFs is reached, or it can be stopped at a limited number of EOFs [*Kondrashov and Ghil*, 2006].

The quality of the filled data can be assessed with a set of simple cross-validation experiments. For this purpose a small fraction of the observations is treated as a gap. To obtain reliable error estimates, this synthetic gap should have the same shape as the other gaps present in the time series [*Kondrashov and Ghil*, 2006]. By computing the RMS-deviation between the reconstruction and the time series in the synthetic gap as a function of retained EOFs and window widths, one can find the optimal parameters L and M corresponding to the minimum error [*Kondrashov and Ghil*, 2006].

³See <http://www.spectraworks.com/Help/mssatheory.html> for helpful figures and more detailed explanations of the method.

4.2.5 EOF and SVD analysis

To find correlations of atmospheric and oceanic variables with the ice draft, EOF analysis⁴ was applied in this work. EOFs are functions that describe a certain fraction of the variance of a field of anomalies (e.g. drift anomalies). They are obtained by diagonalising a covariance or correlation matrix of the field [Björnsson and Venegas, 1997]. This procedure is similar to step two of SSA (see above). The first EOF explains the largest amount of variance, the second one

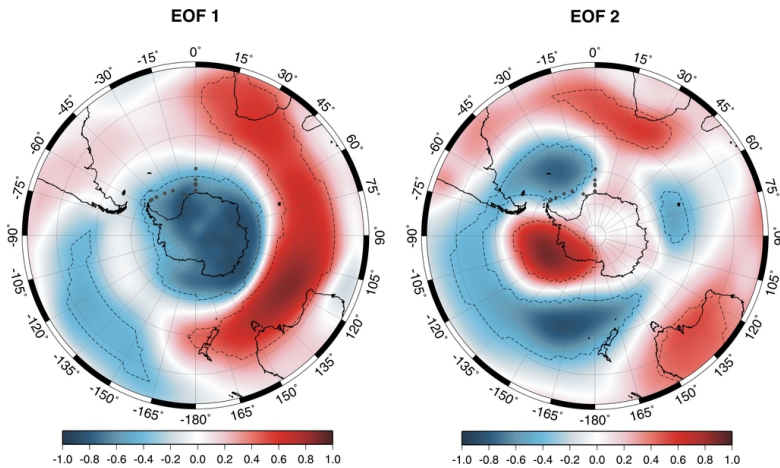


Fig. 4.3: Two examples of homogeneous correlation maps of EOFs of the mass-weighted and vertically integrated (1000-300 hPa) July-September mean geopotential height anomalies between 1979 and 2003. EOF-1 shows the SAM and EOF-2 shows the PSA. Dashed lines indicate 95% statistical confidence based on t tests.

A heterogeneous correlation map on the contrary shows the correlation of the EOF with time series on the grid points of another field in the same domain, e.g. sea ice drift. Thus, it shows how well the grid point values of the drift field can be predicted from the knowledge of the EOF of the SLP field [Björnsson and Venegas, 1997].

For a physical interpretation of localised EOFs it is often recommended to use "rotated" EOFs. For example, if the first EOF has a monopole pattern in the domain, the second EOF will most probably have a dipole pattern, only because of the orthogonality constraint, regardless of whether such a physical pattern really exists in the field [Dommenges and Latif, 2002]. Rotated EOFs are obtained by retaining some of the eigenvectors and reconstructing the data using this truncated basis [Björnsson and Venegas, 1997]. In the next step a new basis is found by maximising a function of simplicity⁵. In this thesis, the average values of a small box in one of the action centres of each EOF were correlated with the full field (*box regression*) to test whether the calculated EOF represents a real physical mode of variability, following the approach of Dommenges and Latif [2002]. Based on the result, it was decided whether the rotated or unrotated EOF shall be considered. A good review of EOF methods is given by Hannachi et al. [2007].

To investigate coupled modes of variability - mainly between wind and ice drift - *singular value decomposition* (SVD) was applied. SVD differs from EOF analyses in that the covariance ma-

the second largest and so on. Each EOF is orthogonal to the other ones in time and space, i.e. it is not correlated with other EOFs. Furthermore, it has a spatial pattern which displays how the variance is distributed over the considered domain. Their *principal components* (sometimes also called *expansion coefficients*) are dimensionless time series that describe how the pattern evolves in time. This pattern is displayed by homogeneous correlation maps (Fig. 4.3). Such a map, e.g. for sea level pressure (SLP), is obtained by correlating the calculated EOF of SLP with the SLP time series on each grid point in the domain.

⁴Sometimes it is also called *principal component analysis* (PCA).

⁵See von Storch and Navarra [1995] or Hannachi et al. [2007] for details. The various functions (e.g. VARIMAX or QUATIMAX) are implemented in the packages *GPArotation* and *psych* of the R language.

trix is calculated from two fields instead of one. The EOF patterns therefore display coupled modes of variability [Björnsson and Venegas, 1997]. Correspondingly, the SVD analysis yields two principal components, e.g. one for the wind field and one for the ice drift. The principal components explain certain fractions of the total squared covariance between the two fields and describe how these coupled modes evolve in time. Examples of SVD analyses can be found in the study of Yuan and Li [2008].

The significance in correlation maps (Fig. 4.3) was tested using a standard t test [Schönwiese, 1992]:

$$\hat{t} = r\sqrt{n - 2/(1 - r^2)}, \quad (4.20)$$

where r is the correlation coefficient, n the length of the principal component and \hat{t} the t value. The correlation was considered as significant at the 95% level if $\hat{t} \geq 2$. According to the t distribution, this value (rounded) is in good approximation valid for the lengths of all time series considered here [Schönwiese, 1992].

*"It has been my experience
that every time I think I
know where it's at, it's usu-
ally somewhere else."*

Blake Edwards, 1922-2010

5

Data Processing and Data Quality

In chapter five the methods and results of the data processing are presented and the advantages and weaknesses are discussed. The data accuracy is analysed in detail, including thorough calculations and some considerations about the systematic error. Furthermore, the results of the data gap filling are presented.

5.1 Data processing

The raw 8/16-bit voltage data are stored in ASCII files which include the time of flight for each of the four sonar signals in one burst, their envelope voltages, the temperature, pressure, tilt of the instrument in x and y direction and date/time. In software version 1.0 only the two most similar times of flight and only one envelope voltage for every second measurement were recorded. For every deployed instrument the calibration coefficients, system settings etc. are stored in a configuration file. Each time a parameter is changed, e.g. the lograte, the configuration file is automatically updated. The conversion of the 8/16-bit decimal values into engineering units is made according to the standard formulae given by *Lothe and Baker* [2000]. A serious error source is the variation of the vertical mean sound speed in the water column above the ULS. Sound speed profiles depend on temperature and salinity. For example, when a colder water mass drifts through the area in which the ULS is located, the thermocline is lowered and reduces the vertical mean temperature. This in turn reduces the vertical mean sound speed. Measured density profiles, from which the sound speed can be calculated, are not available at the required temporal resolution. Therefore, a fixed value is assumed for the mean sound speed (1442 m s^{-1}) and density (1027 kg m^{-3}). The draft calculated in this way is called "pseudo draft". The variations of the true sound speed and density result in a varying offset between the zero-line in the pseudo draft (i.e. 0 m draft) and the true zero-level (i.e. the sea surface). The zero-level correction is based on the identification of open water areas in the data series at which the spatially varying offset of the pseudo draft can be determined.

A comprehensive discussion of error sources and a possible way of correcting the zero-level is provided by Melling et al. [1995].

For the conversion and processing of the ULS data presented here, an automated procedure has been developed at AWI. The *AWI ULS Processing Chain* (AUPC) is a set of IDL-routines written by Wolfgang Dierking and basically consists of three steps:

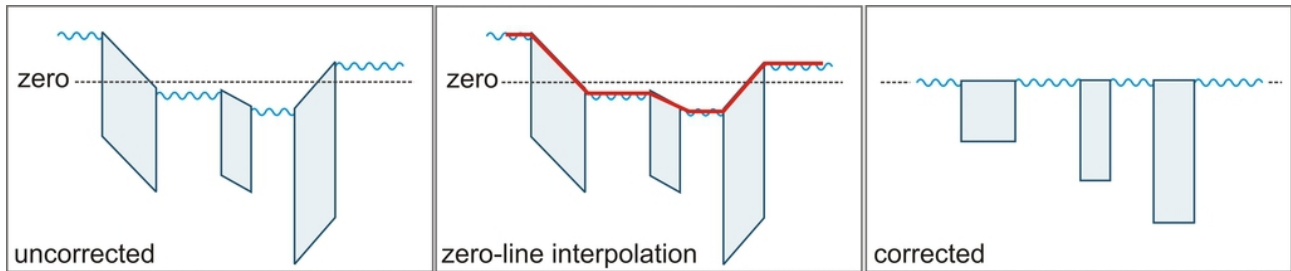


Fig. 5.1: Correction of the ice draft by interpolation of a zero-line. The blue rectangles represent ice.

Step 1: Programme **ULS_step_01**: In step one the raw data are read and converted into physical quantities according to the given configuration files. For a qualitative check of the raw data the programme **ULS_plot_01** plots histograms of pressure, temperature, tilt, travel time and echo level for each of the four pings. The echo level is derived from V_{env} .

Step 2: Programme **ULS_step_02**: The second step checks whether the measured data are within realistic boundaries. The following data are rejected: measurements where $T > 10^{\circ}\text{C}$ or $T < -10^{\circ}\text{C}$, measurements where $p > 200$ dbar or $p < 20$ dbar, measurements where $Tilt > 5^{\circ}$ and draft values with $d > 30$ m or $d < -10$ m, where T stands for temperature and p for pressure. This programme uses ECMWF data for the correction of the measured pressure. The distance between the ULS and the reflecting target is calculated from the mean of the four (or two) recorded travel times.

The programme **ULS_plot_02** plots pseudo draft, ULS-depth and echo level for each month of data acquisition. Based on these plots, the data analyst visually identifies longer open water periods (i.e. no leads). If accepted, these data sequences are automatically set to zero draft. The detection of larger open water areas in step two is aided by the auxiliary variable V_{env} , from which the echo level can be derived. As the echo level is not only lower for ice but also due to increased scattering by gravity waves in open water, the programme additionally displays ECMWF wind speeds to reduce the risk of misinterpretation. The operator also has the possibility to reject obviously erroneous data that occur e.g. when the ULS is depressed to large depths by a passing iceberg, tides or ocean currents.

Step 3: Programme **ULS_step_03**: The identification of the reference level and the correction of the pseudo draft is performed in step three. The deviations of the pseudo draft zero-line from the true zero-level are assumed to originate from natural variations in the true values of c and ρ .¹

Step 3:

(continued) The pseudo draft zero-line is determined as follows: Within pre-defined windows of 24-96 hours width (depending on the sample rate) the algorithm finds the median of the 5% lowest data points classified as ice. Data points within a range of five centimetres below and above the median are then defined as local minima (open water or thin lead ice). The correction line (i.e. the pseudo draft zero-level) is interpolated between these points. After the interpolation process the calculated zero-level is displayed together with the draft for each day of data acquisition by the programme `ULS_plot_03`. Additionally, it indicates periods classified as thin ice/open water with a blue line. In step three the operator has the possibility to further correct the zero-line interactively, if some leads were not captured by the search algorithm. Based on the interpolated zero-line, the full draft record is corrected by setting the line to zero draft (Fig. 5.1). As demonstrated later, this method may induce a sizeable error in the winter months at times. Finally, the programme creates a file with file extension `.dra` and adds the following identification flags to the data: **0**: open water, **1**: ice, **2**: thin ice/open water (draft ≤ 5 cm), **9**: rejected/erroneous data.

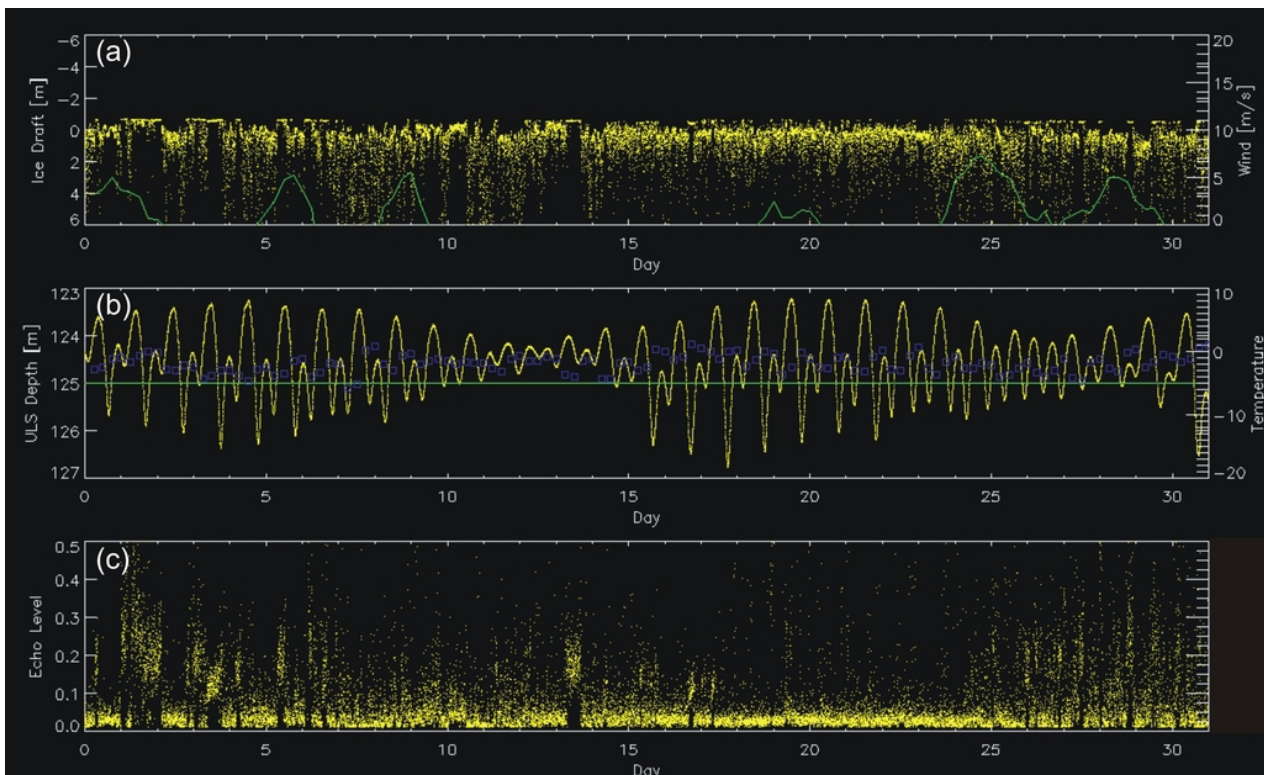


Fig. 5.2: (a) Example of draft data from AWI 232-8 in December 2006 before the zero-level correction. Each dot stands for one draft measurement. In this case the zero-level in the draft record can be easily identified as straight line near a draft value of about -1 m. The sample rate is two minutes. The green line represents the ECMWF wind speed. (b) ULS depth as measured by the pressure sensor. The blue squares are ECMWF surface air temperatures. (c) The echo level as calculated from the envelope voltage (V_{env}) after *Lothe and Baker* [2000]. The plot is taken from `ULS_plot_02`.

An example of the second processing step is given in figure 5.2. The upper panel shows a sequence of raw draft data interspersed with open water patches. Open water can be seen e.g.

on day 4 or 14 and is marked by grouped echoes at the zero-level and black space (i.e. no echoes) further below. If a constant mean drift speed of 5 cm s^{-1} is assumed, the patch on day 14 corresponds to a period of approximately nine hours and an ice-free area of around 1.5 km width. At the same drift speed, a lead of 100 m width would pass the sonar footprint in approximately half an hour. This demonstrates that narrow leads can not be detected visually. However, the algorithm mostly detects such small scale open water features as tie points for the zero-line or as thin ice/open water (flag 2). Other leads, like the ones between days 27 and 29, are easier to identify, although it is not guaranteed that these are completely ice-free. Leads often refreeze rapidly and can be covered by thin ice, whose echo strength may be similar to that of open water. For data sets with low sample rates of eight or even 15 minutes (not shown) it is more difficult to visually assess whether certain features represent open water or periods of thin ice. The middle panel in figure 5.2 demonstrates the necessity of measuring pressure.

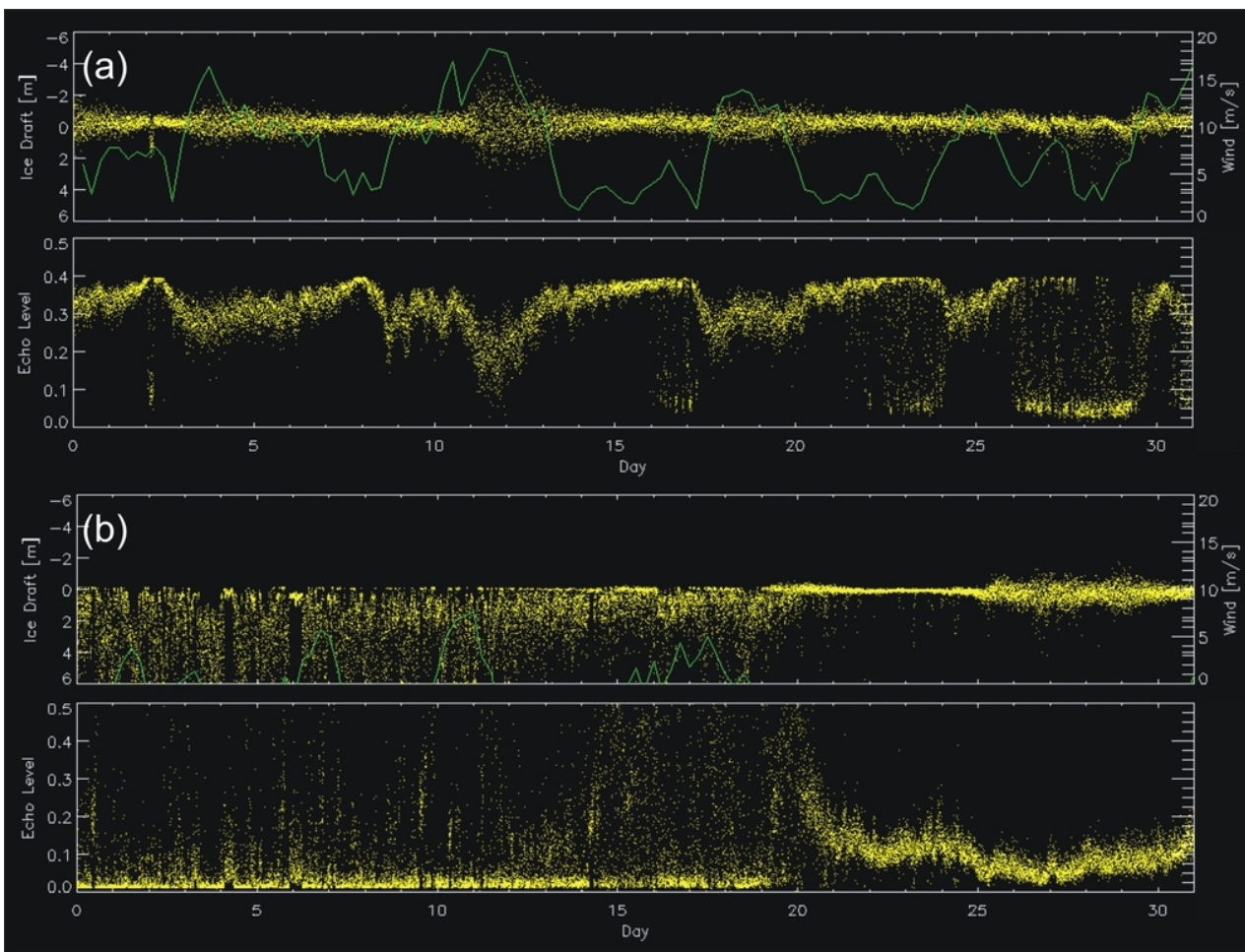


Fig. 5.3: (a) Ice draft and echo level of AWI 233-2 in March 1997. (b) Ice draft and echo level of AWI 232-8 in January 2008. Both plots are taken from ULS_plot_02. The green line represents the ECMWF wind speed.

The ULS depth shows variations of up to 4.5 m caused by a semi-diurnal tide superimposed by a fortnightly tide. In other cases (e.g. at AWI 229-1) the amplitudes of the depth oscillations were larger than 50 m. Not correcting for these depth variations would result in draft errors of equal size. Figure 5.2c highlights the merits of the auxiliary variable V_{env} , from which the echo level is derived. The higher reflectivity of open water compared to the ice bottom can be

clearly seen on day 14. Figure 5.3a shows a nearly ice-free month with the draft data almost symmetrically scattered around the zero-level. Around the days 5, 12 and 19 the increased scattering indicates larger surface gravity waves during storm events, which also coincide with high ECMWF wind speeds. The echo level during these events is reduced, due to the increased scattering of the sonar signal by the surface waves. At the beginning of day 3, a short period of passing sea ice was detected, which is identifiable in both the draft data and the echo level. On day 17 and during the periods of days 22-24 and days 27-30, the low echo level indicates the appearance of first ice patches that mark the beginning of the sea ice season. The draft data between days 27-30 are not symmetrically scattered around the zero-level as it would be typical of open water. But it also does not show a straight zero-line, like the long ice period in figure 5.3b. At the same time the wind speeds are comparably low, which in combination with the low echo level indicates ice. The young ice is still very thin and easily bends on the water surface. The resulting scatter of the data prevents the automatic identification as thin ice/open water, although the echo level during this period indicates a mixture of ice and water. This kind of echo may be created by pancake ice which prevents the identification of a straight zero-level. This case demonstrates the difficulties during the data processing that may arise for certain periods. Either the operator defines such a period as open water in step two, or it will be treated as ice by the processing algorithm. The open water detection is therefore somewhat subjective. The fact that it depends exclusively on visual inspection gives rise to an "operator uncertainty", which in turn depends on the experience of the data analyst. Figure 5.3b shows the transition between ice and open water at the end of the ice season. The echo level jumps from low to high values on day 20, indicating the appearance of open water. Between day 20 and day 25 open water prevails, with some ice draft values in between. The scatter of the draft values in this period is very low, which also indicates that the surface is still very calm and not completely ice-free. On day 26 the echo levels near zero completely disappear. At the same time the symmetric scatter of the draft data displays the occurrence of open water.

The zero-level in the pseudo ice draft generally shows good agreement with open water periods adjacent to periods of ice coverage. The level can be assumed to lie roughly in the centre of the open water echo distribution. In some ice periods, however, a manual correction is necessary. But the ice/open water transition is not always as sharp as in figure 5.3b. The visual identification of open water and the correction of the reference level may therefore be very difficult, as shown in figure 5.4. This uncertainty in the zero-level also contributes to the "operator uncertainty". In such cases, e.g. in figure 5.4a, it may be helpful to visually track the centre of long open water periods nearby (days one and two). Or the operator can use short periods of thin ice/open water, such as the ones on day 11 and 12. It is therefore advantageous when a zero-line correction is applied in the transition times. In periods where a closed ice cover lasts for several weeks the correction may be complicated and more subjective. This problem is discussed in the section *data quality*.

At the onset of the ice season sea ice first appears as frazil crystals, which can be mixed down to 20 m depth [Drucker *et al.*, 2003]. Like in figure 5.4a, the strongly scattered draft values with weak echoes between day 3 and day 8 can be assumed to originate from frazil crystals that formed at the beginning of the ice season. As this suspension can not be regarded as a solid sea ice cover, it is not possible to assign a certain draft value to it. In this case it is recommended that the operator defines such a period as open water.

In leads and larger open water areas breaking waves generate subsurface clouds of air bubbles, that can reflect the ULS signal and could erroneously be interpreted as ice. However, the used sonar frequency lies above the resonance frequency of typical air bubbles at shallow depth.

Furthermore, this error source is reduced by the narrow beam and the very short pulse length of the sonar [Melling, 1998, and references therein]. Nevertheless, it can not be fully excluded that single echoes result from objects suspended in the water column, such as fish and high concentrations of zooplankton [Drucker *et al.*, 2003]. But these echoes are generally not expected to last for several days or weeks.

The data processing algorithm described by Strass [1998] applies an open water detection based on visual inspection and the auxiliary variables V_{env} and d_{diff} . The latter describes the short-term draft variation (i.e. ice roughness) and is calculated from draft variations between the four pings of one sonar burst. This detection of open water requires either V_{env} or d_{diff} to be high². However, this automatic procedure may also produce biased results, for example when d_{diff} is high for rough ice. A slightly improved version of the algorithm was used in the studies of Harms *et al.* [2001] and Drinkwater *et al.* [2001].

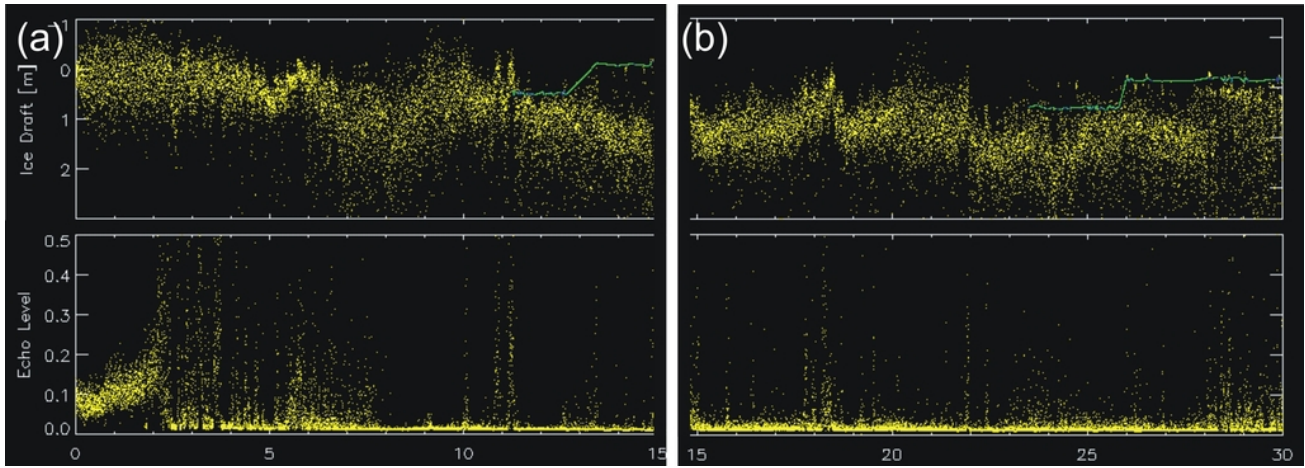


Fig. 5.4: (a) Ice draft and echo level of AWI 232-8 in April 2007. The transition from open water to ice occurs between day 3 and day 8. (b) Ice draft and echo level of AWI 232-8 in April 2006. The echo level displays prevailing ice conditions, but the position of the reference level is not clear (see also part (a) of this figure). Both plots are taken from ULS_plot_03.

Since the first measurements in the early 1990s, improved versions of the ULSs were developed. The increasing data storage capacity allowed for higher sampling rates (see Table II), which strongly increased the data quality and made the processing easier. Some of the ULS types VI or VIII were upgraded with *extended dynamic range* (XDR). For XDR models the gain of the two last echoes of one burst is reduced by a constant offset relative to the two first ones. This allows for a better identification of false targets and requires modified formula in step one of the processing procedure.

To restore comparability and to enable a stable data quality, all data used in this thesis were processed with the AUPC by two analysts. To take the subjective element of the method into account, daily mean files (file extension *.mda*) and monthly mean files (file extension *.mmo*) were calculated from the two draft files and were then averaged. Examples of different *.dra* files are given in figure 5.5. For AWI 229-1 the largest differences occur in the beginning of the ice season in 1996. End of June, part of the data were rejected by one data analyst, whereas the other one classified these data as ice. The differences decrease as the ice draft approaches

²For details see Strass [1998].

its peak at the beginning of November 1996. In 1997 differences also occur in the middle of the ice season in September. These are largely due to the manual correction of the zero-level. Differences in ice draft during transition times of ice and water occur due to differences in the number and length of open water periods, but also due to differently corrected zero-levels. The plot of AWI 231-1 again shows the largest differences in the beginning of each ice season (June/July). The maximum deviations of the running mean values amount to approximately 15 cm. For AWI 232-5 the pattern is almost reversed. At the beginning of the sea ice season the differences are lowest and increase while approaching the peak of ice draft in the period September-October/November. In this case it is very likely that one data analyst corrected the zero-level, whereas the other one largely accepted the level calculated by the algorithm. The red curve is consistently higher than the blue curve, which is responsible for the high RMS-deviation of 23 cm. The plot of AWI 232-8 shows largely good agreement between the filtered daily mean ice drafts of the two operators.

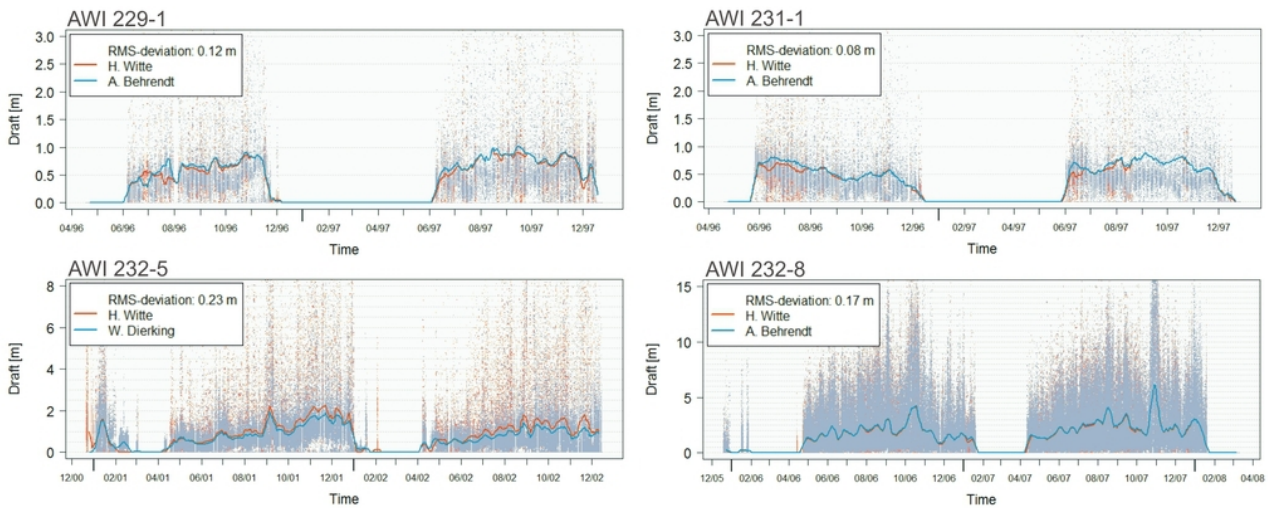


Fig. 5.5: Four examples of *.dra* files processed by two data analysts. Blue and red colours indicate the results of the different analysts. Dots represent single draft echoes. Bold lines are 10-day running means of daily averages. The higher density of dots at AWI 232-5 and AWI 232-8 indicates the higher sampling rate compared to the two upper plots.

However, the RMS-deviation of the single echoes is relatively high (Table III). The best agreement between two files was obtained for the ULSs near Maud Rise. The high RMS values, for example at AWI-207, can be attributed to data cycles identified as ice by one data analyst and as water by the other data analyst.

Figure 5.6a demonstrates that most of the differences between data cycles classified as ice are found during the ice season between June and November. All of these deviations can be attributed to differences in the zero-level. Differences in the range 5 cm to 10 cm, the largest group, occur in more than 250,000 data cycles between June and August. But also the largest numbers of deviations in the ranges 11 cm to 20 cm and 21 cm to 50 cm occur in this period. Only the numbers in the class 0.51 m to 2 m are higher in the period September-November. Most of the deviations in the summer months (DJF) can be attributed to the ULSs near the coast, where the ocean does not become totally ice-free during this period. The number of differences increase in the freeze-up season of the ice cover (MAM). The total number of available valid data cycles in the full ULS data set is about 6×10^6 . The number of 250,000 differing

data cycles (Fig. 5.6a) therefore corresponds to only four percent of the available data. To account for the different treatment of the zero-level, the data cycles from two operators were averaged.

The pattern is almost reversed in figure Figure 5.6b, which shows deviations as a result of different classification of open water. The largest numbers in almost all of the difference classes are found in the period December-February, which is not surprising, as the summer months are dominated by open water. Here, the differences arise due to different lengths of the open water periods identified by the two operators. The fact that large deviations also occur during the freeze-up period (MAM) suggests that periods of frazil may have been treated differently. The deviations of up to 1.1 m to 5 m in the period June-August can also be largely attributed to episodes of frazil, but at ULS positions in lower latitudes, where the freeze-up starts in June. As the differences of the data cycles identified as ice and open water by two operators were considered as too large, these cycles were set to zero draft (open water) and were therefore excluded from the averaging.

**Table III: RMS-deviations of
ULS-data processed by different analysts**

ULS File	RMS-Dev.	ULS File	RMS -Dev.	ULS File	RMS-Dev.
AWI 207-2	68 cm	AWI 229-2	7 cm	AWI 231-6	10 cm
AWI 207-4	31 cm	AWI 229-3	23 cm	AWI 231-7	10 cm
AWI 207-6	31 cm	AWI 229-4	10 cm	AWI 232-1	69 cm
AWI 208-3	23 cm	AWI 229-5	5 cm	AWI 232-4	6 cm
AWI 209-3	6 cm	AWI 229-6	36 cm	AWI 232-5	23 cm
AWI 210-2	13 cm	AWI 230-2	8 cm	AWI 232-6	21 cm
AWI 212-2	40 cm	AWI 230-3	7 cm	AWI 232-8	17 cm
AWI 217-1	29 cm	AWI 231-1	8 cm	AWI 233-2	52 cm
AWI 227-4	8 cm	AWI 231-2	5 cm	AWI 233-6	6 cm
AWI 227-6	14 cm	AWI 231-3	5 cm		
AWI 229-1	12 cm	AWI 231-4	5 cm		

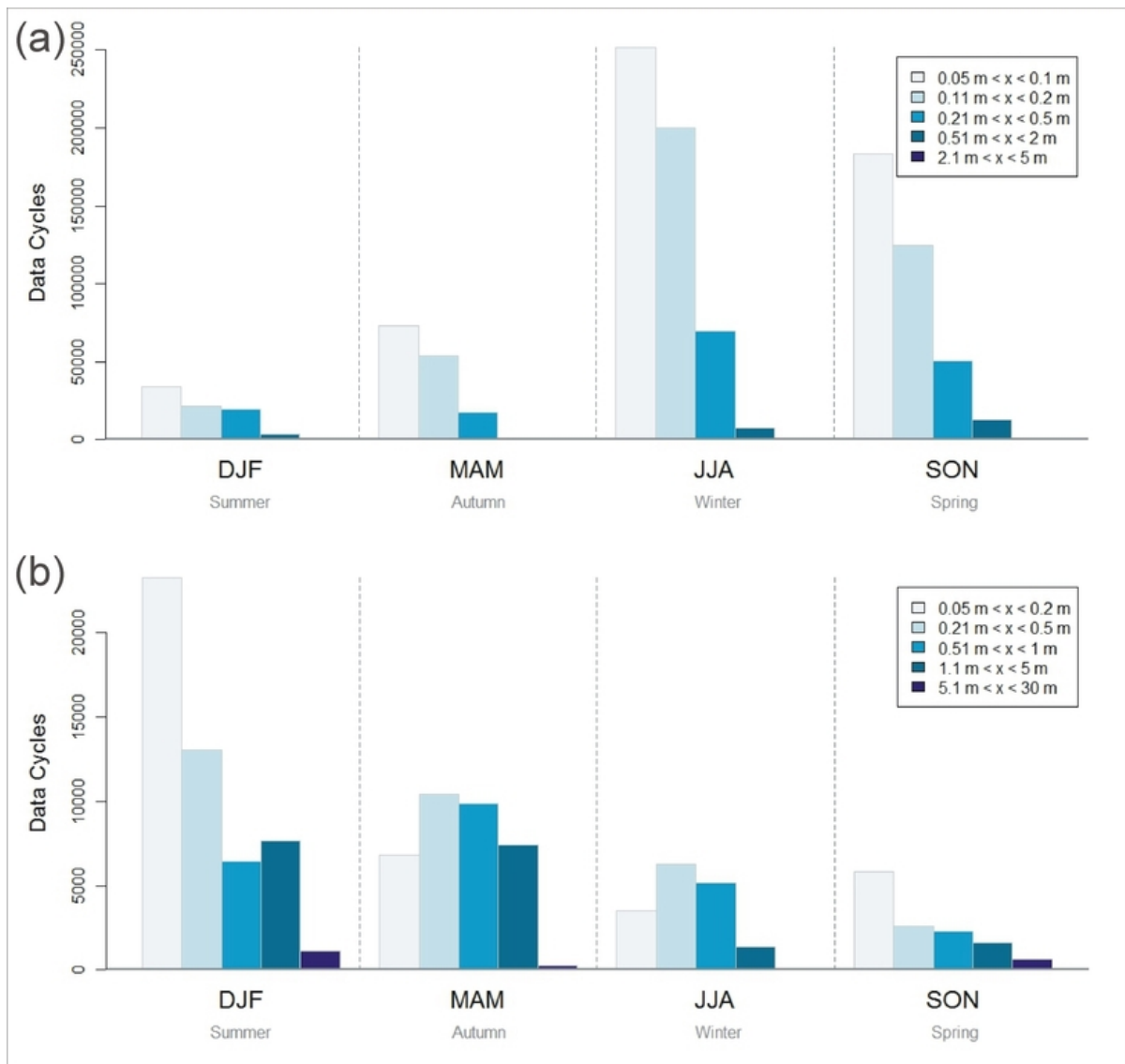


Fig. 5.6: Absolute differences between single data cycles (echoes) of files processed by two analysts. The differences of all ULS files (Table II) were cumulated for this plot, partitioned in classes and then segregated by season. Data flagged with g were excluded. (a) Differences between data cycles classified as ice by both operators. (b) Differences between data cycles classified as water by one operator and as ice by the other. DJF: December-February, MAM: March-May, JJA: June-August, SON: September-November.

5.2 Data quality

The results presented in the following section have been published in *Behrendt et al.* [2012]. However, in this section they are discussed in more detail.

According to ISO³ standard, the term "accuracy" refers to a combination of random error and systematic error components [*Hauck et al.*, 2008, and references therein]. The random error is called "precision" and refers to the degree of scatter between a number of repeated measurements under the same conditions. It is measured by the standard deviation of the test results and can therefore be regarded as a statistical error. In the following, the terms "uncertainty" and "standard error" are used as synonym for precision. A systematic error, also called "bias", defines the deviation of the average value of repeated measurements from a reference quantity value [*Hauck et al.*, 2008, and references therein]. The term "accuracy" will be used for a combination of bias and precision.

5.2.1 Accuracy

The measured distances, from which the ice draft is derived, are several orders of magnitude greater than typical ice drafts. Small errors in these distances therefore result in comparably large errors in the ice draft estimates [*Shcherbina et al.*, 2005]. The full ULS-equation from which the ice draft is derived is composed of the equations (3.3) and (3.4):

ULS-Equation

$$d = \frac{p - p_a}{g\rho} - \frac{1}{2}ct \cos(\alpha) \quad (5.1)$$

Each input variable in this equation is burdened with a specific uncertainty. The law of error propagation describes how the errors in the input variables are propagated to the output variable⁴. The general form of an error propagation is

$$\Delta d = \sqrt{\sum_{i=1}^n \left(\frac{\partial d}{\partial x_i} \Delta x_i \right)^2 + 2 \sum_{j=1}^p \sum_{\substack{k=1 \\ j \neq k}}^p r_{x_j x_k} \left(\frac{\partial d}{\partial x_j} \Delta x_j \right) \left(\frac{\partial d}{\partial x_k} \Delta x_k \right)}, \quad (5.2)$$

where n is the number of variables in the function, p is the number of correlated variables, x_i stands for all variables in the function, all delta values stand for the respective uncertainties in the variables, and x_j and x_k stand for any two variables which are correlated with the correlation coefficient $r_{x_j x_k}$ [*Gränicher*, 1996]. The numerator of a standard correlation coefficient contains the covariance of the two correlated variables. As the covariance measures the degree of correlation of errors between any two variables, correlations in the error propagation can be

³ISO: International Organization for Standardization.

⁴See e.g. *Schönwiese* [1992] or *Gränicher* [1996].

regarded as correlations in the uncertainties of the variables⁵ [Gränicher, 1996]. If all variables were uncorrelated, the right hand term under the square root in equation (5.2) would vanish and the equation then describes the Gaussian error propagation.

Calculating a Gaussian error propagation for the ULS-equation is not readily possible, because the values for c and ρ are fixed numbers in the AUPC ($c = 1442 \text{ m s}^{-1}$, $\rho = 1027 \text{ kg m}^{-3}$). These values, especially the sound velocity, are naturally highly variable and therefore not known for each ULS measurement. The values of c and ρ are in this sense no experimentally determined mean values with known statistical uncertainties. They are more or less realistic estimates which are used to calculate a "first guess" of sea ice draft (pseudo draft). However, an error propagation was applied to estimate the accuracy of drafts corrected by a sound speed model (see below).

Sensitivity study

To estimate the theoretical contribution of each uncertainty of the variables, one can use realistic estimates of all variables in the ULS-equation and alter each value by its uncertainty. The uncertainties of the instrument sensors and geophysical parameters are given in table IV. The absolute values used for the sensitivity study are: $t = 0.205275 \text{ s}$, $p = 16.1347 \text{ bar}$, $\alpha = 0^\circ$, $g = 9.8231 \text{ m s}^{-2}$, $c = 1442 \text{ m s}^{-1}$, $p_a = 990 \text{ hPa}$ and $\rho = 1027.8 \text{ kg m}^{-3}$. The parameters p , p_a , g and ρ are chosen in such a way that they correspond to a ULS depth of 150 m. The measured signal travel time is valid for an ice draft of 2 m. The influence of each uncertainty on the ice draft was estimated with the signal travel time given above, and altering step by step each absolute value by its uncertainty.

a) Instrument parameters:

The ice draft error induced by the small uncertainties in the time measurement is less than 1 cm. Also the error in the tilt sensor would account for at most 2-3 cm ice draft.

Table IV: ULS uncertainties

Instrumental parameters	
pressure	$\Delta p = 0.009\text{-}0.024 \text{ bar}$
time	$\Delta t = 4.3 \mu\text{s}$ (ES-300 VI/VIII) $= 13 \mu\text{s}$ (ES-300 V)
tilt	$\Delta\alpha = 1^\circ$
Geophysical parameters	
atm. pressure	$\Delta p_a = 1 \text{ hPa}$
sound velocity	$\Delta c = \text{unknown}$
water density	$\Delta\rho = \text{unknown}$

The error sources in a calibrated pressure sensor can be divided into two groups: those that are dependent on applied pressure and those that are not (Fig. 5.7). The three offset errors - offset temperature coefficient, offset repeatability and offset stability - are independent of applied pressure. The three span errors - span temperature coefficient, linearity-hysteresis-repeatability and span stability - on the contrary are proportional to pressure, as they affect the linear response (sensitivity) of the sensor to the applied pressure range [Honeywell, 2004].

The *Lucas Schaevitz* sensor (Table II) is based on a foil strain gauge. Its temperature coefficient is given as a combined thermal offset and span coefficient of $\pm 0.004\%$

temperature coefficient is given as a combined thermal offset and span coefficient of $\pm 0.004\%$

⁵The product $r_{x_j x_k} \Delta x_j \Delta x_k$ on the right hand side of equation (5.2) is equal to the covariance between x_j and x_k .

F.R.O.⁶/°C. The combined coefficient is often given, when both contributions (offset and span) are of the same size. The same applies to the long-term drift. If only a temperature error (total error band) were given, one could derive the temperature coefficient from the slope of the error lines (similar to the example in figure 5.7). At room temperature, a temperature error is equal to the linearity-hysteresis-repeatability error (see below) [Beyer, 2008]. The temperature coefficient of the *Lucas Schaevitz* sensor is valid for the full compensated 100°C temperature range (-20°C to 80°C). This would result in a temperature coefficient of $\pm 0.004\% \text{ F.R.O.}/^\circ\text{C} \times 100^\circ\text{C} = \pm 0.4\% \text{ F.R.O.}$ (total error band). In practice, the encountered temperature ranges are much smaller (usually not more than 2-3°C). The temperature coefficient is therefore reduced. For a temperature range of 2°C it is $\pm 0.004\% \text{ F.R.O.}/^\circ\text{C} \times 2^\circ\text{C} = \pm 0.008\% \text{ F.R.O.}$, which translates into approximately 2 cm ice draft. The long-term drift (also *long-term stability*) according to the instrument specifications is $< 0.1\% \text{ F.R.O.}$ per year.

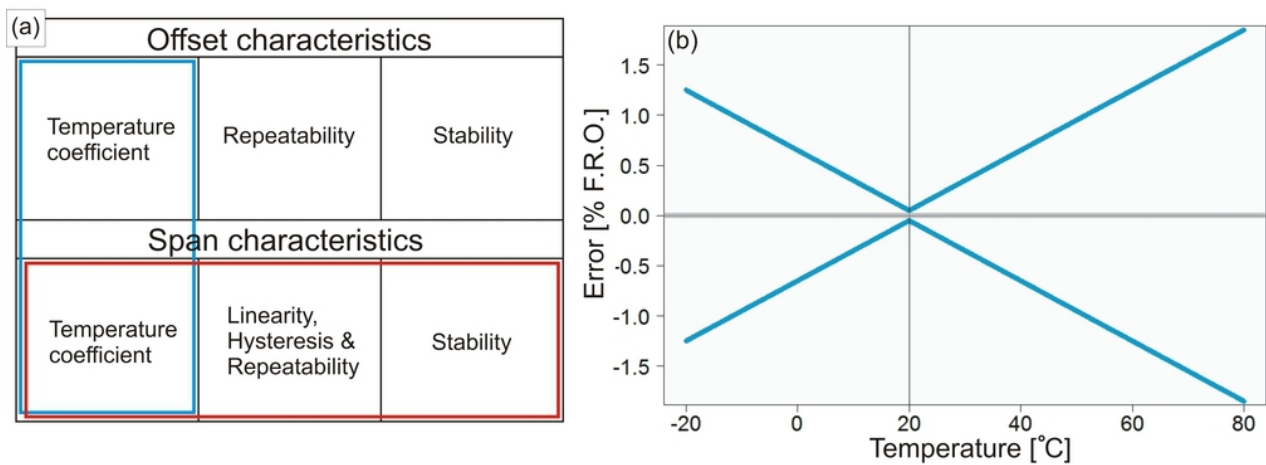


Fig. 5.7: (a) Pressure sensor errors after *Honeywell* [2004]. The blue framed errors are reduced by temperature range correction and the red framed errors are reduced by pressure range correction. (b) Temperature error of the *Druck PDCR 130/W* pressure transducer. The temperature error takes its minimum at room temperature (20°C).

It can be assumed that this error results from 50% span stability and 50% offset stability. The linearity-hysteresis-repeatability error is given as $\pm 0.05\% \text{ F.R.O.}$, which translates into 10 cm ice draft. Overall, the most probable pressure sensor error would then be

$$\Delta p = \sqrt{0.008^2 + 0.1^2 + 0.05^2} = 0.11\% \quad (5.3)$$

of the full range pressure output, which translates into 22 cm ice draft for one year of measurement. For a two years period it would result in a change of 41 cm draft. However, only a small part of the full pressure range of 0-20 bar is encountered during the deployment period. A ULS can oscillate between 150 m and 190 m depth due to ocean currents and tides. The encountered pressure range is only 4 bar. This affects all span errors of the pressure sensor, and they can be scaled by the factor $R = (4 \text{ bar}/20 \text{ bar})$ [Honeywell, 2004]. From the instrument specifications it is not clear whether offset repeatability is included in the linearity-hysteresis-repeatability

⁶F.R.O.: Full Range Output: The difference in the output signal between the minimum and maximum measurable pressure (0-20 bar).

error, as it is not given separately. If it were included, only a certain fraction of the linearity-hysteresis-repeatability error would have to be multiplied by R . However, as the largest part (>96%) of the overall pressure sensor error results from the drift error, this unawareness can be neglected. Multiplying 50% of the temperature error, 50% of the drift error and the full linearity-hysteresis-repeatability error by R then leads to the reduced Δp of 0.061% F.R.O. This translates into $\Delta p = \pm 0.012$ bar total error band plus one year drift, i.e. 12 cm ice draft (24 cm for two years).

The pressure sensor *Druck PDCR 130/W* is based on a silicon strain gauge. Its combined temperature error is given as $\pm 1.5\%$ F.R.O. total error band (BSL⁷). From this value one can derive a temperature coefficient of $\pm 0.03\%$ F.R.O./°C (i.e. the slope of the lines in figure 5.7b). For a temperature range of 2°C it is $\pm 0.03\%$ F.R.O./°C \times 2°C = $\pm 0.06\%$ F.R.O., which translates into 12 cm ice draft. The combined linearity-hysteresis-repeatability error is $\pm 0.05\%$ F.R.O. As a value for the long-term drift is not given in the instrument specifications, it can be assumed to be negligible. Silicon strain gauges do not have chemical bonds that deteriorate over time and are therefore generally very stable. In the example given in *Honeywell* [2004], the offset repeatability error would approximately constitute 37% of a combined offset and span linearity-hysteresis-repeatability error. Multiplying 63% of this error and 50% of the reduced thermal error by R leads to an overall reduced Δp of $\pm 0.044\%$ F.R.O., which translates into 9 cm ice draft.

However, the above values have to be considered as theoretical values, because significant drifts were found in the Druck PDCR 130/W transducer, and the drifts found in the Lucas Schaevitz transducer exceeded those given in the instrument specifications.

b) Geophysical parameters:

The latitude-dependent acceleration of gravity is calculated after *Roedel* [1994]:

$$g(z, \varphi) = 9.806(1 - 0.0026 \cos(2\varphi)) * (1 - 3.1 \times 10^{-7} z), \quad (5.4)$$

where z is the height (depth) above (below) the zero-level and φ is the latitude. As the dependence on z is negligible for usual ULS depths, the last term of the equation can be ignored. The value for g is calculated for each ULS-latitude. However, ignoring this latitude-dependence would result in a draft bias of only a few centimetres. The uncertainty in the ECMWF pressure is the average standard deviation of the differences between ECMWF pressure and the pressure measured by several sensors on ice floes in the Bellinghausen Sea between February and May 2001 [*King*, 2003]. As the study region is close to the Weddell Sea, the value of 1 hPa is assumed to be a reasonable estimate for the Weddell Sea as well. A pressure variation of 1 hPa would alter the draft estimate by about 1 cm.

The values $\Delta\rho$ and Δc can be estimated from CTD measurements. The standard deviations of the plotted values in figure 5.8 are $\Delta\rho = 0.05 \text{ kg m}^{-3}$ and $\Delta c = 2.6 \text{ m s}^{-1}$. These values can be used to alter the absolute values, like in the examples above. An uncertainty of 0.05 kg m^{-3} in the density would cause an error in the ice draft of less than 1 cm. The uncertainty in the sound speed of 2.6 m s^{-1} on the contrary would cause an ice draft error of 27 cm. The value of Δc can therefore be assumed to dominate the uncertainties of the geophysical variables.

⁷BSL: Best Straight Line. See *Beyer* [2008].

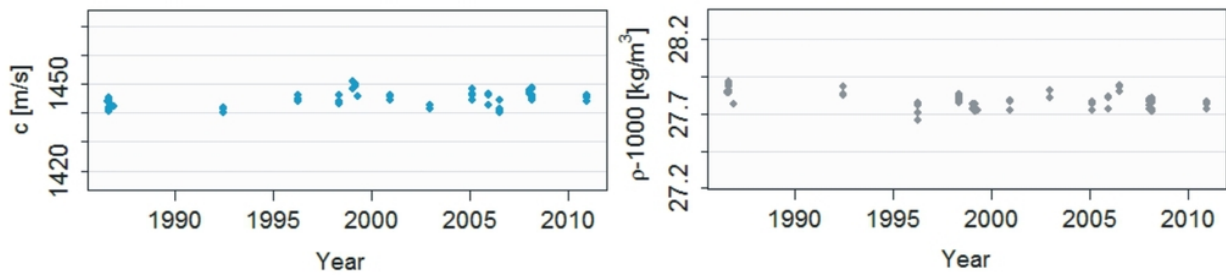


Fig. 5.8: Vertical mean sound velocity (left) and density (right) for the upper 150 m, calculated from CTD measurements on the position of AWI-231. The y-axes span the range $\pm 2\%$ of the mean value of the respective data.

The appearance of the pseudo draft is depicted in figure 5.9. As the pre-set values of c and ρ differ from the unknown true values, the resulting offset in the ice draft zero-line (and thus in the draft itself) has to be corrected as described in the previous section. This offset is mainly due to the unawareness of c and sometimes also due to drift in the pressure sensors. The combination of these errors is expressed in a variable offset between the pseudo draft zero-line (i.e. zero draft) and the zero-level. As the winter temperature profile above the ULS usually includes a thermocline⁸ whose depth is variable, the vertical mean sound velocity also varies over the entire deployment period. The zero-level in the pseudo draft record is therefore not always easily identifiable as straight line. Only in those cases where the ULS depth is less than 110 m or the instrument is moored near the coast, the zero-line is visually identifiable as straight line at the upper edge in the pseudo draft plot, provided that enough leads or very thin ice is present (Fig. 5.9a). The respective vertical temperature and sound speed profiles are constant from the surface to the ULS depth over the whole winter season, i.e. the water temperature at both the ice underside and the ULS is at the freezing point. The vertical harmonic mean sound velocity is therefore constant and has a constant offset to the pre-set value of 1442 m s^{-1} . When the temperature profile includes thermocline whose depth varies over time, the position of the zero-line is often less obvious (Fig. 5.9b).

⁸Temperature and sound velocity profiles are shown further below.

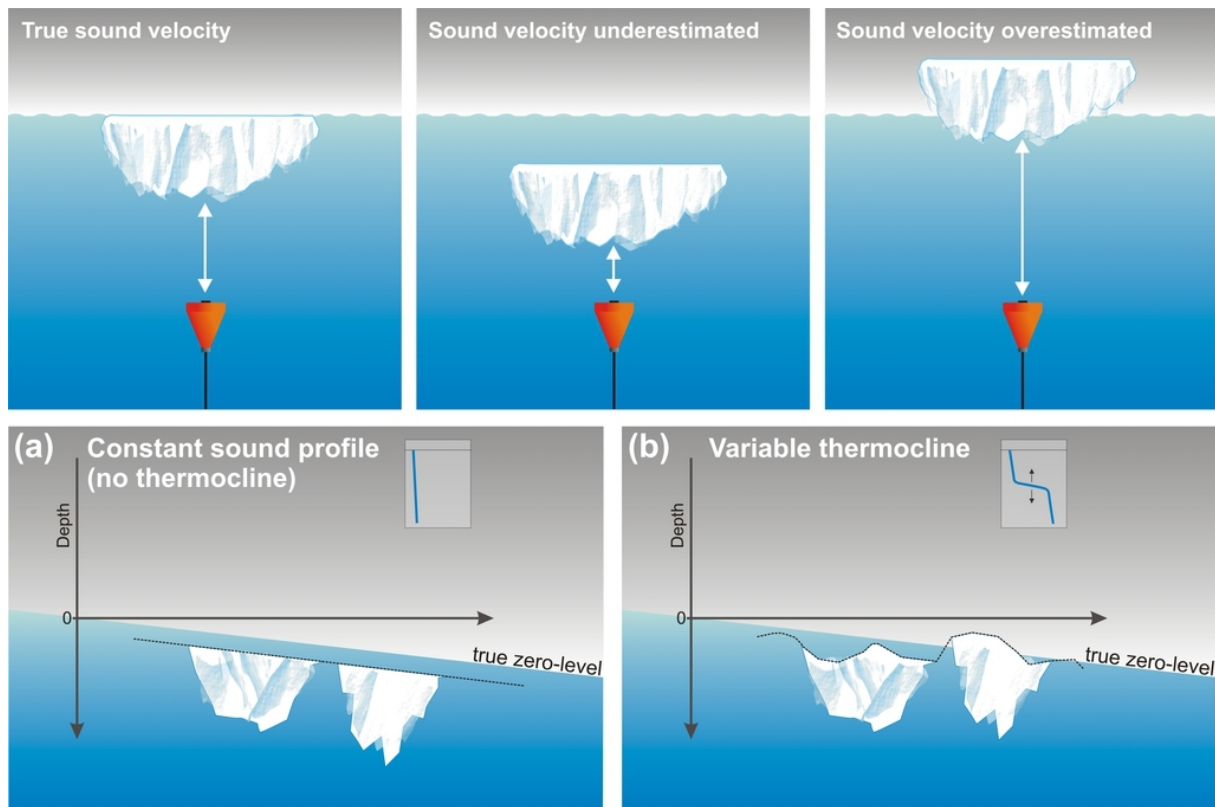


Fig. 5.9: Upper panels: Simplified illustration of errors induced by false estimation of the vertical mean sound velocity. Lower panel: Appearance of the uncorrected pseudo draft: (a) Pseudo draft for ULS moored at small depths or near the coast with a constant sound speed profile. The linear drift in the pressure sensor results in a growing deviation of the data from zero draft on the y-axis. The lead between the ice floes is used for zero-line interpolation. The constant deviation of the data from the true zero-level is a result of the constant difference between the true sound speed and the sound speed used to calculate the pseudo draft. The thin dashed line marks the level of leads and minimum ice draft. (b) Pseudo draft for deeper ULS. The variable winter thermocline leads to variable vertical mean sound velocities and densities. This in turn leads to variations in the minimum ice draft and leads around the true zero-level. The drift induced by the pressure sensor remains linear.

Ice draft error estimation

The variations in the pseudo draft result from a superposition of (1) true ice draft variations, (2) variations in the vertical mean sound speed, (3) small variations in the vertical mean water density and (4) drift and offsets in the pressure sensors. If the real zero-line is found in the pseudo draft by the interpolation, the errors (2-4) and the uncertainties (Δ -terms) are eliminated by the zero-level correction in the AUPC. To what extent they are eliminated can only be estimated. As described above, the operator identifies longer periods of open water during the processing of the data. Smaller open water features, such as leads, are in most cases detected as draft minima by the interpolation algorithm. However, the algorithm does not capture every small crack in the ice. These remaining cracks and leads can be identified and used to estimate the error of the zero-level correction by investigating the statistical distribution of the ice draft that remains after the correction. The identification of cracks and leads is aided by the echo level.

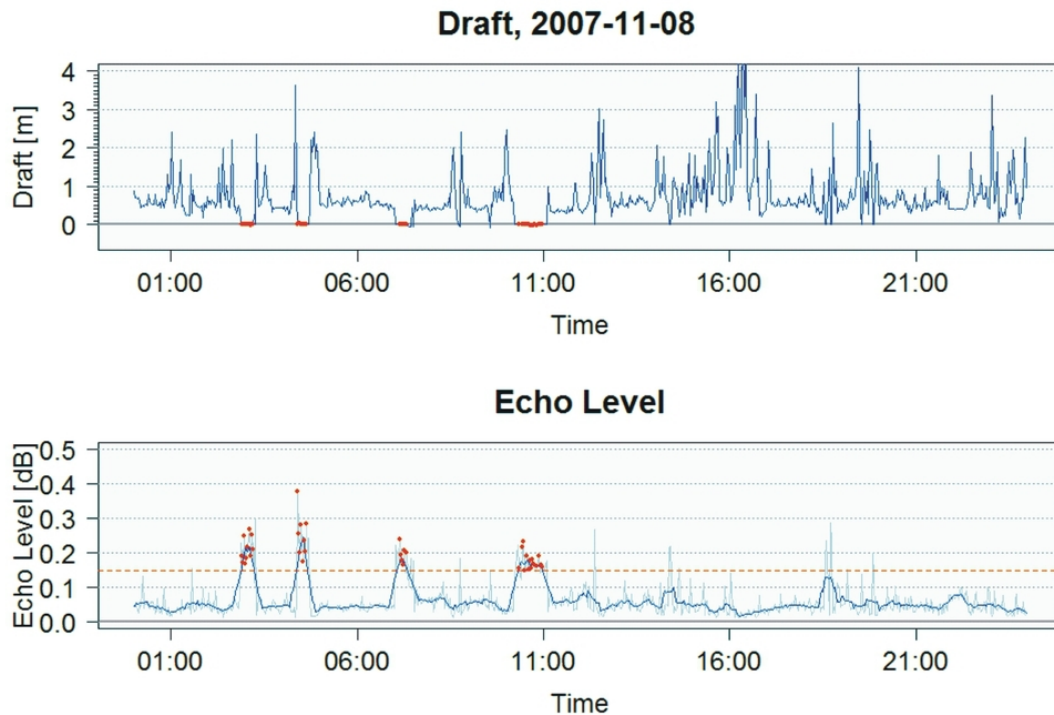


Fig. 5.10: Upper panel: Ice draft of AWI 231-7 on November 08, 2007. The red dots in both plots represent times of open water. Lower panel: Echo level of the same period. The red dashed line depicts the selected echo threshold for open water detection. Light blue line: unfiltered echo level. Dark blue line: filtered echo level.

The discrimination between echoes from ice and water depends on the sample rate of the instrument. Only those instruments with a rate of four minutes or lower were found to be suitable for the procedure. The number of usable records was further reduced, as the quality of the echo level turned out to be crucially dependent on the sensitivity and gain settings of the ULS-receiver. Eventually, only six data sets (AWI 207-6, AWI 227-4, AWI 231-7, AWI 232-6, AWI 232-8 and AWI 233-2) were found to be useful for a reliable ice/water discrimination. The detection algorithm was programmed in such a way that leads are detected when the echo level crosses a predefined threshold. Typical echo levels of open water can be obtained from the measurements in austral summer, in periods when the wind speeds are low and the sea surface is calm. As the echo level is highly variable and not every single peak above the threshold represents open water, the echo signal was filtered as a 10 points running mean. This guarantees that the threshold is passed only by those signals that on average remain high for a longer time period, which is typical for leads. Within these time windows the times of open water were then defined as the points of the unfiltered echo level that lie above the echo threshold (Fig. 5.10). The performance of this method can be assessed with the respective pseudo draft plot. Leads within the ice appear as mostly rectangular-shaped gaps in the draft record (Fig. 5.10). Intervals with strongly wind-disturbed open water were excluded to avoid a bias of the surface level offset. Leads that were correctly captured by the search algorithm - i.e. the tie points of the interpolated zero-line - have zero draft. Thus, their error is zero. The resulting elevation distribution of the remaining leads is approximately Gaussian-shaped (Fig. 5.11). In this time series the open water draft mode was detected similarly to the method of *Strass* [1998]: Single modes were detected for leads long enough to remove the noise resulting

from short surface gravity waves. The final mode was then calculated as the mean of the open water draft modes from those leads in the six data sets that were identified by their echo level but not detected by the search algorithm. The mean open water draft mode found in this way is 4 cm. The standard deviation of the mean open water draft mode is ± 6 cm. The mode represents a bias, whereas the standard deviation represents the dispersion (precision) of the corrected draft data around the location of undetected leads. The overall accuracy is then calculated as the root mean square (rms) error, which accounts for both types of errors [Hauck *et al.*, 2008]:

$$\epsilon_{rms} = \sqrt{\sigma^2 + bias^2}. \quad (5.5)$$

The accuracy found in this way is about ± 7 cm. Note that this estimate is strictly valid for the data sets investigated here and depends on the subjective control of data minima described below. Another problem is that tie points can mistakenly or on purpose be selected within thin ice. For spring and autumn, the tie points selected by the search algorithm could be shown to represent open water by assessing their echo level. In winter, the algorithm sometimes uses ice because of the lack of leads. This problem is further discussed below.

The error is a local estimate which is valid for leads that were not detected. To estimate the error of the full data record one also has to consider all leads that were correctly detected for the zero-line interpolation by the processing algorithm. About 55% of all leads identified by the echo level were found to be detected by the search algorithm. These detected leads have zero mean and standard deviation. If the above procedure is repeated, the mean open water draft mode reduces to 2 cm and the standard deviation of the mean open water draft mode to 4.5 cm. The corresponding rms-error is ± 5 cm. One has to be aware that the calculation is based on only 6 out of 31 data sets and therefore may not reflect the accuracy of all available data. However, the six data sets used for the calculation were acquired from 59°S to 69°S latitude on the prime meridian and include a record from the Antarctic Peninsula, thus representing different ice regimes. Therefore, they can be regarded as a reasonable estimate for the remaining data sets as well. *Melling and Riedel* [1995] and *Melling et al.* [1995] deployed ULS instruments for 5-6 months in the Arctic and fitted curves through the available open water points. The fitting error of these curves was $\pm 2-5$ cm and represents the precision of measurement, which is comparable to the value presented here.

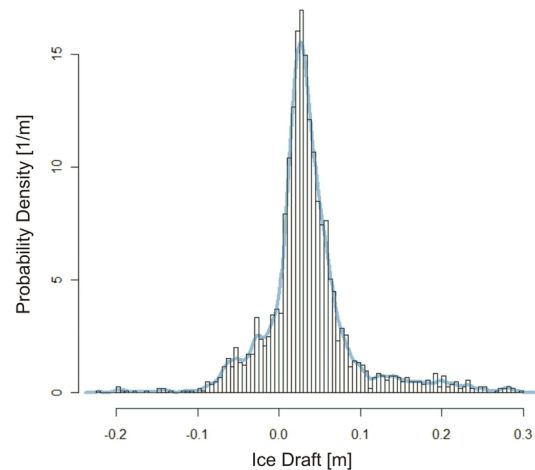


Fig. 5.11: Probability density of ice draft in leads that were not detected by the AUPC search algorithm. The slight skewness to positive drafts suggests that some ice drafts were falsely identified as open water. This may introduce a bias of 2-3 cm into the error estimation.

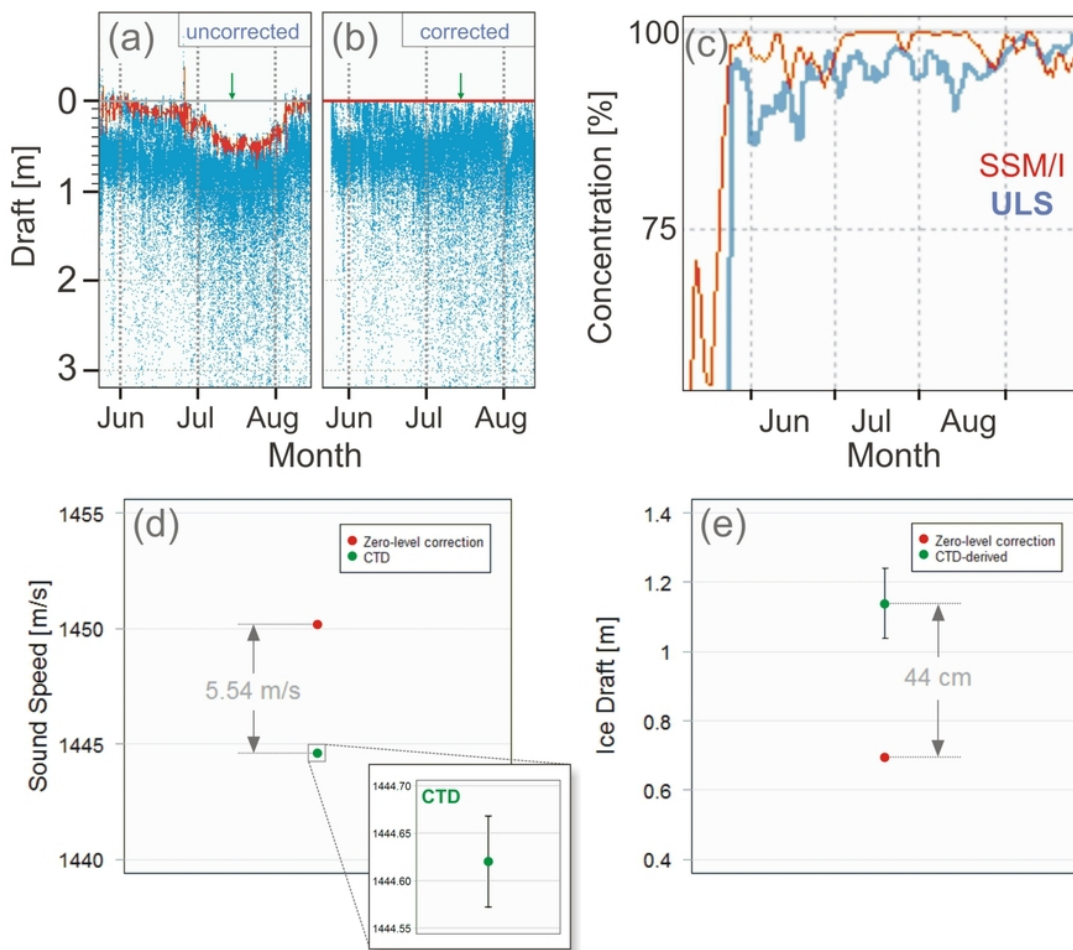


Fig. 5.12: (a) Pseudo draft of AWI 231-7 in winter 2006 (sample rate: 4 min). The red line depicts the interpolated zero-line through ice draft minima. The green arrow marks the time of CTD measurement. (b) Corrected ice draft with the interpolated line levelled to zero draft. (c) Sea ice concentration on the position 231 in the same period from SSM/I and ULS. (d) Mean sound speed calculated from a CTD measurement on July 13, 2006, 20:03:00, and mean sound speed that would be needed to obtain the corrected ice draft in (b) at the same time with the respective ULS parameters. (e) Corrected ice draft on July 13, 2006 at the time of the CTD measurement, and ice draft calculated with the CTD-derived sound speed. The error bars of the ice draft were obtained through error propagation, using the uncertainty Δc from the CTD sound speed in (d) and neglecting $\Delta \rho$.

However, an additional problem arises if no leads are present over long periods in winter. In these cases the zero-line interpolation is biased. If no leads are present for a longer period, the search algorithm picks the thinnest ice as minima and incorporates it into the zero-line interpolation. The bias therefore depends on the mean thickness of the thin ice. The problem can be illustrated by calculating the ice draft for times when the true sound speed profile in the water column is known from CTD measurements. The draft calculated from the CTD measurement in winter 2006 (Fig. 5.12⁹) shows that the true ice draft is reduced by more than 40 cm due to the false interpretation of draft minima. Figure 5.12 shows that in July the ice concentration from SSM/I in the vicinity of the ULS was 100% for several weeks. Therefore, this

⁹The error bars on the sound velocity in figure 5.12 were obtained by calculating an error propagation for the sound speed equation of MacKenzie [1981] and using salinity, temperature and depth from CTD measurements on the position of AWI-231.

error is expected to appear only in the winter months. The winter months are thus alternatively corrected by a simple sound speed model.

Sound speed model

The model basically approximates the temperature profile in the winter mixed layer and translates it into a sound speed profile. It is based on the assumption that the temperature profile in winter can be approximated by a hyperbolic tangent function (Fig. 5.13) [Strass, 1998]:

$$T(z) = T_{uls} + 0.5(T_{sst} - T_{uls}) [1 - \tanh(s(z - h))], \quad (5.6)$$

where T_{sst} is the sea surface temperature, T_{uls} is the temperature at the ULS depth, z is the depth, and s and h the steepness and the depth of the inflection point, respectively. The sea surface temperature is set to a constant value of -1.8°C , since only the winter months are considered here.

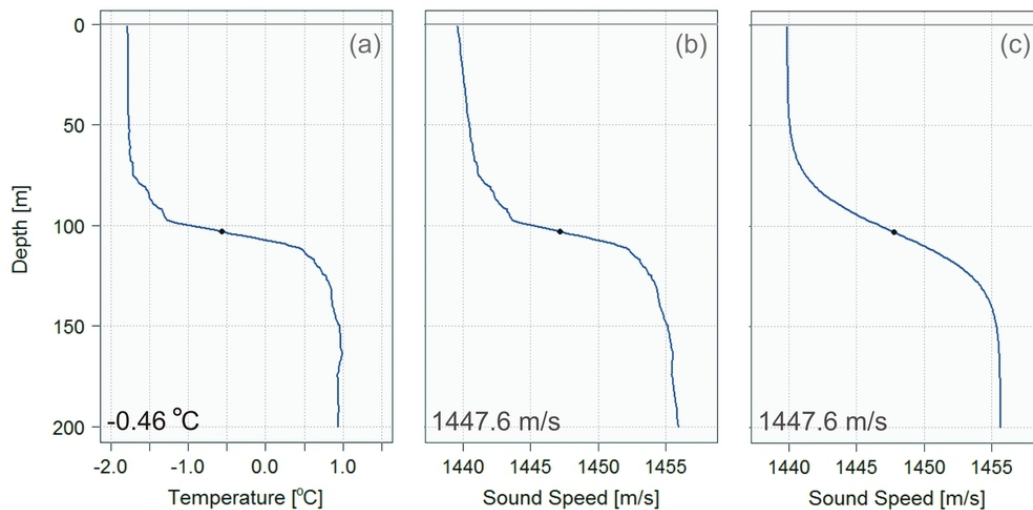


Fig. 5.13: (a) CTD profile of temperature on the position of AWI-231. (b) Sound speed profile calculated from the CTD measurement using the *TEOS-10 Gibbs SeaWater Library* [Wright et al., 2010]. (c) Hyperbolic tangent fit to the sound speed profile. The numbers are the vertical averages of the profiles. The black dot represents the inflection point.

In fact, CTD measurements on the mooring positions in winter showed that the temperature of the surface layer - at least the upper 50 m - is always at the freezing point. The lower bound is given by the temperature record of the ULS. The steepness s does not significantly alter the vertical mean sound velocity. It is set to a constant value of 0.05, which was found to match most of the CTD profiles well. The depth of the inflection point on the contrary does alter the vertical mean sound velocity significantly. For a ULS at 150 m and $T_{uls} = 1.2^\circ\text{C}$, a change in depth of the inflection point from 40 m to 80 m would alter the sound velocity by about 3.8 m s^{-1} . Keeping the measured travel time of the sonar signal constant, this would alter the calculated ice draft by about 40 cm. The depth of the inflection point can be derived from T_{uls} . For most of the ULS data a significant negative correlation between h and T_{uls} could be determined from CTD observations at the respective mooring positions. It follows that if T_{uls}

is equal to $T_{sst} = -1.8^\circ\text{C}$, the temperature profile is constant from the surface to the ULS depth. The depth oscillations of the ULS instruments due to ocean currents and tides can have amplitudes of more than 60 m. As this affects the vertical mean sound speed, the depth changes of the ULS are also considered in the model.

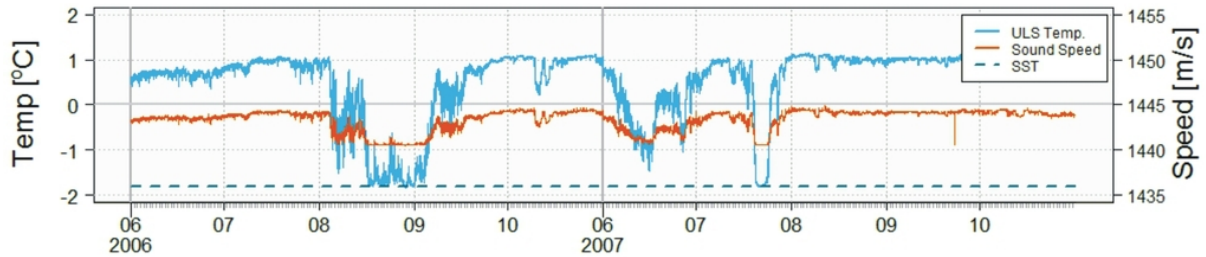


Fig. 5.14: T_{uls} , sea surface temperature (SST) and model-derived vertical mean sound speed for the winter months of AWI 231-7. In periods at which T_{uls} drops to SST, the sound speed profile becomes constant and the vertical mean sound speed reaches its minimum.

More than 400 CTD profiles measured in the Weddell Sea during the years 1986-2010 were investigated for correlation between temperature and sound speed. The measurements were made around the mooring positions within a radius of 50 nautical miles. The correlation coefficient between the two quantities is always very close to one. The temperature profile can therefore be directly translated into a sound speed profile by a linear fit to the scatterplot of temperature and sound speed. Each time a sonar echo is received (every 2-15 minutes) one vertical mean sound speed is calculated from the profiles. In the following, all vertical means of sound speeds from the model or CTD are calculated as harmonic means. If an ice draft of e.g. 5 m occurs, the upper 5 m of the profile would have to be excluded from the averaging. But as the ice draft is calculated from the sound speed and therefore not known before, the influence of the ice thickness on the calculation of the mean is ignored. In the case of 5 m ice draft it would cause an ice draft error of about 2 cm. Most of the encountered ice drafts are considerably smaller than 5 m, and the error can be assumed to be negligible. The calculated sound speeds (Fig. 5.14) were used to correct the pseudo draft of each ULS file. The mean rms-difference in the winter months between data corrected by zero-line interpolation and the sound speed model is about 27 cm (Table V). However, the comparably high rms-differences of AWI 231-6 (Figs. 5.15C,D), AWI 232-8 and AWI 233-2 suggest that quality of the sound speed model is limited at times.

The described correction could not be applied to ULS instruments on the position of AWI-229, as the variations of the thermocline depth (inflection point) were found to be strongly independent of T_{uls} at times. This behaviour seems to originate from oceanic processes, because the position 229 lies in an oceanic frontal zone, where strong north-south gradients in the salinity of the surface waters and also in the eastward geostrophic transport are observed [Whitworth and Nowlin, 1987]. In these frontal zones mesoscale eddy activity enhances the cross-frontal exchange [Whitworth and Nowlin, 1987], which might destroy the correlation between T_{uls} and h through entrainment of water from further north or south into the upper water layers. As indicated by the echo level of AWI 229-4, and the ice concentration that rarely reaches 100%, leads seem to appear frequently in that region. The data sets of AWI-229 were therefore completely corrected by the zero-level interpolation. As discussed above, this is an accurate correction method if enough leads are present in the ice.

Table V: RMS-deviations of ice draft in the winter months of data corrected by two different methods

AWI 207-2:	17 cm	AWI 212-2:	20 cm	AWI 231-2:	23 cm	AWI 232-4:	23 cm
AWI 207-4:	33 cm	AWI 217-1:	18 cm	AWI 231-3:	15 cm	AWI 232-5:	29 cm
AWI 207-6:	21 cm	AWI 227-4:	22 cm	AWI 231-4:	32 cm	AWI 232-6:	33 cm
AWI 208-3:	22 cm	AWI 227-6:	22 cm	AWI 231-6:	52 cm	AWI 232-8:	41 cm
AWI 209-3:	19 cm	AWI 230-3:	39 cm	AWI 231-7:	28 cm	AWI 233-2:	44 cm
AWI 210-2:	20 cm	AWI 231-1:	18 cm	AWI 232-1:	27 cm	AWI 233-6:	25 cm

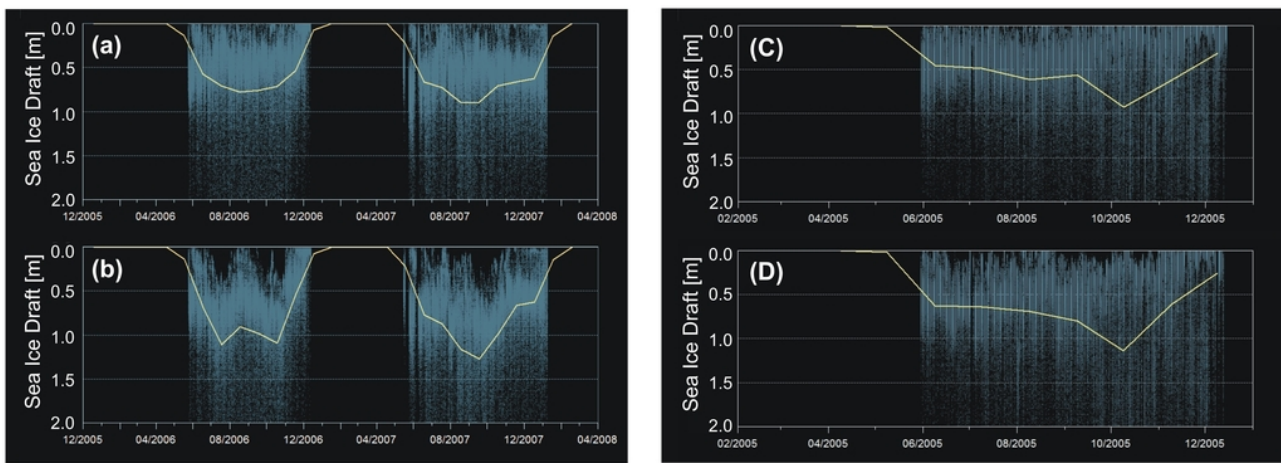


Fig. 5.15: (a) Ice draft of AWI 231-7, corrected by zero-line interpolation. (b) The same ice draft, but with the months June-October corrected by the sound speed model (incl. pressure drift correction) and the remaining months by zero-line interpolation. The solid lines are monthly mean ice drafts. (C) Ice draft of AWI 231-6, corrected by zero-line interpolation. (D) The same ice draft, but with the months June-October corrected by the sound speed model (incl. pressure drift correction) and the remaining months by zero-line interpolation.

Pressure sensor drift

The sound speed correction does not account for drifts in the pressure sensor. The pressure drift can be responsible for an apparent change in ice draft of almost 0.5 m within eight months, which is much larger than given in the instrument specifications of the pressure sensor. The drift could be easily identified only in those data sets, in which the sound speed profile is constant throughout the winter months. This applies only for ULS instruments moored at depths of less than 120 m or near/on the continental shelf. The constant difference between the vertical mean sound speed and the pre-set sound speed of 1442 m s^{-1} used to calculate the pseudo draft results in a very clear and straight zero-line in the ice draft. This enables the visual correction of the pressure drift (Fig. 5.16). However, pressure drift was not found in all data sets. In cases of variable vertical mean sound speed, drifts were corrected by using additional information from the signal travel time. Contrary to the pressure sensor, the clock measuring the signal travel time is not expected to show a significant drift. A linear fit to the signal travel times of the whole period therefore is assumed to display the true change in depth

of the instrument. In most cases the trend in time was negative, i.e. the sonars tend to rise by a few meters. This upward movement may result from twisted mooring lines that slowly stretch during the measuring period. In the next step it was checked to what extent a linear trend in pressure explains the trend in time. The pressure record is always a superposition of true depth changes, due to ocean currents, tides or stretching mooring lines, and the pressure drift. After fitting a line to the pressure record, the trends in time and pressure were compared. The amount of depth change which was not displayed by the linear trend in measured time was then interpreted as linear pressure drift. In most cases the drift was in the direction from low to high pressure. In some data sets an offset remained after the drift and sound speed corrections. Offsets could be easily corrected by levelling the upper bound of the ice draft echoes to zero draft. These offsets could not be explained by sound speed or sensor specifications and are believed to originate from instabilities or calibration errors in the pressure sensors.

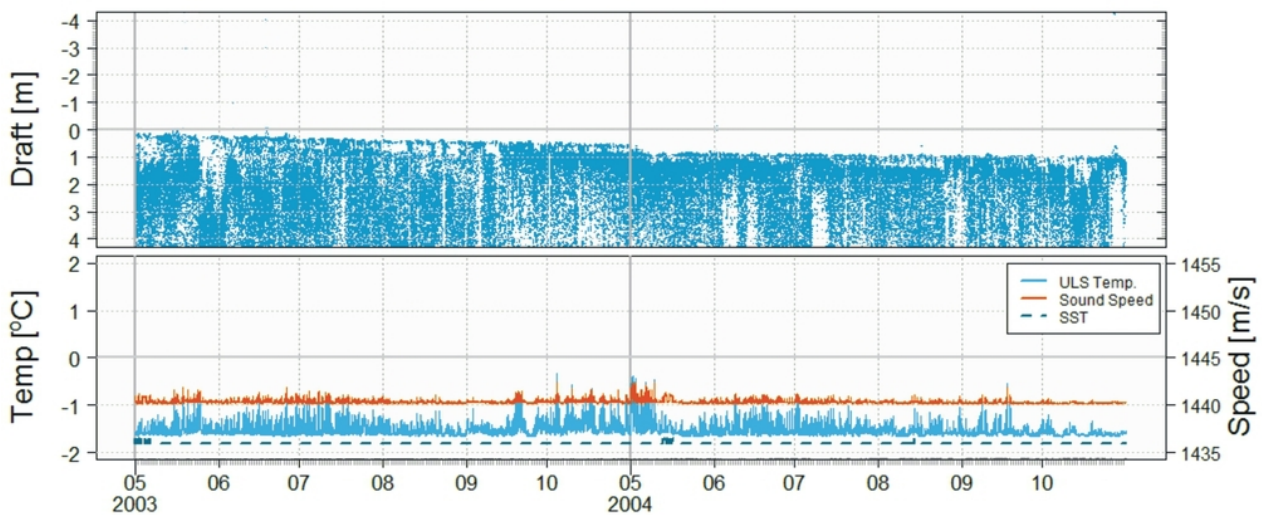


Fig. 5.16: Upper panel: Draft data of AWI 233-6 in the winters 2003 and 2004, corrected with the sound speed model. The effect of pressure drift is evident in the draft record. It results in an apparent change in ice draft of about 1 m over almost 1.5 years. Lower panel: Temperature at the ULS, sea surface temperature, and sound speed calculated with the model. Since the ULS temperature is always close to the freezing point, the vertical sound speed profile above the ULS is constant. This results in an almost constant vertical mean sound speed of about 1440 m s^{-1} . The linear change in ice draft can therefore not be explained by changes in the sound velocity and is interpreted as pressure drift.

Winter ice draft error estimation

The remaining error of the winter ice drafts corrected by the model was estimated in a similar manner as above, i.e.: the mean open water draft mode of identified leads was determined, and together with its standard deviation the rms-error was calculated. The number of identified leads in winter was about two thirds lower than in spring and autumn. The final winter rms-error was derived from the data sets AWI 207-6, AWI 231-7, AWI 232-6, AWI 232-8 and AWI 233-2. It amounts to $\pm 23 \text{ cm}$, with a mean open water draft mode of 20 cm and its standard deviation of 11 cm. This value represents the measurement accuracy of the winter ice drafts corrected by the model (Fig. 5.17).

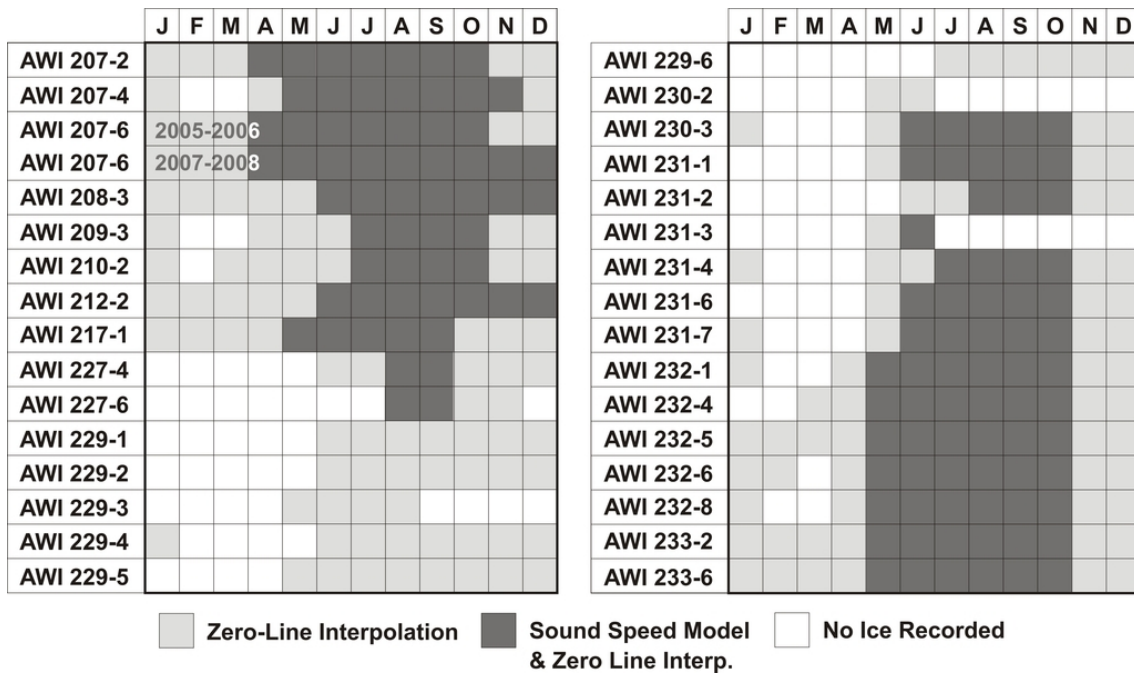


Fig. 5.17: Periods of different ice draft correction in all available data sets. The winter months (dark colour) were identified by visually checking their draft values for possible leads. The winter months were corrected by the sound speed model and the zero-line interpolation (see text).

To validate the accuracy of data corrected by the model, CTD profiles can be used to calculate a Gaussian error propagation by directly determining the uncertainty Δc . This can be achieved by comparing the CTD-derived vertical mean sound velocities to the model-derived sound velocities (Fig. 5.18). However, due to the lack of winter expeditions, only two winter CTD profiles are available directly on ULS positions with the ULS still moored: one on July 13, 2006, in a period of ice coverage at AWI 231-7 (Figs. 5.12 & 5.18), and one on December 16, 2002, in an open water period at AWI 232-5 (Fig. 5.18). The mean difference between the vertical mean sound velocities from CTD and the model is 1.1 m s^{-1} . The standard deviation of the two differences is 0.6 m s^{-1} . To estimate the standard error of the mean from such a small sample size, the t -distribution has to be assumed [Schönwiese, 1992]. The standard error can then be calculated by

$$\Delta c = 1.84 \frac{0.6 \text{ m s}^{-1}}{\sqrt{2}} = 0.78 \text{ m s}^{-1}, \quad (5.7)$$

where 1.84 is the correction factor from the t -distribution for $n=2$. The uncertainties Δt , Δp and $\Delta \alpha$ are instrumental parameters and are therefore not correlated with any other variable in the ULS-equation. The uncertainty in the ECMWF atmospheric pressure is also not correlated with other variables. The same applies to the acceleration of gravity. However, the parameters ρ and c are correlated¹⁰. The error propagation after equation 5.2 then becomes

¹⁰See box *Underwater Acoustics*.

$$\Delta d = \left[\underbrace{\left(\frac{\partial d}{\partial p} \Delta p\right)^2}_a + \underbrace{\left(\frac{\partial d}{\partial p_a} \Delta p_a\right)^2}_b + \underbrace{\left(\frac{\partial d}{\partial \rho} \Delta \rho\right)^2}_c + \underbrace{\left(\frac{\partial d}{\partial c} \Delta c\right)^2}_d + \underbrace{\left(\frac{\partial d}{\partial t} \Delta t\right)^2}_e + \underbrace{\left(\frac{\partial d}{\partial \alpha} \Delta \alpha\right)^2}_f + \underbrace{2r_{c,\rho} \left(\frac{\partial d}{\partial c} \Delta c\right) \left(\frac{\partial d}{\partial \rho} \Delta \rho\right)}_g \right]^{0.5}, \quad (5.8)$$

where the terms $a - f$ correspond to Gaussian error propagation and the term g is the correlation term between c and ρ :

$$\begin{aligned} a &= \left(\frac{1}{\rho g} \Delta p\right)^2, & b &= \left(-\frac{1}{\rho g} \Delta p_a\right)^2, & c &= \left(-\frac{p-p_a}{\rho^2 g} \Delta \rho\right)^2, \\ d &= \left(-\frac{1}{2} \cos(\alpha) t \Delta c\right)^2, & e &= \left(-\frac{1}{2} \cos(\alpha) c \Delta t\right)^2, & f &= \left(\frac{1}{2} \sin(\alpha) ct \Delta \alpha\right)^2, \\ g &= r_{c,\rho} t \cos(\alpha) \Delta c \frac{p-p_a}{\rho^2 c} \Delta \rho. \end{aligned}$$

The magnitude of the correlation coefficient $r_{c,\rho}$ varies little around 0.95, as determined from 60 CTD profiles. The error propagation is calculated exemplarily for the two years period of AWI 231-7. The values chosen are: $p = 13.6$ bar, $p_a = 990$ hPa, $\rho = 1027.7$ kg m⁻³, $\alpha = 0$, $g = 9.82$ m s⁻², corresponding to a depth of 125 m, t corresponding to a draft of 2 m and a sound velocity of 1442 m s⁻¹.

Using $\Delta c = 0.78$ m s⁻¹ and the uncertainties Δp , Δp_a , Δt and $\Delta \alpha$ described above ($\Delta \rho$ neglected), yields a standard error of $\Delta d = \pm 22$ cm, which almost matches the value found by lead detection. About 89% of this error is due to the pressure sensor uncertainties and about 9% due to the uncertainty of the sound velocity. The worst case error is 34 cm. If the uncertainty in the density is included as $\Delta \rho = 0.05$ kg m⁻³ (Fig. 5.8), the Gaussian law of error propagation has to be extended by the correlation term between c and ρ . The standard error would increase to ± 23 cm, and the worst case error would increase to 36 cm. So far, the model was run with ULS temperatures on two positions and compared to CTD profiles. To obtain a larger sample ($n \gg 2$) of differences between the modelled and CTD-derived sound speed, one can run the model with temperatures measured by CTD. In this case, T_{uls} is the CTD temperature at the depth level of the ULS. The obtained uncertainty Δc using a set of 60 CTD profiles is nearly the same as estimated above (0.75 m s⁻¹). This does not change the calculated error significantly.

Like the accuracy of the zero-line method, the winter accuracy of the sound speed model determined by lead detection is composed of two components. The standard deviation of the mean open water draft mode is determined by the accuracy of the modelled sound speeds. This accuracy, in turn, is to a large extent determined by the correlation between the model parameters h and T_{uls} . The mean offset of the drafts, i.e. the mean open water draft mode, mainly depends on how well the linear drifts and offsets in the individual data sets were corrected. Therefore, the rms-error may not seem fully related to the value of ± 22 cm obtained by error propagation. The latter depends on the magnitude of the pressure sensor drift and Δc determined from the difference between sound speed model and CTD profiles. For the uncertainty Δp a linear drift over two years was assumed. Most of the five data sets used for the error estimation by lead

identification consist of measurement periods of two years or longer. It is therefore reasonable to compare the uncertainty of ± 22 cm from error propagation and the uncertainty of ± 23 cm from lead identification. The agreement between these two uncertainties suggests that the given error is a realistic estimate.

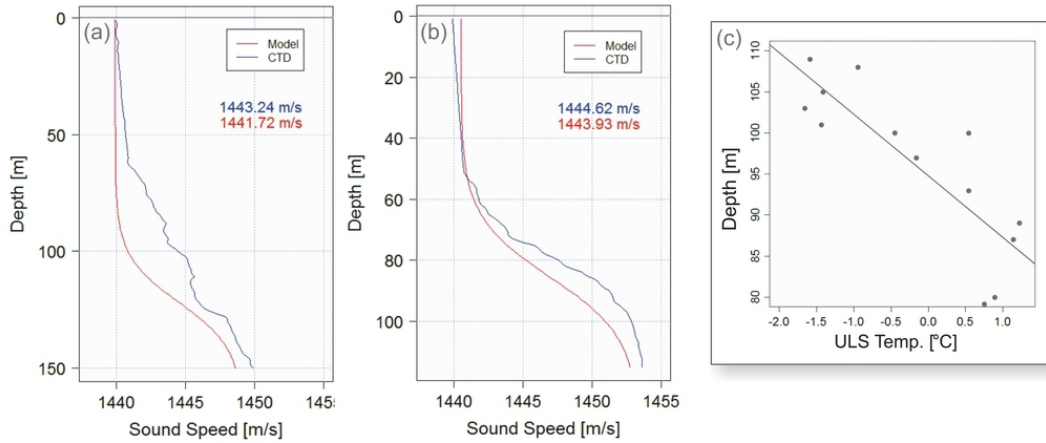


Fig. 5.18: (a) Vertical sound speed profile on December 16, 2002 (AWI 232-5), from CTD and calculated by the sound speed model. The CTD profile was calculated using the *TEOS-10 Gibbs Sea Water Library* [Wright et al., 2010]. The numbers are the vertical harmonic averages of the profiles. (b) Vertical sound speed profiles on July 13, 2006 (AWI 231-7). (c) Correlation between T_{uls} (x-axis) and the depth of the inflection point (y-axis), determined from CTD measurements on the position AWI-231. This correlation is not always very high and is the main reason for the comparably large statistical error of ± 22 cm.

For comparison, the winter ice drafts were also corrected by zero-line interpolation. The rms-error in this case is ± 14 cm, with 3.8 cm mean open water draft mode and 13 cm standard deviation of the mean open water draft mode. If all leads detected by the search algorithm are additionally included into the estimation, the error reduces to ± 12 cm. In winter, the zero-line interpolation therefore results in a smaller statistical error compared to the model correction. On the other hand, the model correction has a stronger capability in correcting ice periods in which no open water occurs for a longer period (Fig. 5.12).

As these situations are expected to be rare, the data used for further analysis in this thesis are the versions fully corrected by zero-line interpolation. In few cases, however, the versions corrected by the model are tested additionally.

5.2.2 Systematic error

Another bias which is not considered in the accuracy estimation above is the systematic overestimation of the sea ice draft due to the finite footprint size of the ULS in combination with the skewed ice draft distribution within the footprint [Strass, 1998]. The true thickness of an ice floe is related to the mode of this draft distribution. In this sense, it is the thickness that would be measured most frequently, rather than the thickness of the deepest protruding points of the ice underside.

Under the assumption of a uniform distribution of reflectivity under the ice, the shape of the echo intensity distribution is related to the thickness distribution in the footprint [Strass, 1998], i.e. the peak value (the envelope voltage: V_{env}) of the amplified echo corresponds to the ice thickness mode. But the arrival time of a ULS echo is detected when the amplified signal exceeds a pre-set threshold value (Fig. 5.19b). The detection threshold of the amplified echo is at 150 mV for the ES-300 V and 100 mV for the ES-300 VI and VIII (voltage U_2 in figure 5.19c). The arrival time is therefore measured before the appearance of the maximum voltage (V_{env}). As a result, the ice draft is overestimated (Fig. 5.19a). For a completely flat ice underside (i.e. level ice) or for an extremely small opening angle of the sonar beam the bias could be assumed to be zero.

The technical influence on the bias could be reduced by measuring the time of flight when the peak value V_{env} is reached. But for technical reasons this is not possible. One would have to record the times of flight for the whole echo distribution and finally store that of the peak amplitude as the true value. Another way could be to measure the time of flight when the signal strength decreases the first time. But this would be problematic for echo distributions with bimodal shape.

The bias may also be altered by different geophysical influences. For example, it may occur when deep ridge keels enter the sonar beam. Normally, the sonar echoes are assumed to originate from ice above the central axis of the sonar beam. But echoes from ice keels at an off-axis position may arrive earlier at the ULS than echoes from the beam axis (Fig. 5.20). If these signals exceed the detection threshold, the ice draft attributed to ice at the beam axis will be overestimated [Melling *et al.*, 1995]. This is not necessarily the case, if the

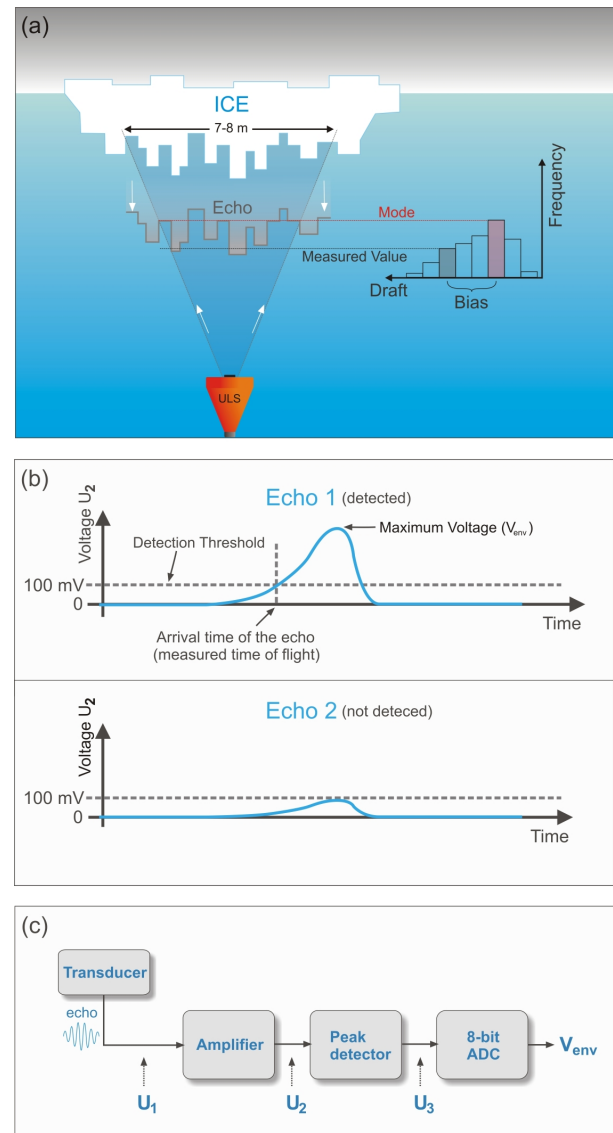


Fig. 5.19: (a) Simplified scheme of the ULS bias. (b) Echo signals and the detection threshold. (c) Scheme of echo detection and conversion of voltages for ES-300 V.

ice in the central axis is level ice, which on average has a much higher reflectivity than ridged ice [Melling, 1998]. If a keel drifts through the sonar footprint, it will be measured repeatedly, which may significantly alter the derived mean ice thickness. This contribution to the overall bias is reduced to a practical minimum (a few percent in the mean) by the narrow sonar beams, low side lobes in the sonar directivity pattern and a high system gain [Melling *et al.*, 1995]. The bias may also vary over time, as it depends on ice thickness, the degree of ridging and the age of the ice. A variable bias may also be induced by ocean currents and tides. Some pressure records of the ULS instruments show significant depth oscillations with amplitudes of up to 70 m. This periodically alters the size of the sonar footprint and thus the bias.

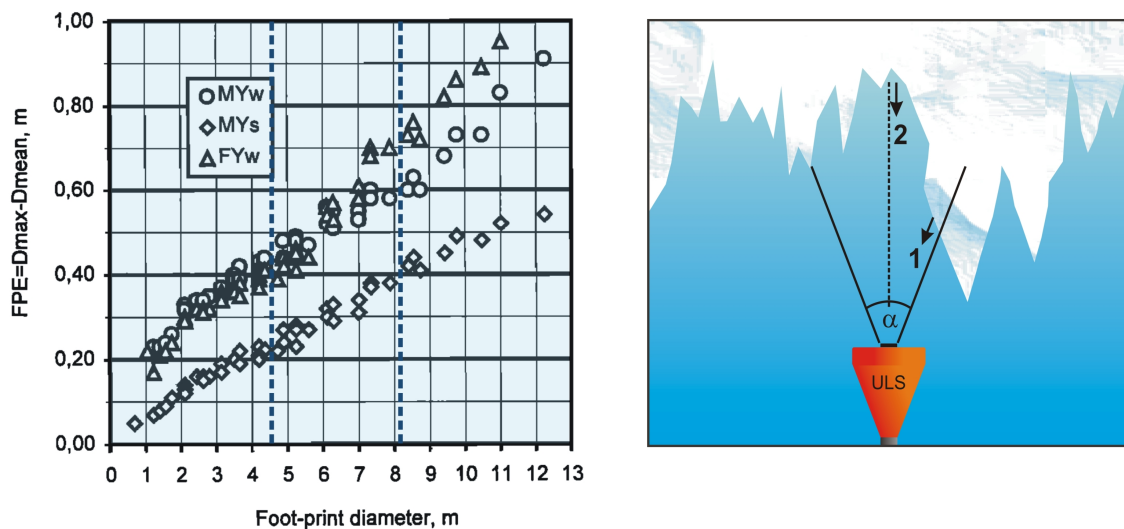


Fig. 5.20: Left: The bias (or *footprint error* (FPE)) after Vinje *et al.* [1998] versus the footprint diameter for Arctic multiyear ice (MY) in summer (s) and winter (w) and for first-year ice (FY) in winter [Vinje *et al.*, 1998]. The range of occurring ULS footprints according to the depths given in table VI is marked by blue dashed lines (roughly between 4.5 m and 8 m). Right: The off-axis echo (1) arrives earlier at the ULS than the echo from the central sonar beam axis (2).

To quantify the bias, Strass [1998] used technical information of the ES-300 V to calculate the distance between the detection threshold and the mean value of the encountered envelope voltages for the ULSs 207-2, 210-2, 212-2, and 217-1. For this purpose, the author converted V_{env} into corresponding values of U_2 (Fig. 5.19c) and found that the detection threshold of the ES-300 V corresponds to about 1/4 of the overall mean value of all encountered envelope voltages. Then, 1742 Antarctic sea ice drill hole measurements were subdivided into 10 m long segments, approximately corresponding to the ULS footprint size. The bias was then inferred from the drill hole draft distributions. It is given by the difference between the draft mode and that larger draft that has 1/4 the probability of the mode [Strass, 1998]. The overall mean bias found in this way is 11.5%. From the results of Kvambekk and Vinje [1992] one can derive a bias of 6% for a ULS with 2° opening angle (ES-300 IV) and a bias of 11% for a ULS with 5° opening angle (ES-300 II).

Information on how to convert the voltages U_1 , U_2 and U_3 are not available for the ULS types ES-300 VI and VIII. But as the detection threshold is smaller than that of ES-300 V, the bias is expected to be larger. Using the voltage conversion rules of the ES-300 V with data from AWI 207-6 (ES-300 VIII) showed that the 100 mV threshold is about 1/3.6 of the overall mean

value of V_{env} calculated in this way. This demonstrates, that if the voltage conversion had not changed from ES-300 V to ES-300 VIII (which is unlikely), the bias for AWI 207-6 would be about the same as given by *Strass* [1998] for the older ULS types.

A bias can also be estimated from investigations in the Arctic. *Johnsen* [1989] used a scanning sonar with 1.7° opening angle at a depth of 15 m under Arctic sea ice to map its bottom topography in different seasons with high resolution. *Vinje et al.* [1998] used this information to derive a bias as the difference between maximum draft and mean draft, depending on the footprint size and the ice type. *Rothrock and Wensnahan* [2007] fitted lines through these data and obtained the equation:

$$d_{max} - \bar{d} = a + \left[2 \tan \left(\frac{\alpha}{2} \right) \right] b D_T \quad (5.9)$$

for a sonar with opening angle of 2° . Here, d_{max} is the deepest draft, \bar{d} the mean draft, D_T the ULS depth and the factors a and b depend on ice type and season (first-year ice in winter: $a=0.08$, $b=0.077$, multiyear ice in winter: $a=0.18$, $b=0.055$, multiyear ice in summer: $a=0.04$, $b=0.044$). The factor in the square brackets equals 0.035 and relates the footprint diameter to the ULS depth. It is valid for the opening angle of 2° and increases to 0.044 for 2.5° opening angle. Using this value in the equation yields the bias values shown in Table VI. These biases are mean biases. The actual bias varies during the ULS measurement campaign, as the ULS depth is periodically altered tides, ocean currents and mooring motions (Fig. 5.2).

**Table VI: ULS biases calculated after
Rothrock and Wensnahan [2007] for different ULS depths**

Ice Type	ULS Depth								
	100 m	110 m	120 m	130 m	140 m	150 m	160 m	170 m	180 m
FY winter	42 cm	45 cm	48 cm	52 cm	55 cm	58 cm	62 cm	65 cm	68 cm
MY winter	42 cm	44 cm	47 cm	49 cm	52 cm	54 cm	56 cm	59 cm	61 cm
MY summer	23 cm	25 cm	27 cm	29 cm	31 cm	33 cm	35 cm	37 cm	39 cm

A relative bias of 11.5% as given by *Strass* [1998] is obtained for a ULS at 150 m depth and a measured first-year winter ice draft of approximately 5 m. However, equation (5.7) was obtained by measurements in the Arctic. The bias values in Table VI are expected to be smaller in the Antarctic, as the sea ice is generally younger and less deformed than in the Northern Hemisphere [*Haas*, 2008]. Note that the biases in Table VI are based on a relation between the maximum and mean ice draft. The bias estimated by *Strass* [1998] for the AWI ULS-types is based on a relation between the draft mode and the measured draft which occurs at the detection threshold. However, the difference between maximum draft and mean draft may be of similar magnitude as the difference between the threshold draft and the modal draft. Overall, the bias results from the complex interplay determined by technical parameters, i.e. the detection threshold and gain settings of the receiver, and geophysical parameters, i.e. sea ice age, geometry and scattering strength of the ice underside and the sonar footprint size. The bias is therefore hard to quantify. The drillings used by *Strass* [1998] were made in the vicinity of the ULS positions, and they were grouped in order to approximate the ice conditions at the mooring sites AWI-207, AWI-217, AWI-210 and AWI-212 in 1990-1992. This attempt showed that the relative bias may vary between 7.5% and 20% from region to region. However,

the drillings do not represent the ice conditions on the other ULS positions, e.g. on the prime meridian. A large-scale drilling program or measurements from electromagnetic induction (EM) sounding [*Haas et al.*, 2008] on all ULS positions is yet not available. The bias is therefore not considered in the presented data. More detailed investigations of the ULS bias may become available in the near future, if large-scale EM-surveys are conducted with a sufficiently high accuracy and spatial resolution.

5.3 M-SSA gap filling

Gaps in the time series were filled for five ULS time series (channels) on the Greenwich meridian (AWI-227, AWI-229, AWI-230, AWI-231, AWI-232) for the period 1996-2007. Wherever a data gap in this period is present in one time series, there are data in at least two other time series.

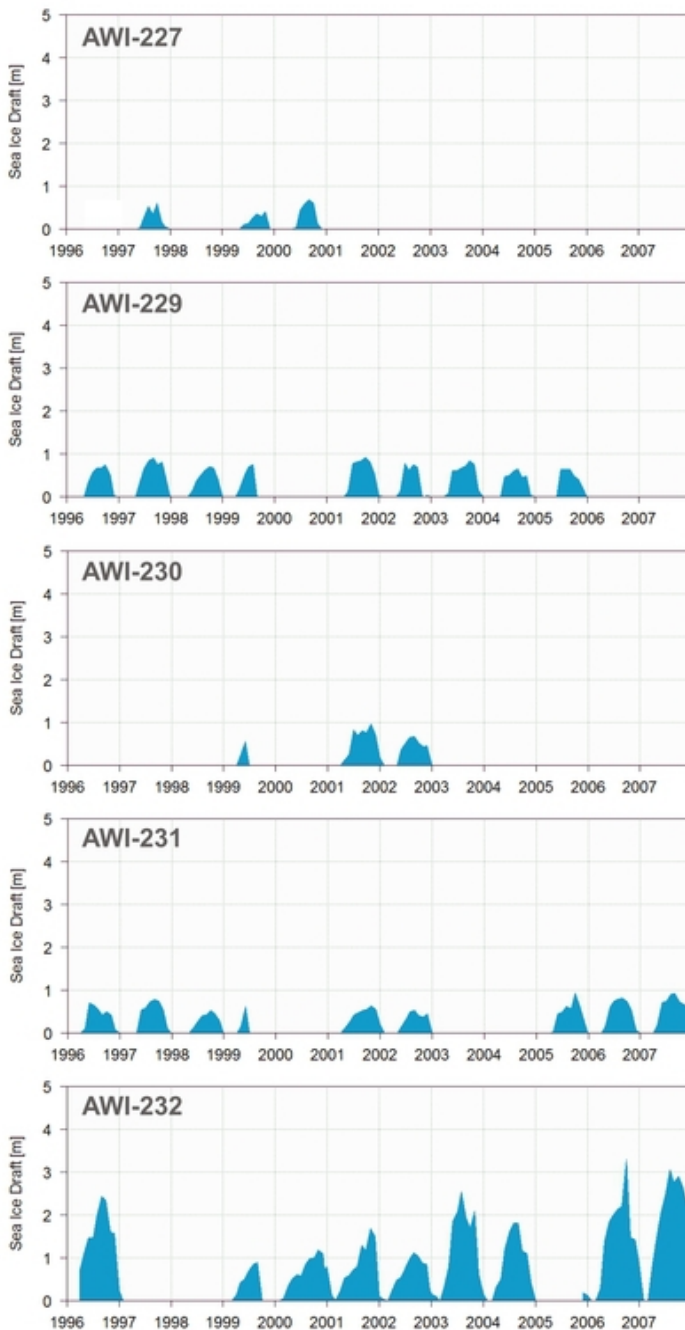


Fig. 5.21: Monthly mean sea ice drafts on the Greenwich meridian section, measured in the period 1996-2007.

The basis for applying M-SSA to this field is the presence of both temporal and spatial correlations. Temporal correlation in single channels over the considered time scale is largely given by the annual cycle. The existence of significant spatial correlations becomes clear when single years of different channels are compared (Fig. 5.21). **AWI-229 and AWI-231:** The monthly mean sea ice draft increases from 1996 to 1997 and again decreases in 1998. **AWI-229, AWI-230, AWI-231 and AWI-232:** The ice draft in 2001 is higher than in 2002, and in AWI-229, AWI-230 and AWI-231 the ice season duration in 2002 is shorter than in the year before. A decrease of sea ice draft from 2003 to 2004 is present in **AWI-229 and AWI-232**, and an increase from 2006 to 2007 can be seen in **AWI-231 and AWI-232**.

Before filling the data gaps, a number of cross validation experiments were conducted (see section 4.2). According to *Kondrashov and Ghil* [2006] the data set aside for cross validation (i.e. the artificial gaps) should reflect the pattern of missing points in the data set to obtain a realistic result. The artificial data gaps were therefore formed as long, continuous random gaps, corresponding to 5% of the data present in the respective time series. However, in the case of short monthly mean time series (e.g. AWI-227) the artificial gaps may comprise only two or three data points, which may give misleading results in the cross validation. The results of the gap filling with the optimal set of parameters were therefore finally assessed by visual

inspection. In some cases the shapes and amplitudes of the filled ice draft were found to be unrealistic. The gap-filling procedure was then repeated with a reduced number of eigenvectors,

until the amplitudes remained within realistic boundaries.

As M-SSA is based on EOF analysis, the used eigenvectors always point in the direction of the highest variance. By changing the M-SSA window width the reconstruction can be adjusted to more spatial covariances (short window widths) or more temporal covariances (long window widths). As shown in figure 5.22, a good quality for the reconstruction of the five ULS channels is already obtained with small window widths and a small number of EOFs.

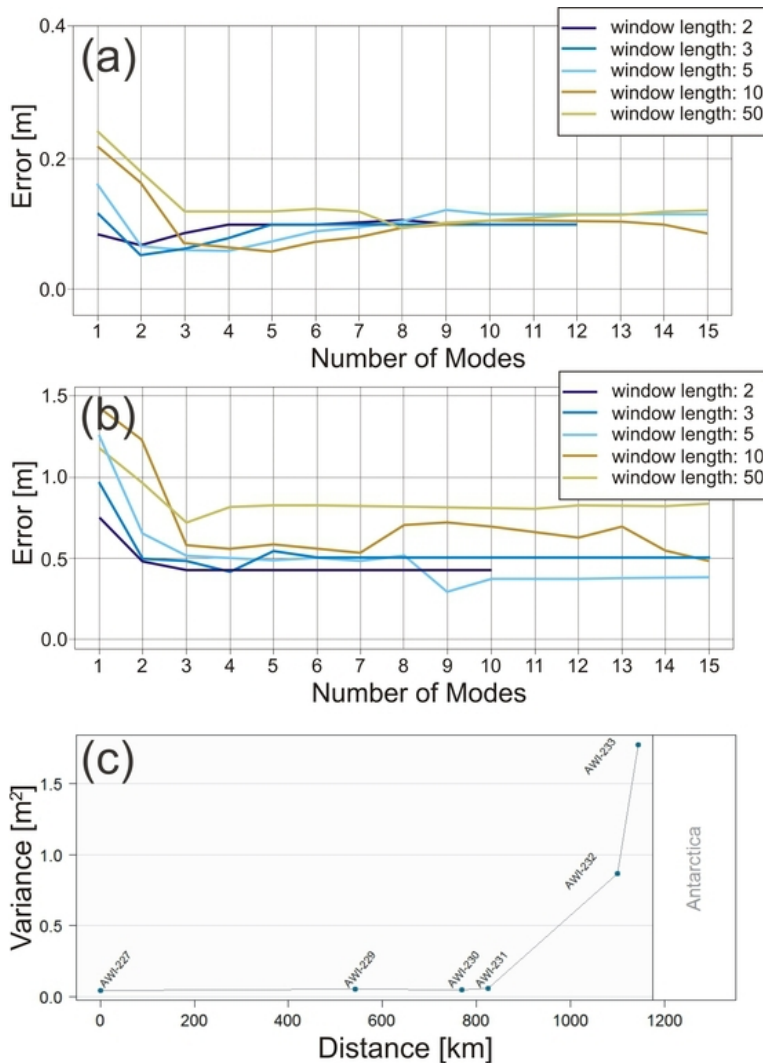


Fig. 5.22: (a) Result of a M-SSA cross-validation experiment (see section 4.2) with channels 1-4, averaged over all channels. (b) Result of a cross validation experiment for AWI-232 using 5 channels. Window lengths used were $M \in \{2, 3, 5, 10, 50\}$. (c) Variance of daily mean sea ice draft on the Greenwich meridian.

the few measured years. The ice season duration on the contrary seems to be overestimated, as the small window width prefers spatial correlations. The reconstruction is therefore based on the neighbouring channels (AWI-229 - AWI-231) which exhibit a longer ice season duration. The cross validation error of AWI-227 is also high, which indicates the low reliability of the reconstruction. But the reason for the large error may also be the cross validation itself, as it is based on very few data points at AWI-227 (5% of the

Different M-SSA channels dominate the variance on different space and time scales [Allen and Robertson, 1996]. Channel five (AWI-232) contributes the largest variance (Fig. 5.22c), as the sea ice near the coast is much more deformed through the ice drift in the Antarctic Coastal Current than further away from the coast. The ice season duration and the ice draft amplitudes of the filled sequences in channels 1-4 (AWI-227 - AWI-231) were therefore overestimated when all five channels were used. Thus, for the reconstruction of channels 1-4, channel five was omitted. The best result for channel five in both daily and monthly time series was obtained by using all five channels for the reconstruction. AWI-233 was excluded from the gap filling procedure, as its data gaps are too large and no similar time series (i.e. without ice-free season) is present in the field. All results of experiments including AWI-233 were considered as unrealistic. Small window widths and a small number of modes were sufficient to reconstruct the daily and monthly ice draft time series (Fig. 5.23). The time series of daily sea ice draft at AWI-227 shows that most of the filled ice draft amplitudes seem to be underestimated in comparison to

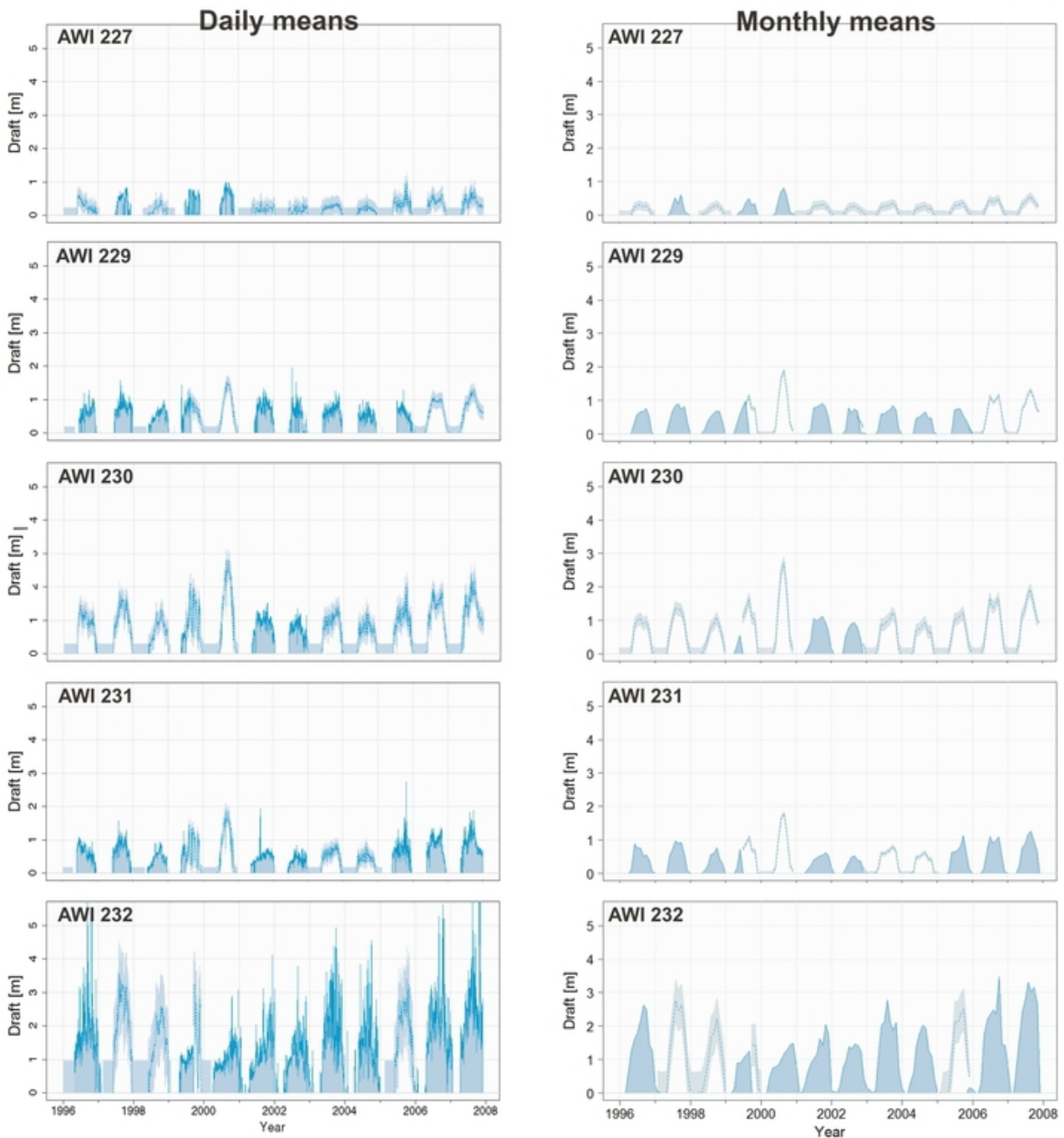


Fig. 5.23: Sea ice draft time series completed by M-SSA. Left: Daily means. Right: Monthly means. The winter months of the ice draft shown here were corrected by the sound speed model. The data fully corrected by the zero-line method, which were used for the analyses in this thesis, were filled in the same way. Their filled data have similar shapes and amplitudes as the data shown here. Years filled with blue colour are measured by ULS. The other years (dashed lines) are filled by M-SSA. The shaded areas are the errors determined through cross validation. Left column: Daily sea ice draft. M-SSA parameters used (see section 4.2) for the first four channels: Window width: $M=3$. Number of modes: $N=3$. Parameters used for AWI-232: $M=3$, $N=2$. Right column: Monthly sea ice draft. Parameters used were: $M=2$ and $N=2$.

measured data). The error of AWI-229 is much lower, because more measured data are available. The comparably high peak in the year 2000 at AWI-229, AWI-230 and AWI-231 results from AWI-227. It is the only of the first four channels having data in that year, and compared to the other measured years at AWI-227 the year 2000 shows a higher ice draft amplitude and a shorter ice season duration. This peak in AWI-229, AWI-230 and AWI-231 is not very realistic, as the shorter ice season duration is not present in the SSM/I data (Fig. 5.24). The weakly positive trend in ice draft amplitude and ice season duration at AWI-231 in the years 2006 and 2007 is also present in the reconstruction of AWI-229 and AWI-230. The cross validation error of AWI-230 is higher compared to AWI-229 and AWI-231, again indicating that filled, large and continuous data gaps are less reliable. The filled time series of AWI-227 and AWI-230 therefore have to be considered with care. The large error in the reconstruction of AWI-232 is an artefact of the method. M-SSA is an EOF-based technique. The variance of the reconstructed signal is therefore always lower than the variance of the original time series, and with a low number of EOF modes it is difficult to reconstruct the high variance signal of AWI-232. However, all reconstructions of AWI-232 using more than two modes resulted in unrealistic amplitudes and were discarded.

The filled monthly mean time series have a similar shape as the daily means, with a strong peak in the year 2000. As monthly mean time series naturally have less variance than daily means, the cross validation errors are also lower.

The only way of validating the filled data is the comparison with ice concentration data from SSM/I. The ice concentration shows significant variations in the length of the sea ice season over the period 1996-2007 (Fig. 5.24). The data confirm the assumption that the duration of the sea ice season at AWI-227 is strongly overestimated in the filled draft sequences. While the season length in 2000 fits well at AWI-229, the length in the years 2006 and 2007 is slightly overestimated. The filled data of AWI-230 and AWI-231 compare well to the concentration data, except the peak in 2000, which appears too narrow. The measured ice draft and ice concentration at AWI-227 in 1999 suggests that the ice cover opened frequently in that year. This feature is also present in the ice concentrations at AWI-230 and AWI-231 and in the reconstructed ice draft. The comparably short ice season duration at AWI-232 in 1999 and 2005 is well reproduced in the filled draft data (Fig. 5.25). However, the draft time series of AWI-232 demonstrates that the filled sequences have a lower variance compared to the measured years, owing to the EOF method.

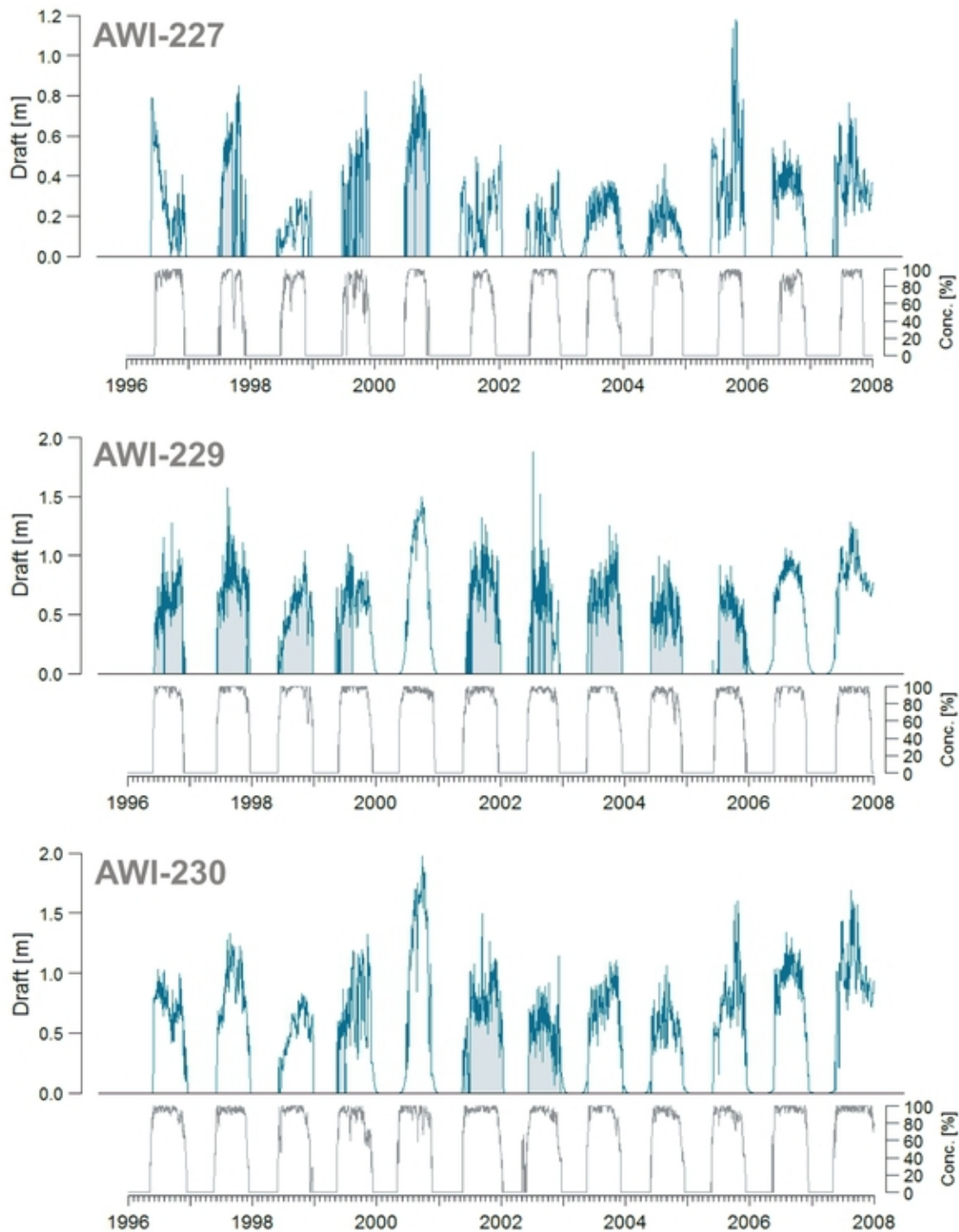


Fig. 5.24: Filled daily mean time series of sea ice draft (blue) and sea ice concentration (grey) from SSM/I [Comiso, 1999/2008] on grid points closest to the respective ULS positions from 1996-2007. The coloured draft data are years with ULS measurements. The shown draft data were completely corrected by zero line interpolation.

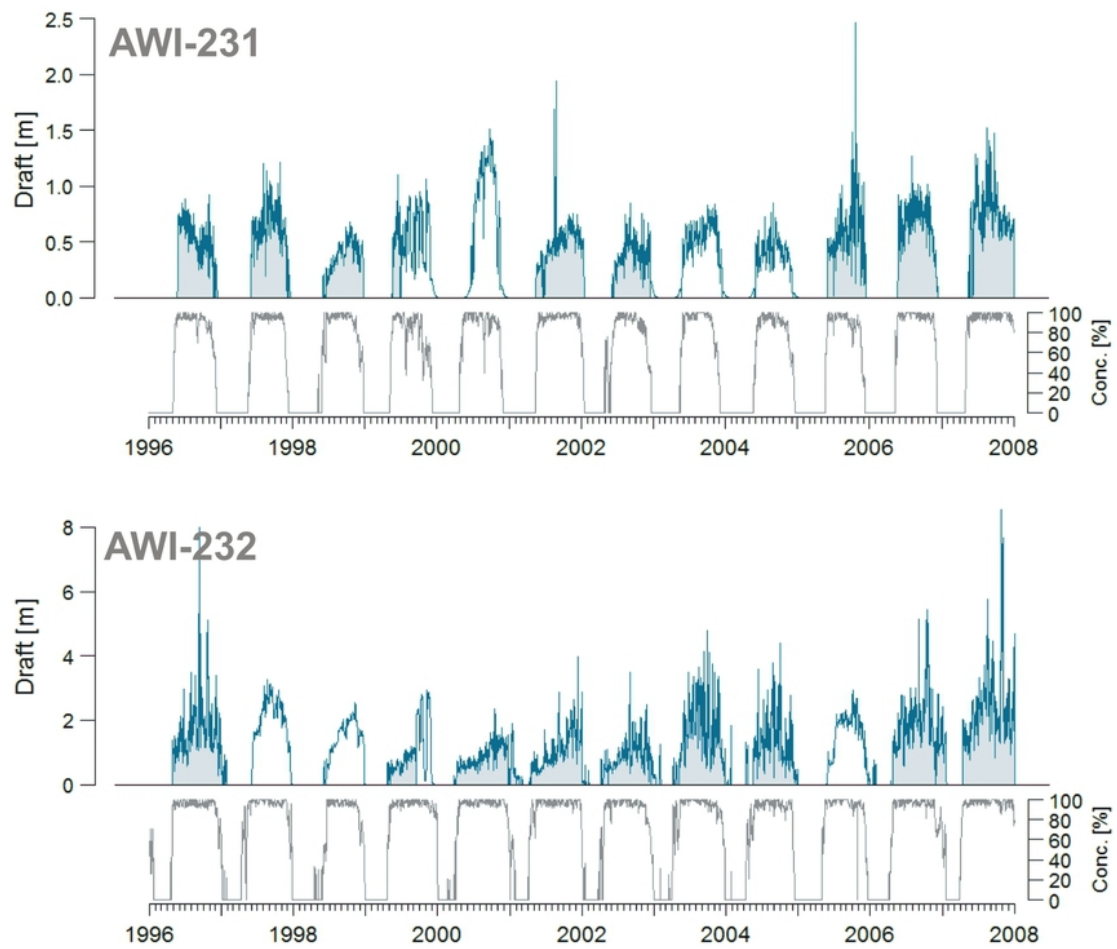


Fig. 5.25: Same as in figure 5.24, but for AWI-231 and AWI-232.

5.4 Summary

The data processing (AUPC) developed at AWI works reliably for ice periods in which enough leads occur. As the procedure includes steps that depend on visual inspection, the data quality increases significantly with the sample rate of the ULS instrument. In the different data processed by two operators, the differences in data cycles classified as ice in winter and spring are smaller than 20 cm for about 89% of the valid data cycles. The differences can generally be attributed to the manual correction of the interpolated zero-line and are accounted for by the averaging of the final draft data.

The sensitivity study demonstrated that the accuracy of ice draft derived from the ULS-equation is dominated by the uncertainties of the pressure sensor and of the sound velocity. The final error could therefore be reduced by using pressure sensors with higher precision and better long-term stability. However, as the sound speed and its uncertainty is not known, a zero-line correction would still be necessary. In this case the pressure sensor uncertainty would also be corrected, regardless of how large it is. If a highly accurate sound speed model were used to calculate sound velocities, the data quality would benefit significantly from better pressure sensors, and a correction by zero-line interpolation would become obsolete.

Note that the uncertainties and variations may have different time scales. Whereas the uncertainties in the density ($\Delta\rho$) and in the sound velocity (Δc) are expected to vary slowly over time, the uncertainty in time (Δt) may introduce an error on shorter time scales. The quality of a correction method, i.e. sound speed model or zero-line interpolation, depends on its ability to resolve all these time scales. Both correction methods perform better when the sound speed profile above the ULS is constant. The depth of the instrument therefore should not be too large in order to ensure a constant vertical sound velocity profile. A constant profile makes the processing of the data much easier and guarantees a stable data quality. When deploying ULS instruments at shallower depths, one has to avoid regions where large icebergs are frequent. However, this may significantly reduce the size of the possible study area.

The draft errors were corrected using two approaches. The first approach uses a correction line which is interpolated through leads present in the ice cover. Draft data corrected by this method were estimated to have an accuracy of ± 5 cm in spring and autumn and ± 12 cm in winter. The estimation was made by investigating the statistical properties of ice drafts in leads that were not captured by the correction line. This error is expected to decrease in daily or monthly averages of sea ice draft. In this case, the autocorrelation would have to be considered to estimate the number of independent data. It could be demonstrated from CTD measurements that missing leads in winter can result in an underestimation of the ice draft by 44 cm, as leads (i.e. the tie points for the correction line) are less frequent in the winter months. The winter drafts were therefore alternatively corrected by a sound speed model.

The model was developed on the basis of temperature data from ULS and CTD measurements and approximates the sound speed profile in the winter mixed layer. It could be shown that, in single cases, the model may have a better capability in correcting ice draft when no leads are present in the ice. However, the winter drafts corrected in this way have an accuracy of about ± 23 cm. This empirical value was also estimated on the basis of leads and was confirmed by error propagation. This comparably large error mainly results from weak correlations between the depth of the thermocline and the temperature at the ULS. Another reason is the correction of the pressure drift, which turned out to be difficult in cases of variable thermocline depth. The sound speed model therefore needs to be further improved. This could be achieved by thoroughly comparing CTD and model-derived sound speeds or by improving the correlation

between the temperature at the ULS level and the depth of the winter thermocline. However, the winter error estimation is based on previously unidentified leads, which are naturally less frequent in this season. Thus, the winter error of the zero-line method itself may be biased. The presented error estimation does not include long periods of closed ice cover, where the sound model is expected to perform better. The error of ± 12 cm therefore has to be considered as a minimum error.

A problem with the presented ULS data is the lack of ice drift information. Contrary to the studies of *Melling et al.* [1995], the AWI ULS instruments were deployed without Acoustic Doppler Current Profilers (ADCP). Their data can therefore not be converted into space-referenced data. Spatially weighted statistics of sea ice are of greater interest than temporally weighted statistics, as they better reflect the true profile of the ice thickness. The sampling problem without ADCP is induced by the character of the ice drift. If, by chance, only thick ice classes are present when the ice drift is slow, these classes will be more common in the draft statistics. The differences between the spatial and temporal distributions are expected to decrease in daily or even more in monthly mean sea ice drafts. The conversion of the observations into regular intervals of space would eliminate the problem. However, interpolation of the temporally sampled data to regular increments in the coordinate of the ice drift is always a smoothing process that lowers the fractal dimension of the ice thickness sequence [*Melling et al.*, 1995]. And as noted above, the ice motion itself might be very irregular and could therefore complicate the spatial separation of consecutive measurements. *Melling et al.* [1995] used ULSs in combination with ADCPs and demonstrated that significant differences can occur between the distributions of time-referenced and space-referenced draft data. The difference between time-referenced and space-referenced data would disappear, if sequences of observations longer than two months were averaged [*Melling et al.*, 1995]. The lack of local near real-time ice drift information is the major drawback of the AWI ULS array in the Southern Ocean.

The ULS bias remains elusive. More Antarctic ice thickness data, e.g. from EM-surveys or high-resolution sonar measurements of the underside topography, are needed for a thorough estimation.

The gap filling by M-SSA can be successfully applied to sea ice draft data that show some degree of spacial correlation. Nevertheless, the method shows clear weaknesses in time series with long, continuous data gaps, especially in AWI-227 and AWI-230. The quality of the filled series is further examined in the following chapters. Because the shapes and amplitudes of the daily and monthly mean reconstructions are nearly the same, the filled monthly mean time series could be obtained by simply calculating monthly means from the filled daily mean time series. This would also reduce the computational burden.

"Doch an den Fenster-
scheiben, wer malte die
Blätter da?

Ihr lacht wohl über den
Träumer, der Blumen im
Winter sah?"

Wilhelm Müller, 1794-1827

6

Variability of Sea Ice Draft

This chapter contains discussions and analyses of the regional and temporal development of the measured sea ice draft. Furthermore, the statistical properties of the ice draft and the ice season duration are investigated. The time series are analysed for significant periodic signals and autocorrelation. All analyses in this chapter are based on data corrected with the zero-line approach, as they exhibit a smaller statistical error, and longer periods of a fully closed ice cover were found to be relatively rare. The results are discussed in each section. A brief summary of the findings is given at the end of the chapter.

6.1 Qualitative descriptions

In this section, the major temporal development of the ice draft is described. The plots show each recorded and processed draft signal of the single time series. They were investigated in terms of (a) differences to earlier data processings (b) annual cycles and ice-free periods/seasons, (c) occurrence of thin ice (0-20 cm) and open water, (d) clusters of ice drafts and their development and (e) a first look at possible dominating forcing mechanisms, such as thermodynamics and ice deformation. The latter part is investigated in more detail in the next section. The time series of AWI 207-2, 208-3, 209-3, 210-2, 212-2 and 217-1 (Fig. 6.1) were discussed in detail by *Strass and Fahrbach* [1998]. As these data sets were reprocessed with the new methods introduced in chapter five, they are also briefly discussed here.

The ice draft in the western boundary region of the Weddell Sea at AWI 207-2 shows no clear annual cycle (Fig. 6.1). Contrary to the results of *Strass and Fahrbach* [1998] the ice draft shows no clear monotonic growth in the beginning winter season of 1992. In the summer months (November-February) thin ice with 15-20 cm draft was very common. Open water occurred throughout the year but reduced significantly from May to July in 1991 and from April to August in 1992. Thick ridged ice (>1 m) appeared throughout the summer seasons and the number of very large ice drafts (>2 m) increased in winter. Most of the winter ice drafts re-

mained between 1 m and 2.5 m. These clusters largely disappeared in August-October. The record of AWI 217-1 is very similar to AWI 207-2. However, it shows a clear annual cycle with the ice draft increasing monotonically from March/April to September in 1991 and to October/November in 1992. There was no ice-free summer season. Open water areas were rarely measured between May and June. The number of larger ice drafts (>1.5 m) increased clearly in June/July of both years. Compared to AWI 207-2 there was a larger amount of ice drafts >1 m in the summer seasons. The records of AWI 208-3 and AWI 209-3 show clear annual cycles of thermodynamic ice growth (compare to figure 2.9). The ice growth at AWI 209-3 occurs more irregularly, which is not the case in the version of *Strass and Fahrbach* [1998]. The summer seasons were largely ice-free.

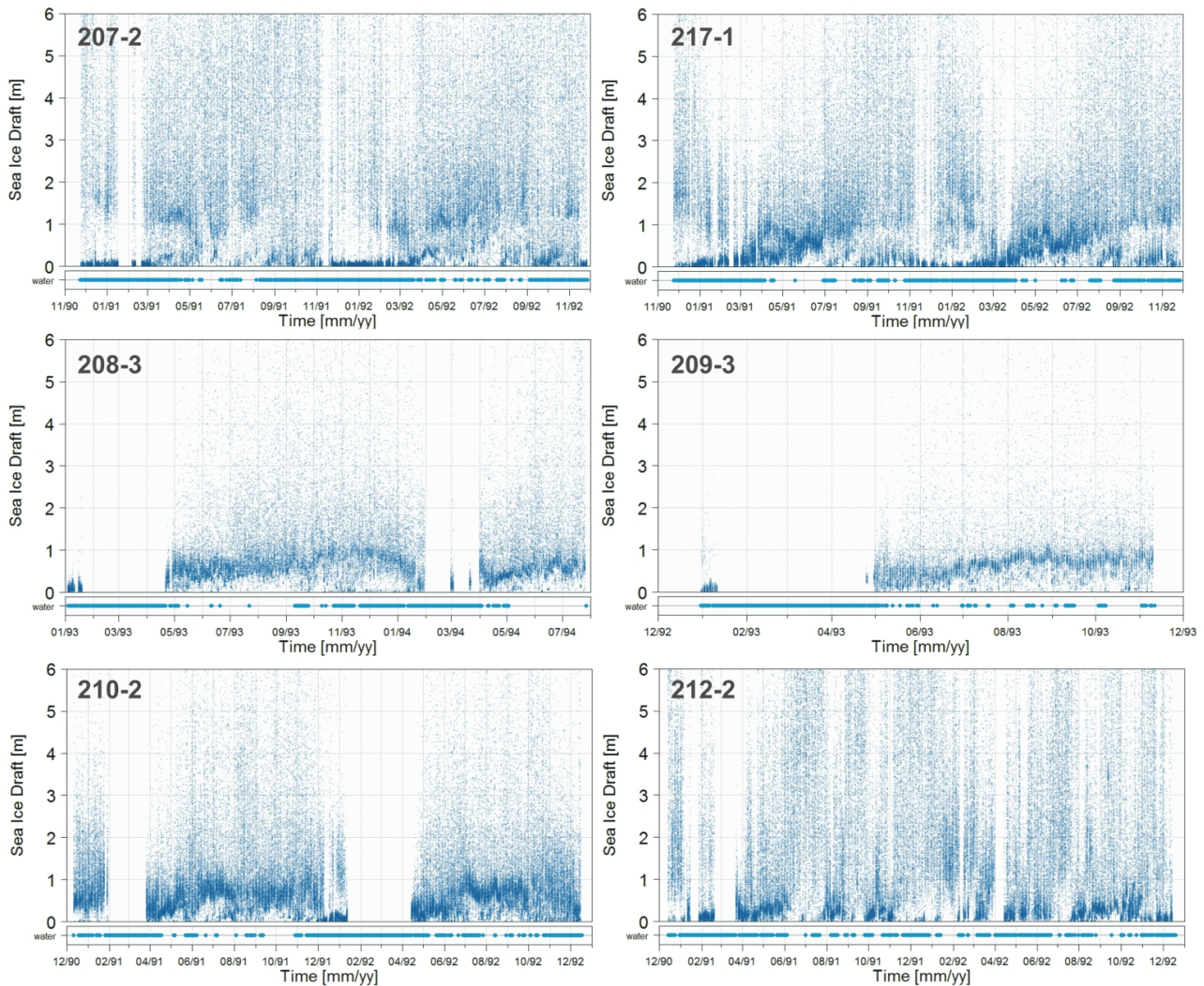


Fig. 6.1: Time series of sea ice draft as obtained from the ULS measurements. Each blue dot stands for one draft measurement. The shown draft was corrected by the zero-line approach and averaged between the results processed by two data analysts. The occurrence of open water is indicated by light blue points in the respective sub-plots. Note that the ULS instruments have different sampling rates.

The growth season at AWI-208 started with scattered ice drafts between 0 m and 1 m, which may indicate that ice from further south was advected into the region. Another reason for this scatter could be a large amount of frazil, which was mixed into the upper water layer and

could not be clearly separated from thin ice during the data processing. The end of this period corresponds to the closing of the ice cover, i.e. when the ice concentration rapidly increases to 100% [Strass and Fahrbach, 1998].

There was almost no thin level ice in both records. Open water areas were rare between May and October. The narrow band of clustered ice drafts indicate level ice that stayed largely below 1 m draft. At AWI 208-3 it increased slowly to a maximum in November and then quickly dropped to zero within two months. At AWI 209-3 the maximum was already reached in August and stayed until November. If a draft bias of 11% is assumed, the data points correspond well to a thermodynamic growth maximum of 0.7-0.8 m [Strass and Fahrbach, 1998]. Ridged ice of more than 1 m draft occurred more frequently at AWI-208 than at AWI-209 further east. The record of AWI-210 shows a clear annual cycle with no ice in the summer season. However, the ice draft was more variable compared to AWI-208 and AWI-209, and thermodynamic ice growth is not as easily identifiable. The ice close to the coast off *Kapp Norvegia* is more deformed than in the central Weddell Sea. AWI-212 shows no annual cycle, i.e. sea ice was present for most of the year. Very thick ice of more than 2 m draft was common in this region. The clusters of drafts between 0 m and 0.5 m indicate that the ice cover opened frequently on time scales of several months, and the resulting leads and polynyas quickly refroze.

The newer data of AWI-207 indicate distinct changes in the ice regime at the Antarctic Peninsula (Fig. 6.2). AWI 207-4 shows an annual cycle with an ice-free period in summer. The ice draft in 1997 shows a monotonic increase between April and August. Very thin ice occurred at the end of the year 1996. Open water areas seem to have occurred more often at AWI 207-4 than at AWI 207-2. The ice drafts are roughly clustered between 0.5 m and 2 m. By comparing the plots of AWI 207-2 and AWI 207-4 it is obvious that ice above 1 m draft was much less abundant in 1996/1997. The amount of thick ice of more than 2 m draft remained high throughout the year, which indicates that ridged ice and possibly also fragments of small icebergs were continuously advected northwards along the Antarctic Peninsula. Given the Eulerian character of the ULS measurements, one has to be aware that the measured sea ice may have developed in regions far away from the ULS position. Eight years later, in the record of AWI 207-6, the picture again changes drastically. The ULS had a higher sampling rate (three minutes) compared to the other two records of AWI-207, which creates a high density of the measurements. The three years show a clear annual cycle with a monotonic increase of the ice draft starting in March. Very thin ice was more frequent compared to the previous records. The gap in August/September 2005 is due to erroneous data. It is therefore not clear whether there was ice or open water in this period. The gaps in January-March 2006 and in December 2006 and January-March 2007 on the contrary are due to open water. The drafts are still mainly clustered between 0 m and 2 m, but ridged ice above 2 m draft is less abundant in this record.

In the eastern Weddell Sea at AWI-227, on the prime meridian at 59°S, the ice season is very short (Fig. 6.2). The ice drafts in 1997 showed thermodynamic ice growth from July to October with the drafts clustering mainly between 0.5 m and 1 m. As the ice growth did not start at zero draft or with possible frazil periods such as at AWI-208, one can assume that the ice growth started further south and thicker ice was advected to the position as the ice boundary migrated northward. The draft of the congelation ice reached its growth maximum in October. At the end of the ice season the draft reached its minimum.

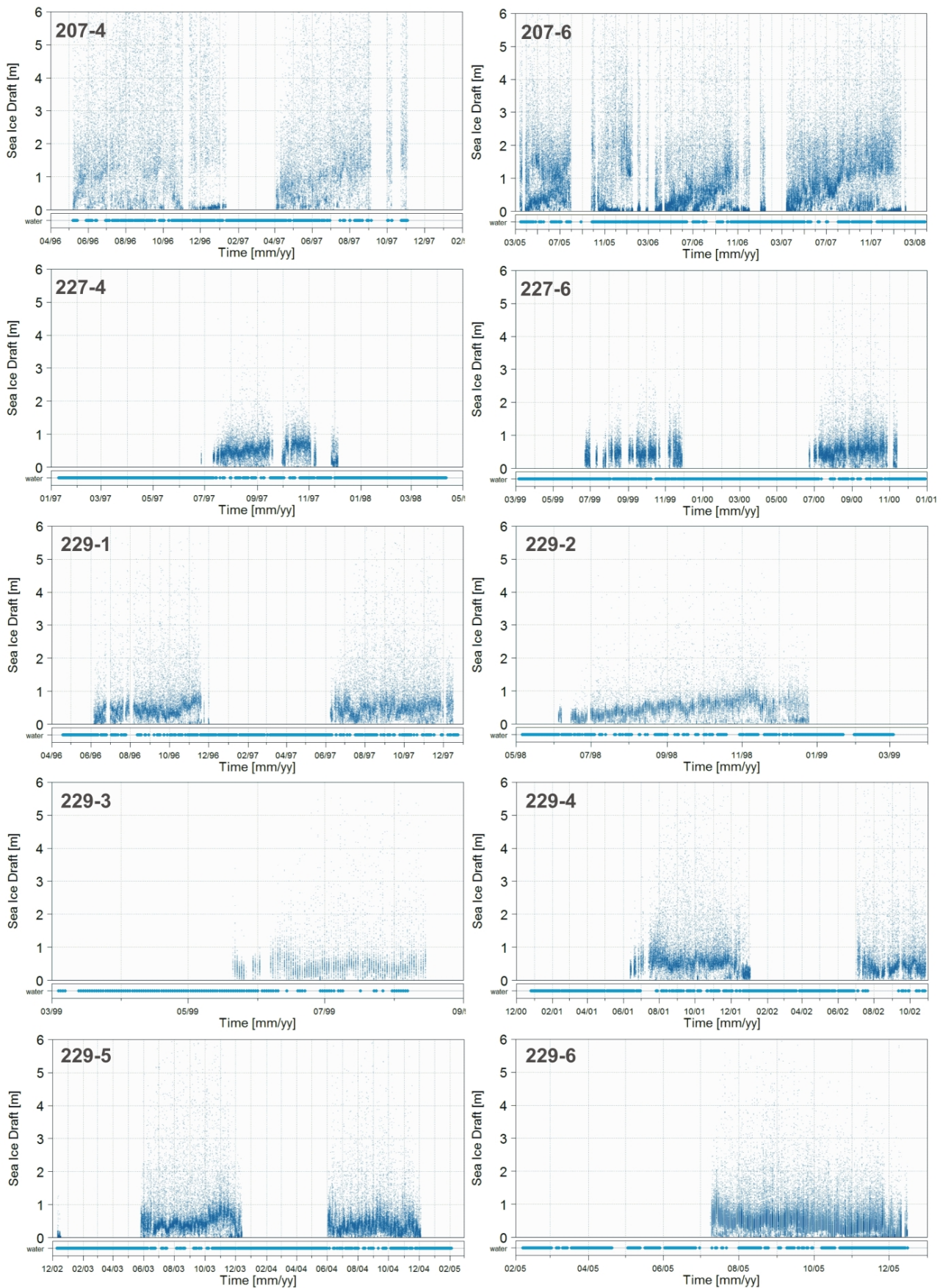


Fig. 6.2: Same as in figure 6.1, but for the newer data of AWI-207 and for AWI-227 and AWI-229. Note the different sampling rates (between 1 and 15 minutes).

The thermodynamic cycle is comparable to the records of AWI-208 and AWI-209, but with a shorter ice season and a lower maximum of the ice draft mode, as the ice at the northern rim of the Weddell gyre encounters higher winter temperatures than in the central Weddell Sea. In 1999, the ice at AWI-227 was thinner than two years before and interspersed with longer open water patches. The ice season in this year was shorter, and the thermodynamic growth seems to be less steep. Almost no ice drafts larger than 4 m were recorded. This changed in the year 2000. While the ice season was slightly shorter, both the congelation ice and ridges were thicker. Open water is very frequent at the position of AWI-227.

North of Maud Rise, at AWI-229 (Fig. 6.2), the thermodynamic growth maximum is comparable to the one of AWI-227. On average, the ice season at Maud Rise started three to four weeks earlier. Furthermore, the ice drafts display a higher degree of ridging. However, like at AWI-227 most of the drafts clustered between 0 m and 1 m. Overall, there is a high variability in (1) the length of the ice season, (2) the occurrence of open water, (3) the temporal development of the main draft clusters and (4) in the degree of ridging at AWI-229. For example, at AWI 229-1 between October and November 1996 the ice draft mode increased and then suddenly disappeared. This suggests that the ice did not gradually melt in this region, like at AWI-208, but was rather drifted southward as it melted. Or AWI 229-2: It shows a clear thermodynamic growth cycle which is comparable to the one of AWI-209. The ice growth seems to have started in June near the ULS position. The main cluster of the ice draft increased monotonically until November and dropped in the same month. In December most of the ice became thinner than 25 cm. Ice drift data from SSM/I indicate that the meridional drift in 1998 was extremely low at the positions of AWI-229 to AWI-231. Therefore, almost no thicker or thinner ice from regions further south or north was advected into the footprint of the sonar. This could be an explanation for the undisturbed record of the congelation growth. AWI 229-6 on the contrary shows an almost reversed pattern.

South of Maud Rise the record of AWI 230-2 (Fig. 6.3) shows a very similar behaviour as AWI 229-3, but with the ice season starting about one week earlier. The instrument failed in July 1999. Also AWI 230-3 and AWI 229-4 are very similar, with peaks of the main ice draft cluster in July and November 2001. At AWI 229-4 this behaviour was delayed by approximately one month. In 2002 the ice was thinner than the year before.

The ice draft on position AWI-231 again shows a very variable behaviour (Fig. 6.3). The records of AWI-229 and AWI-231 are similar in the years 1998 and 2005, except for ice season duration. Like at AWI-229 and AWI-230 very thin ice could be observed mainly at the beginning and the end of the ice season. Also most of the drafts mainly cluster between 0 m and 1 m. However, the mean ice thickness seems to be lower at AWI-231. A clear difference between AWI-231 and AWI-229 can be seen in the years 1996 and 1997. Whereas the main clusters of drafts tend to slightly increase at AWI-229, they show a clear decreasing tendency at AWI-231. On average, the plots of AWI-229 and AWI-230 display a higher degree of ridging than the ones of AWI-231. However, AWI 231-7 shows a large number of ice drafts above 2 m (no records of AWI-229 and AWI-230 in this period). The main ice draft clusters seem to have remained almost constantly at 0.5 m throughout the ice season. This suggests that the ice neither grew nor melted in the vicinity of the ULS position. Open water areas seem to be less common at AWI-231 than further north.

Closer to the coast, at AWI-232, the ice regime again changes significantly. The data (Fig. 6.4) indicate the strong interannual variability in sea ice thickness near the coast. All time series show a clear annual cycle with ice-free summer periods.

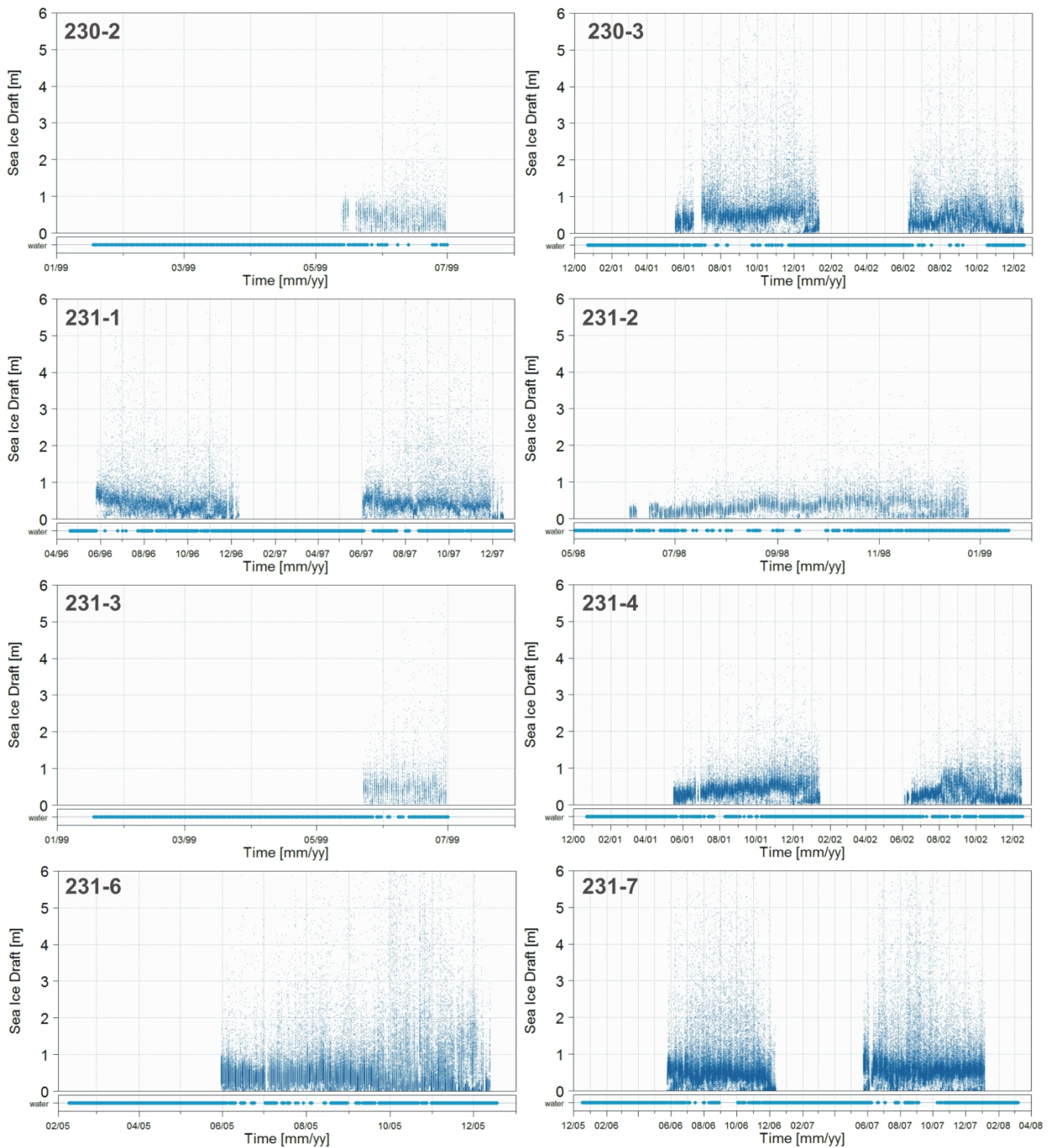


Fig. 6.3: Same as in figure 6.1, but for the records of AWI-230 and AWI-231. Note the different sampling rates (between 1 and 15 minutes).

The plots display a very high degree of ridging, while most of the drafts cluster between 0 m and 2 m. The main clusters sometimes increase monotonically, sometimes increase in steps and sometimes vary irregularly. Very thin ice below 20 cm draft could mainly be observed in spring and autumn. Some of the records (232-4 and 232-5) show more concentrated ice drafts that grew up to the thermodynamic maximum below 1 m and were then distorted towards higher drafts in late winter/early spring. In 1996, between August and December the ice draft shows

some indication of a periodic variation with a period of roughly one month. The peaks of ice draft can be seen in the second half of August, September and October, respectively. They are marked by a higher amount of ice drafts above 2 m and only few ice drafts below 1 m. A fourth peak occurred at the beginning of December.

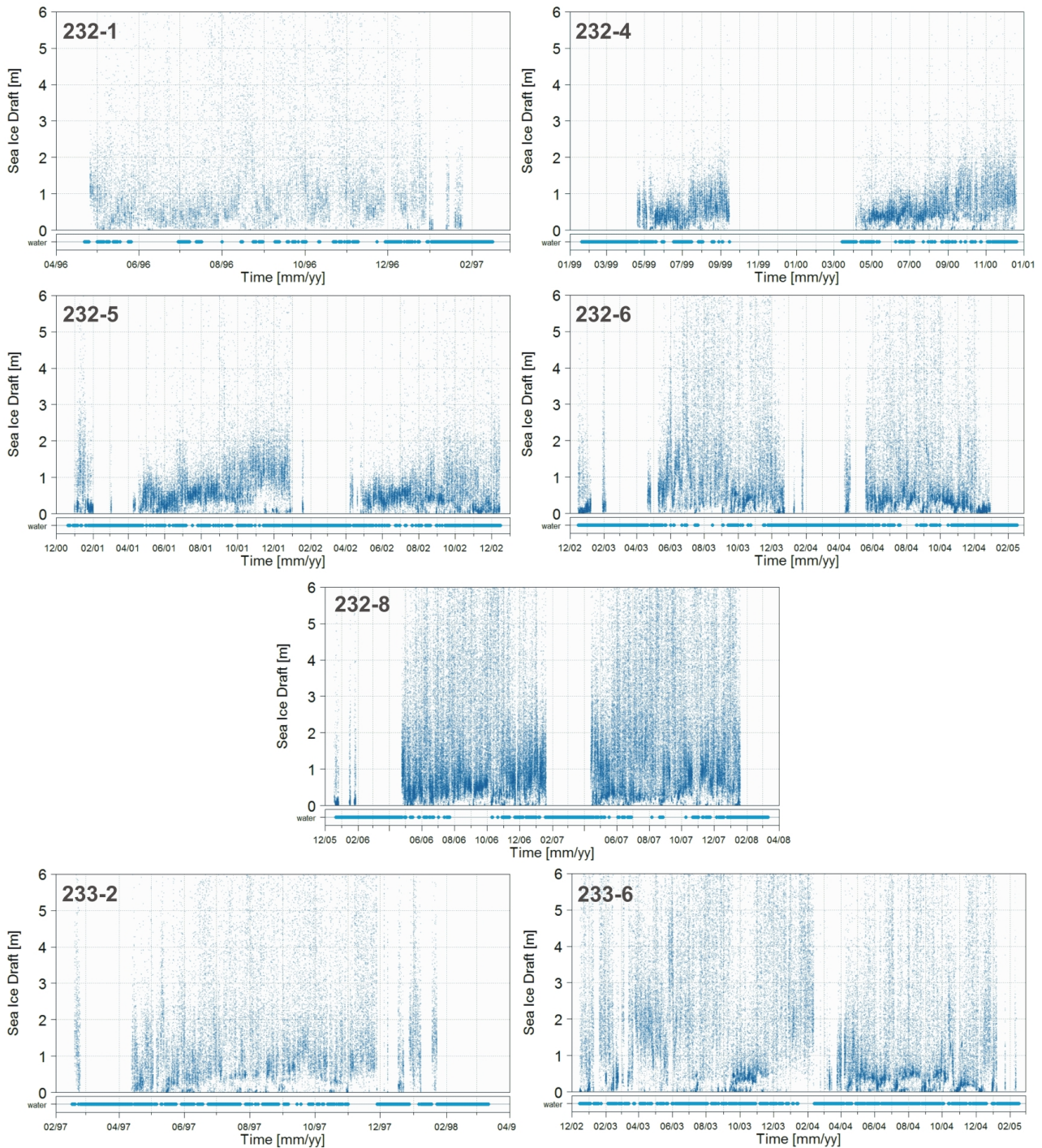


Fig. 6.4: Same as in figure 6.1, but for the records of AWI-232 and AWI-233. Note the different sampling rates (between 2 and 15 minutes).

The instrument deployed in 1999 failed in September¹. Open water areas were less common in years of very thick ice (1996, 2006 and 2007).

At AWI-233 (Fig. 6.4) the draft shows no pronounced annual cycle. The formation of monotonically increasing ice draft clusters is assumed to be prevented by the high degree of ice deformation. Ice-free summer seasons were only recorded at AWI 233-2. The much thicker ice at AWI 233-6 occasionally shows concentrated clusters of ice drafts at around 0.5 m and below, especially in 2004. In both records very small ice drafts below 20 cm indicate refrozen leads.

¹Note that AWI-229, AWI-230, AWI-231 and AWI-232 failed nearly at the same time. The reason is not known. It can be of technical nature, e.g. through declining battery power.

6.2 Monthly draft statistics

Investigations of probability density distributions and draft statistics were already presented for the data of AWI 207-2, 208-3, 209-3, 210-2, 212-2 and 217-1 by *Strass and Fahrbach* [1998]. An annual cycle could be found in three statistical quantities - draft mean, draft mode and ice coverage - only in the central Weddell gyre at AWI-208. In the other regions the annual cycle was most evident in the ice coverage [*Strass and Fahrbach*, 1998]. It was also found that the summer minima in the three statistical quantities occur simultaneously in February, while the time of occurrence of the winter maxima is different: ice coverage in June/July, draft mode in September and draft mean in September/October. Spatially, the ice draft mean takes its maximum values at the boundaries of the Weddell gyre (AWI-207 and AWI-212), while the minimum occurs in the central gyre (AWI-209). For the ice draft mode the situation is reversed: maximum values in the central gyre and minima in the boundary regions [*Strass and Fahrbach*, 1998]. The authors also estimated that almost 75% of the thin ice at AWI-212 is transformed to thicker ice at AWI-207 during circulation through the Weddell gyre. Furthermore, they demonstrated that the statistical ice draft distributions allow for a discrimination between level ice and deformed ice.

As the ice draft variation is described in detail in the previous section, only selected data with significant variations are discussed here. The detailed treatment of the ice draft statistics may give some additional information for the correlation analysis in the next chapter. Therefore, the discussion is mainly restricted to the ULS positions with the highest amount of data. Contrary to *Strass and Fahrbach* [1998] the statistical distributions are considered here on a monthly scale to allow for a more detailed investigation of thermodynamic growth and ice deformation. Besides the distributions, the considered quantities are: monthly mean, mode, median and 95% percentile.

The plot of AWI 207-2 (Fig. 6.5) shows that most of the ice drafts remained below 11 m in this record. The ice draft median mainly follows the pattern of the mean ice draft. In 1991 the most frequently measured ice class (mode) was 0-10 cm (except for May). A secondary mode formed in March at around 1.2 m and could be observed until August in the range 1.2-1.5 m, except for June, where it dropped to 1 m. In 1992 the main mode varied between 0-10 cm and 1.4-1.5 m. While the mode increased, the mean draft decreased, and vice versa. Compared to 1991 the second mode at 1.5 m became more dominant and increased to 1.7 m in August. The monthly draft distributions of 1992 were less skewed than in the year before.

In 1996 and 1997 most of the measured ice drafts remained below 8 m. The bimodal shape with modes at 0-10 cm and around 1-1.5 m was still present. Compared to 1996 the monthly distributions in 1997 were less skewed. Whereas in 1996 small ice drafts (0-10 cm) were most abundant throughout the year, in July and August 1997 the mode around 1.5 m dominated.

The period 2005-2007 shows a completely different picture, reflecting significant changes in the ice regime since 1997. Most of the ice drafts remained below 4 m. The bimodal shape was not as consistent as in the years 1991-1997, and the monthly ice draft distributions were more variable. The main mode was still largely at 0-10 cm and increased only between May and August.

The two data with the clearest annual cycles (Fig. 6.6) display thermodynamic ice growth in the central Weddell gyre, where the drift speeds are lower than in the boundary regions [*Fahrbach*, 1994]. At AWI-208 the ice draft distributions took an almost Gaussian shape in May 1993. As the mode increased until October, the monthly distributions widened and became mode skewed

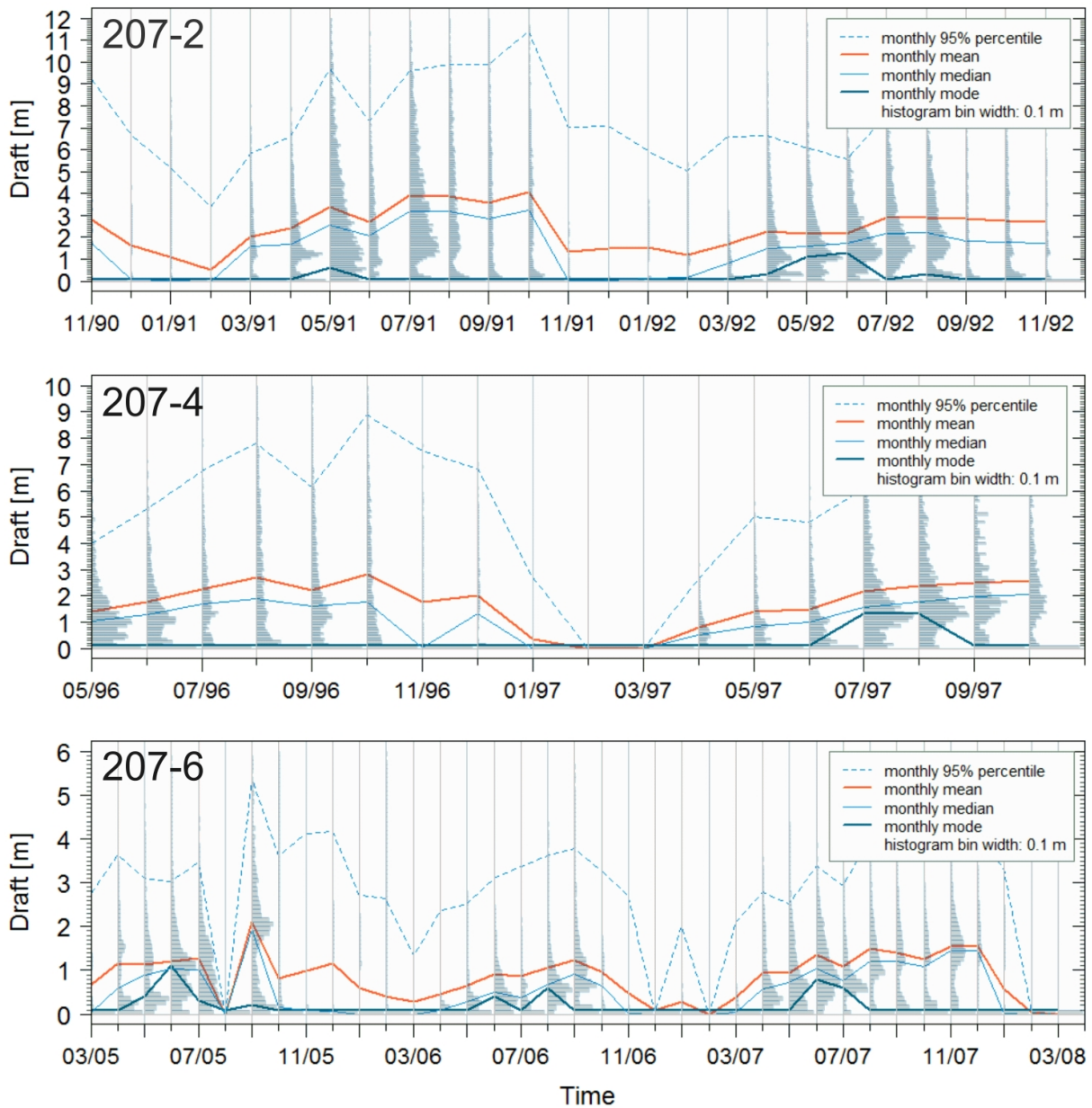


Fig. 6.5: Monthly mean, mode, median and 95% percentile of ice draft and monthly draft distributions of AWI 207-2, 207-4 and 207-6. There were no valid data in August 2005. The mean value is the *effective mean*, i.e. the mean ice draft calculated by including data cycles classified as open water. Also the mode (thick blue line) was calculated for data including ice and water. All histograms have been scaled by the maximum bar of the respective month to ensure equal distance between the time steps in the plot. The bin width of 10 cm was selected according to the measurement accuracy of 5-12 cm.

towards larger ice drafts. In November the median still continued on its level at around 1 m, whereas the mode dropped to 0-10 cm, indicating that open water and thin ice became dominant. Between November and January the second (thermodynamic) mode dropped rapidly together with the median. In the following year significant ice growth started one month earlier.

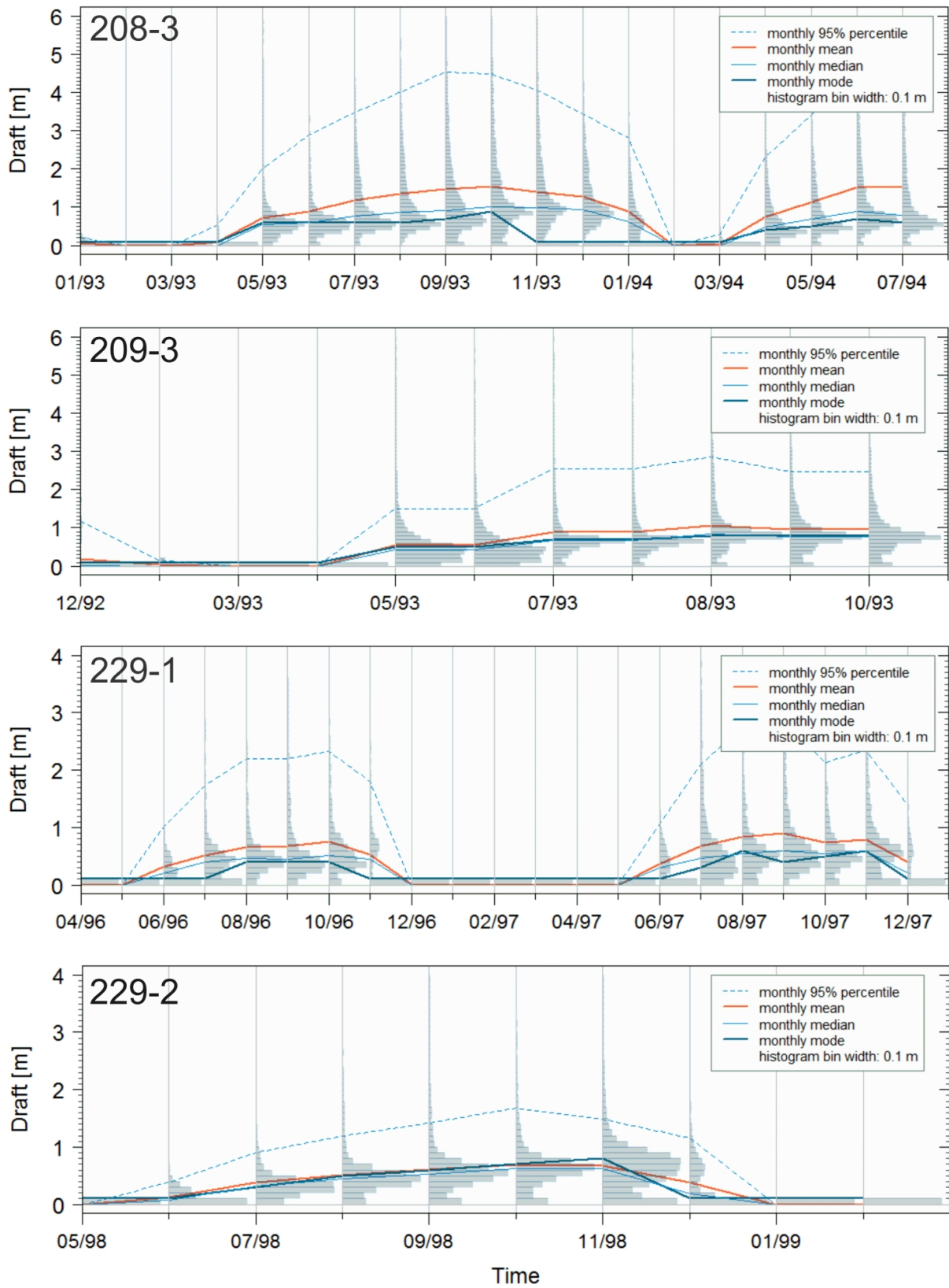


Fig. 6.6: The same as in figure 6.5, but for AWI 208-3, AWI 209-3, AWI 229-1 and AWI 229-2.

At AWI-209 the three quantities mean, median and mode almost coincide over the entire record. The distributions were almost Gaussian between July and October. The maximum mode between August and October remained between 70 cm and 80 cm, displaying the maximum of thermodynamic ice growth ².

At AWI 229-1 (Fig. 6.6) the median and the mode largely coincided, except for times when the class 0-10 cm was dominant. The larger mean draft indicates the degree of skewness of the distributions. Thus, the deviation of the mean from the median and the mode can be assumed to display the degree of ice deformation. Depending on the year, the mode reached maximum values of 60-70 cm and 70-80 cm, which displays changing thermodynamic conditions.

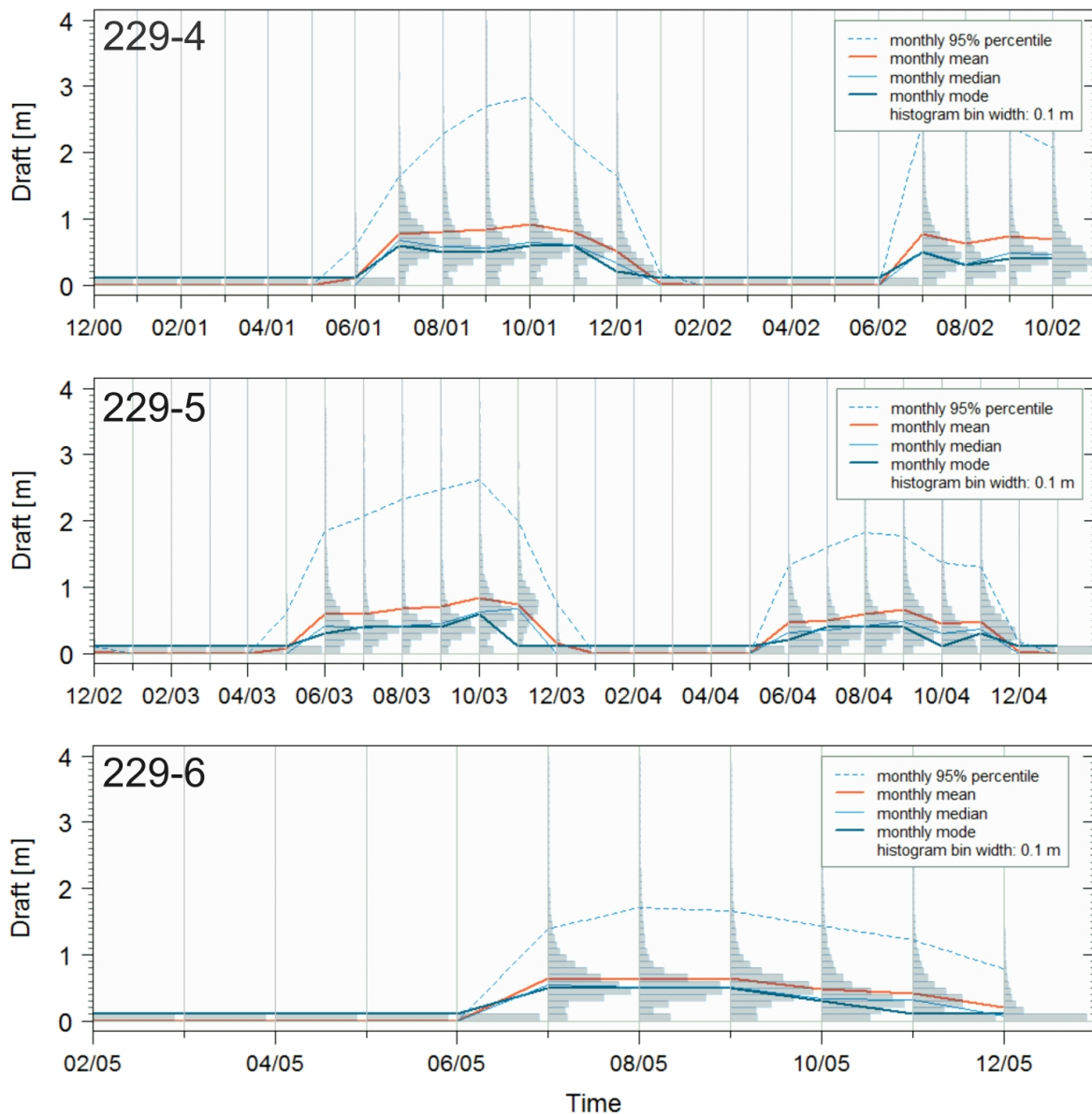


Fig. 6.7: The same as in figure 6.5, but for AWI 229-4, AWI 229-5 and AWI 229-6.

²Note that the mode is also determined by the snowload on top of the ice

At AWI 229-2 mean, mode and median took the same values, which indicates a low degree of ice deformation and a dominating influence of thermodynamics. The draft distributions of AWI 229-4 and AWI 229-5 (Fig. 6.7) are very similar to AWI 229-1. AWI 229-6 indicates a low degree of ice deformation, i.e. almost Gaussian shaped distributions in winter, which were only slightly skewed towards larger drafts.

The plot of AWI 231-1 (Fig. 6.8) shows slightly higher ice deformation in 1997 compared to 1996. In 1998 the monthly distributions were almost Gaussian between July and October, with the respective medians, modes and means almost coinciding. In November the ice started disintegrating, and thin ice classes and open water became dominant.

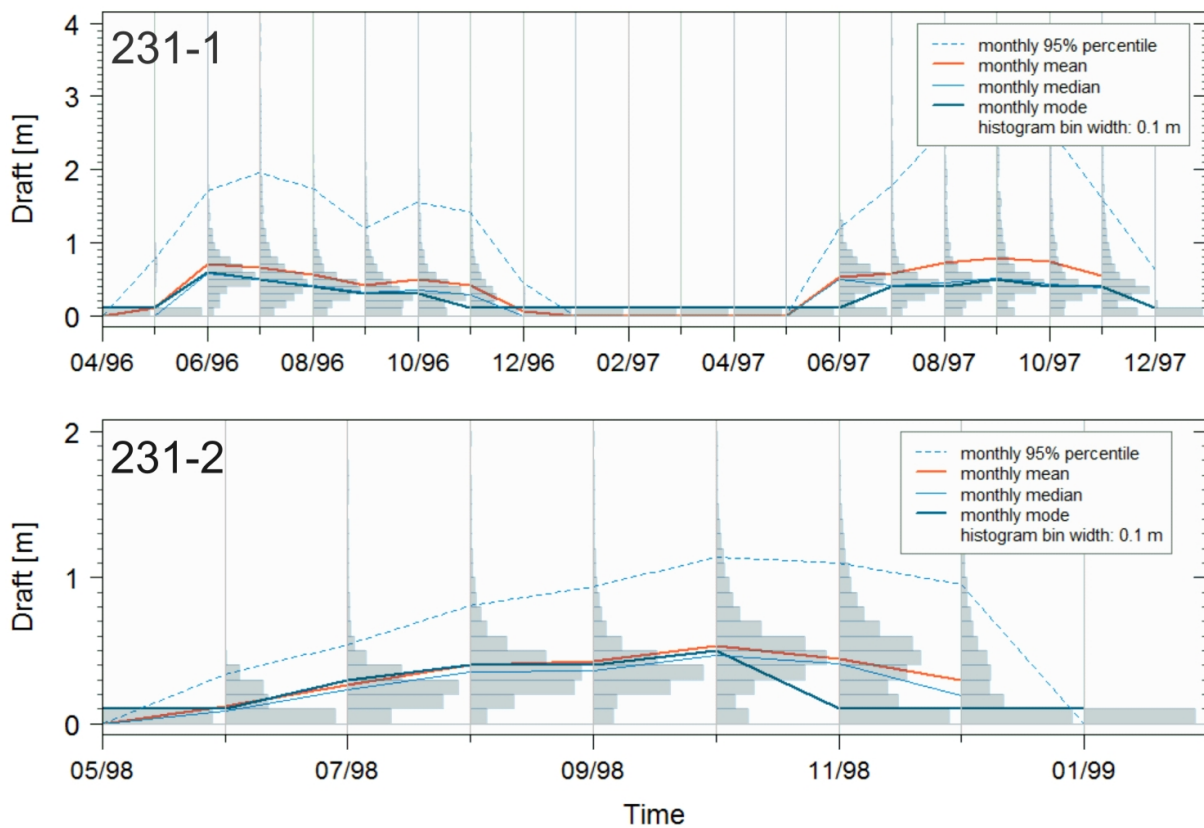


Fig. 6.8: The same as in figure 6.5, but for AWI 231-1 and AWI 231-2.

At AWI 231-4 (Fig. 6.9) the monthly distributions were almost symmetric and displayed an only weak influence of ice deformation in 2001. One year later, mean, mode and median did not differ significantly from each other until September. In contrast to 2001, the distributions in August and September 2002 became flatter from zero ice draft to the draft mode. Mean, mode and median started deviating from each other in August. The same applies to AWI 231-6. At AWI 231-7 the deviation of median and mode in June and November indicates dominating open water and thin ice. The positive deviation of the mean from the median between June and October indicates deformed ice. However, as discussed in the chapter about data quality, the record of AWI 231-7 is affected by biases resulting from high ice concentration. The distributions of winter ice drafts in 2006 corrected by the sound model are shown in the inset. Mainly the

distributions in July and October shift towards higher values, which corresponds to thicker ice and low ice concentration.

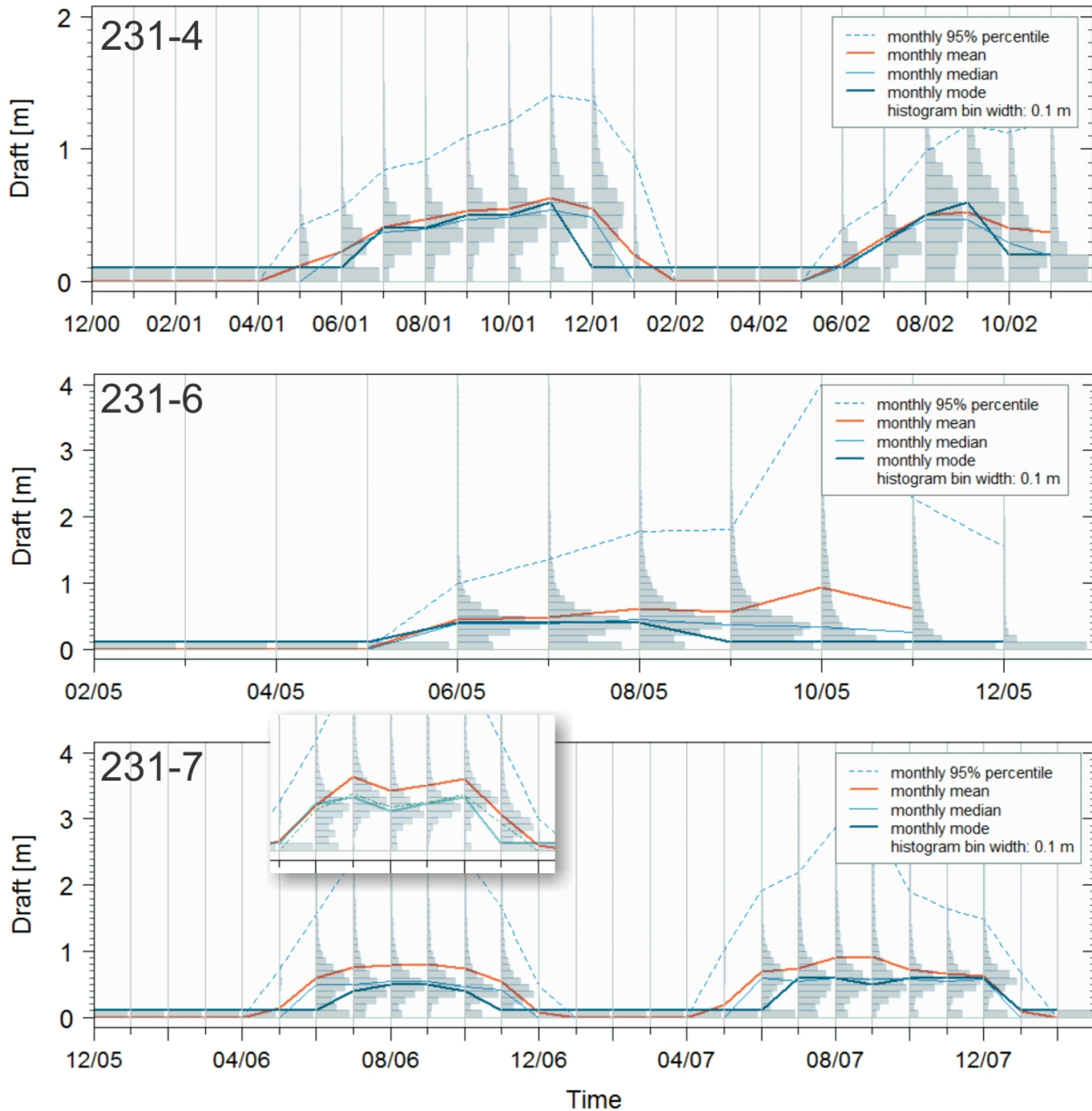


Fig. 6.9: The same as in figure 6.5, but for AWI 231-4, AWI 231-6 and AWI 231-7. The inset shows data corrected by the sound model.

At AWI 232-1 (Fig. 6.10) the draft mode reached a maximum value of 0.9 m. Strongly skewed monthly distributions and deviating statistical quantities indicate a high degree of ice deformation. This changes at AWI 232-4. The record shows a monotonic growth of mean, mode and median until September. The mode reached maximum values of only 0.6 m in August/September. In 2000 it increased to almost 1 m in September, which indicates colder temperatures in that year. In contrast to 1996, most of the ice drafts did not exceed 2 m. AWI 232-5 shows monotonic increase of the three main statistical quantities until August in

2001 and until July in 2002. After that, the rising mean indicates the growing influence of ice dynamics. The August mode was comparable in both years. However, after August the ice deformation seems to have played a larger role in the first year of AWI 232-5.

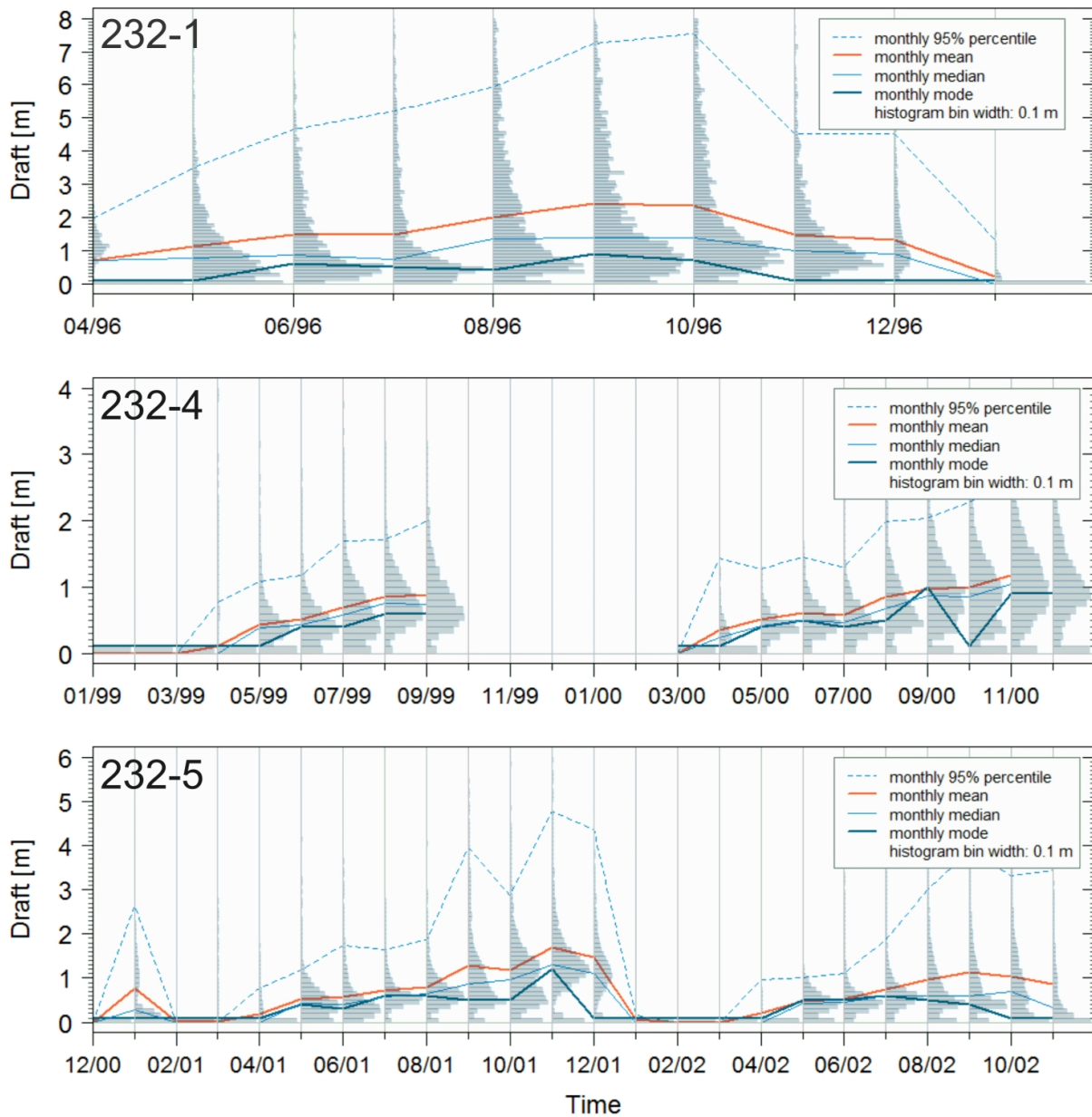


Fig. 6.10: The same as in figure 6.5, but for AWI 232-1, AWI 232-4 and AWI 232-5.

AWI 232-6 (Fig. 6.11) displays a high degree of ice deformation. A monotonic increase of the draft mode is hardly detectable. Most of the ice drafts remained below 6-7 m. Mean, mode and median deviated by up to 2 m from each other. The modes of 2003 and 2004 were comparable. Less deformation occurred in 2004. In 2006 and 2007 ice drafts of up to 10 m were measured. The modes never exceeded 0.7 m, except for October 2007. However, the thermodynamic modes were still visible around 1 m between August and November 2007. It seems that the thicker

ice in 2007 was due to a combination of both thermodynamics and dynamics.

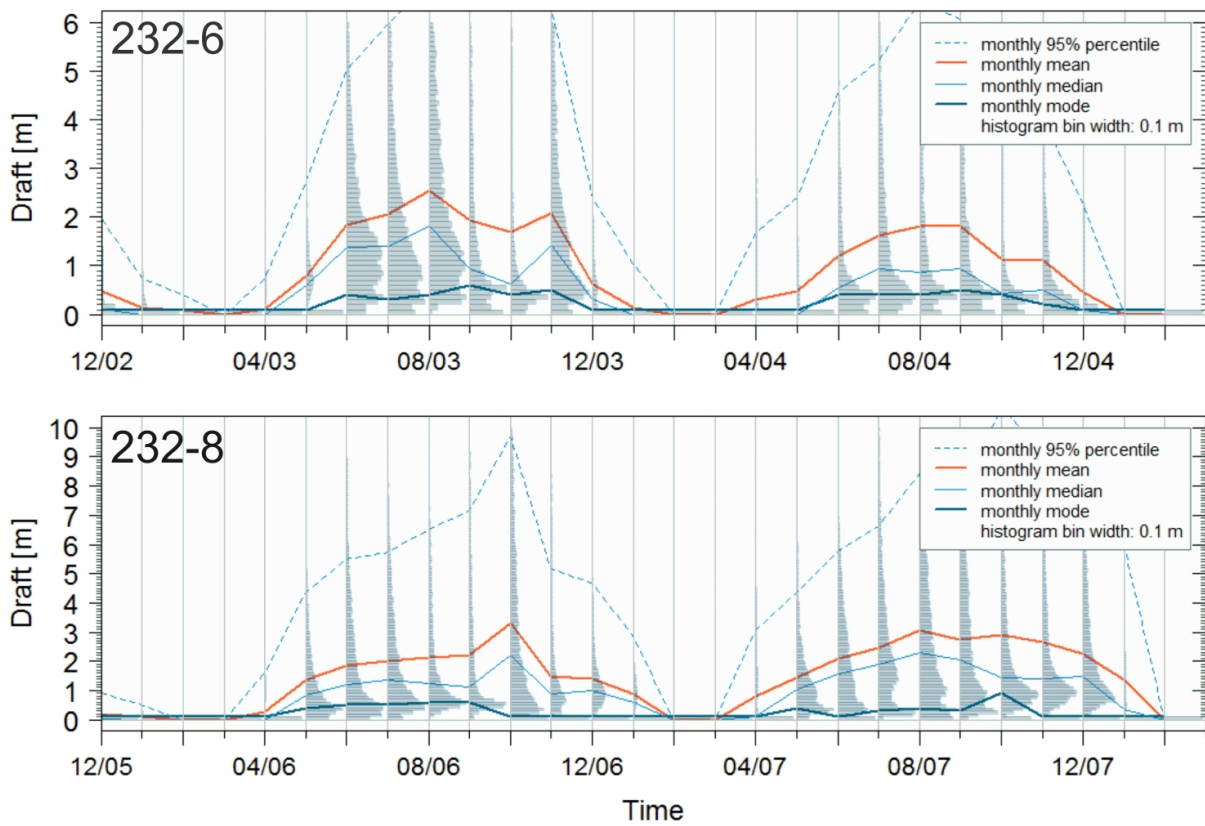


Fig. 6.11: The same as in figure 6.5, but for AWI 232-6 and AWI 232-8.

Averaged statistical values, such as monthly mean ice draft and monthly draft mode, are shown below (Table VII & Table VIII).

Table VII: Monthly mean ice drafts [m]

The monthly averages were calculated as effective means from all available draft measurements. The respective lower values (\pm) are standard errors of the means.

	Jan	Feb	Mar	Apr	May	Jun	Jul	Aug	Sep	Oct	Nov	Dec
207-2	1.32 ± 0.02	0.87 ± 0.02	1.85 ± 0.02	2.32 ± 0.02	2.79 ± 0.02	2.44 ± 0.02	3.4 ± 0.03	3.39 ± 0.03	3.2 ± 0.03	3.4 ± 0.03	2.07 ± 0.03	1.57 ± 0.02
207-4	0.34 ± 0.02	- $\pm -$	- $\pm -$	0.8 ± 0.02	1.41 ± 0.02	1.63 ± 0.02	2.22 ± 0.03	2.54 ± 0.03	2.25 ± 0.04	2.74 ± 0.04	1.91 ± 0.05	2 ± 0.05
207-6	0.49 ± 0.01	0.14 ± 0.00	0.3 ± 0.00	0.84 ± 0.01	0.9 ± 0.01	1.15 ± 0.01	1.08 ± 0.01	1.29 ± 0.01	1.38 ± 0.01	1.01 ± 0.01	0.98 ± 0.01	0.91 ± 0.01
208-3	0.5 ± 0.01	- $\pm -$	0.02 ± 0.00	0.42 ± 0.00	0.92 ± 0.01	1.2 ± 0.01	1.35 ± 0.01	1.36 ± 0.01	1.47 ± 0.01	1.55 ± 0.02	1.39 ± 0.01	1.28 ± 0.01
209-3	0.05 ± 0.00	- $\pm -$	- $\pm -$	0.01 ± 0.00	0.55 ± 0.01	0.74 ± 0.01	0.88 ± 0.01	1.06 ± 0.01	0.99 ± 0.01	0.95 ± 0.01	0.96 ± 0.01	0.18 ± 0.03
210-2	0.58 ± 0.01	- $\pm -$	0.04 ± 0.00	0.4 ± 0.01	0.92 ± 0.01	1.25 ± 0.01	1.14 ± 0.01	1.46 ± 0.01	1.25 ± 0.01	1.54 ± 0.02	1.14 ± 0.01	0.74 ± 0.01
212-2	1.86 ± 0.02	1.33 ± 0.02	0.94 ± 0.02	0.74 ± 0.01	1.58 ± 0.02	2.84 ± 0.02	3.78 ± 0.03	1.3 ± 0.02	3.29 ± 0.03	1.29 ± 0.02	2.93 ± 0.03	3.07 ± 0.03
217-1	1.39 ± 0.02	0.72 ± 0.01	0.5 ± 0.01	0.9 ± 0.01	1.12 ± 0.01	1.22 ± 0.01	1.9 ± 0.02	2.19 ± 0.02	2.8 ± 0.03	2.41 ± 0.02	1.65 ± 0.02	2.09 ± 0.02
227-4	- $\pm -$	0.24 ± 0.00	0.53 ± 0.00	0.33 ± 0.00	0.61 ± 0.00	0.12 ± 0.00	0.04 ± 0.00					
227-6	- $\pm -$	0.06 ± 0.00	0.25 ± 0.00	0.41 ± 0.00	0.52 ± 0.00	0.42 ± 0.00	0.23 ± 0.00	- $\pm -$				
229-1	- $\pm -$	0.34 ± 0.01	0.6 ± 0.01	0.75 ± 0.01	0.79 ± 0.01	0.75 ± 0.01	0.66 ± 0.01	0.19 ± 0.01				
229-2	- $\pm -$	0.13 ± 0.00	0.38 ± 0.00	0.51 ± 0.00	0.61 ± 0.01	0.69 ± 0.01	0.67 ± 0.01	0.38 ± 0.00				
229-3	- $\pm -$	- $\pm -$	- $\pm -$	- $\pm -$	0.09 ± 0.00	0.47 ± 0.01	0.69 ± 0.01	0.75 ± 0.01	- $\pm -$	- $\pm -$	- $\pm -$	- $\pm -$
229-4	0.01 ± 0.00	- $\pm -$	- $\pm -$	- $\pm -$	- $\pm -$	0.06 ± 0.00	0.77 ± 0.01	0.73 ± 0.01	0.8 ± 0.01	0.81 ± 0.01	0.8 ± 0.01	0.42 ± 0.01
229-5	- $\pm -$	- $\pm -$	- $\pm -$	- $\pm -$	0.04 ± 0.00	0.53 ± 0.00	0.55 ± 0.00	0.63 ± 0.01	0.68 ± 0.01	0.65 ± 0.01	0.61 ± 0.00	0.07 ± 0.00
229-6	- $\pm -$	0.64 ± 0.00	0.63 ± 0.00	0.64 ± 0.00	0.48 ± 0.00	0.41 ± 0.00	0.2 ± 0.00					
230-2	- $\pm -$	- $\pm -$	- $\pm -$	- $\pm -$	0.23 ± 0.00	0.56 ± 0.01	- $\pm -$					
230-3	0.09 ± 0.00	- $\pm -$	- $\pm -$	- $\pm -$	0.07 ± 0.00	0.3 ± 0.00	0.68 ± 0.00	0.68 ± 0.00	0.74 ± 0.01	0.64 ± 0.00	0.69 ± 0.01	0.52 ± 0.00
231-1	- $\pm -$	- $\pm -$	- $\pm -$	- $\pm -$	0.05 ± 0.00	0.61 ± 0.01	0.62 ± 0.01	0.65 ± 0.01	0.6 ± 0.01	0.61 ± 0.01	0.48 ± 0.01	0.07 ± 0.00
231-2	- $\pm -$	0.12 ± 0.00	0.26 ± 0.00	0.4 ± 0.00	0.42 ± 0.00	0.53 ± 0.00	0.44 ± 0.00	0.29 ± 0.00				
231-3	- $\pm -$	- $\pm -$	- $\pm -$	- $\pm -$	0.14 ± 0.00	0.62 ± 0.01	- $\pm -$					
231-4	0.1 ± 0.00	- $\pm -$	- $\pm -$	- $\pm -$	0.06 ± 0.00	0.18 ± 0.00	0.37 ± 0.00	0.48 ± 0.00	0.53 ± 0.00	0.47 ± 0.00	0.5 ± 0.00	0.43 ± 0.00
231-6	- $\pm -$	- $\pm -$	- $\pm -$	- $\pm -$	0.02 ± 0.00	0.45 ± 0.00	0.48 ± 0.00	0.61 ± 0.00	0.56 ± 0.00	0.93 ± 0.01	0.61 ± 0.00	0.26 ± 0.00
231-7	0.03 ± 0.00	- $\pm -$	- $\pm -$	- $\pm -$	0.16 ± 0.00	0.64 ± 0.00	0.74 ± 0.00	0.85 ± 0.00	0.86 ± 0.00	0.73 ± 0.00	0.6 ± 0.00	0.29 ± 0.00

	Jan	Feb	Mar	Apr	May	Jun	Jul	Aug	Sep	Oct	Nov	Dec
232-1	0.22 ±0.01	- ± -	- ± -	0.71 ± 0.03	1.13 ± 0.03	1.47 ± 0.03	1.47 ± 0.03	2 ± 0.04	2.43 ± 0.06	2.34 ± 0.05	1.47 ± 0.03	1.32 ± 0.03
232-4	- ± -	- ± -	- ± -	0.19 ± 0.00	0.47 ± 0.00	0.56 ± 0.00	0.63 ± 0.01	0.85 ± 0.01	0.94 ± 0.01	0.99 ± 0.01	1.18 ± 0.01	1.09 ± 0.01
232-5	0.4 ±0.01	- ± -	0.01 ± 0.00	0.19 ± 0.00	0.5 ± 0.00	0.55 ± 0.00	0.73 ± 0.01	0.88 ± 0.01	1.21 ± 0.01	1.11 ± 0.01	1.28 ± 0.01	1.13 ± 0.01
232-6	0.09 ±0.00	0.04 ± 0.00	- ± -	0.21 ± 0.00	0.64 ± 0.01	1.52 ± 0.01	1.83 ± 0.01	2.18 ± 0.02	1.87 ± 0.02	1.42 ± 0.01	1.6 ± 0.01	0.52 ± 0.01
232-8	0.77 ±0.01	- ± -	- ± -	0.54 ± 0.00	1.41 ± 0.01	1.97 ± 0.01	2.22 ± 0.01	2.6 ± 0.01	2.48 ± 0.01	3.1 ± 0.02	2.06 ± 0.01	1.56 ± 0.01
233-2	0.81 ±0.01	0.22 ± 0.01	- ± -	0.55 ± 0.01	1.21 ± 0.01	1.64 ± 0.02	2.09 ± 0.02	2.46 ± 0.02	2.51 ± 0.02	1.89 ± 0.02	2.43 ± 0.02	0.54 ± 0.01
233-6	1.95 ±0.01	1.13 ± 0.01	1.01 ± 0.01	1.68 ± 0.01	1.94 ± 0.01	2.06 ± 0.01	2.07 ± 0.02	3.15 ± 0.02	2.24 ± 0.02	1.52 ± 0.01	2.75 ± 0.02	2.72 ± 0.02

6.3 Ice season duration

As the beginnings and the ends of the sea ice seasons vary over time, the mean annual cycles (Fig. 6.12) include years in which the measured annual cycle starts earliest and ends latest, i.e. they display the maximum possible period of ice coverage at the respective mooring positions.

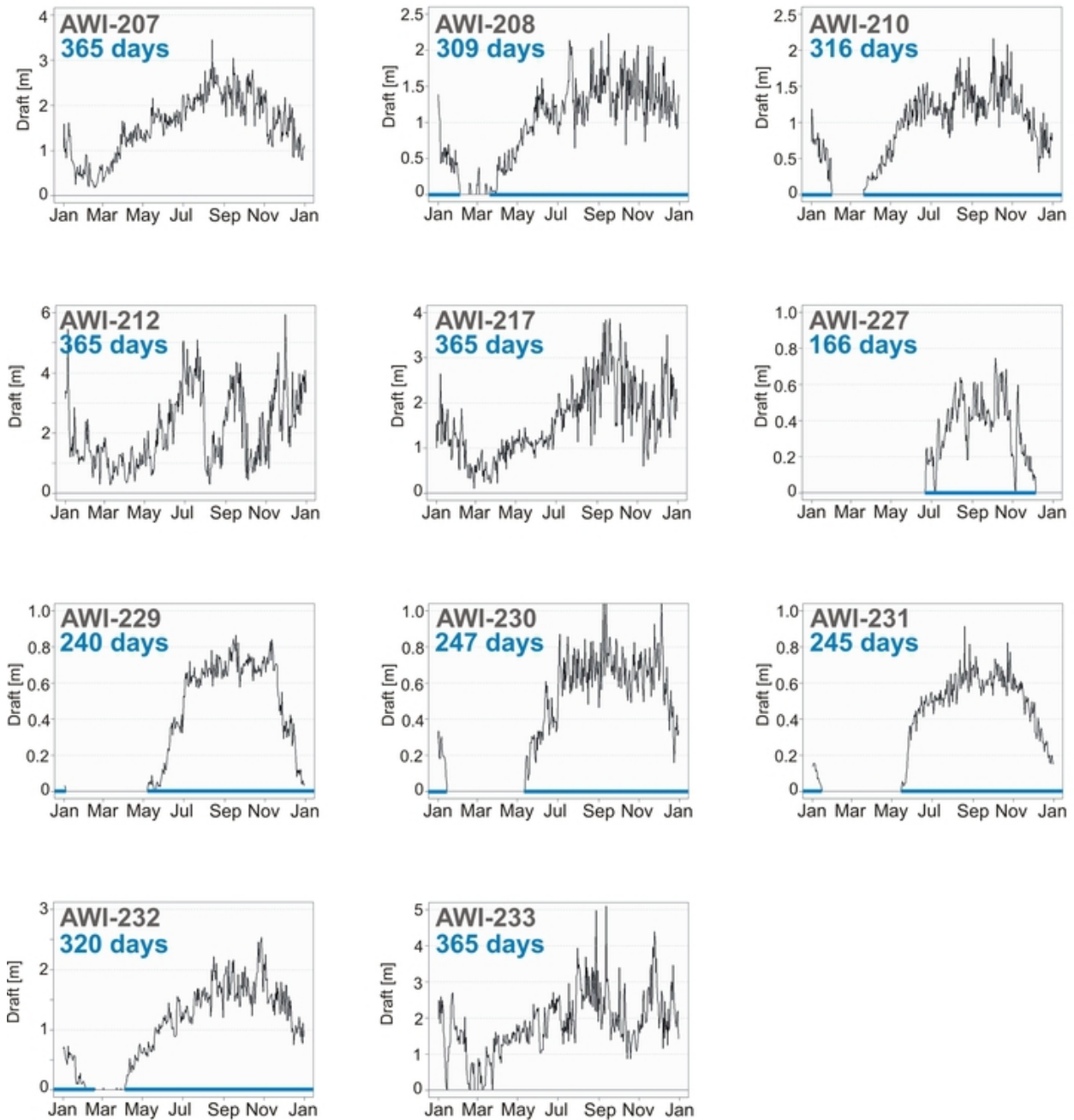


Fig. 6.12: Mean annual cycles of the daily mean ice draft for all ULS positions. The calculations were made only for measured data (i.e. no filled gaps). For AWI-209 no full annual cycle was measured. The blue bars mark the period of possible ice appearance given by the blue numbers.

At only four locations sea ice can appear year-round: AWI-207, AWI-212, AWI-217 and AWI-233. However, also at AWI-208 some ice remained in the observed summer season.

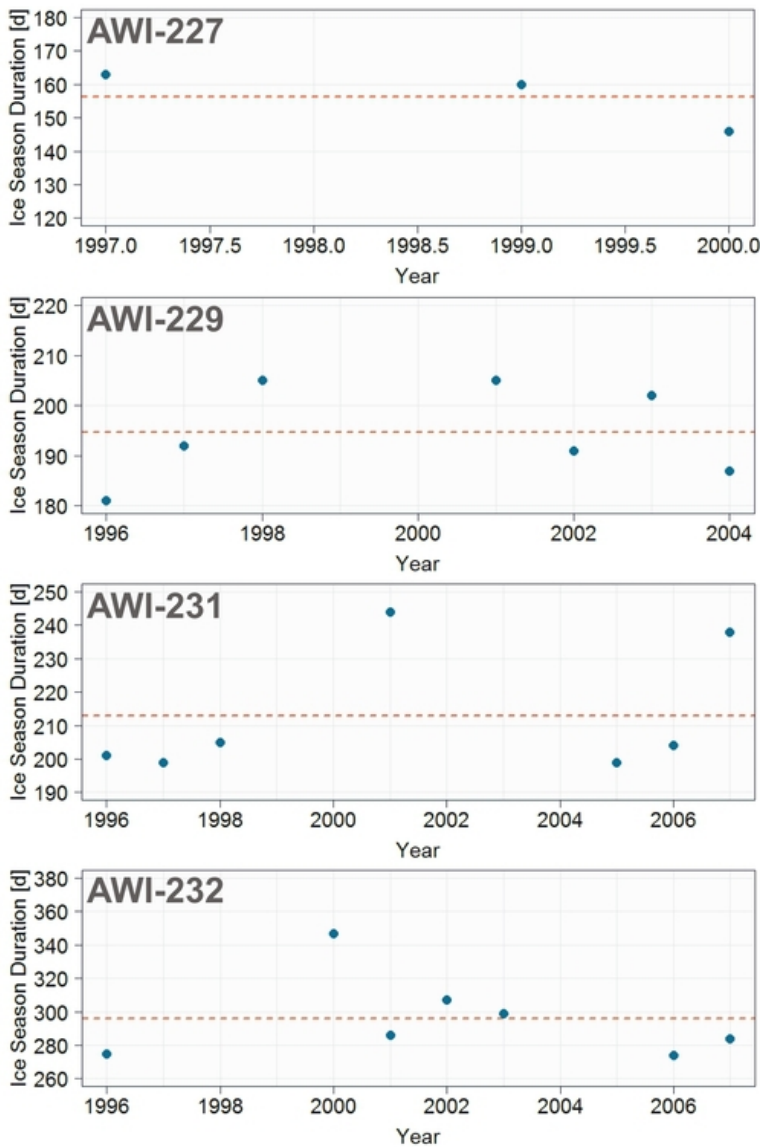


Fig. 6.13: Ice season durations (in days) of the measured years on the prime meridian. The red dashed line marks the average ice season duration.

sometimes no full annual cycle was measured. At AWI-232 years with thicker ice seem to have a shorter ice season duration and vice versa (compare to figure 5.21). At AWI-210 the ice season duration in 1991/1992 was 299 days, and at AWI-208 it was 288 days in 1993/1994.

The variance in the mean annual cycle decreases with increasing number of observations. In the central Weddell Sea (AWI-208 and AWI-210) the ice seasons cover a period of 309-316 days (Table IX). The period of possible ice coverage near the northern boundary of the sea ice field (AWI-227) is 166 days long. At AWI-229, AWI-230 and AWI-231 the length of this period is similar and differs by one week at maximum. The annual cycle is least pronounced at AWI-212. The ice draft rises and declines steepest in the regions with short ice season duration (AWI-227 - AWI-231). Note that the ice draft at AWI-231 is on average thinner than at AWI-230 and AWI-229, although the ice thickness on the prime meridian declines almost exponentially from AWI-233 to AWI-227. At AWI-232 the period of possible ice coverage is 320 days long.

The lengths of the individual annual cycles at AWI-227, AWI-229, AWI-231 and AWI-232 vary strongly and show no trend (Fig. 6.13). The averages are 156 ± 5 , 195 ± 4 , 213 ± 7 , 296 ± 10 days, respectively. The variance of the ice season duration increases from north to south. For AWI-207 no clear annual cycle could be extracted, as the variations in the individual years are too strong and some-

Table IX: Days of earliest and latest ice occurrence, based on the ULS measurements

Position	Earliest	Latest	Position	Earliest	Latest
AWI-207	17. Feb.	17. Feb.	AWI-227	22. Jun.	5. Dec.
AWI-208	31. Mar.	2. Feb.	AWI-229	8. May	3. Jan.
AWI-210	21. Mar.	31. Jan.	AWI-230	12. May	14. Jan.
AWI-212	10. Mar.	10. Mar.	AWI-231	15. May	15. Jan.
AWI-217	27. Feb.	27. Feb.	AWI-232	6. Apr.	19. Feb.
			AWI-233	3. Mar.	3. Mar.

6.4 Spectral analysis

To obtain some first information on the driving mechanisms of variations in sea ice thickness, spectral analysis of the draft time series and time series of possible forcings, such as wind and drift, was conducted. As shown above, the regions with the most distinct changes in sea ice thickness are the positions AWI-207 and AWI-232. Further analyses were therefore focused on these regions. In addition, two more positions with quasi-continuous time series were considered: AWI-231 and AWI-229. Local time series (i.e. on the grid points closest to the ULS positions) of ice drift, ice concentration, ECMWF surface air temperature and ECMWF surface winds were analysed in order to assess whether the ice draft shares significant periods with these parameters. SSA was also applied to large-scale processes, such as SAM, SAO, ZW3, PSA and *El Niño* (see section 2.5). Finally, spectral analysis was applied to time series of ice thickness from the MIT and FESOM³ models to investigate whether the models are capable of reproducing significant oscillations in the ice draft.

The SAM-Index (SLP-based) was taken from the *Joint Institute for the Study of the Atmosphere and Ocean*⁴ (JISAO) in Washington and the ENSO indices were taken from NOAA⁵. The ZW3-Index was calculated after *Yuan and Li* [2008], i.e. as the first EOF of the vertically integrated, mass-weighted meridional wind anomalies (NCEP) over the full hemisphere south of 20°S latitude, with the only difference that it was calculated for the pressure levels 1000-925 hPa, i.e. for the lower atmosphere. The anomalies were weighted by area before the calculation, using the square root of the cosine of latitude to ensure equal area weighting for the covariance matrix [*Udagawa et al.*, 2009]. Also the PSA-Index and the SAO-Index were calculated after *Yuan and Li* [2008]. The PSA-Index was calculated from the 500 hPa geopotential height field (NCEP) according to the three typical pressure centres and the SAO-Index as the difference between the zonal mean SLP between 50°S and 65°S.

Spectral analysis was conducted by applying SSA (see section 4.2) to monthly anomaly time series. As the analysis focuses on more or less regular oscillations in the data, the anomalies were calculated as follows: First, SSA was applied to the data retaining the annual cycle. Then, the EOFs representing the annual cycle were determined and fitted to the data. Before the fit, the EOFs were set to zero in the ice-free summer seasons in all ice-related time series. The fitted EOFs were then subtracted from the initial time series. In this way, only the annual oscillations are removed and other regular oscillations, e.g. semi-annual cycles, remain in the data. Only the anomalies of the data in the period AWI 207-6 were calculated in the common way, i.e. by subtracting from each month its long-term mean. This was done because the annual cycle detected by SSA was considered too weak to apply the above procedure. The draft record of AWI 207-6 contained no data in 8/2005 and a very low amount of valid data in 9/2005. These two months were therefore filled by draft data derived from the MIT sea ice model. This was possible, because the simulated thickness is very close to the observed draft in the period of AWI 207-6, and the draft anomalies were found to correlate well ($r=0.68$) with the MIT model ice thickness anomalies. The ice thickness of the MIT model in the two months was converted into draft values based on empirical relations obtained from drillings in the Weddell Sea [*Harms et al.*, 2001] and filled into the draft record of 207-6. As the record at AWI-207 is very gappy, the anomalies of the three subintervals were calculated with the respective base periods, e.g. 04/05-12/07 for AWI 207-6. To avoid the detection of artificial signals that only result from

³The results of FESOM were omitted at AWI-207 as they were considered unrealistic in this region.

⁴<http://www.jisao.washington.edu/aao/slp/>

⁵<ftp://ftp.cpc.ncep.noaa.gov/wd52dg/data/indices/>

the calculation of anomalies, significant oscillations were additionally analysed and confirmed by retaining the annual cycle in the respective time series.

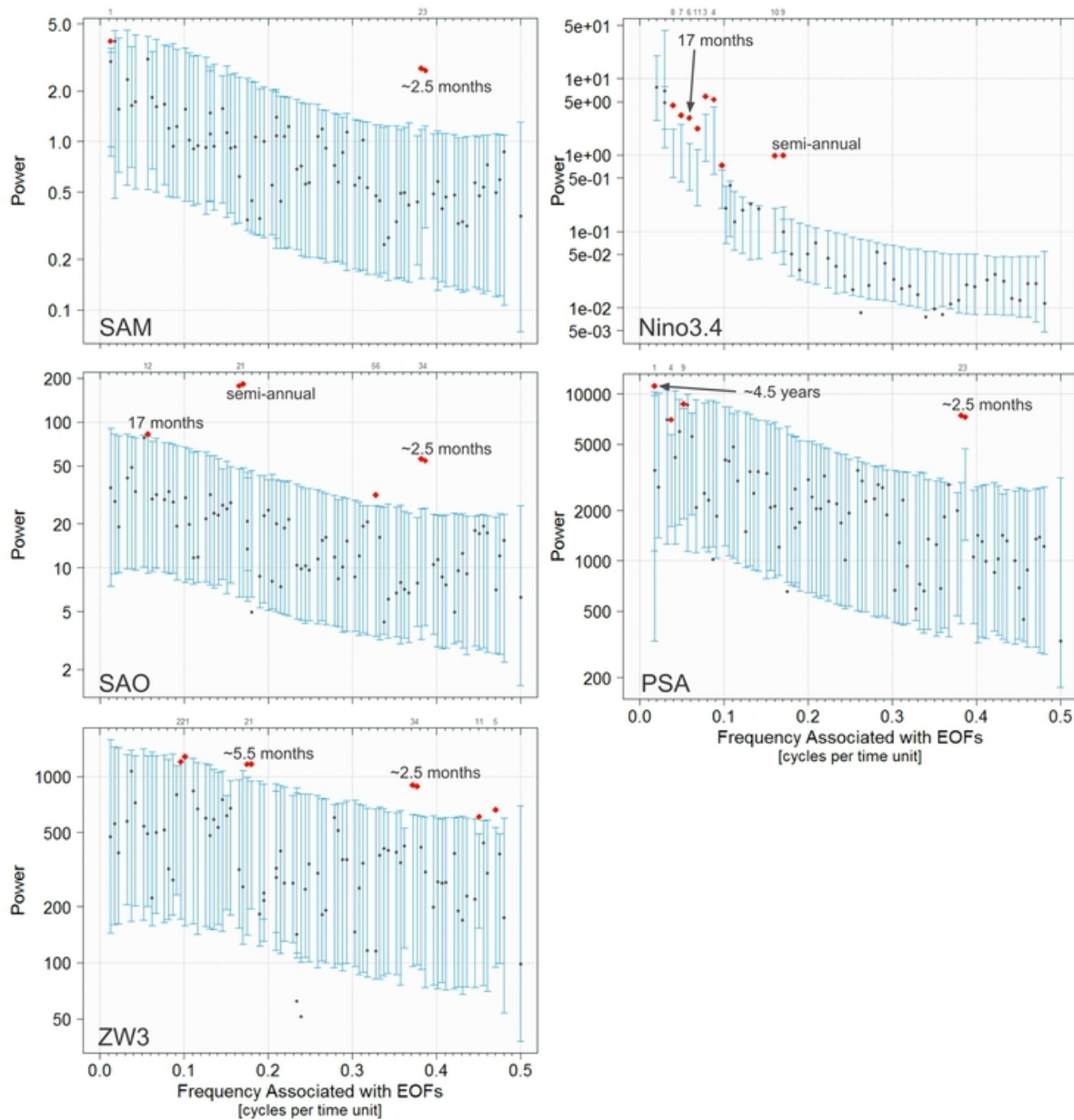


Fig. 6.14: Eigenvalues of the lag-covariance matrices (see section 4.2), plotted against the dominant frequency associated with their corresponding EOFs. Shown are the spectra of different climate modes over the period 1990-2007. SSA-window width for all time series: 80 months. Red diamonds mark significant EOFs. Note the logarithmic scale of the y-axis.

The SSA window widths used were not longer than half the length of the time series, as recommended by *Hassani* [2007]. To generate error bars (97.5th and 2.5th percentiles), 2000 Monte Carlo simulations were performed. The frequencies of the EOFs were determined by maximising the correlation with a sine function [*Allen and Smith, 1996*]. Shown are eigenvalue spectra (scree diagrams) of climate modes, the ice draft and selected parameters which show the same or similar significant oscillations as the ice draft. The diagrams show the eigenvalues

ordered by frequency after step two of the SSA significance test. The significant frequencies found in all parameters are summarised in tables. Discussed in the text are mainly those periods that are shared by the ice draft and other parameters. Experiments with artificial white noise time series showed that in about one out of three random time series of 12 years length, SSA detected significant periods around 2.5 and 3 months. These periods were therefore considered as artefacts of SSA and are not discussed in the text.

Table X: Significant SSA periods in climate modes 1990-2007

Mode	Period [months] (explained variance)					
<i>Niño</i> 3.4	31 (5.5%)	27 (5%)	19 (6.5%)	17.5 (2%)	12 (20%)	6 (6.5%)
PSA	54 (5.5%)	27 (3.5%)	19 (2.5%)	2.5 (9%)		
SAM	80 (5.5%)	2.5 (9%)				
SAO	17.5 (1.8%)	6 (20%)	3 (0.5%)	2.5 (10%)		
ZW3	10 (3%)	5.5 (7.5%)	2.5 (6.5%)	2.2 (5.5%)		

The SAM shows significant variability with a period of 80 months (Fig. 6.14 & Table X). A property of the SSA method is that oscillations with significant power at frequencies below the detection threshold (which is defined by the maximum window width) are sometimes displayed by a significant frequency corresponding to the one at the detection threshold [Allen and Smith, 1996]. The 80-month period therefore may display all significant variability in the SAM above 80 months, e.g. the long-term trend in SAM. When a longer period is analysed (1948-2008), SAM variability is dominated by a 60-months period (27% variance explained). The 2.5-months period is shared by SAM, SAO, PSA and ZW3. However, this signal is believed to be an artefact of the SSA method or the reanalysis data. A semi-annual signal is naturally present in the SAO, but also in the *Niño*3.4-Index and to some extent in ZW3. A significant 17-months period is present in the SAO-Index and the *Niño*3.4-Index. The periods of 19, 17.5 and 12 months in the *Niño*3.4-Index could indicate that its annual cycle is irregular to some extent and was split by SSA into discrete frequencies.

Besides analysing the anomalies of AWI-207, the three time series were additionally analysed retaining the annual cycle, as they are very short. An analysis retaining the annual cycle was also applied by Allen and Smith [1996]. No significant oscillations were found for AWI 207-2 and AWI 207-4. For AWI 207-6 no significant oscillation was found in the first step of the SSA significance test. However, EOF 1 represents the annual cycle at 11.6 months - which is not very pronounced in this time series - and EOF 2 represents a period of 17 months. Together both EOFs explain 50% of the variance. If these EOFs are identified as signal, they stand out as significant after step two of the significance test (Fig. 6.15). One can therefore reject the null hypothesis that both EOFs are part of AR(1)⁶ noise at the 97.5% confidence level (see section 4.2).

⁶AR(1): Autoregressive process with only the noise term and the previous term in the process contributing to the output (*red noise*) [Allen and Smith, 1996].

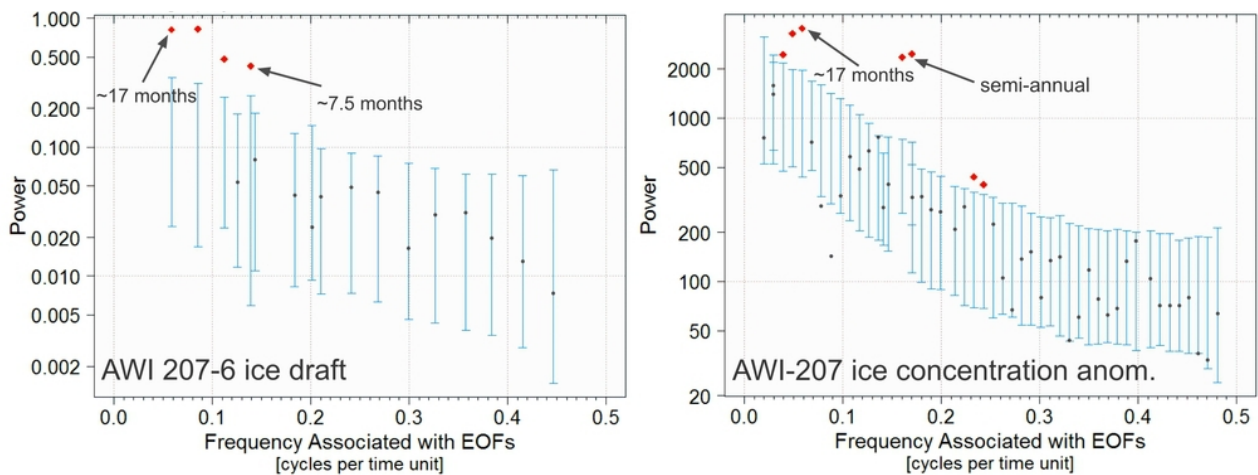


Fig. 6.15: SSA spectra for AWI-207 (see figure 6.14 for more information). SSA window width: Ice draft: 17 months, ice concentration (SSM/I): 60 months. The ice draft was analysed retaining the annual cycle. Analysed period of ice concentration: 1990-2007.

The origin of EOF 2 is unclear. Note that the association of frequencies with the EOFs via lag correlation may be slightly biased. It is possible that EOF 2 has a period of 16 or 18 months. Two additional periods (9 and 7.5 months) stand out as significant after step two of the test. When draft anomalies were analysed, the 7-month (quasi semi-annual) and the 17-month period remained. The 17-months period is also present in the sea ice concentration anomalies at AWI-207 (Fig. 6.15). As discussed in section 2.5, the SAM has a large influence on the sea ice region around the Antarctic Peninsula. No significant frequency could be detected for the SAM in the period of AWI 207-6 (04/2005-12/2007), and for 1990-2007 (Fig. 6.14) only significant periods at around 2.5 months were detected. However, a significant period of 17.5 months appears in the *Niño*3.4-Index and the SAO-Index (Fig. 6.14). In the SAO-Index it explains only a very small fraction of the variance and is barely significant. Also in the *Niño*3.4-Index the explained variance is very small, but when anomalies of the index are calculated to remove the annual cycle of ENSO, the 17.5-month period explains 15% of the variance. Note that regardless of the amount of explained variance, SSA is very powerful in detecting even extremely weak signals in geophysical data [Allen and Smith, 1996]. The explained variance also depends to some extent on the SSA window width and on the selection of signals that are used for the second stage of the SSA significance test. As the explained variances of the EOF representing the annual cycle and the EOF representing the 17-months period are equal, the 17-month period may also result from the strongly varying length of the sea ice season at the tip of the Antarctic Peninsula. A varying length of the ice season would produce a broadband signal which is split by SSA into discrete frequencies, e.g. 9, 12 and 17 months. As the 17 months correspond to the maximum window width for this time series, this EOF could also represent all significant variability >17 months, as explained above. However, the correlation with ENSO-Indices is high and statistically significant, as shown in the next chapter.

A semi-annual signal is present in the surface temperature anomalies (1990-2007) and could therefore represent a real forcing of sea ice thickness. Over the period 2005-2007 (AWI 207-6) a quasi semi-annual signal with a period of 7-7.5 months was detected in the anomalies of ice draft (20% explained variance), ice concentration (28% explained variance), surface air temperature

(17% explained variance)⁷, meridional ice drift (15% explained variance) and meridional surface wind (30% explained variance) (Fig. 6.16). The phasing of the signals suggests that a quasi semi-annual oscillation in the meridional winds carried cold air from the southern Weddell Sea to AWI-207. This would also explain the time lag of about one month between wind and temperature.

Table XI: Significant SSA periods for AWI-207 and AWI-229

Period analysed at AWI-207: 2005-2007 for ice draft and thickness (SSA window width: M=17 months) and 1990-2007 for the remaining parameters (M=60). Period analysed at AWI-229: 1996-2007 (M=60).

Parameter/ULS	Period [months] (explained variance [%])					
	← Range [months] →					
	4-4.5	5-7.5	8-9	9.5-12	16-27	30-80
AWI-207						
Draft 207-6 (+annual cycle)		7.5 (14)	9 (16)	12 (25)	17 (25)	
Draft 207-6		7.5 (20)			17 (30)	
MIT ice thickness 207-6		7.5 (18)				
Ice conc. (SSM/I)	4 (1.5)	6 (19)			17 (13) 20 (12) 25 (3)	
Ice drift (zonal)		6 (10.5)				
Ice drift (meridional)		6 (10.5)				33 (1)
Surface wind (zonal)		6 (5.5)			25 (11)	
Surface wind (meridional)	4 (3)	6 (5.5)			25 (11) 20 (5)	
Surface temperature		6 (3.5)				
AWI-229						
Ice draft 96-07	4 (9)	6 (14)				
Ice draft 01-05	4.5 (10)					
FESOM 96-07	4 (14)	6.5 (5)				32 (10)
MIT 96-07	4 (12)	6 (22)				
Ice conc. (SSM/I)	4 (1)					
Ice drift (zonal)		6 (2)				
Ice drift (meridional)		7 (4)			24 (4)	
Surface wind (zonal)		6 (9)			21 (9)	
Surface wind (meridional)						
Surface temperature	4 (9)	6 (23)				

⁷The signal was a little bit more pronounced at the 925 hPa level (NCEP) (21% variance).

The advected cold air in turn favoured ice growth in this region. In addition, the meridional ice drift anomalies roughly oscillated with the same frequency between positive and negative values. This results in periodic slow and fast ice advection of thicker ice from the south⁸. The

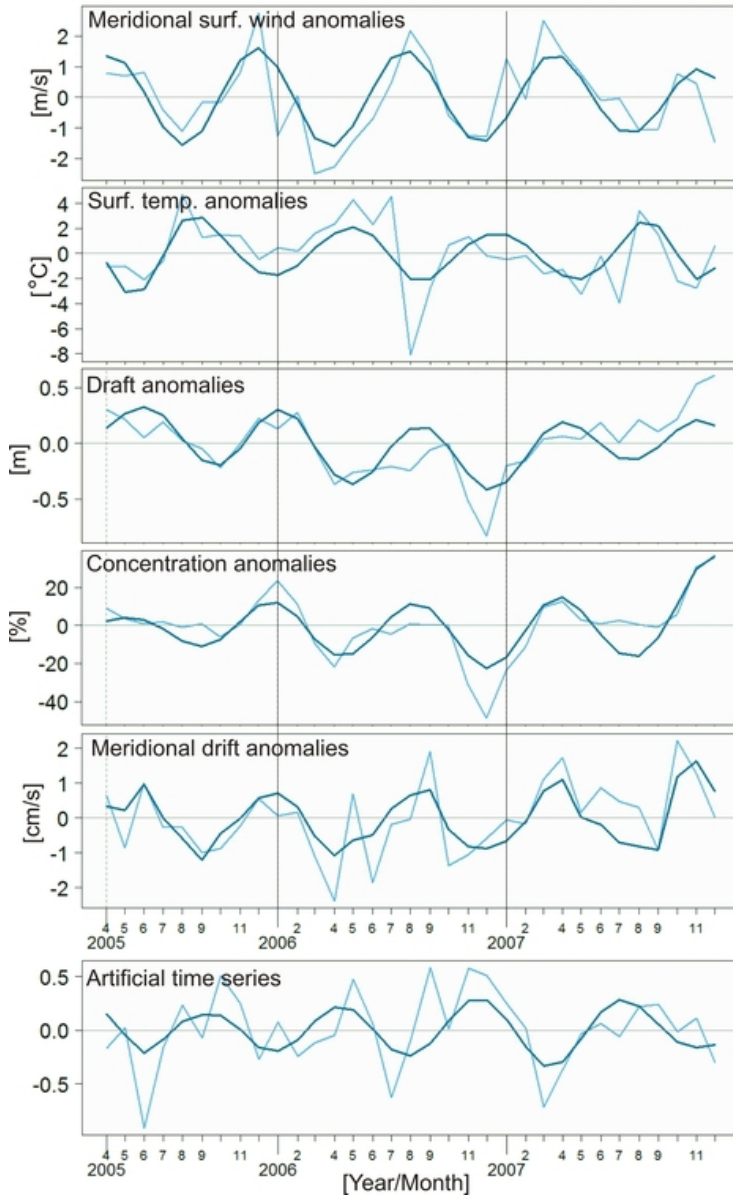


Fig. 6.16: Anomalies of local meridional surface wind, surface air temperature (both ECMWF), ice draft, ice concentration (SSM/I) and meridional ice drift at the position of AWI 207-6. Light blue: Original time series. Dark blue: Significant EOF signals. Positive wind and drift anomalies are from south to north. Lowermost time series: SSA sensitivity test (see text).

the time series, e.g. the ice draft (Fig. 6.16), additional SSA experiments with artificial time series were conducted to test the sensitivity of SSA. To do this, time series of white noise with 36-months length and the same standard deviation as the ice draft anomalies were created and

amplitude of the drift signal is considered too weak to cause significant ice ridging and thickening. The same 7-months cycle in phase with the ice draft was found in the MIT model ice thickness (18% explained variance). Over the period 1990-2007 the semi-annual signal in the air temperature explains only a very small fraction of the variability (see Table XI). One reason for this is that the amplitude of the signal was extremely weak in the period 1990-1999. From 1999 on, it started growing to the higher values observed in 2005-2007. But the five signals are not perfectly in phase with the SAO-Index which has a slightly shorter period during this time (6 months). A 7-months oscillation was found by SSA in the PSA-Index during 2005-2007, exactly in phase with the temperature anomalies. Note that a negative PSA-Index - especially during an *El Niño* event - results in transport of cold continental air from the southern Weddell Sea to the tip of the Antarctic Peninsula [Yuan and Li, 2008]. This is followed by higher ice concentration and larger sea ice extent in this region (see section 2.5). The signal did not pass the SSA significance test. One reason might be that it could not be observed in the PSA-Index over a longer time period (2000-2010). Thus, it is likely that the 7-months signal in the parameters is not part of a long-term oscillation. This is also supported by the fact that it was not found in the ice concentrations and winds in 2000-2005. However, as shown in the next chapter, there is a significant correlation of sea ice parameters at AWI 207-6 with ENSO-Indices and the PSA. As the signal seems to be very arbitrary in some of

⁸Note that the mean ice drift at AWI-207 is always directed northwards.

superimposed with a weak sine-function with 7-months period. As shown in figure 6.16, SSA was able to detect the periodic signal in the white noise time series with high confidence, which confirms the sensitivity of SSA. Moreover, the 7-months signal in the ice draft was very stable against varying SSA window widths. It can be assumed that the oscillation in the ice draft represents a thermodynamically forced PSA signal, which varied in concert with ice concentration and periodic ice advection from higher latitudes. Ice concentration and surface air temperature are negatively correlated in the region of AWI-207 [Schwegmann, 2012]. The peak of the signal in the ice draft and concentration in 2006 is below zero and therefore no positive anomaly. This is a result of the base period used (2005-2007). When ice concentration anomalies are calculated with a longer base period (e.g. 2000-2007), the peak in 2006 becomes positive. As shown in the next chapter, ice draft and concentration are highly correlated in 2005-2007. The ice draft anomaly in 2006 can therefore be assumed to become positive as well, if more draft data were available to use a longer base period.

The full 12-year ice draft anomaly time series of AWI-229 (filled by M-SSA) exhibits significant oscillations with periods of four months and six months. For the measured years 2001-2005 only a 4-months period was detected. Thus, the semi-annual signal in the long time series may result from the filling of data gaps by M-SSA (see section 4.2). The semi-annual cycle was also found in the ice drift, zonal surface winds and surface air temperature. Both model time series contain a semi-annual cycle (especially the MIT model) and 4-months periods. In the temperature anomalies the semi-annual signal explains a large amount of variance (see Table XI). The semi-annual cycle in the modelled ice thickness was

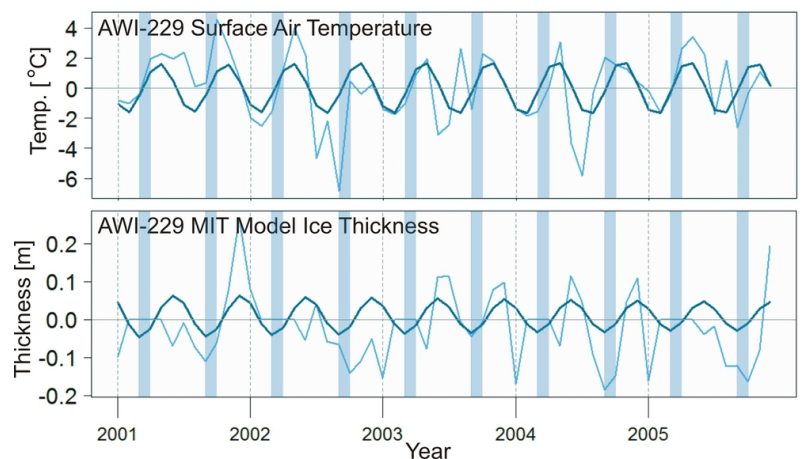


Fig. 6.17: Anomalies of ECMWF surface air temperature and MIT model ice thickness at AWI-229 in the period 2001-2005. Light blue: Original time series. Dark blue: Significant semi-annual signal detected by SSA. The blue shaded periods mark the spring and autumn equinoxes in March and September.

therefore assumed to represent a thermodynamic SAO signal. A typical indication of a high SAO-Index are negative peaks in air temperature around the spring and autumn equinoxes [van den Broeke, 2000b]. The temperature signal in figure 6.17 shows negative peaks in February and August. However, it seems contradictory that almost at the same time, the anomaly of the modelled ice thickness attains its lowest values. In the FESOM model the signal is very weak, but the phase relation with temperature is more obvious, i.e. thicker ice in February and August. But as shown in the next chapter, the measured sea ice draft in the period 2001-2005 was positively correlated with air temperature, which indicates that the observed sea ice was not primarily influenced by thermodynamic effects. This explains why the ice draft time series for that period does not contain a significant semi-annual oscillation. However, it remains hard to conclude whether the signal originates from thermodynamics or dynamics.

The semi-annual cycle is also very pronounced in many parameters at AWI-231 (see Table XII). However, it was not detected in the filled 12-years time series of ice draft and meridional ice drift and wind. In the ice draft and the FESOM ice thickness a significant 4-months cycle was found, while the MIT-model simulates a pronounced semi-annual cycle at AWI-231. Addition-

ally, the MIT model simulates a 5-year cycle in the ice thickness, which is close to the period of 4.5-6 years at AWI-232 (see below). Both at AWI-231 and AWI-229 the FESOM model simulates an oscillation with a period of almost three years.

SSA was also applied to the filled 12-year anomaly time series of AWI-232 (Fig. 6.18). The semi-annual cycle was again found in many parameters at AWI-232, including the modelled ice thicknesses and ice concentrations (see Table XII). The high amount of explained variance was found to result partly from the way the anomalies were calculated, but the signal was also found in the time series when retaining the annual cycle. In the measured ice draft, the signal was only found in the draft anomalies and not when retaining the annual cycle.

Table XII: Significant SSA periods for AWI-231 and AWI-232
The period analysed was 1996-2007. SSA window width: M=72 months.

Parameter/ULS	Period [months] (explained variance [%])					
	← Range [months] →					
	4-4.5	5-7	7.5-9	9.5-12	16-27	30-80
AWI-231						
Ice draft 96-07	4 (7)					
FESOM 96-07	4 (21)					32 (5.5)
MIT 96-07		6 (28)				60 (8)
Ice conc. (SSM/I)	4 (14)	6 (16)				
Ice drift (zonal)		6 (11)				
Ice drift (meridional)						
Surface wind (zonal)		6 (3.5)	7.5 (7)		18 (3)	
Surface wind (meridional)						
Surface temperature	4 (11)	6 (18)			18 (2.5) 20 (5)	
AWI-232						
Ice draft 96-07		6 (13)(anom.)				53 (15), 42 (4) 72 (15), 34 (4)
FESOM 96-07	4 (7)	6 (30)				
MIT 96-07		6 (22)				53 (10) 72 (9)
Ice conc. (SSM/I)		6 (45)				53 (4) 72 (4)
Ice drift (zonal)		6 (13)			15 (3)	53 (6) 72 (5)
Ice drift (meridional)						
Surface wind (zonal)		5.5 (2.5)	7.5 (6)			
Surface wind (meridional)		6 (2.7)				
Surface temperature		6 (13)				

The amount of explained variance is also very small. The signal could not be detected in the measured years 2000-2004. Experiments with artificial time series revealed that even fragments of oscillations hidden in random time series stand out as significant if they are long enough and their amplitudes are big enough. Thus, significant oscillations found by SSA do not necessarily have to span the full data record. It is therefore possible that some of the detected SSA signals occur only over certain periods of time. This may also be an explanation for the low amount of explained variance in some of the time series.

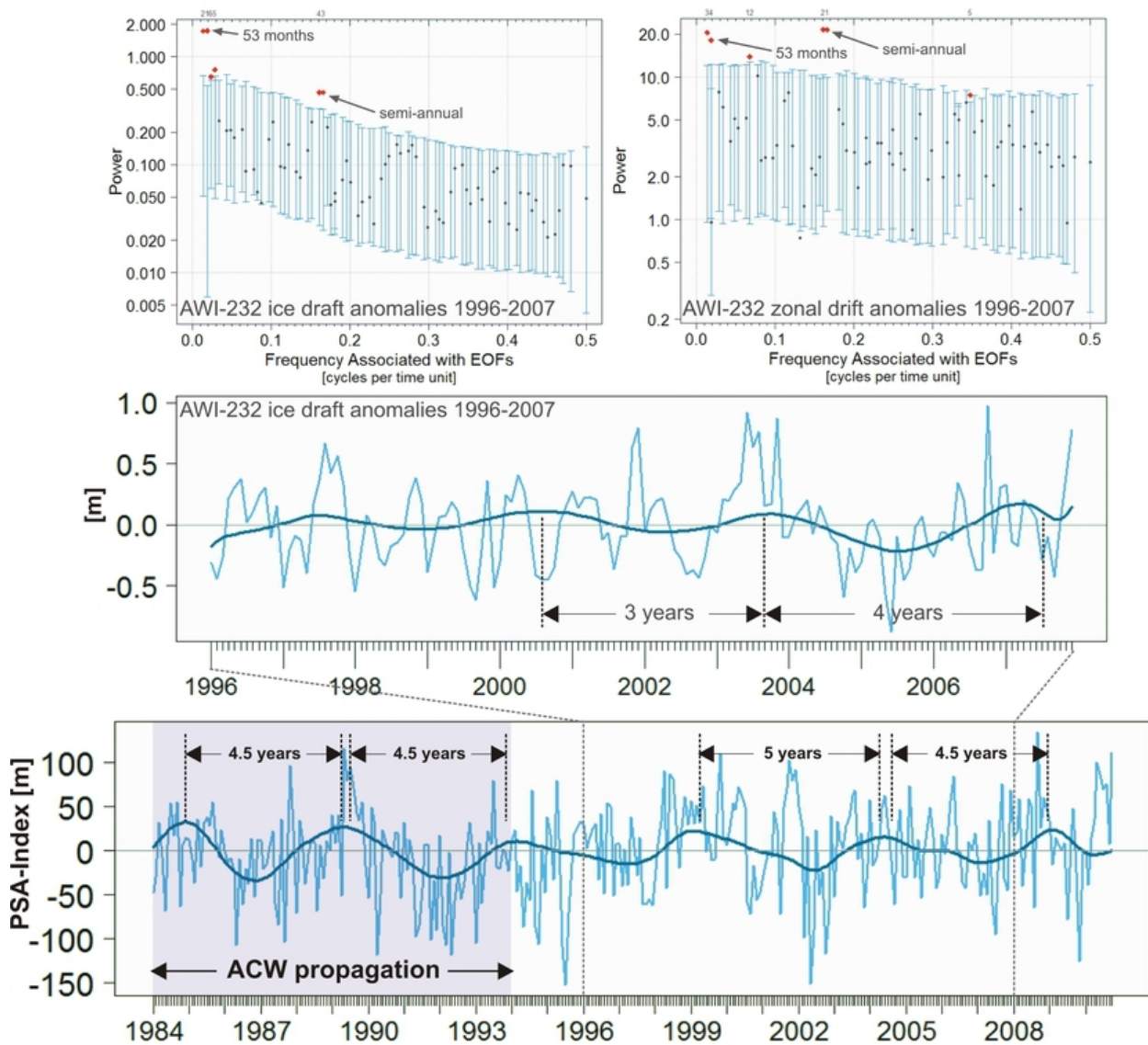


Fig. 6.18: SSA spectra for ice draft and drift at AWI-232 (see figure 6.14 for more information). The time series below shows the ice draft anomalies (light blue) and the significant EOF signal with a period of 3-4 years (dark blue) between 1996 and 2007. For a better overview in this plot, both time series were detrended after the SSA analysis. SSA window width used: $M=60$ months. The lowermost time series shows the PSA-Index from 1984 to 2010 and the significant 4.5-years oscillation detected by SSA. SSA window width used: $M=90$ months.

In the region of AWI-232 and AWI-233 the sea ice concentrations are positively correlated

with surface air temperature for most of the year [Shu *et al.*, 2012], which indicates that the sea ice there is not primarily influenced by thermodynamics. A significant positive correlation between surface air temperatures (NCEP) and bootstrap sea ice concentrations for the period 1979-2006 was also found by Schwegmann [2012] for this region. The semi-annual signal in ice draft and thickness was therefore assumed to be an effect of ice dynamics. By comparing the semi-annual signal of the zonal ice drift and the MIT model ice thickness it was found that an anomalously fast ice drift in the coastal current was followed by anomalously thick ice, which suggests periodic ice ridging simulated by the model. However, in the FESOM model the phase relation of both signals is reversed (see AWI-229). The signal in the measured ice draft is very weak, so that a clear phase relation could not be extracted. Thus, it again remains hard to conclude whether the semi-annual oscillation in the ice drift results in periodic ice ridging.

The draft anomalies, the SSM/I ice concentration anomalies and the zonal ice drift anomalies at AWI-232 exhibit anomalous power at a frequency corresponding to a period between 3 and 4.5 years, depending on the SSA window width used. A period of 3-4 years is in accordance with the Weddell Sea Oscillation [Venegas and Drinkwater, 2001], which is associated with ENSO and the ACW (see section 2.5). The joint variability of sea ice drift, concentration and sea level pressure in the whole Weddell Sea has a significant spectral peak at periods of around 3-4.5 years [Venegas and Drinkwater, 2001]. Figure 6.18 shows that the signal is irregular. Until 2003 its amplitude is very weak and its period is about 3 years. Between 2003 and 2007 its period increases to almost 4 years and its amplitude increases as well. The 4-year signals in the ice drift and ice concentration could not be extracted like in figure 6.18, as they could not be clearly separated from other signals with periods of 5-8 years. This results from the *degeneracy problem* of SSA: Sometimes SSA is not able to clearly separate EOF signals whose eigenvalues are of similar size [Groth and Ghil, 2011]. However, the ice drift had negative peaks, i.e. strong westward drift, in 2002/2003 and 2007, and the ice concentration a positive peak in 2007. During the recent cruise ANT-XXIX/2, *Polarstern* encountered strong ice drift and very thick ice at AWI-232, so that the mooring could not be recovered [G. Rohardt, personal communication, 2013]. This would roughly correspond to another peak in ice drift and thickness 4.5 years after 2007/2008. The fact that the signal occurs only in the ice parameters suggests that it is an oceanic phenomenon, corresponding to the ACW. Moreover, the PSA pattern - the main forcing of the ACW - exhibits a significant oscillation with a period of 53 months (Fig. 6.14). The signal had a high amplitude only during the period 1984-1994. According to Udagawa *et al.* [2009], the ACW propagated in 1984-1994 and was inactive in 1995-2003. But it is still detectable after 1995 (Fig. 6.18). Venegas and Drinkwater [2001] suggested that the Weddell Sea Oscillation is associated with the ACW but has a life of its own. It is therefore likely to be independent of the propagation of the ACW. The authors also found that the oceanic response of the Weddell gyre to the atmospheric forcing has a significant time lag of several years. Both time series in figure 6.18 therefore are not expected to oscillate in phase. The signal in the ice thickness seems to be reproduced by the MIT model, but it is degenerate with a period of 5-6 years and could not be clearly separated. The signal in the three parameters should be further investigated including the most recent draft data after 2007. Nevertheless, what they have in common is increasing ice drift, draft and concentration between 2006 and 2007.

To further test the validity of the signal, an artificial 12-year random (white noise) time series was created and superimposed with a sine function with a 4-year period. This time series was analysed with SSA with varying window widths. It was found that for the window widths 60, 72 and 90 months the period of the detected signal was between 46 and 53 months. As noted by Simmonds [2003], in band-pass filtered time series the only signals which survive are in

the admittance window and hence the only variability which is left will have frequencies corresponding to the size of the window. Thus, they do not have to have a real physical meaning. A similar window effect may occur in SSA. However, the quasi 4-year signal was stable against varying window sizes both in the artificial time series and the time series of concentration, draft and drift.

Generally, SSA analyses of ice draft records are to some extent influenced by the gap-filling method and the data processing. As both the correction by zero-line interpolation and by the sound model significantly affect the amplitudes of the ice draft, biases that occur more or less regularly in time may create significant peaks in the SSA spectrum. When the model-corrected 12-years draft time series of AWI-231 was analysed, no signals were detected. This indicates that some high-frequency components may result from the data processing and have no physical meaning. But this is not necessarily the case if the data corrected by zero-line interpolation are closer to reality.

The spectra of ice concentrations were found to be less steep than spectra of ice draft. This means that there is more power in the red part of the ice draft spectra than in the red part of the ice concentration spectra, i.e. the ice concentrations are closer to a random time series (white noise) than the ice draft. Closest to white noise is the ice drift, with an almost flat spectrum, except at AWI-232 in the Antarctic coastal current.

Some of the periods found by SSA are hardly significant. Conducting 5000 Monte Carlo simulations instead of 2000 may slightly broaden the error bars that would "swallow" the weakly significant signals. However, the error bars shown are 97.5th and 2.5th percentiles. The weakly significant signals then still may be significant at the 95% level. The quasi 4-year cycle in the ice draft anomalies at AWI-232 remained significant at the 97.5% level even after 5000 Monte Carlo simulations.

6.5 Autocorrelation

6.5.1 Short-range correlation

In this subsection the autocorrelation behaviour of the measured ice draft on time scales of up to 10 days is briefly investigated. The purpose of this analysis was to demonstrate that sea ice thickness in coastal regions has higher decorrelation times than further away from the coast. As noted by *Chatfield* [1984], the interpretation of autocorrelation functions requires some experience and great care. Most difficult is often the determination of the non-correlation lags, i.e. the lag at which the data become linearly independent. A value for this lag, which is frequently cited in the literature, is the lag at which the autocorrelation function first reaches a value of zero [e.g. *Romanou et al.*, 2006]. However, this can sometimes be misleading as shown in figure 6.19.

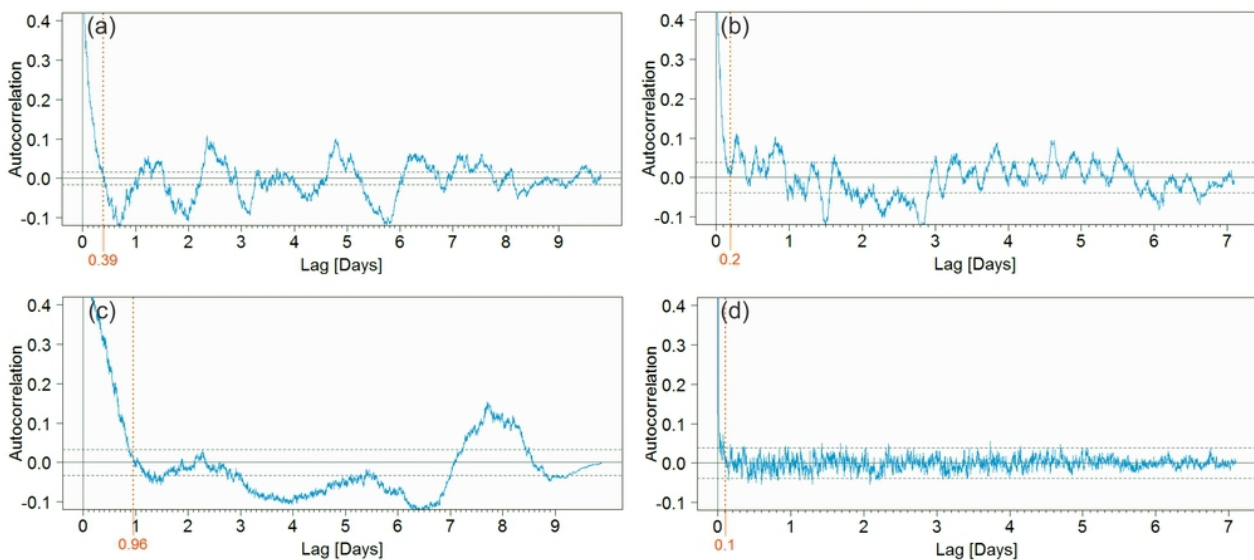


Fig. 6.19: Four arbitrary examples of autocorrelation functions of sea ice draft for periods of 7-10 days. The horizontal dashed lines are 2σ confidence intervals for white noise [*Chatfield*, 1984]. The red vertical line denotes the lag at which the function first reaches a value of zero.

The first function (a) shows clear signs of a cyclic behaviour. The decorrelation time of 0.39 days is therefore not a good choice. A similar argument applies to function (b). The value of 0.96 days in function (c) also has to be regarded as critical, as obviously many values of the function lie outside the confidence limits above the decorrelation time. Some authors therefore use other measures of autocorrelation, such as "mutual information" [*Strickert*, 2003]. The least critical decorrelation scale is the value of 0.1 days in function (d). It shows decorrelation of the data on very small time scales, and the autocorrelation function indicates noisy data. As these examples indicate, the interpretation of the short-range autocorrelation of the ice draft would require a very thorough treatment which would be far beyond the scope of this section.

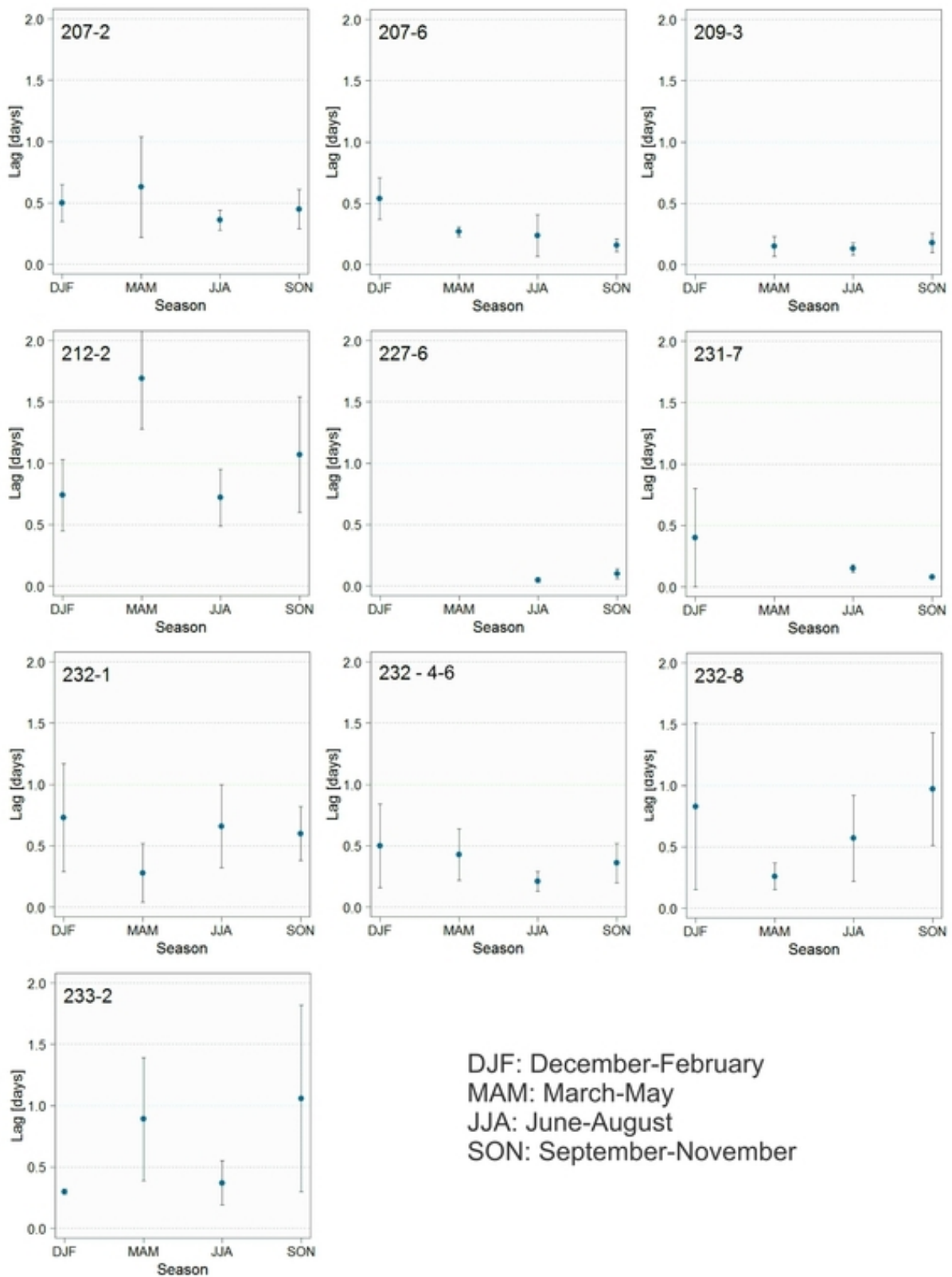


Fig. 6.20: Mean decorrelation times of selected ULS records. The means were calculated from values of 3-6 autocorrelation functions of ice draft in four seasons, respectively. Periods with data gaps were avoided. The error bars are standard deviations of the means, corrected by the t-factor for small sample sizes [Schönwiese, 1992].

The decorrelation time scales discussed in the following are intrinsic to the time-referenced ULS data and can not be readily used to gain detailed information on the characteristics of the sea ice thickness distribution. However, selected decorrelation time scales are compared to obtain some additional information which might be helpful to understand the discussed changes in sea ice thickness. There are several possible reasons for high decorrelation time scales, e.g. slow ice drift, refrozen leads, a folded drift path (i.e. repeated sampling of the same features) or a combination of these factors. Low decorrelation time scales are conceivable for weakly deformed ice with a highly varying underside, the strongly eroded underside of undeformed ice or a high degree of ice deformation and pressure ridges of different sizes.

The broad error bars in figure 6.20 indicate that the decorrelation time scale changes significantly within one season. Using the zero-crossing approach discussed above, the data at AWI 207-2 become independent after approximately 12 hours on average. The data of AWI 207-6 decorrelate somewhat earlier. However, the mean values are not significantly different from AWI 207-2, except the value for spring (SON), which may reflect the changes in the ice regime between these two records. At AWI-209 very low decorrelation time scales were found. The same values were found for AWI-208 (not shown). This indicates that the ice drafts decorrelate quickly in the centre of the Weddell gyre. In the highly dynamic boundary region at AWI-212 high decorrelation time scales indicate heavy ridging and possibly also refreezing leads. This is most obvious in autumn (MAM). The lowest of all decorrelation values were found at AWI-227 at the northern rim of the Weddell gyre. Similar values were found for AWI-229 and most of the records of AWI-231. At AWI-232 the two records with very thick ice (232-1 and 232-8) show low decorrelation time scales in autumn (MAM) compared to the other seasons.

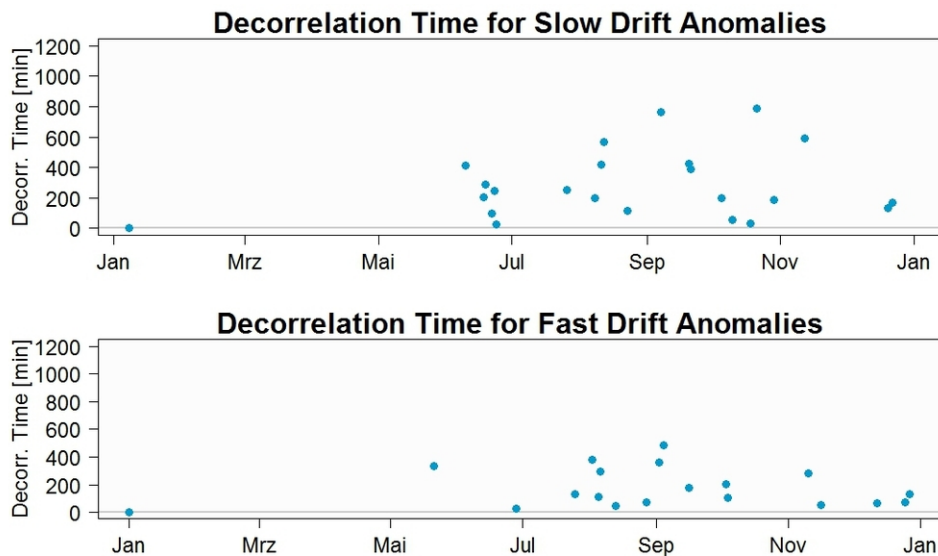


Fig. 6.21: Decorrelation times of the ice draft at AWI 232-1 (1996) for days of slow and fast ice drift. The daily ice draft data in 1996 decorrelate on average 2.5 hours later on days with slow ice drift.

Compared to the records of AWI 232-4-6, the record of AWI 232-8 shows high decorrelation time scales, especially in winter and spring. At AWI-233 the data show high mean decorrelation time scales in the transition times, i.e. autumn and spring. However, also the scatter of the values is very high, so that the means are not significantly different from the winter value.

To estimate the influence of the ice drift on the decorrelation time scales, an experiment was conducted using SSM/I drift data at the position of AWI-232. For all records of AWI-232 only days without data gaps were selected. Then, the days were separated into days with positive and negative ice drift anomalies, i.e. days with anomalously slow and fast westward drift in the coastal current. Next, the decorrelation time scales of the ice draft were estimated based on the zero-crossing approach (Fig. 6.21). The ice draft data of AWI-232 (all years with measurements) decorrelate on average 1.5 hours later at days with ice drift anomalies > 0 , i.e. slow westward drift, compared to days with ice drift anomalies < 0 , i.e. fast westward drift. The differences vary from year to year, e.g. for 2006 and 2007 they were found to be negligible. A significant correlation between ice drift anomalies and decorrelation time was not found.

6.5.2 Long-range correlation

As shown in the previous subsection, the ice draft in coastal regions can have decorrelation time scales of above one day. To investigate whether ice draft is serially correlated over even longer time scales, DFA was applied (see section 4.2). Another purpose of the DFA analysis was to take a first look on possible linear or higher-order trends in the data. As a reminder: DFA systematically eliminates trends of different orders from the data on all time scales and analyses the remaining fluctuations for autocorrelation. The analysis was conducted up to DFA5. This means that fourth-order trends were eliminated by DFA5 and trends up to this order may be reflected in the fluctuation functions DFA1-4. The analysis was exemplarily performed for AWI-232, as this record contains five consecutive years of measured sea ice draft.

The fluctuation functions of the daily ice draft anomalies for the five measured years 2000-2004 rise with $\alpha \approx 0.8$ (Fig. 6.22). It can therefore be concluded that the detrended ice draft autocorrelation function declines on time scales of up to at least 456 days according to the power law

$$C(s) \sim s^{-\gamma}, \quad (6.1)$$

with $\gamma = 0.4$. Note that only the first fourth of the fluctuation functions can be considered, as the fluctuations generally become overly large for values $s > N/4$, where N is the length of the time series [J. W. Kantelhardt, personal communication, 2010]. Therefore, it is not possible to conclude that the detected long-range correlation is valid for the full 5-years period. This is investigated further below using model data. The value of $\alpha \approx 0.8$ is significant at the 99% level according to the confidence intervals given by Weron [2002]. The crossover starting at approximately 100 days in DFA1 and increasingly later up to DFA4 may be indicative of a fourth-order trend in the data [Kantelhardt *et al.*, 2001]. However, in an experiment an artificial time series with $\alpha=0.8$ was generated according to the procedure explained by Kantelhardt *et al.* [2001] and then modified by trends of different orders. Only the first-order trend displayed by DFA1 could be reproduced. Ice draft time series naturally contain longer times of zero ice draft in summer. In another experiment it was tested whether this affects the slope of the fluctuation functions by simply removing the ice-free periods. The slope, and therefore the scaling law, was found to be unaffected by the short ice-free seasons at AWI-232. However, when the summer season is longer, e.g. at AWI-227, the slope of the fluctuation functions may not reflect the true scaling behaviour any more.

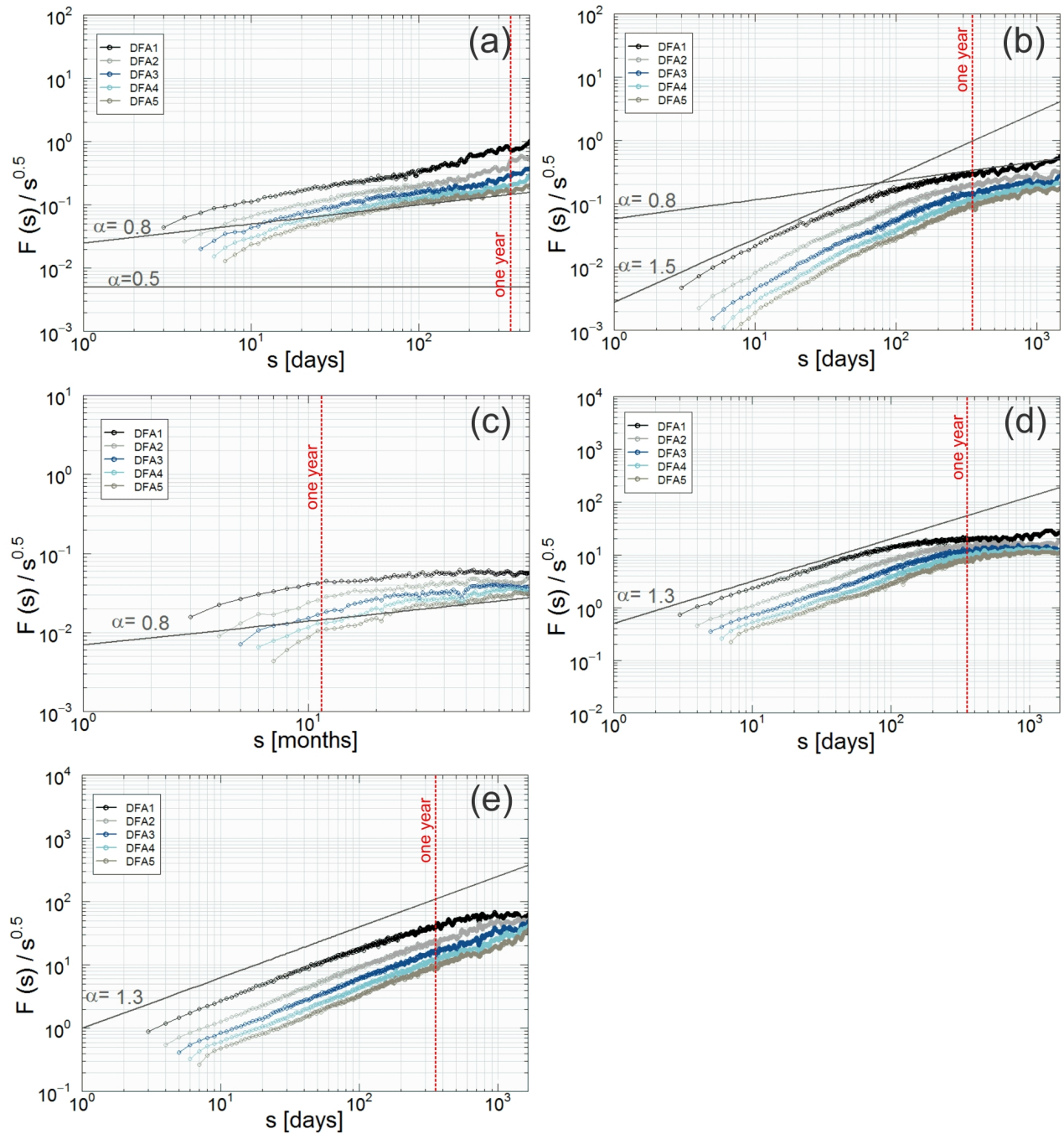


Fig. 6.22: (a) Double logarithmic plot of DFA fluctuation functions for the measured daily ice draft anomalies of AWI-232 in the period 2000-2004. The deviations from the scaling law at small scales s are intrinsic to the DFA method and were reduced by applying the correction function described by *Kantelhardt et al.* [2001]. For comparison, the line $\alpha=0.5$ for completely uncorrelated data is also shown. (b) DFA fluctuation functions for the MIT model daily ice thickness anomalies at AWI-232 in the period 1992-2007. (c) DFA fluctuation functions for the FESOM model monthly ice thickness anomalies at AWI-232 in the period 1979-2010. (d) DFA fluctuation functions for the SSM/I-derived daily ice concentration anomalies at AWI-232 in the period 1990-2007. (e) DFA fluctuation functions for the SSM/I-derived daily ice concentration anomalies at AWI-207 in the period 1990-2007.

As the measured time series between 2000 and 2004 is very short, the modelled ice thicknesses were also investigated by DFA. The fluctuation functions of the time series of the MIT model show a steep rise ($\alpha=1.5$) up to approximately 100 days, indicative of strong short-range correlations on small time scales [Rybski, 2006]. According to Kantelhardt *et al.* [2001] the position of a real crossover is best approximated by DFA1. Between 200 and 1500 days the modelled ice thicknesses show the same scaling behaviour as the measured ice draft ($\alpha=0.8$). A possible explanation for the high correlation up to 100 days could be that the models still fail to reproduce the complex ice dynamics, which may result in more or less chaotic - and therefore less correlated - signals of ice thickness on sub-annual time scales. The FESOM modelled ice thicknesses were in this study only available on a monthly basis. The FESOM data show the same scaling behaviour as the previous data ($\alpha=0.8$) between approximately 20 months and 95 months. The functions DFA1-DFA3 seem to display a value of $\alpha=0.5$, i.e. no long-range correlation. To investigate this behaviour the 226 years temperature time series (monthly means) from Prague [Bunde and Kantelhardt, 2001] was analysed. The value of $\alpha=0.65$ could be confirmed. Then, only the first 32 years were analysed according to the length of the FESOM time series. It was found that the correct value of α on these time scales is displayed by DFA4 and DFA5, just like in the example of the FESOM data. However, as the behaviour of DFA1 is somewhat misleading, it is not possible to determine the crossover exactly. The real crossover in the FESOM fluctuation functions is therefore expected to appear earlier than at 20 months. The results from both model-derived ice thickness seem to confirm that the power law of the measured ice draft is valid over time scales of up to 8 years. The fluctuation functions of the modelled ice thicknesses do not display any trend at AWI-232.

The high long-range correlation of the ice thickness can be explained by stable atmospheric and oceanic boundary conditions, i.e. wind/drift fields and temperature, which are constrained by the geographical setting. The high long-range correlations ($\alpha=0.65$) over centuries in temperature time series was interpreted as a sign of coupling of surface temperature to the ocean which has very long time scales [Bunde and Kantelhardt, 2001]. Thus, the even higher values of long-range correlation in sea ice thickness can be explained by its strong coupling to the ocean and its dependence on surface air temperatures and winds. However, the ice concentrations at AWI-232 behave differently.

The fluctuation functions of the SSM/I ice concentration anomalies at AWI-232 show a steep rise up to approximately 100 days (Fig. 6.22), which is again indicative of strong short-range correlations on time scales of less than one year. After approximately one year the fluctuation function DFA1 levels off, indicating that ice concentrations become fully uncorrelated ($\alpha=0.5$). As mentioned above, the ice concentrations in the region of AWI-232 are positively correlated with air temperature. At AWI-207 - a region where ice concentrations are negatively correlated with air temperature [Shu *et al.*, 2012] - the fluctuation functions of the ice concentration in the period 1990-2007 rise with $\alpha=1.3$ up to 1500 days and are therefore highly correlated over time scales of up to 4 years. This highlights the different ice regimes at AWI-207 and AWI-232. Unfortunately, the time series of ice draft at AWI-207 are too short to detect long-range correlation of above one year.

6.6 Summary

The plotted ice drafts in the first section of this chapter demonstrate the Eulerian character of the ULS measurements. Ice that developed away from the ULS position is advected over the sonar footprint and recorded by the ULS. This is especially visible in the records north and south of Maud Rise, which do not show clear freeze-melt cycles. A similar behaviour was already observed by *Strass and Fahrbach* [1998], who noted that the initial opening of the ice cover is sometimes more related to ice divergence rather than melting of the ice. Many ice draft records, e.g. AWI-229, show significant year-to-year variability. Only in certain years undisturbed thermodynamic ice growth cycles - more or less superimposed by ridging - are reflected in the measurements, such as AWI 231-2, AWI-208 and AWI 229-2. At Maud Rise these years correspond to situations with low ice drift, especially in meridional direction, as less thicker or thinner ice from latitudes further north or south was advected over the ULS position. A comparison of the records of AWI-229 and AWI-230, and to some extent AWI-231, revealed that the behaviour of the ice draft in these regions is very similar. This could indicate that the filled 12-years time series of AWI-230 is more reliable than expected. The ice at AWI-231 seems to be thinner than at AWI-230 and AWI-229 further north. The position of AWI-231 lies at the southern tip of a halo of anomalously warm water over the flanks of the Maud Rise sea mount [*Lindsay et al.*, 2008], the region in which the Weddell Polynya appeared in the mid 1970s [*Holland*, 2001]. This may affect the ice growth near AWI-231 and could provide a possible explanation for the phenomenon. At the tip of the Antarctic Peninsula (AWI-207) the sea ice draft shows a strongly negative trend since 1990. This is consistent with negative trends of sea ice concentration in this region [*Schwegmann*, 2012]. At AWI-232 the sea ice draft shows a positive trend since 2000. This trend is not reflected in the ice concentrations.

The monthly statistical ice draft distributions indicate that the thermodynamic ice growth maximum lies between 0.5 and 0.8 m at positions near Maud Rise and around 0.9-1 m at AWI-232. Although Maud Rise and AWI-208 are almost at the same latitude, the thermodynamic growth maxima of 0.7-0.9 m in the central Weddell Sea at AWI-208 and 209 seem to be slightly higher than at Maud Rise. In the work of *Schwegmann* [2012] the mean surface air temperatures between 1979 and 2006 at 65°S latitude are slightly higher on the prime meridian than in the central Weddell Sea.

By considering the statistical distributions on a monthly scale it is possible to discriminate between periods of dominating thermodynamic ice growth and periods of ice ridging by dynamic processes. In the years of dominating thermodynamic growth the three statistical quantities mean, mode and median were found to coincide as the monthly draft distributions are almost Gaussian. The statistical mode mostly displays the thermodynamic growth, i.e. the draft of the level ice, except for periods with a high amount of leads and/or new ice or periods of extreme ice deformation. The degree of ridging can then be roughly estimated by the degree the mean deviates from the mode.

Similar to the ice draft, the ice season duration varies strongly from year to year. The variance on the prime meridian increases from north to south. There is some indication that at AWI-232 ice seasons with thick ice are shorter than ice seasons with thin ice.

Spectral analysis by *singular spectrum analysis* (SSA) is a very powerful method for detecting irregular and regular oscillations in geophysical time series. The sensitivity of SSA together with its ability to detect irregular signals can pose problems to the interpretation of the detected signals. SSA therefore requires some experience and a rough idea of the frequencies to search for. However, a persistent and significant oscillation with a 17-month period was identified

by SSA in the ice draft over the period 2005-2007 (AWI 207-6) and in the SSM/I-derived ice concentrations at AWI-207 in the period 1990-2007. The significant 17-months period was also found in the SSA spectrum of the *Niño*3.4-Index. The period of 17 months in both data may be indicative of an ENSO forcing (see section 2.5). Further correlation analysis is necessary to confirm a possible ENSO forcing of sea ice thickness at the tip of the Antarctic Peninsula. An attribution solely based on significant frequencies is not feasible. For a thorough examination of the 17-months period the draft time series of AWI-207 should also be extended by the most recent data from 2008-2011, which are still to be processed. A significant 7-month period in the ice draft anomalies of AWI 207-6 is also present in the ice concentration anomalies, meridional wind and drift anomalies and the surface air temperature anomalies. The phasing of the signals suggests that it represents a thermodynamically and dynamically driven signal in the ice draft, which is forced by the PSA pattern. The PSA forcing of sea ice is very pronounced in the northwestern Weddell Sea [Yuan and Li, 2008] (see also section 2.5). The signal is well reproduced by the MIT sea ice model.

At AWI-229 a significant semi-annual cycle was detected in the ice draft anomalies of the filled 12-years period 1996-2007. The signal was not found in the measured ice draft between 2001 and 2005, but it is present in the time series of modelled ice thickness, especially in the MIT model. The same significant period was found in the anomalies of surface air temperature and zonal wind and drift in this region. The semi-annual signal in the air temperature explains the largest amount of variance. However, based on the model results it remains difficult to conclude that the signal represents a thermodynamic SAO forcing, because it was found to be anticorrelated between the MIT and FESOM model.

At AWI-232 a weak semi-annual cycle was found in the anomalies of the filled draft time series (1996-2007). The signal is more pronounced in the ice concentrations (SSM/I) and in the modelled ice thickness (MIT and FESOM). It could not be detected in the measured ice draft between 2000 and 2004. Again, it remains hard to conclude whether the signal is a thermodynamic or a dynamic effect. Like at AWI-229, the signals are anticorrelated between both models. A signal with a quasi-quadrennial period (46-53 months) was detected in the ice draft anomalies (filled by M-SSA), ice concentration anomalies and the zonal ice drift anomalies for the period 1996-2007. This can be attributed to the *Weddell Sea Oscillation*, which is associated with a 4-yearly ice accumulation in the Weddell Sea. The joint variability of sea ice drift, concentration and sea level pressure in the whole Weddell Sea has a significant spectral peak at periods of around 4-4.5 years [Venegas and Drinkwater, 2001]. This oscillation is linked to ENSO and the Antarctic Circumpolar Wave (ACW). A quasi-quadrennial signal linked to ENSO was also identified in the Weddell Sea by Gloersen [1995]. The five consecutive years (2000-2004) of measured ice draft are too short to detect the signal. A clear phase relation between the 4-year signals in draft, drift and concentration could not be found, most likely due to the shortness of the time series and the degeneracy of the signals with other frequencies. However, the signal is believed to originate from the Weddell Sea Oscillation as (1) it appears only in oceanic parameters and not in wind and air temperature and (2) the Pacific South America Pattern (PSA) - which is the forcing of the ACW - shows a similar period of 4.5 years. It remains unclear how the detected signals in the four time series are associated. The records should be extended by the most recent data (2008-2011) to further investigate the phenomenon. A semi-annual cycle was found in the ice concentrations, ice drift as well as surface wind and surface air temperature. It was not detected in the measured ice draft, neither with nor without the annual cycle removed. It is assumed that in the Antarctic coastal current the chaotic ridging processes prevent a clear occurrence of the semi-annual cycle in the

ice draft. The semi-annual cycle at AWI-232 was also found in both sea ice models (FESOM and MIT), which may indicate that the signal results from periodic thermodynamic forcing as the models still fail to simulate the complex ice dynamics.

Decorrelation time scales of the ice draft data were estimated to be low in the centre of the Weddell gyre (5-6 hours at AWI-208 and AWI-209) and comparably higher in the dynamic boundary regions (12-36 hours at AWI-212 and AWI-207). On the prime meridian the decorrelation time scale was estimated to be very low at the northern rim of the gyre (3-4 hours at AWI-227) and in the centre at AWI-229 and AWI-231. The decorrelation time increases towards the coast (AWI-232 and AWI-233), where it is very variable. There are indications at AWI-207 and AWI-232 that the draft data in years with thicker ice exhibit higher decorrelation times than draft data in years with thinner ice. Comparison of days with fast ice drift and days with slow ice drift suggests a weak and insignificant influence of the ice drift speed on decorrelation time of the ice draft.

The results of the *detrended fluctuation analysis* (DFA) indicate that sea ice thickness exhibits significant long-range correlation. The time series of measured ice draft at AWI-232 (5 years) indicate that the autocorrelation function C obeys the power law $C(s) \sim s^{-0.4}$ over time scales of above one year. This corresponds to a DFA fluctuation exponent of $\alpha=0.8$. The same behaviour was found for the long-range correlation of the modelled ice thickness (MIT and FESOM). This suggests that the power law of the measured ice draft is valid over time scales of up to 8 years. The time series of consecutive measured ice draft data should be extended to better investigate the long-range correlation. However, this seems difficult due to the high failure rate of the ULS instruments. The high long-range correlation is explained by stable atmospheric boundary conditions and the long time scales of the ocean. The most striking difference between models and measurements is the strong short-range correlation over time scales of several months, which is only present in the model data. This indicates that models still fail to reproduce the complex ice dynamics, which may result in more or less chaotic - and therefore less correlated - signals of ice thickness on short time scales. Contrary to the ice thickness, the ice concentrations at AWI-232 are completely uncorrelated on time scales of above one year. As mentioned above, the ice concentrations in the region of AWI-232 are positively correlated with air temperature. At AWI-207 - a region where ice concentrations are negatively correlated with air temperature [Shu *et al.*, 2012] - the fluctuation functions of the ice concentration in the period 1990-2007 were found to be strongly correlated on time scales of up to 4 years.

"Erst im Bunde mit dem
Wind wird ein Meer aus dem
Meer [...], denn das Meer an
sich ist weniger."

Hörspiel von Peter
Wawerzinek

7

Correlation Analysis

This chapter presents correlations of sea ice draft with other oceanic and atmospheric parameters on different time scales. Correlations were performed using standard linear correlation analysis. The analyses were aimed to investigate the main drivers of sea ice thickness in different regions of the Atlantic sector and to reveal their connection with large-scale climate patterns of the Southern Hemisphere. The first section gives a qualitative overview of the covariation of sea ice draft with water masses. The following sections contain a more detailed and quantitative treatment of correlations.

7.1 Covariation with water masses

On the basis of oceanographic data obtained between 1984 and 2008, decadal-scale variations in the properties of the Winter Water and the sea ice draft on the Greenwich meridian could be identified [Behrendt *et al.*, 2011]. The Weddell Sea is one of the most important regions of bottom water formation and thus represents a driving mechanism of the Atlantic meridional overturning circulation [Heywood and Stevens, 2007]. The dense water is formed through sea ice formation over the continental shelves. These waters mix with Warm Deep Water (WDW) from the ACC further north, and together they form the Weddell Sea Bottom Water (WSBW). The salinity of the surface layer is the dominant factor in destabilising the stratification and initiating deep convection [Behrendt *et al.*, 2011]. Surface salinity is therefore an important quantity in monitoring the changes in deep water formation in the Weddell Sea. There are several clues in the literature to a trend towards a freshening of the Weddell Sea and the correlation of the SAM with WSBW¹.

The oceanographic data presented here include surface salinities from traditional hydrography [Fahrbach *et al.*, 2007] and recent float data, covering a period of 20 years. The used hydrographic data were collected by moorings and during cruises with the ice breaker R.V. Polarstern

¹See Behrendt *et al.* [2011] and references therein.

between 1992 and 2008². Since 1999, AWI deployed more than 130 Argo floats within the Weddell gyre. The accuracy of the float data is better than 0.01°C in temperature and 0.01 in salinity (Argo standard). Data of float WMO 7900093, deployed in March 2005 and active until December 2008, were used for the analysis. Since 2005, under-ice profiles were stored successfully throughout winter and transmitted during subsequent summer seasons. In this way, float WMO 7900093 performed 135 profiles covering three winter seasons. Owing to not resolved technical problems of different origin, the under-ice data are still rare [Behrendt *et al.*, 2011]. Since the lag between the different data sections varies from one to eight years, only variations from multi annual to decadal time scales are considered here.

The upper water layer in the Weddell Sea consists of Antarctic Surface Water (AASW) and Winter Water (WW). Their temperatures range from the freezing point in winter to a few degrees above that in summer [Behrendt *et al.*, 2011]. The WW fills the upper layer in winter, and its temperature is close to the freezing point. It is also observed during spring and early summer, when the upper part of the surface layer is heated up. Due to the stable stratification, the lower part of the winter surface layer cannot be reached by the heating from above. It thus keeps its near-freezing temperature. This lower part forms a remnant of WW in the summer season (Fig. 7.2). Only due to WDW entrainment or diffusion from below during summer it may increase its temperature. At the Greenwich meridian section, the WW is visible at depths of 50-120 m all across the gyre [Behrendt *et al.*, 2011]. In March/April, winter convection erodes the summer layer within about a month and reaches the WW from the previous year which is slightly warmer than freezing temperature (Fig. 7.2). With ongoing convection the new WW layer deepens and increases slightly in salinity until August/September, when the ice cover is fully established [Behrendt *et al.*, 2011]. After that, with decreasing intensity of convection, upward motion in the Weddell gyre becomes dominant, shifting the lower boundary of WW upwards. In December after the melt-back of the sea ice, a warm and low saline summer layer is formed at the surface. The WW gradually warms and the temperature minimum becomes less saline [Behrendt *et al.*, 2011]. The year to year variations in the float data are to some extent due to the northeastward propagation of the float (Fig. 7.2).

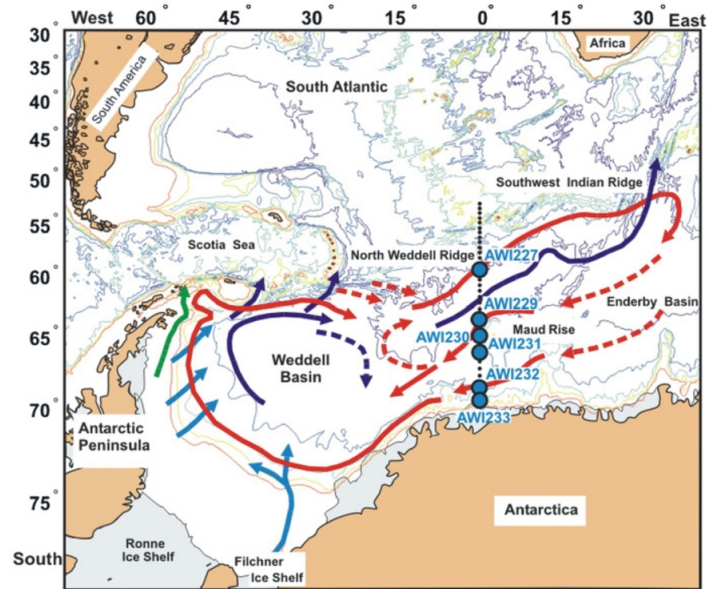


Fig. 7.1: Map of the Atlantic sector of the Southern Ocean including the generalized circulation of the Weddell gyre, the location of the section at the Greenwich meridian and of the moorings AWI-227 - AWI-233. Red arrows indicate circulation of circumpolar (Warm) Deep Water, light blue arrows sinking water masses along the continental slope. Dark blue arrows depict deep and bottom water circulation and water masses leaving the basin. The green arrow indicates shelf water leaving the western Weddell Sea. Dashed arrows indicate either transient currents or eddy exchanges [Behrendt *et al.*, 2011].

²See Fahrbach *et al.* [2011] and Behrendt *et al.* [2011] for details.

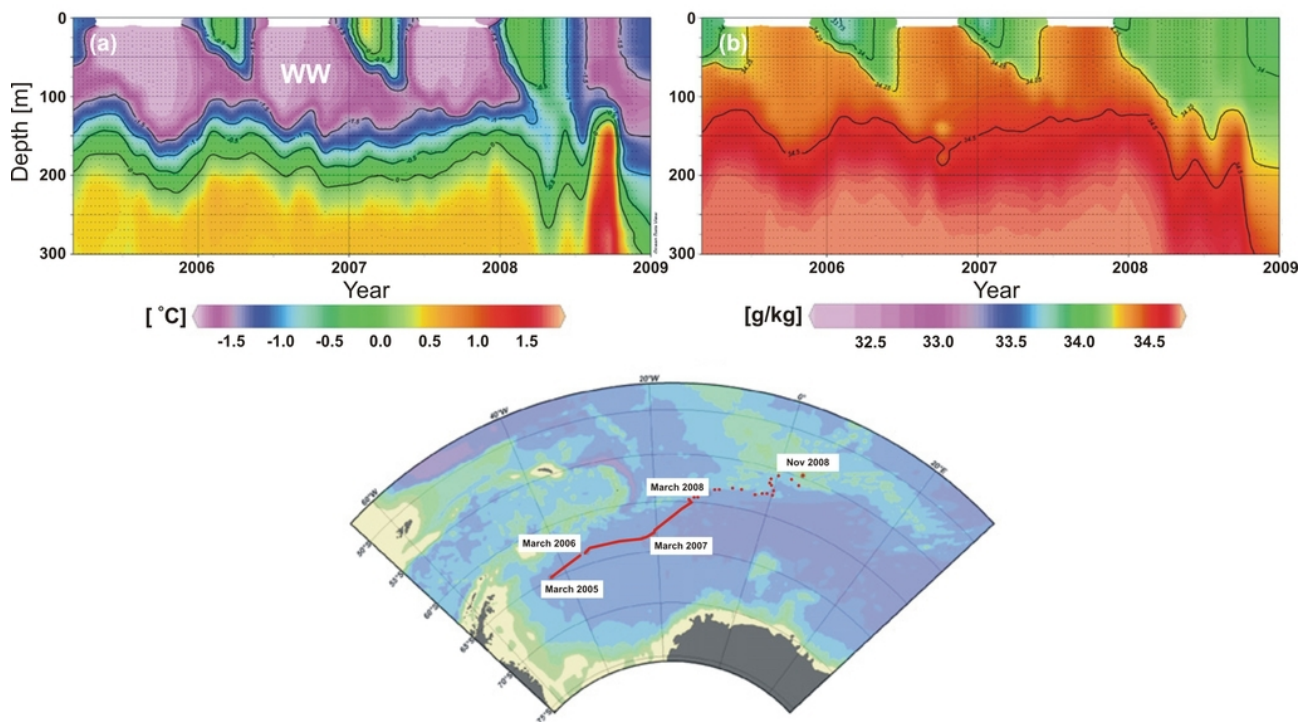


Fig. 7.2: Isopleth diagrams of in-situ temperature (a) and salinity (b) of the upper layers in the Weddell Sea from vertically profiling float WMO 7900093. Contour plots were created with ODV [Schlitzer, 2010]. WW: Winter Water. The drift track (map) is depicted by dots 10 days apart at each location at which the float came to the surface. Under the sea ice the tracks were linearly interpolated east and west of 40°W , 30°W and east of 20°W [Behrendt *et al.*, 2011].

As the CTD transects were conducted at different times of the summer season, the seasonal aliasing in the estimates of the different WW properties has to be taken into account. This was achieved by deriving the initial WW properties from the float data³. As shown in figure 7.3 the salinity had a maximum in 1984 and decreased to a minimum in 1992. Due to the lack of data in between one can not exclude interannual variations in the data gap. From 1992 on, a positive trend is observed until 2003, where the WW starts freshening again. A higher WW salinity would ease convective overturning and vice versa. The positive trend between the early 1990s to the middle 2000s is obvious in both the adjusted and the unadjusted data. Comparative investigations of Fahrbach *et al.* [2011] on WDW with CTD and moorings suggest that the variations in the water mass properties are well captured by the CTD sections. Therefore, the results shown here are believed to be a good estimate of the WW variations [Behrendt *et al.*, 2011].

A salinity budget of the Weddell Sea must include advection, diffusion, upwelling/entrainment, and freshwater fluxes [Behrendt *et al.*, 2011]. Three processes are involved in changing the WW properties in the Weddell gyre: (1) variation of the interactions with the underlying WDW, (2) variations of sea ice formation and (3) variations of external freshwater sources.

The variations in the WDW properties are discussed in detail by Fahrbach *et al.* [2011]. The authors found decadal-scale fluctuations in the temperature and salinity and also in the layer thickness of the WDW. The average of the WDW temperature and salinity over the full transect

³See Behrendt *et al.* [2011] for details.

from 56°S to 69.4°S had maxima in 1998 and minima in 2005. The maxima and minima in the WDW layer thickness preceded those of average temperature and salinity by about 2-4 years [Fahrbach *et al.*, 2011]. An increased inflow of WDW - evidenced by the increasing layer thickness - tends to increase the salinity of the WW. This is due to the entrainment of the saline WDW into the WW layer. An increased WW salinity, in turn, would be followed by a stronger convective overturning. However, entrainment can only explain a certain fraction of the observed salinity variations in figure 7.3. For example, during the first inflow event of WDW in 1992 the WW salinity has a minimum. Thus, the potential density difference - i.e. the stability - (Fig. 7.3b) of the upper water layers has a maximum at the same time, despite the WDW entrainment.

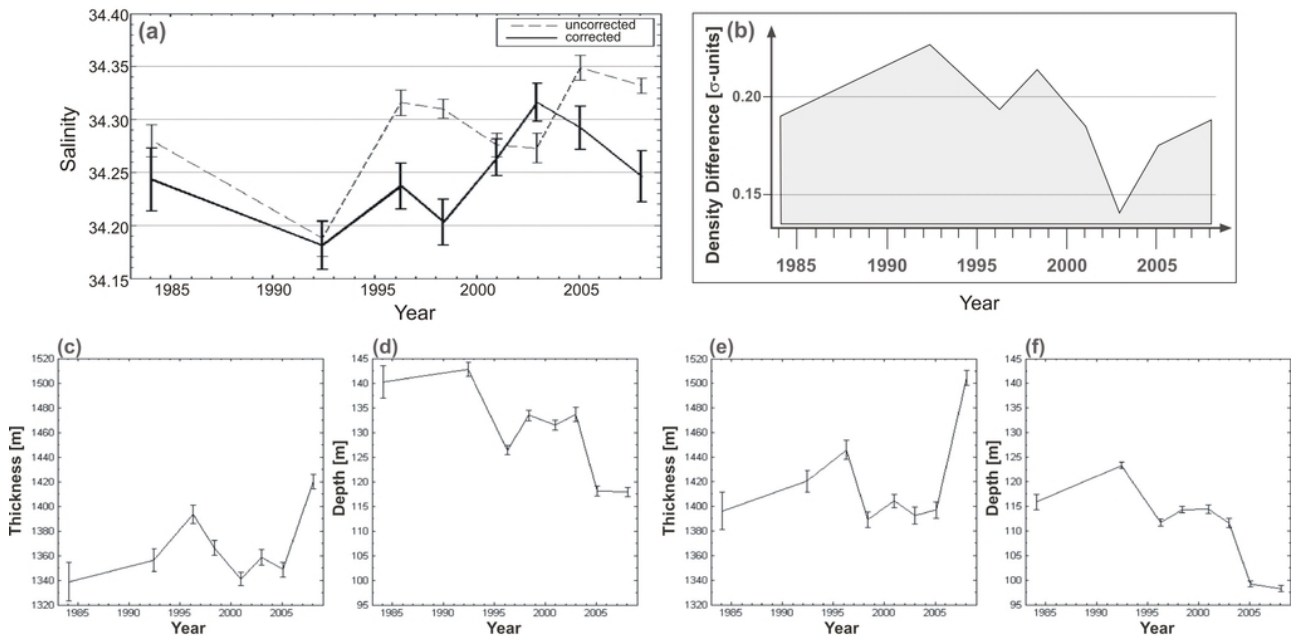


Fig. 7.3: (a) Time series of the mean salinity of the WW derived from the all-section data along the Greenwich meridian. The dashed line represents measured values, the solid line values adjusted to winter conditions according to the correction procedure. The error bars were calculated as the error of the mean values of independent samples. (b) Time series of the difference in potential density between WW and WDW. (c-f) Time series of properties of the Warm Deep Water as defined by neutral density over the section along the Greenwich meridian as averages over the full transect from 56°S to 69.4°S (c) and (d) and over the southern gyre limb from 60° to 69.4°S (e) and (f). The thickness of the WDW layer is displayed in (c) and (e) and the depth of the upper limit of the WDW (at $\gamma^n = 28.0 \text{ kg/m}^3$) in (d) and (f) [modified from Behrendt *et al.*, 2011].

Between 1992 and 1996 the upper boundary of WDW decreased from 142 m to 127 m (Fig. 7.3d), thereby increasing the layer thickness. The latter then decreased until 2001 and remained almost constant for four years. Then, further warming again increased the layer thickness rapidly from 2005 to 2008 (Fig. 7.3c). By the end of 2008 the upper boundary of WDW had moved upwards to approximately 118 m. At the same time the WW salinity decreased again. The two phases of decreasing WW layer thickness and first increasing and then decreasing salinity suggest a different origin of the causes [Behrendt *et al.*, 2011]. It would take about one year for an entrainment of the upper 25 m of WDW into the WW layer. This lost WDW

must be resupplied to the gyre under steady conditions, and the salinity gain of WW must be compensated by a freshwater gain of about 0.3 m [Behrendt *et al.*, 2011, and references therein]. The increase in WW salinity from 34.18 to 34.23 between 1992 and 1996 can be explained by the erosion of a 15 m layer of WDW from 142 to 127 m as observed during that period. Between 1998 and 2003 the salinity further increased from 34.21 to 34.32. At the same time, the depth of the WW layer remains almost constant. This suggests an influence of variations in the sea ice thickness.

The following investigations are focused on the influence of the WDW on the sea ice thickness changes, i.e. the thermal forcing from below. Figures 7.3e and f show the layer thicknesses of WDW and WW in the southern limb of the gyre, where the decadal sea ice draft variations are strongest. In the southern limb of the gyre (at AWI-232) the variations in sea ice thickness correlate with the WDW layer thickness, with the strongest increase between 2005 and 2008 [Behrendt *et al.*, 2011]. However, it seems contradictory that the WW is shallow when thick sea ice is present, as the thicker WDW layer would provide more heat to reduce the sea ice growth. This suggests that the sea ice thickness growth in this region is to a large extent determined by processes other than oceanic heat transport. This is supported by Fahrback *et al.* [2011], who found that the wind-driven westward current measured by moorings in this region increased from 1998 onwards. This would imply dynamical reasons, e.g. ice convergence, for the increasing sea ice thickness. A sea ice thickness increase of 0.45 m over the time period from 1998 to 2003 is able to explain the WW salinity increase displayed for this period (Fig. 7.3). This is consistent with the sea ice thickness observations [Behrendt *et al.*, 2011]. However, the third phase of WW salinity decrease from 2003 to 2008 can neither be explained by interaction with WDW, since the WW is getting shallower again and sea ice is increasing in thickness. Therefore, external freshwater inflow can be assumed. Possible sources of freshwater can be the break-off events at the Larsen Ice Shelf between 1995 and 2003 or the direct melt of ice shelves [Behrendt *et al.*, 2011, and references therein].

7.2 Linear correlation

As discussed in the previous chapters, sea ice is influenced by several dynamic and thermodynamic parameters. The monthly ice draft statistics revealed that thermodynamics and dynamics affect the sea ice thickness with varying strength in different years. Therefore, correlations of the ice draft with surface air temperature, ice drift, surface winds and pressure fields were expected. Furthermore, there are clear indications that the ice observed at the ULS positions developed in other regions. This implies that the measured changes in sea ice draft are forced by ice dynamics and thermodynamics on a more regional scale, rather than in the direct vicinity of the ULS position. The ice draft was therefore correlated with atmospheric parameters from reanalysis data (surface: ECMWF, higher levels: NCEP) and oceanic parameters from satellite data (SSM/I) not only on a local scale, but also on a regional scale. To investigate the regional

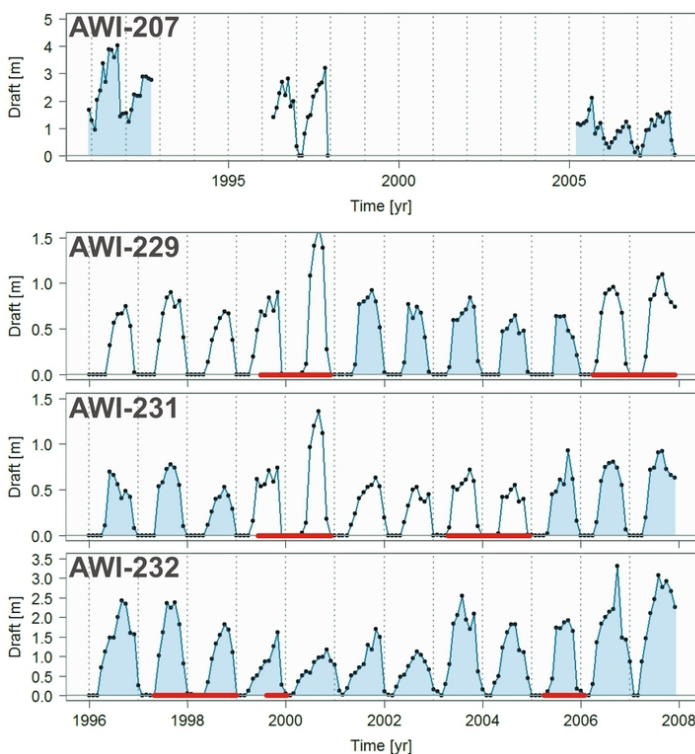


Fig. 7.4: The time series analysed in this section. The periods marked with blue colour were selected for the correlation analysis. Red bars indicate periods that were filled by M-SSA (see section 4.2).

is focused on ice draft anomalies⁵ of AWI-207, AWI-229, AWI-231 and AWI-232 (Fig. 7.4) (see also Appendix). To estimate the significance levels by means of random correlations, the time series of parameters assumed to influence the sea ice draft were shuffled (1000 times) by the bootstrapping method of *Ebisuzaki* [1997] (see section 4.2). The shuffled time series was treated in the same way as in the initial correlation, e.g. after bootstrapping only selected months were correlated with the ice draft or the random time series was lag-shifted and correlated with the ice draft.

⁴See "spectral analysis" in the previous chapter for details on how the indices were calculated.

⁵The anomalies in this section were calculated in the common way, i.e. by subtracting the long-term mean from each month.

influence on the sea ice draft, EOFs and SVDs were calculated from selected fields of atmospheric and oceanic variables after *Björns-son and Venegas* [1997] (see section 4.2). By correlating these EOFs (i.e. their principal components) with the ice draft, the regional patterns of variability and their influence on sea ice thickness were assessed. Additionally, the ULS data were correlated with thickness data from sea ice models (MIT and FESOM) to test their capability of simulating sea ice thickness. As regional patterns of sea ice variability are connected to large-scale processes, such as ENSO and SAM, the ice draft was additionally correlated with the respective indices (ENSO, SAM, SAO, PSA, ZW3⁴). This investigation was also motivated by the spectral analysis in the previous chapter, which suggested possible forcings of sea ice thickness by these processes. Some atmospheric and oceanic forcings do not translate linearly into ice thickness. However, the simple linear correlations performed in this section may give first clues on the dominating forcing mechanisms in different months and seasons. As in the previous chapter, the analysis

Monthly anomaly time series were used for the analysis. For example, an anomalously fast ice drift was assumed to result in anomalously thick ice through ridging. Anomalies were also calculated from the ENSO-Indices *Niño*3.4 and *Niño*1+2 to remove the annual cycle of ENSO. For ice draft the effective mean (i.e. calculated from ice and water cycles) was used. In the first step of the analysis, data on the respective grid points closest to the ULS positions were used. In the second step, regional or hemispheric EOFs of the different quantities were calculated and correlated with the ULS data. EOFs marked with "VARIMAX" were rotated. High correlations that were found only for certain periods are described in the text. For brevity, the results are not shown if the data were found to be completely uncorrelated. Significant correlations over the full data period are presented in tables, including the periods of highest correlation. Percentages indicate the significance level determined after the method of *Ebisuzaki* [1997]. The influence of climate modes on sea ice draft was investigated in three steps: (1) Based on the correlations with atmospheric and oceanic parameters, it was assessed to what extent the ice draft is influenced by thermodynamics and/or dynamics. (2) The influence of climate modes on air temperature, ice concentration, air pressure, winds and ice drift was assessed. (3) Selected periods of minimum and maximum ice draft were analysed regarding the association of atmospheric/oceanic parameters with the climate modes. The abbreviations used in the tables are:

r	-	Correlation coefficient after Pearson
r_{sp}	-	Rank correlation coefficient after Spearman
PHC	-	Period of Highest Correlation (+: positive, -: negative) e.g. 5 for May or 11 for November
SLP	-	Sea Level Pressure
GPH	-	Geopotential Height
M-Wind	-	Meridional Wind
Z-Wind	-	Zonal Wind
M-Drift	-	Meridional Drift
Z-Drift	-	Zonal Drift

The time lag given in the tables is the lag at which the highest correlation was found and is meant as the number of months the ice draft lags behind the other variable. It has to be noted that the reanalysis models still have problems in reproducing data for the atmospheric boundary layer in the polar regions. For example, the ECMWF reanalysis data were found to be not very consistent with measured data from the *Neumayer* research station of AWI [*G. König-Langlo* (AWI), personal communication, 2012]. The analysis was therefore completed with reanalysis data on the 925 hPa level or averaged up to 1000 hPa or higher levels to reduce the boundary layer problem, following the approach of *Hobbs and Raphael* [2010]. To demonstrate the applied procedure, the analysis of the first time series (AWI-207) is presented in a very detailed manner. The following time series are more briefly discussed.

AWI-207

For AWI-207 the anomalies were calculated for each record separately, as the full record contains large gaps that could not be filled. The analysis of AWI-207 is focused on 207-2 and 207-6 as the ice thicknesses of these records differ significantly. Furthermore, the record of 207-4 is too short to calculate anomalies. The anomalies of all quantities the ice draft was correlated with were calculated with the same base periods, i.e. 12/90-10/92 for AWI 207-2 and 04/05-12/07 for AWI 207-6. The data of the first two months of 2008 were omitted, as the ice drift data for this study were only available up to 2007.

AWI 207-2 local correlations:

The following correlations with the ice draft were found only for certain periods of the time series:

- ECMWF surface air temperature anomalies (March-July: $r = 0.7$, $r_{sp} = 0.83$)
- ice concentration anomalies (SSM/I) (April-August: $r = -0.58$, $r_{sp} = -0.59$)
- zonal ice drift anomalies (February-June: $r = 0.7$, $r_{sp} = 0.93$)
- SAM-Index (March-June: $r = 0.73$, $r_{sp} = 0.79$)

Table XIII: Correlations with monthly ice draft anomalies for the full period of AWI 207-2

EOFs marked with • are shown in figures further below.

AWI 207-2	lag	r	r^2	r_{sp}	PHC
Local					
ECMWF SLP	0	-0.47 (99%)	0.22	-0.51 (99%)	4-8 (-)
NCEP GPH (925 hPa)	0	-0.44 (99%)	0.19	-0.5 (99%)	4-8 (-)
ECMWF Z-Wind (surface)	0	0.27 (99%)	0.07	0.29 (99%)	2-6 (+)
ECMWF M-Wind (surface)	0	0.44 (99%)	0.19	0.45 (99%)	4-7 (+)
NCEP M-Wind (925 hPa)	0	0.55 (99%)	0.30	0.57 (99%)	4-7 (+)
Regional					
• EOF-3 Z-Wind (925 hPa)	0	0.86 (99%)	0.74	0.86 (99%)	/
• EOF-2 Z-Drift	0	0.67 (99%)	0.45	0.67 (99%)	/
• EOF-3 M-Drift (VARIMAX)	0	0.55 (99%)	0.30	0.46 (99%)	/
• EOF-2 M-Drift	0	0.81 (99%)	0.66	0.88 (99%)	/
SVD-1 Z-Wind (925 hPa) + M-Drift	0	0.89 (99%)	0.79	0.89 (99%)	/
Large-Scale & Hemispheric					
<i>Niño</i> 3.4-Index (anomaly)	0	0.28 (99%)	0.07	0.24 (99%)	3-5 (-)
• ZW3 (1000-925 hPa)	0	0.32 (99%)	0.1	0.32 (99%)	5-7 (+)
EOF-2 GPH (1000-925 hPa)	0	0.39 (99%)	0.15	0.41 (99%)	5-6 (+)

Next, the significant correlations valid for the full time series (i.e. all months) are discussed (see Table XIII). The sea ice draft anomalies of AWI 207-2 correlate negatively with sea level pressure anomalies and 925 hPa geopotential height anomalies. There is a weak but significant positive correlation with zonal surface wind anomalies, i.e. westerly wind anomalies lead to thick ice. The record of AWI-206 shows that the ice west of AWI-207 was thicker, at least in the period of AWI 207-4. The assumption that thicker ice was advected eastwards is supported by the positive correlation with the zonal ice drift⁶ in the period February-June. The ice draft anomalies of AWI 207-2 are positively correlated with meridional wind anomalies, i.e. anomalous southerly winds lead to thick ice.

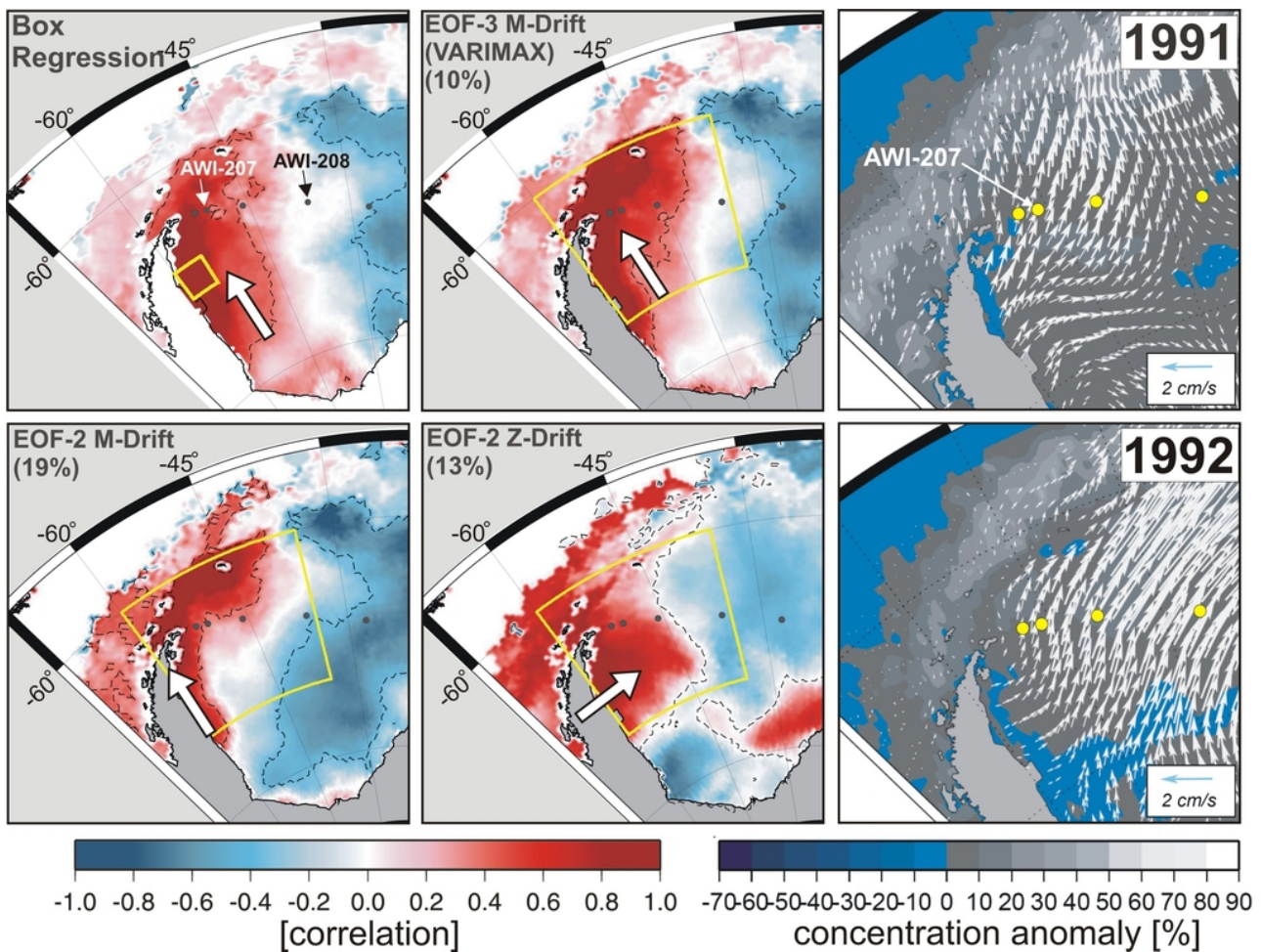


Fig. 7.5: Left and middle panels: Box regression of meridional ice drift anomalies and homogeneous correlation maps of the EOFs for meridional and zonal ice drift anomalies in the period of AWI 207-2, showing the spatial patterns of the EOFs. Shown are those EOFs that were found to have the highest correlation with the ice draft anomalies. The yellow frames mark the region for which the EOF was calculated or the region of box regression. The white arrows indicate the direction of the flow anomalies for situations of thick ice according to the correlations (see Table XIII). Dashed lines indicate 95% statistical confidence based on t tests. The percentages indicate the explained variance of each EOF. The right panels show the ice drift anomalies and concentration anomalies (SSM/I) from the 1990-2006 mean, averaged for 1991 and 1992.

⁶Positive direction for wind and drift is always from south to north (upwards) and from west to east (to the right).

These correlations are higher and more consistent than the correlation with zonal wind. Although there is no local (i.e. grid point) correlation between ice draft and meridional drift, the relation with meridional winds is assumed to be dynamical rather than thermodynamical. The draft seems to be positively correlated with temperature in the period of highest correlation with meridional winds (April-July). Furthermore, a significant negative correlation ($r = -0.63$, $r_{sp} = -0.35$) between surface air temperature anomalies and ice concentration anomalies was found, with the temperature lagging the concentrations by one month. This indicates that in the period of AWI 207-2 the ice had a larger influence on the air temperature than vice versa.

AWI 207-2 regional/hemispheric correlations:

There is a weakly positive correlation with the anomalies of the *Niño*3.4-Index. As mentioned in section 2.5, an *El-Niño* event brings cool continental air to the northwestern Weddell Sea and increases the sea ice extent. The ice draft anomalies of AWI 207-2 correlate positively with the second EOF of the geopotential height field (1000-925 hPa) south of 20°S latitude. This EOF (not shown) has the pattern of SAM, which confirms the correlation with the SAM-Index between March and June (see above). Between 1985 and 1994 the PSA was the dominating pattern (EOF-1) and SAM was sub dominant (EOF-2) [Udagawa *et al.*, 2009]. However, no correlation between the ice draft and the PSA-Index was found. The ice draft anomalies are correlated with the ZW3-Index of the lower atmosphere, which confirms the local correlation with meridional winds (see above).

On a regional scale, the most significant correlations were found with the wind and drift fields. The box regression (see subsection 4.2.5) in figure 7.5 shows the typical ice drift pattern in the Weddell Sea with strong northward transport along the eastern coast of the peninsula. This drift pattern is part of the Weddell gyre [Fahrbach, 1994] (Fig. 7.1) and is located southwest of AWI-207. There is a narrow band with strongly variable meridional ice drift along the coast (dark red colour) and a zone with less variable northward ice drift further east. This pattern is well described by the third rotated EOF of the meridional drift⁷. The first two rotated EOF patterns (not shown) exclude the band of coastal drift. The ice draft anomalies of AWI 207-2 correlate significantly with the rotated EOF-3 (Fig. 7.5), indicating that the drift pattern describes transport of thick ice from the southern Weddell Sea towards AWI-207. This thick ice includes second-year ice which is heavily deformed through ridging [Schwegmann, 2012]. If the EOFs are not rotated, the second mode (EOF-2) describes only the coastal band of ice drift (Fig. 7.5). The correlation of this mode with the ice draft anomalies is even higher and explains 2/3 of the shared variance (see Table XIII). It includes significant time lags of up to 5 months. This indicates that the thick ice needed a certain time to travel along the coast and to reach the position of AWI-207. The drift anomalies in 1991 and 1992 also had a zonal component (Fig. 7.5). At the observed mean drift speeds of 3-5 cm/s the ice could have travelled the distance between the northeastern coast off the Larsen ice shelves and AWI-207 within 2-4 months. Especially in 1991, the ice drift anomalies were high and oriented in northeastern direction, away from the Larsen ice shelves towards AWI-207. This explains the high ice thickness measured at AWI-207 in this year. In 1992 the ice drift anomalies away from the shelves were smaller and not directly oriented towards AWI-207. The pattern of zonal ice drift away from the coast is described by the unrotated second EOF of the zonal drift (Fig. 7.5). Its correlation with the ice draft anomalies is also significant (see Table XIII). A box regression - like in the example above - confirmed the validity of the pattern. The first zonal drift EOF of

⁷The first 10 EOF patterns were rotated, following the approach of Dommenget and Latif [2002].

the same domain (not shown) describes a pattern of strong drift in the northwestern Weddell Sea, which seems to be part of the circumpolar current.

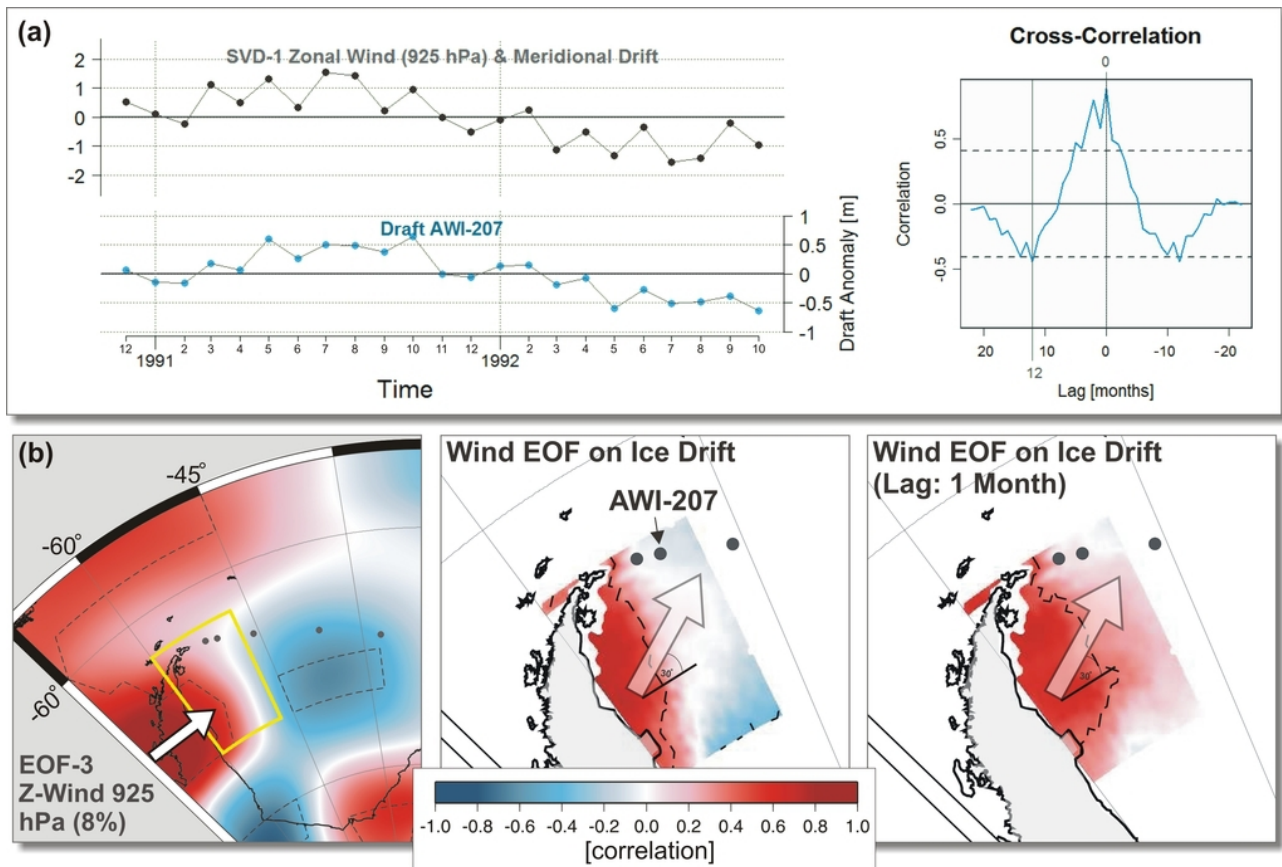


Fig. 7.6: (a) Left: Principal component of the ice drift of the leading SVD mode between zonal wind anomalies and the meridional drift anomalies southwest of AWI-207 (black). Ice draft anomalies of AWI 207-2 (blue). Correlation coefficient: $r = 0.89$. Right: Cross-correlation plot for both time series. Dashed lines: 95% confidence limits [Chatfield, 1984]. (b) Left panel: Third EOF pattern of the zonal wind anomalies (see figure 7.5 for more information). Middle panel: Heterogeneous correlation map of the wind EOF and the drift-anomaly component 30° to the left of the zonal drift. Right panel: Heterogeneous correlation map of the wind EOF and the drift-anomaly component 30° to the left of the zonal direction with the drift lagging the wind by one month. Dashed lines: 95% statistical confidence based on t tests. Arrows show the direction of the flow anomalies for situations of thick ice.

To investigate the influence of wind patterns on the observed ice drift and thickness, EOFs of the meridional and zonal wind field were calculated. A high correlation between ice draft anomalies and wind anomalies was found for the unrotated third EOF of the zonal wind field southeast of AWI-207 (Fig. 7.6). This correlation also includes significant time lags of up to 4 months and explains almost 3/4 of the shared variance (see Table XIII). Thus, the westerly winds blowing across the Antarctic Peninsula drove the thick ice from coastal regions towards the central and northern Weddell Sea. The correlation between the zonal wind EOF and the zonal drift EOF is significant ($r = 0.63$, $r_{sp} = 0.65$), as well as the correlation between the zonal wind EOF and the meridional drift EOF ($r = 0.63$, $r_{sp} = 0.89$). Thus, the westerly winds also contributed to the northward ice drift along the tip of the Antarctic Peninsula. This assumption is supported by the very high correlation between the ice draft and the leading

SVD mode between the zonal wind anomalies and the meridional drift anomalies (Fig. 7.6a) in the same domain. This mode explains 60% of the total squared covariance. The correlation includes time lags of up to 4 months, with the ice draft lagging the SVD mode. Because of the relative positions of the wind EOF pattern and AWI-207, it can be assumed that zonal winds induced Ekman drift, which transported thick ice in northeastern direction towards the position of AWI-207. To investigate the Ekman drift, the wind EOF was correlated with drift-anomaly components to the left of the zonal drift. The Ekman components were obtained by projecting the ice drift vectors onto unit vectors of different angles to the left of the zonal direction. The heterogeneous correlation maps show significant correlations between the zonal wind EOF and the Ekman drift 30° to the left (Fig. 7.6). High turning angles of $20\text{--}30^\circ$ between surface wind and drift in this region were reported by *Kimura* [2004]. The region of significant correlation extends further east when a time lag of one month is considered (Fig. 7.6). The significant

correlations disappeared for a time lag of two months, which suggests that the thick ice reached AWI-207 in less than two months.

Data from the *European Remote Sensing Satellite* (ERS) show high average radar backscatter from sea ice east of the Larsen ice shelves and over the position of AWI-207 in 1992 [*Drinkwater et al.*, 1993]. The high average backscatter near the tip of the peninsula is associated with deformed second-year ice [*Schwegmann*, 2012].

The ice draft at AWI 207-2 showed significant negative correlations ($r = -0.83$, $r_{sp} = -0.83$) with a meridional wind pattern (EOF-2) along the eastern coast of the peninsula, i.e. the ice was thick when the southerly winds were weak. This wind pattern did not show significant correlations with the ice drift in the vicinity of AWI-207. As this pattern is significantly anticorrelated with the zonal wind pattern shown above, it can be assumed that the correlation between ice draft and the meridional wind pattern results from the fact that the westerly winds across the peninsula were strong when the southerly winds were weak and vice versa. However, weak but significant correlations with ZW3 were found (see Table XIII). The ZW3 pattern (Fig. 7.7) shows significant meridional wind anomalies at the tip of the peninsula, which can be assumed to contribute to the northward transport of thick ice in that region. Model data from FESOM were considered unrealistic at AWI-207 over the period 1990-2007, and data from the MIT model were available only from 1992 on. The correlation with model data was therefore omitted at AWI 207-2.

AWI 207-6 local correlations:

When compared to AWI 207-2, the record of AWI 207-6 not only shows a strong decline of the

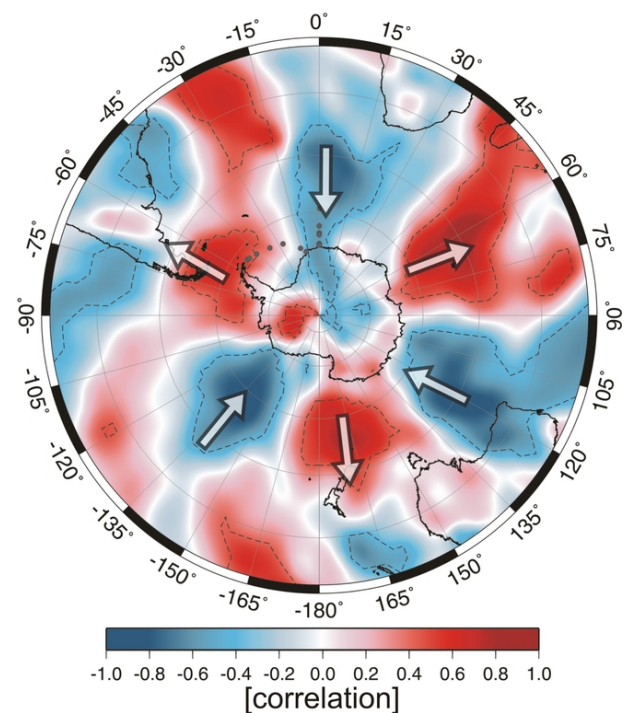


Fig. 7.7: Leading EOF mode of the vertically averaged (1000-925 hPa) and mass-weighted meridional wind anomalies (NCEP) for the period of AWI 207-2, showing the ZW3 pattern. The arrows indicate the direction of the flow anomalies for situations of thick ice. Dashed lines: 95% statistical confidence based on t tests.

Model data from FESOM were considered unrealistic at AWI-207 over the period 1990-2007, and data from the MIT model were available only from 1992 on. The correlation with model data was therefore omitted at AWI 207-2.

ice thickness (Fig. 7.4), but also associations with other parameters. The data gaps in 8/2005 and 9/2005 were filled by deriving draft values from the MIT model (see *spectral analysis* in the previous chapter).

Table XIV: Correlations with monthly ice draft anomalies for the full period of AWI 207-6

EOFs marked with • are shown in figures further below.

AWI 207-6	lag	r	r ²	r _{sp}	PHC
Local					
MIT Model Ice Thickness	0	0.75 (99%)	0.56	0.77 (99%)	/
SSM/I Ice Concentration	0	0.9 (99%)	0.81	0.84 (99%)	/
ECMWF Air Temperature (surface)	1	-0.4 (99%)	0.16	-0.51 (99%)	/
ECMWF Meridional Wind (surface)	1	0.4 (99%)	0.16	0.43 (99%)	/
SSM/I Zonal Drift	0	-0.32 (99%)	0.1	-0.38 (99%)	3-7 (-)
SSM/I Meridional Drift	1	0.6 (99%)	0.36	0.6 (99%)	/
Regional					
• EOF-1 Ice Concentration (SSM/I)	0	0.9 (99%)	0.81	0.81 (99%)	/
EOF-1 Temp (1000-925 hPa)	1	-0.45 (99%)	0.20	-0.54 (99%)	/
EOF-1 M-Wind (surface)	1	0.45 (99%)	0.20	0.46 (99%)	/
EOF-1 Z-Drift	1	-0.45 (99%)	0.20	-0.52 (99%)	/
• EOF-1 M-Drift	1	0.48 (99%)	0.23	0.48 (99%)	/
Large-Scale & Hemispheric					
<i>Niño</i> 1+2-Index (anomaly)	1	-0.68 (99%)	0.46	-0.62 (99%)	/
<i>Niño</i> 3.4-Index (anomaly)	0	-0.7 (99%)	0.49	-0.56 (99%)	8-2 (-)
PSA-Index	1	-0.38 (99%)	0.14	-0.42 (99%)	/
SAM-Index	1	-0.48 (99%)	0.23	-0.58 (99%)	/
SAO-Index	1	-0.42 (99%)	0.18	-0.44 (99%)	/
• EOF-1 GPH (1000-925 hPa)	2	-0.54 (99%)	0.29	-0.68 (99%)	/
ZW3 (1000-925 hPa)	2	0.54 (99%)	0.29	0.68 (99%)	/

The correlation of the draft anomalies with thickness anomalies of the MIT model is very high. Before filling the two months with model data, the correlation was also high ($r=0.68$). FESOM data were unrealistic and omitted. The negative correlation with local ECMWF surface air temperature anomalies is highest when the draft lags the temperature by one month. The ice of AWI 207-6 was on average about two metres thinner compared to AWI 207-2 (Fig. 7.4). At AWI 207-2 the mean ice thickness was strongly determined by deformed ice, whereas at AWI 207-6 the mean ice thickness was closer to the thermodynamic growth maximum below 1 m. It can therefore be assumed to have been more sensitive to variations in atmospheric temperature. The highest correlation was found with ice concentrations (SSM/I), indicating that highly concentrated ice was thicker than weakly concentrated ice in this period. The ice draft is positively correlated with meridional winds and drift⁸, again confirming the regular pattern in figure 6.16. The correlation with meridional ice drift is higher than the correlation

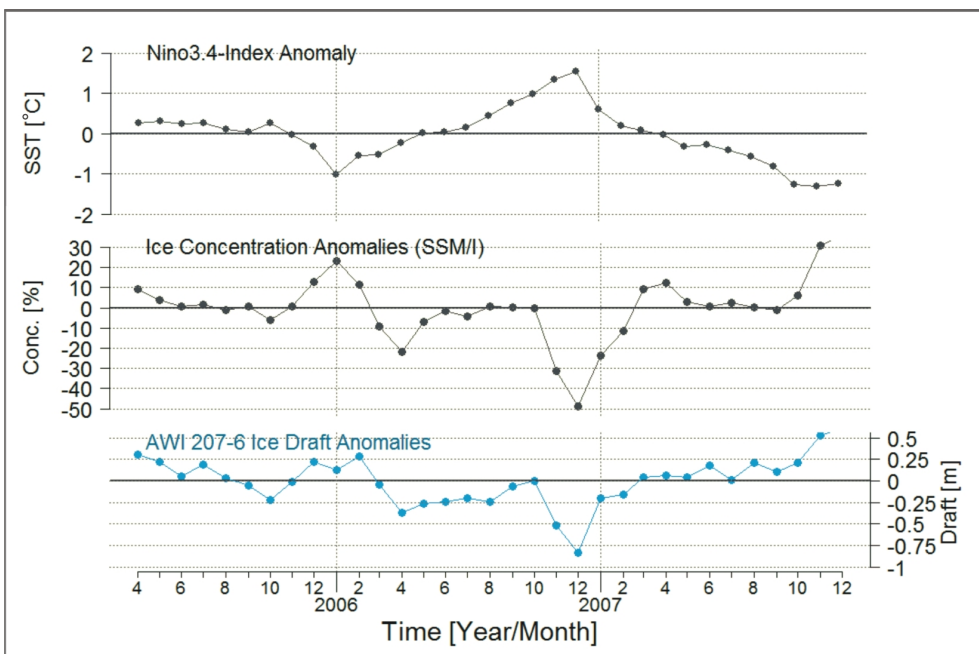


Fig. 7.8: Anomalies of *Niño*3.4-Index, local ice concentration (black) and ice draft (blue) at AWI 207-6 (base period 2005-2007).

drift anomalies. This suggests that the ice at AWI-207 was thick when the drift anomalies had an east-to-west component, i.e. directed from the central Weddell Sea towards AWI-207 and the coast of the peninsula.

AWI 207-6 regional/hemispheric correlations:

The correlations of EOF time series (principal components) with the ice draft anomalies at AWI 207-6 were found to be slightly higher when using a smaller EOF domain (Fig. 7.9) compared to AWI 207-2. The correlation with the meridional ice drift pattern along the Antarctic Peninsula is still present, albeit weaker compared to AWI 207-2. The pattern was confirmed by box regression (see subsection 4.2.5) and was also found when the EOF domain was increased. The narrow band of ice drift near the coast is not present in the EOF pattern any more (Fig. 7.9), regardless of the size of the EOF domain. The meridional ice drift east of the peninsula

with temperature. However, it was found to be highest in summer/autumn. The correlation with meridional ice drift could therefore be more valid for thin ice. The correlation with air temperature is highest over winter, which is not surprising, as the air temperature exerts more influence on the sea ice field in winter than in any other season [Yuan and Li, 2008]. Contrary to AWI 207-2 there is a negative correlation with local zonal ice

⁸The drift data after 2006 were kindly provided by Dr. Stephan Kern, University of Hamburg.

decreased with a statistically significant trend of about 1 cm s^{-1} per decade over the period 1988-2006 [Schwegmann, 2012]. The correlation with the zonal drift is assumed to result from the fact that at times of peaking sea ice draft and concentration, the drift anomalies were oriented in northwestern direction, i.e. ice was advected from southeast of AWI-207. The meridional and zonal wind anomalies were found to be anticorrelated, i.e. strong southerly winds also had a strong easterly component. The same applies to the ice drift. This could lead to increased ice compaction at the coast of the peninsula. Additionally, the winds carried cold air from the southern Weddell Sea towards AWI-207 (Fig. 7.10). Like the EOF of the zonal drift, the EOF-1 of near surface air temperature (1000-925 hPa, not shown) has no pattern, i.e. it has the same intensity over the entire EOF domain. As for zonal and meridional drift, the correlation with the temperature EOF is highest with the ice draft anomalies lagging by one

month. For ice concentration, the correlation with air temperature is highest at lag 0. This was also discussed by Schwegmann [2012], who concluded that it remains unclear whether sea ice primarily affects air temperatures or vice versa. From the correlations presented here, it is very likely that air temperatures affect sea ice thickness because of the time lag of one month. The correlation with ice drift also included a time lag of one month, but this correlation was higher in summer. The influence of air temperature on ice thickness in winter is therefore evident in the correlations.

In the following, the correlations between ice draft and climate modes is investigated. From the correlations in table XIV it can be concluded that ice draft at AWI 207-6 is mainly correlated with ice concentrations, meridional ice drift and surface air temperature. It was therefore investigated how the climate modes are associated with these parameters. Only selected figures can be shown here. A significant correlation was found between ice draft and the ZW3 pattern, with the ice draft lagging by 2 months. In the period of AWI 207-6 the ZW3 pattern (not shown) is described by the second EOF of the meridional wind anomaly field, while the first EOF describes a ZW4 pattern. ZW3 mainly affected the air temperatures in the period 2005-2007 at AWI 207-6, but also had a very small influence on the meridional ice drift. A time lag of two months was also found for a significant correlation with the first EOF of the hemispheric geopotential height field. This EOF (Fig. 7.10c) has a SAM pattern superimposed by a slightly shifted PSA pattern. A time lag of two months was also found by Yuan and Li [2008] for correlations of large-scale climate modes with sea ice concentrations.

PSA had a stronger influence on the air temperatures at AWI-207 than ZW3. The influence of PSA is most evident in the meridional ice drift along the peninsula. The correlation of PSA

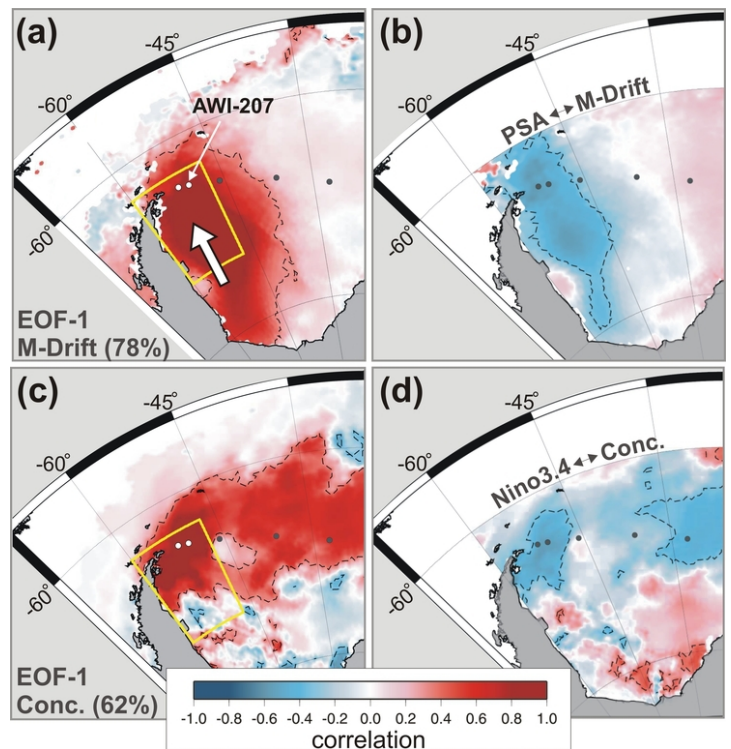


Fig. 7.9: (a) Leading EOF pattern of meridional ice drift in 2005-2007 (see figure 7.5 for more information). (b) Correlation of the PSA-Index with meridional ice drift (2005-2007). (c) Leading EOF pattern of ice concentration in 2005-2007. (d) Correlation of the Niño3.4-Index with ice concentration (2005-2007).

with the meridional drift almost equals the pattern of the first EOF of the meridional drift (Fig. 7.9), especially in the region of highest variability (dark red). The long-term changes in PSA could therefore provide an explanation for the decreasing northward ice drift along the Antarctic Peninsula. PSA shows a significant trend towards its positive phase [Yuan and Li, 2008] which would be associated with decreasing northward advection of continental air in the western Weddell Sea through the central pressure system of PSA.

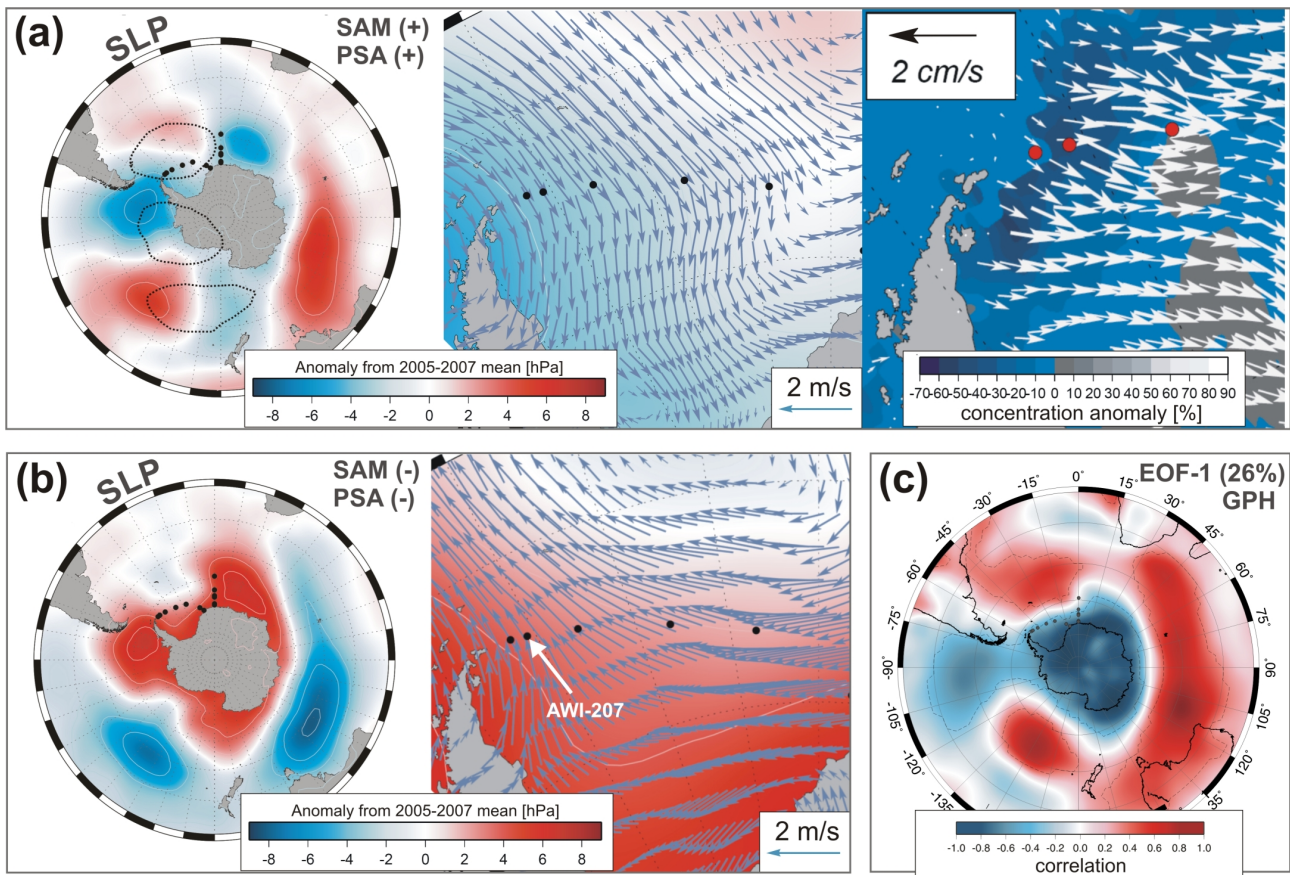


Fig. 7.10: (a) Left: Mean sea level pressure anomalies, averaged over November and December 2006 (low ice draft, positive PSA-Index and SAM-Index). The black lines mark the usual positions of the PSA pattern. Middle: Anomalies of sea level pressure and surface wind, averaged over the same period. Right: Anomalies of ice drift and concentration (SSM/I), averaged over the same period. (b) Left: Mean sea level pressure anomalies, averaged over November and December 2005 (high ice draft, negative PSA-Index and SAM-Index). Right: Anomalies of sea level pressure and surface wind, averaged over the same period. (c) Leading EOF pattern of the vertically averaged geopotential height field (NCEP, 1000-925 hPa) in 2005-2007.

The only significant influence on ice concentrations around AWI 207-6 was found for the *Niño*3.4-Index. The first EOF of the ice concentration shows a region of high variability (dark red) at the tip of the peninsula which seems to be associated with the *Niño*3.4-Index during 2005-2007 (Fig. 7.9). Both the surface air temperature and the meridional ice drift were significantly correlated with the ice concentration in this small region (not shown). However, the sign of the correlation between the *Niño*3.4-Index and the ice concentration was not expected. The correlation was negative with and without the annual cycle removed from the index. An

analysis of the *Niño*3.4-Index and ice concentration anomalies over a longer time period (1990-2007) in the full Southern Hemisphere showed significant correlations in the Antarctic Dipole (ADP). The values were positive in the Bellinghausen Sea and large parts of the Weddell Sea and negative in the Amundsen/Ross seas. *Stammerjohn et al.* [2008] found that the correlation between the *Niño*3.4-Index and ice concentration reversed its sign between the 1980s and 1990s. A similar effect may have occurred during 2005-2007. Nevertheless, the correlation with the *Niño*3.4-Index shows that the sea ice thickness in the northwestern Weddell Sea is to some extent associated with tropical Pacific sea surface temperature variability.

The correlation of ice draft with the SAM-Index is higher than with the PSA-Index (see Table XIV). SAM had the highest influence on surface air temperature at AWI 207-6 and also showed a small influence on the meridional ice drift. The only significant influence of SAO was found for air temperatures, but it was smaller than the influences of SAM, PSA and ZW3.

The correlation of sea ice parameters and the SAM-Index together with the PSA-Index was further investigated by considering the wind and pressure fields. Figure 7.10 shows the situations during the times of maximum and minimum ice draft at the ends of 2005 and 2006, respectively. SAM and PSA were found to correlate significantly during 2005-2007 ($r = 0.69$, $r_{sp} = 0.65$). The two examples of positive and negative indices show the direction of the wind anomalies in the Weddell Sea, caused by the pressure systems of PSA and SAM. During the low of both indices in late 2005, the pressure over Antarctica was anomalously high and the central pressure system of the PSA pattern was a high pressure anomaly. This caused northward transport of cold air and probably northward advection of thicker ice from the southern Weddell Sea towards AWI-207. During this period, higher ice concentration and ice draft could be observed. During the high of the indices in late 2006, the central pressure system of PSA was a low pressure anomaly which caused anomalous northerly winds, high air temperatures and less northward advection of thick ice at AWI-207. During this time, ice concentration and ice draft were in a minimum (Fig. 7.8). A similar situation occurred in March-May 2006.

Overall, it can be concluded that the interplay mainly of SAM, PSA, ZW3 and *Niño*3.4 was responsible for the observed changes in sea ice concentration and thickness in the period of AWI 207-6 at the tip of the Antarctic Peninsula. The thermodynamic forcing of sea ice thickness was mainly determined by SAM and ZW3 and to a lesser extent by PSA and SAO. The dynamic part, i.e. meridional ice advection, was mainly determined by PSA and to a lesser extent by SAM. The influence of ZW3 and SAO on the drift was negligible. How the ENSO-Indices affected the ice concentration and thickness remains to be investigated, especially as the indices of PSA and ENSO were not correlated in 2005-2007. In the period of AWI 207-2 (1991-1992) the association of sea ice thickness with climate modes was much lower. Both the SAM-Index and the PSA-Index were in a low during the period of AWI 207-2. Correlations in both periods are compared in table XV.

Table XV: Significant local/regional correlations with ice draft at AWI-207

Large symbols denote correlations with $|r| \geq 0.5$ and/or $|r_{sp}| \geq 0.5$.

Parameter	AWI 207-2	AWI 207-6
Air Temperature		—
Air Pressure (or GPH)	—	
Ice Concentration		+
Zonal Wind	+	
Meridional Wind	+	+
Zonal Drift	+	—
Meridional Drift	+	+
<i>Niño</i> -Indices	+	—
SAM-Index		—
SAO-Index		-
PSA-Index		-
ZW3-Index	+	+

AWI-229

Correlations of the filled (see section 4.2) 12-year time series were generally very weak, which indicates that the gap-filling at AWI-229 was not successful. The analysis was therefore focused on the five measured years 2001-2005. In this time series only data for November 2002 were filled by M-SSA. All anomalies were calculated with the base period 2001-2005. The variation of sea ice draft anomalies during 2001-2005 was very small, with a standard deviation of only ± 12 cm.

Table XVI: Correlations with monthly ice draft anomalies for the full period of AWI-229 (2001-2005)

EOFs marked with • are shown in figures further below.

AWI-229	lag	r	r ²	r _{sp}	PHC
Local					
FESOM Model Ice Thickness	1	-0.44 (99%)	0.19	-0.43 (99%)	/
MIT Model Ice Thickness	0	0.65 (99%)	0.42	0.64 (99%)	/
Ice Concentration (SSM/I)	0	0.66 (99%)	0.44	0.38 (99%)	/
NCEP Air Temp. (925 hPa)	1	0.41 (99%)	0.17	0.42 (99%)	/
ECMWF Z-Wind (surface)	0	0.39 (99%)	0.15	0.25 (99%)	/
ECMWF M-Wind (surface)	1	-0.54 (99%)	0.29	-0.58 (99%)	/
Z-Drift	0	0.32 (99%)	0.10	0.25 (99%)	/
M-Drift	2	-0.44 (99%)	0.19	-0.24 (95%)	/
Regional					
• EOF-2 Concentration (SSM/I)	0	0.6 (99%)	0.36	0.62 (99%)	/
EOF-1 Temp. (1000-925 hPa)	1	0.42 (99%)	0.18	0.43 (99%)	/
EOF-1 Z-Wind (1000-925 hPa)	1	0.39 (99%)	0.15	0.3 (99%)	/
EOF-1 M-Wind (1000-925 hPa)	1	-0.51 (99%)	0.26	-0.55 (99%)	/
EOF-1 Z-Drift	1	0.42 (99%)	0.18	0.4 (99%)	/
EOF-1 M-Drift	2	-0.51 (99%)	0.26	-0.28 (95%)	/
Large-Scale & Hemispheric					
<i>Niño</i> 1+2-Index (anomaly)	1	-0.42 (99%)	0.18	-0.41 (99%)	/
<i>Niño</i> 3.4-Index (anomaly)	0	-0.36 (95%)	0.13	-0.36 (95%)	/
PSA-Index	0	0.34 (99%)	0.12	0.28 (95%)	8-12 (+)
SAO-Index	1	0.32 (95%)	0.10	0.22 (68%)	/
ZW3-Index	0	-0.38 (99%)	0.14	-0.3 (95%)	10-12 (-)

AWI-229 local correlations:

The only significant correlation with data from the FESOM model is negative with a time lag of one month. While the ULS-derived ice draft shows a statistically significant negative trend of -3 cm per year, the modelled ice thickness increases during the 5-years period. A better correlation was detected between the ice draft and the ice thickness of the MIT model.

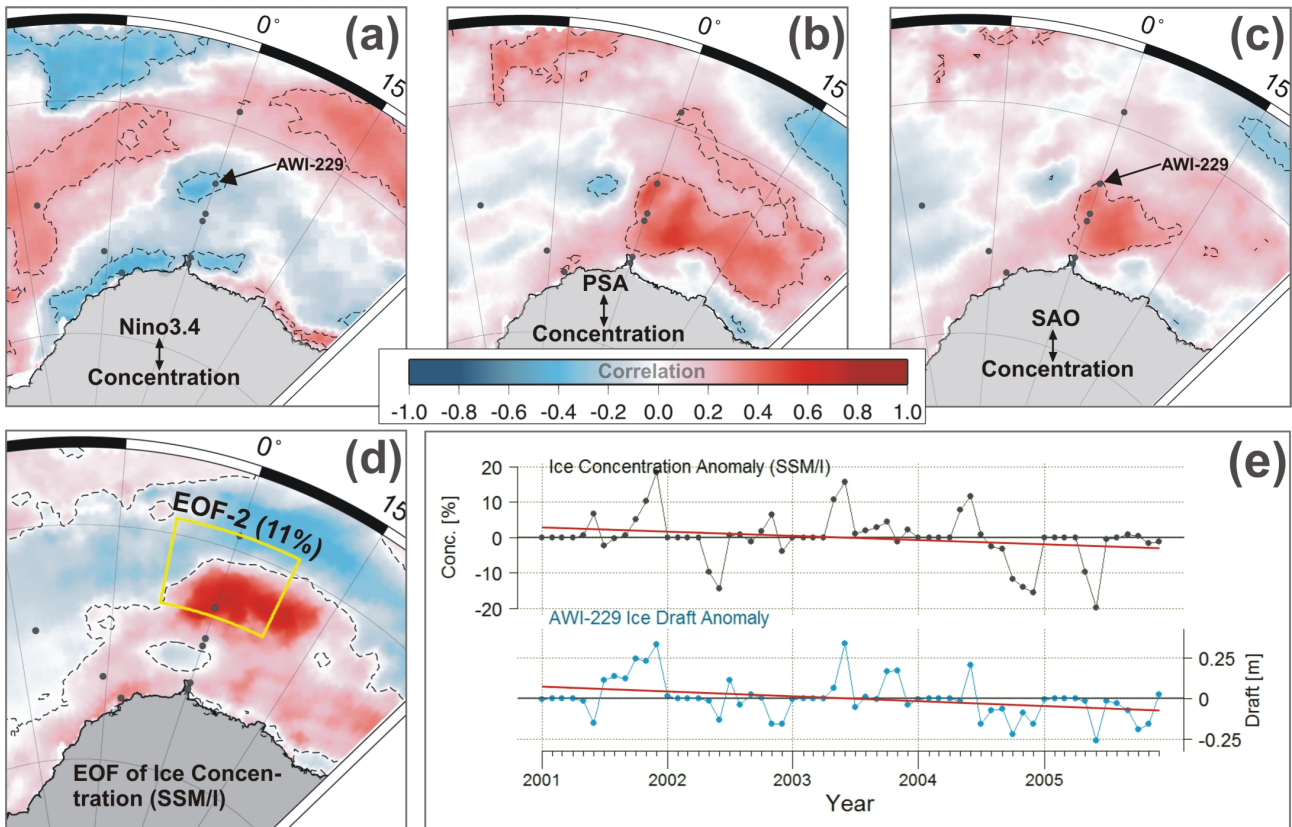


Fig. 7.11: Correlation of (a) Nino3.4-Index anomaly, (b) PSA-Index and (c) SAO-Index with ice concentration anomalies (SSM/I) in 2001-2005. Dashed lines: 95% statistical confidence based on t tests. The influence of ZW3 (not shown) was similar to the one of SAO. (d) Second EOF mode of ice concentration during 2001-2005 (see figure 7.5 for more information). (e) Local anomalies of ice concentration (black) and ice draft (blue) at AWI-229 (base period 2001-2005). The red lines show the statistically significant trends of -1.2% ice concentration per year and -3 cm ice draft per year.

Interestingly, there is a positive correlation between ULS ice draft and air temperatures, which indicates that the measured ice draft was not primarily influenced by thermodynamics. The ice draft at AWI-229 correlates well with local ice concentrations from SSM/I. The correlations with wind and drift anomalies indicate that the ice was anomalously thick when (1) meridional drift and wind anomalies were low, i.e. directed from north to south and (2) when the zonal drift and wind anomalies were high, i.e. directed from west to east. This phenomenon is investigated further below.

AWI-229 regional/hemispheric correlations:

The correlations discussed above are also reflected in the correlations with regional EOFs (see Table XVI). The selected EOF domain reaches from 8°W to 8°E and spans a range of 5.5° in latitude. To find the highest correlations, the domain was slightly shifted in both directions.

The EOF of ice concentration (Fig. 7.11) shows a region of high variability around AWI-229, exceeding the EOF domain and reaching to about 14°E longitude. This pattern was confirmed by box regression (see section 4.2). The correlation of this principal component with the ice draft was the highest correlation found for EOFs of ice concentration. The correlations of ice draft with EOFs of meridional wind and drift were highest when the EOF domain was not centred on AWI-229, but shifted southward (8°W - 8°E ; 63.5°S - 69°S). This, in combination with the time lags of 1-2 months, suggests that thinner ice was advected from a position south of AWI-229. Comparing the records of AWI-229, AWI-230 and AWI-231 (Fig. 5.21) indeed suggests that the ice south of AWI-229 is on average thinner. In the months June-October in 2001 and 2002 the ice at AWI-230 was 5% thinner and the ice at AWI-231 35% thinner than at AWI-229⁹. This also explains the positive correlation with air temperature: Southerly winds not only carried cold air masses but also caused northward advection of thinner ice.

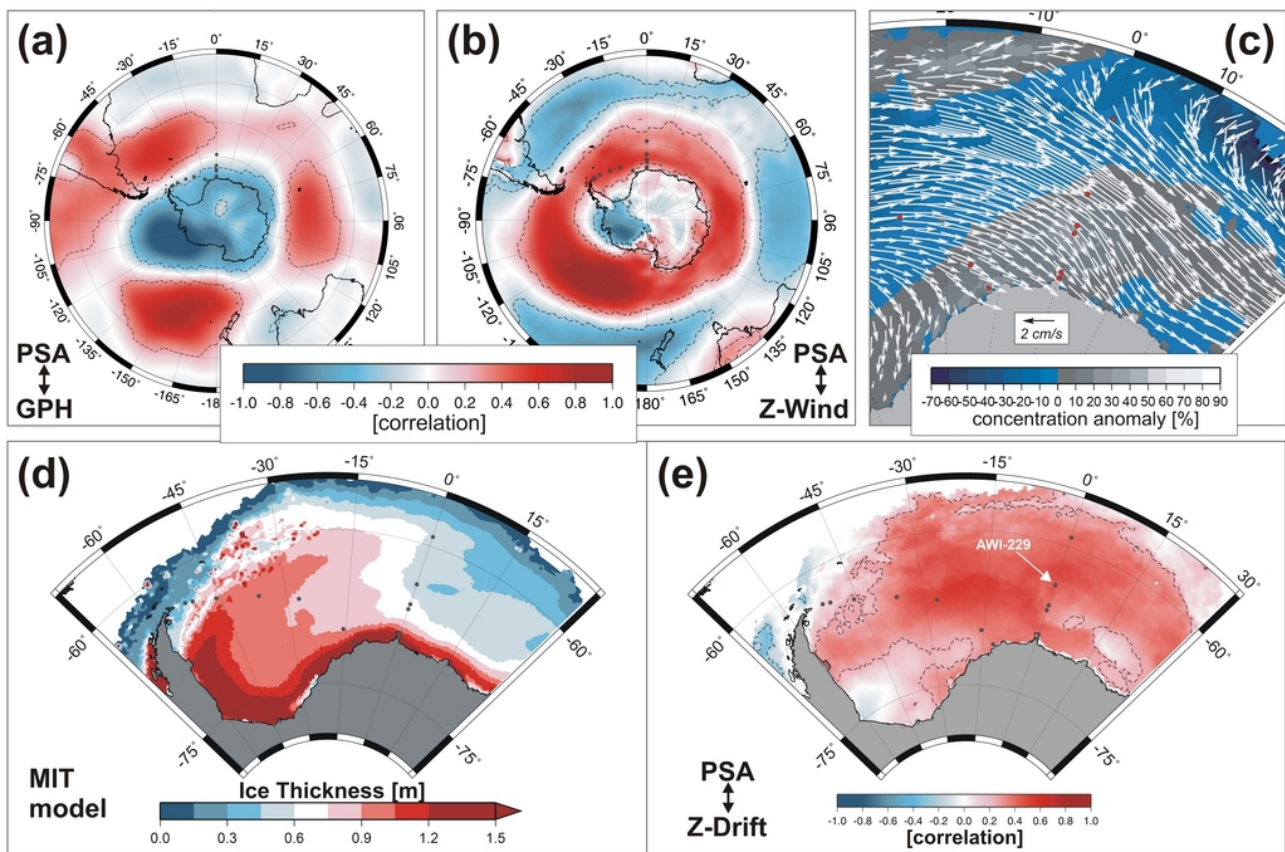


Fig. 7.12: Correlation of the PSA-Index with (a) mean geopotential height anomalies (1000-925 hPa) and (b) mean zonal wind anomalies (1000-925 hPa) during 2001-2005. (c) Anomalies (base period 2001-2005) of ice drift and concentration (SSM/I), averaged over the period September-November 2001, i.e. the time of a draft maximum (see also figure 7.11e). (d) Absolute ice thickness from the MIT model, averaged over the period September-November 2001. (e) Correlation of the PSA-Index with zonal ice drift anomalies during 2001-2005. Dashed lines: 95% statistical confidence based on t tests. Positive wind and drift directions are from south to north (upwards) and from west to east (to the right).

⁹This feature is not simulated by the models.

The signs of the correlations therefore indicate that dynamical effects dominate the ice thickness at AWI-229. The correlation with EOFs of zonal wind and drift indicate that the ice west of AWI-229 was thicker and east of AWI-229 thinner. The average ice thickness from the MIT model (Fig. 7.12d) confirms this.

Significant negative correlations were found for the anomalies of both ENSO-Indices (see Table XVI). The highest correlation with the *Niño*1+2-Index anomaly was found for a time lag of one month, while the correlation with the *Niño*3.4-Index anomaly was highest at lag 0 but also included a significant correlation at lag 1. Moderate correlations were found with the indices of PSA, SAO and ZW3. The ZW3-Index (not shown) does not correlate significantly with the meridional winds on the prime meridian. The correlation of ice draft with ZW3 is therefore believed to result from the correlation with the PSA-Index, as the PSA-Index in the period 2001-2005 shows an association with ZW3 (see figure 7.12).

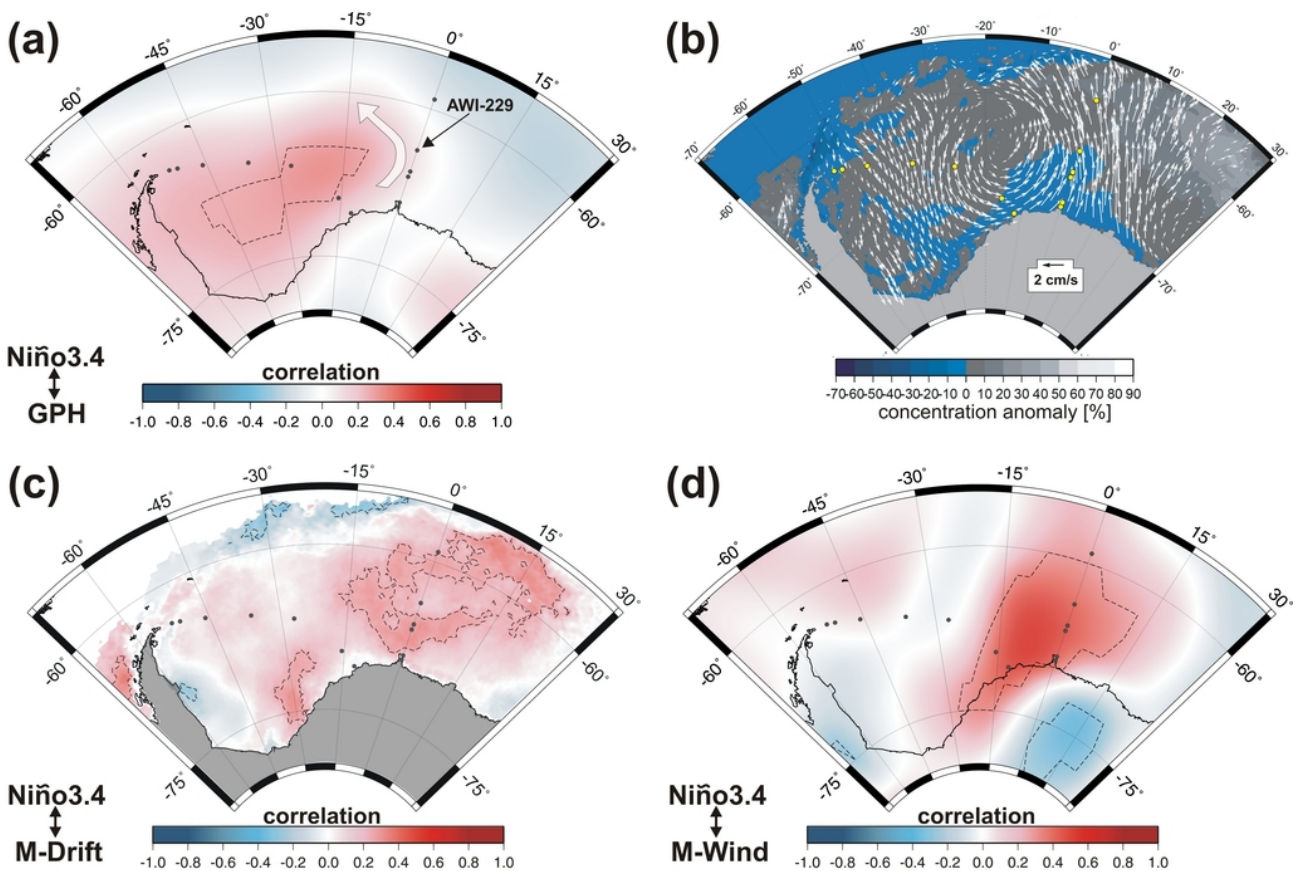


Fig. 7.13: (a) Correlation of the *Niño*3.4-Index anomaly with mean geopotential height anomalies (1000-925 hPa) during 2001-2005. The white arrow marks the direction of wind anomalies for a high pressure anomaly and positive *Niño*3.4-Index anomaly. (b) Anomalies (base period 2001-2005) of ice drift and concentration (SSM/I), averaged over the period July-October 2004, i.e. the time of a draft minimum (see figure 7.11e) and a positive *Niño*3.4-Index anomaly. (c) Correlation of the *Niño*3.4-Index anomaly with meridional ice drift anomalies during 2001-2005. (d) Correlation of the *Niño*3.4-Index anomaly with mean meridional wind anomalies (1000-925 hPa) during 2001-2005. Dashed lines: 95% statistical confidence based on t tests. Positive meridional wind and drift directions are from south to north (upwards).

As shown in table XVI, the ice draft correlates with ice concentrations and dynamical parameters. Furthermore, it is associated with ENSO-Indices and to a lesser extent with PSA, SAO and ZW3. All indices affected the ice concentrations around AWI-229 (Fig. 7.11). The only significant effect on meridional ice drift on the prime meridian was found for the *Niño*3.4-Index. Zonal ice drift was mainly affected by PSA and to a lesser extent by ZW3 and SAO.

In the following, the situation of the ice draft maximum in September-November 2001 and its association with the PSA-Index is discussed (Fig. 7.12). The PSA-Index shows clear associations with SAM and ZW3 during 2001-2005 (Fig. 7.12a). Its influence on the zonal winds was circumpolar and strongest in the Pacific sector (Fig. 7.12b). Compared to other climate modes (SAM, SAO and ENSO-Indices) the PSA-Index had the largest influence on the zonal ice drift in the Weddell Sea during 2001-2005 (Fig. 7.12e). During September-November 2001 the index was in a very high state compared to the other years in the period 2001-2005. This caused strong westerly wind anomalies across the entire Weddell Sea and anomalously high ice draft and ice concentrations at AWI-229 (Fig. 7.11e). The zonal winds are usually very strongly associated with SAM. However, only weak correlations between ice draft and SAM could be found. A reason for this could not be found. However, during the draft maximum at the end of 2001 the SAM and SAO-Indices were also anomalously high. SAO and SAM therefore also contributed to some extent to the ice draft and concentration maximum in 2001.

Next, the situation of the ice draft minimum in July-October 2004 and its association with the *Niño*3.4-Index is discussed (Fig. 7.13). As shown in figure 7.13a, a positive anomaly of the *Niño*3.4-Index was associated with positive geopotential height anomalies in the lower atmosphere over the Weddell Sea. The correlation is relatively small but statistically significant. This action centre was part of the PSA pattern with a positive anomaly in the Amundsen, Bellinghousen and Weddell Seas and negative anomalies near New Zealand and the eastern coast of South America. A positive pressure anomaly in the central Weddell Sea resulted in southerly wind and ice drift anomalies near the prime meridian. This situation occurred in July-October 2004 (Fig. 7.13b) and created a negative anomaly of ice draft and concentration at AWI-229. During this time, the anomalies of both *Niño*-Indices were in a positive phase. The correlation of the *Niño*1+2-Index anomaly and the geopotential height field over the Weddell Sea was similar to *Niño*3.4 during 2001-2005, but also statistically significant over the southern and western Weddell Sea.

The other negative and positive anomalies in the ice draft, e.g. in 2003 or 2005, were found to be a result of the combined effects of the patterns of PSA, SAO and *El Niño*, i.e. ice draft minima during ice drift anomalies from southeast of AWI-229 and ice draft maxima during ice drift anomalies from northwest of AWI-229. None of the parameters or climate indices shows a significant trend over the period 2001-2005. Therefore, it remains unclear why the ice draft shows the trend of -3 cm per year. However, *Schwegmann* [2012] found a decrease of the westerly winds over the eastern Weddell Sea for the period 1979-2006. The trends point to a more southerly direction, which could explain the decreasing ice thickness at AWI-229.

AWI-231

The correlations with anomalies of the filled 12-year draft time series were again very weak. The two periods 1996-1998 and 2005-2007 with measured data were therefore analysed separately. The first time series is called 231-a henceforth and includes the data of AWI 231-1 and AWI 231-2. The second time series is called 231-b and includes the data of AWI 231-6 and AWI 231-7. All anomalies the ice draft was correlated with were calculated with the respective base periods (1996-1998 and 2005-2007).

Table XVII: Correlations with monthly ice draft anomalies for AWI-231 (1996-1998)

EOFs marked with ● are shown in figures further below.

AWI 231-a	lag	r	r ²	r _{sp}	PHC
Local					
MIT Model Ice Thickness	-1	0.49 (99%)	0.24	0.59 (99%)	/
FESOM Model Ice Thickness	0	0.83 (99%)	0.69	0.79 (99%)	/
Ice Concentration (SSM/I)	1	0.53 (99%)	0.28	0.39 (99%)	/
ECMWF Air Temp. (surface)	1	-0.71 (99%)	0.5	-0.55 (99%)	/
ECMWF Z-Wind (surface)	-2	-0.44 (99%)	0.19	-0.35 (99%)	/
ECMWF M-Wind (surface)	1	0.32 (95%)	0.1	0.28 (95%)	/
Regional					
● EOF-1 Concentration (SSM/I)	0	0.67 (99%)	0.45	0.47 (95%)	/
EOF-1 Temp. (surface)	1	-0.74 (99%)	0.55	-0.77 (99%)	/
EOF-1 M-Wind (surface)	1	0.39 (99%)	0.15	0.27 (68%)	/
EOF-1 M-Drift	1	0.39 (95%)	0.15	0.34 (68%)	/
Large-Scale & Hemispheric					
PSA-Index	0	-0.45 (95%)	0.2	-0.32 (68%)	/
SAM-Index	-1	-0.48 (99%)	0.23	-0.37 (68%)	/
SAO-Index	-2	-0.44 (99%)	0.19	-0.36 (95%)	/
ZW3-Index	-1	-0.42 (99%)	0.28	-0.39 (95%)	/
EOF-1 GPH (1000-925 hPa)	-1	-0.69 (99%)	0.48	-0.64 (99%)	/

AWI 231-a local correlations:

A significant correlation with thickness data from the MIT model was found, with the model data lagging the measured ice draft by one month (see Table XVII). The FESOM model ice thickness shows an even higher correlation with the ice draft during 1996-1998 at lag 0. The ice thickness at AWI 231-a was strongly influenced by surface air temperatures and also associated with ice concentrations. The time lag of one month indicates that declining temperatures

went along with rising ice concentrations and were followed by increasing ice thickness. The correlations with air temperature and ice concentration were also significant at lag 0. The relatively weak correlation with meridional winds suggests that cold temperatures at AWI-231 were not exclusively determined by southerly winds (see figure 7.14). The negative correlation with zonal winds shows a time lag of -2 months, i.e. anomalously thick ice was followed by weak westerly winds (see climate mode correlation below).

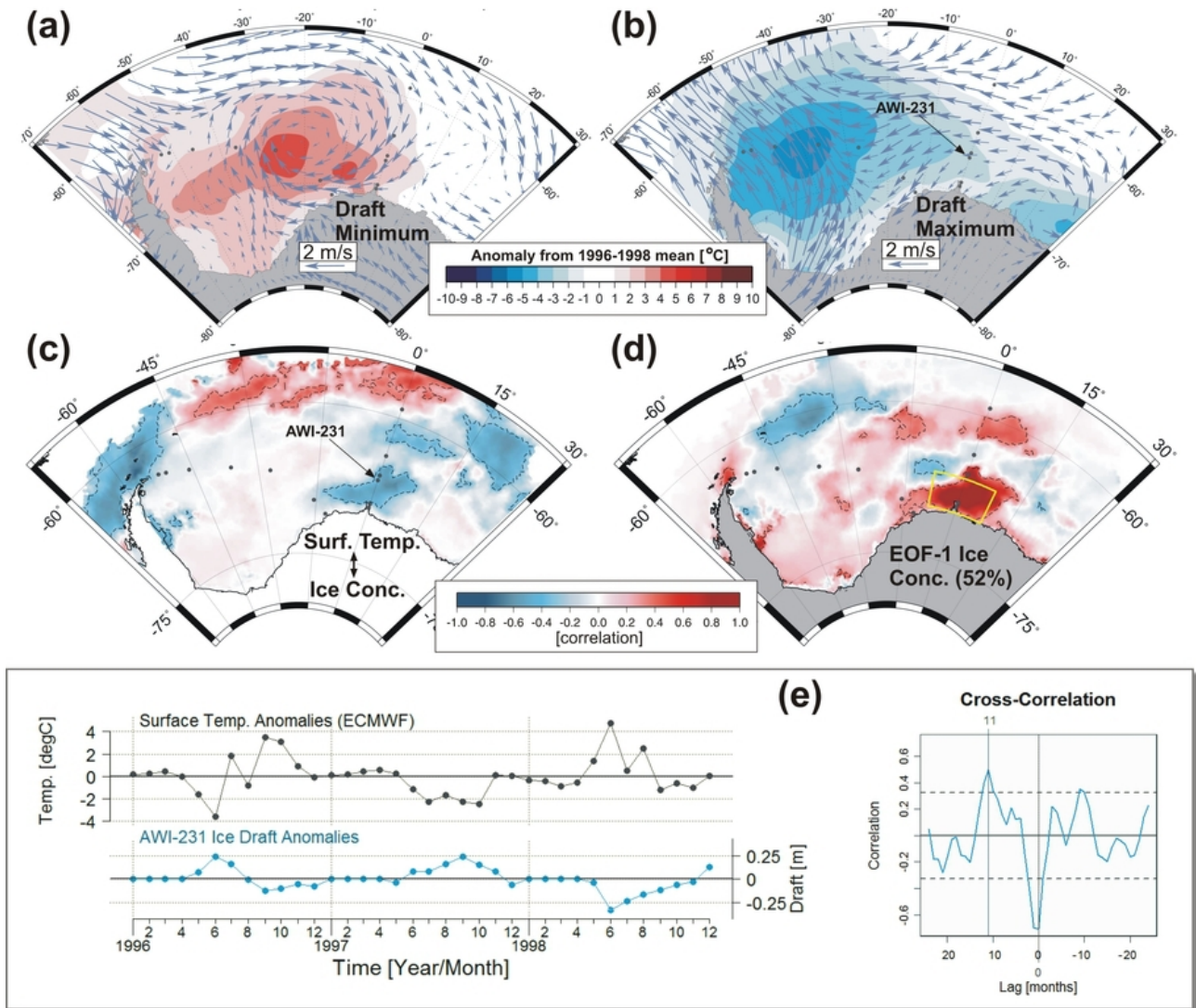


Fig. 7.14: (a) Anomalies of surface air temperature and surface wind (both ECMWF), averaged over June and July 1998 (draft minimum). (b) Anomalies of surface air temperature and surface wind, averaged over September and October 1997 (draft maximum). (c) Correlation between mean surface air temperature in the region 8°W - 8°E longitude and 66.5°S - 69°S latitude and ice concentration (SSM/I) during 1996-1998. (d) Leading EOF pattern of ice concentration for the period 1996-1998 (see figure 7.5 for more information). Dashed lines: 95% statistical confidence based on t tests. (e) Local anomalies of surface air temperature and ice draft at AWI-231 (base period 1996-1998). Right: Cross-correlation plot for both time series. Dashed lines: 95% confidence limits [Chatfield, 1984].

AWI 231-a regional/hemispheric correlations:

The mechanisms described in the following can be regarded as valid also for AWI-229 in this period (Fig. 7.4). Except for air temperature, the correlations with EOFs were highest, when the EOF domain was slightly shifted southward of AWI-231 (Fig. 7.14). The leading EOF pattern of ice concentration was confirmed by box regression (see section 4.2). The EOF pattern of air temperature (not shown) has a monopole structure. A similar monopole structure was found for the leading EOFs of meridional wind and drift. The positive correlations of ice draft with these modes indicate that thicker ice was advected from south of AWI-231. This is also suggested by the time lag of one month. Both EOFs (meridional wind and drift) are significantly correlated ($r = 0.67$, $r_{sp} = 0.56$).

Figure 7.14 shows situations of a draft minimum in 1998 and a draft maximum in 1997 and how air temperatures affected ice concentrations around AWI-231. During the period June-July 1998 a large low-pressure anomaly over the Weddell Sea - indicated by vortex-shaped wind anomalies - created positive air temperature anomalies over the central Weddell Sea and parts of the prime meridian. During the period September-October 1997 a strong high pressure anomaly over the Amundsen/Bellinghausen Seas and the Antarctic Peninsula created strong southerly wind anomalies in the central Weddell Sea which were associated with negative temperature anomalies spreading across the entire Weddell Sea. At the same time, a small high pressure anomaly at 25°E longitude carried cold air to the eastern Weddell Sea. This demonstrates how the air temperature anomalies affected the sea ice concentration around AWI-231 and, in turn, sea ice thickness.

The pressure anomalies during the discussed draft minimum and maximum did not show clear associations with patterns of SAM, SAO, PSA or ZW3. Moreover, the correlations with indices of SAM, SAO, PSA and ZW3 together with the time lags suggest that sea ice thickness was not influenced by these modes. It rather seems that changes in sea ice thickness at AWI-231 displayed the onset of changes in large-scale atmospheric circulation in the period 1996-1998. Only the correlation between ice draft and the PSA-Index was equally high for lag 0 and lag 1. This indicates the association of surface air temperature in the Weddell Sea with the intense central pressure system of the PSA pattern in 1996-1998. The leading hemispheric EOF pattern of geopotential height (1000-925 hPa, not shown) for 1996-1998 describes a dipole pattern with one pole of very high variability in the Amundsen/Bellinghausen Seas and another pole spreading over large parts of the South Pacific. This can be attributed to the exceptionally strong *El Niño* event in 1997/1998. However, correlations of sea ice draft with the indices of ENSO were not found.

AWI 231-b local correlations:

The driving mechanisms of variations of sea ice draft at AWI 231-b were difficult to determine. At AWI 231-b there is a high correlation with thickness data of the MIT model (see Table XVIII). The correlations with FESOM data are lower, but show two significant peaks, one at lag 0 and one at lag 3. Interestingly, a significant negative correlation with surface air temperature could only be found for the ice draft lagging the temperature by three months. No significant correlation exists at smaller lags. The same applies to the sea level pressure. The FESOM model seems to simulate the phenomenon. An analysis of sea ice concentration and surface air temperature showed the highest correlations in the Weddell Sea between 30°W and 20°E longitude when the concentration lags the temperature by three months. However, the reason for this time lag remains unclear. Possibly, surface processes - such as snow accumulation and snow melt - played a role in delaying the effect of temperature on ice thickness. In the

correlation between data from FESOM and ULS, the peak at lag 3 results from air temperature and the peak at lag 0 from meridional ice advection. The latter can be concluded as both time series show the same lag of one month when correlated with the meridional ice drift.

The position of AWI-231 is close to the Antarctic Coastal Current, in which the direction of the ice drift is clearly from east to west and less variable than further north. The negative correlation with zonal ice drift can therefore be interpreted as an increased degree of ice ridging for decreasing ice drift anomalies, i.e. a stronger westward flow (note that negative ice drift is from east to west). The positive correlation with meridional ice drift anomalies with a time lag of one month indicates advection of thicker ice from higher latitudes.

AWI 231-b regional/hemispheric correlations:

The EOF domain was centred on the position of AWI-231: 8°W-8°E longitude and 63.5°S-69.5°S latitude. Only the domain for the meridional ice drift was shifted southward, like in the example of AWI 231-a (see above), as the correlations were higher in this case.

Table XVIII: Correlations with monthly ice draft anomalies for AWI-231 (2005-2007)

AWI 231-b	lag	r	r ²	r _{sp}	PHC
Local					
MIT Model Ice Thickness	0	0.61 (99%)	0.37	0.66 (99%)	/
FESOM Model Ice Thickness	0	0.36 (99%)	0.13	0.42 (99%)	/
	3	0.5 (99%)	0.25	0.42 (99%)	/
Ice Concentration (SSM/I)	0	0.62 (99%)	0.38	0.51 (99%)	/
ECMWF Air Temp. (surface)	3	-0.76 (99%)	0.58	-0.69 (99%)	/
ECMWF Sea Level Pressure	3	0.55 (99%)	0.3	0.54 (99%)	/
Z-Drift	0	-0.37 (95%)	0.14	-0.28 (68%)	7-9 (-)
M-Drift	1	0.43 (99%)	0.18	0.31 (99%)	/
Regional					
EOF-1 Concentration (SSM/I)	0	0.61 (99%)	0.37	0.55 (99%)	/
EOF-1 Surface Temp. (ECMWF)	3	-0.73 (99%)	0.53	-0.7 (99%)	/
EOF-1 SLP (ECMWF)	3	0.52 (99%)	0.27	0.52 (99%)	/
EOF-1 Z-Drift	0	-0.36 (95%)	0.13	-0.42 (95%)	7-9 (-)
EOF-1 M-Drift	1	0.41 (99%)	0.17	0.31 (99%)	/
Large-Scale & Hemispheric					
<i>Niño</i> 3.4-Index (anomaly)	1	-0.5 (99%)	0.25	-0.48 (99%)	/
<i>Niño</i> 1+2-Index (anomaly)	1	-0.5 (99%)	0.25	-0.48 (99%)	/

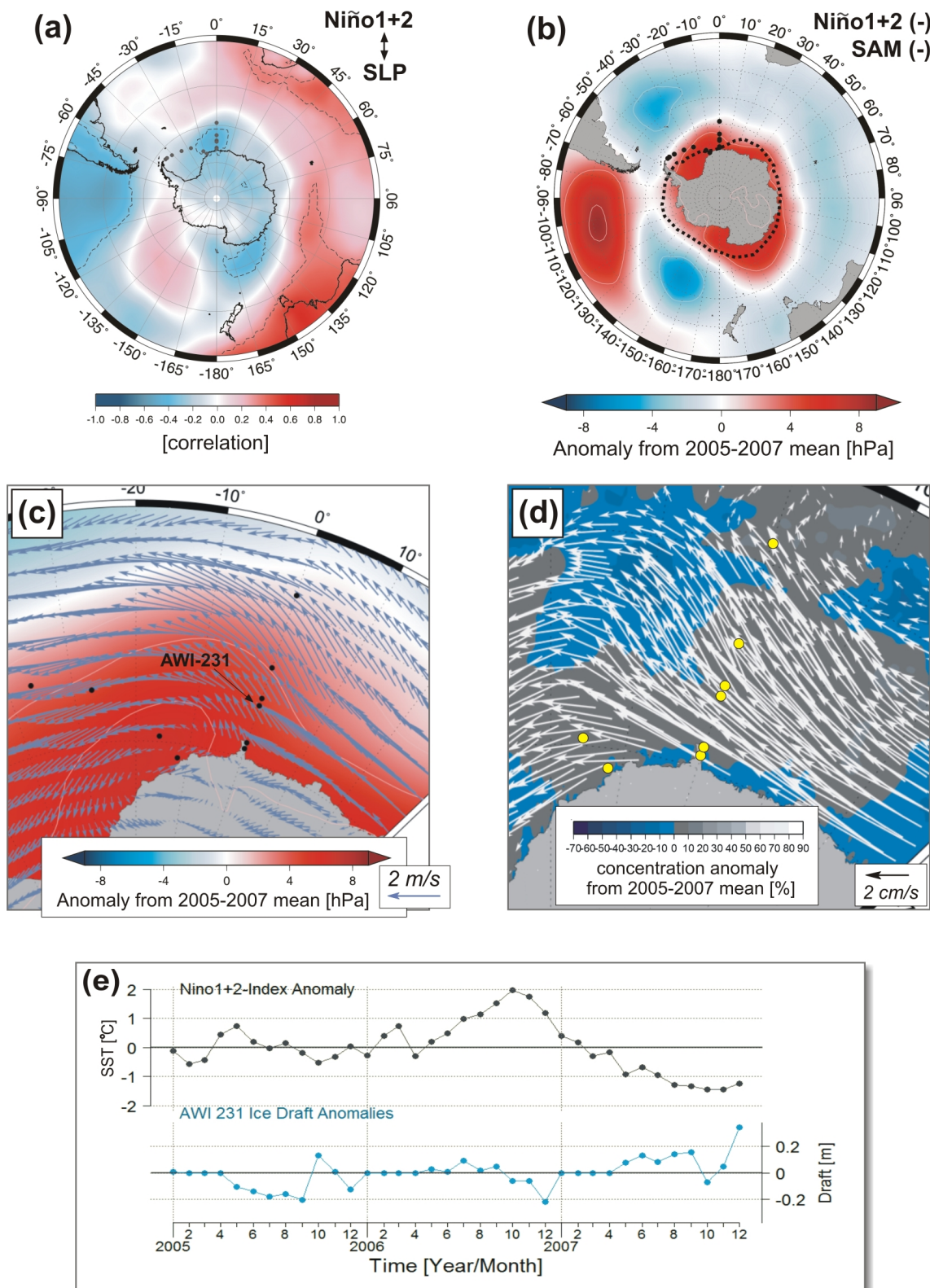


Fig. 7.15: (a) Correlation between the *Niño*1+2-Index anomaly and sea level pressure (ECMWF) for 2005-2007. Dashed lines: 95% statistical confidence based on t tests. (b) Sea level pressure anomalies (ECMWF), averaged over May-August 2007. The black dotted line marks the influence of SAM on sea level pressure during 2005-2007. (c) Anomalies of surface wind and sea level pressure (both ECMWF), averaged over May-August 2007. (d) Anomalies of ice drift and ice concentration (SSM/I), averaged over May-August 2007. (e) Anomalies of the *Niño*1+2-Index (black) and ice draft (blue) at AWI 231-b (base period 2005-2007).

Contrary to AWI 231-a, the EOF for ice concentration was centred on AWI-231, because the region of highest variability spread over a larger area, reaching up to AWI-229. Overall, the correlations with regional EOF patterns reflect the local correlations discussed above.

The sea ice draft of AWI 231-b is significantly correlated with both indices of ENSO (see Table XVIII). This relation is discussed exemplarily for the anomaly of the *Niño*1+2-Index, as this index showed stronger associations with other parameters (e.g. sea level pressure) than the *Niño*3.4-Index. Figure 7.15a shows negative correlations of sea level pressure with the *Niño*1+2-Index anomaly in the southeast Pacific and close to the Antarctic continent on the prime meridian and off Oates Land. The pattern was slightly weaker for the *Niño*3.4-Index. The *Niño*1+2-Index was also positively correlated with surface air temperature at AWI-231 and further north on the prime meridian. This correlation was associated with air pressure over the prime meridian, i.e. advection of warm air from northwest of AWI-231 during a high index state and advection of cold air from southeast of AWI-231 during a low index state.

During the draft maximum in the period May-August 2007 (Fig. 7.15e), the SAM was in a very low state. A low SAM-Index is associated with a more or less symmetric high pressure anomaly over the Antarctic continent (see section 2.5). In 2007 the low SAM-Index was responsible for strong easterly wind and ice drift anomalies (drift: up to 7.5 cm/s) in the eastern Weddell Sea (Fig. 7.15d). This resulted in ridging processes, as indicated by the ice draft statistics of AWI 231-7 and AWI 232-8 (see section 6.2). In the same period, a moderate *La Niña* event (low *Niño*-Indices) was associated with anomalously high pressure in the southeast Pacific, on the prime meridian and off Oates Land (Fig. 7.15b). These anomalies superimposed onto the SAM pattern and resulted in a slight asymmetry of the high pressure anomaly. The easterly wind anomalies associated with the low SAM-Index therefore received a southerly component near the prime meridian, and thick ice was advected from the coast towards AWI-231. The measured sea ice draft was therefore determined by a combined effect of low indices of SAM and *Niño*. The correlation of ice draft with the SAM-Index for 2005-2007 was not significant, as the correlation with SAM only occurred in 2007.

During the ice draft minima in 2005 and at the end of 2006 the ice drift in the eastern Weddell sea was anomalously low. However, the ice was less deformed in 2005 (see section 6.2) than during the strongly positive anomaly of *Niño*1+2 in 2006. This indicates that also other processes, like advection of cold and warm air, contributed to the variations of sea ice thickness at AWI-231 in the period 2005-2007. As the sea ice thickness at AWI-231 seems to respond consistently to variations in surface air temperature over long time scales, the negative trend in air temperature in this region [Schwegmann, 2012] can be expected to result in a positive trend in ice thickness. Correlations in both periods of AWI-231 are compared in table XIX.

Table XIX: Significant local/regional correlations with ice draft at AWI-231

Large symbols denote correlations with $|r| \geq 0.5$ and/or $|r_{sp}| \geq 0.5$.

Parameter	AWI 231-a	AWI 231-b
MIT model	+	+
FESOM model	+	+
Air Temperature	—	—
Air Pressure (or GPH)		+
Ice Concentration	+	+
Zonal Wind		
Meridional Wind	+	
Zonal Drift		-
Meridional Drift	+	+
<i>Niño</i> -Indices		—
PSA-Index	-	

AWI-232

Compared to AWI-229 and AWI-231, the quality of the filled 12-years time series of AWI-232 was considered better for two reasons: (1) The unrealistic peak in the year 2000 is not present and (2) the spectral analysis in the previous chapter suggested that the filled draft time series contains oscillations which are also present in time series of ice concentration and ice drift. However, some care is required as the time series north of AWI-232 were used to fill the record of AWI-232 (see chapter 5). The following discussion therefore also includes the separate analysis of the measured years 2000-2004. At AWI-232 the direction of the ice drift is clearly defined by the coastal current, i.e. the ice drifts from east to west all the year. The EOFs were therefore calculated for positions east of AWI-232.

Table XX: Correlations with monthly ice draft anomalies for AWI-232 (2000-2004)

EOFs marked with • are shown in figures further below.

AWI-232	lag	r	r ²	r _{sp}	PHC
Local					
Ice Concentration (SSM/I)	0	0.28 (99%)	0.08	0.18 (68%)	/
ECMWF Air Temp. (surface)	1	-0.22 (95%)	0.05	-0.17 (68%)	4-7 (-)
Z-Drift	2	0.33 (99%)	0.11	0.16 (95%)	/
Regional					
EOF-1 Surface Temp. (ECMWF)	1	-0.33 (99%)	0.11	-0.38 (99%)	/
• EOF-1 M-Wind (1000-500 hPa)	0	0.25 (99%)	0.06	0.29 (99%)	6-10 (+)
EOF-1 Z-Drift	3	0.36 (99%)	0.13	0.3 (99%)	/
Large-Scale & Hemispheric					
<i>Niño</i> 1+2-Index (anomaly)	2	-0.56 (99%)	0.31	-0.55 (99%)	/
PSA-Index	1	0.33 (95%)	0.11	0.27 (95%)	/
• ZW3-Index (1000-500 hPa)	0	0.41 (99%)	0.17	0.38 (99%)	6-12 (+)

AWI-232 correlations (1996-2007):

As the length of the ice season differs from year to year, a significant amount of the annual cycle remained in the ice draft anomalies. The remnant of the annual cycle was removed by identifying the EOFs of the annual cycle by SSA (see previous chapter), fitting them to the data and subtracting them. The correlations found for the 12-years time series were low. As indicated by the analyses of AWI-207, AWI-229 and AWI-231, the forcings of ice thickness and the ice conditions may change from year to year. The highest correlation with ice draft was found for EOF-1 of meridional wind anomalies over Dronning Maud Land (Fig. 7.16), i.e. thick ice was measured at AWI-232 during strong southerly wind anomalies. The correlations were highest for winds averaged over 1000-500 hPa ($r = 0.43$ [99%], $r_{sp} = 0.46$ [99%]).

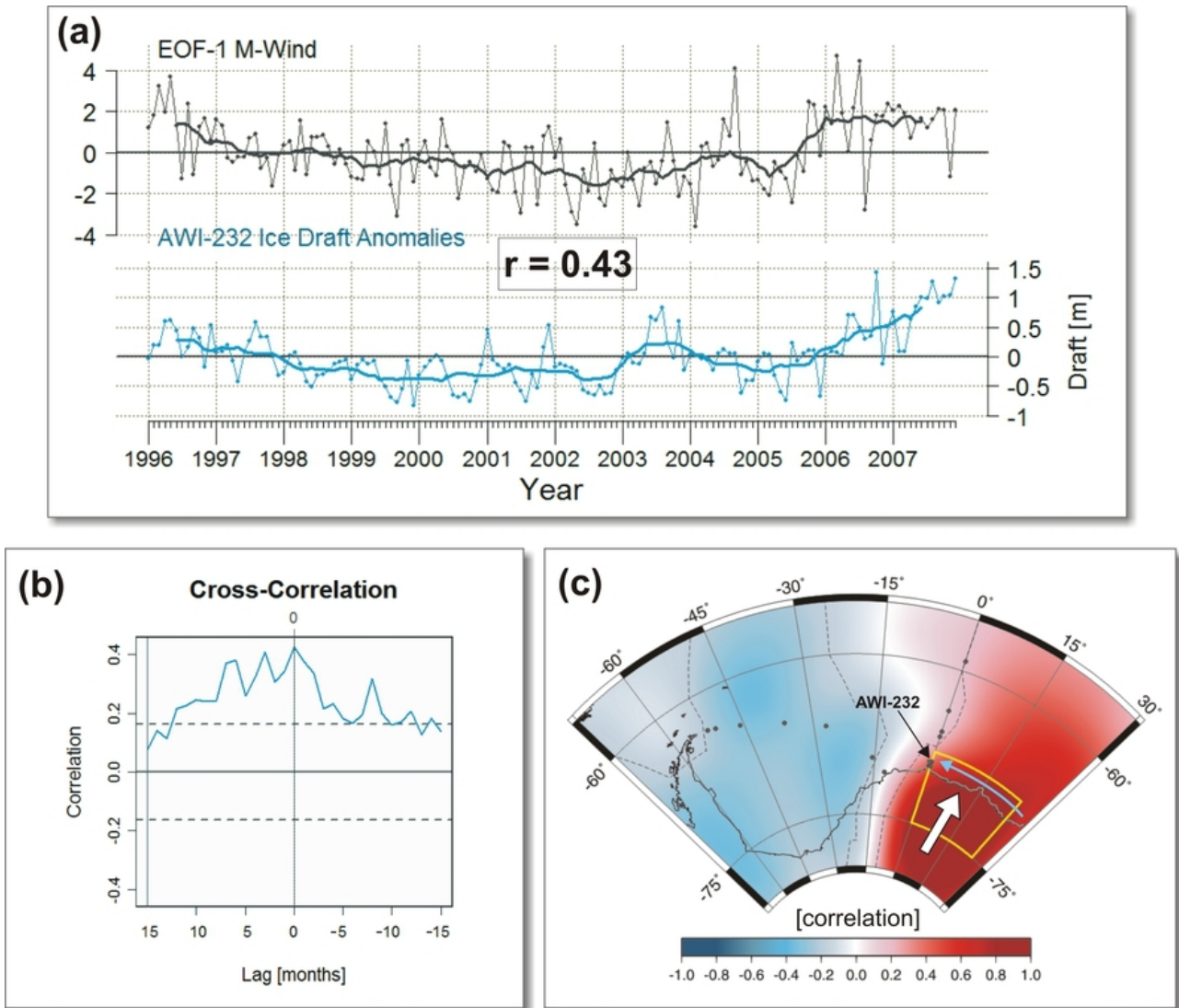


Fig. 7.16: (a) Black: Principal component of the leading EOF mode of meridional wind anomalies (NCEP, 1000-500 hPa) over Dronning Maud Land. Blue: Ice draft anomalies at AWI-232 of the filled (M-SSA, see section 4.2) 12-years time series (see also figure 7.4). Thin lines: monthly means. Bold lines: 12-months running means. (b) Cross correlation plot for both time series. Dashed lines: 95% confidence limits [Chatfield, 1984]. (c) Leading EOF pattern of meridional winds. Yellow frame: EOF domain. White arrow: Wind direction for situations of thick ice at AWI-232. Blue arrow: Flow direction of the coastal current. Dashed lines: 95% statistical confidence based on t tests.

But also for near-surface winds the correlation was significant. This indicates that the katabatic winds blowing from the Antarctic continent affect the sea ice thickness in the coastal current. The cross-correlation (Fig. 7.16) shows that the correlation is positive over a wide range of lead-lag relationships. But the slight asymmetry of the graph indicates that the relation in which the winds lead the ice thickness is stronger. The long time scales of up to one year suggest that the winds affect ice thickness over a large region east of AWI-232. Several mechanisms are conceivable for the correlation: (1) The winds create coastal polynyas. This initiates the production of new ice which is then transformed by ridging into thicker ice. (2) The winds drive thicker ice away from the coast, which is then measured by the ULS. (3) The katabatic winds result in

cold temperatures over the coastal ocean, which favours ice growth. The wind EOF and mean surface air temperatures in the northern, oceanic part of the EOF domain are significantly correlated ($r = -0.45$ [99%], $r_{sp} = -0.48$ [99%]). The correlation of ice draft with surface air temperatures is only significant for the months April-June ($r = -0.39$ [95%], $r_{sp} = -0.44$ [99%]), i.e. for the growth phase of the ice. Correlations with ice concentration (SSM/I) over the full year are weak, as they are positive over the first half of the year and negative over the second half. This means that thick new ice had a high concentration and thick, deformed first-year ice a low concentration later in the year. Next, only the measured years 2000-2004 are discussed.

AWI-232 local correlations (2000-2004):

No correlations could be found for the MIT and FESOM models. This indicates that the models still fail to simulate the complex processes of ice deformation. The correlation with ice concentrations is again very weak and barely significant for the rank correlation (Table XX). The same applies to surface air temperature. The latter correlation increases when only the months April to July - i.e. months in the growth phase - are considered: ($r = -0.59$ [99%], $r_{sp} = -0.62$ [99%]). The correlation with zonal ice drift is significant for time lags of 1-3 months. The correlation with zonal surface wind anomalies is significant only for the months March-June ($r = 0.5$ [99%], $r_{sp} = 0.65$ [99%]). Both correlations indicate that a slow ice drift in the coastal current is followed by thicker ice, which contradicts the assumption of ice ridging and thickening due to fast ice drift (note that positive in zonal direction is from west to east). However, the mean zonal and meridional wind anomalies east of AWI-232 were found to be significantly correlated with positive sign, i.e. strong southerly wind anomalies are associated with strong westerly wind anomalies. This means that thick ice at AWI-232 could be more related to southerly winds and meridional ice advection, which would be associated with a slowdown of the coastal current. This seems possible as the coastal current is mainly driven by easterly winds [*Núñez-Riboni and Fahrbach, 2009*]. A slow ice drift in the coastal current might also mean that less thinner ice from further east is advected over the ULS position. However, results from the MIT model indicated that during the period 2000-2004 the ice east of AWI-232 was not significantly thinner than the ice at AWI-232 and further west.

AWI-232 regional/hemispheric correlations (2000-2004):

Except for meridional wind, the EOFs were calculated for the oceanic part of the wind EOF shown in figure 7.16, i.e. $0^{\circ}\text{W}-25^{\circ}\text{E}$ and $68^{\circ}\text{S}-70^{\circ}\text{S}$. The correlation with surface air temperature and the time lag of one month confirms that the ice thickness measured at AWI-232 is to some extent influenced by the air temperature east of the ULS position. This correlation is also significant for a lag of two months, albeit weaker. The correlation with the katabatic winds is lower compared to the full 12-years period (Table XX), but slightly increases when only the months June-October are considered ($r = 0.36$ [99%], $r_{sp} = 0.32$ [95%]). The correlation with zonal ice drift (see above) is also confirmed by the EOF correlation.

The highest correlation with ice draft was found for the *Niño*₁₊₂-Index. The significant time lags span the period 1-5 months. No correlation between the index and ice concentrations around AWI-232 could be found. The index correlated significantly with zonal winds and ice drift across the Weddell Sea (see below). A positive correlation was found for the surface air temperatures over the continent in the region of the wind EOF shown in figure 7.16. Figure 7.17a shows the influence of *Niño*₁₊₂ on sea level pressure. The influence is significant roughly in the PSA regions, with the pressure system near New Zealand slightly shifted eastward and the Atlantic pressure system stretched to the prime meridian. This also explains to some extent

the low correlation with the PSA-Index: The index was calculated for the centres of the three typical pressure systems of PSA¹⁰. If the systems migrate, the index does not capture the full variability any more. This is also the reason for the comparably weak response of the index (Fig. 2.17) to the strong *El Niño* event in 1997/1998, compared to the weaker *El Niño* in 1991/1992.

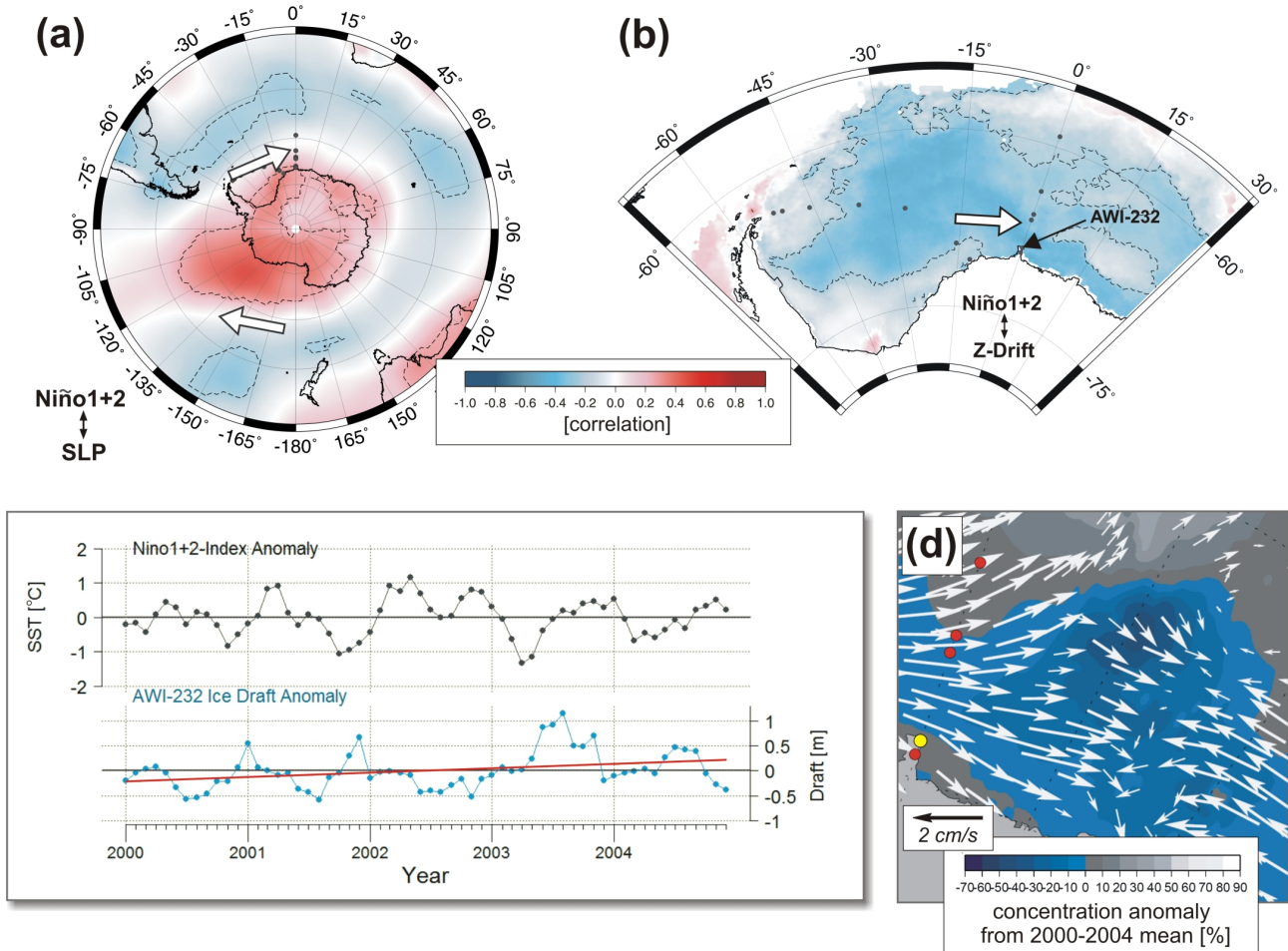


Fig. 7.17: (a) Correlation of the *Niño*1+2-Index anomaly with sea level pressure anomalies (ECMWF) for the period 2000-2004. Dashed lines: 95% statistical confidence based on t tests. The white arrows indicate the direction of the flow anomalies (wind and ice drift) for situations of thick ice at AWI-232, i.e. a low *Niño*1+2-Index. (b) Correlation of the *Niño*1+2-Index anomaly with zonal ice drift anomalies for the period 2000-2004. (c) Anomalies of the *Niño*1+2-Index (black) and ice draft at AWI-232 (blue). Base period: 2000-2004. The red line shows the statistically significant trend of +9 cm ice draft per year. (d) Anomalies of ice drift and concentration (SSM/I), averaged over a period of thick ice at AWI-232 (April-June 2003). The situation shows ice drift convergence east of AWI-232 (yellow circle).

The highest impact of *Niño*1+2 on pressure during 2000-2004 was in the central Amundsen Sea system and also in parts of the Weddell Sea (Fig. 7.17). Due to this configuration, the *Niño*1+2-Index was associated with zonal winds and ice drift in the Weddell Sea. Figure 7.17d

¹⁰See Yuan and Li [2008].

suggests that the westerly winds may have encountered easterly winds in the region east of AWI-232, which caused convergence in the ice drift and was associated with dynamical ice thickening. The ZW3 pattern for 2000-2004 is shown in figure 7.18a. The correlation of ice draft with this index shows significant time lags of 1-2 months. The katabatic winds are part of this pattern and affected the surface air temperature east of AWI-232 (Fig. 7.18b). But a high ZW3-Index also reduced the westward drift in the Weddell Sea (Fig. 7.18c).

The following examples explain the ice draft minimum in 2002 and the draft maximum in 2004. During the first half of 2002 the *Niño*1+2-Index was in a very high state, which caused fast ice drift in the coastal current east of AWI-232. At the same time, the ZW3-Index was in a negative state, i.e. the region east of AWI-232 was influenced by northerly winds which created positive average air temperature anomalies of about 3-4°C. Contrary, in early 2004 the *Niño*1+2-Index was in a low state and the ZW3-Index was positive. The strong southerly winds from the continent created negative air temperature anomalies of 2-3°C above the coastal current, which was followed by thick ice at AWI-232 a few months later.

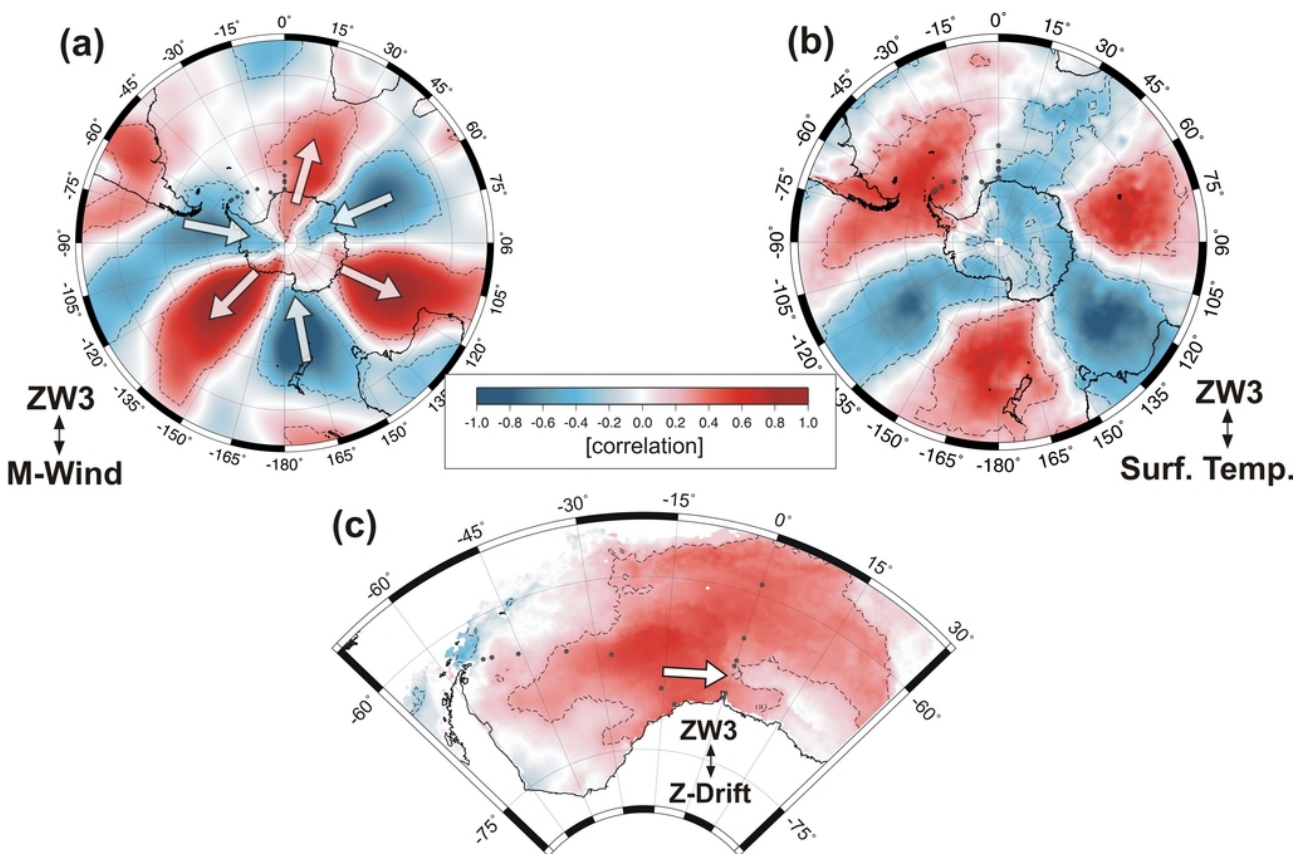


Fig. 7.18: (a) Correlation of the ZW3-Index (1000-500 hPa) with meridional wind anomalies for the period 2000-2004, showing its EOF pattern. The white arrows indicate the direction of the flow anomalies (wind and ice drift) for situations of thick ice at AWI-232, i.e. a high ZW3-Index. (b) Correlation of the ZW3-Index with surface air temperature anomalies (ECMWF) for the period 2000-2004. (c) Correlation of the ZW3-Index with zonal ice drift anomalies for the period 2000-2004.

For the big ice draft anomaly in 2003 the relations with *Niño*1+2 and ZW3 were less obvious. It has to be noted that the drift data from SSM/I have some weaknesses, especially near the coast and in zonal direction [Schwegmann *et al.*, 2011]. Strong southerly winds east of AWI-232

also caused a negative air temperature anomaly in 1996, a year in which very thick ice was measured.

The ice draft anomalies at AWI-232 show a statistically significant positive trend of 9 cm per year over the period 2000-2004. The only parameter showing a significant trend (+0.13 m/s per year) over the same period is the mean meridional wind anomaly in the EOF region east of AWI-232 (Fig. 7.16). The anomalies of the mean air temperatures east of AWI-232 showed a statistically significant trend of -1°C over 2002-2004 and the anomalies of the mean meridional ice drift a statistically significant trend of +0.36 cm/s per year over 2001-2004. This suggests that both thermodynamics and ice advection contributed to the trend in ice draft over 2001-2004. A trend in meridional winds is consistent with the positive trend in ZW3 [*Raphael, 2007*] and the increasing meridional ice drift around Antarctica [*Holland and Kwok, 2012*]. The ice thickness at AWI-232 can therefore be expected to further increase in the coming years. But the EOF-based ZW3-Index [*Yuan and Li, 2008*] used here shows a statistically significant positive trend only during the period 2003-2007. To what extent both types of the ZW3-Index are different should be further investigated (see also figure 2.20).

To account for processes of ice deformation, divergences/convergences of ice drift were calculated for different regions centred on the ULS position and east of the position, but without success. This can be attributed to a low quality of the drift data or to the fact that ice deformation is a very small-scale process which can not be resolved by the drift data.

7.3 Summary

The measured sea ice thickness at the tip of the Antarctic Peninsula (AWI-207) shows a strong decline between 1991 and 2007. In 1991 and 1992, 3-4 m thick, deformed ice was advected from the eastern coast of the peninsula by westerly winds towards the position of AWI-207. This ice did not show any correlation with ice concentration and air temperature, and was only weakly correlated with large-scale climate modes, such as SAM, ZW3 and the *Niño*3.4-Index. It was concluded that the measured ice draft at AWI 207-2 was mainly determined by dynamical mechanisms: Intense northward ice drift along the coast together with zonal ice advection away from the tip of the peninsula. The ice draft of AWI 207-6 (2005-2007) was more determined by meridional ice advection from positions north and south of AWI-207. Furthermore, it was highly correlated with ice concentration and air temperature. The ice draft of AWI 207-6 was also significantly correlated with large-scale climate modes, such as SAM, SAO, PSA, ZW3 and *Niño*-Indices. It was found that the surface air temperature in the northwestern Weddell Sea was mainly determined by SAM and ZW3, but also to some extent by PSA and SAO. A high SAM-Index causes strong northwesterly winds that blow across the tip of the peninsula towards the central Weddell Sea [Schwegmann, 2012, and references therein]. The higher temperatures affect the sea ice concentrations in the Weddell Sea [Liu *et al.*, 2004; Yuan and Li, 2008] and can be assumed to affect sea ice thickness as well. The meridional ice drift along the peninsula in 2005-2007 was mainly determined by PSA. As the PSA shows a significant trend toward its positive phase [Yuan and Li, 2008], it could explain the significant slowdown of the ice drift along the Antarctic Peninsula, which was discussed by Schwegmann [2012]. The PSA pattern was sometimes shifted to the east. For future work, the PSA-Index should therefore be calculated based on pressure averages over three regions and not based on three grid points as done in this work. This would take the migration of the pressure systems into account. Also an EOF-based PSA-Index could be used (Fig. 4.3). The ice concentrations around AWI-207 during 2005-2007 were strongly associated with the *Niño*3.4-Index. However, the reason for this could not be found.

The measured ice draft at AWI-229 during 2001-2005 was mainly determined by ice advection. It was not determined by air temperatures but was significantly correlated with ice concentrations. The ice draft and ice concentrations were significantly correlated with the PSA-Index. Driven mainly by PSA, thicker ice was advected eastwards from the central Weddell Sea towards AWI-229 during positive phases of the index. The significant negative correlation found between ice draft and the indices of ENSO can be explained by meridional ice advection. During positive phases of the indices, it seems that thinner ice from further south was advected northward towards AWI-229. This would confirm the assumption made in the previous chapter, that the ice south of AWI-229 is on average thinner. The significant negative trend in the ice draft of AWI-229 over the period 2001-2005 can be explained by the decreasing westerly winds over the eastern Weddell Sea¹¹.

The ice draft at AWI-231 in 1996-1998 was correlated with ice concentrations and it was strongly dependent on surface air temperature. Contrary to AWI-229, southerly winds and ice drift cause advection of thicker ice on this position. There are indications that the ice draft was influenced by PSA through advection of cold air masses into the central Weddell Sea. Changes in the ice draft at AWI-231 during 1996-1998 lead changes in climate modes - such as SAM, SAO and ZW3 - by a few months. Thus, the ice draft displayed the onset of changes in large-scale

¹¹See Schwegmann [2012].

atmospheric circulation. In the period 2005-2007 the ice draft was also strongly correlated with ice concentrations and surface air temperature. During this period, the zonal ice drift in the coastal current and ice deformation also played a role. The combination of a low SAM-Index and a moderate *La Niña* event caused the advection of thick, deformed ice over the position of AWI-231 in 2007.

For the ice draft of AWI-232 in the Antarctic Coastal Current only weak correlations were found. The highest correlations with surface air temperature were found for the growth phase of the ice, i.e. the months April-July. The ice draft correlated significantly with katabatic winds east of AWI-232. The meridional winds affect the surface air temperature above the coastal current and, in turn, the ice thickness. But also the northward advection of thicker ice from the coast may have played a role in affecting the ice draft measured at AWI-232. The meridional winds are part of the ZW3 pattern which, in its positive phase, slows down the westward ice drift in the coastal current east and west of AWI-232. The correlation with zonal ice drift implies that the ice grew thicker when the drift in the coastal current was slow, which contradicts the assumption of increased ice ridging in a fast ice flow. The meridional winds east of AWI-232 have increased significantly during 2000-2004, which explains the increasing ice draft. The ice draft of AWI-232 was significantly correlated with the indices of ENSO and to some extent with the PSA-Index. This correlation is associated with a slowdown of the westward ice drift through westerly wind anomalies. The high ice thickness in 2007 was the result of high ice deformation due to a low SAM-Index in combination with a moderate *La Niña* event (see AWI-231). The assumption of ice deformation is also supported by the correlation with Warm Deep Water (WDW). Between 2005 and 2008 the ice draft correlated with the layer thickness of the WDW. This correlation suggests that the ice growth during this period was not determined by oceanic heat flux. An increase in ice thickness through deformation could also be observed in east Antarctic coastal regions over the last five years [*Jan L. Lieser*, personal communication, 2013]. Between 1998 and 2003 thermodynamic ice growth can explain the increase in the salinity of the Winter Water (WW). As suggested by the ice draft statistics in the previous chapter, the ice draft in 1999-2002 was indeed to a large extent determined by thermodynamic growth.

Overall, the MIT sea ice model performs better in simulating the variations in sea ice thickness. Only in the period 1996-1998 at AWI-231 the thickness anomalies from the FESOM model show a higher correlation with the anomalies of the measured ice draft.

"Jeder nennt klare Gedanken jene, die denselben Verwirrungsgrad aufweisen wie seine eigenen."

Marcel Proust, 1871-1922

8

Summary and Conclusions

The thickness of polar sea ice is still one of the most unknown geophysical parameters. The present study is concerned with measurements of sea ice draft as a proxy for sea ice thickness by upward looking sonars (ULS) in the Weddell Sea, Antarctica. The ice thickness can be estimated from a simple linear relation with the ice draft. The study was aimed at (1) the production of a consistent data set of Antarctic sea ice draft for climate studies and the validation of sea ice models and satellite algorithms, (2) the assessment of its quality, (3) localising significant changes in sea ice thickness and (4) the identification of its geophysical forcing mechanisms and the connections to large-scale climate variability in the Southern Hemisphere. The available ULS data from 1990-2007 were reprocessed with a sophisticated processing algorithm and thereby assimilated to a consistent quality. The measurement accuracy was estimated and discussed in detail. The obtained time series were analysed in terms of variability, statistical properties, autocorrelation and significant oscillations. Furthermore, the draft time series were correlated with atmospheric and oceanic variables - such as wind, ice drift and air temperature - to find the dominant forcing mechanisms and their connection to different modes of climate variability. Analysed were mainly ULS data from the tip of the Antarctic Peninsula (AWI-207) and on the prime meridian north of the Maud Rise sea mount (AWI-229), south of Maud Rise (AWI-231) and in the Antarctic Coastal Current (AWI-232). Additionally, the analysed draft data were compared to ice thickness data from two different sea ice models (MIT and FESOM).

A thorough error analysis confirmed the unique quality of the presented ULS data set. Normally, the accuracy of ULS data would be mainly dependent on the knowledge of the sound speed in the water column above the ULS as well as the accuracy and stability of the pressure sensor in the instrument. However, the sound speed is generally not known over long periods of time. To correct for the unawareness of the sound speed, sophisticated processing algorithms including the possibility of an interactive correction are needed. Such a correction method - such as the one used in this work - identifies open water leads in the ice and interpolates a correction line through these reference points which is used to correct the full range of data. This

method is not only aimed at the correction of errors induced by the unawareness of sound speed but also at the correction of errors induced by the instrument sensors. The method was shown to work reliably. An error estimation confirmed previous studies from the Arctic, that sea ice draft processed in such a way has an accuracy of 5-12 cm. Upward looking sonars therefore still provide the most accurate tool to measure sea ice draft and its long-term development. It was found that the quality of the processed data depends on different factors: (1) The number of open water leads in the ice. (2) A relatively stable average sound speed above the ULS. (3) The quality of the processing algorithm. (4) The experience of the data analyst. If the number of leads is low, biases of up to 0.45 m ice draft might be introduced. For such cases a sound speed model was developed, which was shown to correct the draft data with sufficient accuracy. For future work, the draft data could be corrected by using a combination of automatic/interactive data correction at times of low ice concentration and a sound speed model at times of high ice concentration.

In the time series analysis of monthly mean ice draft it was shown that the statistical quantities mean, mode and median allow for a qualitative assessment of thermodynamic ice growth and dynamic ice deformation. This analysis showed that in some years the monthly mean sea ice draft is more determined by thermodynamic ice growth, while in other years ice deformation plays a larger role. This may on the one hand indicate changing forcing mechanisms of sea ice thickness; on the other hand this could demonstrate the Eulerian character of ULS draft measurements, as the direction of the ice drift in some regions changes on a monthly scale. This is most evident in regions in which the direction of the ice drift is not clearly defined by ocean currents and persistent winds, i.e. away from the coast in the central or eastern Weddell Sea. For determining the physical forcing mechanisms of variations in sea ice thickness it is therefore recommended to deploy ULS instruments in regions of the Antarctic Coastal Current, at the eastern coast of the Antarctic Peninsula or in the northern marginal ice zone.

The maximum of thermodynamic ice growth was found to be 0.8-0.9 m in the central Weddell Sea (AWI-208/209), 0.5-0.8 m near Maud Rise in the eastern Weddell Sea (AWI-229/230/231) and up to 1 m on the prime meridian about 70 km away from the coast (AWI-232). The ice draft at the tip of the Antarctic Peninsula shows a strong decline from 1991 to 2007. In the period 1991-1992 the average maximum ice draft of 3.4 m occurred in July and October. In the period 2005-2007 the average maximum ice draft was only 1.38 m and occurred in September. In the eastern Weddell Sea at AWI-229, a statistically significant negative trend of -3 cm per year could be observed in the monthly ice draft anomalies over the period 2001-2005. At AWI-232 the monthly draft anomalies showed a statistically significant positive trend of +9 cm per year over the period 2000-2004.

A spectral analysis of the draft anomalies indicated that the ice draft exhibits significant oscillations on different time scales. The analysis suggested a possible forcing of sea ice draft by meridional ice drift and surface temperature in association with the Pacific South America (PSA) pattern at AWI-207 in the period 2005-2007. At AWI-232, the ice draft oscillates with a period of 3-4 years, which was assumed to be associated with the Weddell Sea Oscillation. This process is associated with atmospherically driven ice accumulation in the eastern Weddell Sea every 3-4 years. Further extension of the draft data set is needed to investigate the phenomenon. There are indications of a semi-annual oscillation in the ice draft at AWI-229 and AWI-232. However, based on ULS draft and model data of ice thickness it could not be concluded whether the oscillation is driven by thermodynamics or ice drift dynamics.

Detrended Fluctuation Analysis (DFA) revealed that ice draft exhibits strong autocorrelation

over long time scales of above one year. Thickness data from two sea ice models confirmed the degree of autocorrelation and showed the same value up to eight years. This strong long-range correlation was interpreted as the result of stable geographic boundary conditions and the coupling of sea ice to the ocean.

The identification of physical forcings of sea ice thickness by linear correlation was complicated mainly by four factors: (1) The Eulerian character of the ice drift. A correlation between a physical variable, such as air temperature, and ice draft may be disturbed by sudden swings in the direction of the ice drift. This could advect sea ice over the ULS footprint whose thickness might be more determined by other processes. (2) The multivariate character of the ice thickness. The ice thickness is determined by a variety of physical processes in a non-linear way. (3) The time-referenced ULS measurements. The draft time series used in this study are no spatial profiles of ice thickness. Thus, the time series may include biases induced by the erratic character of the ice drift. (4) Due to the varying ice conditions from year to year, the correlation coefficients were found to decrease with increasing length of the draft time series. For the above reasons, the ULS data have an only limited capability in determining physical ice processes in a very detailed manner. However, the linear correlations obtained in this study can explain why thicker or thinner ice was measured in different years and provide a first look on possible mechanisms that may be responsible for the observed changes in sea ice thickness. The results of the correlation analysis can be summarised as follows:

AWI-207 (Antarctic Peninsula): It could not be concluded that the strongly positive trends in air temperature over the Antarctic Peninsula are responsible for the detected decline of sea ice thickness at AWI-207. The thick ice in 1991-1992 was highly deformed. It was advected from the coast over the ULS position by westerly winds that blew across the tip of the Antarctic Peninsula. These strong wind anomalies were not found for the period 2005-2007. The ice draft in 2005-2007 was more correlated with meridional winds and drift as well as air temperature and ice concentration. It can therefore not be concluded that ZW3 was responsible for the contrasting trends in ice draft between AWI-207 and AWI-232. Contrary to the early 1990s, the ice draft was significantly correlated with climate modes, such as the Southern Annular Mode (SAM), the PSA pattern, the Semi-Annual Oscillation (SAO), Zonal Wave Three (ZW3) and *El Niño* Southern Oscillation (ENSO), through thermodynamic and dynamic processes. This large number of correlations was found as AWI-207 is deployed in a region where sea ice changes are most pronounced: The Antarctic Dipole. Due to the positive trend in most of these modes, it was concluded that the ice thickness in the northern peninsula region will further decrease in the coming years.

AWI-229 (north of Maud Rise): At AWI-229, the measured ice draft in the analysed period 2001-2005 was determined by: (1) Advection of thicker ice from the central Weddell Sea in association with the PSA-Index and (2) advection of thinner ice from further south in association with ENSO and the ZW3. The sea ice draft in this region was furthermore significantly correlated with ice concentrations. Air temperature did not play a role in determining the ice thickness. The negative trend in ice draft over the period 2001-2005 was explained by decreasing westerly winds in the eastern Weddell Sea.

AWI-231 (south of Maud Rise): At AWI-231 the ice draft was strongly influenced by surface air temperatures and also correlated with ice concentrations in the analysed periods 1996-1998 and 2005-2007. Contrary to AWI-229, the meridional ice drift in this region caused northward advection of thicker ice from higher latitudes. During 2005-2007 the ice draft at

AWI-231 was found to correlate significantly with indices of ENSO, which were associated with the meridional ice advection. The ice thickness at AWI-231 is expected to increase in the coming years, due to the negative trend in surface air temperature.

AWI-232 (coastal current): The ice draft at AWI-232 was determined by katabatic winds east of the ULS position. These meridional winds are part of ZW3 and result in cold temperatures over the Antarctic Coastal Current which influence the ice thickness in the growth season. It could not be excluded that also advection of thicker ice from the coast contributed to the measured ice draft at AWI-232. The positive trend in ice draft over the period 2000-2004 was explained by the positive trend in meridional winds. The ice thickness at AWI-232 can therefore be expected to increase in the coming years, if the meridional winds and ice drift further increase. The correlation with zonal ice drift associated with ENSO during 2000-2004 implies that the ice grew thicker when the drift was slow or that less thinner ice was advected from positions east of AWI-232. In 2007, fast ice drift associated with SAM and ENSO resulted in strongly deformed ice at AWI-232.

Sea Ice Models: Compared to the finite element sea ice model (FESOM), the variations in sea ice thickness simulated by the MIT general circulation model were found to be in closer agreement with the ULS draft data.

Overall, the ice draft in the Weddell Sea responds to climate modes, like ENSO and PSA, and is therefore associated with changes in tropical Pacific sea surface temperature variability. The Southern Annular Mode was found to play a smaller role, which agrees with previous studies of climate modes and Antarctic sea ice concentration. On the prime meridian, the correlation between ice draft and the *Niño*₁₊₂-Index increases, the closer one approaches the coast. The *Niño*₁₊₂-Index describes the sea surface temperature variability in the tropical Pacific Ocean off the coasts of Ecuador and Peru. Most of the correlations with climate modes result from "indirect" forcing of the measured sea ice draft, i.e. advection of thinner or thicker ice from other regions. A direct forcing through variations in air temperature or ice deformation by dynamic processes could be identified only in few cases. This problem indicates the limited power of time-referenced Eulerian draft measurements and demonstrates that satellite algorithms for sea ice thickness measurements from space need to be quickly developed.

However, this study provides for the first time a detailed view on changes in Antarctic sea ice thickness and their relation to large-scale climate variability in the Southern Hemisphere. The produced data set will also serve as a valuable tool for the validation of satellite algorithms and climate models.

Recommendations for future ULS deployments and ULS studies:

- The quality of the data processing strongly depends on the sampling rate of the ULS instrument. It is therefore recommended to select a sampling rate not lower than four minutes.
- As the quality of the processed data increases if the sound speed profile above the ULS is stable, the instruments should be moored not deeper than 100 m (away from the coast) and not deeper than 150 m (near or on the continental shelf). This would guarantee a stable data quality.
- More CTD measurements should be conducted during ice coverage directly on the mooring positions. This would significantly improve the quality control of sound speed models.

-
- ULS deployments should be avoided in regions of very high ice concentration to enable a high quality of the data processing. This could be assessed by investigating concentration data from SSM/I.
 - The draft data should be converted into space-referenced data by deploying the ULS instruments together with ADCP instruments.
 - To enhance the possibility of investigating correlations with climate modes, more ULS instruments should be deployed in the Antarctic Dipole region, i.e. the northwestern Weddell Sea or the Bellinghausen Sea, or in the marginal ice zone.
 - Due to the above mentioned shortcomings of ULS draft measurements, a promising way for correlation analysis with ULS data could be non-linear, multiple correlation analysis with EOFs of regional variability.

List of Acronyms

AABW	-	Antarctic Bottom Water
AAO	-	Antarctic Oscillation
AASW	-	Antarctic Surface Water
ACC	-	Antarctic Circumpolar Current
ACW	-	Antarctic Circumpolar Wave
ADCP	-	Acoustic Doppler Current Profiler
ADP	-	Antarctic Dipole
AMSR-E	-	Advanced Microwave Scanning Radiometer - Earth Observing System
ASPeCt	-	Antarctic Sea Ice Processes and Climate
AUPC	-	AWI ULS Processing Chain
AVHRR	-	Advanced Very High Resolution Radiometer
AWI	-	Alfred Wegener Institute for Polar and Marine Research
CMR	-	Christian Michelsen Research
DFA	-	Detrended Fluctuation Analysis
DMS	-	Dimethylsulfide
DMSP	-	Defense Meteorological Satellite Program
DT	-	Detection Threshold
ECMWF	-	European Centre for Medium-Range Weather Forecasts
EM	-	Electromagnetic
ENSO	-	<i>El Niño</i> Southern Oscillation
EOF	-	Empirical Orthogonal Function
ESA	-	European Space Agency
FESOM	-	Finite Element Sea Ice Ocean Model
GCM	-	General Circulation Model
GLAS	-	Geoscience Laser Altimeter System
GPR	-	Ground Penetrating Radar
GPS	-	Global Positioning System
HadISST1	-	Hadley Centre sea ice and sea surface temperature data set version 1
IGOS	-	Integrated Global Observing Strategy
IMU	-	Inertial Measurement Unit
IPCC	-	Intergovernmental Panel on Climate Change
JISAO	-	Joint Institute for the Study of the Atmosphere and Ocean (Washington)
LIDAR	-	Light Detection And Ranging
MIT	-	Massachusetts Institute of Technology
MIZ	-	Marginal Ice Zone

MSA	-	Methanesulphonic Acid
M-SSA	-	Multi-Channel Singular Spectrum Analysis
NADW	-	North Atlantic Deep Water
NASA	-	National Aeronautics and Space Administration
NCAR	-	National Center for Atmospheric Research
NCEP	-	National Centers for Environmental Prediction
NOAA	-	National Oceanographic and Atmospheric Administration
NSIDC	-	National Snow and Ice Data Center
PC	-	Principal Component
PDF	-	Probability Density Function
PSA	-	Pacific-South America Pattern
RL	-	Reverberation Level
RMS	-	Root Mean Square
SAM	-	Southern Annular Mode
SAO	-	Semi-Annual Oscillation
SAR	-	Synthetic Aperture Radar
SCAR	-	Scientific Committee on Antarctic Research
SIC	-	Sea Ice Concentration
SL	-	Source Level
SLP	-	Sea Level Pressure
SMMR	-	Scanning Multichannel Microwave Radiometer
SMOS	-	Soil Moisture and Ocean Salinity
S/N	-	Signal-to-noise Ratio
SOI	-	Southern Oscillation Index
SSA	-	Singular Spectrum Analysis
SSM/I	-	Special Sensor Microwave/Imager
SST	-	Sea Surface Temperature
SVD	-	Singular Value Decomposition
THC	-	Thermohaline Circulation
TL	-	Transmission Loss
TS	-	Target Strength
ULS	-	Upward Looking Sonar
WSBW	-	Weddell Sea Bottom Water
WDW	-	Warm Deep Water
WW	-	Winter Water
XDR	-	Extended Dynamic Range
ZW3	-	Zonal Wave Three

List of Symbols

- α - angle of incidence/ULS inclination angle
- β - compressibility of sea water
- c - sound velocity
- c_{si} - specific heat capacity of sea ice
- $c_{i,0^\circ}$ - specific heat capacity of freshwater ice at 0°C
- c_{solid} - specific heat capacity of deposited salts
- \mathbf{C}_D - lag-covariance matrix
- \mathbf{C}_R - surrogate lag-covariance matrix
- d - sea ice draft
- \mathbf{D} - SSA trajectory matrix
- \mathbf{E}_D - matrix of eigenvectors
- \mathbf{E}_R - matrix of surrogate eigenvectors
- F - sea ice freeboard
- F_L - latent heat flux
- F_w - oceanic heat flux
- F_c - conductive heat flux
- F_l - longwave heat flux
- F_{sw} - shortwave heat flux
- F_t - turbulent atmospheric sensible and latent heat fluxes
- F_a - net atmospheric heat flux
- f - Coriolis parameter (also thermodynamic growth term in $g(H)$)
- g - gravitational acceleration on Earth's surface
- $g(H)$ - sea ice thickness distribution
- γ - signal-to-noise ratio
- H - sea ice thickness
- H_{eq} - equilibrium sea ice thickness
- h - snow layer thickness
- k - heat transfer coefficient
- L_{si} - latent heat of fusion of sea ice
- L_i - latent heat of fusion of freshwater ice
- L_{solid} - latent heat of fusion of deposited salts
- λ_{si} - thermal conductivity of sea ice

λ_s	- thermal conductivity of snow
λ_i	- thermal conductivity of freshwater ice
λ_b	- thermal conductivity of brine
Λ_D	- eigenvalue matrix
Λ_R	- eigenvalue matrix of surrogates
N	- geoid height
Ω	- mechanical deformation term in $g(H)$
p	- pressure/measured pressure at ULS
p_a	- atmospheric pressure
p_h	- hydrostatic pressure
r	- correlation coefficient (Pearson)
r_{sp}	- correlation coefficient (Spearman)
R	- reflection coefficient
ρ_{si}	- density of sea ice
ρ_i	- density of freshwater ice
ρ_b	- density of brine
ρ_a	- density of air
ρ_w	- density of sea water
S_{si}	- salinity of sea ice
S_b	- salinity of brine
T	- temperature
τ_a	- wind stress vector
τ_w	- water stress vector
τ_c	- Coriolis force
τ_i	- internal ice stress
τ_t	- force due to sea surface tilt
u	- propagation velocity of a fluid parcel
\mathbf{V}_i	- vector of horizontal sea ice velocity
\mathbf{V}_a	- vector of horizontal wind velocity
\mathbf{V}_{ag}	- vector of geostrophic wind velocity
\mathbf{V}_{wg}	- velocity vector of geostrophic ocean current
V_{env}	- envelope voltage (echo amplitude)
z	- ULS depth
z_s	- snow layer thickness

References

- Abrahamsen E.P., S. Østerhus, T. Gammelsrød** (2006) *Ice draft and current measurements from the north-western Barents Sea, 1993-96*, Polar Research 25(1), 25-37
- ACIA** (2004) *Impacts of a Warming Arctic: Arctic Climate Impact Assessment.*, Cambridge University Press, Cambridge, UK.
- Ackley S., P. Wadhams, J.C. Comiso, A.P. Worby** (2003) *Decadal decrease of Antarctic sea ice extent inferred from whaling records revisited on the basis of historical and modern sea ice records*, Polar Research, 22(1), 19-25
- Allen M.R., A.W. Robertson** (1996) *Distinguishing modulated oscillations from coloured noise in multivariate datasets*, Climate Dynamics, 12, 775-784
- Allen M.R., L.A. Smith** (1996) *Monte Carlo SSA: Detecting Irregular Oscillations in the Presence of Colored Noise*, Journal of Climate, Vol. 9, 3373-3404
- Allison I.** (1979) *Antarctic sea ice growth and oceanic heat flux*, Sea Level, Ice, and Climatic Change (Proceedings of the Canberra Symposium, December 1979), IAHS Publ. no. 131
- Allison I.** (1997) *Physical Processes determining the Antarctic Sea Ice Environment*, Australian Journal of Physics, Vol. 50, 759-771
- Allison I., N.L. Bindoff, R.A. Bindshadler, P.M. Cox, N. de Noblet, M.H. England, J.E. Francis, N. Gruber, A.M. Haywood, D.J. Karoly, G. Kaser, C. Le Quéré, T.M. Lenton, M.E. Mann, B.I. McNeil, A.J. Pitman, S. Rahmstorf, E. Rignot, H.J. Schellnhuber, S.H. Schneider, S.C. Sherwood, R.C.J. Somerville, K. Steffen, E.J. Steig, M. Visbeck, A.J. Weaver** (2009) *The Copenhagen Diagnosis, 2009: Updating the World on the Latest Climate Science.*, The University of New South Wales Climate Change Research Centre (CCRC), Sydney, Australia, 60pp.
- Anisimov O.A., D.G. Vaughan, T.V. Callaghan, C. Furgal, H. Marchant, T.D. Prowse, H. Vilhjálmsson and J.E. Walsh** (2007) *Polar regions (Arctic and Antarctic)*, Climate Change 2007: Impacts, Adaptation and Vulnerability. Contribution of Working Group II to the Fourth Assessment Report of the Intergovernmental Panel on Climate Change (IPCC), M.L. Parry, O.F. Canziani, J.P. Palutikof, P.J. van der Linden and C.E. Hanson (eds.), Cambridge University Press, Cambridge, 653-685
- Arrigo K.R., T. Mock, M.P. Lizotte** (2010) *Primary Producers in Sea Ice*, In: Sea Ice (second edition), D.N. Thomas and G.S. Dieckmann (eds.), Blackwell Publishing Ltd
- Assur A.** (1960) *Composition of sea ice and its tensile strength*, SIPRE Research Report, 44
- Baba K., S. Minobe, N. Kimura, M. Wakatsuchi** (2006) *Intraseasonal variability of sea-ice concentration in the Antarctic with particular emphasis on wind effect*, Journal of Geophysical Research, Vol. 111, C12023, doi:10.1029/2005JC003052
- Babko O., D.A. Rothrock, G.A. Maykut** (2002) *Role of rafting in the mechanical redistribution of sea ice thickness*, Journal of Geophysical Research, Vol. 107, No. C8, 3113, doi:10.1029/1999JC000190
- Baede A.P.M., E. Ahlonsou, Y. Ding, D. Schimel** (2001) *The Climate System: An Overview*, Climate Change 2001: The Scientific Basis. Contribution of Working Group I to the Third Assessment Report of the Intergovernmental Panel on Climate Change (IPCC), B. Bolin, S. Pollonais (eds.), p. 85-98, Cambridge University Press, Cambridge
- Behrendt A., E. Fahrbach, M. Hoppema, G. Rohardt, O. Boebel, O. Klatt, A. Wisotzki, H. Witte** (2011) *Variations of Winter Water properties and sea ice along the Greenwich meridian on decadal time scales*, Deep-Sea Research II, 58, 2524-2532, doi:10.1016/j.dsr2.2011.07.001
- Behrendt A., W. Dierking, E. Fahrbach, H. Witte** (2012) *Sea ice draft in the Weddell Sea, mea-*

- ured by upward looking sonars, Earth System Science Data Discussions, 5, 805-851, doi:10.5194/essdd-5-805-2012
- Bernstein et al.** (2007) *Climate Change 2007: Synthesis Report*, Based on the Working Group contributions to the Fourth Assessment Report of the Intergovernmental Panel on Climate Change (IPCC), Cambridge University Press, Cambridge
- Beyer M.** (2008) *Do You Know the Accuracy of your Pressure Sensor?*, Sensor Magazin, 4, 2008, Sensor Markt
- Bigg G.** (2003) *The Oceans and Climate*, Second Edition, Cambridge University Press, New York
- Björnsson H., S.A. Venegas** (1997) *A Manual for EOF and SVD Analyses of Climatic Data*, C²GCR Report No. 97-1, available online at: <http://www.geog.mcgill.ca/gec3/wp-content/uploads/2009/03/>
- Blender B., K. Fraedrich** (2003) *Long time memory in global warming simulations*, Geophysical Research Letters, Vol. 30, No. 14, 1769, doi:10.1029/2003GL017666
- Bradley D.L., R. Stern** (2008) *Underwater Sound and the Marine Mammal Acoustic Environment: A Guide to Fundamental Principles*, Marine Mammal Commission, Bethesda, USA
- Broecker W.S.** (1991) *The great ocean conveyor*, Oceanography, 4, 79-89
- Broomhead D.S., G.P. King** (1986) *Extracting qualitative dynamics from experimental data*, Physica D, **20**, 217-236
- Bunde A., J.W. Kantelhardt** (2001) *Langzeitkorrelationen in der Natur: von Klima, Erbgut und Herzrhythmus*, Physikalische Blätter, 57, Nr. 5, 49-54
- Cai W., P.G. Baines** (2001) *Forcing of the Antarctic Circumpolar Wave by El Niño-Southern Oscillation teleconnections*, Journal of Geophysical Research, Vol. 106, No. C5, 9019-9038
- Carleton A.M.** (1988) *Sea ice-atmosphere signal of the southern oscillation in the Weddell Sea, Antarctica*, Journal of Climate, Vol. 1, 379-388
- Carleton A.M.** (1989) *Antarctic sea-ice relationships with indices of the atmospheric circulation of the Southern Hemisphere*, Climate Dynamics, 3:207-220, Springer Verlag
- Carleton A.M.** (2003) *Atmospheric teleconnections involving the Southern Ocean*, Journal of Geophysical Research, Vol. 108, No. C4, 8080, doi:10.1029/2000JC000379
- Cavalieri D.J., P. Gloersen, C.L. Parkinson, J.C. Comiso, H.J. Zwally** (1997) *Observed Hemispheric Asymmetry in Global Sea Ice Changes*, Science, Vol. 278, 1104, doi:10.1126/science.278.5340.1104
- Cavalieri D.J., C.L. Parkinson** (2008) *Antarctic sea ice variability and trends, 1979-2006*, Journal of Geophysical Research, Vol. 113, C07004, doi:10.1029/2007JC004564
- Chatfield C.** (1984) *The Analysis of Time Series: An Introduction*, Third Edition, Chapman and Hall, London/New York
- Clark P.U., N.G. Pisias, T.F. Stocker, A.J. Weaver** (2002) *The role of the thermohaline circulation in abrupt climate change*, Nature, Vol. 415, 863-869
- Collins M., S.I. An, W. Cai, A. Ganachaud, E. Guilyardi, F.F. Jin, M. Jochum, M. Lengaigne, S. Power, A. Timmermann, G. Vecchi, A. Wittenberg** (2010) *The impact of global warming on the tropical Pacific Ocean and El Niño*, Nature Geoscience, published online: 23 May 2010, doi:10.1038/ngeo868
- Comiso J.C.** (1999, updated 2008) *Bootstrap sea ice concentrations from NIMBUS-7 SMMR and DMSP SSM/I*, Boulder, Colorado USA: National Snow and Ice Data Center. Digital media.
- Comiso J.C.** (2010) *Variability and Trends of the Global Sea Ice Cover*, In: Sea Ice (second edition), D.N. Thomas and G.S. Dieckmann (eds.), Blackwell Publishing Ltd
- Connolley W.M.** (2005) *Sea ice concentrations in the Weddell Sea: A comparison of SSM/I, ULS, and GCM data*, Geophysical Research Letters, Vol. 32, L07501, doi:10.1029/2004GL021898
- Cotté C., C. Guinet** (2007) *Historical whaling records reveal major regional retreat of Antarctic sea ice*, Deep-Sea Research I 54, 243-252, doi:10.1016/j.dsr.2006.11.001
- Crepeau J.** (2008) *Josef Stefan and his contribu-*

- tions to heat transfer, Proceedings of the ASME 2008 Heat Transfer Conference, August 10-14, 2008, Jacksonville, Florida, USA
- Curran M.A.J., T.D. van Ommen, V.I. Morgan, K.L. Phillips, A.S. Palmer** (2003) *Ice Core Evidence for Antarctic Sea Ice Decline Since the 1950s*, Science Vol. 302, 1203, doi:10.1126/science.1087888
- Dee D.P., S.M. Uppala, A.J. Simmons, P. Berrisford, P. Poli, S. Kobayashi, U. Andrae, M.A. Balmaseda, G. Balsamo, P. Bauer, P. Bechtold, A.C.M. Beljaars, L. van de Berg, J. Bidlot, N. Bormann, C. Delsol, R. Dragani, M. Fuentes, A. J. Geer, L. Haimberger, S. B. Healy, H. Hersbach, E.V. Hólm, L. Isaksen, P. Kállberg, M. Köhler, M. Matricardi, A.P. McNally, B.M. Monge-Sanz, J.-J. Morcrette, B.-K. Park, C. Peubey, P. de Rosnay, C. Tavolato, J.-N. Thépaut, F. Vitart** (2011) *The ERA-Interim reanalysis: configuration and performance of the data assimilation system*, Quarterly Journal of the Royal Meteorological Society, **137**: 553-597
- de la Mare W.K.** (1997) *Abrupt mid-twentieth-century decline in Antarctic sea-ice extent from whaling records*, Nature, Vol. 389, 57-60
- de Magalhães Neto N., H. Evangelista, K. Tanizaki-Fonseca, M.S.P. Meirelles, C.E. Garcia** (2012) *A multivariate analysis of Antarctic sea ice since 1979*, Climate Dynamics, 38:1115-1128, doi:10.1007/s00382-011-1162-6
- Dieckmann G.S., H.H. Hellmer** (2010) *The Importance of Sea Ice: An Overview*, In: Sea Ice (second edition), D.N. Thomas and G.S. Dieckmann (eds.), Blackwell Publishing Ltd
- Dierking W.** (1995) *Laser profiling of the ice surface topography during the Winter Weddell Gyre Study 1992*, Journal of Geophysical Research, Vol. 100, No. C3, pages 4807-4820
- Dommenget D., M. Latif** (2002) *A Cautionary Note on the Interpretation of EOFs*, Journal of Climate, Vol. 15, 216-225
- Dommenget D., J. Flöter** (2011) *Conceptual understanding of climate change with a globally resolved energy balance model*, Climate Dynamics, 37, doi:10.1007/s00382-011-1026-0
- Doronin Y.P., D.E. Kheisin** (1977) *Sea Ice*, Amerind Publishing Co. Pvt. Ltd., New Delhi
- Drinkwater M., D.G. Long, D.S. Early** (1993) *Enhanced-Resolution ERS-1 Scatterometer Imaging of Southern-Ocean Sea Ice*, ESA Journal, Vol. 17, 307-322
- Drinkwater M., X. Liu** (2000) *Seasonal to inter-annual variability in Antarctic sea-ice surface melt*, IEEE Transactions on Geoscience and Remote Sensing, Vol. 38, No. 4, 1827-1842
- Drinkwater M., X. Liu, S. Harms** (2001) *Combined satellite- and ULS-derived sea-ice flux in the Weddell Sea*, Annals of Glaciology, Vol. 33
- Drucker R., S. Martin, R. Moritz** (2003) *Observations of ice thickness and frazil ice in the St. Lawrence Island polynya from satellite imagery, upward looking sonar, and salinity/temperature moorings*, Journal of Geophysical Research, Vol. 108, No. C5, 3149, doi:10.1029/2001JC001213
- Ducklow H.W., D.K. Steinberg, K.O. Bueseler** (2001) *Upper Ocean Carbon Export and the Biological Pump*, Oceanography, Vol. 14, No. 4, 50-58
- Dukes J.S.** (2003) *Burning Buried Sunshine: Human Consumption of Ancient Solar Energy*, Climatic Change 61: 31-44
- Ebisuzaki W.** (1997) *A Method to Estimate the Statistical Significance of a Correlation When the Data Are Serially Correlated*, Journal of Climate, Vol. 10, 2147-2153
- Eicken H.** (1992) *The role of sea ice in structuring Antarctic ecosystems*, Polar Biol., 12, 3-13
- Eicken H., M.A. Lange** (1989) *Sea ice thickness data: the many vs. the few*, Geophysical Research Letters, Vol. 16, No. 6, 495-498
- Endlicher W., F.W. Gerstengarbe** (2007) *Der Klimawandel -Einblicke, Rückblicke und Ausblicke-*, Potsdam/Berlin
- Enomoto H., A. Ohmura** (1990) *The Influences of Atmospheric Half-Yearly Cycle on the Sea Ice Extent in the Antarctic*, Journal of Geophysical Research, Vol. 95, No. C6, 9497-9511
- Fahrbach E.** (1994) *Zirkulation und Wassermassenbildung im Weddellmeer*, Die Geowissenschaften, Nr. 7, 11. Jahrgang, 246-253, Ernst & Sohn, Berlin

- Fahrbach E., M. Hoppema, G. Rohardt, M. Schröder, A. Wisotzki (2004) *Decadal-scale variations of water mass properties in the deep Weddell Sea*, *Ocean Dynamics*, 54: 77-91, doi:10.1007/s10236-003-0082-3
- Fahrbach E., G. Rohardt, R. Sieger (2007) *25 Years of Polarstern Hydrography (1982-2007)*, WDC-MARE Reports, 5, AWI, Bremerhaven and MARUM, Bremen, 94pp.
- Fahrbach E., M. Hoppema, G. Rohardt, O. Boebel, O. Klatt, A. Wisotzki (2011) *Warming of deep and abyssal water masses along the Greenwich meridian on decadal time scales: the Weddell gyre as a heat buffer*, *Deep-Sea Research II*, 58, 2509-2523.
- Feltham D.L., N. Untersteiner, J.S. Wettlaufer, M.G. Worster (2006) *Sea ice is a mushy layer*, *Geophysical Research Letters*, Vol. 33, L14501, doi:10.1029/2006GL026290
- Flato G.M. (1998) *The Thickness Variable in Sea-Ice Models*, *Atmosphere-Ocean*, 36 (1), 29-36, Canadian Meteorological Society
- Forsberg R., K. Keller, S. M. Jacobsen (2001) *Laser Monitoring of Ice Elevations and Sea-Ice Thickness in Greenland*, *International Archives of Photogrammetry and Remote Sensing*, Volume XXXIV-3/W4 Annapolis, MD, 163-168
- Forsberg R., H. Skourup (2005) *Arctic Ocean gravity, geoid and sea-ice freeboard heights from ICE-Sat and GRACE*, *Geophysical Research Letters*, Vol. 32, L21502, doi:10.1029/2005GL023711
- Foster A.F.M., M.A.J. Curran, B.T. Smith, T.D. van Ommen, V.I. Morgan (2006) *Covariation of sea ice and methanesulphonic acid in Wilhelm II Land, East Antarctica*, *Annals of Glaciology*, 44, 429-432
- Fowler C. (2003, updated 2007) *Polar Pathfinder Daily 25 km EASE-Grid Sea Ice Motion Vectors*, Boulder, Colorado USA: National Snow and Ice Data Center. Digital media.
- Francois R.E., G.R. Garrison (1982) *Sound absorption based on ocean measurements. Part II: Boric acid contribution and equation for total absorption*, *Journal of the Acoustical Society of America*, Vol. 72, Nr. 6
- Friedlingstein P., R.A. Houghton, G. Marland, J. Hackler, T.A. Boden, T.J. Conway, J.G. Canadell, M.R. Raupach, P. Ciais, C. Le Quéré (2010) *Update on CO₂ emissions*, *Nature Geoscience*, published online: 21 November 2010,
- Fukumachi Y., G. Mizuta, K.I. Ohshima, H. Melling, D. Fissel, M. Wakatsuchi (2003) *Variability of sea-ice draft off Hokkaido in the Sea of Okhotsk revealed by a moored ice-profiling sonar in winter of 1999*, *Geophysical Research Letters*, Vol. 30, No. 7, 1376, doi:10.1029/2002GL016197
- Furukawa Y. (1997) *Faszination der Schneekristalle - wie ihre bezaubernden Formen entstehen*, *Chemie in unserer Zeit*, 31. Jahrg., Nr. 2, 58-65, Wiley-VCH Verlag GmbH & Co. KGaA, Weinheim
- Garrison G.R., R.E. Francois, T. Wen (1991) *Acoustic reflections from arctic ice at 15-300 kHz*, *Journal of the Acoustical Society of America*, Vol. 90, Nr. 2, Pt 1
- Gerland S., J. Aars, T. Bracegirdle, E. Carmack, H. Hop, G.K. Hovelsrud, K. Kovacs, C. Lydersen, D.K. Perovich, J. Richter-Menge, S. Rybråten, H. Strøm, J. Turner (2007) *Ice in the Sea*, In: *Global Outlook for Ice and Snow*, J. Eamer (ed.), United Nations Environment Programme (UNEP)
- Gildor H., E. Tziperman (2003) *Sea-ice switches and abrupt climate change*, *Philosophical Transactions of the Royal Society A*, 361, 1935-1944, doi:10.1098/rsta.2003.1244
- Giles K.A., S.W. Laxon, A.P. Worby (2008) *Antarctic sea ice elevation from satellite radar altimetry*, *Geophysical Research Letters*, Vol. 35, L03503, doi:10.1029/2007GL031572
- Gille S.T. (2008) *Decadal-Scale Temperature Trends in the Southern Hemisphere Ocean*, *Journal of Climate*, Vol. 21, 4749-4765, American Meteorological Society
- Gillet N.P., T.D. Kell, P.D. Jones (2006) *Regional climate impacts of the Southern Annular Mode*, *Geophysical Research Letters*, Vol. 33, L23704, doi:10.1029/2006GL027721
- Gillet N.P., D.A. Stone, P.A. Stott, T. Nozawa, A.YU. Karpechko, G.C. Hegerl, M.F. Wehner, P.D. Jones (2008) *Attribution of polar warming to human influence*, *Nature Geoscience*, published online: 30 Oct. 2008, doi:10.1038/ngeo338

- Gloersen P.** (1995) *Modulation of hemispheric sea-ice cover by ENSO events*, *Nature*, Vol. 373, 503-506
- Gloersen P., W.B. White** (2001) *Reestablishing the circumpolar wave in sea ice around Antarctica from one winter to the next*, *Journal of Geophysical Research*, Vol. 106, No. C3, 4391-4395
- Gong D., S. Wang** (1999) *Definition of Antarctic oscillation index*, *Geophysical Research Letters*, Vol. 26, No.4, 459-462
- Graf H.** (2002) *Klimaänderungen durch Vulkane*, *promet*, Jahrg.28, Nr.3/4, 117-122, Deutscher Wetterdienst
- Granberg H.G., M. Leppäranta** (1999) *Observations of sea ice ridging in the Weddell Sea*, *Journal of Geophysical Research*, Vol. 104, No.C11, 25,735-25,745
- Gränicher H.** (1996) *Messung beendet - was nun?*, 2. Auflage, vdf Hochschulverlag, Zürich
- Groth A., M. Ghil** (2011) *Multivariate singular spectrum analysis and the road to phase synchronization*, *Physical Review E*, Vol. 84, Issue 3, doi:10.1103/PhysRevE.84.036206
- Haas C., S. Gerland, H. Eicken, H. Miller** (1997) *Comparison of sea-ice thickness measurements under summer and winter conditions in the Arctic using a small electromagnetic induction device*, *Geophysics*, Vol. 62, No. 3, 749-757
- Haas C.** (1998) *Evaluation of ship-based electromagnetic-inductive thickness measurements of summer sea-ice in the Bellingshausen and Amundsen Seas, Antarctica*, *Cold Regions Science and Technology*, 27, 1-16
- Haas C., S. Goebell, S. Hendricks, T. Martin, A. Pfaffling, C. von Saldern** (2005) *Airborne Electromagnetic Measurements of Sea Ice Thickness: Methods and Applications*, In: *Arctic Sea Ice Thickness: Past, Present and Future*, Scientific Report of the International Workshop in Rungstedgaard, Denmark, 8.-9. November 2005, P. Wadhams and G. Amanatidis (eds.)
- Haas C., M. Nicolaus, S. Willmes, A. Worby, D. Flinspach** (2008) *Sea ice and snow thickness and physical properties of an ice floe in the western Weddell Sea and their changes during spring warming*, *Deep-Sea Research II*, 55, 963-974, doi:10.1016/j.dsr2.2007.12.020
- Haas C.** (2010) *Dynamics versus Thermodynamics: The Sea Ice Thickness Distribution*, In: *Sea Ice* (second edition), D.N. Thomas and G.S. Dieckmann (eds.), Blackwell Publishing Ltd
- Haas C., S. Hendricks, H. Eicken, A. Herber** (2010) *Synoptic airborne thickness surveys reveal state of Arctic sea ice cover*, *Geophysical Research Letters*, Vol. 37, L09501, doi:10.1029/2010GL042652
- Hannachi A., I.T. Jolliffe, D.B. Stephenson** (2007) *Empirical orthogonal functions and related techniques in atmospheric science: A review*, *International Journal of Climatology*, 27, 1119-1152, doi:10.1002/joc.1499
- Hansen J., R. Ruedy, M. Sato, K. Lo** (2010) *Global Surface Temperature Change*, *Reviews of Geophysics*, 48, RG4004, doi:10.1029/2010RG000345
- Harangozo S.A.** (2006) *Atmospheric circulation impacts on winter maximum sea ice extent in the west Antarctic Peninsula region (1979-2001)*, *Geophysical Research Letters*, Vol. 33, L02502, doi:10.1029/2005GL024978
- Harms S., E. Fahrbach, V.H. Strass** (2001) *Sea ice transports in the Weddell Sea*, *Journal of Geophysical Research*, Vol. 106, No. C5, 9057-9073
- Hassani H.** (2007) *Singular Spectrum Analysis: Methodology and Comparison*, *Journal of Data Science*, 5, 239-257
- Hauck W.W., W. Koch, D. Abernethy, R.L. Williams** (2008) *Making Sense of Trueness, Precision, Accuracy, and Uncertainty*, *Pharmaceutical Forum*, Vol. 34(3), 838-842
- Hauck J., M. Hoppema, R.G.J. Bellerby, C. Völker, D. Wolf-Gladrow** (2010) *Data-based estimation of anthropogenic carbon and acidification in the Weddell Sea on a decadal timescale*, *Journal of Geophysical Research*, Vol. 115, C03004, doi:10.1029/2009JC005479
- Hense A.** (2002) *Klimavariabilität durch interne Wechselwirkungen*, *promet*, Jahrg.28, Nr.3/4, 108-116, Deutscher Wetterdienst
- Herterich K.** (2002) *Variabilität der Erdbahnparameter und Klimaänderungen*, *promet*, Jahrg.28, Nr.3/4, 117-122, Deutscher Wetterdienst
- Heywood K.J., D.P. Stevens** (2007) *Merid-*

- ional heat transport across the Antarctic Circumpolar Current by the Antarctic Bottom Water overturning cell*, *Geophys. Res. Lett.*, 34, L11610.doi:10.1029/2007GL030130
- Hobbs W.R., M.N. Raphael** (2010) *The Pacific zonal asymmetry and its influence on Southern Hemisphere sea ice variability*, *Antarctic Science*, 22(5), 559-571, doi:10.1017/S0954102010000283
- Holladay J.S., J.R. Rossiter, A. Kovacs** (1990) *Airborne measurements of sea-ice thickness using electromagnetic induction sounding*, 9th Conf. of Offshore Mechanics and Arctic Engineering. Houston, USA, Conference Proceedings, 309-315
- Holland M.M., J.A. Curry, J.L. Schramm** (1997) *Modeling the thermodynamics of a sea ice thickness distribution, 2. Sea ice/ocean interactions*, *Journal of Geophysical Research*, Vol. 102, No. C10, 23,093-23,107
- Holland D.M.** (2001) *Explaining the Weddell Polynya - a large ocean eddy shed at Maud Rise*, *Science*, Vol. 292, 1697-1700
- Holland P.R., R. Kwok** (2012) *Wind-driven trends in Antarctic sea-ice drift*, *Nature Geoscience*, published online: 11 November 2012, doi:10.1038/NCEO1627
- Holt B., P. Kanagaratnam, S.P. Gogineni, V.C. Ramasami, A. Mahoney, V. Lytle** (2009) *Sea ice thickness measurements by ultrawideband penetrating radar: First results*, *Cold Regions Science and Technology*, 55, 33-46
- Honeywell** (2004) *Pressure Transducer Accuracy in Application*, Technical Note, Honeywell International Inc., Freeport (Illinois)
- Hvidegaard S.M., R. Forsberg** (2002) *Sea-ice thickness from airborne laser altimetry over the Arctic Ocean north of Greenland*, *Geophysical Research Letters*, Vol. 29, NO. 20, 1952, doi:10.1029/2001GL014474
- Hyatt J., M. Visbeck, R.C. Beardsley, W. Brechner Owens** (2008) *Estimating sea-ice coverage, draft, and velocity in Marguerite Bay (Antarctica) using a subsurface moored upward-looking acoustic Doppler current profiler (ADCP)*, *Deep-Sea Research II*, 55, 351-364, doi:10.1016/j.dsr2.2007.11.004
- IGOS - Integrated Global Observing Strategy** (2007) *Cryosphere Theme Report - For the Monitoring of our Environment from Space and from Earth*, Geneva: World Meteorological Organization (WMO), WMO/TD-Nr. 1405
- IPCC** (2007) *Climate Change 2007: The Physical Science Basis.*, Contribution of Working Group I to the Fourth Assessment Report of the Intergovernmental Panel on Climate Change, S. Solomon, D. Qin, M. Manning, Z. Chen, M. Marquis, K.B. Averyt, M.Tignor and H.L. Miller (eds.), Cambridge University Press, Cambridge, United Kingdom and New York, NY, USA
- Jezek K.C., T.K. Stanton, A.J. Gow, M.A. Lange** (1990) *Influence of environmental conditions on acoustical properties of sea ice*, *Journal of the Acoustical Society of America*, Vol. 88, Nr. 4
- Johnsen Å.S.** (1989) *Relation between top and bottom ice topography using scanning sonar*, in: *Proceedings of the Tenth International Conference on Port and Ocean Engineering Under Arctic Conditions*, edited by K. B. E. Axelsson and L. Fransson, pp. 77-86, Luleå Univ. of Technol., Luleå, Sweden
- Jones J.M., R.L. Fogt, M. Widmann, G.J. Marshall, P.D. Jones, M. Visbeck** (2009) *Historical SAM Variability. Part I: Century-Length Seasonal Reconstructions*, *Journal of Climate*, Vol. 22, 5319-5345, doi:10.1175/2009JCLI2785.1
- Kaleschke L.** (2003) *Fernerkundung des Meereises mit passiven und aktiven Mikrowellensensoren*, Dissertation, Universität Bremen
- Kaleschke L., N. Maaß, C. Haas, S. Hendricks, G. Heygster, R. T. Tonboe** (2010) *A sea-ice thickness retrieval model for 1.4 GHz radiometry and application to airborne measurements over low salinity sea-ice*, *The Cryosphere*, 4, 583-592, doi:10.5194/tc-4-583-2010
- Kantelhardt J.W., E. Koscielny-Bunde, H.H.A. Rego, S. Havlin, A. Bunde** (2001) *Detecting long-range correlations with detrended fluctuation analysis*, *Physica A* 295, 441-454
- Kalnay E., M. Kanamitsu, R. Kistler, W. Collins, D. Deaven, L. Gandin, M. Iredell, S. Saha, G. White, J. Woollen, Y. Zhu, M. Chelliah, W. Ebisuzaki, W. Higgins, J. Janowiak, K.C. Mo, C. Ropelewski, J. Wang, A. Leetmaa, R. Reynolds, R. Jenne, D. Joseph** (1996) *The NCEP/NCAR 40-Year Reanalysis Project*, *Bulletin of the American Meteorological Society*, Vol. 77, Nr. 3

- Karl T.R., K.E. Trenberth** (2003) *Modern Global Climate Change*, Science 302, 1719, doi: 10.1126/science.1090228
- Karoly D.J.** (1989) *Southern Hemisphere Circulation Features Associated with El Niño-Southern Oscillation Events*, Journal of Climate, Vol. 2, 1239-1252
- Kiene R.P., D.J. Kieber, D. Slezak, D.A. Toole, D.A. del Valle, J. Bisgrove, J. Brinkley, A. Rellinger** (2007) *Distribution and cycling of dimethylsulfide, dimethylsulfoniopropionate, and dimethylsulfoxide during spring and early summer in the Southern Ocean south of New Zealand*, Aquatic Sciences, 69, 305-319, doi:10.1007/s00027-007-0892-3
- Kimura N.** (2004) *Sea Ice Motion in Response to Surface Wind and Ocean Current in the Southern Ocean*, Journal of the Meteorological Society of Japan, Vol. 82, No. 4, 1223-1231
- King J.C.** (2003) *Validation of ECMWF Sea Level Pressure Analyses over the Bellingshausen Sea, Antarctica*, Weather and Forecasting, Vol. 18, 536-540
- Knorr G., G. Lohmann** (2003) *Southern Ocean origin for the resumption of Atlantic thermohaline circulation during deglaciation*, Nature, Vol. 424, 31. July 2003
- Kondrashov D., M. Ghil** (2006) *Spatio-temporal filling of missing points in geophysical data sets*, Non-linear Processes in Geophysics, 13, 151-159
- Kottmeier C., L. Sellmann** (1996) *Atmospheric and oceanic forcing of Weddell Sea ice motion*, Journal of Geophysical Research, Vol. 101, No. C9, 20,809-20,824
- Kuhlbrodt T., A. Griesel, M. Montoya, A. Levermann, M. Hofmann, S. Rahmstorf** (2007) *On the Driving Processes of the Atlantic Meridional Overturning Circulation*, Reviews of Geophysics, 45, RG2001, Paper number 2004RG000166
- Kurtz N.T., T. Markus** (2012) *Satellite observations of Antarctic sea ice thickness and volume*, Journal of Geophysical Research, Vol. 117, C08025, doi:10.1029/2012JC008141
- Kvambekk A.S., T. Vinje** (1992) *Ice draft recordings from upward looking sonars (ULSs) in the Fram Strait and the Barents Sea in 1987/88 and 1990/91*, Norsk Polarinstitutt Rapportserie, Vol. 79, Oslo, Norway, 43pp.
- Kwok R., J.C. Comiso** (2002a) *Spatial patterns of variability in Antarctic surface temperature: Connections to the Southern Hemisphere Annular Mode and the Southern Oscillation*, Geophysical Research Letters, Vol. 29, No. 14, doi:10.1029/2002GL015415
- Kwok R., J.C. Comiso** (2002b) *Southern Ocean Climate and Sea Ice Anomalies Associated with the Southern Oscillation*, Journal of Climate, Vol. 15, 487-501
- Kwok R., G.F. Cunningham** (2008) *ICESat over Arctic sea ice: Estimation of snow depth and ice thickness*, Journal of Climate, Journal of Geophysical Research, Vol. 113, C08010, doi:10.1029/2008JC004753
- Kwok R., D.A. Rothrock** (2009) *Decline in Arctic sea ice thickness from submarine and ICESat records: 1958-2008*, Geophysical Research Letters, Vol. 36, L15501, doi:10.1029/2009GL039035
- Kwok R., G.F. Cunningham, M. Wensnahan, I. Rigor, H.J. Zwally, D. Yi** (2009) *Thinning and volume loss of the Arctic Ocean sea ice cover: 2003-2008*, Journal of Geophysical Research, Vol. 114, C07005, doi:10.1029/2009JC005312
- Lange M.A., S.F. Ackley, P. Wadhams, G.S. Dieckmann, H. Eicken** (1989) *Development of Sea Ice in the Weddell Sea*, Annals of Glaciology, 12
- Lange M.A., H. Eicken** (1991) *The Sea Ice Thickness Distribution in the Northwestern Weddell Sea*, Journal of Geophysical Research, Vol. 96, No. C3, 4821-4837
- Langleben M.P.** (1970) *Reflection of Sound at the Water-Sea Ice Interface*, Journal of Geophysical Research, Vol. 75, No. 27, 5243-5246
- Laxon S.W., N. Peacock, D. Smith** (2003) *High interannual variability of sea ice thickness in the Arctic region*, Nature, 425, 947-950, doi:10.1038/nature02050
- Lemke P.** (1994) *Meereis und Schelfeis*, Lecture Script, Alfred Wegener Institute, Bremerhaven
- Lemke P., M. Hilmer** (2003) *Meereismodelle*, *promet*, Jahrg.29, Nr.1-4, 90-97, Deutscher Wetterdienst

- Lemke P., D. Olbers** (2007) *On the Physics of the Climate System: Ice Age or Greenhouse Climate?*, Lectures on Climate Physics, University of Bremen
- Lemke P., J. Ren, R.B. Alley, I. Allison, J. Carrasco, G. Flato, Y. Fujii, G. Kaser, P. Mote, R.H. Thomas and T. Zhang** (2007) *Observations: Changes in Snow, Ice and Frozen Ground.*, In: Climate Change 2007: The Physical Science Basis. Contribution of Working Group I to the Fourth Assessment Report of the Intergovernmental Panel on Climate Change (IPCC), S. Solomon, D. Qin, M. Manning, Z. Chen, M. Marquis, K.B. Averyt, M. Tignor and H.L. Miller (eds.), Cambridge University Press, Cambridge, United Kingdom and New York, NY, USA
- Leppäranta M.** (1993) *A Review of Analytical Models of Sea-Ice Growth*, Atmosphere-Ocean 31 (1), 123-138, Canadian Meteorological and Oceanographic Society
- Leppäranta M.** (1998) *The Dynamics of Sea Ice*, In: Physics of Ice-Covered Seas, Lecture notes from a summer school in Savonlinna, Finland, Vol. 1, University of Helsinki, Department of Geophysics
- Le Quééré C., M.R. Raupach, J.G. Canadell, G. Marland et al.** (2009) *Trends in the sources and sinks of carbon dioxide*, Nature Geoscience, published online: 17 Nov. 2009, doi:10.1038/ngeo689
- Lee T., W.R. Hobbs, J.K. Willis, D. Halkides, I. Fukumori, E.M. Armstrong, A.K. Hayashi, W. Timothy Liu, W. Patzert, O. Wang** (2010) *Record warming in the South Pacific and western Antarctica associated with the strong central-Pacific El Niño in 2009-10*, Geophysical Research Letters, Vol. 37, L19704, doi:10.1029/2010GL044865
- L'Heureux M.L., D.W.J. Thompson** (2006) *Observed Relationships between the El Niño-Southern Oscillation and the Extratropical Zonal-Mean Circulation*, Journal of Climate, Vol. 19, 276-287
- Lindsay R.W., R. Kwok, L. de Steur, W. Meier** (2008) *Halo of ice deformation observed over the Maud Rise seamount*, Geophysical Research Letters, Vol. 35, L15501, doi:10.1029/2008GL034629
- Lisiecki L.E.** (2010) *Links between eccentricity forcing and the 100,000-year glacial cycle*, Nature Geoscience, published online: 4 Apr. 2010, doi:10.1038/ngeo828
- Liu J., J.A. Curry** (2010) *Accelerated warming of the Southern Ocean and its impacts on the hydrological cycle and sea ice*, PNAS, Vol. 107, No. 34, 14987-14992, doi:10.1073/pnas.1003336107
- Liu J., X. Yuan, D. Rind, D.G. Martinson** (2002) *Mechanism study of the ENSO and southern high latitude climate teleconnections*, Geophysical Research Letters, Vol. 29, No. 14, doi:10.1029/2002GL015143
- Liu J., J.A. Curry, D.G. Martinson** (2004) *Interpretation of recent Antarctic sea ice variability*, Geophysical Research Letters, Vol. 31, L02205, doi:10.1029/2003GL018732
- Lohmann G., R. Gerdes** (1998) *Sea Ice Effects on the Sensitivity of the Thermohaline Circulation*, Journal of Climate, Vol. 11, 2789-2803
- Losch M., D. Menemenlis, J.M. Campin, P. Heimbach, C. Hill** (2010) *On the formulation of sea-ice models. Part 1: Effects of different solver implementations and parameterizations*, Ocean Modelling, 33, 129-144, doi:10.1016/j.ocemod.2009.12.008
- Løset S., K. Shkhinek, O.T. Gudmestad, K. Høyland** (2006) *Actions from Ice on Arctic Offshore and Coastal Structures*, Publisher LAN, Trondheim, St. Petersburg, Moscow, Krasnodar, ISBN: 5-8114-0703-3, 271 pp.
- Lothe T., A. Baker** (2000) *Processing of Data from ES 300 Upward Looking Sonars*, A guide to data conversion and processing, CMR Report, Ref.Nr.:CMR-00-A10031, Bergen, Norway
- Ludwig R., D. Paschek** (2005) *Wasser - Anomalien und Rätsel*, Chemie in unserer Zeit, 39, 164-175, Wiley-VCH Verlag GmbH & Co. KGaA, Weinheim
- Lyman J.M., S.A. Good, V.V. Gouretski, M. Ishii, G.C. Johnson, M.D. Palmer, D.M. Smith, J.K. Willis** (2010) *Robust warming of the global upper ocean*, Nature, Vol. 465, doi:10.1038/nature09043
- MacKenzie K.V.** (1981) *Nine-term equation for sound speed in the oceans*, Journal of the Acoustical Society of America, Vol. 70, Nr. 3
- Maksym T., S.E. Stammerjohn, S. Ackley, R. Massom** (2012) *Antarctic Sea Ice - A Polar Opposite?*, Oceanography, Vol. 25, No. 3, http://dx.doi.org/10.5670/oceanog.2012.88
- Mandelbrodt B.B.** (1987) *Die fraktale Geometrie*

der Natur, Birkhäuser Verlag, Basel

Marshall J., F. Schott (1999) *Open-Ocean Convection: Observations, Theory, and Models*, Reviews of Geophysics, 37, pages 1-64, Paper number 98RG02739

Marshall G.J. (2003) *Trends in the Southern Annular Mode from Observations and Reanalyses*, Journal of Climate, Vol. 16, 4134-4143

Marshall G.J., A. Orr, N.P.M. van Lipzig, J.C. King (2006) *The Impact of a changing Southern Hemisphere Annular Mode on Antarctic Peninsula Summer Temperatures*, Journal of Climate, Vol. 19, 5388-5404

Martinson D.G., C. Wamser (1990) *Ice Drift and Momentum Exchange in Winter Antarctic Pack Ice*, Journal of Geophysical Research, Vol. 95, No. C2, 1741-1755

Martinson D.G., R.A. Iannuzzi (2003) *Spatial/temporal patterns in Weddell gyre characteristics and their relationship to global climate*, Journal of Geophysical Research, Vol. 108, No. C4, 8083, doi:10.1029/2000JC000538

Massom R.A., H. Eicken, C. Haas, M.O. Jeffries, M.R. Drinkwater, M. Sturm, A.P. Worby, X. Wu, V.I. Lytle, S. Ushio, K. Morris, P.A. Reid, S.G. Warren, I. Allison (2001) *Snow on Antarctic Sea Ice*, Reviews of Geophysics, 39, 3, 413-445

Massom R.A., S.E. Stammerjohn, W. Lefebvre, S.A. Harangozo, N. Adams, T.A. Scambos, M.J. Pook, C. Fowler (2008) *West Antarctic Peninsula sea ice in 2005: Extreme ice compaction and ice edge retreat due to strong anomaly with respect to climate*, Journal of Geophysical Research, Vol. 113, C02S20, doi:10.1029/2007JC004239

Mayewski P.A., M.P. Meredith, C.P. Summerhayes, J. Turner, A. Worby, P.J. Barrett, G. Casassa, N.A.N. Bertler, T. Bracegirdle, A.C. Naveira Garabato, D. Bromwich, H. Campbell, G.S. Hamilton, W.B. Lyons, K.A. Maasch, S. Aoki, C. Xiao, T. van Ommen (2009) *State of the Antarctic and Southern Ocean Climate System*, Reviews of Geophysics, 47, RG1003, Paper number 2007RG000231

Maykut G.A., N. Untersteiner (1971) *Some Results from a Time-Dependent Thermodynamic Model of Sea Ice*, Journal of Geophysical Research, Vol. 76,

No. 6, 1550-1575

Meehl G. (1991), *A Reexamination of the Mechanism of the Semiannual Oscillation in the Southern Hemisphere*, Journal of Climate, Vol. 4, 911-926

Meier W., J. Wolfe, S. Renfrow, K. Pharris, K. Barton, R. Barry, M. Serreze, J. Stroeve, T. Arbetter, F. Fetterer, D. Scott (2009, 2010), *All about sea ice*, Web Page: <http://nsidc.org/seaice>, National Snow and Ice Data Center, Institute for Research in Environmental Sciences, University of Boulder, Colorado

Melling H., D.A. Riedel (1995) *The underside topography of sea ice over the continental shelf of the Beaufort Sea in the winter of 1990*, Journal of Geophysical Research, Vol. 100, No. C7, 13,641-13,653

Melling H., P.H. Johnston, D.A. Riedel (1995) *Measurements of the Topography of Sea Ice by Moored Subsea Sonar*, Journal of Atmospheric and Oceanic Technology, Vol. 12, 589-602

Melling H., D.A. Riedel (1996) *Development of seasonal pack ice in the Beaufort Sea during the winter of 1991-1992: A view from below*, Journal of Geophysical Research, Vol. 101, No. C5, 11,975-11,991

Melling H. (1998) *Sound Scattering from Sea Ice: Aspects Relevant to Ice-Draft Profiling by Sonar*, Journal of Atmospheric and Oceanic Technology, Vol. 15, 1023-1034

Melling H., D.A. Riedel (2005) *Trends in the draft and extent of seasonal pack ice, Canadian Beaufort Sea*, Geophysical Research Letters, Vol. 32, L24501, doi:10.1029/2005GL024483

Müller J., G. Massé, R. Stein, S.T. Belt (2009) *Variability of sea-ice conditions in the Fram Strait over the past 30,000 years*, Nature Geoscience, published online: 25 Oct. 2009, doi:10.1038/ngeo665

Nørgaard-Pedersen N. (2009) *Tracking ancient sea ice*, Nature Geoscience, published online: 25 Oct. 2009, doi:10.1038/ngeo665

Notz D. (2005) *Thermodynamic and Fluid-Dynamical Processes in Sea Ice*, PhD-Thesis, Trinity College, University of Cambridge

Notz D., M.G. Worster (2009) *Desalination processes of sea ice revisited*, Journal of Geophysical Research, Vol. 114, C05006, doi:10.1029/2008JC004885

- NSIDC (National Snow and Ice Data Center)** (2009, 2010, 2012), Web Page: <http://nsidc.org/>, Institute for Research in Environmental Sciences, University of Boulder, Colorado
- Núñez-Riboni I., E. Fahrbach** (2009), *Seasonal variability of the Antarctic Coastal Current and its driving mechanisms in the Weddell Sea*, Deep-Sea Research I, 56, 1927-1941, doi:10.1016/j.dsr.2009.06.005
- Olbers D.** (2002) *Der Ozean als Wärmemaschine unseres Planeten*, In: Eiskalte Entdeckungen: Forschungsreisen zwischen Nord- und Südpol, zweite Auflage, Delius/Klasing, Bielefeld
- Parkinson C.L.** (2002) *Trends in the length of the Southern Ocean sea-ice season, 1979-99*, Annals of Glaciology, 34, 435-440
- Parkinson C.L.** (2004) *Southern Ocean sea ice and its wider linkages: insights revealed from models and observations*, Antarctic Science, 16 (4), 387-400, doi:10.1017/S0954102004002214
- Parkinson C.L., J.C. Comiso** (2008) *Antarctic sea ice parameters from AMSR-E data using two techniques and comparisons with sea ice from SSM/I*, Journal of Geophysical Research, Vol. 113, C02S06, doi:10.1029/2007JC004253
- Parkinson C.L., D.J. Cavalieri** (2012) *Antarctic sea ice variability and trends, 1979-2010*, The Cryosphere, 6, 871-880, doi:10.5194/tc-6-871-2012
- Peters G.P., R.M. Andrew, T. Boden, J.P. Canadell, P. Ciais, C. Le Quéré, G. Marland, M.R. Raupach, C. Wilson** (2012) *The challenge to keep global warming below 2° C*, Commentary in: Nature Climate Change, published online: 2 December 2012
- Peterson R.G., W.B. White** (1998) *Slow oceanic teleconnections linking the Antarctic Circumpolar Wave with the tropical El Niño-Southern Oscillation*, Journal of Geophysical Research, Vol. 103, No. C11, 24,573-24,583
- Petrenko V.F.** (1993) *Electrical Properties of Ice*, Cold Regions Research and Engineering Laboratory, CRREL Special Report 93-20, 69pp
- Petrich C., H. Eicken** (2010) *Growth, Structure and Properties of Sea Ice*, In: Sea Ice (second edition), D.N. Thomas and G.S. Dieckmann (eds.), Blackwell Publishing Ltd
- Pfaffling A., C. Haas, J.E. Reid** (2005) *Key Characteristics of Helicopter Electromagnetic Sea Ice Thickness Mapping: Resolution, Accuracy and Footprint*, In: Arctic Sea Ice Thickness: Past, Present and Future, Scientific Report of the International Workshop in Rungstedgaard, Denmark, 8.-9. November 2005, P. Wadhams and G. Amanatidis (eds.)
- Pierrehumbert R.T.** (2011) *Infrared radiation and planetary temperature*, Physics Today, January 2011, 33-38, American Institute of Physics
- Prestrud P.** (2007) *Why are Snow and Ice Important to Us?*, In: Global Outlook for Ice and Snow, J. Eamer (ed.), United Nations Environment Programme (UNEP)
- Pringle D.J., J.E. Miner, H. Eicken, K.M. Golden** (2009) *Pore space percolation in sea ice single crystals*, Journal of Geophysical Research, Vol. 114, C12017, doi:10.1029/2008JC005145
- Purdie C.R., P.J. Langhorne, G.H. Leonard, T.G. Haskell** (2006) *Growth of first-year landfast Antarctic sea ice determined from winter temperature measurements*, Annals of Glaciology, 44, 170-176
- Qiu B., F.F. Jin** (1997) *Antarctic circumpolar waves: An indication of ocean-atmosphere coupling in the extratropics*, Geophysical Research Letters, Vol. 24, No. 21, 2585-2588
- Rahmstorf S.** (2002) *Ocean circulation and climate during the past 120,000 years*, Nature, Vol. 419, 207-214
- Rahmstorf S.** (2006) *Thermohaline Ocean Circulation*, In: Encyclopedia of Quaternary Sciences, S.A. Elias (ed.), Elsevier, Amsterdam
- Raphael M.N.** (2004) *A zonal wave 3 index for the Southern Hemisphere*, Geophysical Research Letters, Vol. 31, L23212, doi:10.1029/2004GL020365
- Raphael M.N.** (2007) *The influence of atmospheric zonal wave three on Antarctic sea ice variability*, Journal of Geophysical Research, Vol. 112, D12112, doi:10.1029/2006JD007852
- Reid J.E., A.P. Worby, J. Vrbancich, A.I.S. Munro** (2003) *Shipborne electromagnetic measurements of Antarctic sea-ice thickness*, Geophysics, Vol. 68, No. 5, 1537-1546
- Renner A.H.H., V. Lytle** (2007) *Sea-ice thick-*

- ness in the Weddell Sea, Antarctica: a comparison of model and upward-looking sonar data, *Annals of Glaciology*, 46, 419-427
- Renwick J.A.** (2004) *Trends in the Southern Hemisphere polar vortex in NCEP and ECMWF reanalyses*, *Journal of Geophysical Research*, Vol. 31, L07209, doi:10.1029/2003GL019302
- Reson** (2010) *Catalogue - Standard Transducers and Hydrophones*, Version: A032-090804-US, downloaded in August 2010 from: www.reson.com
- Roedel W.** (1994) *Physik unserer Umwelt - Die Atmosphäre*, 2. Auflage, Springer, ISBN 3-540-57885-4
- Romanou A., W.B. Rossow, S.H. Chou** (2006) *Decorrelation Scales of High-Resolution Turbulent Fluxes at the Ocean Surface and a Method to Fill in Gaps in Satellite Data Products*, *Journal of Climate*, Vol. 19, 3378-3393
- Rothrock D.A.** (1986) *Ice thickness distribution - measurement and theory*, In: *The Geophysics of Sea Ice* (ed. N. Untersteiner), Plenum, New York, 551-575
- Rothrock D.A., M. Wensnahan** (2007) *The Accuracy of Sea Ice Drafts Measured from U.S. Navy Submarines*, *Journal of Atmospheric and Oceanic Technology*, Vol. 24, 1936-1949, doi: 10.1175/JTECH2097.1
- Rothrock D.A., D.B. Percival, M. Wensnahan** (2008) *The decline in arctic sea-ice thickness: Separating the spatial, annual, and interannual variability in a quarter century of submarine data*, *Journal of Geophysical Research*, Vol. 113, C05003, doi:10.1029/2007JC004252
- Rybski D., A. Bunde, S. Havlin, H. v. Storch** (2006) *Long-term persistence in climate and the detection problem*, *Geophysical Research Letters*, Vol. 33, L06718, doi:10.1029/2005GL025591
- Rybski D.** (2006) *Untersuchung von Korrelationen, Trends und synchronem Verhalten in Klimazeitreihen*, PhD-Thesis, University of Gießen, Germany
- Sabine C.L., R.A. Feely, N. Gruber, R.M. Key, K. Lee, J.L. Bullister, R. Wanninkhof, C.S. Wong, D.W.R. Wallace, B. Tilbrook, F.J. Millero, T.H. Peng, A. Kozyr, T. Ono, A.F. Rios** (2004) *The Oceanic Sink for Anthropogenic CO₂*, *Science* 305, 367, doi: 10.1126/science.1097403
- Sandven S., O.M. Johannessen** (2006) *Sea ice monitoring by Remote Sensing*, In: *Remote Sensing of the Marine Environment, Manual of Remote Sensing, Third Edition, Volume 6*, J. Gower (ed.), American Society for Photogrammetry and Remote Sensing, Maryland, USA
- SCAR** (2009) *Antarctic Climate Change and the Environment (A Contribution to the International Polar Year 2007-2008)*, J. Turner, R. Bindshadler, P. Convey, G. di Prisco, E. Fahrbach, J. Gutt, D. Hodgson, P. Mayewski, C. Summerhayes (eds.), published by the Scientific Committee on Antarctic Research, Scott Polar Research Institute, Lensfield Road, Cambridge, UK
- Schlitzer R.** (2010) *Ocean Data View*, [/http://odv.awi.de](http://odv.awi.de)
- Schmitt C.** (2005) *Interannual Variability in Antarctic Sea Ice Motion*, PhD-Thesis, University of Karlsruhe, Germany
- Schönwiese C.D.** (1992) *Praktische Statistik für Meteorologen und Geowissenschaftler*, Zweite Auflage, Gebrüder Borntraeger, Berlin/Stuttgart
- Schwarz J., W.F. Weeks** (1977) *Engineering Properties of Sea Ice*, *Journal of Glaciology*, Vol. 19, No. 81
- Schwegmann S., C. Haas, C. Fowler, R. Gerdes** (2011) *A comparison of satellite-derived sea-ice motion with drifting-buoy data in the Weddell Sea, Antarctica*, *Annals of Glaciology* 52(57), 103-110
- Schwegmann S.** (2012) *Interannual and decadal variability of sea ice drift, concentration and thickness in the Weddell Sea*, PhD-Thesis, University of Bremen, Germany
- Scott M., R. Simmon** (2009) *Sea Ice*, NASA Feature Article, Web Page: <http://earthobservatory.nasa.gov/Features/SeaIce>
- Screen J.A., I. Simmonds** (2010) *The central role of diminishing sea ice in recent Arctic temperature amplification*, *Nature*, Vol. 464, doi:10.1038/nature09051
- Screen J.A.** (2011) *Sudden increase in Antarctic sea ice: Fact or artifact?*, *Geophysical Research Letters*, Vol. 38, L13702, doi:10.1029/2011GL047553
- Shcherbina A.Y., D.L. Rudnick, L.D. Talley** (2005) *Ice-Draft Profiling from Bottom-Mounted ADCP Data*, *Journal of Atmospheric and Oceanic*

Technology, Vol.22, 1249-1266

Shin S.I., Z. Liu, B.L. Otto-Bliesner, J.E. Kutzbach, S.J. Vavrus (2003) *Southern Ocean sea-ice control of the North Atlantic thermohaline circulation*, Geophysical Research Letters, Vol. 30, No. 2, 1096, doi:10.1029/2002GL015513

Shu Q., F. Qiao, Z. Song, C. Wang (2012) *Sea ice trends in the Antarctic and their relationship to surface air temperature during 1979-2009*, Climate Dynamics, 38:2355-2363, doi:10.1007/s00382-011-1143-9

Sigmond M., J.C. Fyfe (2010) *Has the ozone hole contributed to increased Antarctic sea ice extent?*, Geophysical Research Letters, Vol. 37, L18502, doi:10.1029/2010GL044301

Simmonds I. (2003) *Modes of atmospheric variability over the Southern Ocean*, Journal of Geophysical Research, Vol. 108, No. C4, 8078, doi:10.1029/2000JC000542

Skinner L.C., S. Fallon, C. Waelbroeck, E. Michel, S. Barker (2010) *Ventilation of the Deep Southern Ocean and Deglacial CO₂ Rise*, Science 328, 1147, doi:10.1126/science.1183627

Smith S.D., R.D. Muench, C.H. Pease (1990) *Polynyas and Leads: An Overview of Physical Processes and Environment*, Journal of Geophysical Research, Vol. 95, No. C6, pages 9461-9479

SpectraWorks (2011) *KSpectra Toolkit - M-SSA Theory*, Web Page: <http://www.spectraworks.com/Help/mssatheory.html>

Spindler M. (1994) *Notes on the biology of sea ice in the Arctic and Antarctic*, Polar Biol., 14, 319-324

Spreen G., S. Kern, D. Stammer, R. Forsberg, J. Haarpainter (2006) *Satellite-based estimates of sea-ice volume flux through Fram Strait*, Annals of Glaciology, 44, 321-328

Stammerjohn S.E., D.G. Martinson, R.C. Smith, X. Yuan, D. Rind (2008) *Trends in Antarctic annual sea ice retreat and advance and their relation to El Niño-Southern Oscillation and Southern Annular Mode variability*, Journal of Geophysical Research, Vol. 113, C03S90, doi:10.1029/2007JC004269

Stanton T.K., K.C. Jezek, A.J. Gow (1986) *Acoustical reflection and scattering from the underside of laboratory grown sea ice: Measurements and predictions*, Journal of the Acoustical Society of

America, Vol. 80, Nr. 5

Steig E., D.P. Schneider, S.D. Rutherford, M.E. Mann, J.C. Comiso, D.T. Shindell (2009) *Warming of the Antarctic ice-sheet surface since the 1957 International Geophysical Year*, Nature, Vol. 457, doi:10.1038/nature07669

Stewart R.H. (2006) *Introduction To Physical Oceanography*, Department of Oceanography, Texas A & M University, available online at: http://oceanworld.tamu.edu/home/course_book.htm

Stocker T.F., R. Knutti, G.K. Plattner (2001) *The Future of the Thermohaline Circulation - A Perspective*, AGU Monograph Series edited by D. Seidov, M. Maslin and B. Haupt

Strass V.H. (1998) *Measuring sea ice draft and coverage with moored upward looking sonars*, Deep-Sea Research, I, 45, 795-818

Strass V.H., E. Fahrbach (1998) *Temporal and Regional Variation of Sea Ice Draft and Coverage in the Weddell Sea Obtained from Upward Looking Sonars*, Antarctic Sea Ice: Physical Processes, Interactions and Variability, Antarctic Research Series, Vol. 74, 123-139

Strickert M. (2003) *Time Series and Data Analysis*, Lecture Script, Department of Mathematics and Computer Science, University of Osnabrück, Germany

Su H., Y. Wang (2012) *Using MODIS data to estimate sea ice thickness in the Bohai Sea (China) in the 2009-2010 winter*, Journal of Geophysical Research, Vol. 117, C10018, doi:10.1029/2012JC008251

Sun B., J. Wen, M. He, J. Kang, Y. Luo, Y. Li (2003) *Sea ice thickness measurement and its underside morphology analysis using radar penetration in the Arctic Ocean*, Science in China (Series D), Vol. 46, No. 11

Tan B., Z.j. Li, P. Lu, C. Haas, M. Nicolaus (2012) *Morphology of sea ice pressure ridges in the northwestern Weddell Sea in winter*, Journal of Geophysical Research, Vol. 117, C06024, doi:10.1029/2011JC007800

Thomas D.N., G.S. Dieckmann (2002) *Antarctic Sea Ice - a Habitat for Extremophiles*, Science 295, 641, doi:10.1126/science.1063391

Thompson D.W.J., J.M. Wallace (2000) *Annu-*

- lar Modes in the Extratropical Circulation. Part I: Month-to-Month Variability, *Journal of Climate*, Vol. 13, 1000-1016
- Thompson D.W.J., S. Solomon** (2002) *Interpretation of Recent Southern Hemisphere Climate Change*, *Science*, Vol. 296, 895-899
- Thorndike A.S., D.A. Rothrock, G.A. Maykut, R. Colony** (1975) *The Thickness Distribution of Sea Ice*, *Journal of Geophysical Research*, Vol. 80, No. 33, 4501-4513
- Thorndike A.S.** (1992) *Estimates of Sea Ice Thickness Distribution Using Observations and Theory*, *Journal of Geophysical Research*, Vol. 97, No. C8, 12,601-12,605
- Timco G.W., W.F. Weeks** (2010) *A review of the engineering properties of sea ice*, *Cold Regions Science and Technology*, 60, 107-129, doi:10.1016/j.coldregions.2009.10.003
- Timmermann R., A. Beckmann, H.H. Hellmer** (2002) *Simulations of ice-ocean dynamics in the Weddell Sea 1. Model configuration and validation*, *Journal of Geophysical Research*, Vol. 107, No. C3, 3024, 10.1029/2000JC000741
- Timmermann R., A. Worby, H. Goosse, T. Fichefet** (2004) *Utilizing the ASPeCt sea ice thickness data set to evaluate a global coupled sea ice-ocean model*, *Journal of Geophysical Research*, Vol. 109, C07017, doi:10.1029/2003JC002242
- Timmermann R., S. Danilov, J. Schröter, C. Böning, D. Sidorenko, K. Rollenhagen** (2009) *Ocean circulation and sea ice distribution in a finite element global sea ice-ocean model*, *Ocean Modelling*, 27, 114-129, doi:10.1016/j.ocemod.2008.10.009
- Trenberth K.E.** (1997) *The Definition of El Niño*, *Bulletin of the American Meteorological Society*, Vol. 78, No. 12
- Trenberth K.E., J.T. Fasullo, J. Kiehl** (2009) *Earth's Global Energy Budget*, *Bulletin of the American Meteorological Society*, Vol. 90, Issue 3, doi:10.1175/2008BAMS2634.1
- Turner J.** (2004) *The El Niño-Southern Oscillation and Antarctica*, *International Journal of Climatology*, 24: 1-31, doi:10.1002/joc.965
- Turner J., S.R. Colwell, G.J. Marshall, T.A. Lachlan-Cope, A.M. Carleton, P.D. Jones, V. Lagun, P.A. Reid, S. Iagovkina** (2005) *Antarctic climate change during the last 50 years*, *International Journal of Climatology*, 25: 279-294, doi:10.1002/joc.1130
- Turner J., J.C. Comiso, G.J. Marshall, T.A. Lachlan-Cope, T. Bracegirdle, T. Maksym, M.P. Meredith, Z. Wang, A. Orr** (2009) *Non-annular atmospheric circulation change induced by stratospheric ozone depletion and its role in the recent increase of Antarctic sea ice extent*, *Geophysical Research Letters*, Vol. 36, L08502, doi:10.1029/2009GL037524
- Turner J., J. Overland** (2009) *Contrasting climate change in the two polar regions*, *Polar Research*, 28, 146-164, doi:10.1111/j.1751-8369.2009.00128.x
- Tynan C., D.G. Ainley, I. Stirling** (2010) *Sea Ice: A Critical Habitat for Polar Marine Mammals and Birds*, In: *Sea Ice* (second edition), D.N. Thomas and G.S. Dieckmann (eds.), Blackwell Publishing Ltd
- Udagawa Y., Y. Tachibana, K. Yamazaki** (2009) *Modulation in interannual sea ice patterns in the Southern Ocean in association with large-scale atmospheric mode shift*, *Journal of Geophysical Research*, Vol. 114, D21103, doi:10.1029/2009JD011807
- Urlick R.J.** (1983) *Principles of Underwater Sound*, 3d edition, McGraw-Hill Book Company
- van den Broeke M.R.** (2000) *On the Interpretation of Antarctic Temperature Trends*, *Journal of Climate*, Vol. 13, 3885-3889
- van den Broeke M.R.** (2000b) *The semiannual oscillation and Antarctic climate. Part 5: impact on the annual temperature cycle as derived from NCEP/NCAR re-analysis*, *Climate Dynamics*, 16, 369-377
- van Loon H., R.L. Jenne** (1972) *The Zonal Harmonic Standing Waves in the Southern Hemisphere*, *Journal of Geophysical Research*, Vol. 77, No. 10, 992-1003
- Vautard R., M. Ghil** (1989) *Singular Spectrum Analysis in non-linear dynamics with applications to paleoclimatic time series*, *Physica D*, 35, 395-424
- Venegas S.A., M.R. Drinkwater** (2001) *Sea ice, atmosphere and upper ocean variability in the Weddell Sea, Antarctica*, *Journal of Geophysical Research*, Vol. 106, No. C8, pages 16,747-16,765

- Venegas S.A., M. Drinkwater, G. Shaffer** (2001) *Coupled oscillations in Antarctic sea ice and atmosphere in the South Pacific sector*, Journal of Geophysical Research, Vol. 28, No. 17, 3301-3304
- Venegas S.A.** (2003) *The Antarctic Circumpolar Wave: A Combination of Two Signals?*, Journal of Climate, Vol. 16, 2509-2525
- Vinje T., N. Nordlund, A. Kvambekk** (1998) *Monitoring ice thickness in Fram Strait*, Journal of Geophysical Research, Vol. 103, No. C5, 10,437-10,449
- von Storch H., A. Navarra (eds.)** (1995) *Analyses of Climate Variability - Applications of Statistical Techniques*, Springer
- Wadhams P., M.A. Lange, S.F. Ackley** (1987) *The Ice Thickness Distribution Across the Atlantic Sector of the Antarctic Ocean in Midwinter*, Journal of Geophysical Research, Vol. 92, No. C13, pages 14,535-14,552
- Wadhams P.** (1994) *Sea Ice Thickness Changes and Their Relation to Climate*, The Polar Oceans and Their Role in Shaping The Global Environment, Geophysical Monograph 85, American Geophysical Union, Washington D.C., USA
- Wadhams P.** (2000) *Ice in the Ocean*, Gordon and Breach Science Publishers (Overseas Publishers Association)
- Watkins A.B., I. Simmonds** (1999) *A late spring surge in the open water of the Antarctic sea ice pack*, Geophysical Research Letters, Vol. 26, No. 10, 1481-1484
- Weeks W.F., A.J. Gow** (1978) *Preferred Crystal Orientations in the Fast Ice Along the Margins of the Arctic Ocean*, Journal of Geophysical Research, Vol. 83, No. C10, 8C0361
- Weeks W.F.** (1998) *Growth Conditions and the Structure and Properties of Sea Ice*, In: Physics of Ice-Covered Seas, Lecture notes from a summer school in Savonlinna, Finland, Vol. 1, University of Helsinki, Department of Geophysics
- Weron R.** (2002) *Estimating long-range dependence: finite sample properties and confidence intervals*, Physica A 312, 285-299
- Weissling B.P., M.J. Lewis, S.F. Ackley** (2011) *Sea-ice thickness and mass at Ice Station Belgica, Bellingshausen Sea, Antarctica*, Deep-Sea Research II, 58, 1112-1124, doi:10.1016/j.dsr2.2010.10.032
- Wettlaufer J.S.** (1998) *Introduction to Crystallization Phenomena in Natural and Artificial Sea Ice*, In: Physics of Ice-Covered Seas, Lecture notes from a summer school in Savonlinna, Finland, Vol. 1, University of Helsinki, Department of Geophysics
- White W.B., R.G. Peterson** (1996) *An Antarctic circumpolar wave in surface pressure, wind, temperature and sea-ice extent*, Nature, Vol. 380, 699-702
- Whitworth III T., W.D. Nowlin Jr.** (1987) *Water Masses and Currents of the Southern Ocean at the Greenwich Meridian*, Journal of Geophysical Research, Vol. 92, No. C6, 6462-6476
- Wilson P.W., A.F. Heneghan, A.D.J. Haymet** (2003) *Ice nucleation in nature: supercooling point (SCP) measurements and the role of heterogeneous nucleation*, Cryobiology, 46, 88-98, doi:10.1016/S0011-2240(02)00182-7
- Wolff E.W., H. Fischer, F. Fundel, U. Ruth, B. Twarloh, G.C. Littot, R. Mulvaney, R. Röthlisberger, M. de Angelis, C.F. Boutron, M. Hansson, U. Jonsell, M.A. Hutterli, F. Lambert, P. Kaufmann, B. Stauffer, T.F. Stocker, J.P. Steffensen, M. Bigler, M.L. Siggaard-Andersen, R. Udisti, S. Becagli, E. Castellano, M. Severi, D. Wagenbach, C. Barbante, P. Gabrielli, V. Gaspari** (2006) *Southern Ocean sea-ice extent, productivity and iron flux over the past eight glacial cycles*, Nature, Vol. 440, doi:10.1038/nature04614
- Worby A.P., M.O. Jeffries, W.F. Weeks, K. Morris, R. Jaña** (1996) *The thickness distribution of sea ice and snow cover during late winter in the Bellingshausen and Amundsen Seas, Antarctica*, Journal of Geophysical Research, Vol. 101, No. C12, 28,441-28,455
- Worby A.P., P.W. Griffin, V.I. Lytle, R.A. Massom** (1999) *On the use of electromagnetic induction sounding to determine winter and spring sea ice thickness in the Antarctic*, Cold Regions Science and Technology, 29, 49-58
- Worby A.P., G.M. Bush, I. Allison** (2001) *Seasonal development of the sea-ice thickness distribution in East Antarctica: measurements from upward-looking sonar*, Annals of Glaciology, 33, 177-180
- Worby A.P., J.C. Comiso** (2004) *Studies of the*

Antarctic sea ice edge and ice extent from satellite and ship observations, Remote Sensing of Environment, 92, 98-111, doi:10.1016/j.rse.2004.05.007

Worby A.P., C.A. Geiger, M.J. Paget, M.L. Van Woert, S.F. Ackley, T.L. DeLiberty (2008) *Thickness distribution of Antarctic sea ice*, Journal of Geophysical Research, Vol. 113, C05S92, doi:10.1029/2007JC004254

World Ocean Review (2010) *T. Bosch, F. Colijn, R. Ebinghaus, A. Körtzinger, M. Latif, B. Matthiessen, F. Melzner, A. Oeschies, S. Petersen, A. Proelß, M. Quaas, T. Requate, T. Reusch, P. Rosenstiel, K. Schrottko, H. Sichts Schmidt, U. Siebert, R. Soltwedel, U. Sommer, K. Stattegger, H. Sterr, R. Sturm, T. Treude, A. Vafeidis, C.v. Bernem, J.v. Beusekom, M. Visbeck, M. Wahl, K. Wallmann, F. Weinberger, M. Bollmann, R. Froese, S. Khalilian, J. Reichenbach, J.O. Schmidt, R. Voss, N. Gelpke, J. Lehmköster, T. Schröder, D. Ladischenski, K. Schäfer, E. Söding, M. Zeller, S. Hoschack, P. Kossmann, W.M. Scheid*, maribus, Hamburg

Wright D.G., R. Feistel, J.H. Reissmann, K. Miyagawa, D.R. Jackett, W. Wagner, U. Overhoff, C. Guder, A. Feistel, and G.M. Marion (2010) *Numerical implementation and oceanographic application of the thermodynamic potentials of liquid water, water vapour, ice, seawater and humid air - Part 2: The library routines*, Ocean Science, 6, 695-718, doi:10.5194/os-6-695-2010

Xie H., S.F. Ackley, D. Yi, H.J. Zwally, P. Wagner, B. Weissling, M. Lewis, K. Ye (2011) *Sea-ice thickness distribution of the Bellingshausen Sea from surface measurements and ICESat altimetry*, Deep-Sea Research II, 58, 1039-1051, doi:10.1016/j.dsr2.2010.10.038

Yi D., H.J. Zwally, J.W. Robbins (2011) *ICE-*

Sat observations of seasonal and interannual variations of sea-ice freeboard and estimated thickness in the Weddell Sea, Antarctica (2003-2009), Annals of Glaciology, 52(57), p. 43-51

Yu Y., R.W. Lindsay (2003) *Comparison of thin ice thickness distributions derived from RADARSAT Geophysical Processor System and advanced very high resolution radiometer data sets*, Journal of Geophysical Research, Vol. 108, No. C12, 3387, doi:10.1029/2002JC001319

Yuan X. (2004) *ENSO-related impacts on Antarctic sea ice: a synthesis of phenomenon and mechanisms*, Antarctic Science, 16 (4): 415-425, doi:10.1017/S0954102004002238

Yuan X., C. Li (2008) *Climate modes in southern high latitudes and their impacts on Antarctic sea ice*, Journal of Geophysical Research, Vol. 113, C06S91, doi:10.1029/2006JC004067

Yuan X., D.G. Martinson (2000) *Antarctic Sea Ice Extent Variability and Its Global Connectivity*, Journal of Climate, Vol. 13, 1697-1717

Yuan X., D.G. Martinson (2001) *The Antarctic Dipole and its Predictability*, Geophysical Research Letters, Vol. 28, No. 18, 3609-3612

Zhang J. (2007) *Increasing Antarctic Sea Ice under Warming Atmospheric and Oceanic Conditions*, Journal of Climate, Vol. 20, doi:10.1175/JCLI4136.1

Zwally H.J., D. Yi, R. Kwok, Y. Zhao (2008) *ICESat measurements of sea ice freeboard and estimates of sea ice thickness in the Weddell Sea*, Journal of Geophysical Research, Vol. 113, C02S15, doi:10.1029/2007JC004284

List of Figures

1.1	Global average surface temperature 1900-2012	7
1.2	Processes altered or inhibited by sea ice	8
1.3	Cross section through the Atlantic Ocean	9
1.4	Ice-associated animals and diatoms	11
1.5	Shrinking Arctic sea ice	13
1.6	Antarctic sea ice thickness and freeboard derived from three different methods .	16
1.7	AWI ULS mooring positions in the Weddell Sea	17
2.1	Ice crystal structure and S-T diagram for water	20
2.2	Phase diagram of sea ice and X-ray tomography of brine pockets	21
2.3	Columnar structure of sea ice	22
2.4	Ice types formed under calm conditions	23
2.5	Ice types formed under agitated conditions	24
2.6	The life cycle of sea ice	25
2.7	Multiyear ice	26
2.8	Simple ice growth model	28
2.9	Ice growth diagram after Stefan's law	31
2.10	Momentum balance for drifting sea ice	34
2.11	Pressure ridges	35
2.12	Sea ice thickness distribution	37
2.13	Circumpolar Antarctic sea ice thickness	38
2.14	Annual cycle of Antarctic sea ice extent	39
2.15	SAM-Index	41
2.16	SAM effects on sea ice	42
2.17	PSA-Index	44
2.18	ENSO effects on sea ice	45
2.19	ZW3-Index	47
2.20	ZW3 & ACW effects on sea ice	48
2.21	Dominant patterns during ACW propagation	49
2.22	Multivariate correlations with Antarctic sea ice	50
2.23	Trends in sea ice extent	52
3.1	Sea ice drilling	55
3.2	Ground penetrating radar	56
3.3	LIDAR	58
3.4	EM measurement technique	59
3.5	EM-Bird	60
3.6	Satellite altimetry	61
3.7	ULS measurement principle	63

3.8	Sonar directivity pattern	64
3.9	Mooring arrangement with ULS	65
3.10	Ice thickness measurement techniques	66
3.11	Echo amplitudes	68
4.1	The AWI ULS array and available data	72
4.2	SSA	81
4.3	EOF examples	84
5.1	Zero-level correction	88
5.2	Data processing 1	89
5.3	Data processing 2	90
5.4	Data processing 3	92
5.5	Examples of data processing differences I	93
5.6	Examples of data processing differences II	95
5.7	Pressure sensor errors	98
5.8	Sound speed and density from CTD	100
5.9	Sound speed estimation errors	101
5.10	Detection of leads	102
5.11	Probability density of leads	103
5.12	Ice draft of 231-7 derived from CTD and ULS	104
5.13	CTD profiles of temperature and sound speed	105
5.14	Model-derived sound speeds for 231-7	106
5.15	Differences between the winter ice draft corrections	107
5.16	Pressure sensor drift	108
5.17	Overview of draft periods corrected by different methods	109
5.18	CTD profile and model sound speed profile	111
5.19	ULS bias	112
5.20	Bias after <i>Vinje et al. (1998)</i>	113
5.21	Greenwich meridian monthly mean ice draft	116
5.22	M-SSA cross validation	117
5.23	M-SSA filled time series	118
5.24	M-SSA filled time series & SSM/I concentration a	120
5.25	M-SSA filled time series & SSM/I concentration b	121
6.1	Sea ice draft measurements 1	126
6.2	Sea ice draft measurements 2	128
6.3	Sea ice draft measurements 3	130
6.4	Sea ice draft measurements 4	131
6.5	Sea ice draft statistics AWI-207	134
6.6	Sea ice draft statistics AWI-208, AWI 209 and AWI 229 1-2	135
6.7	Sea ice draft statistics AWI-229 b	136
6.8	Sea ice draft statistics AWI-231 a	137
6.9	Sea ice draft statistics AWI-231 b	138
6.10	Sea ice draft statistics AWI-232 a	139
6.11	Sea ice draft statistics AWI-232 b	140
6.12	Mean annual cycles	144
6.13	Ice season durations	145

6.14	SSA spectra of climate modes	148
6.15	SSA spectra AWI-207	150
6.16	7-months signal in time series at AWI 207-6	152
6.17	Semi-annual signal in time series at AWI-229	153
6.18	SSA spectra AWI-232	155
6.19	Autocorrelation functions of sea ice draft	158
6.20	Decorrelation time scales of selected records	159
6.21	Autocorrelation and ice drift velocity	160
6.22	DFA fluctuation functions for AWI-232	162
7.1	Map of Weddell Sea circulation	168
7.2	Temperature and salinity from float data	169
7.3	WDW variations	170
7.4	Periods used for correlation analysis	172
7.5	EOFs at AWI 207-2	175
7.6	Correlation with EOFs (AWI 207-2)	177
7.7	ZW3 for period of AWI 207-2	178
7.8	Time series AWI 207-6	180
7.9	EOFs at AWI 207-6	181
7.10	PSA pattern in period AWI 207-6	182
7.11	Correlations: climate modes with ice concentration (AWI-229)	186
7.12	Effects of PSA-Index on sea ice during a draft maximum at AWI-229	187
7.13	Effects of <i>Niño</i> 3.4 on sea ice during a draft minimum at AWI-229	188
7.14	Situations of draft minima and maxima at AWI-231a	191
7.15	Situation of a draft maximum at AWI-231b	194
7.16	Correlations at AWI-232 a	198
7.17	Correlations at AWI-232 b	200
7.18	ZW3 effects at AWI-232	201

Sources

Figure 1.4:

- (a) Photo by Gary Miller, © Commonwealth of Australia (<http://www.aad.gov.au/>)
- (b) <http://thundafunda.com/33/travel-world-pictures> (free online pictures)
- (c) Photo by Kai-Uwe Ludwigowski (AWI), *Polarstern* cruise ARK XXIII-2, summer 2008
- (d) Photo by Gordon T. Taylor, Stony Brook University, © National Oceanic and Atmospheric Administration/Department of Commerce (<http://www.photolib.noaa.gov>)
- (e) Photo by Stephen Brookes, © Commonwealth of Australia (<http://www.aad.gov.au/>)

Figure 2.4:

- (a) University of Fairbanks, Alaska (<http://www.gi.alaska.edu>)
- (b) Photo by Don Perovich, Cold Regions Research and Engineering Laboratory (CRREL)
- (c) Canadian Ice Service (<http://ice-glaces.ec.gc.ca>)

Figure 2.5:

- (a) Notz [2005]
- (b) Photo by Andy Mahoney, NSIDC

Figure 3.1:

Image courtesy of Arctic Exploration 2002, NOAA/OER
(<http://oceanexplorer.noaa.gov/explorations/02arctic>)

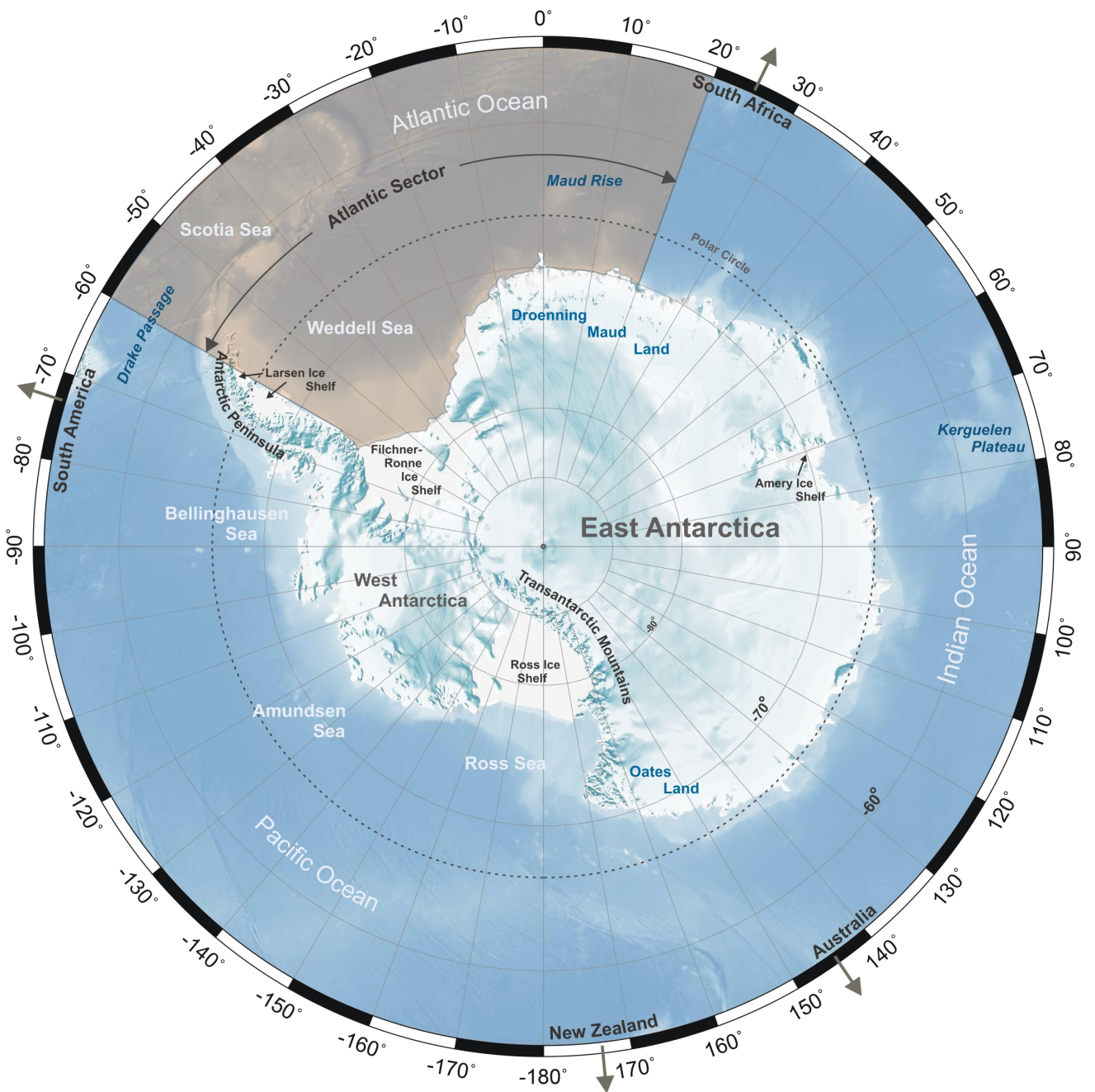
Figure 3.3:

Image courtesy by Jan L. Lieser, Antarctic Climate and Ecosystems
Cooperative Research Centre (ACE CRC)
Helicopter courtesy www.3Dkitbuilder.com and TheyerGFX Pty Ltd.

List of Tables

I - Antarctic sea ice trends	52
II - ULS data overview	73
III - ULS data RMS deviations (a)	94
IV - ULS uncertainties	97
V - ULS data RMS deviations (b)	107
VI - ULS biases	114
VII - Mean ice drafts	142
VIII - Statistical ice draft modes	143
IX - Earliest and latest ice occurrence	146
X - SSA periods in climate modes	149
XI - SSA periods for AWI-207 and AWI-229	151
XII - SSA periods for AWI-231 and AWI-232	154
XIII - Correlation coefficients AWI 207-2	174
XIV - Correlation coefficients AWI 207-6	179
XV - Correlations AWI 207-2 and AWI 207-6	184
XVI - Correlation coefficients AWI-229	185
XVII - Correlation coefficients AWI 231-a	190
XVIII - Correlation coefficients AWI 231-b	193
XIX - Correlations AWI 231-a and AWI 231-b	196
XX - Correlation coefficients AWI-232	197

Appendix





- 300kHz transducer
- Narrow beam
- Excellent piezo-ceramics element
- Transducer fits into ATLAS SW60/28/6029 housing

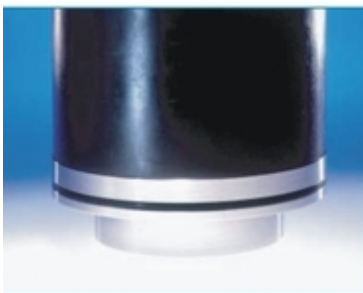
TC2078

Universal 300kHz narrow beam transducer ideal for navigation and hydrographic echosounding.

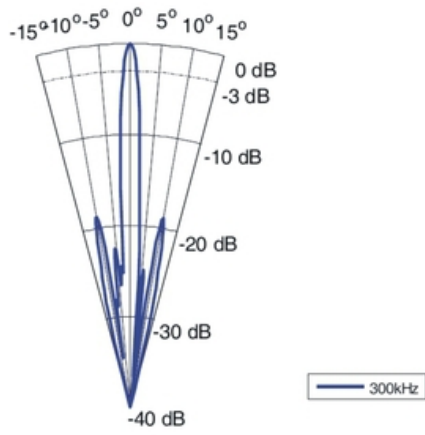
The TC2078 can be fitted into Atlas SW 60/28/6029 housings and RESON steel housings for full mounting on vessels.

TECHNICAL SPECIFICATIONS

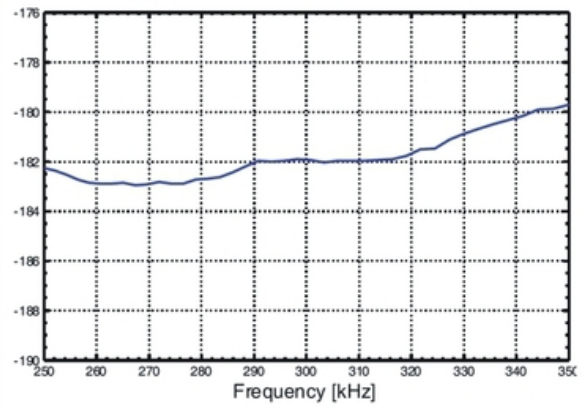
Resonant Frequency:	300kHz \pm 15kHz
Transmitting Sensitivity:	179dB \pm 3dB re 1 μ PA/V at 1m
Receiving Sensitivity:	-184dB \pm 3dB re 1V/ μ Pa
Impedance:	100ohm \pm 30ohm at 300kHz
Beam width	2.6° \pm 0.3°
Beam shape:	Conical beam
Max input Power:	1000W at 1% duty cycle
Operating depth:	400m
Operating temperature range:	+2°C to +35°C
Storage temperature range:	-40°C to +50°C
Housing:	Special Formulated NBR
Weight in Air Incl. cable:	7.8kg



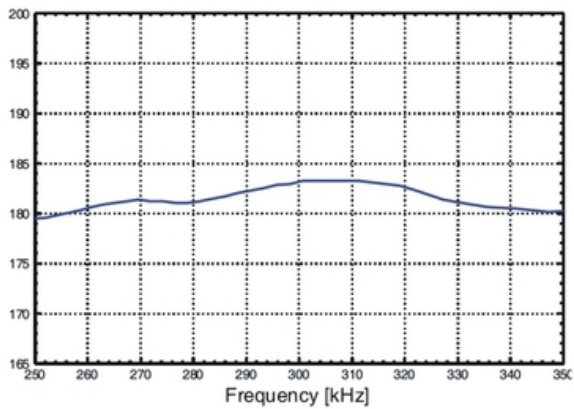
Horizontal Directivity Pattern



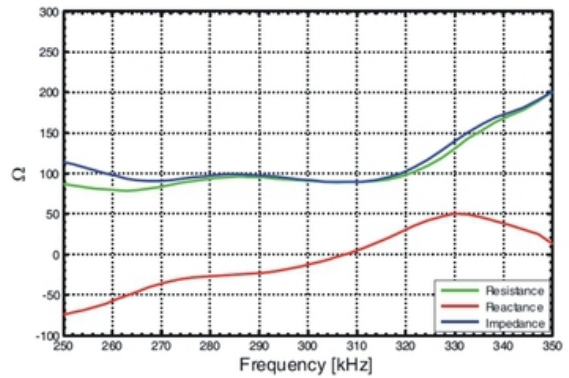
Receiving Sensitivity [dB re 1V/μPa @ 1m]



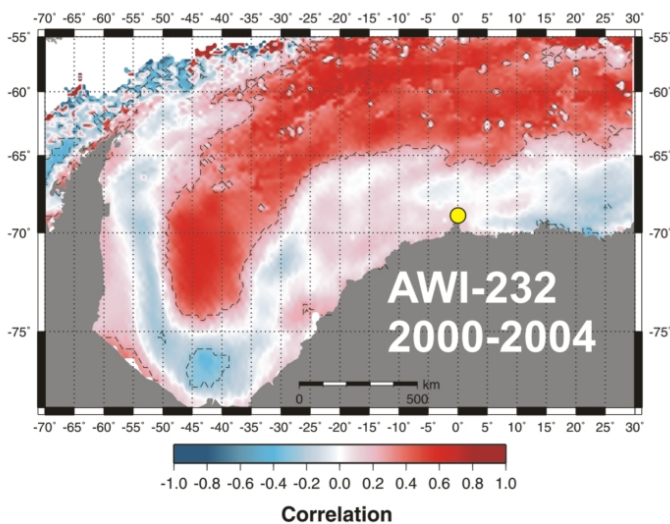
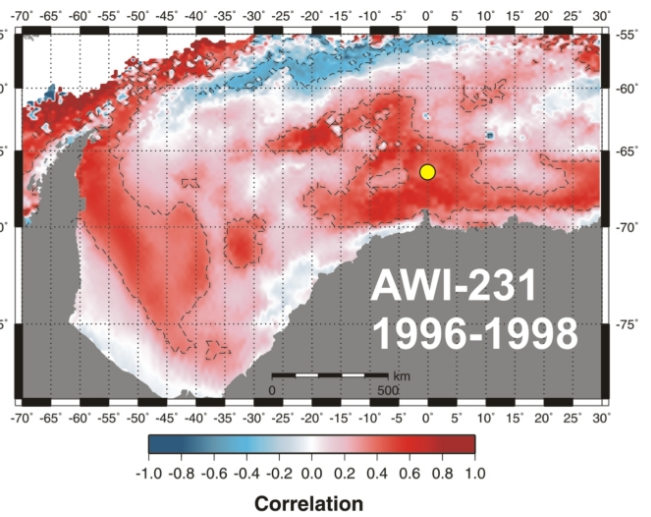
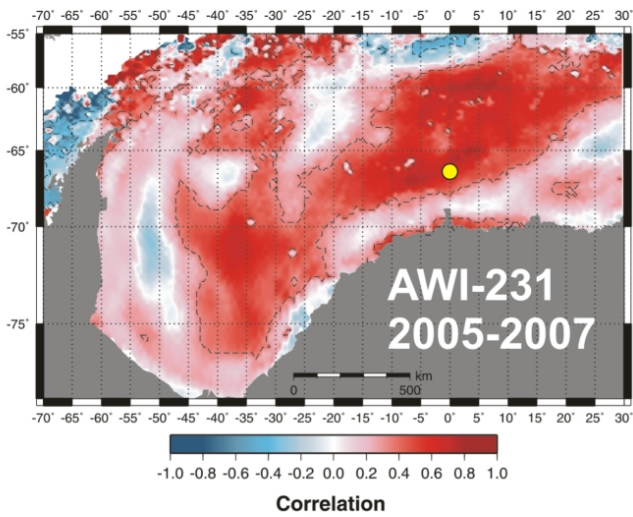
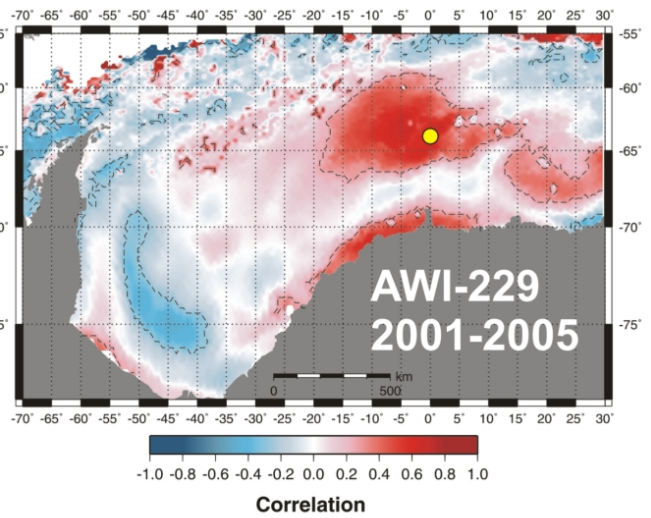
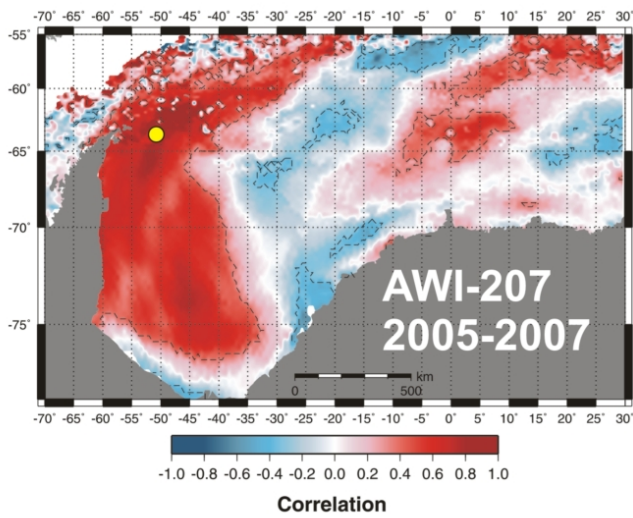
Transmitting Sensitivity [dB re 1μPa/V @ 1m]



Impedance

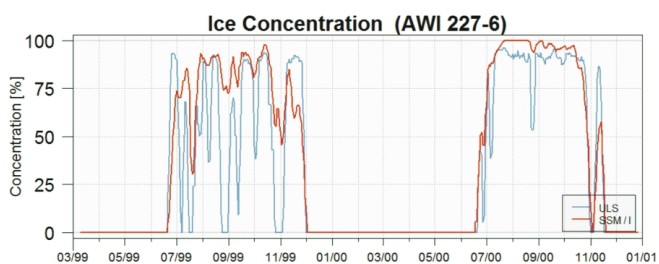
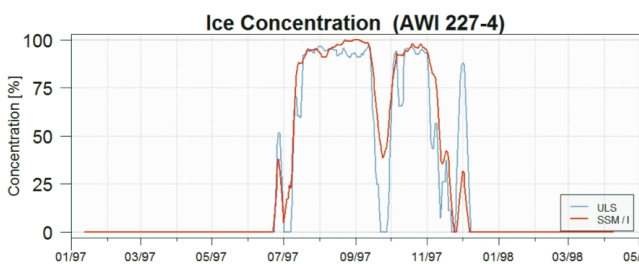
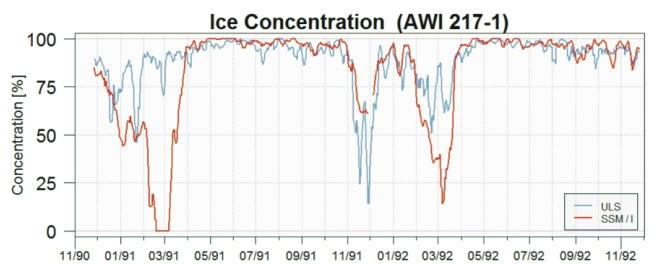
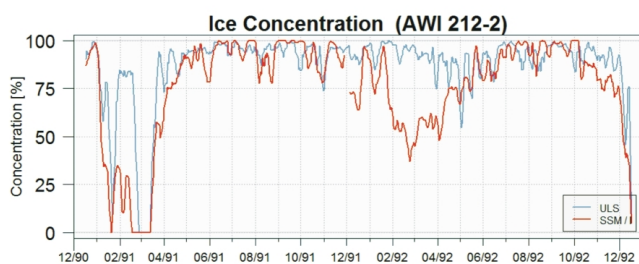
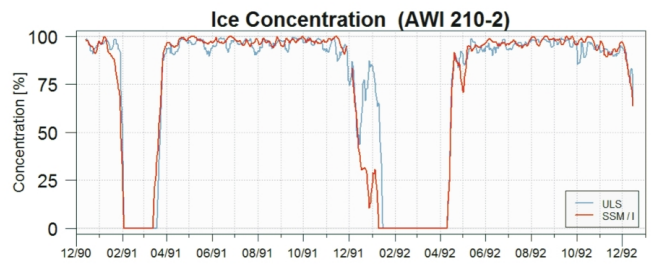
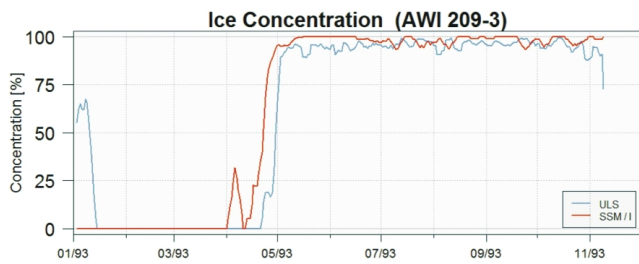
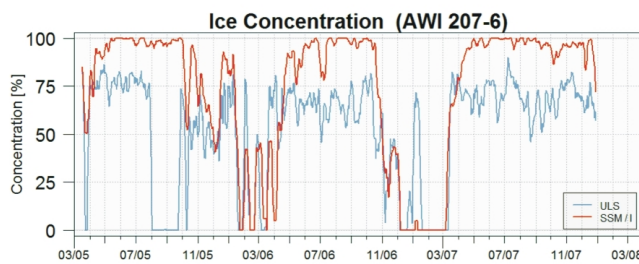


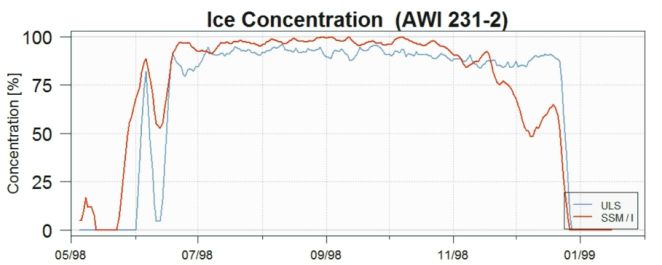
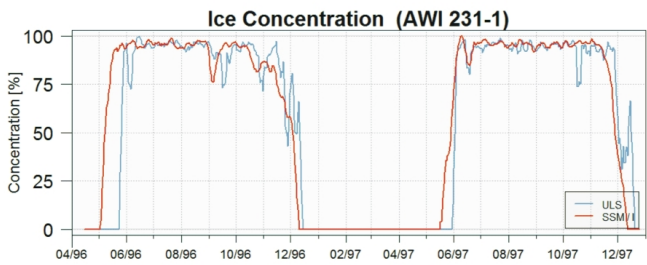
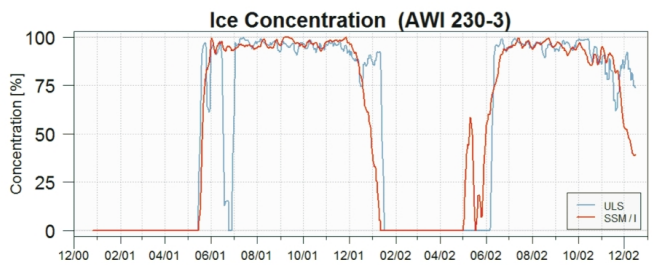
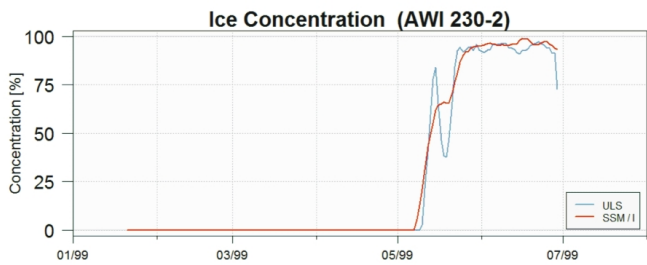
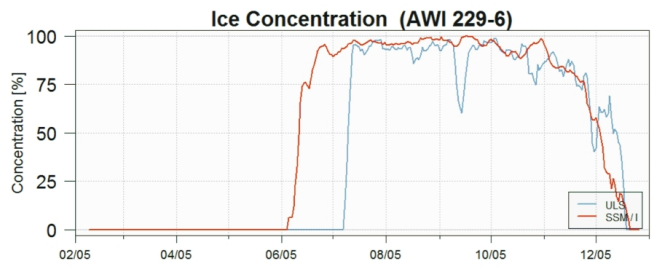
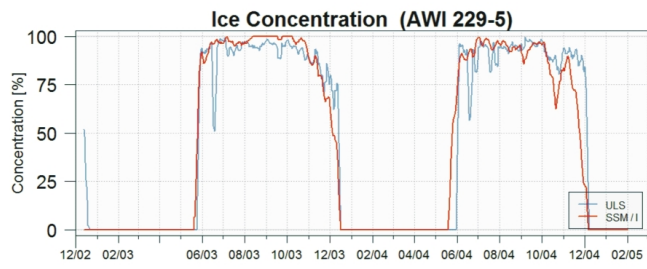
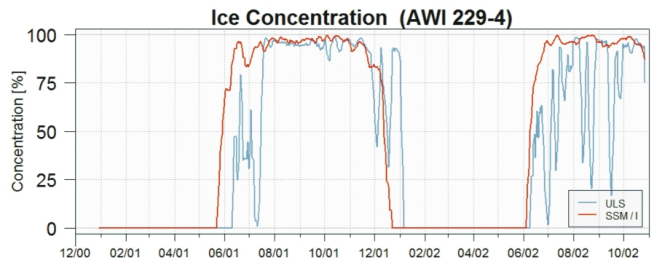
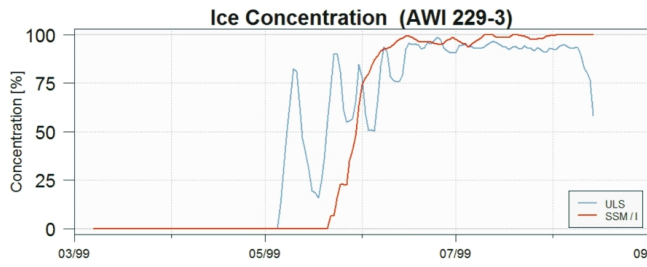
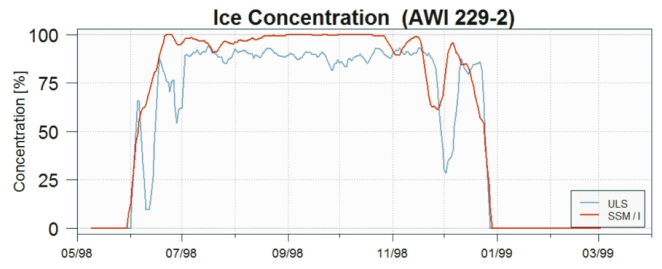
[Reson, 2010]

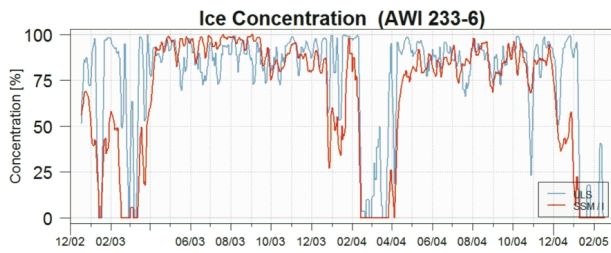
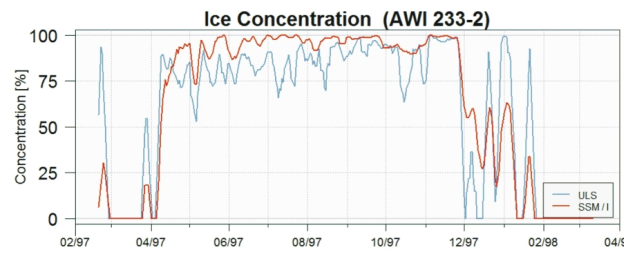
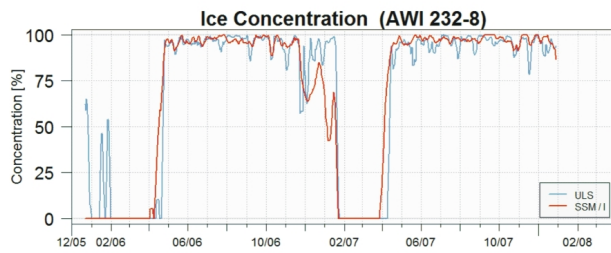
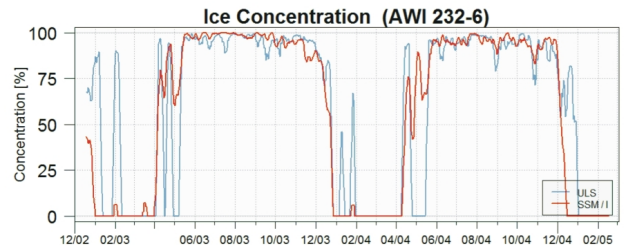
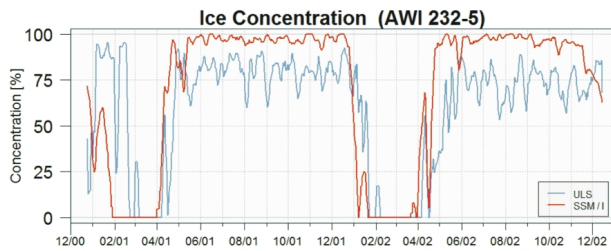
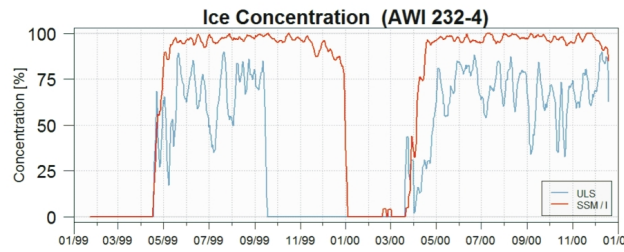
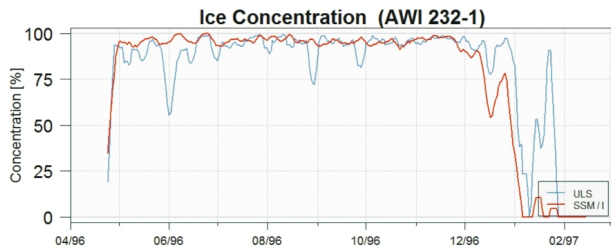
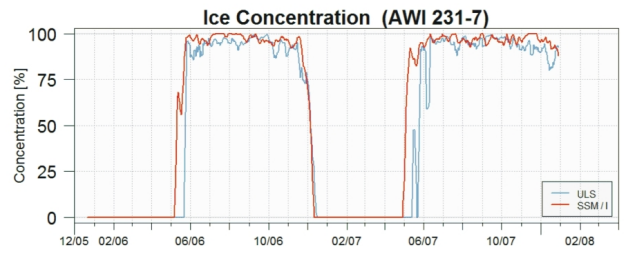
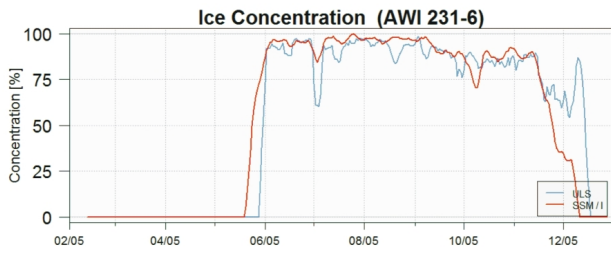
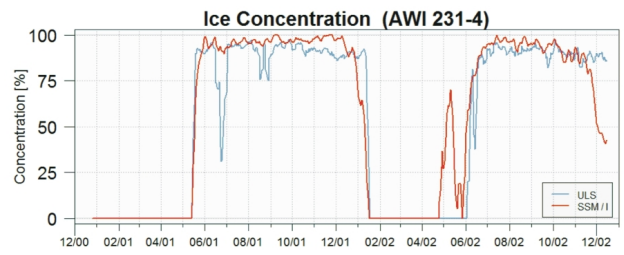
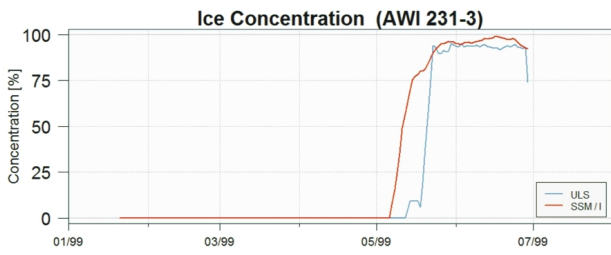


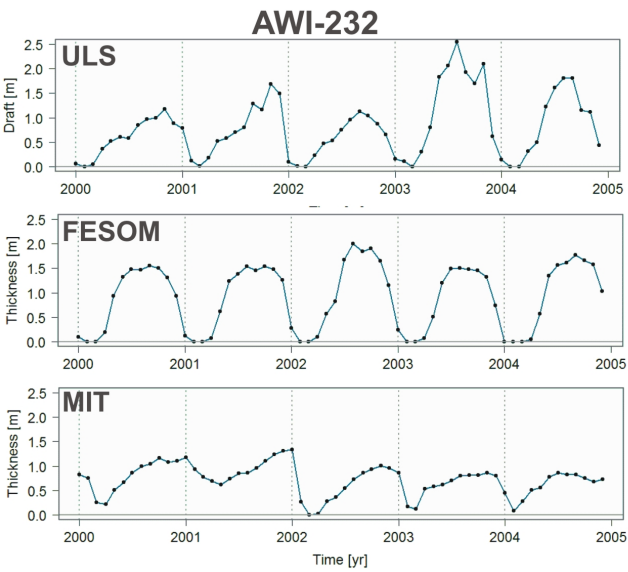
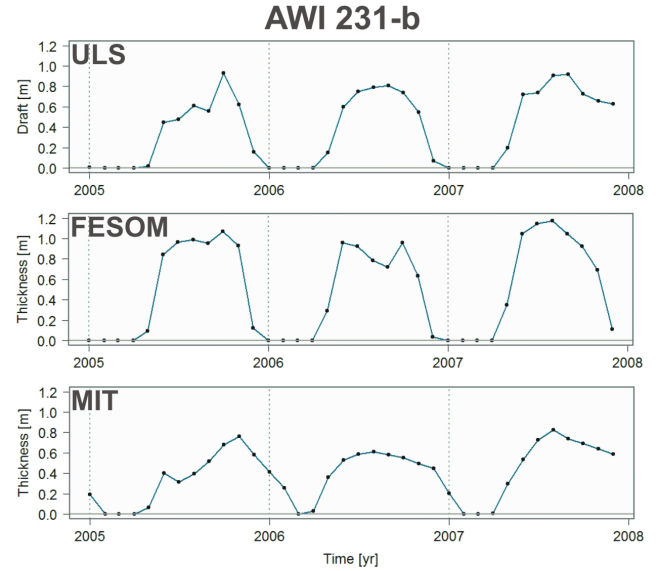
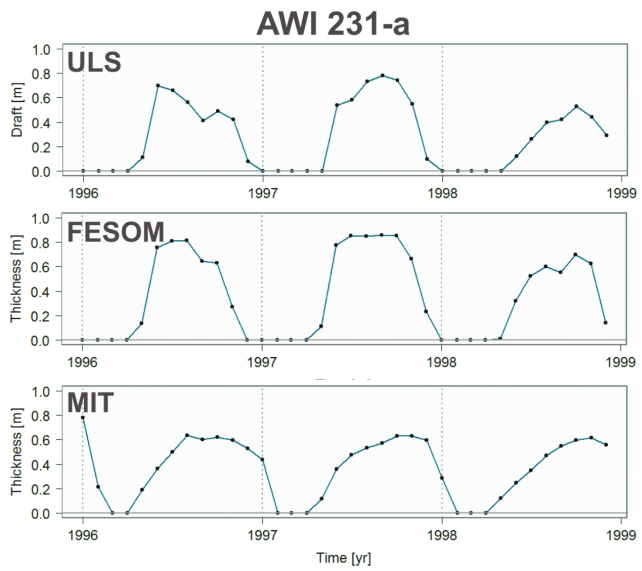
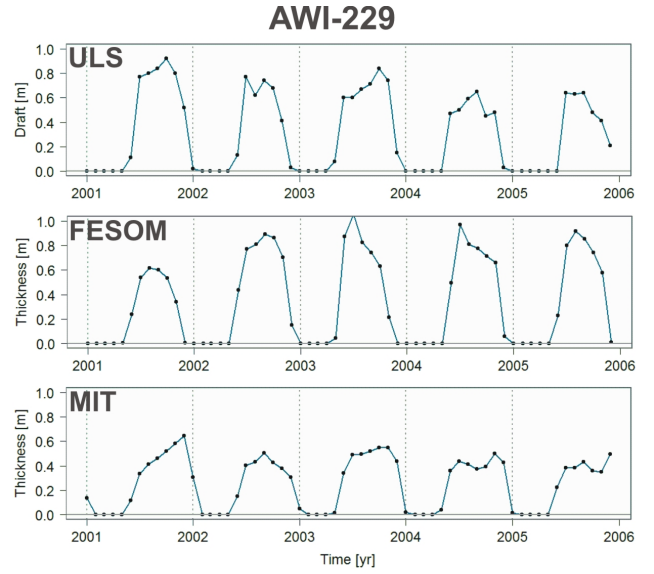
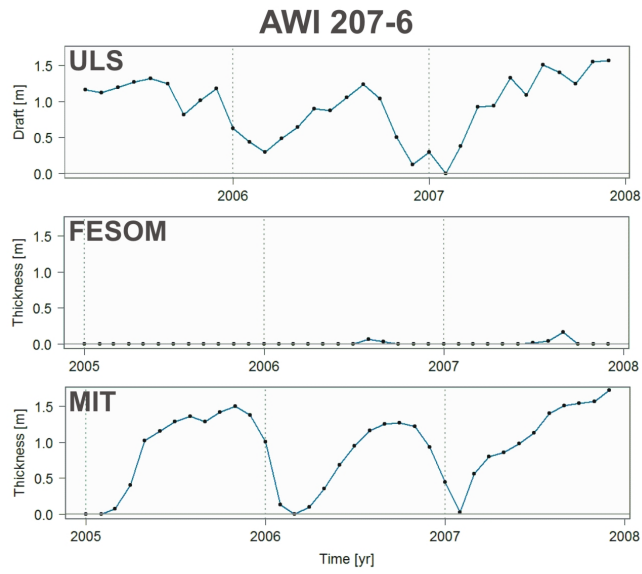
Correlation between ULS ice draft anomalies and MIT model ice thickness anomalies

Ice concentration from ULS and SSM/I (5-days running means)

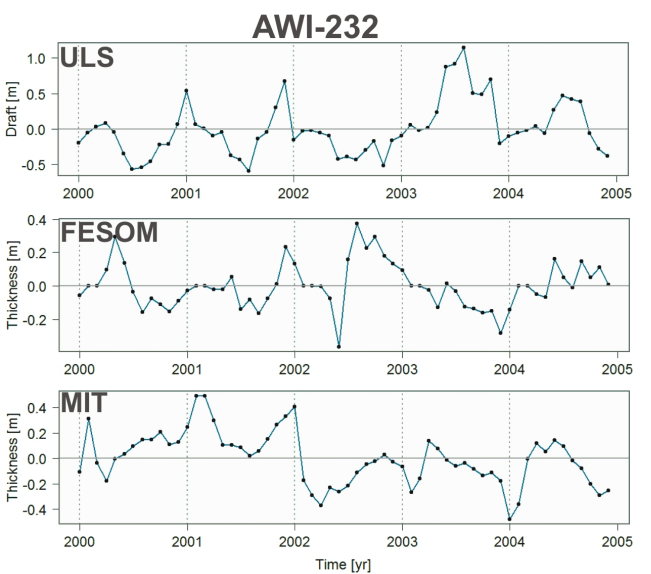
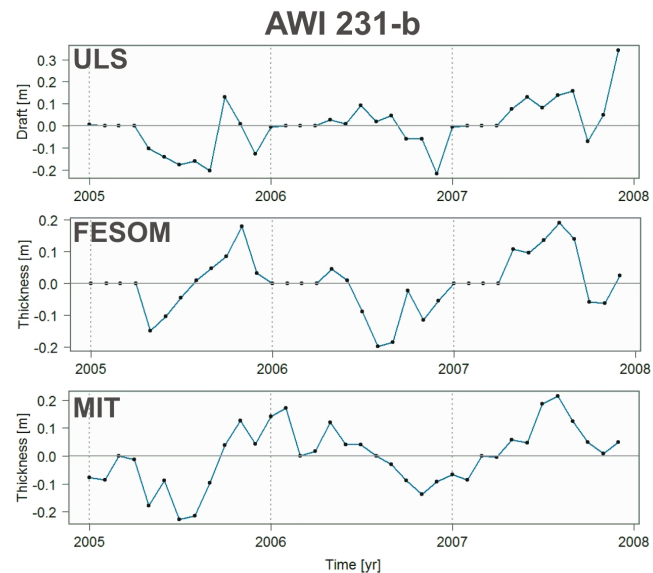
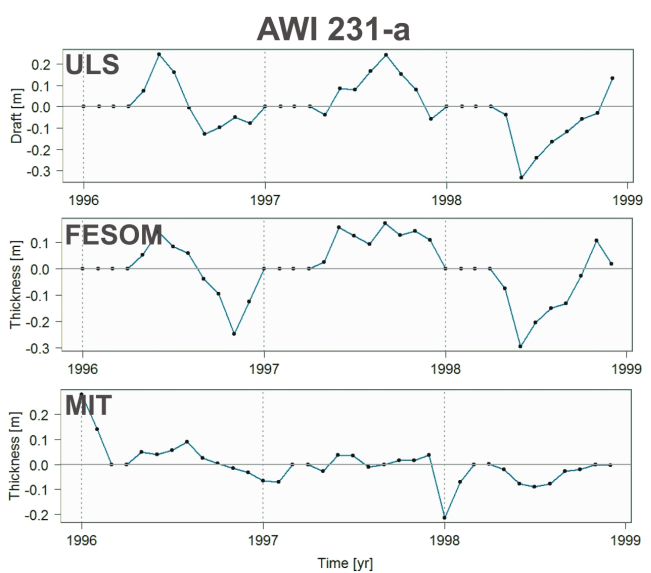
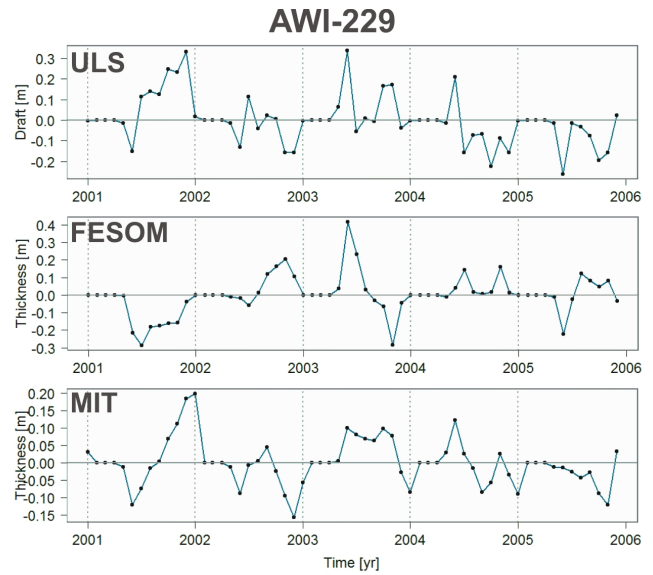
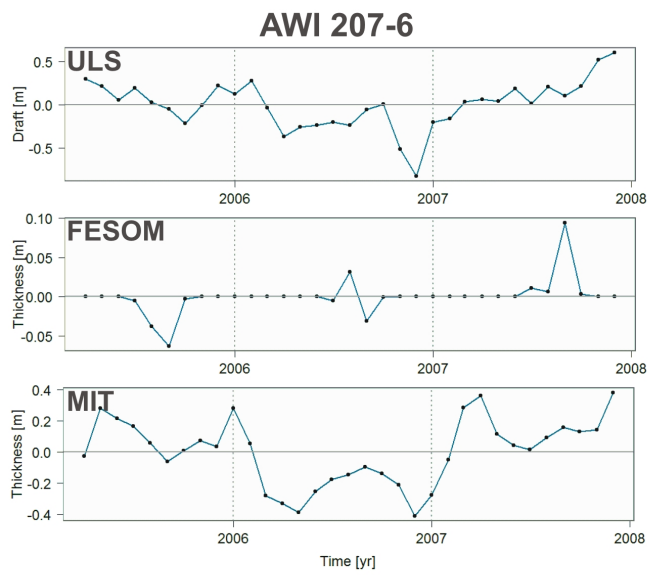








Monthly ice draft from ULS and ice thickness from two models



Anomalies of ice draft from ULS and ice thickness from two models

Danksagung

Zunächst möchte ich Prof. Lemke für die Ermöglichung und Begutachtung dieser Arbeit danken. Ich danke ihm auch für seine lehrreichen und gut organisierten Vorlesungen in Klimaphysik, die immer sehr motivierend für mich waren. Ich danke auch meinem ursprünglichen Zweitgutachter Prof. Gerdes für seine wertvollen Ratschläge und Tipps und die Zeit, die er sich für unsere Komitee-Treffen genommen hat (zum Dank habe ich ihm für ein paar Wochen den Parkplatz weggenommen...). Weiterhin danke ich Prof. Kaleschke von der Uni Hamburg, dass er so schnell bereit war, für Rüdiger Gerdes einzuspringen und die Begutachtung zu übernehmen. Ein ganz besonders großer Dank geht an Dr. Eberhard Fahrbach. Er hat mich für diese Arbeit angeworben, mir stets ein produktives Arbeitsumfeld ermöglicht und immer sehr viel Geduld mit mir gehabt. Ohne ihn und seine Förderung wäre die Arbeit in dieser Form nicht möglich gewesen. Danke! Ich danke auch besonders Dr. Wolfgang Dierking. Er hat sich viel Zeit genommen, mit mir schwierige Details zur Datenqualität durchzusprechen und mir die komplizierte Datenprozessierung verständlich gemacht. Außerdem half er mir sehr dabei, die Qualität des Textes deutlich zu verbessern.

Besonders geholfen hat mir auch Hannelore Witte. Sie war immer wieder meine Ansprechpartnerin für die ULS-Daten, hat mit großem Einsatz den Bias bekämpft und mir sehr bei der Datenprozessierung geholfen. Danke dafür! Weiterhin danke ich meinem "Büro-Mitbewohner" Mario Hoppema für zahlreiche Gespräche und Tipps und die angenehme, ruhige Arbeitsatmosphäre. Großer Dank gilt auch dem Ozi Gerd Rohardt, der mir sehr bei MatLab, TEOS-10 und CTD geholfen hat. Andreas Wisotzki danke ich für ein paar Hilfen bei GMT und den CTD-Daten. Wenn Computer verrückt spielten, Drucker streikten oder ich mal wieder wichtige Daten gelöscht hatte, war Computerfachmann Wolfgang Cohrs zur Stelle und immer sehr hilfsbereit. Ein wichtiger Job, vielen Dank dafür! Volker Strass von gegenüber danke ich für wichtige Infos und die Bereitstellung von ULS-Dokumenten, und der gesamten messenden Ozeanographie von Deck II danke ich für den mordsmäßigen Mampf mit leckerem Kuchen. Für Gespräche, Hilfen, Infos und Daten danke ich außerdem David Peddie von CMR, Jan W. Kantelhardt von der Uni Halle, Diego Rybski vom Potsdam-Institut für Klimafolgenforschung, Stefan Kern vom KlimaCampus Hamburg sowie Martin Losch, Frank Kauker, Christine Wesche, Sandra Schwegmann, Gert König-Langlo, Rainer Sieger und Ulrike Wacker vom AWI. Nicht zuletzt möchte ich mich auch bei meiner früheren Betreuerin Ursel Schauer für ihre Offenheit und ihre ermutigenden Worte bedanken.

Finanziert wurde diese Arbeit zu großen Teilen von den Deutschen Forschungsgemeinschaft (DFG). Ich danke speziell den Organisatoren des DFG-Schwerpunktprogramms Antarktisforschung (SPP-1158) für die gute Unterstützung. Danken möchte ich auch den zahlreichen Besatzungsmitgliedern und Technikern der *Polarstern*, die mit großem Einsatz und unter schwierigen Bedingungen die harte Verankerungsarbeit auf sich nehmen und so die ULS-Messungen erst möglich machen (danke an Matthias und Olaf!). Dem AWI danke ich ganz besonders dafür, dass auch diejenigen, die etwas langsamer sind eine Chance bekommen. Hier danke ich speziell Frau Krämer von der Personalabteilung sowie Eberhard und Ursel. Auch Herrn Nashef möchte ich danken, für viele hilfreiche Gespräche und die gute Unterstützung.

Möglich wurde diese Arbeit nur aufgrund zahlreicher öffentlich zugänglicher Datensätze. Ein zusätzlicher Dank geht daher an: ECMWF, NCEP/NCAR und das NSIDC. Außerdem danke ich der *R Foundation for Statistical Computing* für ihre hervorragende freie Programmiersprache R, die mir vieles leichter gemacht hat.

Der allergrößte Dank geht jedoch an meine lieben Eltern: Auch ihr habt mir diese Arbeit ermöglicht, mich während dieser schwierigen und intensiven Zeit moralisch unterstützt und mir auch einiges abgenommen. Herzlichen Dank an Euch!

Die "**Berichte zur Polar- und Meeresforschung**" (ISSN 1866-3192) werden beginnend mit dem Heft Nr. 569 (2008) als Open-Access-Publikation herausgegeben. Ein Verzeichnis aller Hefte einschließlich der Druckausgaben (Heft 377-568) sowie der früheren "**Berichte zur Polarforschung**" (Heft 1-376, von 1981 bis 2000) befindet sich im open access institutional repository for publications and presentations (**ePIC**) des AWI unter der URL <http://epic.awi.de>. Durch Auswahl "Reports on Polar- and Marine Research" (via "browse"/"type") wird eine Liste der Publikationen sortiert nach Heftnummer innerhalb der absteigenden chronologischen Reihenfolge der Jahrgänge erzeugt.

To generate a list of all Reports past issues, use the following URL: <http://epic.awi.de> and select "browse"/"type" to browse "Reports on Polar and Marine Research". A chronological list in declining order, issues chronological, will be produced, and pdf-icons shown for open access download.

Verzeichnis der zuletzt erschienenen Hefte:

Heft-Nr. 656/2012 — "The Expedition of the Research Vessel 'Sonne' to the Manihiki Plateau in 2012 (So 224)", edited by Gabriele Uenzelmann-Neben

Heft-Nr. 657/2012 — "The Expedition of the Research Vessel 'Polarstern' to the Antarctic in 2011 (ANT-XXVIII/1) ", edited by Saad El Naggat

Heft-Nr. 658/2013 — "The Expedition of the Research Vessel 'Polarstern' to the Arctic in 2012 (ARK-XXVII/2)", edited by Thomas Soltwedel

Heft-Nr. 659/2013 — "Changing Polar Regions - 25th International Congress on Polar Research, March 17-22, 2013, Hamburg, Germany, German Society for Polar Research", edited by Eva-Maria Pfeiffer, Heidemarie Kassens, and Ralf Tiedeman

Heft-Nr. 660/2013 — "The Expedition of the Research Vessel 'Polarstern' to the Arctic in 2012 (ARK-XXVII/1)", edited by Agnieszka Beszczynska-Möller

Heft-Nr. 661/2013 — "The Expedition of the Research Vessel 'Polarstern' to the Antarctic in 2012 (ANT-XXVIII/3)", edited by Dieter Wolf-Gladrow

Heft-Nr. 662/2013 — "Climate Change in the Marine Realm: An international summer school in the framework of the European Campus of Excellence", edited by Angelika Dummermuth and Klaus Grosfeld

Heft-Nr. 663/2013 — "The Expedition of the Research Vessel 'Polarstern' to the Arctic in 2012 (ARK-XXVII/3)", edited by Antje Boetius

Heft-Nr. 664/2013 — "Russian-German Cooperation SYSTEM LAPTEV SEA: The Expeditions Laptev Sea - Mamontov Klyk 2011 & Buor Khaya 2012", edited by Frank Günther, Pier Paul Overduin, Aleksandr S. Makarov, and Mikhail N. Grigoriev

Heft-Nr. 665/2013 — "The Expedition of the Research Vessel 'Polarstern' to the Antarctic in 2013 (ANT-XXIX/3)", edited by Julian Gutt

Heft-Nr. 666/2013 — "The Expedition of the Research Vessel 'Polarstern' to the Antarctic in 2013 (ANT-XXIX/5)", edited by Wilfried Jokat

Heft-Nr. 667/2013 — "The Sea Ice Thickness in the Atlantic Sector of the Southern Ocean", by Axel Behrendt